

Sheffield Hallam University

Processing-composition-structure effects on the optical band gap of KNbO₃-based ceramics

PASCUAL-GONZALEZ, Cristina

Available from the Sheffield Hallam University Research Archive (SHURA) at:

<http://shura.shu.ac.uk/18746/>

A Sheffield Hallam University thesis

This thesis is protected by copyright which belongs to the author.

The content must not be changed in any way or sold commercially in any format or medium without the formal permission of the author.

When referring to this work, full bibliographic details including the author, title, awarding institution and date of the thesis must be given.

Please visit <http://shura.shu.ac.uk/18746/> and <http://shura.shu.ac.uk/information.html> for further details about copyright and re-use permissions.



**Processing-composition-structure effects on the
optical band gap of KNbO₃-based ceramics**

Cristina Pascual-González

A thesis submitted in partial fulfilment of the requirements of
Sheffield Hallam University for the degree of Doctor of Philosophy

October 2017

A mis padres.

A Bryan.

Acknowledgements

First of all, I would like to acknowledge the financial support of the Vice-Chancellor scholarship from Sheffield Hallam University, my main supervisor, Dr Antonio Feteira, for his support and guidance throughout my studies and my second supervisor, Dr Iasmi Sterianou, for her willingness to answer my 'silly questions'.

I would also like to thank TO-BE cost action, which made possible my attendance to a summer school, different meetings and short term scientific mission in Universitat de Barcelona. Thank you to Dr. Ignasi Fina and Prof. Manuel Varela for their warm hospitality and sharing their knowledges about PLD with me.

I would also like to thank Dr Giorgio Schileo for his support since my first day in Sheffield and the band-gap measurements, and Carolina Elicker for her kindness and photovoltaic measurements.

At Sheffield Hallam University, I would like to thank Deeba Zahoor, Dr. Anthony Bell, Stuart Creasey and Paul Alender for their help with the instrumentation and the facilities in the laboratory and of course my colleagues of the Ceramic and Glass group, for their support every day and lovely company, specially Alex Scrimshire and Benjamin Allsopp, for their 'english lessons' and Georgia Christopoulou, for all the shared laughter and tears (but mostly, laughter) at the university. At Sheffield University, I would like to thank to Amir Kreshor, Shunshuke Murakani and Dawei Wang for the dielectric measurement and Raman Spectroscopy with temperature. At Instituto de Ciencia de Materiales de Madrid, I would like to express my gratitude to Miguel Algueró and Harvey Amorín for their encouragement and help to find a PhD position.

The PhD experience has been a crucial experience in my life and I would like to thank all who have helped me during this long journey.

Primero agradecer a la gente que me he encontrado en el camino, como Noemí y Lidia que hicieron insuperable el primer año en Sheffield y a Conchi, por ayudar a levantarme en el segundo. Además, un enorme y sincero gracias a todos mis amigos que me han ayudado de una manera u otra en algún momento durante estos tres últimos años y siempre han creído en mí, como Eva, Héctor, Jesús o Joaquín que vinieron a verme a

Sheffield; Vero y Paula que hicieron aún mejor mi estancia en Barcelona y los que siempre están ahí en Madrid esperándome, como Antonio (Cuqui), Vero, Paola y Benja. Pero sobre todo quiero agradecer a Rebe todo su apoyo, cariño y compañía cada día, que ha sido fundamental durante mi estancia aquí.

Gracias a mi pequeña pero gran familia, sobre todo a mis padres por su apoyo y amor incondicional, a los que les debo todo lo que tengo.

Y por último, gracias a Bryan por todo su amor, apoyo, ayuda y por todos los kilómetros que ha recorrido para estar conmigo.

Declaration and published work

I declare this thesis has been composed by myself, except collaborations that has been specified in the text, that were carried out at the University of Sheffield (Sheffield, United Kingdom), Universidade Federal de Pelotas (Pelotas, Brazil) and in the company Greatsolarcell (Manchester, United Kingdom). The work reported here has not been submitted for any other degree or professional qualification.

Some parts of the work reported in this thesis have been published or submitted for publication, as listed below. It is anticipated that further parts of this work will be submitted for publication in due course. The rest of papers published during the last three years are listed in APPENDIX H (section H.1.1).

1. C. Pascual-Gonzalez, G. Schileo, S. Murakami, A. Khesro, D. Wang, I. M. Reaney and A. Feteira. *Continuously controllable optical band gap in orthorhombic ferroelectric $KNbO_3$ - $BiFeO_3$ ceramics*. Applied Physics Letters, 110, 179202 (2017).
2. C. Pascual-González, G. Schileo, A. Kherso, I. Sterianou, D. Wang, I. M. Reaney and A. Feteira. *Band gap evolution and piezoelectric-to-electrostrictive crossover in $(1-x)KNbO_3 - x(Ba_{0.5}Bi_{0.5})(Nb_{0.5}Zn_{0.5})O_3$ ceramics*. Journal of Materials Chemistry C, 5 (8). pp. 1990-1996. (2017). Electronic Supplementary Information (ESI) available.

Abstract

This present work is focused on band-gap engineering of solid-solutions based on KNbO_3 , which was proposed as a promising photoferroelectric (Grinberg et al., 2013). The strategy to narrow the band-gap of the parent KNbO_3 (3.22 eV), relies on replacing Nb^{5+} by lower valence transition metals (Me^{3+}) and K^{+1} by cations which maintain the compositions stoichiometric.

Ceramic processing of KNbO_3 by conventional route was optimised in order to minimise K losses, which leads to the formation of a hygroscopic secondary phase, $\text{K}_4\text{Nb}_6\text{O}_{17}$. This phase impairs the structural integrity of the samples. In addition, single-phase KNbO_3 ceramics have the tendency to absorb moisture from the environment, increasing its conductivity near room temperature. Subsequently, all solid-solutions presented in this work, $(1-x) \text{KNbO}_3-x \text{Ba}_{0.5}\text{Bi}_{0.5}\text{Nb}_{0.5}\text{Zn}_{0.5}\text{O}_3$ and $(1-x) \text{KNbO}_3-x \text{BiMeO}_3$ (Me= Mn, Co and Ni) systems in a compositional range of $0 \leq x \leq 0.25$, $0.90 \text{KNbO}_3-0.1 \text{BaNb}_{0.5}\text{Ni}_{0.5}\text{O}_3$ and $0.98 \text{K}_{0.5}\text{Na}_{0.5}\text{NbO}_3-0.02 \text{BaNb}_{0.5}\text{Ni}_{0.5}\text{O}_3$ compounds, were prepared by the same route as KNbO_3 . X-Ray Diffraction (XRD), Raman spectroscopy and Scanning Electron Microscopy (SEM) revealed compositionally inhomogeneities, suggesting difficulties in cation diffusion for low concentration of solutes by conventional routes.

The systems evolve from orthorhombic ($x=0$) to pseudo-cubic symmetry with an increase of x , suggested by XRD, Raman spectroscopy, ferroelectric and dielectric response. Indeed, these two symmetries seem to coexist for intermediary concentrations. A solubility limit for orthorhombic KNbO_3 phase is determined for each system. In addition, a continuous band-gap narrowing was observed in all systems.

Nevertheless, $(1-x) \text{KNbO}_3-x \text{BiFeO}_3$ ($0 \leq x \leq 0.25$) system maintained the polar phase up to $x=0.25$ and its band-gap was narrowed down to 2.22 eV. Indeed, a photocurrent of $0.24 \mu\text{A}/\text{cm}^2$ was measured for $0.75 \text{KNbO}_3-0.25 \text{BiFeO}_3$ which is higher than reported for the controversial $0.90 \text{KNbO}_3-0.1 \text{BaNb}_{0.5}\text{Ni}_{0.5}\text{O}_3$ compound (Grinberg et al., 2013). The literature does not agree about its band-gap value, which varies from 1.3 eV to 3 eV. Hypothetically, the impossibility of preparing chemically homogenised samples by solid-state reaction may lead to the occurrence of intraband states, which can be misinterpreted. Similar conclusions are reached for $0.98 \text{K}_{0.5}\text{Na}_{0.5}\text{NbO}_3-0.02 \text{BaNb}_{0.5}\text{Ni}_{0.5}\text{O}_3$.

Contents

VOLUME I

Chapter 1: Introduction	1
1.1. Perovskites	1
1.1.1. Structural characteristics	1
1.1.2. Solid solutions	3
1.2. Dielectrics.	4
1.2.1. Definitions.	4
1.2.2. Piezoelectrics.....	5
1.2.3. Ferroelectrics	6
1.2.3.1. Historical background	6
1.2.3.2. Phenomenology.....	7
1.2.3.3. Origin of ferroelectricity.	9
1.2.4. Piezoelectricity in ferroelectrics	13
1.2.5. Literature review of KNbO_3 (KN).....	6
1.2.6. Applications of piezo- and ferroelectrics	21
1.3. Photoferroelectrics	22
1.3.1. Electronic band structure of solids.	22
1.3.2. Photovoltaic effect.....	26
1.3.3. The anomalous photovoltaic effect in ferroelectrics	28
1.3.3.1. Introduction	28
1.3.3.2. Origin of the photoresponse in ferroelectrics.	29
1.3.3.3. Experimental measurements	30
1.4. Band-gap engineering	34
1.5. Motivations	41
1.6. Aims and Objectives.	42

1.6.1. Aims.	42
1.6.2. Research objectives.	43
1.6.3. Thesis overview.....	43
1.7. References	44
Chapter 2: Methodology.....	57
2.1. Introduction	58
2.2. Ceramic processing	58
2.2.1. Powder Synthesis: Solid State Reaction.....	59
2.2.2. Raw materials	60
2.2.3. Sintering	60
2.2.4. Density of materials	61
2.2.5. Fabricated compositions.....	62
2.3. Film preparation.	63
2.3.1. Pulsed laser deposition (PLD).....	63
2.3.2. Photoresponse measurements.....	64
2.4. Chemical and structural characterisation	66
2.4.1. X-ray diffraction (XRD).....	66
2.4.2. Rietveld Refinement.....	68
2.4.3. Raman Spectroscopy	70
2.4.4. Scanning Electron Microscopy.	72
2.4.5. EDX.....	73
2.5. Electrical characterisation.	74
2.5.1. LCR	74
2.5.2. Ferroelectric and piezoelectric measurements	75
2.6. Optical characterisation.....	77
2.6.1. Diffuse reflectance spectroscopy.....	77
2.7. References	79

Chapter 3: Processing and Characterisation of KNbO₃ ceramics.....	81
3.1. Introduction.....	82
3.2. Method 1	86
3.2.1. Purity and crystal structure.....	86
3.3. Method 2.....	89
3.3.1. Purity and crystal structure.....	89
3.4. Comparison between method 1 and 2.....	94
3.4.1. X-Ray diffraction data.....	94
3.4.2. Stability in water	96
3.5. Structural and chemical characterisation.	99
3.5.1. Raman Spectroscopy	99
3.5.2. SEM.....	101
3.5.3. EDX.....	102
3.6. Electric characterisation of stoichiometric KNbO ₃ prepared via 2.....	103
3.6.1. Dielectric characterisation	103
3.6.2. Ferroelectric Characterisation	104
3.7. Optical characterisation	110
3.7.1. Diffuse Reflectance Spectroscopy.....	110
3.8. Discussion.....	112
3.9. Conclusions.....	114
3.10. References	114
Chapter 4: System (1-x) KNbO₃-x(Ba_{0.5}Bi_{0.5})(Zn_{0.5}Nb_{0.5})O₃	118
4.1. Introduction.....	119
4.2. Structural and chemical characterisation	120
4.2.1. Purity and X-ray powder diffraction.	120
4.2.2. Raman Spectroscopy	124
4.2.3. SEM.....	128

4.2.4. EDX.....	131
4.3. Electrical Characterisation	137
4.3.1. Dielectric Characterisation	137
4.3.2. Piezo- and Ferroelectric Characterisation	142
4.4. Optical Characterisation.....	148
4.4.1 Diffuse reflectance spectroscopy.....	148
4.5. Discussion	151
4.6. Conclusions	153
4.7. References	154
Chapter 5: System (1-x) KNbO₃- x BiFeO₃.....	156
5.1. Introduction.....	157
5.2. Structural and chemical characterisation	158
5.2.1. Purity and X-ray powder diffraction.	158
5.2.2. Raman spectroscopy.....	162
5.2.3. SEM.....	167
5.2.4. EDX.....	168
5.3. Electrical Characterisation	173
5.3.1. Dielectric Characterisation	173
5.4. Optical Characterisation.....	180
5.4.1 Diffuse reflectance spectroscopy.....	180
5.5. Preparation of thin films.....	182
5.5.1. Pulsed laser deposition.	182
5.5.2. Photovoltaic cell	185
5.5. Discussion.	187
5.6. Conclusions.	190
5.7. References	190
Chapter 6: System (1-x) KNbO₃-x BiMnO₃.....	193

6.1. Introduction	194
6.2. Structural and chemical characterisation	195
6.2.1. Purity and X-ray diffraction.	195
6.3.2. Raman spectroscopy.....	200
6.3.3. SEM.....	204
6.3.4. EDX.....	205
6.4. Electrical Characterisation	210
6.4.1. Dielectric Characterisation	210
6.5. Optical Characterisation.....	214
6.5.1 Diffuse reflectance spectroscopy.....	214
6.6. Discussion	217
6.7. Conclusions	218
6.8. References	219
Chapter 7: System (1-x) KNbO₃- x BiCoO₃.....	221
7.1. Introduction	222
7.2. Structural and chemical characterisation	223
7.2.1. Purity and X-ray powder diffraction.	223
7.2.2. Raman spectroscopy.....	227
7.2.3. SEM.....	230
7.2.4. EDX.....	231
7.3. Electrical Characterisation	237
7.3.1. Dielectric Characterisation	237
7.4. Optical Characterisation.....	241
7.4.1 Diffuse reflectance spectroscopy.....	241
7.5. Discussion	244
7.6. Conclusions.....	245
7.7. References	245

Chapter 8: System (1-x) KNbO₃- x BiNiO₃.....	247
8.1. Introduction	248
8.2. Structural and chemical characterisation	249
8.2.1. Purity and X-ray diffraction	249
8.2.2. Raman spectroscopy.....	254
8.2.3. SEM.....	257
8.2.4. EDX.....	260
8.3. Electrical Characterisation	265
8.3.1. Dielectric Characterisation	265
8.4. Optical Characterisation.....	270
8.4.1 Diffuse reflectance spectroscopy.....	270
8.5. Discussion.	272
8.6. Conclusions	273
8.7. References	274
Chapter 9: Ferroelectric and optical properties for KNbO₃ vs K_{0.90}Ba_{0.1}Nb_{0.95}Ni_{0.05}O₃ and K_{0.5}Na_{0.5}NbO₃ vs K_{0.49}Na_{0.49}Ba_{0.02}Nb_{0.99}Ni_{0.01}O₃	276
9.1. Introduction	277
9.2. Structural and chemical characterisation	279
9.2.1. Purity and X-ray powder diffraction.	279
9.2.1.1. Results for KN and KN-BNN powders and ceramics.....	279
9.2.1.2. Results for KNN and KNN-BNN powders and ceramics.....	281
9.2.2. Raman spectroscopy.....	283
9.2.3. SEM.....	286
9.2.4. EDX.....	287
9.3. Electrical Characterisation	295
9.3.1. Dielectric measurements	295
9.3.2. Piezo- and Ferroelectric Characterisation	297

9.4. Optical Characterisation.....	300
9.4.1 Diffuse reflectance spectroscopy.....	300
9.5. Discussion	303
9.6. Conclusions	308
9.7. References	308
Chapter 10: Discussion	311
10.1. Ceramic processing	312
10.2. (1-x) KNbO ₃ -x BiMeO ₃ (Me=Fe, Mn, Co, Ni) (0≤x≤0.25) systems	316
10.3. Photovoltaic effect in orthorhombic 0.75 KNbO ₃ -0.25 BiFeO ₃ solid-solution	321
10.4. Experimental validation and non-reproducibility of band-gap narrowing in solid solutions based on KNbO ₃ from literature.	322
10.4. Band-gap narrowing.....	323
10.5. References	326
Chapter 11: Conclusions, contributions to the field and future work	331
11.1. Conclusions	332
11.2. Contributions to the field	335
11.3. Future work	335
11.4. References	336

Chapter 1

Introduction

1.1. Perovskites

1.1.1 Structural characteristics

1.1.2 Solid solutions

1.2. Dielectrics.

1.2.1 Definitions

1.2.2 Piezoelectrics

1.2.3 Ferroelectrics

1.2.4. Piezoelectricity in ferroelectrics

1.2.5. Literature review of KNbO_3

1.2.6. Applications of piezo- and ferroelectrics

1.3. Photoferroelectrics

1.3.1. Electronic band structure of solids

1.3.2. Photovoltaic effect

1.3.3. The anomalous photovoltaic effect in ferroelectrics

1.4. Band-gap engineering

1.5. Motivations

1.6. Aims and Objectives

1.6.1. Aims

1.6.2. Research objectives

1.6.3. Thesis overview

1.7. References

1. Introduction

1.1 Perovskites

1.1.1 Structural characteristics

Perovskites have the chemical formula ABO_3 , where the A-site cations are typically larger than the B-site cations and similar in size to the O^{2-} anions.

The name of this structure derives from the mineral $CaTiO_3$ called perovskite, which was discovered by the geologist Gustav Rose in 1839 from samples found in the Ural Mountains and named after Count Lev Aleksevich von Perovski. (Hazen, 1988).

Figure 1. 1 shows the structure of an ideal cubic perovskite. A-cations are located at the corners of the cube (blue spheres), and the B cation at the centre (orange sphere) with oxygen ions (red spheres) at the face-centred positions in octahedra coordination. The space group that describes the crystal symmetry of cubic perovskites is $Pm\bar{3}m$ (No 221). Table 1.1 details the atomic positions in cubic perovskites.

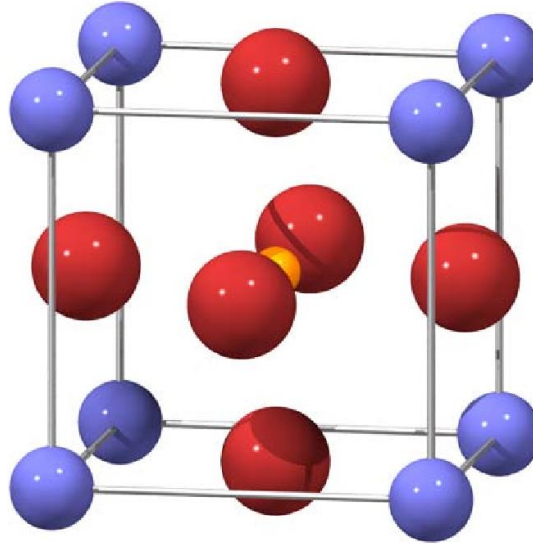


Figure 1. 1: Cubic perovskite unit cell. Blue spheres represent the A cations, the orange sphere represents the B cation, and red spheres represent oxygen anions (O) in octahedral coordination.

Site	Coordinates
A cation	(0, 0, 0)
B cation	(0.5, 0.5, 0.5)
O anion	(0.5, 0, 0), (0, 0.5, 0), (0, 0, 0.5)

Table 1. 1: Equivalent positions of the atoms in cubic perovskites.

The perovskite structure enables a wide range of physical phenomena, depending on the atomic species occupying the A and B-sites. Indeed, piezo- and ferroelectric, magnetic, catalytic, photovoltaic, ionic and electronic conduction properties can be observed in materials with this structure (Dogan, Lin, Guilloux-Viry, & Peña, 2015). Consequently, perovskites can be adapted to a wide range of applications such as electromechanical devices, transducers, capacitors, actuators, fuel cells, memory devices, transistors and sensors.

The first reference found on the design of perovskite compounds was published in 1927 by Goldschmidt, who is considered to be the founder of modern geochemistry and crystal chemistry. Goldsmith introduced important concepts such as the tolerance factor. Assuming an ideal cubic phase, a relation between the ionic radii and the lattice parameter, a , can be expressed as $a = 2R_O + 2R_B$, going through the centre, and as $a = \sqrt{2}(2R_O + 2R_A)$, through the diagonal. The relation between these expressions is an indicator of the stability and distortion of perovskite structures and it is expressed by Equation 1.1.

$$t = \frac{R_O + R_A}{\sqrt{2}(R_O + R_B)} \quad \text{Eq. 1.1.}$$

Where t is the tolerance factor and R_A , R_B and R_O , correspond to the ionic radii of A, B and O^{2-} ions, respectively. A perovskite structure is considered stable when t varies from 0.75 to 1. Many possible combinations of cations and anions have been designed using this expression (Bhalla, Guo, & Roy, 2000).

Most compounds with the perovskite structure present distortions from the ideal cubic structure that lower the crystal symmetry. These deviations may have different origins, as for example, displacements of A or B cations (Jaffe, Cook, & Jaffe, 1971). An example of B-cationic displacement can be found in $BaTiO_3$ at room temperature and it is accompanied with the appearance of spontaneous polarisation. Indeed, one of the most studied properties in perovskite oxides is the ferroelectricity, which will be described in detail below.

1.1.2. Solid solutions

Solid solution is a solid-state solution where one or more solutes coexist in a solvent. The solute-solvent coexistence is considered a solution, when the solvent structure remains unchanged by addition of solutes and it is still single phase. There are two types of solid-solutions: substitutional (Figure 1. 2 (a)), where the atoms of the solvent are replaced by the atoms of the solutes, and interstitial (Figure 1. 2 (b)), where the atoms of the solutes fit into the space between solvent atoms.

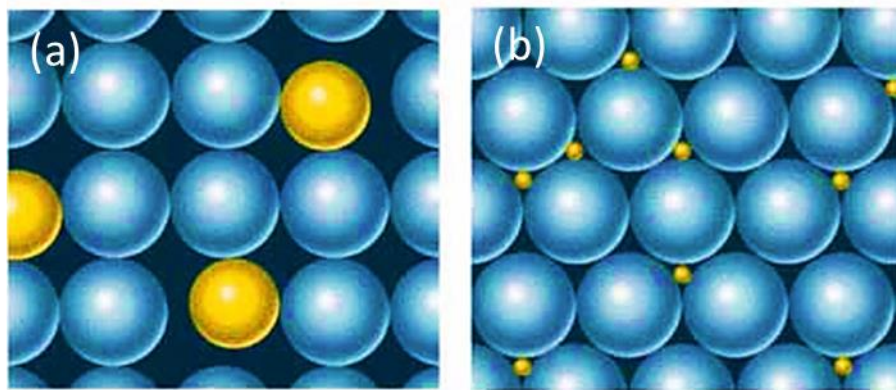


Figure 1. 2: Types of solid solutions: (a) Substitutional solid solution and (b) Interstitial solid solution

Both types of solid solution modify the properties of the material by distorting the crystal lattice and changing the physical and electrical properties of the solvent material (Groover, 1997). After the discovery and development of the perovskites in the 1950s, R. Roy and colleagues moved the research on these materials to the next level, by synthesizing the first substitutional solid solutions with perovskite structure (Roy, 1954). Later, this research group created maps with regions of stability, where it is possible to carry out ionic substitutions and correctly predict which polymorph forms. These maps are still used today, in order to validate or discard substitutions of a specific perovskite phase (Bhalla et al., 2000).

Vegard's law is an approximate empirical rule which holds that a linear relation exists, at constant temperature, between the lattice parameters of the solid solution and the solute content (Denton, 1991). In this work, it was used to study the formation of the solid-solutions.

Often, the creation of solid solutions is motivated by the improvement of specific properties of the solvent compound. An example, is the solid solution $x \text{PbTiO}_3$ - $(1-x) \text{PbZrO}_3$ (PZT), which shows high piezoelectric coefficients (Cao & Cross, 1993). This is also the case of the materials prepared for this thesis, where the impact of different chemical substitutions into KNbO_3 (KN), a well-known perovskite oxide, is investigated in particular the ferroelectric and optical properties.

1.2. Dielectrics

1.2.1 Definitions

A dielectric material is defined as an electrical insulator that can store charge by applying an electric field (E). The polarisation vector, P ($\mu\text{C}/\text{cm}^2$), that is induced in the material is given by Equation 1.2.:

$$P = \varepsilon_0 \cdot \chi \cdot E \quad \text{Eq. 1.2.}$$

where χ (F m^{-1}) is the dielectric susceptibility of the material and ε_0 is the dielectric permittivity of vacuum and it has a constant value of $8.854 \cdot 10^{-12} \text{ F m}^{-1}$. The total quantity

of charge density accumulated on the surface of the material when E is applied, is defined as the dielectric displacement vector, D ($C\ m^{-2}$) (Equation 1.3.):

$$D = \varepsilon_0 \cdot E + P \quad \text{Eq. 1.3.}$$

Equation 1.4. is obtained by combining Eq. 1.2. and Eq. 1.3.:

$$D = \varepsilon_0 \cdot E + \varepsilon_0 \cdot \chi \cdot E = \varepsilon_0 \cdot (1 + \chi) \cdot E \quad \text{Eq. 1.4.}$$

where $\varepsilon = 1 + \chi$ is the dielectric permittivity of the material. This value gives information about how easily a material is polarised under an electric field. When a dielectric material is not able to withstand an electric field and electricity starts to flow through the material, it has reached the dielectric breakdown limit.

1.2.2 Piezoelectrics

Among dielectrics, there is a group of materials that develop electric displacements (in other words, spontaneous polarization) by the application of a mechanical pressure and they are known as piezoelectric materials. Piezoelectricity is an intrinsic property related with the crystal structure. There are 32 crystallographic point groups (Table 1. 2) depending on their symmetry characteristics, 11 of them possess a centre of symmetry and are non-polar. The remaining 21 point groups are non-centrosymmetric groups but only 20 exhibit piezoelectricity. Non-centrosymmetric point groups are further divided into polar (10) and nonpolar types (11).

Materials that present temperature dependence of the spontaneous polarization are called pyroelectrics. In these materials, a change in temperature of the crystal produces electric charges on the surface of the crystal corresponding to a change of spontaneous polarization.

Polarity	Symmetry	Crystal System										
		Cubic		Hexagonal		Tetragonal		Rhomboidal		Orthorhombic	Mono-clinic	Triclinic
Nonpolar (22)	Centro (11)	$m3m$	$m3$	$6/mmm$	$6/m$	$4/mmm$	$4/m$	$\bar{3}m$	$\bar{3}$	mmm	$2/m$	$\bar{1}$
	Noncentro (21)	432	23	622	$\bar{6}$	422	$\bar{4}$	32		222		
		$\bar{4}3m$		$\bar{6}m2$		$\bar{4}2m$						
Polar (pyroelectric) (10)				$6mm$	6	$4mm$	4	$3m$	3	$mm2$	2 m	1

Table 1. 2: Classification according to crystal centrosymmetry and polarity. Inside the bold line are piezoelectrics (Uchino, 2009).

1.2.3 Ferroelectrics

Ferroelectric materials have all these properties explained above and furthermore their spontaneous polarization can be reversed by an external electric field. For determining ferroelectricity, it is required to apply an electric field to a pyroelectric material and experimentally observe the switching of the spontaneous polarisation without exceeding the dielectric breakdown limit.

1.2.3.1 Historical background

The first ferroelectric material, Rochelle salt, was discovered in 1922 by Valasek. Development of ferroelectric materials was driven by military applications during World War II in the early 1940s. Then, switchable orientation of BaTiO_3 was reported for first time in 1949 (Grey, 1949) and by the mid-1950s, $\text{Pb}(\text{Zr}_x\text{Ti}_{1-x})\text{O}_3$ (PZT) was already known. Since then, continuous innovation and improvement of materials and technologies has led to a large number of industrial and commercial applications, such as capacitors, actuators, sonars and transducers, among others (Haertling, 1999).

1.2.3.2. Phenomenology

The polarisation response under an electric field can be plotted as a characteristic curve known as ferroelectric hysteresis loop. It is possible to observe an example in Figure 1. 3. This behaviour is directly related with the switching of the domains. Once almost all domains are aligned, polarisation achieves its maximum value (P_s) and it is maintained constant. It means the ferroelectric material is saturated. However, it is not possible to achieve complete alignment of the dipoles due to defects and impurities in the ceramic. At zero field, the ferroelectric material exhibits remanent polarisation (P_r) and the field necessary to bring polarization to zero is called the coercive field, E_c .

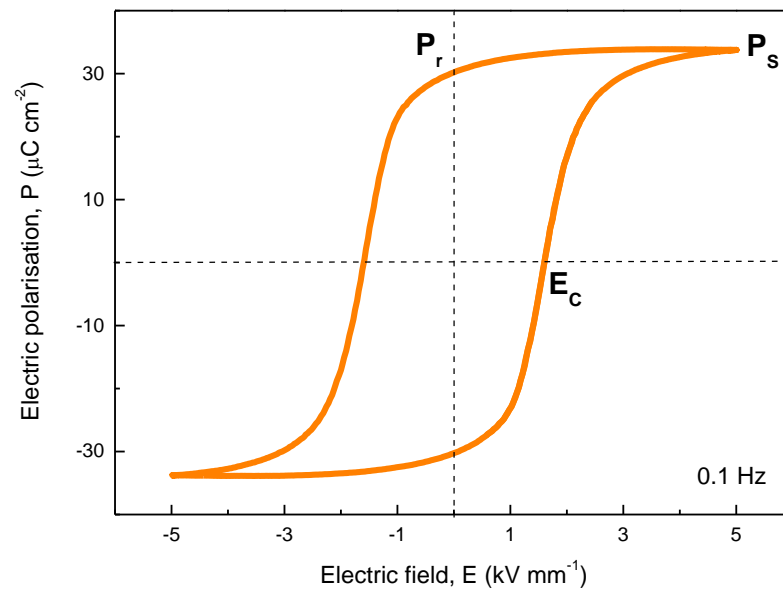


Figure 1. 3: Ferroelectric ($P-E$) hysteresis loop. Spontaneous polarisation (P_s), remanent polarisation (P_r) and coercive field (E_c) are noted in the figure.(Pascual-Gonzalez et al 2016).

One of the characteristics of ferroelectric materials is the formation of ferroelectric domains. These domains are crystal regions where the spontaneous polarization is orientated in the same direction. The interface between domains is called a domain wall.

In the case of a well-known ferroelectric material, $BaTiO_3$ (BT), that will be examined in detail in the next section, domain walls of 180° and 90° can be observed, which means the polarization vectors are either in completely opposite directions or at 90° angles, respectively. Figure 1. 4 shows an illustration of 90° and 180° domain walls (Fang et al.,

2013) and a SEM (backscattered electron detector) image of BT microstructure where ferroelectrics domains can be detected (Cheng, Ho, & Lu, 2008).

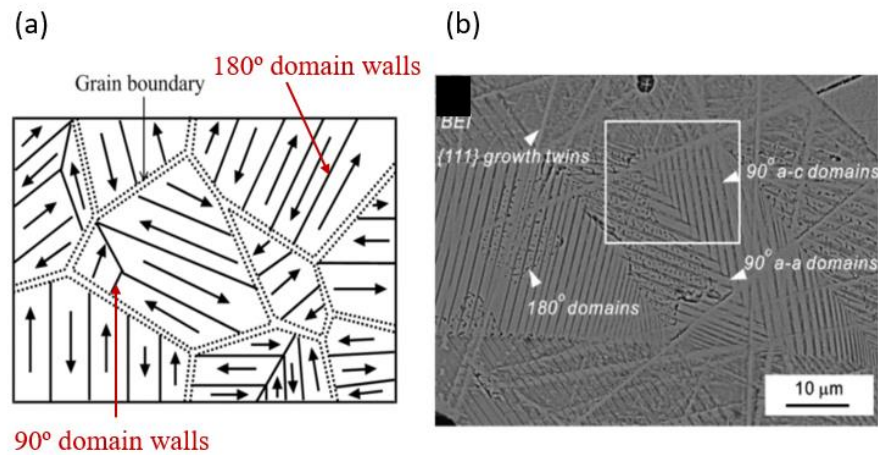


Figure 1. 4: (a) Representation of ferroelectric domains (180° and 90°) in different grains. (b) Backscattered electron SEM image of the BT polished. Ferroelectric domains of 90° and 180° are pointed in the image (Cheng et al., 2008).

When cubic BT is cooled down, it acquires a ferroelectric phase and the polarisation vector could be oriented in any direction along the cubic axis of the structure (Figure 1. 5). The electrical and mechanical boundary conditions are what really determine the direction at which the spontaneous polarisation will be established. In the phase transition when spontaneous polarisation starts to appear, some charge is accumulated on the surface of the material. It generates an electric field, also known as depolarising field E_d ; and its direction is opposite to the spontaneous polarisation, P_s , as shown in Figure 1. 5. It may be the case that the depolarising field will be strong enough to fragment a single-domain energetically unfavourable into many domains with oppositely oriented polarization (Damjanovic, 1998). This phenomenon is related with the creation of 180° domain walls. On the other hand, when a crystal is mechanically stressed along the $[100]$ cubic direction and cooled down, the long axis (c_T -axis in Figure 1. 5) of the tetragonal distortion will develop perpendicularly to the stress in order to minimize the elastic energy.

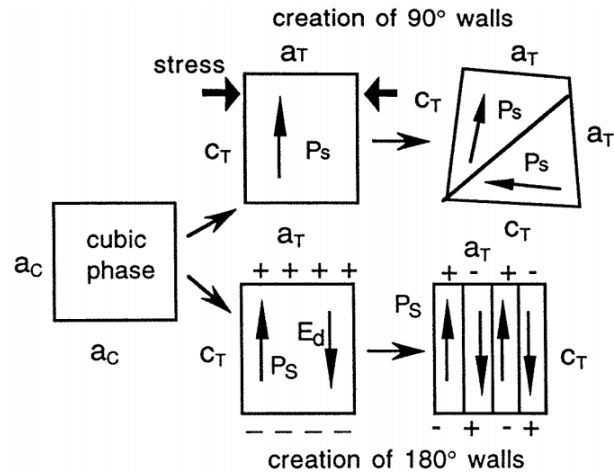


Figure 1. 5: Formation of 90° and 180° ferroelectric domain walls in a tetragonal perovskite ferroelectric, such as BaTiO₃. (Damjanovic, 1998)

The ferroelectric domains are randomly oriented due to the complexity of electric and elastic conditions in each grain (Figure 1. 6). Even if materials exhibit spontaneous polarisation locally, the net polarisation is zero. In order to reorient all domains and bring the ceramic to a polar state, it is necessary to apply an electric field strong enough to switch all dipoles. This process is called poling and usually is done at high temperature for increased domain wall mobility.

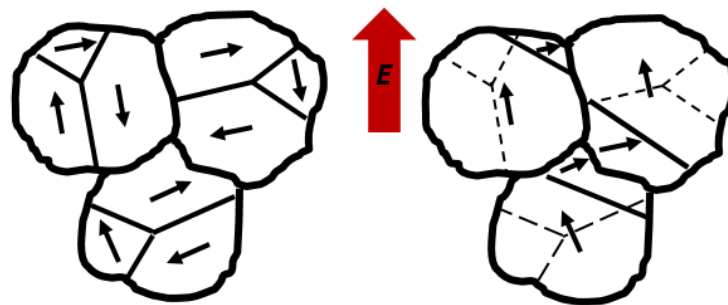


Figure 1. 6: Ferroelectric ceramic with random orientation of grains before and after poling.

1.2.3.3. Origin of ferroelectricity

The origin of the ferroelectricity in perovskites may arise from different sources as:

- (i) Cation-displacements
- (ii) Lone pair electrons
- (iii) Geometry

(iv) Charge ordering

(i) Cation-displacements

Barium titanate, BaTiO_3 (BT), is a classical ferroelectric material. From its discovery to the present, it has been extensively investigated, being possible to find a large number of works about its structure and properties in the literature (Ahn, Rabe, & Triscone, 2004; Cohen, 1992; Merz, 1954).

With a tolerance factor of 1.06, BaTiO_3 has a typical perovskite structure with a tetragonal distortion, space group $P4mm$ (No. 99) as shown in Figure 1. 7 (a).

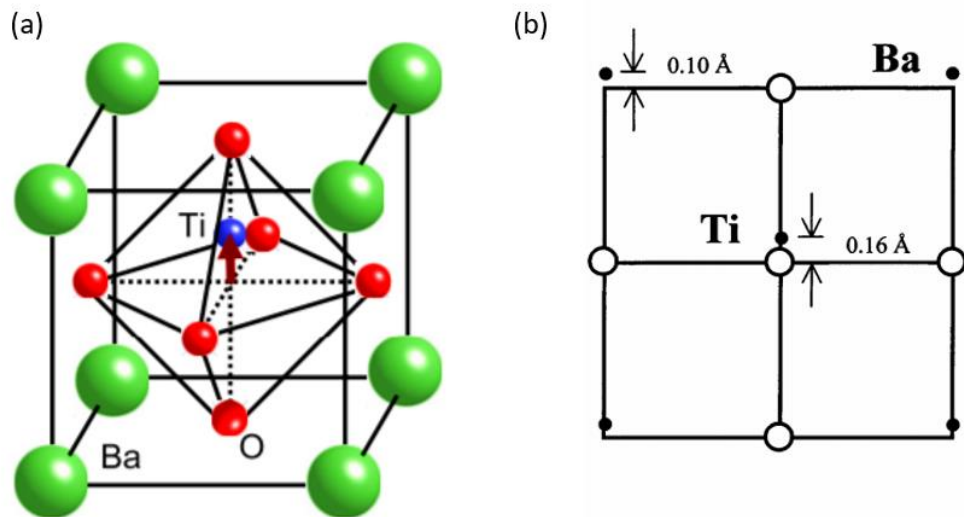


Figure 1. 7: Displacement of the A and B cations in BaTiO_3 . Green spheres represent the A cations (Ba), the blue sphere represent the B cation (Ti), and red spheres represent oxygen anions in octahedral coordination (Tazaki et al 2009).

Ferroelectricity arises by Ti off-centering, generating distortion and the appearance of spontaneous polarization in the material.

BT undergoes a series of phase transitions with temperature. Figure 1. 8 illustrates these successive phase transitions (Rhombohedral-to-orthorhombic, orthorhombic-to-tetragonal, tetragonal-to-cubic) which are accompanied by dielectric anomalies. Above 130°C , the unit cell acquires a cubic form and consequently, spontaneous polarisation disappears. Overall, the transition from polar to non-polar phase in ferroelectrics occurs at certain temperature, also called Curie temperature and it is characteristic of each

material. At this temperature, dielectric permittivity presents a maximum value (Jona & Shirane, 1962).

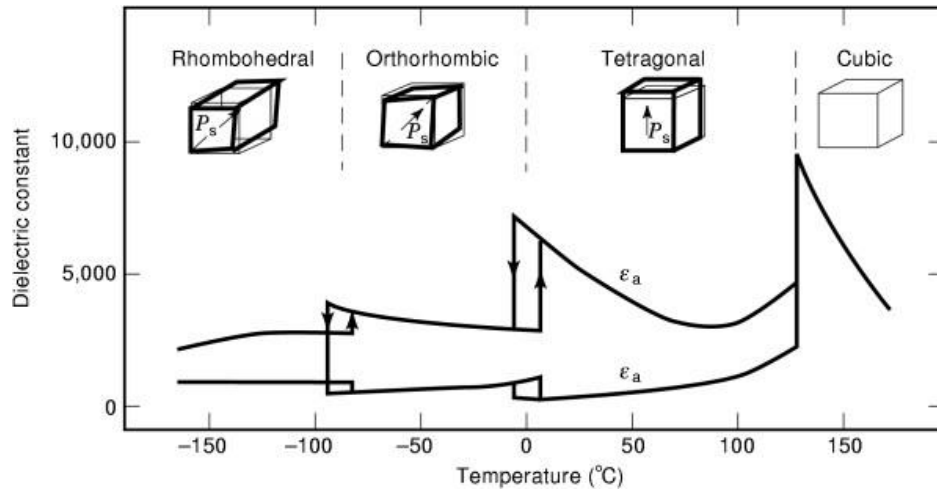


Figure 1. 8: The temperature dependence of the dielectric constant for BaTiO₃ and the various phase transitions (Ito & Uchino, 2005).

Lead titanate, PbTiO₃, is also a well-known ferroelectric perovskite oxide (Arlt, 1990; Jaffe et al., 1971; Moulson & Herbert, 1990). The ferro- to paraelectric phase transition occurs at higher temperature than BaTiO₃, around 490°C (Sani, Hanfland, & Levy, 2002). This compound presents tetragonal structure (P4mm) at room temperature and it is characterised as having high tetragonal distortion with c/a value of 1.064 (BaTiO₃, $c/a=1.01$) (Cohen, 1992). The high tetragonality of this structure suggests a remarkable displacement of the cations, generating the appearance of a dipole moment in the direction of this axis (Rabe & Ghosez, 2007).

(ii) Lone pair electrons

BiFeO₃ is possibly the only material that is both magnetic and a strong ferroelectric at room temperature and it was one of the first multiferroic materials with perovskite structure to be studied.

BiFeO₃ exhibits a rhombohedral structure (point group R3c) at room temperature (Moreau, Michel, Gerson, & James, 1971). From the electrical point of view, the main problem of this material is its high conductivity. First measurements gave small values of polarisation, between 3-6 $\mu\text{C} / \text{cm}^2$ (Teague, Gerson, & James, 1970). However, an order of magnitude higher has been reported later on high quality thin films (Eerenstein, Mathur, & Scott, 2006; J. Wang et al., 2003; Xie et al., 2017), single crystals (Lebeugle et al., 2007) and ceramics (Shvartsman, Kleemann, Haumont, & Kreisel, 2007).

Ferroelectricity in BiFeO_3 is originated by the lone pair electrons (s^2) of Bi^{3+} , which shifts Bi^{3+} to give rise to a spontaneous polarization along the $[111]$ direction (Catalan & Scott, 2009). The lone pair is visualized by red surface in Figure 1. 9.

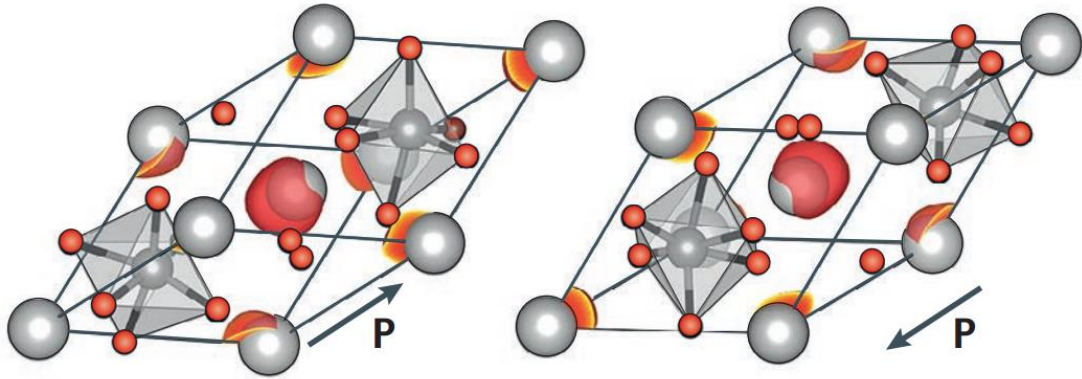


Figure 1. 9: Schematic representation of BiFeO_3 showing that the lone pair (red surface) promotes the appearance of spontaneous polarisation (Fiebig, Lottermoser, Meier, & Trassin, 2016).

(iii) Geometry

Other mechanism that generates ferroelectricity is due to geometric factors (Spaldin, 2017). Spontaneous polarisation in hexagonal RMnO_3 (where $R = \text{Sc}, \text{Y}, \text{In}$ or Dy) compounds arises from a tilt and deformation of MnO_5 bipyramids, which shift the rare-earth ions as pointed by the arrows on Figure 1. 10.

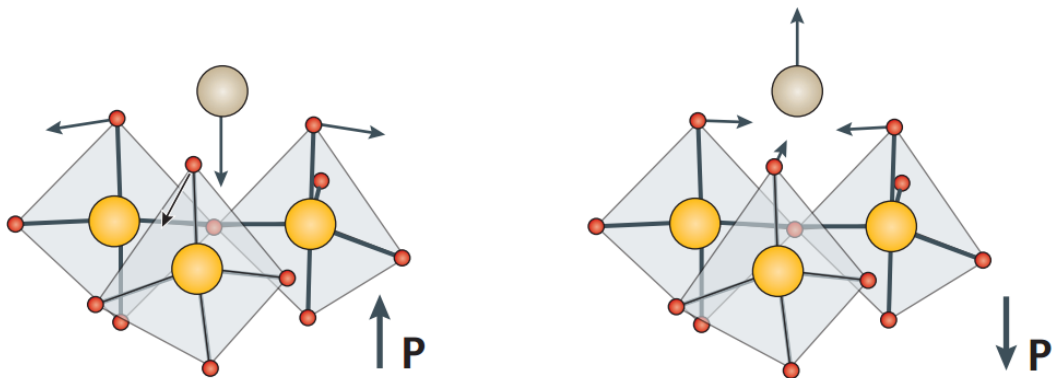


Figure 1. 10: Schematic representation of YMnO_3 . Spontaneous polarisation (P) arises when the MnO_5 pyramids (yellow and red spheres represent manganese and oxygen respectively) tilts and therefore the Y ion (grey sphere) shifts towards one of the oxygens.(Fiebig et al., 2016).

(iv) Charge ordering

Furthermore, the occurrence of ferroelectricity in LuFe_2O_4 is explained by other mechanism, charge-ordering (Ikeda et al., 2005). Fe^{2+} and Fe^{3+} ions are arranged in alternating chains in a superlattice. The spontaneous polarization arises between the two layers (Figure 1. 11).

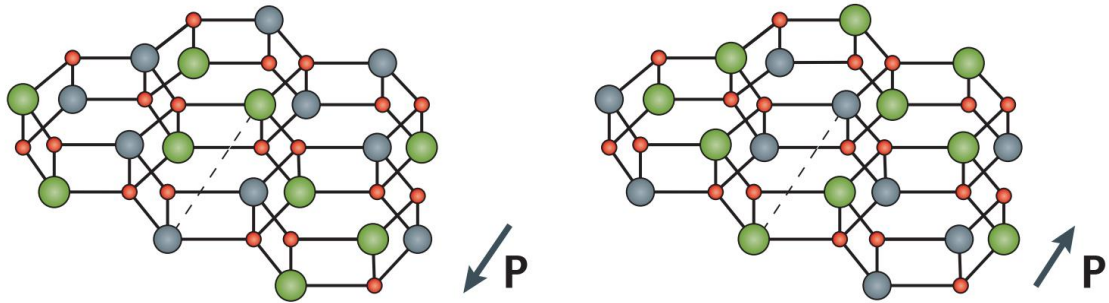


Figure 1. 11: Charge ordering is the source of an electric polarization in LuFe_2O_4 , which is illustrated in this figure. Green, grey and red sphere represent Fe^{+2} , Fe^{+3} and O, respectively. (Fiebig et al., 2016)

Finally, an alternative way to induce ferroelectricity is the magnetic order. Spin interactions can drive to a non-polar state and it is related to the generation of multiferroicity (Cheong & Mostovoy, 2007; Mostovoy, 2006).

1.2.4. Piezoelectricity in ferroelectrics

The direct piezoelectric effect (Equation 1.5.) relies on the accumulation of electric charge density (D), which is generated by an applied mechanical stress (T). On the other hand, the indirect piezoelectric effect (Equation 1.6) occurs when an electric field (E) is applied on solids and causes stress, and consequently, a proportional strain (S). The basic relationships between the electrical and elastic properties can be represented as follows:

$$D = d \cdot T + \varepsilon \cdot E \quad \text{Eq. 1.5}$$

$$S = s \cdot T + d \cdot E \quad \text{Eq. 1.6}$$

Where d , s and ε are the piezoelectric charge coefficient, compliance coefficient and the permittivity characteristics of each material, respectively.

In addition, electromechanical coupling factor, k_T , is an indicator of how effective a piezoelectric material is in converting electrical energy into mechanical energy and vice versa.

Figure 1. 12 shows an illustration of a strain (S) versus electric field (E) curve for ferroelectrics. The shape looks like a butterfly, and it is usually known as the “butterfly loop”.

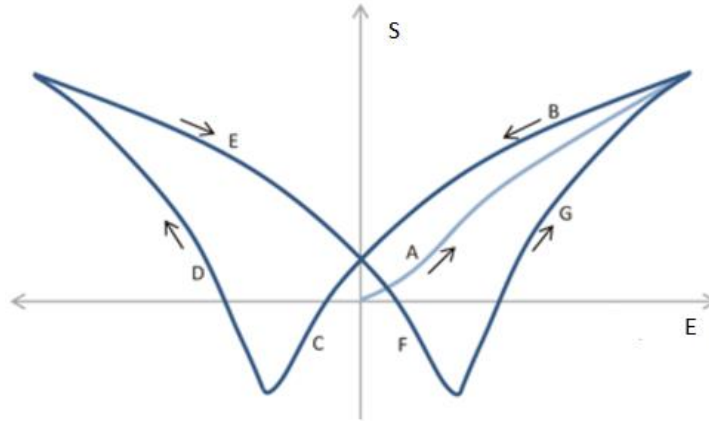


Figure 1. 12: Typical strain- electric field response curve for a ferroelectric material.

Firstly, strain increases with electric field (A). The dipoles of all the grains start to align with the electric field and the ceramic expands through the piezoelectric effect. The expansion continues until the maximum field is reached. When the field changes orientation, strain decreases more slowly due to the reoriented dipoles (B). As the field becomes negative the dipoles are forced away from their original orientation. At the critical point, the field is large enough to switch the direction of polarization (C). After polarization reversal (D), the crystal expands again until it reaches its physical strain limit. The electric field is again reversed, and the line E-F-G is analogous to that explained for B-C-D in the other direction.

Among solid solutions with perovskite structure, a type of ferroelectric systems has emerged that have a morphotropic phase boundary (MPB). An MPB is defined as the compositional barrier between two phases, in a phase diagram with identical Gibbs energy (Cao & Cross, 1993)

This phenomenon occurs in a solid solution between compounds that have different polymorphs derived from the perovskite structure. With the increase of substituted cations in the solid solution, the crystal structure of the solvent phase is distorted and a transition to the other polymorph happens. That composition or range of compositions in which the phase transition appears, is known as MPB.

Even if the two phases involved in the MPB have similar energies, they have different elasticity, consequently the solvent phase tends to maintain its structure with the addition

of solute until it reaches the MPB. In this region, it is observed that electrical properties have a tendency to increase, achieving maximum values in parameters such as dielectric constant, piezoelectricity, electromechanical properties, spontaneous polarization and pyroelectric coefficient (Bhalla et al., 2000).

One of the most investigated solid solutions that presents this phenomenon is $x \text{PbTiO}_3 - (1-x) \text{PbZrO}_3$ (PZT). This ferroelectric system exhibits the highest piezoelectric coefficients known in the MPB region ($x \sim 0.47$). Controversy about the origin of the high piezoelectric response in the MPB is found in the literature. Finally this behaviour in PZT was explained by Guo et al. in 2000 through the presence of a phase with monoclinic structure (space group Cm), which is considered intermediate between rhombohedral and tetragonal. Modifications on PZT phase diagram, after the discovery of the monoclinic phase is shown in Figure 1. 13.

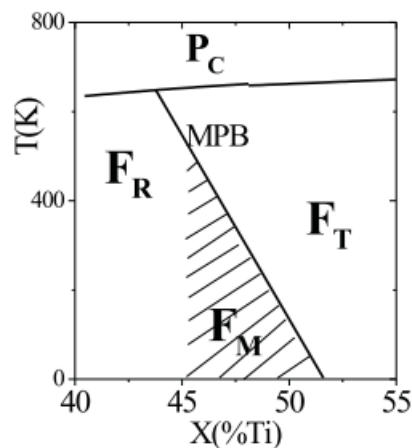


Figure 1. 13: PZT phase diagram around the MPB showing the monoclinic region (Guo et al., 2000)

The electrostrictive effect is the non-linear deformation of a solid under an electric field (E). The induced strain (S) is proportional to the square of electric field (E) and it is expressed in the following Equations 1.7-8:

$$S = Q \cdot P^2 \quad \text{Eq. 1.7.}$$

$$S = M \cdot E^2 \quad \text{Eq. 1.8}$$

where Q and M are electrostrictive coefficients. According to Eq. (1.7.) and Eq. (1.8.), the electrostrictive coefficient Q can be calculated from the linear fitting of the strain-polarization square ($S \cdot P^2$) curve (Li, Jin, Xu, & Zhang, 2014). A classic electrostrictive material is lead magnesium niobate (PMN), which exhibits large electrostriction strains (up to 0.1%) and is used widely in actuator applications (Figure 1. 14).

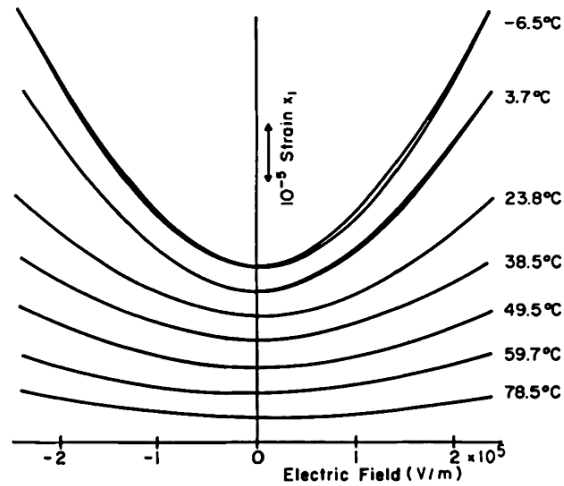


Figure 1. 14: Electric field dependence of the strain in a PMN single crystal at various temperatures. (Nomura & Uchino, 1982).

PMN electrostrictive ceramics belong to a class of relaxor ferroelectrics, materials which shows a strong dispersion of dielectric permittivity. T_C can vary in a temperature interval of hundreds of degrees and the dielectric peak is broader than for normal ferroelectric (Figure 1. 15). However, the mechanism for this effect is still an open question (Cowley, Gvasaliya, Lushnikov, Roessli, & Rotaru, 2011).

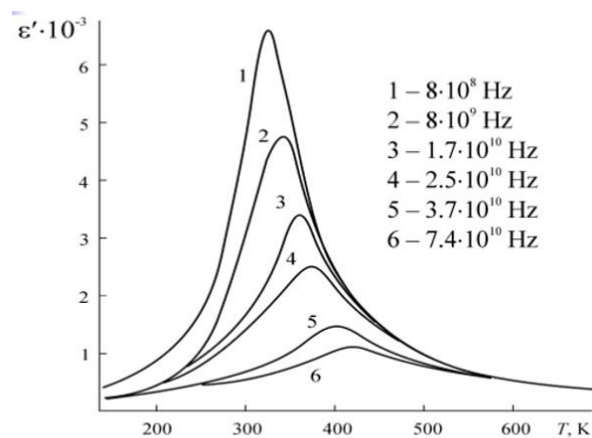


Figure 1. 15: Temperature dependence of the real part of the dielectric permittivity ϵ' of PMN (Smolenskii, 1970).

1.2.5. Literature review of KNbO_3

KN is a well-known ferroelectric perovskite and it is the main compound of this study. Many fundamental and experimental investigations have been carried out since ferroelectricity was discovered in this compound (Matthias, 1949). At room temperature,

the KN crystal symmetry can be described with orthorhombic structure (space group $Amm2$). The orthorhombic $Amm2$ cell contains two $KNbO_3$ units and the lattice parameters are $a = 3.973 \text{ \AA}$, $b = 5.695 \text{ \AA}$ and $c = 5.721 \text{ \AA}$ (Hewat, 1973).

Shirane et al reported in 1954 a value of $41 \pm 2 \mu\text{C}/\text{cm}^2$ for the spontaneous polarisation of KN single-domain at room temperature. This large value is due to cation displacement of Nb^{+5} within the NbO_6 octahedra. The distortion is generated by the hybridisation of the empty d-orbitals of Nb^{+5} with the O^{2-} p-orbitals.

Figure 1. 16 (a) and (b) shows the dielectric constant dependence with the temperature in a KN crystal (Shirane et al., 1954) and a ceramic (Birol, Damjanovic, & Setter, 2005) respectively. The Curie temperature of both, crystal and ceramics, for KN is about 410°C . At -55°C the crystal symmetry changes from rhombohedral ($R3m$) to orthorhombic ($Amm2$) and at 220°C from orthorhombic to tetragonal ($P4mm$). The ferroelectric phase transition behaviour for KN single crystal and ceramic are analogous to $BaTiO_3$ (Figure 1. 8).

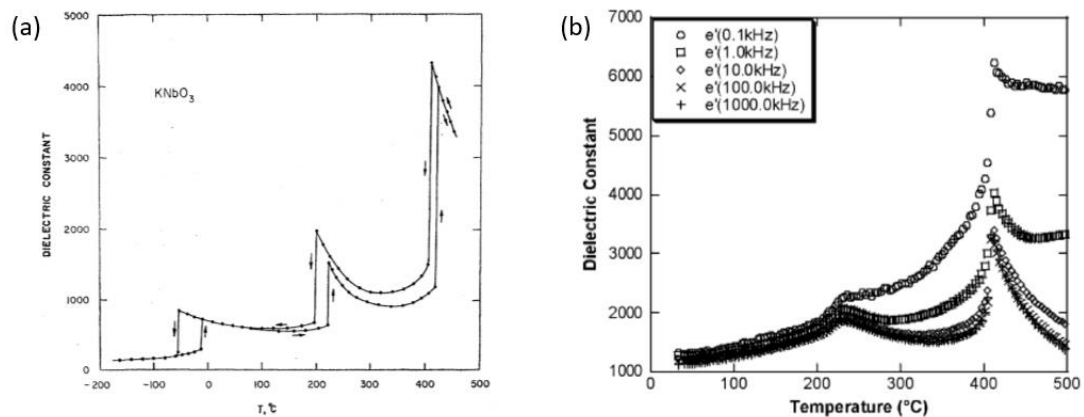


Figure 1. 16: Evolution of the dielectric constant with the temperature in (a) a single crystal (Shirane et al., 1954) and (b) a ceramic (Birol et al., 2005) of KN. Dielectric anomalies are related with the phase transition.

The dielectric constant for the single crystal exhibits maximum value of 4000 (6000 for ceramic) at the Curie temperature, although at room-temperature it is <1000 . In ceramics, the room temperature value varies between $\sim 300 - 1000$ in the literature (Birol et al., 2005; Ken-Ichi Kakimoto, Masuda, & Ohsato, 2005; Kim et al., 2014; Pascual-Gonzalez, Schileo, & Feteira, 2016). This discrepancy on dielectric constant values is related to the final microstructure of the ceramic, such as presence of porosity and different distribution of grain size. The different polymorphs of KN can also be distinguished by Raman spectroscopy (Figure 1. 17, Baier-Saip, Ramos-Moor, & Cabrera, 2005).

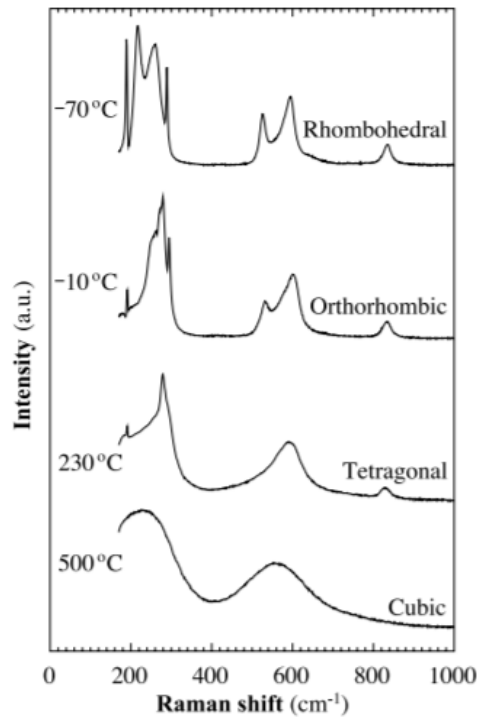


Figure 1. 17: Raman spectra of KNbO_3 . The temperature and the corresponding crystal phase are indicated for each spectrum (Baier-Saip et al., 2005)

The cubic phase displays two large and broad bands. These bands persist in the tetragonal and orthorhombic phases, and they split in narrower modes, which become sharper as temperature decreases. Extra modes emerge in orthorhombic and rhombohedral phase. The intensity of the sharp mode near 192 cm^{-1} increases systematically with the decrease in temperature. Detailed description of Raman modes in KN will be given in Chapter 3.

KN crystals exhibit unusual large mechanical coupling factors, k_T , which presents a maximum value of 0.69 at 40.51° away from the polar axis (Figure 1. 18). This value is the largest k_T reported in literature among piezoelectrics (Rödel et al., 2009), the typical value for PZT is 0.5. Even with this great mechanical coupling value, no practical applications of polycrystalline KNbO_3 piezoelectric ceramics have been found and only few studies about electrical properties of this material have been reported due to difficulties on its densification.

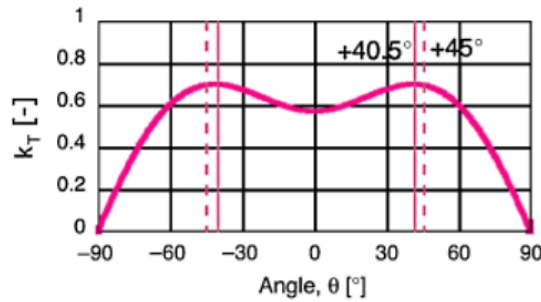


Figure 1. 18: The mechanical coupling factor in KN single crystals. The angle θ specifies the rotation away from the polar axis of the pseudocubic system. The largest K_T (0.69) value is obtained at 40.51° (Rödel et al., 2009).

The preparation of KN by conventional ceramic processing is challenging because of different issues. The evaporation of potassium during the heat treatments of the synthesis and sintering prevent KN ceramics from being fully densified. When the ratio K/Nb differs from unity, an unstable secondary phase, $K_4Nb_6O_{17}$ (or $2K_2O-3Nb_2O_3$) is easily formed. This phase affects the stability of the KN ceramic when exposed to humid environment. Furthermore, other problem that affects the KN preparation is its low melting point (1039°C) which is very close to the sintering temperature, as shown by the Reisman and Holtzberg's phase diagram (Figure 1. 19). These problems are approached in Chapter 3.

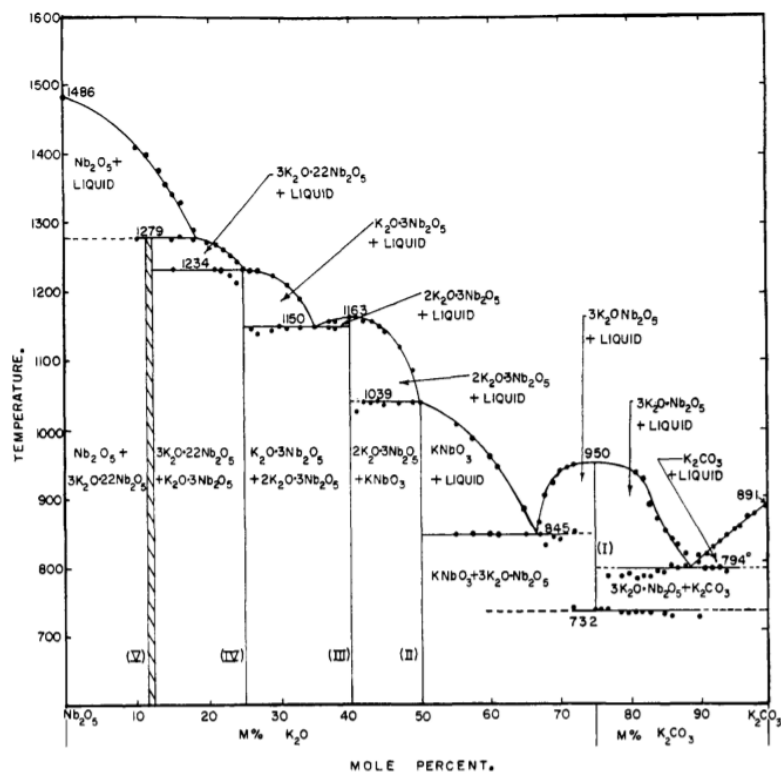


Figure 1. 19: Phase diagram of Nb_2O_5 - K_2CO_3 system. The melting point of KN is indicated at 1039°C . (Reisman, Holtzberg, Triebwasser, & Berkenblit, 1956)

However, Birol et al. achieved to prepare KN ceramics with high relative density (93.9%) after firing the green bodies at 1035 °C in oxygen. The same study shows hysteresis loop of KN at room temperature (Figure 1. 20 (a)). The ceramic was able to withstand an electric field of 80 kV/cm and exhibited a maximum spontaneous polarisation value of 25 $\mu\text{C}/\text{cm}^2$ and a coercive field of 15 kV/cm. Kakimoto et al obtained a density of 4.49 g/cm^3 (97.4%) for KN ceramics which were sintered at 1020 °C in a potassium rich atmosphere provided by covering the green body with additional KN powder. This study also reported an enhancement of the ferroelectric properties for $(1-x) \text{KNbO}_3-x \text{LaFeO}_3$ (Figure 1. 20 (b)) with increasing x content.

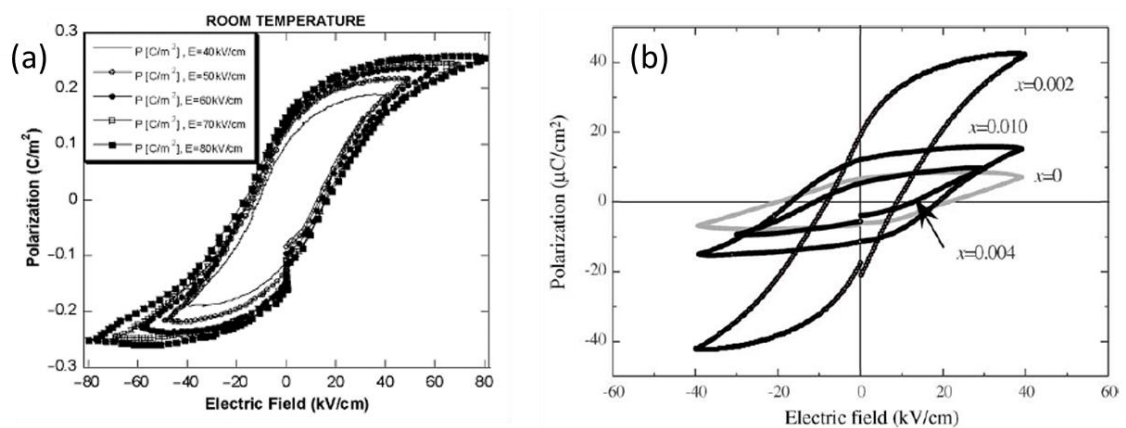


Figure 1. 20: Hysteresis loop of polycrystalline KN ceramic at room temperature reported by (a) Birol and (b) $(1-x) \text{KNbO}_3-x \text{LaFeO}_3$ Kakimoto et al.

In addition, KN also presents promising optical properties, such as nonlinear optics (Pliska, Fluck, Günter, Beckers, & Buchal, 1998), electro-optical coefficients and high refractive indices (Reeves, Jani, Jassemnejad, & Powell, 1991). Indeed, KNbO_3 is a good candidate for photorefractive materials (Ryf, Montemezzani, & Günter, 2001; Yan et al., 2013), electro-optic devices, optical waveguides, optical parametric oscillator (Zaitsev, Kuznetsova, & Joshi, 2001), frequency doublers, sensing, imaging applications (Ladj et al., 2013), cryptography (Montemezzani & Günter, 1990), signal processing circuits, photocatalytic (R. Wang et al., 2013), photovoltaic (Ilya Grinberg et al., 2013) and holographic memory storage devices (Buse, 1993). Due to this wide spectrum of optical applications, the band-gap of KN has been largely reported, that will be shown later, in section 1.4 (Band-gap narrowing).

1.2.6. Applications of piezo- and ferroelectrics

This section provides a general overview about piezo- and ferroelectric applications without going into many details. From their discovery to the present, FE materials have been implemented in wide range of applications. Depending on the application ferroelectrics can be prepared as bulk ceramics or thin films. Figure 1. 21 illustrates the temperature dependence of the spontaneous polarisation (P_s), dielectric constant (ϵ) and its inverse ($1/\epsilon$). Schematically the classic applications of ferroelectrics are indicated in this graph in function of the physical properties required and the operational temperature.

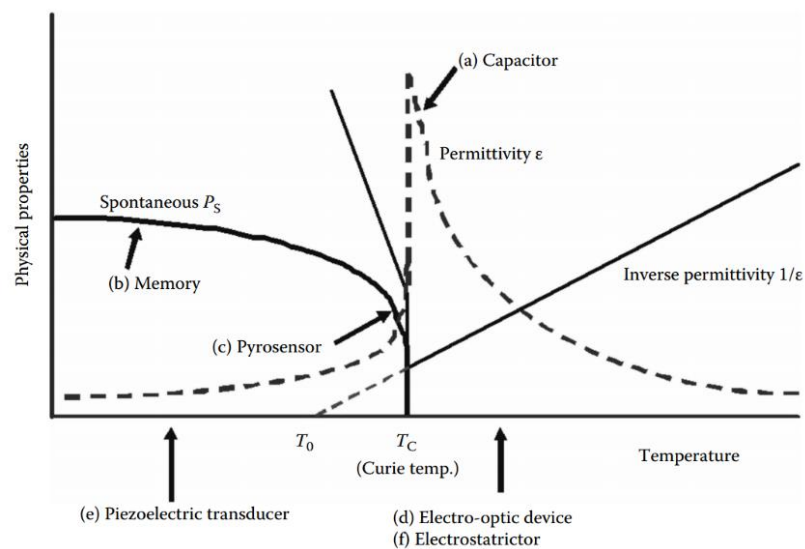


Figure 1. 21: Spontaneous polarization, permittivity and inverse permittivity in a ferroelectric material. (a)–(f) indicate the temperature ranges for each application (Uchino, 2009).

Capacitors (a) need to be easily polarised under an electric field, then they will work in the maximum value of dielectric constant close to the transition (T_C). In memory devices (b) the materials must be FE at RT. Pyroelectric sensors (c) are based on the large temperature dependence of the spontaneous polarisation below T_C .

Piezoelectrics are more utilised as sensors and actuators (e). A requisite of these applications is to exhibit high values of T_C . Direct piezoelectric effect is used in sensors devices that measure force, pressure, vibration or acceleration. Indeed, conventional piezovibrators have already been installed in different equipment such as precision positioners and pulse drive linear motors. Recently, piezoelectric energy harvesting systems have attracted attention. Waste mechanical energy such as noise vibration, wind, and human walking can be transformed into electrical energy and can be used directly for

signal transmission or to charge up batteries for portable electronics (Mitcheson, Yeatman, Rao, Holmes, & Green, 2008). The indirect piezoelectric effect is used in actuators to generate a force, vibration or an acoustic wave. Both effects can be employed in a device to combine actuation and sensing. Finally, T_C for electro-optic (d) and electrostrictive (f) devices are lower than RT to use their paraelectric state.

1.3. Photoferroelectrics

1.3.1. Electronic band structure of solids

A solid is a set of ions and electrons at different energy levels in thermodynamic equilibrium and its band structure gives the allowed and forbidden energy ranges that an electron can have within the solid and consequently informs of many physical properties.

In quantum mechanics, a Hamiltonian (H) is a mathematical operator that corresponds to the total energy in a system. Taking in consideration all the ionic and electronic interactions into the solid, the formulation of the Hamiltonian becomes very complex. In order to make this task easier some approximations are considered: (i) ions are at rest, then ion's kinetic energy term is zero; (ii) ions are fixed, interaction ion-ion term is discarded; and (iii) each electron does not perceive an individualized interaction of each ion and electron, but a resulting effective potential generated by all electrons and ions, $V(r_i)$.

Considering the previous approximations for the Hamiltonian, the evolution over time of an electron is given by the Schrödinger equation (Eq. 1.9).

$$\hat{H}\psi(r, t) = \sum_i \left\{ -\frac{\hbar^2}{2m} \nabla_i^2 + V(r_i) \right\} \cdot \psi_i(r_i, t) \quad \text{Eq. 1.9}$$

The first term represents the kinetic energy of the electrons, where i is the number of electrons, m is the electron mass, \hbar is the Planck constant ($6.58212 \cdot 10^{-16}$ eV·s/rad), ∇_i is the gradient operator and $\psi_i(r_i, t)$ is the electron wave function. The resulting effective potential ($V(r_i)$) is assumed to be a periodic potential of period a and consisting of an infinite series of potential barriers of height V_0 , wide b and separated by a distance $a-b$ (Model Kroning-Peney). (Figure 1. 22).

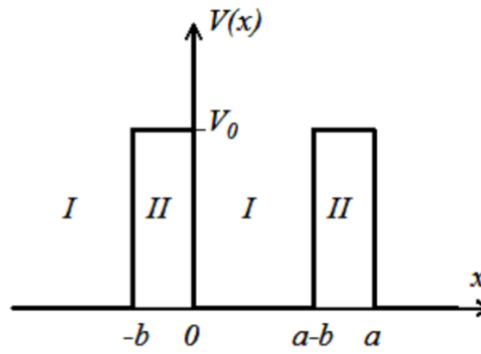


Figure 1. 22: Schematic representation of idealized quantum-mechanical system that consists of an infinite periodic array of rectangular potential barriers.

The solution of the Schrödinger equation for this model is given by the Bloch functions. A 1 dimensional chain of atoms (x direction) separated by a lattice spacing a , is considered (Eq. 1.10).

$$\Psi(r_x) = u(r_x) \cdot e^{ikr_x} \quad \text{Eq. 1.10}$$

The wavefunction $\Psi(r_x)$ is a combination of the periodic potential $u(r_x)$ of each atom with an exponential term that varies with the wavenumber k . The wavefunction is continuous and periodic (Eq. 1.11).

$$\Psi(r_x) = \Psi(r_x + a) \quad \text{Eq. 1.11.}$$

It is convenient to work with wavenumbers, k , instead of time to approach the Schrödinger equation, because k always presents discrete values (Eq. 1.12).

$$k = \left(\frac{2\pi}{a}\right)n \quad \text{Eq. 1.12}$$

Where n is an integer number.

Assuming all the considerations detailed above, the Schrödinger equation can be 'easily' resolved, obtaining the energy as a function of wavenumbers, $E(k)$, also known as "band energy diagram". In this case, the solution, $E(K)$, is a parabola, except for certain energy ranges where the solution does not exist (black curve, Figure 1. 23).

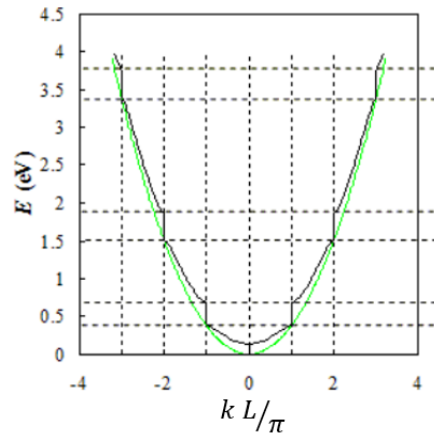


Figure 1. 23: Representation of the band structure $E(K)$. Black curve is the solution assuming a periodic potential (Model Kroning-Peney). and green curve is for a free electron model.

By inspection of the energy band structure we can determine the valence and conduction bands. The valence band (VB) is where the electrons that form the atomic bonds can be found. Nevertheless, there are electronic states with higher energy that form the conduction band (CB). If one electron occupies one of this energy levels, it is not linked to an atom but to all atoms at the same time and the electron can move freely. The range of energy (or band), where electron states cannot be found, is defined as the ‘band-gap’. This interval is defined between the VB and the CB (Figure 1. 24). Depending on the value of the band- gap, the material can be classified as metallic (VB and CB are overlapping), semiconductor ($\sim 1\text{eV}$) or insulator ($\geq 9\text{ eV}$). If the maximum of the VB (MVB) and the minimum of the CB (mCB) are at the same wavenumber, k , it is called direct band-gap. Otherwise, it is called indirect band-gap. (Figure 1. 24). In this type of band-gap, an electron cannot be excited from the MVB to mCB without a change in momentum. This process requires the absorption of a phonon for conservation of momentum. This distinction is important in solar cells because the semiconductors with direct gap absorb more photons than indirect gap.

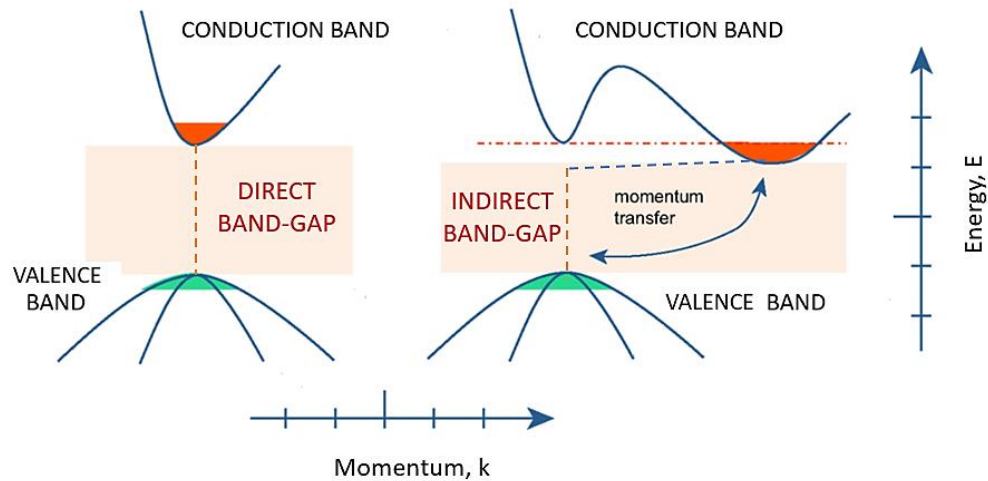


Figure 1. 24: Energy (E) versus momentum (k) plot. Schematic representation of direct and indirect band-gaps.

However, real band structure in solids must consider orbital interactions in 3 dimensions arising from s , p , d , and f orbitals on each atom. This leads to complex energy diagrams with many bands. Thus, the calculation of $E(k)$ is unfeasible and requires computational programs. Extending the system to 3 dimensions, the k vectors comprise the first Brillouin zone of the crystal. Before going deeper in this, it is necessary to explain some crucial concepts. Due to the periodic properties of the lattice and the Bloch functions, every k vector in the real space is equivalent to a k vector inside this Brillouin Zone (also called k -space). Figure 1. 25 shows the Brillouin Zone of a face-centered cubic (FCC) lattice where b_1 , b_2 , and b_3 are the reciprocal vectors and the red points labelled (Γ , L, K, W, X, U) correspond to high symmetry points in the Brillouin Zone.

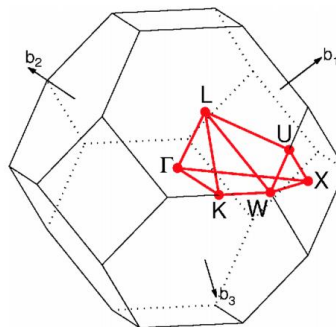


Figure 1. 25: The Brillouin zone of FCC lattice showing the reciprocal vectors and the high symmetry lines and points.

Then the electronic band structure ($E(k)$) is directly obtained by calculating energies in the high symmetry points in the Brillouin Zone, which is the easiest way from a point of view of the calculations (using symmetry conditions). As an example, Figure 1. 26 shows

band diagrams of (a) GaAs (direct band-gap) and (b) Si (indirect band-gap) which are the preferred materials for conventional solar cells. The band-gaps are 1.43 eV and 1 eV, respectively.

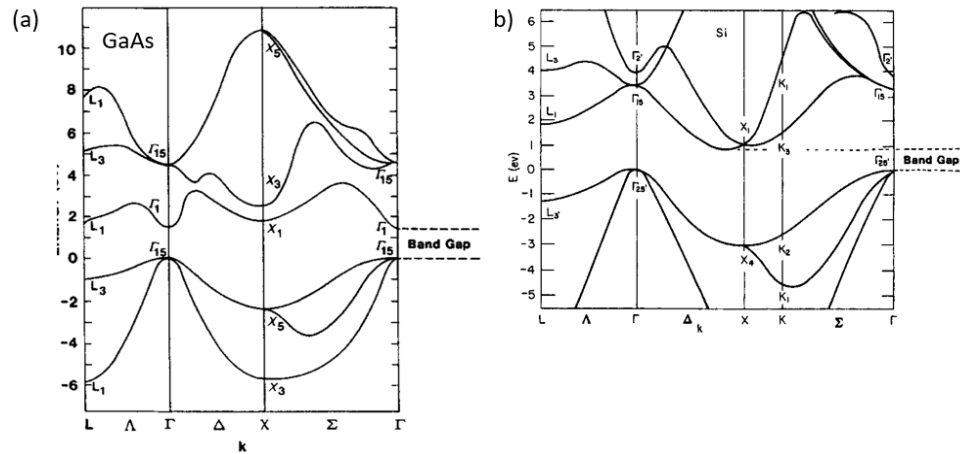


Figure 1. 26: Electronic band structure of (a)GaAs, which exhibits direct band-gap (1.43 eV) and (b) Si with an indirect band-gap of 1 eV.(Rohlfing, Krüger, & Pollmann, 1993).

1.3.2. Photovoltaic effect

As mentioned previously, semiconductors exhibit band-gaps of $\sim 1\text{eV}$ which promotes the absorption of sunlight due to the matching in energy with the solar spectrum, which mostly emits in the visible range (400-700 nm). When the light is absorbed by a semiconductor material, photons transfer the energy to the valence electrons producing the excitation of these from the VB to the CB. This process creates holes in the VB and electrons in the CB (electron-hole pair). After some time, electrons go back to their original electronic state, emitting photons or phonons. This procedure is called recombination. However, if there is an electric potential across the material, it will promote a net flow of photogenerated electrons and holes (photocurrent). The creation of electric current in a material under sunlight illumination is what is known as ‘photovoltaic effect’.

The photovoltaic effect was discovered by A. E. Becquerel in 1839. In the first photovoltaic systems, the charge separation was obtained by the introduction of a selenium layer (Nelson, 2003). In the 1950’s a new method for creating asymmetry in the electric potential was presented, just doping different regions of a single piece of silicon

with phosphorous and boron. This procedure generates an intrinsic electric field (p-n junction) in the material that separates the photocarriers.

The power conversion efficiency (η) of incident light power (P_{in}) to electricity is proportional to the open-circuit voltage (V_{oc}), short-circuit current (J_{sc}) and to the fill-factor (FF) is given by Eq. 1.13.

$$\eta = \frac{V_{oc}J_{sc}FF}{P_{in}} \quad \text{Eq. 1.13.}$$

The maximum voltage which can be generated by conventional semiconductors (V_{oc}) is limited by the band-gap of the material. The photocurrent (J_{sc}) is measured when $V_{oc}=0$ and it is determined by the portion of solar spectrum that the material absorbed. In an ideal solar cell, the power generation would be equal to the product $J_{sc} \cdot V_{oc}$. Real solar cells show a different maximum power point (MPP) (Figure 1. 27). To evaluate the quality of a solar cell the fill factor (FF) is calculated, which is given by the ratio of the products of the current and the voltage at MPP and of V_{oc} and J_{sc} .

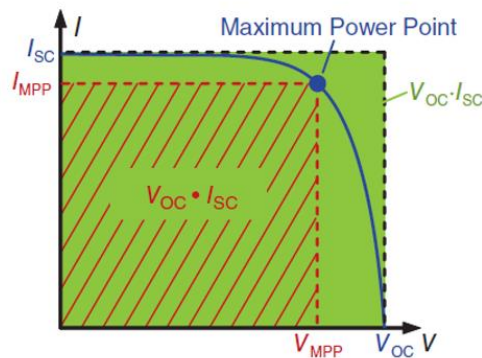


Figure 1. 27: Photovoltaic characteristic curve(I-V). Green square represents the ideal conversion power in a solar cell and the red one the real maximum power. The relation of this quantities gives the fill factor (FF).

A theoretical calculation determines that only 33.7% of the total solar energy can be converted into electric energy in a solar cell with a single p-n junction (Shockley & Queisser, 1961). Nevertheless, this limit can be surpassed by cells with other architectures as shown on the NREL chart (2017) (Figure 1. 28). The multijunction cells are able to reach efficiencies up to 46%. In addition, it is noted that perovskite cells have experienced a promising growth over the last few years. Since 2009, the efficiency of perovskites has increased from 3.8% to 22.1%. One of the biggest problems that presents these cells are the stability and the rapid degradation.

In academia, photoferroelectrics are presented as potential candidates for using in photovoltaic devices due to their anomalous photovoltaic response that will be detailed in the next section. Anyway, these materials do not appear in the NREL chart because of their extremely low efficiency.

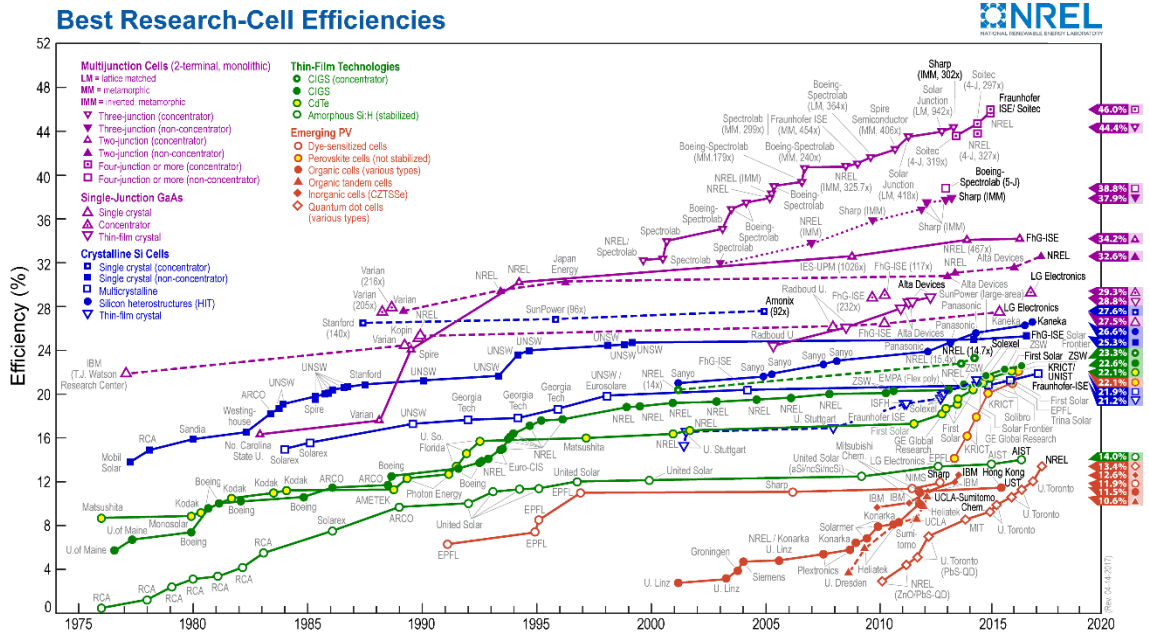


Figure 1. 28: NREL chart show cells efficiencies from 1975 to 2017.

1.3.3. The anomalous photovoltaic effect in ferroelectrics

1.3.3.1. Introduction

Anomalous photovoltaic effect in polar materials was discovered in early 70's (V. M. Fridkin et al., 1974; Grekov, Malitskaya, Spitsina, & Fridkin, 1970). The first explanation of the photovoltaic effect based on the asymmetry of Fe^{+2} -doped LiNbO_3 was reported by Glass in 1974. Since then, photo-response on thin films of classical ferroelectrics have been investigated, such as PZT (Kholkin, Boiarkine, & Setter, 1998) and BaTiO_3 (Dharmadhikari & Grannemann, 1982). Moreover, different theoretical studies have been developed (Sturman & V. M. Fridkin, 1992; Young & Rappe, 2012; Young, Zheng, & Rappe, 2012). In the last 10 years photovoltaic properties in non-centrosymmetric crystals have attracted renewed attention (Choi, Lee, Choi, Kiryukhin, & Cheong, 2009; Ilya Grinberg et al., 2013; Kreisel, Alexe, & Thomas, 2012; Yang et al., 2010).

Different explanations have been proposed to explain the nature of anomalous photovoltaic effect in polar materials. However, all have one point in common: photo-response in ferroelectric is generated by completely different mechanism than observed in non-polar structures such as p-n junctions.

Photovoltages in ferroelectrics can exceed several times their band gaps values, in contrast to conventional semiconductors. Spontaneous polarisation in non-centrosymmetric materials provides an alternative way to separate the photoexcited carriers.

1.3.2.2. Origin of the photoresponse in ferroelectrics

As was introduced, the origin of the bulk photovoltaic effect (BPE) was explained for first time more than 40 years ago (Glass, von der Linde, Auston, & Negran, 1975) and it has been recently reviewed in BaTiO₃ thin films (Zenkevich et al., 2014).

The microscopic mechanism that promotes BPE in Fe doped LiNbO₃ was directly related to asymmetric scattering of excited electrons, in this case due to the ‘iron defects’ (Glass et al., 1975). When some lithium cations (Li⁺) are substituted by iron cations (Fe²⁺) in a LiNbO₃ array, the results are that the potentials barriers for electrons are not equal in all directions (Figure 1. 29(a)). If an electron is excited from the ground state (E₀) to an energy level E₁, the electron remains trapped in the potential well. Nevertheless, if the electron is excited to E₂ level then it will be scattered in a certain direction. Always there is a preferred orientation from a statistic point of view (possible tunnelling) which leads to the presence of more electrons with certain momentum vector value, k . This imbalance gives rise to the appearance of a net flow of electrons in the same direction. These electrons will travel l_0 distance in space before losing their energy and decay to the lowest level of the conduction band (Figure 1. 29 (b)).

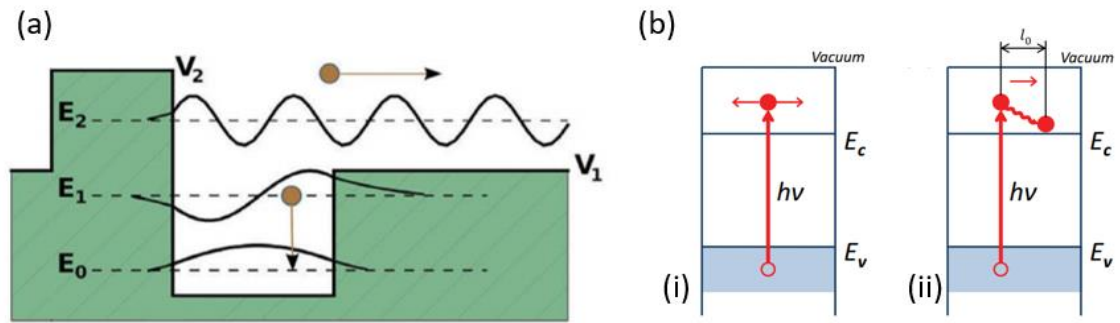


Figure 1. 29: (a) Asymmetric potential well which leads the asymmetric scattering of the excited electrons (Butler, Frost, & Walsh, 2015)(b) While photoelectrons in a centrosymmetric crystals (i) present an homogeneous momentum distribution, in a noncentrosymmetric crystal (ii) a photocurrent appears under illumination due to the asymmetric momentum distribution (Zenkevich et al., 2014a).

However, noncentrosymmetric materials without impurities also exhibit photoresponse under illumination. Fridkin explained in his book ‘Photo-ferroelectrics’ (1979) in a contrived manner and difficult to understand that there are several microscopic mechanisms that can contribute to the photocurrent such as impurity centres and photoinduced fluctuations. In subsequent works, Fridkin directly attributed ‘the violation of the principle of the detailed balancing for photoexcited (non-equilibrium) carriers in noncentrosymmetric crystals’ to the generation of photocurrent. This mechanism would be analogous to the Glass model (explained above) but without making clear the origin of asymmetric scattering of excited electrons.

1.3.2.3. Experimental measurements

The photoresponse in ferroelectrics is measured in the same way as conventional photovoltaics. A homogeneous polar medium with short-circuited electrodes is uniformly illuminated, thus the photocurrent (J_{SC}) is generated. On the other hand, the photovoltage (U_{Ph}) is measured in open-circuit conditions (Figure 1. 30).

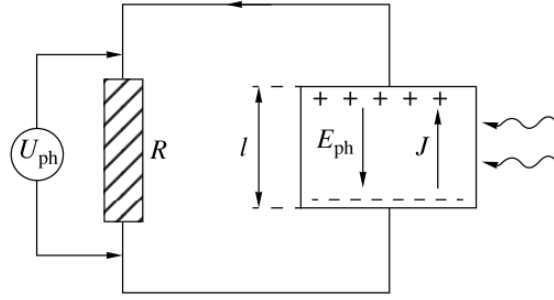


Figure 1. 30: Schematic representation of measurements of the photovoltaic current J and photovoltage U_{ph} . Initially, the Glass model considered that the photovoltaic current was proportional to the intensity of the monochromatic incident light (Eq. 1.14).

$$J_{sc} = \kappa_1 \alpha I \quad \text{Eq. 1.14}$$

where α is the absorption coefficient and κ_1 is a coefficient that relies on the nature and concentration of the impurity centres and the energy of the incident photons. Afterwards quantum mechanics was incorporated to this model for describing the asymmetric scattering of excited electrons in ferroelectrics (von Baltz & Kraut, 1978). However, this model did not consider the dependence of photocurrent with the rotation of the polarization of the incident light. Hence, the expression of the photocurrent was described with a third rank tensor (Eq. 1.15) (V. M. Fridkin, 2001; Kraut & Von Baltz, 1979; Sturman & V. M. Fridkin, 1992; Von Baltz & Kraut, 1981).

$$J_{sc}^i = \alpha \beta_{ijl} p_j p_l I_0 \quad \text{Eq. 1.15}$$

where p_j and p_l are the components of the light polarization vector, I_0 is the amplitude of the light and the scalar value of the tensor β_{ijl} expressed in terms of microscopic quantities is given by Eq. 1.16.

$$\beta = \frac{e l_0 \xi \varphi}{\hbar \omega} \quad \text{Eq. 1.16}$$

where e is the elementary charge of the electron, l_0 is the shift of excited electrons, φ is the quantum yield, $\hbar \omega$ is the energy of the photons and ξ is a parameter that characterises the shift of the electrons in an anisotropy direction.

Currently, the efficiency of conversion of light into electricity through the BPE is extremely low compared with actual commercial values. For example, in the case of BaTiO₃ bulk crystals, the efficiency η was estimated $\sim 10^{-7}$ (Koch, Munser, Ruppel, & Würfel, 1975). Recently, this value has been surpassed in BaTiO₃ thin films, as will be

explained later (Zenkevich et al., 2014). Until few years ago, the highest efficiency (0.28%) among FEs materials was reported in La-doped PZT thin film (Qin, Yao, & Liang, 2008).

Different studies showed that if the thickness of the polar materials, l , is in the same order of magnitude or less than the shift in the nonthermalized electrons l_0 , the photoinduced electric field and the conversion efficiency become much higher.

Zenkevich et al. reported a greatly enhancement of photoinduced electric field (E_{PV}) when the thickness of the BaTiO_3 films was reduced to few tens of nanometres. Figure 1. 31 shows the I-V measurements for 50-nm (a) and 20-nm (b) BaTiO_3 films at different illumination intensities. U_{PV} values are practically equal to both thicknesses. Consequently the E_{PV} values surpass by 4 orders of magnitude those reported for the bulk crystals (Sturman & V. M. Fridkin, 1992).

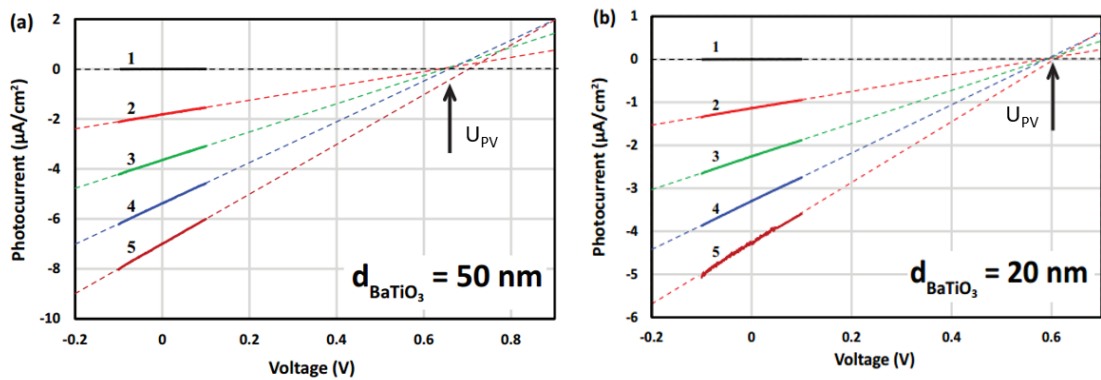


Figure 1. 31: Photocurrent at different light intensities (1: dark current; 2: $I = 1.5 \times 10^{-1} \text{ W/cm}^2$; 3: $I = 3 \times 10^{-1} \text{ W/cm}^2$; 4: $I = 4.5 \times 10^{-1} \text{ W/cm}^2$; and 5: $I = 7.5 \times 10^{-1} \text{ W/cm}^2$) measured on two thin-films of thickness: (a) $l = 50 \text{ nm}$ and (b) $l = 20 \text{ nm}$ in Pt/ BaTiO_3 /Pt sample.

However, Yang et al. described a new mechanism for explaining the nature of the photovoltaic effect in BiFeO_3 thin film and completely refused the BPE detailed above. Linear increase of the photovoltage was observed with the increase of electrode spacing, d (inset Figure 1. 32). This suggests the important role of domain walls in creating the anomalous photovoltages. Authors rejected the BPE due to insignificant values of photovoltage measured in a high purity single domain of BiFeO_3 (Figure 1. 32).

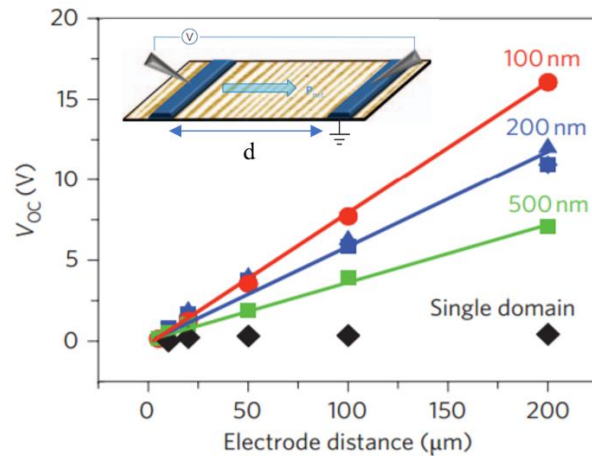


Figure 1. 32: Evolution of V_{OC} versus electrode spacing (inset) for four t samples of high purity BiFeO_3 film with different thicknesses of 100 nm (red), 200 nm (blue) and 500 nm (green) and monodomain (black)(Yang et al., 2010).

The new mechanism proposed for the photovoltaic effect in BiFeO_3 thin films is related with the presence of the 71° (Figure 1. 33 (a)) and 109° domain walls. Separation of photoexcited carriers occur at the ferroelectric domain walls, where the gradient of polarisation gives rise to an internal electric field. Then photoelectrons move to one side of the wall while holes move to the other side (Figure 1. 33 (d)). Indeed, an accumulation of charges is created close to the domain wall under illumination. Figure 1. 33 (b) and (c) show the band diagrams under dark and illumination conditions. So, the net photovoltage is generated across all the sample, resulting from the combined effect of the domain walls and the excess charge created by illumination.

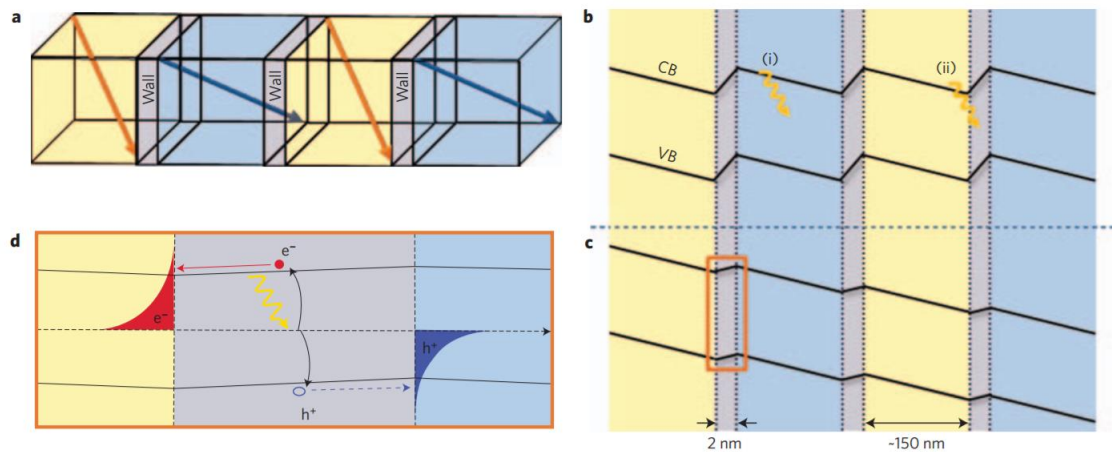


Figure 1. 33: (a) Schematic illustration of ferroelectric domains and 71° domain walls in BiFeO_3 . (b) Band diagram showing the valence band (VB) and conduction band (CB) across these domains and domain walls in the dark and (c) under illumination. (d) Mechanism of photo excited charges at a domain wall. (Yang et al., 2010).

Even if the separation of the carriers at the domain wall is quite similar to the separation at the p-n junction, the main difference resides in the magnitude of the electric field that drives the charge separation, conventional Si systems exhibit 7 kV/cm compared with BiFeO₃ that presents 50 kV/cm.

However, this model has created controversies in the literature, indeed several studies clearly validated both models (Alexe, 2012; Alexe & Hesse, 2011; Bhatnagar, Ayan, Young, Hesse, & Alexe, 2013; Ji, Yao, & Liang, 2011).

In conclusion, the origin of the photocurrent is not generally understood, and it is even difficult to determine whether the effect is due to BPE or domain wall mechanism.

1.4. Band-gap engineering

To enhance the photovoltaic efficiency, the band-gap of ferroelectrics (FE) must be narrowed while maintaining their polar nature. Indeed, band-gaps of FE usually present values above 3 eV (Table 1. 3), which limits their light absorption mostly to the ultraviolet (UV) region that it is equivalent to absorbing only 8% of the solar spectrum. The wide optical bandgaps in oxide FE perovskites arise from the nature of the bonding between O and B ions. Indeed, the large differences in electronegativity between the O and the B ions lead to the valence band to be formed by the 2p O states and the conduction band by the d states of the B transition metals sitting within the O octahedra.

Ideally, a photovoltaic material should have a band gap in between 1.0–1.8 eV in order to match with the maximum emission of the solar spectrum which is the visible range (400-800 nm).

FE material	Band-gap (eV)	Reference
BaTiO₃	3.34	(Wemple, 1970)
PbTiO₃	3.88	(Zelezny et al., 2016)
LiNbO₃	3.78	(Dhar & Mansingh, 1990)
KNbO₃	3.24	(T. Zhang et al., 2013)
BiFeO₃	2.67	(Hung et al., 2012)

Table 1. 3: Band-gap values of classic ferroelectric materials.

In this section, two strategies and several studies on bandgap engineering in ferroelectrics are described.

First approach to narrow the band-gap is by controlling the chemical order of the species. As shown on Table 1. 3, BiFeO_3 exhibits the narrowest band-gap (2.67 eV) among ferroelectrics. However, it is only able to capture 20% of the solar spectrum. The modification of Fe/Cr cationic order into parent BiFeO_3 has been related with lower band-gaps. Theoretical studies predicted a band gap range of 1.4–2.0 eV in $\text{BiFe}_{0.5}\text{Cr}_{0.5}\text{O}_3$ (BFCO) compounds (Zhao, Wen, Wang, Guan, & Liu, 2008), and it was experimentally validated by Nechache et al. in 2011. In this study, a PV power conversion efficiency of 6.5% for red laser was reported in BFCO thin films with a photovoltaic current density of 0.99 mA cm^{-2} , one of the largest recorded at the time. More recently, the same authors obtained an efficiency of 8.1% for optimised multilayer system of BFCO (Figure 1. 34 (a)), the highest efficiency ever recorded on conventional ferroelectrics. Each layer absorbed a different part of the solar spectrum. The tunability of the bandgap in each layer arises from the interaction between Fe and Cr with different oxidation states, alternating at B sites of the perovskite. By inspection of Figure 1. 34 (b) the band-gaps are determined from 1.4 to 3.2 eV (from 885 to 388 nm) which covers wide range of solar spectrum.

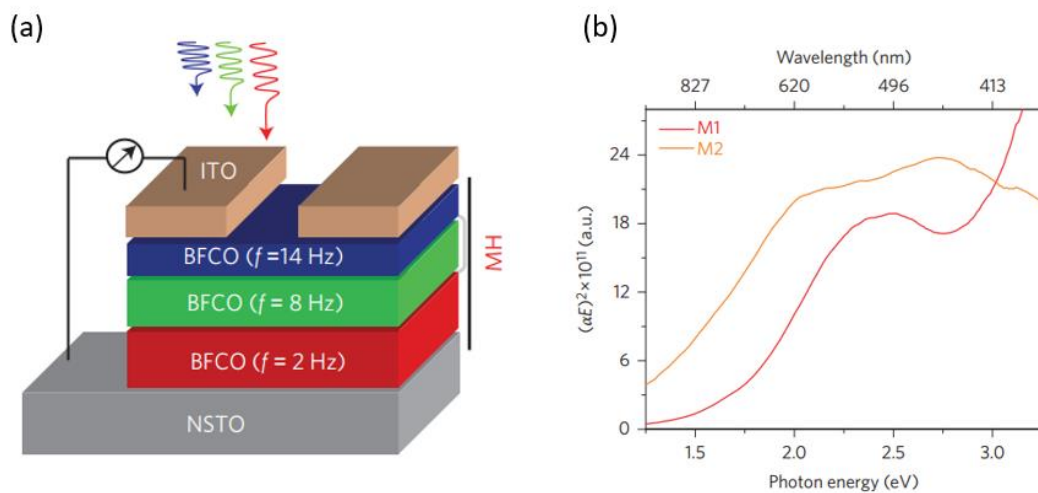


Figure 1. 34: (a) Illustration of the tested BFCO multilayer structure. (b) $(\alpha E)^2$ as a function of photon energy, in arbitrary units (a.u.).

In addition, Zhang et al. reported a new FE compound, KBiFe_2O_5 , which presented a band-gap down to 1.6 eV and obtained photovoltage and photocurrent values comparable to those described for BiFeO_3 .

Second route to reduce the band-gap would be chemical engineering. Indeed, solid solutions permit the properties of different compounds to be adapted.

This thesis is devoted on band-gap engineering for solid solutions based on KNbO_3 .

Different electronic band diagrams of KNbO_3 along the symmetry lines of the Brillouin zone are shown in Figure 1. 35. Both, Okoye and Sinha et al. calculations are in agreement for cubic KNbO_3 , as shown in Figure 1. 35 (a) and (c). The indirect band gap appears between the top valence band at the R point and the bottom of the conduction band at the Γ point. However, Xu et al reported that KNbO_3 exhibits the valence-band maxima at R points and the conduction-band minima at G points, indicating again indirect band-gap (Figure 1. 35 (b)). In contrast, Modak & Ghosh obtained direct band-gap (Figure 1. 35 (d)). Table 1. 4 and Table 1. 5 show theoretical and experimental band-gap values for KN reported in literature.

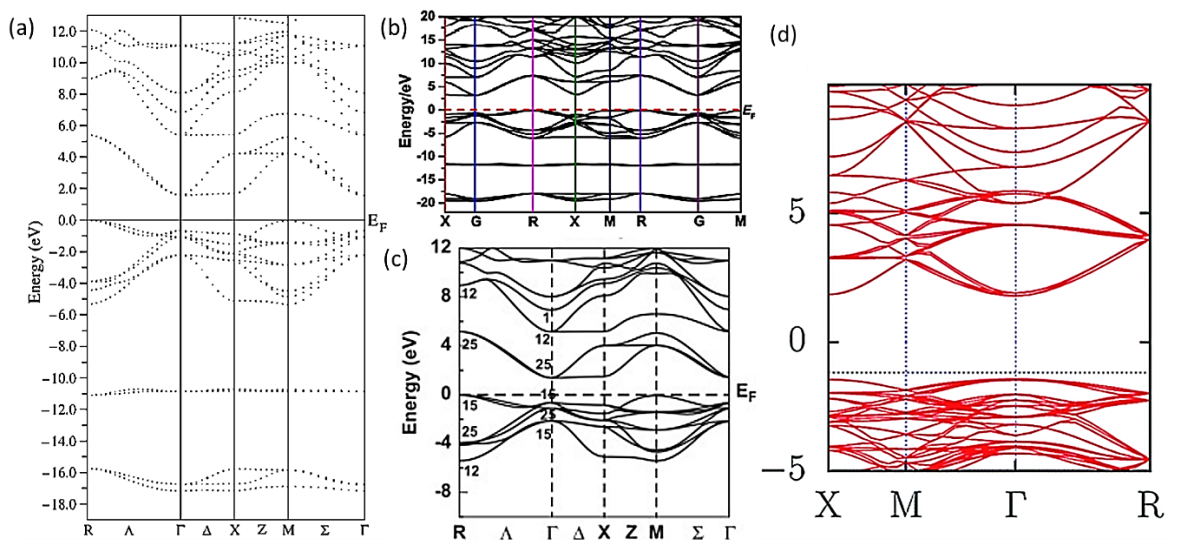


Figure 1. 35: (a), (b), (c) and (d): Different models for the electronic band structure of cubic KNbO_3 along the symmetry lines of the Brillouin zone.

	Methods	Band-gap (eV)	References
Direct Band-gaps	LDA	1.98	(Fengcong Wang & Rappe, 2015; Xu, Wu, Zhang, Wu, & Ding, 2017a)
	PBE	1.98	
	HSE06	3.83, 3.10	
	GWO	3.89	
	FPLAP	1.58	
Indirect Band-gaps	LDA	1.43	(Fengcong Wang & Rappe, 2015; Xu, Wu, Zhang, Wu, & Ding, 2017a)
	PBE	1.42	
	HSE06	3.24	
	GWO	3.28	

Table 1. 4: Calculated direct and indirect band-gaps gaps of KNbO₃ with LDA, PBE, HSE06, and GWO.

Methods	Band-gaps	References
Absorbance	3.24	(T. Zhang et al., 2013)
Spectroscopy	3.14	(Liu, Chen, Li, & Zhang, 2007)
Ellipsometry	3.95	(Tyunina et al., 2015)
spectroscopy	3.80	(Ilya Grinberg et al., 2013)
Diffuse reflectance spectroscopy	3.10	(Eng, Barnes, Auer, & Woodward, 2003)

Table 1. 5: Experimental band-gaps of KNbO₃, measured by absorbance, ellipsometry and diffuse reflectance spectroscopy. Authors do not differentiate between direct and indirect band-gaps.

The interest in KN in this work arises from a crucial study (I. Grinberg et al., 2013) which reported high polarization ($20 \mu\text{C}/\text{cm}^2$, Figure 1. 36 (a)) and narrow band gap never described before (1.1 eV for $x=0.2$) (Figure 1. 36 (b)), in $(1-x) \text{KNbO}_3-x\text{BaNi}_{0.5}\text{Nb}_{0.5}\text{O}_{3-\delta}$ (KN-BNN) 20 μm thick- film. F.Wang & Rappe elucidated the origin of this band-gap narrowing by first principle calculations. Maximum valence band is composed by hybridized Ni 3d and O 2p orbitals, while the minimum conduction band occupied by Nb 4d states. Hence, they suggested that the filled Ni 3d gap states in the KN-BNN ceramics play an important role in narrowing the bandgap, which provides a guide for designing and optimising new FE photovoltaic materials.

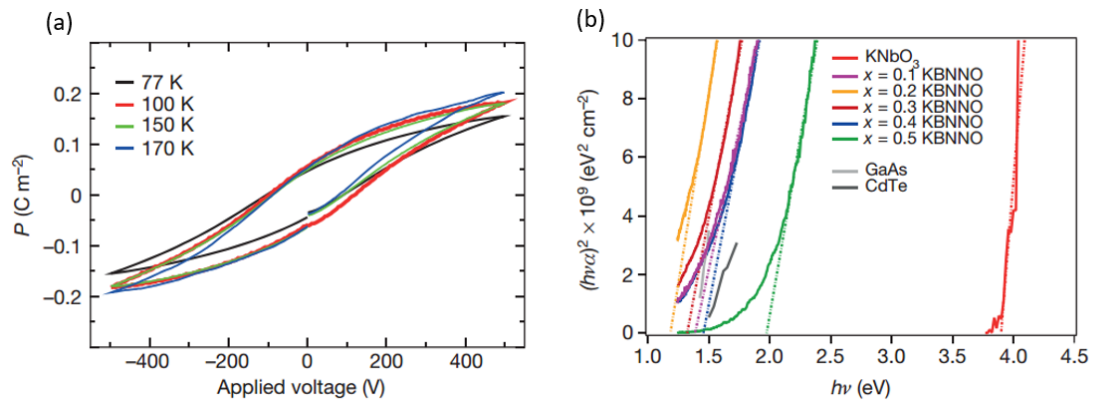


Figure 1. 36: (a) Ferroelectric loops for a thick film KN-BNN $x=0.01$ at 10^{-7} torr and 77–170K (b) Ellipsometry measurements for KN-BNN $x=0.0$ – 0.5 reveal a bandgap narrowing from 3.8 eV to 1.18 eV (I. Grinberg et al., 2013)

Consequently, this composition, KN-BNN, has been largely investigated in the last four years. Two studies reported similar band gap narrowing in the ceramic KN-BNN system and both showed the lowest band-gap (1.18 eV) corresponds to $x=0.2$ (Figure 1. 37 (a) and (b)) (Song et al., 2017). It was also suggested that KN-BNN exhibits ferromagnetism at RT which would offer great potential in multiferroic applications (Zhou, Deng, Yang, & Chu, 2014).

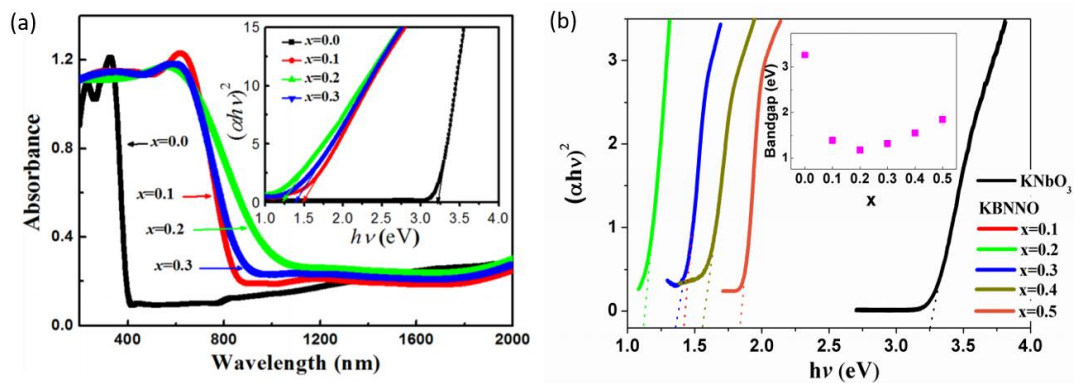


Figure 1. 37: (a) Absorption spectra and $(\alpha h\nu)^2$ versus $h\nu$ (inset) of KN-BNN bulk ceramics ($x=0, 0.1, 0.2, 0.3$) (Zhou et al., 2014) (b) $(\alpha h\nu)^2$ versus photon energy in KN-BNN ($x=0, 0.1, 0.2, 0.3, 0.4$ and 0.5) bulk ceramics sintered by solid state reaction (Song et al., 2017) Both show the narrowest band-gap (~ 1 eV) for $x=0.2$.

Zhang et al reported a narrow band-gap (up to 1.39 eV) and P-E loop ($P_r = 1.4 \mu\text{C}/\text{cm}^2$) in KN-BNN thin films prepared by PLD (Figure 1. 38. (i) and (ii)). The band gap reduction of KN-BNN was attributed to the emergence of Ni 3d gap states. Furthermore, authors proposed a linear dependence between optical band-gap and the Ni content (Figure 1. 38. (i) (c)).

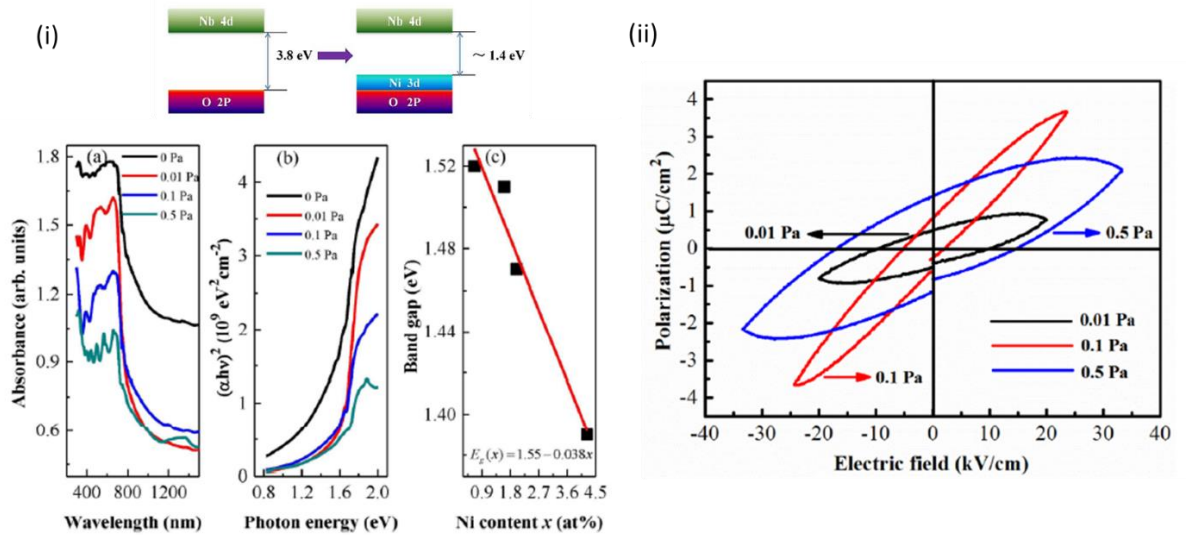


Figure 1. 38: (i) (a) Absorption spectra and (b) absorption coefficient square $(\alpha h\nu)^2$ vs. Photon energy $(h\nu)$ plots of KN-BNN films deposited at different O₂ pressures. (c) The bandgap of the films as a function of the Ni content. (ii) P-E loops for KN-BNN thin films deposited at O₂ pressures of 0.01, 0.1, and 0.5 Pa.

Bai et al studied optic and ferroelectric properties of KN-BNN bulk ceramic with $x=0.01$, stoichiometric (CI) and non-stoichiometric (CII) created by a potassium deficiency. Figure 1. 39 (a) and (b) illustrate absorbance and photon energy for both materials. The authors affirmed that measuring absorbance (Figure 1. 39 (a)) is not a reliable method to determine the band-gap in solid samples. Then they decided to measure diffuse reflectance and to plot the function $(F(R) \cdot hv)^2$ (being $F(R)$ Kubelka-Munk formula) to determine the band-gaps of KN-BNN (Figure 1. 39 (b)). The samples CI and II exhibit band gaps of 1.40 eV and 1.48 eV, respectively. Worth to mention, the sample CI was able to withstand an electric field up to 80 kV/cm (Figure 1. 39 (c)).

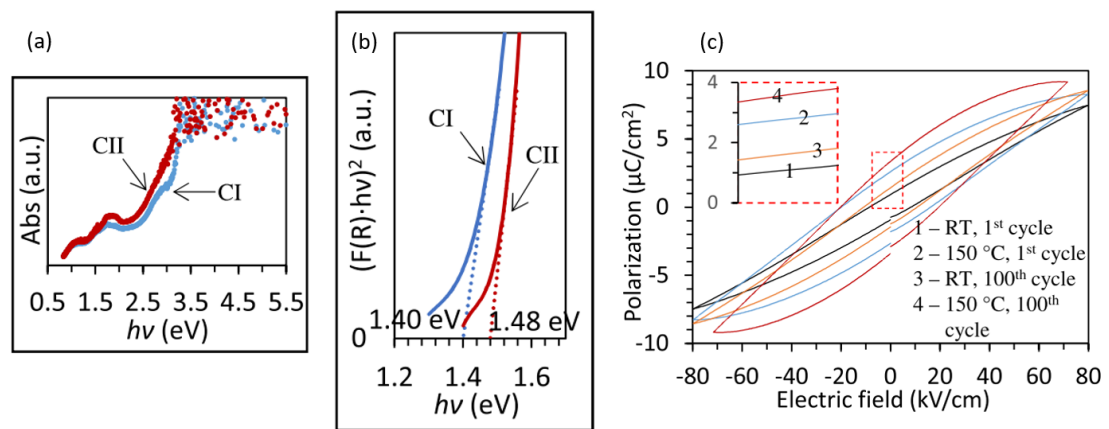


Figure 1. 39: (a) Absorption spectra and (b) $(F(R) \cdot hv)^2$ versus $h\nu$ for KN-BNN ($x=0.01$) bulk ceramic (CI stoichiometry and CII non- stoichiometry). (c) P-E loop of KN-BNN ($x=0.01$) at RT.(Bai, Siponkoski, Peräntie, Jantunen, & Juuti, 2017).

Very recently, a study has been published by the same author (Bai, Tofel, Palosaari, Jantunen, & Juuti, 2017) that compares $(\text{K}_{0.5}\text{Na}_{0.5})\text{NbO}_3$ (KNN) and $0.98(\text{K}_{0.5}\text{Na}_{0.5})\text{NbO}_3 - 0.02\text{Ba}(\text{Ni}_{0.5}\text{Nb}_{0.5})\text{O}_3$ (KNN-BNNO) ceramics. This last compound revealed large ferroelectric ($26\ \mu\text{C}/\text{cm}^2$) and piezoelectric ($100\ \text{pm}/\text{V}$) properties (Figure 1. 40 (b)) accompanied with a surprising narrow bandgap (1.6 eV).

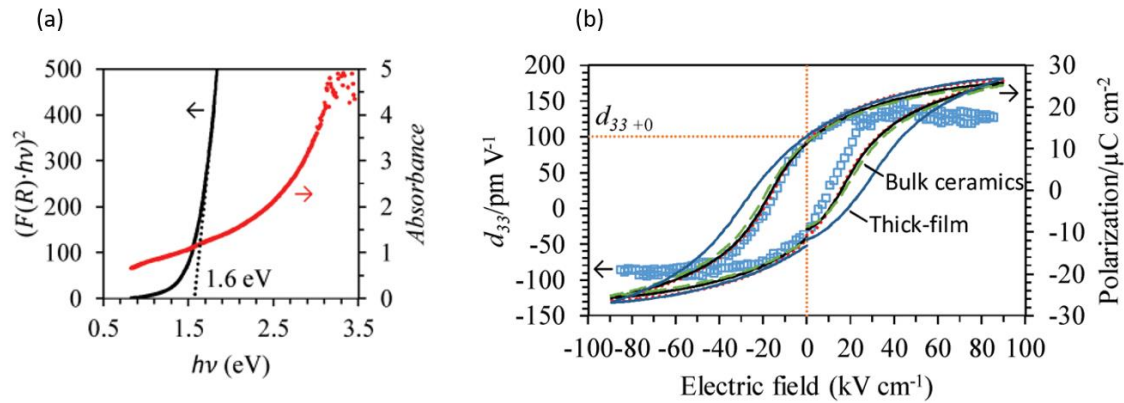


Figure 1. 40: (a) Absorption spectra and Tauc plot of the thick-film KN-BNN. (b) Ferroelectric loop for KN-BNN ceramic and thick-film. (Bai, Siponkoski, et al., 2017)

However, contradictory results for KN-BBNZ band gap are found in literature. (Zhou, Deng, Yang, & Chu, 2016). Figure 1. 41 (a) illustrates the absorption spectra and the $(F(R)/h\nu)^2$ versus the photon energy of KN-BNN thin film. The two slopes pointed at 1.85 eV (2) and at 2.51 eV (1), are attributed, respectively, to intraband transition of Ni 3d orbitals and band-to-band transition from hybridized Ni 3d and O 2p to Nb 4d states (Figure 1. 41 (b)).

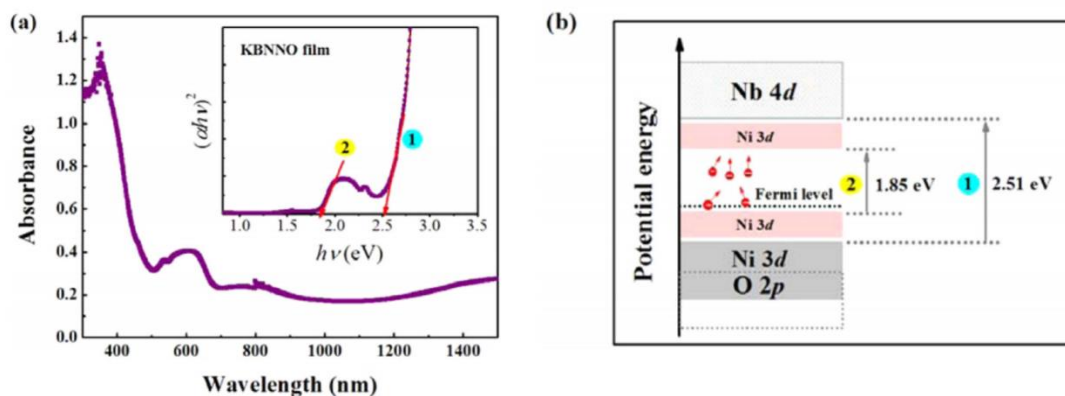


Figure 1. 41: (a) Absorption spectra of the KN-BNN film on Pt(111)/Ti/SiO₂/Si(100) substrate and a plot of $(F(R)/h\nu)^2$ as a function of $h\nu$ (inset). (b) A schematic illustration of intraband electronic transition in KN-BNN. (Zhou et al., 2016).

Moreover, Wu et al. synthesised KN-BNN ($0 \leq x \leq 0.4$) nanocrystals fabricated by sol-gel based on Pechini method and showed that Ba and Ni modifications slightly narrow the original band-gap of KN, only 0.15 eV smaller than KN (Figure 1. 42 (b)). Three broad absorption bands (beside the band-gap) can be found in the absorbance spectra at 450 nm (2.75 eV), at 720 nm (1.72 eV) and at 1150 nm (1.07 eV) (Figure 1. 42 (a)). and attributed to d-d transitions created by Ni^{+2} ions in the crystal of KN-BNN. Authors concluded that previous reports which gave band gap values of 1.1-1.5 eV of KN-BNN may be misinterpreting the 720 nm absorption band in KN-BNN as the intrinsic band-gap absorption

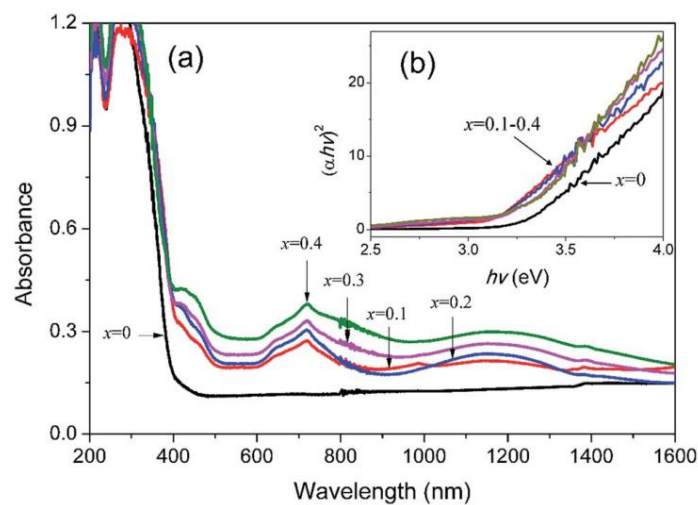


Figure 1. 42: Absorption spectra of KNbO_3 ($x = 0$) and KN-BNN ($x = 0.1-0.4$); (b) plots of $(F(R) h\nu)^2 - h\nu$ (inset). (Wu et al., 2016)

These studies gave a boost to develop theoretical and experimental works based on the band-gap tunability of the compounds based on KN. Systematic band-gap narrowing was reported in different solid solutions based on KN, such as $(1-x) \text{KNbO}_3 - x \text{Ba}(\text{Co}_{0.5}\text{Nb}_{0.5})\text{O}_{3-\delta}$ (KBCNO) which shifts down to 2.4 eV (Limin Yu, Jia, Yi, Shan, & Han, 2016). Very recently systems that has been studied include $\text{KNb}_{1-x}\text{Fe}_x\text{O}_{3-\delta}$ (Nie et al., 2017) and $(1-x) \text{KNbO}_3 - x \text{Ba}(\text{Nb}_{0.5}\text{Fe}_{0.5})\text{O}_3$ (KBNFO) which show a reduction of the band gap from 3.2 eV down to 1.74 eV (Lu Yu, Deng, Zhou, Yang, & Chu, 2017).

1.5. Motivations

These new ferroelectric oxides based on KNbO_3 with lower band-gaps rely on the presence of a large concentration of oxygen vacancies. This fact critically affects the

polarization switching and can also trap the photo-excited carriers and consequently increase the charge recombination rate. Hence, oxygen vacancies are detrimental to ferroelectric and photovoltaic properties. First principle calculations estimated the bandgaps and spontaneous polarisation for vacancy-free KNbO₃ co-doped with Zn⁺² in B-site and A₁⁺² and A₂⁺³ substitution on the A-site (A₁⁺²= Pb²⁺, Ba²⁺, Sr²⁺; A₂⁺³= La³⁺, Bi³⁺) in order to achieve charge neutrality. The calculated band-gaps for these systems present values between 2.92 eV and 2.11 eV (F Wang, Grinberg, & Rappe, 2014).

This motivates us to investigate alternative strategies to lower band-gap while preserving ferroelectricity and without creating oxygen vacancies. The approach to reduce the band-gap of parent KN in this work relies on replacing Nb⁵⁺ cations by lower valence transition metals (Me³⁺) dopants. The transition metals were selected following the periodic table order (Mn, Fe, Co and Ni). Furthermore K⁺¹ will be substituted by Bi⁺³ in order to maintain the compositions stoichiometry. The mechanism which leads to the band-gap narrowing is the repulsion between non-bonding 3dⁿ orbitals of the Me³⁺ and 2p⁶ orbitals of O²⁻ upshifting the VBM.

1.6. Aims and Objectives

1.6.1. Aims

Growing concerns about the impact of burning fossil fuels on the environment and our dependence on these limited resources, it is driving the development and the research of sustainable energies. Among others, the sun is the most abundant supplier of energy on Earth and promising long-term source to replace the traditional fossil fuels. Very recently, ferroelectric materials have emerged as potential candidates as photovoltaic materials. This work aims to provide fundamental knowledge and experimental evidence of the mechanisms which leads to band gap narrowing in ferroelectrics. In more detail, this investigation is focused on systems based on well-known ferroelectric perovskite, KNbO₃. Moreover, one of the aims of this investigation is to contribute to the scientific community the good practice of preparing KNbO₃ by conventional routes and to fill the gap that exists in the literature about the electric properties of this compound, due to difficulties in its preparation and low densification.

1.6.2. Research objectives

To address the key aims, this research has the following objectives:

- ⇒ To determinate the current state of the art knowledge in photo-ferroelectrics and band-gap engineering in ferroelectrics oxides.
- ⇒ To develop a strategy to narrow band-gaps in FE, avoiding oxygen vacancies.
- ⇒ To prepare bulk ceramics by solid state reaction for all the systems explored in this work and to optimise their processing.
- ⇒ Experimental validation of theoretical predictions and controversies in the literature.
- ⇒ To investigate the impact of BiMeO₃ (with Me= Mn, Fe, Co and Ni) doping on the structure, dielectric, ferroelectric and optical properties of KNbO₃.
- ⇒ To prepare thin films by pulsed laser deposition.
- ⇒ To measure photoresponse along the materials which present the most promising characteristics (low band-gaps and ferroelectricity).
- ⇒ Extract significant outcomes regarding the ability to control the band-gap while maintaining the spontaneous polarisation in these compounds.

1.6.3. Thesis overview

The thesis structure is organised as follows:

In **Chapter 1** the bases required to understand this research work even if someone is specialised on another discipline, have been explained. Furthermore, previous studies in this research topic have been reviewed.

Chapter 2 describes the techniques and methods used to prepare and characterise the samples which are the object of this work.

The first part of **Chapter 3** is focused on the optimisation of synthesis and sintering of KNbO₃. In addition, the second part shows the complete characterisation of KN.

Chapter 4 shows the complete characterisation of $(1-x)$ KNbO_{3-x} ($\text{Ba}_{0.5}\text{Bi}_{0.5}$) ($\text{Zn}_{0.5}\text{Nb}_{0.5}$) O_3 ($x=0, 0.05, 0.10, 0.15, 0.20$ and 0.25) system. Experimental results are compared with the predictions of first principles calculations.

Chapters 5,6,7 and 8 include the main results corresponding to the binary systems $(1-x)$ KNbO_{3-x} BiMeO_3 being $\text{Me}=\text{Fe, Mn, Co}$ and Ni with $x=0, 0.05, 0.10, 0.15, 0.20$ and 0.25 , from the point of view of ceramic processing and structural, dielectrical and optical characterisation.

Chapter 9 addresses the controversy found in the literature about the band-gap of KN-BNN and KNN-BNN.

Chapter 10 and 11 contain the discussion and the main conclusions of this research work, respectively.

1.7. References

- Ahn, C. H., Rabe, K. M., & Triscone, J.-M. (2004). Ferroelectricity at the Nanoscale: Local Polarization in Oxide Thin Films and Heterostructures. *Science*, *303*(5657), 488–491. <https://doi.org/10.1126/science.1092508>
- Alexe, M. (2012). Local mapping of generation and recombination lifetime in BiFeO_3 single crystals by scanning probe photoinduced transient spectroscopy. *Nano Letters*, *12*(5). <https://doi.org/10.1021/nl300618e>
- Alexe, M., & Hesse, D. (2011). Tip-enhanced photovoltaic effects in bismuth ferrite. *Nature Communications*, *2*(1). <https://doi.org/10.1038/ncomms1261>
- Arlt, G. (1990). Twinning in ferroelectric and ferroelastic ceramics: stress relief. *Journal of Materials Science*, *25*(6), 2655–2666. <https://doi.org/10.1007/BF00584864>
- Bai, Y., Siponkoski, T., Peräntie, J., Jantunen, H., & Juuti, J. (2017). Ferroelectric, pyroelectric, and piezoelectric properties of a photovoltaic perovskite oxide. *Applied Physics Letters*, *110*(6). <https://doi.org/10.1063/1.4974735>
- Bai, Y., Tofel, P., Palosaari, J., Jantunen, H., & Juuti, J. (2017). A Game Changer : A Multifunctional Perovskite Exhibiting Giant Ferroelectricity and Narrow Bandgap

- with Potential Application in a Truly Monolithic Multienergy Harvester or Sensor, *1700767*, 1–7. <https://doi.org/10.1002/adma.201700767>
- Baier-Saip, J. A., Ramos-Moor, E., & Cabrera, A. L. (2005). Raman study of phase transitions in KNbO₃. *Solid State Communications*, *135*(6), 367–372. <https://doi.org/http://dx.doi.org/10.1016/j.ssc.2005.05.021>
- Bhalla, A. S., Guo, R., & Roy, R. (2000). The perovskite structure. Review of its role in ceramic science and technology. *Materials Research Innovations*, *4*(1), 3–26. <https://doi.org/10.1007/s100190000062>
- Bhatnagar, A., Ayan, R. C., Young, H. K., Hesse, D., & Alexe, M. (2013). Role of domain walls in the abnormal photovoltaic effect in BiFeO₃. *Nature Communications*, *4* (2835). <https://doi.org/10.1038/ncomms3835>
- Birol, H., Damjanovic, D., & Setter, N. (2005). Preparation and characterization of KNbO₃ ceramics. *Journal of the American Ceramic Society*, *88*(7), 1754–1759. <https://doi.org/10.1111/j.1551.2916.2005.00347.x>
- Buse, K. (1993). Thermal gratings and pyroelectrically produced charge redistribution in BaTiO₃ and KNbO₃. *Journal of the Optical Society of America B*, *10*(7), 1266–1275. <https://doi.org/10.1364/JOSAB.10.001266>
- Butler, K. T., Frost, J. M., & Walsh, A. (2015). Ferroelectric materials for solar energy conversion: photoferroics revisited. *Energy & Environmental Science*, *8*(3), 838–848. <https://doi.org/10.1039/c4ee03523b>
- Cao, W., & Cross, L. E. (1993). Theoretical model for the morphotropic phase boundary in lead zirconate-lead titanate solid solution. *Physical Review B*, *47*(9), 4825–4830. <https://doi.org/10.1103/PhysRevB.47.4825>
- Catalan, G., & Scott, J. F. (2009). Physics and applications of bismuth ferrite. *Advanced Materials*, *21*(24), 2463–2485. <https://doi.org/10.1002/adma.200802849>
- Cheng, S. Y., Ho, N. J., & Lu, H. Y. (2008). Polar directions of the 90° and 180° ferroelectric domains in tetragonal barium titanate determined by electron-backscatter diffraction. *Journal of the American Ceramic Society*, *91*(4), 1244–1248. <https://doi.org/10.1111/j.1551-2916.2007.02251.x>
- Cheong, S.-W., & Mostovoy, M. (2007). Multiferroics: a magnetic twist for

- ferroelectricity. *Nature Materials*, 6(1), 13–20. <http://dx.doi.org/10.1038/nmat1804>
- Choi, T., Lee, S., Choi, Y. J., Kiryukhin, V., & Cheong, S.-W. (2009). Switchable ferroelectric diode and photovoltaic effect in BiFeO₃. *Science*, 324(5923). <https://doi.org/10.1126/science.1168636>
- Cohen, R. E. (1992). Origin of ferroelectricity in perovskite oxides. *Nature*, 358(6382), 136. <https://doi.org/10.1038/358136a0>
- Cowley, R. A., Gvasaliya, S. N., Lushnikov, S. G., Roessli, B., & Rotaru, G. M. (2011). Relaxing with relaxors: a review of relaxor ferroelectrics. *Advances in Physics*, 60(2), 229–327. <https://doi.org/10.1080/00018732.2011.555385>
- Damjanovic, D. (1998). Ferroelectric, dielectric and piezoelectric properties of ferroelectric thin films and ceramics. *Reports on Progress in Physics*, 61(9), 1267–1324. <https://doi.org/10.1088/0034-4885/61/9/002>
- Dhar, A., & Mansingh, A. (1990). Optical properties of reduced lithium niobate single crystals. *Journal of Applied Physics*, 68(11). <https://doi.org/10.1063/1.346951>
- Dharmadhikari, V. S., & Grannemann, W. W. (1982). Photovoltaic properties of ferroelectric BaTiO₃ thin films rf sputter deposited on silicon. *Journal of Applied Physics*, 53(12), 8988–8992. <https://doi.org/10.1063/1.330456>
- Denton, A. R., & Ashcroft, N. W. (1991). Vegard's law. *Phys. Rev. A*, 43(6), 3161–3164. <https://doi.org/10.1103/PhysRevA.43.3161>
- Dogan, F., Lin, H., Guilloux-Viry, M., & Peña, O. (2015). Focus on properties and applications of perovskites. *Science and Technology of Advanced Materials*, 16(2), 20301. Retrieved from <http://stacks.iop.org/1468-6996/16/i=2/a=020301>
- Eerenstein, W., Mathur, N. D., & Scott, J. F. (2006). Multiferroic and magnetoelectric materials. *Nature*, 442(7104), 759–765. <http://dx.doi.org/10.1038/nature05023>
- Eng, H. W., Barnes, P. W., Auer, B. M., & Woodward, P. M. (2003). Investigations of the electronic structure of d⁰ transition metal oxides belonging to the perovskite family. *Journal of Solid State Chemistry*, 175(1). [https://doi.org/10.1016/S0022-4596\(03\)00289-5](https://doi.org/10.1016/S0022-4596(03)00289-5)
- Fang, D., Li, F., Liu, B., Zhang, Y., Hong, J., & Guo, X. (2013). Advances in Developing

- Electromechanically Coupled Computational Methods for Piezoelectrics/Ferroelectrics at Multiscale. *Applied Mechanics Reviews*, 65(6), 60802. <https://doi.org/10.1115/1.4025633>
- Fiebig, M., Lottermoser, T., Meier, D., & Trassin, M. (2016). The evolution of multiferroics. *Nature Reviews Materials*, 1(8), 16046. <https://doi.org/10.1038/natrevmats.2016.46>
- Flueckiger, U., & Arend, H. (1977). Synthesis of KNbO₃ Powder. *Journal American Ceramic Society*, 56(575–7).
- Fridkin, V. (2001). Bulk photovoltaic effect in noncentrosymmetric crystals. *Crystallography Reports*, 46(4), 654–658. <https://doi.org/10.1134/1.1387133>
- Fridkin, V. M. (1979). *Photo-ferroelectrics* (Springer). New York.
- Fridkin, V. M., Grekov, A. A., Ionov, P. V., Rodin, A. I., Savchenko, E. A., & Mikhailina, K. A. (1974). Photoconductivity in certain ferroelectrics. *Ferroelectrics*, 8(1), 433–435. <https://doi.org/10.1080/00150197408234118>
- Glass, A. M., von der Linde, D., Auston, D. H., & Negran, T. J. (1975). Excited state polarization, bulk photovoltaic effect and the photorefractive effect in electrically polarized media. *Journal of Electronic Materials*, 4(5). <https://doi.org/10.1007/BF02660180>
- Glass, A. M., Von Der Linde, D., & Negran, T. J. (1974). High-voltage bulk photovoltaic effect and the photorefractive process in LiNbO₃. *Applied Physics Letters*, 25(4), 233–235. <https://doi.org/10.1063/1.1655453>
- Goldschmidt, V. M. (1927). *Geochemisce Verterlungsgesetze der Elemente*. (Norske Vid). Oslo.
- Grekov, A. A., Malitskaya, M. A., Spitsina, V. D., & Fridkin, V. M. (1970). No Title. *Soviet physics Crystallography* (15), 423.
- Grey, R. B. (1949). Transducer and method of making the same. U.S. Pat. No. 2486560. Retrieved from <https://www.google.ch/patents/US2486560>
- Grinberg, I., West, D. V., Torres, M., Gou, G., Stein, D. M., Wu, L., L., Chen G., Gallo E., Akbashev A. R., Davies P.K., Spanier J.E. and Rappe, A. M. (2013). Perovskite

- oxides for visible-light-absorbing ferroelectric and photovoltaic materials. *Nature*, 503(7477) 509. <https://doi.org/10.1038/nature12622>
- Groover, M. P. (1997). *Fundamentos de manufactura moderna: Materiales, Procesos y Sistemas*. (Prentice-H). Mexico.
- Guo, R., Cross, L. E., Park, S.-E., Noheda, B., Cox, D. E., & Shirane, G. (2000). Origin of the high piezoelectric response in $\text{PbZr}_{(1-x)}\text{Ti}_x\text{O}_3$. *Physical Review Letters*, 84(23), 5423–5426. <https://doi.org/10.1103/PhysRevLett.84.5423>
- Haertling, G. (1999). Ferroelectric ceramics: history and technology. *Journal of the American Ceramic Society*, 82(4), 718–818. <https://doi.org/10.1111/j.1151-2916.1999.tb01840.x>
- Hazen, R. M. (1988). Perovskite. *Scientific American*, 258, 52–61.
- Hewat, A. W. (1973). Cubic-tetragonal-orthorhombic-rhombohedral ferroelectric transitions in perovskite potassium niobate: Neutron powder profile refinement of the structures. *Journal of Physics C: Solid State Physics*, 6(16). <https://doi.org/10.1088/0022-3719/6/16/010>
- Hung, C.-M., Tu, C.-S., Yen, W. D., Jou, L. S., Jiang, M.-D., & Schmidt, V. H. (2012). Photovoltaic phenomena in BiFeO_3 multiferroic ceramics. *Journal of Applied Physics*, 111(7). <https://doi.org/10.1063/1.3675984>
- Ikeda, N., Ohsumi, H., Ohwada, K., Ishii, K., Inami, T., Kakurai, K., Murakami, Y., Yoshii, K., Mori, S., Horibe, and Kito, H. (2005). Ferroelectricity from iron valence ordering in the charge-frustrated system LuFe_2O_4 . *Nature*, 436(7054), 1136–1138. <http://dx.doi.org/10.1038/nature04039>
- Ito, Y., & Uchino, K. (2005). Piezoelectricity. In *Encyclopedia of RF and Microwave Engineering*.
- Jaffe, B., Cook, W. R., & Jaffe, H. L. (1971). *Piezoelectric ceramics*. (Academic P). London.
- Ji, W., Yao, K., & Liang, Y. C. (2011). Evidence of bulk photovoltaic effect and large tensor coefficient in ferroelectric BiFeO_3 thin films. *Physical Review B - Condensed Matter and Materials Physics*, 84(9). <https://doi.org/10.1103/PhysRevB.84.094115>

- Jona, F., & Shirane, G. (1962). *Ferroelectric crystals* (Ed. Pergam). New York.
- Kakimoto, K.-I., Masuda, I., & Ohsato, H. (2005). Lead- free KNbO_3 piezoceramics synthesized by pressure- less sintering. *Journal of the European Ceramic Society*, 25(12), 2719–2722. <https://doi.org/10.1016/j.jeurceramsoc.2005.03.209>
- Kholkin, A., Boiarkine, O., & Setter, N. (1998). Transient photocurrents in lead zirconate titanate thin films. *Applied Physics Letters*, 72(1), 130–132. <https://doi.org/10.1063/1.120663>
- Kim, D., Joung, M., Seo, I., Hur, J., Kim, J., Kim, B. and Nahm, S. (2014). Influence of sintering conditions on piezoelectric properties of KNbO_3 ceramics. *Journal of the European Ceramic Society*, 34, 4193–4200.
- Koch, W. T. H., Munser, R., Ruppel, W., & Würfel, P. (1975). Bulk photovoltaic effect in BaTiO_3 . *Solid State Communications*, 17(7), 847–850. [https://doi.org/http://dx.doi.org/10.1016/0038-1098\(75\)90735-8](https://doi.org/http://dx.doi.org/10.1016/0038-1098(75)90735-8)
- Kraut, W., & Von Baltz, R. (1979). Anomalous bulk photovoltaic effect in ferroelectrics: A quadratic response theory. *Physical Review B*, 19(3). <https://doi.org/10.1103/PhysRevB.19.1548>
- Kreisel, J., Alexe, M., & Thomas, P. A. (2012). A photoferroelectric material is more than the sum of its parts. *Nature Materials*, 11(4), 260. <http://dx.doi.org/10.1038/nmat3282>
- Ladj, R., Magouroux, T., Eissa, M., Dubled, M., Mugnier, Y., Dantec, R. Le and Elaissari, A. (2013). Aminodextran-coated potassium niobate (KNbO_3) nanocrystals for second harmonic bio-imaging. *Colloids and Surfaces A: Physicochemical and Engineering Aspects*, 439, 131–137. <http://dx.doi.org/10.1016/j.colsurfa.2013.02.025>
- Lebeugle, D., Colson, D., Forget, A., Viret, M., Bonville, P., Marucco, J. F., & Fusil, S. (2007). Room-temperature coexistence of large electric polarization and magnetic order in BiFeO_3 single crystals. *Physical Review B*, 76(2), 24116. <https://doi.org/10.1103/PhysRevB.76.024116>
- Li, F., Jin, L., Xu, Z., & Zhang, S. (2014). Electrostrictive effect in ferroelectrics: An alternative approach to improve piezoelectricity. *Applied Physics Reviews*, 1(1).

<https://doi.org/10.1063/1.4861260>

- Liu, J. W., Chen, G., Li, Z. H., & Zhang, Z. G. (2007). Hydrothermal synthesis and photocatalytic properties of ATaO₃ and ANbO₃ (A = Na and K). *International Journal of Hydrogen Energy*, 32(13). <https://doi.org/10.1016/j.ijhydene.2006.10.005>
- Lv, X., Li, Z., Wu, J., Xiao, D., & Zhu, J. (2016). Lead-Free KNbO₃:xZnO Composite Ceramics. *ACS Applied Materials & Interfaces*, 8(44), 30304–30311. <https://doi.org/10.1021/acsami.6b11677>
- Malic, B., Jenko, D., Holc, J., Hrovat, M., & Kosec, M. (2008). Synthesis of sodium potassium niobate: A diffusion couples study. *Journal of the American Ceramic Society*, 91(6). <https://doi.org/10.1111/j.1551-2916.2008.02376.x>
- Matsumoto, K., Hiruma, Y., Nagata, H., & Takenaka, T. (2007). Piezoelectric properties of KNbO₃ ceramics prepared by ordinary sintering. *Ferroelectrics*, 358(1 PART 4). <https://doi.org/10.1080/00150190701537166>
- Matthias, B. T. (1949). New Ferroelectric Crystals. *Phys. Rev.*, 75(11), 1771. <https://doi.org/10.1103/PhysRev.75.1771>
- Merz, W. J. (1954). Domain Formation and Domain Wall Motions in Ferroelectric BaTiO₃ Single Crystals. *Physical Review* 95(3), 690–698. <https://doi.org/10.1103/PhysRev.95.690>
- Mitcheson, P. D., Yeatman, E. M., Rao, G. K., Holmes, A. S., & Green, T. C. (2008). Energy harvesting from human and machine motion for wireless electronic devices. *Proceedings of the IEEE*, 96(9), 1457–1486. <https://doi.org/10.1109/JPROC.2008.927494>
- Modak, B., & Ghosh, S. K. (2016). Improving KNbO₃ photocatalytic activity under visible light. *RSC Advances*, 6(12). <https://doi.org/10.1039/c5ra26079e>
- Montemezzani, G., & Günter, P. (1990). Thermal hologram fixing in pure and doped KNbO₃ crystals. *Journal of the Optical Society of America B*, 7(12), 2323–2328. <https://doi.org/10.1364/JOSAB.7.002323>
- Moreau, J. M., Michel, C., Gerson, R., & James, W. J. (1971). Ferroelectric BiFeO₃ X-ray and neutron diffraction study. *Journal of Physics and Chemistry of Solids*, 32(6),

- 1315–1320. [https://doi.org/http://dx.doi.org/10.1016/S0022-3697\(71\)80189-0](https://doi.org/http://dx.doi.org/10.1016/S0022-3697(71)80189-0)
- Mostovoy, M. (2006). Ferroelectricity in Spiral Magnets. *Physical Review Letters*, 96(6), 67601. <https://doi.org/10.1103/PhysRevLett.96.067601>
- Moulson, A. J., & Herbert, J. M. (1990). *Electroceramics : materials, properties, applications*. Chapman & Hall.
- Nechache, R., Harnagea, C., Licoccia, S., Traversa, E., Ruediger, A., Pignolet, A., & Rosei, F. (2011). Photovoltaic properties of Bi₂FeCrO₆ epitaxial thin films. *Applied Physics Letters*, 98(20). <https://doi.org/10.1063/1.3590270>
- Nelson, J. (2003). *The physics of solar cells* (Imperial C). London.
- Nie, D., Zhang, J., Deng, W., Chen, X., Mao, Z., & Tang, L. (2017). Narrow Band Gap and Room-temperature Ferromagnetism in KNb_{1-x}Fe_xO_{3-δ}. *Chinese Journal of Chemical Physics*, 30(1), 97–102. <https://doi.org/10.1063/1674-0068/30/cjcp1608154>
- Nomura, S., & Uchino, K. (1982). Electrostrictive effect in Pb(Mg_{1/3}Nb_{2/3})O₃ -type materials. *Ferroelectrics*, 41(1), 117–132. <https://doi.org/10.1080/00150198208210614>
- Okoye, C. (2003). Theoretical study of the electronic structure , chemical bonding and optical properties of KNbO₃ in the paraelectric cubic phase. *Journal of Physics: Condensed Matter*, 5945, 5945–5958.
- Pascual-González, C., Berganza, E., Amorín, H., Castro, A., & Algueró, M. (2016). Point defect engineering of high temperature piezoelectric BiScO₃-PbTiO₃ for enhanced voltage response. *Materials and Design*, 108, 501–509. <https://doi.org/10.1016/j.matdes.2016.07.015>
- Pascual-Gonzalez, C., Schileo, G., & Feteira, A. (2016). Band gap narrowing in ferroelectric KNbO₃-Bi(Yb,Me)O₃ (Me=Fe or Mn) ceramics. *Applied Physics Letters*, 109(13), 132902. <https://doi.org/10.1063/1.4963699>
- Pascual-Gonzalez, C., Schileo, G., Khesro, A., Sterianou, I., Wang, D., Reaney, I. M., & Feteira, A. (2017). Band gap evolution and a piezoelectric-to-electrostrictive crossover in (1 - x)KNbO₃-x(Ba_{0.5}Bi_{0.5})(Nb_{0.5}Zn_{0.5})O₃ ceramics. *Journal of Materials Chemistry C*, 5(8), 1990–1996. <https://doi.org/10.1039/C6TC05515J>

- Pliska, T., Fluck, D., Günter, P., Beckers, L., & Buchal, C. (1998). Linear and nonlinear optical properties of KNbO₃ ridge waveguides. *Journal of Applied Physics*, *84*(3), 1186–1195. <https://doi.org/10.1063/1.368184>
- Qin, M., Yao, K., & Liang, Y. C. (2008). High efficient photovoltaics in nanoscaled ferroelectric thin films. *Applied Physics Letters*, *93*(12), 1–4. <https://doi.org/10.1063/1.2990754>
- Rabe, K. M., & Ghosez, P. (2007). First-principles studies of ferroelectric oxides. *Topics in Applied Physics*, *105*, 117.
- Reeves, R. J., Jani, M. G., Jassemnejad, B., & Powell, R. C. (1991). photorefractive properties of KNbO₃. *Physical Review B*, *43*(1).
- Reisman, A., Holtzberg, F., Triebwasser, S., & Berkenblit, M. (1956). Preparation of Pure Potassium Metaniobate. *Journal American Ceramic Society*, *78*, 718–19.
- Rödel, J., Jo, W., Seifert, K. T. P., Anton, E.-M., Granzow, T., & Damjanovic, D. (2009). Perspective on the development of lead-free piezoceramics. *Journal of the American Ceramic Society*, *92*(6). <https://doi.org/10.1111/j.1551-2916.2009.03061.x>
- Rohlfing, M., Krüger, P., & Pollmann, J. (1993). Quasiparticle band-structure calculations for C, Si, Ge, GaAs, and SiC using Gaussian-orbital basis sets. *Physical Review B*, *48*(24), 17791–17805. <https://doi.org/10.1103/PhysRevB.48.17791>
- Roy, R. (1954). Multiple Ion Substitution in the Perovskite Lattice. *Journal of the American Ceramic Society*, *37*(12), 581–588. <https://doi.org/10.1111/j.1151-2916.1954.tb13992.x>
- Ryf, R., Montemezzani, G., & Günter, P. (2001). Long dark decay in highly sensitive Ce doped photorefractive KNbO₃ crystals. *Journal of Optics A: Pure and Applied Optics*, *3*(1), 16. <http://stacks.iop.org/1464-4258/3/i=1/a=303>
- Sani, A., Hanfland, M., & Levy, D. (2002). Pressure and temperature dependence of the ferroelectric-paraelectric phase transition in PbTiO₃. *Journal of Solid State Chemistry*, *167*(2), 446–452. [https://doi.org/10.1016/S0022-4596\(02\)99653-2](https://doi.org/10.1016/S0022-4596(02)99653-2)
- Shirane, G., Danner, H., Pavlovic, A., & Pepinsky, R. (1954). Phase Transitions in Ferroelectric KNbO₃. *Physical Review*, *93*(4), 672–673. <https://doi.org/10.1103/PhysRev.93.672>

- Shockley, W., & Queisser, H. J. (1961). Detailed balance limit of efficiency of p-n junction solar cells. *Journal of Applied Physics*, 32(3). <https://doi.org/10.1063/1.1736034>
- Shvartsman, V. V., Kleemann, W., Haumont, R., & Kreisel, J. (2007). Large bulk polarization and regular domain structure in ceramic BiFeO₃. *Applied Physics Letters*, 90(17), 172115. <https://doi.org/10.1063/1.2731312>
- Sinha, T. P., Dutta, A., Saha, S., Tarafder, K., Sanyal, B., Eriksson, O., & Mookerjee, A. (2012). Electronic structure and optical properties of ordered compounds potassium tantalate and potassium niobate and their disordered alloys. *Physica B: Condensed Matter*, 407(24). <https://doi.org/10.1016/j.physb.2012.09.011>
- Smolenskii, G. A. (1970). No title. *Physical Society of Japan*, 28, 26.
- Song, B., Wang, X., Xin, C., Zhang, L., Song, B., Zhang, Y., ... Tang, J. (2017). Multiferroic properties of Ba/Ni co-doped KNbO₃ with narrow band-gap. *Journal of Alloys and Compounds*. <https://doi.org/10.1016/j.jallcom.2017.01.180>.
- Spaldin, N. A. (2017). Multiferroics: Past, present, and future. *MRS Bulletin*, 42(5), 385–390. <https://doi.org/10.1557/mrs.2017.86>
- Sturman, B. S. I., & V. M. Fridkin. (1992). *Photovoltaic and Photorefractive Effects in Noncentrosymmetric Materials* (Gordon). Philadelphia.
- Tazaki, R., Fu, D., Itoh, M., Daimon, M., & Koshihara, S. (2009). Lattice distortion under an electric field in BaTiO₃ piezoelectric single crystal. *Journal of Physics: Condensed Matter*, 21(21), 215903. <https://doi.org/10.1088/0953-8984/21/21/215903>
- Teague, J. R., Gerson, R., & James, W. J. (1970). Dielectric hysteresis in single crystal BiFeO₃. *Solid State Communications*, 8(13), 1073–1074. [https://doi.org/http://dx.doi.org/10.1016/0038-1098\(70\)90262-0](https://doi.org/http://dx.doi.org/10.1016/0038-1098(70)90262-0)
- Tyunina, M., Yao, L., Chvostova, D., Dejneka, A., Kocourek, T., Jelinek, M., ... Van Dijken, S. (2015). Concurrent bandgap narrowing and polarization enhancement in epitaxial ferroelectric nanofilms. *Science and Technology of Advanced Materials*, 16(2). <https://doi.org/10.1088/1468-6996/16/2/026002>
- Uchino, K. (2009). *Ferroelectric Devices 2nd Edition* (2nd ed.).

- Valasek, J. (1922). Properties of Rochelle Salt Related to the Piezo-electric Effect. *Physical Review*, 20(6), 639–664. <https://doi.org/10.1103/PhysRev.20.639>
- Von Baltz, R., & Kraut, W. (1978). A model calculation to explain the existence of bulk photo-currents in ferroelectrics. *Solid State Communications*, 26(12). [https://doi.org/10.1016/0038-1098\(78\)91262-0](https://doi.org/10.1016/0038-1098(78)91262-0)
- Von Baltz, R., & Kraut, W. (1981). Theory of the bulk photovoltaic effect in pure crystals. *Physical Review B*, 23(10). <https://doi.org/10.1103/PhysRevB.23.5590>
- Wang, F., Grinberg, I., & Rappe, A. M. (2014). Semiconducting ferroelectric photovoltaics through Zn^{2+} doping into $KNbO_3$ and polarization rotation. *Physical Review B - Condensed Matter and Materials Physics*, 89(23).
- Wang, F., & Rappe, A. M. (2015). First-principles calculation of the bulk photovoltaic effect in $KNbO_3$ and $(K,Ba)(Ni,Nb)O_{3-d}$. *Physical Review B*, 91(16), 165124. <https://doi.org/10.1103/PhysRevB.91.165124>
- Wang, J., Neaton, J. B., Zheng, H., Nagarajan, V., Ogale, S. B., Liu, B., ... Ramesh, R. (2003). Epitaxial $BiFeO_3$ multiferroic thin film heterostructures. *Science (New York, N.Y.)*, 299(5613), 1719–1722. <https://doi.org/10.1126/science.1080615>
- Wang, R., Zhu, Y., Qiu, Y., Leung, C.-F., He, J., Liu, G., & Lau, T.-C. (2013). Synthesis of nitrogen-doped $KNbO_3$ nanocubes with high photocatalytic activity for water splitting and degradation of organic pollutants under visible light. *Chemical Engineering Journal*, 226, 123–130. <https://doi.org/10.1016/j.cej.2013.04.049>
- Wemple, S. H. (1970). Polarization Fluctuations and the Optical-Absorption Edge in $BaTiO_3$. *Phys. Rev. B*, 2(7), 2679–2689. <https://doi.org/10.1103/PhysRevB.2.2679>
- Wu, P., Wang, G., Chen, R., Guo, Y., Ma, X., & Jiang, D. (2016). Advances Enhanced visible light absorption and photocatalytic activity of gel based Pechini method. *RSC Advances*, 6, 82409–82416. <https://doi.org/10.1039/C6RA15288K>
- Xie, L., Li, L., Heikes, C. A., Zhang, Y., Hong, Z., Gao, P., ... Pan, X. (2017). Giant Ferroelectric Polarization in Ultrathin Ferroelectrics via Boundary-Condition Engineering. *Advanced Materials*.
- Xu, Y.-Q., Wu, S.-Y., Zhang, L.-J., Wu, L.-N., & Ding, C.-C. (2017). First-principles study of structural, electronic, elastic, and optical properties of cubic $KNbO_3$ and

- KTaO₃ crystals. *Physica Status Solidi (B)*, 254(5), 1600620–n/a.
<https://doi.org/10.1002/pssb.201600620>
- Yan, L., Zhang, J., Zhou, X., Wu, X., Lan, J., Wang, Y., Zhi, L. (2013). Crystalline phase-dependent photocatalytic water splitting for hydrogen generation on KNbO₃ submicro-crystals. *International Journal of Hydrogen Energy*, 38(9), 3554–3561.
<https://doi.org/http://dx.doi.org/10.1016/j.ijhydene.2013.01.028>
- Yang, S. Y., Seidel, J., Byrnes, S. J., Shafer, P., Yang, C. H., Rossell, M. D., Ramesh, R. (2010). Above-bandgap voltages from ferroelectric photovoltaic devices. *Nature Nanotechnology*, 5(2), 143–147. <http://dx.doi.org/10.1038/nnano.2009.451>
- Young, S. M., & Rappe, A. M. (2012). First Principles Calculation of the Shift Current Photovoltaic Effect in Ferroelectrics. *Physical Review Letter*, 109(11), 116601.
<https://doi.org/10.1103/PhysRevLett.109.116601>
- Young, S. M., Zheng, F., & Rappe, A. M. (2012). First-Principles Calculation of the Bulk Photovoltaic Effect in Bismuth Ferrite. *Physical Review Letter*, 109(23), 236601.
<https://doi.org/10.1103/PhysRevLett.109.236601>
- Yu, L., Deng, H., Zhou, W., Yang, P., & Chu, J. (2017). Band gap engineering and magnetic switching in a novel perovskite (1-x)KNbO₃-xBaNb_{1/2}Fe_{1/2}O₃. *Materials Letters*, 202, 39–43. <https://doi.org/https://doi.org/10.1016/j.matlet.2017.05.077>
- Yu, L., Jia, J., Yi, G., Shan, Y., & Han, M. (2016). Bandgap tuning of [KNbO₃]_{1-x}[BaCo_{1/2}Nb_{1/2}O_{3-δ}]_x ferroelectrics. *Materials Letters*, 184, 166–168.
<https://doi.org/http://dx.doi.org/10.1016/j.matlet.2016.08.044>
- Zaitsev, B. D., Kuznetsova, I. E., & Joshi, S. G. (2001). Hybrid acoustic waves in thin potassium niobate plates. *Journal of Applied Physics*, 90(7), 3648–3649.
<https://doi.org/10.1063/1.1388596>
- Zelezny, V., Chvostova, D., Simek, D., Maca, F., Masek, J., Setter, N., & Hong Huang, Y. (2016). The variation of PbTiO₃ bandgap at ferroelectric phase transition. *Journal of Physics. Condensed Matter: An Institute of Physics Journal*, 28(2), 25501.
<https://doi.org/10.1088/0953-8984/28/2/025501>
- Zenkevich, A., Matveyev, Y., Maksimova, K., Gaynutdinov, R., Tolstikhina, A., & Fridkin, V. (2014a). Giant bulk photovoltaic effect in thin ferroelectric BaTiO₃

- films. *Physical Review B - Condensed Matter and Materials Physics*, 90(16).
<https://doi.org/10.1103/PhysRevB.90.161409>
- Zhang, G., Wu, H., Li, G., Huang, Q., Yang, C., Huang, F., Lin, J. (2013). New high Tc multiferroics KBiFe₂O₅ with narrow band gap and promising photovoltaic effect. *Scientific Reports*, 3(1), 1265. <https://doi.org/10.1038/srep01265>
- Zhang, Q., Xu, F., Xu, M., Li, L., Lu, Y., Li, M., He, Y. (2017). Lead-free perovskite ferroelectric thin films with narrow direct band gap suitable for solar cell applications. *Materials Research Bulletin*, 95, 56–60.
<https://doi.org/10.1016/j.materresbull.2017.07.020>
- Zhang, T., Zhao, K., Yu, J., Jin, J., Qi, Y., Li, H., ... Liu, G. (2013). Photocatalytic water splitting for hydrogen generation on cubic, orthorhombic, and tetragonal KNbO₃ microcubes. *Nanoscale*, 5(18). <https://doi.org/10.1039/c3nr02356g>
- Zhao, Q.-X., Wen, M.-X., Wang, S.-B., Guan, L., & Liu, B.-T. (2008). No Title. *J. Synth. Cryst.*, 37, 1390.
- Zhou, W., Deng, H., Yang, P., & Chu, J. (2014). Structural phase transition, narrow band gap, and room-temperature ferromagnetism in [KNbO₃]_{1-x}[BaNi_{1/2}Nb_{1/2}O_{3-δ}]_x ferroelectrics. *Applied Physics Letters*, 105(11), 111904.
<https://doi.org/10.1063/1.4896317>
- Zhou, W., Deng, H., Yang, P., & Chu, J. (2016). Investigation of microstructural and optical properties of (K,Ba)(Ni,Nb)O_{3-δ} thin films fabricated by pulsed laser deposition. *Materials Letters*, 181, 178–181.
<https://doi.org/http://dx.doi.org/10.1016/j.matlet.2016.06.032>

Chapter 2

Methodology

2.1. Introduction

2.2. Ceramic processing

2.2.1. Powder Synthesis: Solid State Reaction

2.2.2. Raw materials

2.2.3. Sintering

2.2.4. Fabricated compositions

2.3. Film preparation

2.3.1. Pulsed laser deposition (PLD)

2.3.2. Electrodeposition

2.4. Chemical and structural characterisation

2.4.1. X-ray diffraction (XRD)

2.4.2. Rietveld Refinement

2.4.3. Raman Spectroscopy

2.4.4. Scanning Electron Microscopy

2.4.5. EDX

2.5. Electrical characterisation

2.5.1. Dielectric response

2.5.2. Ferroelectric and piezoelectric measurements

2.6. Optical characterisation

2.3.1. Diffuse reflectance spectroscopy

2.7. References

2. Methodology

2.1. Introduction

This chapter describes the techniques and methods used to prepare and study the materials in this work. Ceramics were synthesised by solid state reaction and pressureless sintered.

Techniques employed for chemical and structural characterisation included powder X-ray diffraction (XRD), Raman spectroscopy and scanning electron microscopy (SEM) combined with energy-dispersive X-ray spectroscopy (EDX). Dielectric and electromechanical measurements were performed on ceramics. Optical characterisation was carried out by diffuse reflectance spectroscopy.

Thin films of $0.75 \text{ KNbO}_3 - 0.25 \text{ BiFeO}_3$ (KNBF $x=0.25$) were prepared by pulsed laser deposition (PLD), but finally, photo-response was measured on KNBF $x=0.25$ coated cell.

2.2. Ceramic processing

Ceramic materials are polycrystalline materials obtained by a process that classically is divided into three steps: powder synthesis (Figure 2. 1. (a)), preparation of the ‘green body’ (Figure 2. 1. (c)) and sintering (Figure 2. 1. (b)).

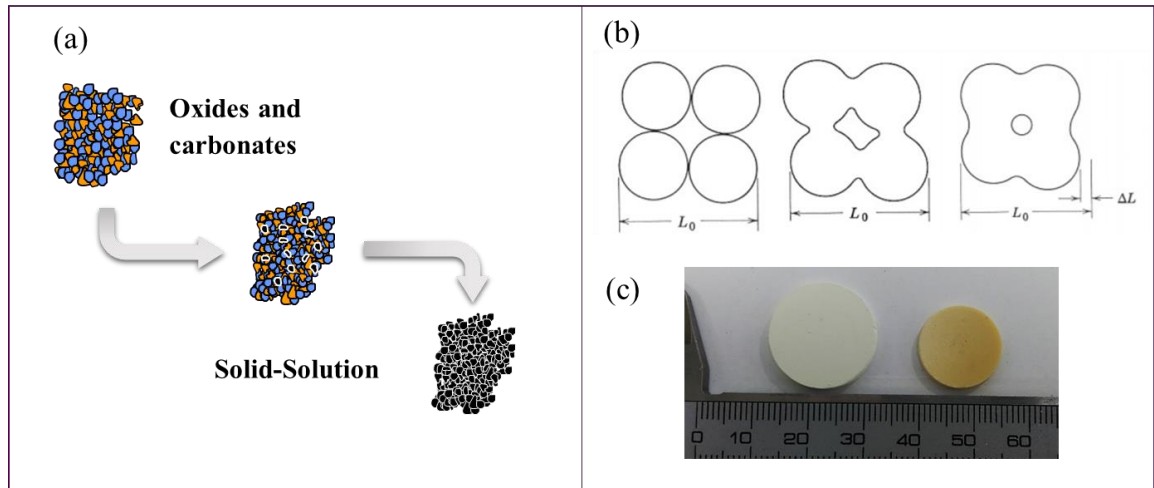


Figure 2. 1.: Schematic representation of (a) powder synthesis and (b) sintering evolution from compact powder to densified ceramic (Carter & Norton, 2007). (c) Picture of green and fired body.

2.2.1. Powder Synthesis: Solid State Reaction

All compositions of the present work were synthesised following the conventional Solid-State Reaction (SSR) method, as detailed below.

First, oxides and carbonates were pre-dried in a drying oven at 200°C for 24 hours to avoid any unwanted moisture. The chemicals were weighed in the required molar ratios, in order to produce 15 g of each composition. The mixture was placed into a polyethylene bottle containing propanol (up to 50 ml) and zirconia media. Then, the bottle was transferred into a ball mill and rotated overnight (for 24 hours) for effective mixing of the reactants.

After milling, the slurry was moved into a stainless-steel pan, which was placed into the drying oven at 100°C. The dried slurries were passed through a 250 μm mesh sieve, to obtain very fine powders. Sieved powders were placed into covered alumina crucible and fired in air for reaction for 4 hours using a heating rate of 3°C/min. The powders were re-milled and the calcination repeated until there was no change in the XRD data. The end of the processing was considered when no change in the XRD data were observed.

Chapter 3 of this work addresses the optimisation of the ceramic processing for KNbO_3 . However, the solid-solutions based on KNbO_3 present some modifications on the synthesis and sintering routes.

2.2.2. Raw materials

All the materials presented in this study were prepared from the oxides and carbonates listed in Table 2. 1.

Compound formulae	Supplier	Lot n°	Purity
K₂CO₃	Sigma-Aldrich	069K1682	≥99%
Nb₂O₅	Aldrich	MKBN8594V	99.9%
BaCO₃	Sigma-Aldrich	BCBM2121V	≥99%
Na₂CO₃	Sigma-Aldrich	040M0040	≥99%
Bi₂O₃	Fluka Analytical	BCBC0495V	98%
ZnO	Sigma-Aldrich	BCBC7947V	≥99%
Fe₂O₃	Sigma-Aldrich	MKB56874V	≥99%
Co₃O₄	Aldrich	MKBB0427V	99%
Mn₂O₃	Aldrich	MKBB0427V	99%
NiO	Sigma-Aldrich	BHCF3223V	99.9%
Propanol	Fischer	1421368	≥99.5%

Table 2. 1.: List of reactants used in this study.

2.2.3. Sintering

Pellets of 10 mm in diameter and approximately 2 mm in thickness were fabricated by uniaxial pressing of ~ 1 g of powder. Applied pressure was less than 1 ton. Higher applied pressure would lead to the appearance of cracks in the pellets. Green bodies were thermally treated at high temperatures in order to obtain dense ceramics. The thermal treatments were carried out in a range of temperatures from 1070°C to 1185°C (depending on the composition, Table 2. 2) for 4-12 hours and the heating rate was 3°C min⁻¹.

2.2.4. Density of materials

Usually, bulk density of sintered pellets is measured by Archimedes method. A liquid displacement method was rejected due to the high sensitivity of the samples to moisture from the environment, as will be described in detail later. In this thesis, the density of sintered pellets was estimated from the sample mass and volume. The mass, M , was measured using a digital balance ($\Delta M=0.001\text{g}$) and sample volume was calculated from the external dimensions of the samples, diameter, d , ($\Delta d=0.01\text{ mm}$) and thickness, t , ($\Delta t=0.01\text{ mm}$), using a micrometre. Bulk density was calculated by the weight of the ceramic sample divided by its volume, without considering open pores (Eq. 2.1.). The total error for density (Eq. 2.4.) is given by experimental error (Eq. 2.2.) and statistical error (Eq. 2.3).

$$\rho = \frac{M}{t \cdot \pi \cdot \frac{d^2}{4}} \quad \text{Eq. 2.1.}$$

$$\begin{aligned} \Delta\rho_{exp} &= \sqrt{\left(\frac{\partial\rho}{\partial M}\Delta M\right)^2 + \left(\frac{\partial\rho}{\partial t}\Delta t\right)^2 + \left(\frac{\partial\rho}{\partial d}\Delta d\right)^2} \quad \text{Eq. 2.2.} \\ &= \sqrt{\left(\frac{\Delta M}{t \cdot \pi \cdot r^2}\right)^2 + \left(-\frac{M}{t^2 \cdot \pi \cdot r^2}\Delta t\right)^2 + \left(-\frac{8M}{t \cdot \pi \cdot d^3}\Delta d\right)^2} \end{aligned}$$

$$\Delta\rho_{sta} = \left(\frac{\sum_{i=1}^N (\bar{\rho} - \rho_i)^2}{N}\right)^{1/2} \quad \text{Eq. 2.3.}$$

$$\Delta\rho_{tot} = \sqrt{\Delta\rho_{exp}^2 + \Delta\rho_{sta}^2} \quad \text{Eq. 2.4.}$$

2.2.5. Fabricated compositions

The nominal compositions studied in this work with corresponding temperatures for calcination and sintering, are listed in Table 2. 2.

Systems	x	Calcination Temperatures (°C)	Sintering Temperature (°C)
KNbO₃	-	850+850	1085
K_{0.95}NbO₃	-	850+850	1080
KNb_{0.95}O₃	-	850+850	1070
(1-x) KNbO₃- x Ba_{0.5}Bi_{0.5}Nb_{0.5}Zn_{0.5}O₃	0.5, 0.10, 0.15, 0.20, 0.25	850+850	1100
(1-x) KNbO₃- x BiFeO₃	0.5, 0.10, 0.15, 0.20, 0.25	850+850	1080-1085
(1-x) KNbO₃- x BiMnO₃	0.5, 0.10, 0.15, 0.20, 0.25	800+900	1070-1080
(1-x) KNbO₃- x BiCoO₃	0.5, 0.10, 0.15, 0.20, 0.25	850+850	1080-1090
(1-x) KNbO₃- x BiNiO₃	0.5, 0.10, 0.15, 0.20, 0.25	850+850+850	1070-1085
(1-x) KNbO₃- x BaNb_{0.5}Ni_{0.5}O₃	0.10	850+850	1085
K_{0.5}Na_{0.5}NbO₃	-	850+850	1100
(1-x) K_{0.5}Na_{0.5}NbO₃- x BaNb_{0.5}Ni_{0.5}O₃	0.02	850+850	1185

Table 2. 2.: Fabricated compositions object in this research. Calcination and sintering temperatures are also included in the table.

2.3. Film preparation

2.3.1. Pulsed laser deposition (PLD)

0.75 KNbO₃- 0.25 BiFeO₃ films were grown on STO (001) and MgO (001) substrates by Pulsed laser deposition (PLD) at temperatures of 600 and 650°C, at the Universitat de Barcelona with the collaboration of Institut de Ciència de Materials de Barcelona (ICMAB-CSIC), Barcelona, Spain.

Schematic representation of the pulsed laser deposition is shown in (Figure 2. 2.(a)). Once starting configurations were set up (vacuum, oxygen pressure and substrate temperature), the high-energy pulsed laser beam passed through a series of lenses, in order to be focused on the target, inside the vacuum chamber. Subsequently, the sample target starts to instantaneously vaporise and ionise, generating plasma that contains atoms, molecules, ions, and neutral particles. Then, the plasma is ejected perpendicular to the target surface, forming a plasma plume. In the diffusion process, the plume interacts with the oxygen atmosphere, which increases the ionization process, and thereby promotes the collisions among the components of the plasma. Finally, the atoms from the target are sprayed onto a substrate placed on a heater. By optimizing the factors such as laser density, pressure of the atmosphere, and heating temperature, epitaxial thin films can be prepared with the same composition as the target (Chrissey & Hubler, 1994; Martin, Chu, & Ramesh, 2010; Martín et al., 1997). Figure 2. 2.(b) and (c) illustrate the PLD equipment used in this work at the Universitat de Barcelona, Barcelona, Spain. The chamber was evacuated by an ion pump to a base pressure of $\sim 10^{-5}$ mBar. Pulsed KrF excimer laser was operated at a repetition rate of 5 Hz. The laser energy density was about 2 J/cm². In this work, results are presented for only one composition, 0.75 KNbO₃-0.25BiFeO₃. A dense ceramic of 2 cm of diameter prepared at Sheffield Hallam University, was used as the target. The substrate holder was placed at 50 mm from the target, which was rotated at 5 rpm to prevent holes formation in the target and to ensure uniform ablation. The 0.75 KNbO₃-0.25BiFeO₃ films were deposited on STO (001) and MgO (001) substrates, at temperatures of 600 and 650°C under oxygen pressure of 0.1 mBar and 0.75 mBar for 20 minutes.

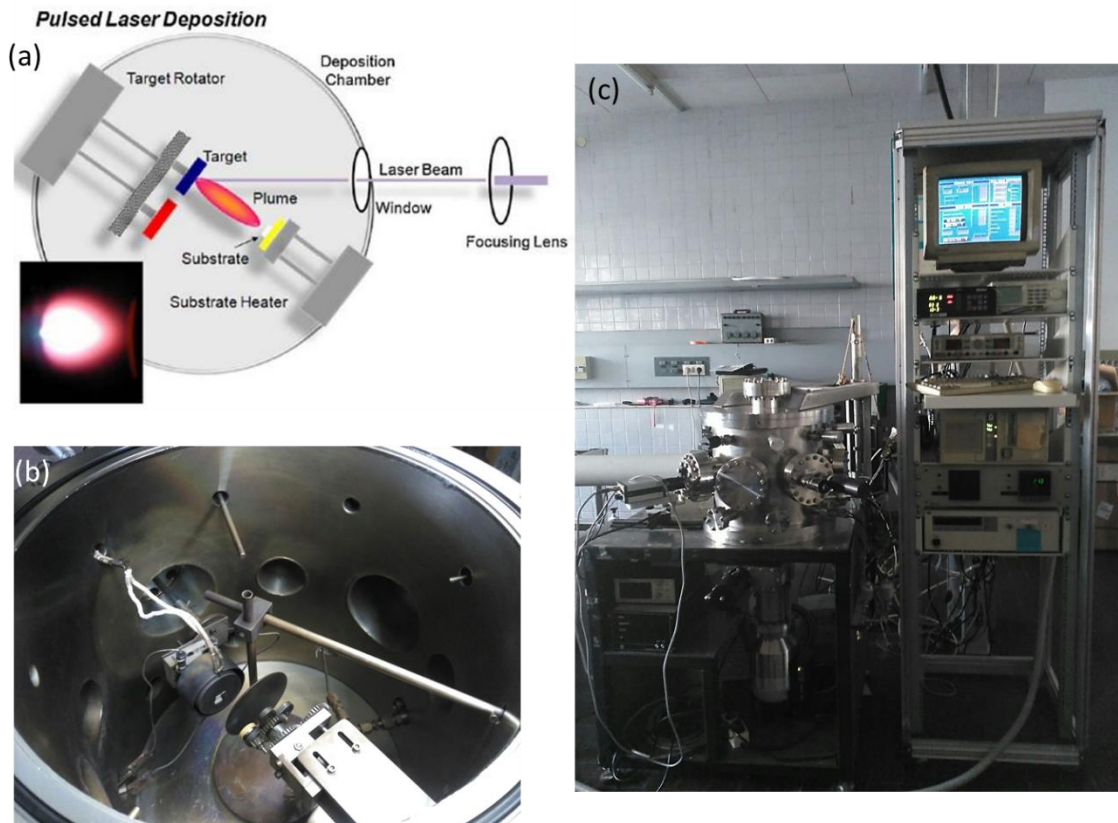


Figure 2. 2.: (a) Schematic representation of operational pulsed laser deposition (PLD) equipment. Pictures of (b) the interior of the chamber and (c) the complete equipment for PLD at the Universitat de Barcelona, Barcelona, Spain.

2.3.2. Photoresponse measurements

The photoresponse of $0.75 \text{ KNbO}_3\text{-}0.25 \text{ BiFeO}_3$ was measured at the Universidade Federal de Pelotas, Pelotas, Brasil, where the ferroelectric cell was also fabricated.

First, a ferroelectric paste was prepared, mixing 0.3 g of $\text{KNbO}_3\text{-}0.25\text{BiFeO}_3$ powder, 15 μL of ethylene glycol, 15 μL of Triton-X (adherent) and 100 μL of ethanol (dispersant). This solution was mixed in Vortex mixer (~ 5 minutes), homogenized in ultrasound bath (~ 30 minutes) (Figure 2. 3).

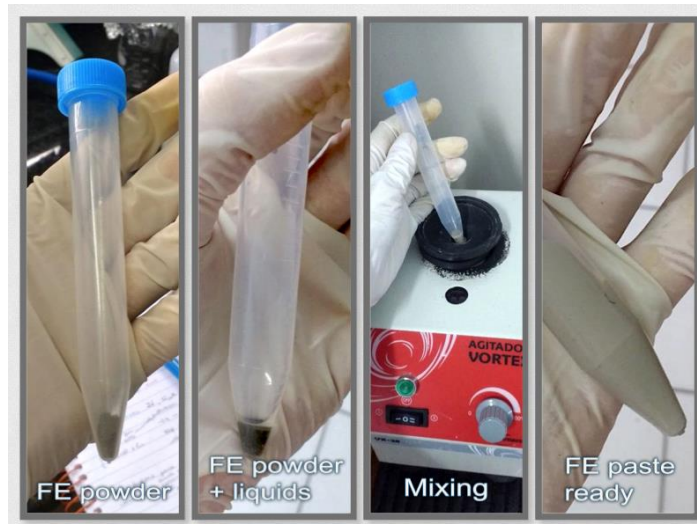


Figure 2. 3.: Preparation of the ferroelectric phase.

Secondly, the fabrication of the cell was performed. Electrodes were prepared on FTO coated glass. The counter-electrode was made with carbon (pencil) (Figure 2. 4 (a)). The photoelectrode (FE paste) was deposited by casting (Figure 2. 4 (b), (c) and (d)). After deposition, the photoelectrode was thermally treated first, at 125 °C for 5 minutes and then at 450 °C for 30 minutes in a tubular furnace to eliminate organic compounds from FE paste. Finally, the sealing gasket was made with one thermoplastic polymer.

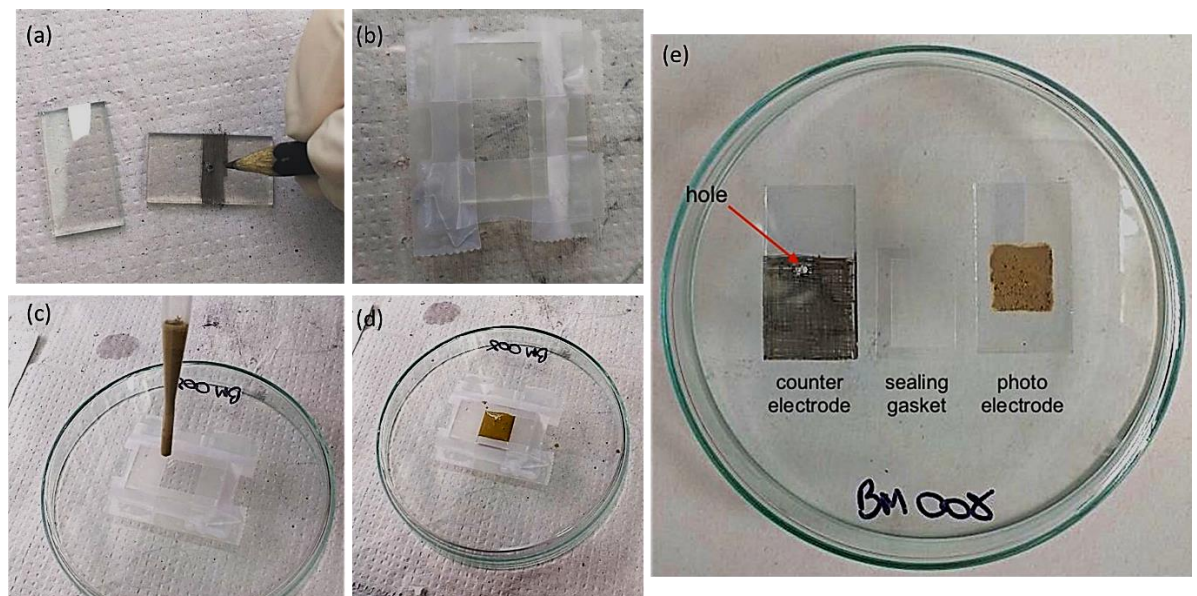


Figure 2. 4. Components on the FEPV cell: (a) the counter-electrode. (b),(c) and (d) deposited photoelectrode and (e) sealing gasket.

Third, all components are set together (counter eletrode + sealing gasket + photoelectrode) and sealed with epoxy resin (Scotch Mix transparent epoxy adhesive)

(Figure 2. 5). After 24 hours, an electrolyte was inserted (redox couple I^-/I^{3-}) through the small hole in counter electrode side in order to favour the transport of the photo-charges.

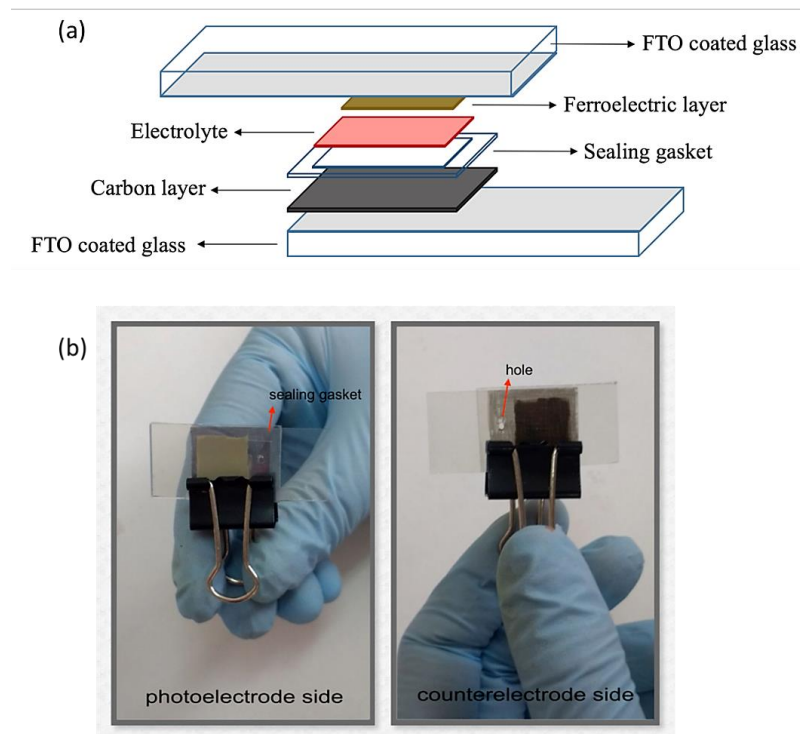


Figure 2. 5: (a) Schematic representation of the setting and components of photo-ferroelectric cell. (b) Final aspect of cell by both sides.

The photoresponse of KNBF $x=0.25$ was measured under white light (210-1500nm) and in the dark. The active area of cell is 1 cm^2 .

2.4. Chemical and structural characterisation

2.4.1. X-ray diffraction (XRD)

Geometrically, it is possible to think of a crystal as different families of parallel atomic planes (Kittel & Hellwarth, 1957), as shown in Figure 2. 6. All the atoms are placed in a regular periodic array. Each family of atomic planes is determined by three integers (h, l, k) also denominated Miller indices. From them, it is possible to calculate the interplanar spacing, d_{hkl} .

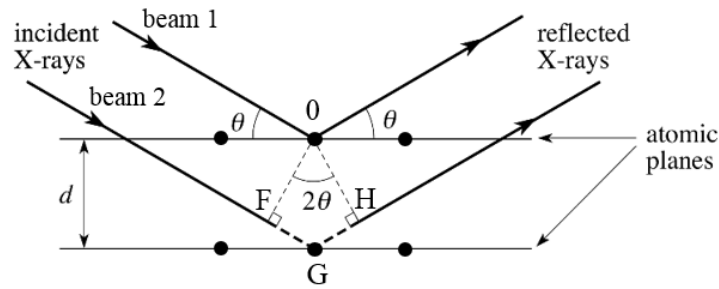


Figure 2. 6.: Schematic representation of Bragg's law (Cullity, 2014).

When an X-ray beam interacts with a single-crystal, diffraction occurs, because the wavelength, λ , of the incident beam is on the same order as the spacing between atoms ($\sim 1\text{\AA}$). Diffracted rays produce interference phenomena, most of them destructive. However, constructive interference also occurs. Indeed, it is possible to detect a diffraction beam with sufficient intensity, if the incident beam and the detector are placed in a specific Bragg angle, as discussed below.

The assumption made in deriving the Bragg equation is that the planes of atoms responsible for a diffraction peak behave as a specular mirror, so that the angle of incidence is equal to the angle of reflection. Constructive interference of beam 1 and 2 (Figure 2. 6) is produced when they are in phase after reflection. Then the extra-distance that beam 2 travels ($FG+GH$) must be an integer number of wavelength λ . FG and GH paths are easily calculated by trigonometry. A relationship between the X-ray wavelength λ , the spacing d between lattice planes, d , and the angle of incidence θ , is derived and known as Bragg's law (Eq. 2.5)(Waseda, Matsubara, & Shinoda, 2011):

$$n\lambda = 2d_{hkl}\sin\theta_{hkl} \quad \text{Eq. 2. 5}$$

Where n is taken as integer number. Summarising, the Bragg angle (θ_{hkl}) depends on the inter-plane spacing d_{hkl} , which itself depends on the size of the atoms/ions building up the structure. From the X-ray powder diffraction pattern, it is possible to extract useful information about the crystal structure, such as the symmetry and the dimensions of the unit cell. Furthermore, the intensity of the peaks in the diffraction pattern is related with the atoms nature and their position, so it is also possible to obtain information about the internal structure of the crystal.

In this work, powder X-ray diffraction (XRD) analyses were used to study the crystal structure and the purity of the prepared materials. Measurements were carried out at room temperature with a diffractometer (model: Empyrean XRD, PANalytical™, Almelo, The

Netherlands) (Figure 2. 7 (a) and (b)) equipped with a Cu ($\lambda = 1.5418 \text{ \AA}$) and Co ($\lambda = 1.7890 \text{ \AA}$) tube operated at 40 kV and 40 mA, normally in the 2θ range between 20 and 80, with 2θ increments of 0.013° and counting time of ~ 70 s per step. Both powders and pellets were analysed using the reflection spinner sample holder, which spins at 0.25 Hz. Lattice parameters were calculated from Rietveld refinement of XRD data using the X'Pert High Score software (produced by: PANalytical B.V., Almelo, The Netherlands, license number: 42001164).



Figure 2. 7.: (a) PANalytical Empyrean X-Ray diffractometer. (b) Internal structure.

2.4.2. Rietveld Refinement

Rietveld method calculates X-ray diffraction pattern of a specimen and compares it to the measured pattern. It is important to note that this method is a refinement, not a solution method, because the structure of the model must be known in advance.

The peak profile function is used to model the shape of diffraction peaks. The most common peak profile functions are: Gaussian (Equation 2.6), Lorentzian (Equation 2.7), modified Lorentzian, Pearson VII and pseudo-Voigt (Equation 2.8). However, the best option has long been established to be the pseudo-Voigt (Young & Wiles, 1982), which is a linear combination of Gaussian and Lorentzian functions:

$$\text{Gaussian: } G = \frac{e^{-\frac{x^2}{2\sigma^2}}}{\sigma\sqrt{2\pi}} \quad \text{Eq. 2. 6}$$

$$\text{Lorentzian: } L = \frac{\gamma}{\pi(x^2 + \gamma^2)} \quad \text{Eq. 2. 7}$$

$$\text{Pseudo - Voigt: } \eta L + (1 - \eta)G \quad \text{Eq. 2. 8}$$

The calculated pattern is fitted to the experimental pattern by changing various refinable parameters, such as atomic positions, site occupancies, peak shape parameters, etc., until a best-fit match is obtained with the measured pattern. The purpose of the fitting is to minimize the following difference, S_y . (Equation 2.9):

$$S_y = \sum_{i=1}^n \frac{1}{y_i} (y_{i,obs} - y_{i,calc})^2 \quad \text{Eq. 2.9}$$

The quality of the fitting is determined by the visual check of the difference between the calculated and the experimental pattern; There are also quantitative indicators: the weighted-profile R value (R_{wp}) (Equation 2.10) and the expected residual value (R_{exp}) (Equation 2.11):

$$R_{wp} = \sqrt{\frac{\sum_i w_i (y_{i,obs} - y_{i,calc})^2}{\sum_i w_i (y_{i,obs})^2}} \quad \text{Eq. 2. 10}$$

$$R_{exp} = \sqrt{\frac{N - P}{\sum_i w_i (y_{i,obs})^2}} \quad \text{Eq. 2. 11}$$

where N is the number of observations and P the number of parameters. R_{wp} is therefore the ratio of the difference between the two patterns to the observed pattern, whereas R_{exp} is a measure of the quality of the data (statistically). The ratio between R_{wp} and R_{exp} is often given as a measure of the goodness of fit (GOF, or χ^2). (Equation 2.12):

$$GOF = \chi^2 = \left(\frac{R_{wp}}{R_{exp}} \right)^2 \quad \text{Eq. 2. 12}$$

If the experimental pattern has more data points than needed, χ^2 can be much larger than 1, whereas if the data points are not sufficient (i.e. low sensitivity of the detector or scan time too short), χ^2 can be even smaller than 1, which is an indication that the data

acquisition should be repeated (McCusker, Dreele, Cox, Lou\er, & Scardi, 1999). However, as for every empirical manipulation of data, the results must make physical sense, no matter how good the fitting is (Buchsbaum & Schmidt, 2007).

Rietveld Refinement was used to determine the lattice parameters of each composition and for monitoring the evolution of the crystal structure upon doping.

2.4.3. Raman Spectroscopy

Raman spectroscopy permits the measurements of vibrational transitions by observing inelastically scattered radiation. In general, every molecule has unique Raman response, which is a finger print of the material and allows identifying or measuring properties of its own nature, including the effects of composition and temperature on phase transformations (Perry & Hall, 1965). The intensity of the inelastically scattered light is graphically represented as a function of Raman shift of the light (wavenumbers).

The electric field of the incident light makes the electron cloud oscillate around the molecule (in simpler words, electrons get polarised). Therefore, electrons go up to a virtual vibrational state. Rayleigh scattering occurs when electrons go down to the same vibrational level, which means there is no loss of energy (elastic scattering). However, Raman scattering involves a shift in the vibrational energy level of the emitted radiation (and therefore in its wavelength) (Figure 2. 8.) This is due to a sizeable change of the electronic polarisation of the molecule during the vibration. Considering the symmetry properties of a molecule, the vibrations that transform similarly to the products of the x, y or z coordinates (i.e. xx, yy, zz, xy, xz, yz) can be observed in the Raman spectrum. Raman activity is determined by inspection of the character tables usually reported in the vibrational spectroscopy books for each symmetry point group.

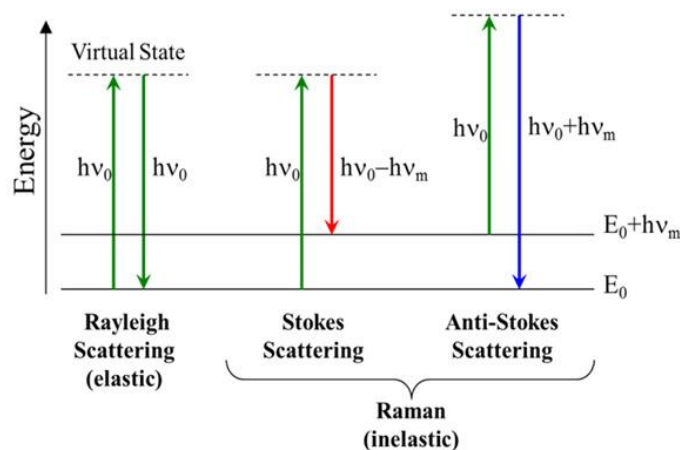


Figure 2. 8.: Vibrational energy level diagram showing the state involved in Raman spectra.

Lattice vibrations in crystalline solids can be transverse (if the polarization is perpendicular to the direction of propagation) or longitudinal (if polarization and propagation vectors are parallel); each of these modes can be acoustic (atoms moves in phase) or optical (adjacent atoms are out-of-phase) (Figure 2. 9).

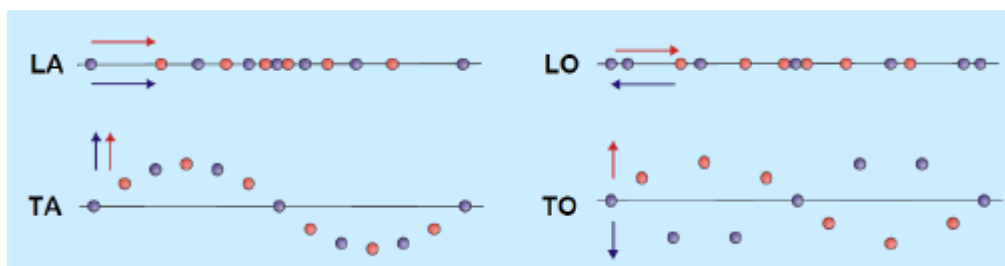


Figure 2. 9.: Schematic representation of phonon modes, or lattice vibrations (LA =longitudinal acoustic, LO = longitudinal optical, TA = transverse acoustic, TO =transverse optical).

Depolarised Raman spectra were recorded in backscattering geometry with a spectrometer (Thermo Scientific DXR2) equipped with a microscope objective of 10x magnification and using the 520 nm laser (Figure 2. 10.).

The laser enters the main compartment and is guided through mirrors to the sample. The back-scattered radiation is collected and re-enters the main compartment through a filter that cuts off the Rayleigh scattering (thus enabling us to see the much weaker Raman signal) up to 50 cm^{-1} above the laser frequency. A diffraction grid rotates to bring the intensity of separate wavelengths to the CCD detector, which finally converts the incoming photons into electrons to be stored digitally in a PC.

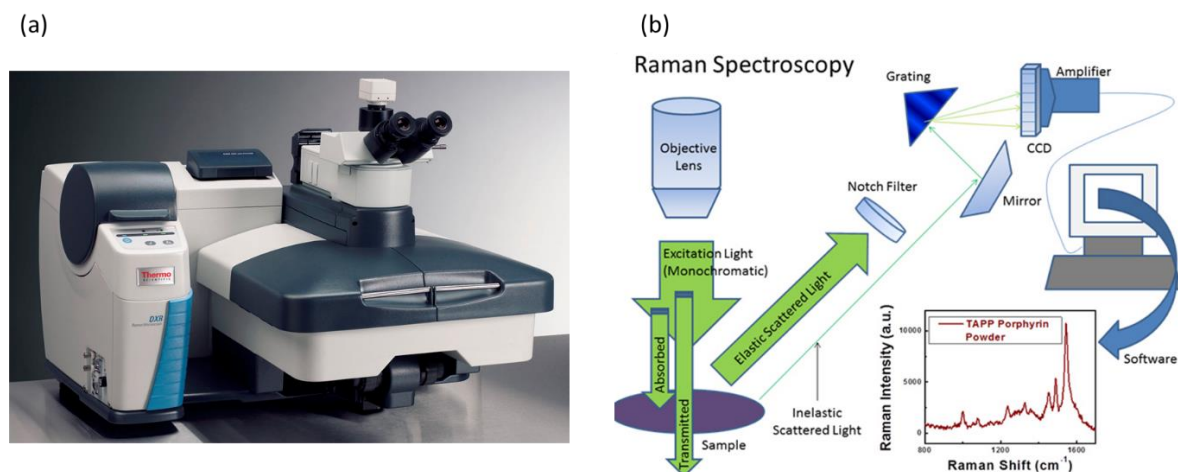


Figure 2. 10.: (a) The Raman instrumentation is a Thermo Scientific DXR2. (b) schematic representation

2.4.4. Scanning Electron Microscopy

Scanning electron microscopy (SEM) provides information relating topographical features, morphology, phase distribution and compositional differences. This technique is able to analyse materials that cannot be observed with the resolution offered by optical techniques.

During SEM study, a variety of signals are produced by accelerated electrons with significant amounts of kinetic energy interacting with the specimen. These signals include: secondary electrons, backscattered electrons, X-rays, photons, visible light and heat. Secondary electrons and backscattered electrons are commonly used for imaging samples. In this investigation, samples are examined by secondary electron detector which is more valuable for showing morphology and topography on samples and present greater resolution.

Figure 2. 11 (a) and (b) shows the scanning electron microscope (SEM) and the internal structure representation of a conventional SEM, respectively.

Firstly, the electron gun (top of the column), produces the electrons and accelerates them. The diameter of electron beam produced is too large to form a high-resolution image. Hence, electromagnetic lenses and apertures are used to focus and define the electron beam and to form a small focused electron spot on the specimen. Then, high-vacuum environment allows electrons to travel without scattering by the air. Finally, the specimen

stage, electron beam scanning coils, signal detection, and processing system provide real-time observation and image recording of the specimen surface.

Ceramic microstructures were examined using scanning electron microscope (model: Nova Nano 200, FEI, Brno, Czech Republic). The samples were carbon coated before SEM inspection, in order to avoid charging. Scanning electron images were taken with the following parameters: voltage of 15 kV, working distance of 5 mm and spot size 4.

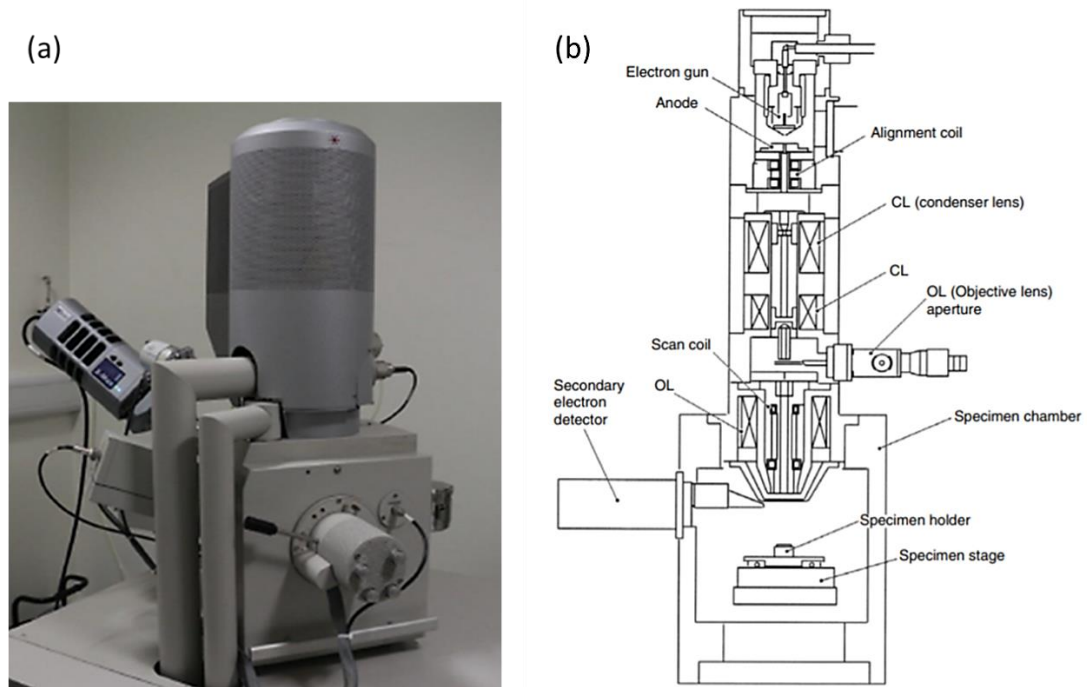


Figure 2. 11.: (a) Actual picture and (b) schematic representation of the internal structure of the FEI Nova Nano 200 Scanning electron

2.4.5. EDX

Energy-dispersive X-ray spectroscopy (EDX), is a technique used for elemental analyses and chemical characterization of a specimen.

As mentioned previously, X-ray are also produced by the interaction of the primary electrons with the specimen. This radiation is generated when the incident electron beam excites an electron of the specimen in an inner shell, ejecting it from a discrete level of energy while creating an electron hole. An electron from a higher energy level then fills the hole, and the energy difference in between the levels may be released in the form of an X-ray. The emitted characteristic X-ray energies for elements will generally be

different from element to element with only a few spectral peaks overlapping. If the identification of one peak is ambiguous, other peaks or limited knowledge of the sample history will often allow a reasonable elemental identification of the peak.

2.5. Electrical characterisation

In order to measure the electrical properties, parallel plate capacitors were fabricated (Figure 2. 12.). The ceramic discs were polished and thinned down to ~ 1 mm of thickness. Then, Pt electrodes were applied and treated at 600°C for 30 min, to improve the mechanical and electrical properties of the electrode and the interface with the ceramic.

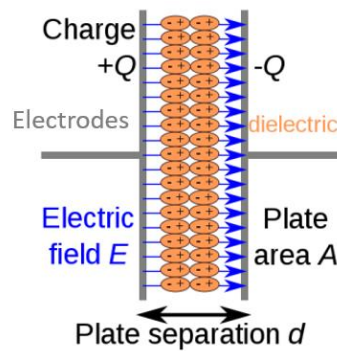


Figure 2. 12: Capacitor fabricated for electrical measurements. Electric dipoles aligning themselves with the electric field E

2.5.1. Dielectric response

The relative permittivity was calculated from the capacitance (C) measurements of the capacitor under an AC electric field at the University Sheffield, Sheffield, United Kingdom. The capacitance values were then converted to relative permittivity using the formula (Equation 2.13).:

$$\epsilon_r = \frac{Ct}{\epsilon_0 A} \quad \text{Eq. 2. 13}$$

where ϵ_0 is the dielectric permittivity of vacuum ($8.85 \cdot 10^{-12}$ F/m), A and t , the area and the thickness of the parallel plate capacitor fabricated, respectively.

Dielectric loss ($\tan\delta$) was measured and it is very useful to verify the quality of the capacitor. This value is highly dependent on the frequency because of different types of polarization can occur. Capacitance measurements in the frequency range 10 kHz to 1 MHz were carried out in unpoled ceramics using an LCR meter coupled with a furnace applying a heating/cooling rate of 1 C°/min.

2.5.2. Ferroelectric and piezoelectric measurements

To study the ferroelectric properties, polarization-electric field (P-E) hysteresis loops were measured at room temperature. The polarization (P) of the ferroelectric material is calculated by measuring the stored electric charge in the system (Q), by using the following expression (Equation 2.14), also including the area of the capacitor (A):

$$P = Q/A \quad \text{Eq. 2.14}$$

By the observation of the P-E hysteresis loop, the identification of ferroelectric materials was possible, as well as the determination of the spontaneous (P_{sat}) and remanent (P_r) polarizations and the coercive field (E_c) of the different ferroelectric compositions of the system (Figure 2. 13.)

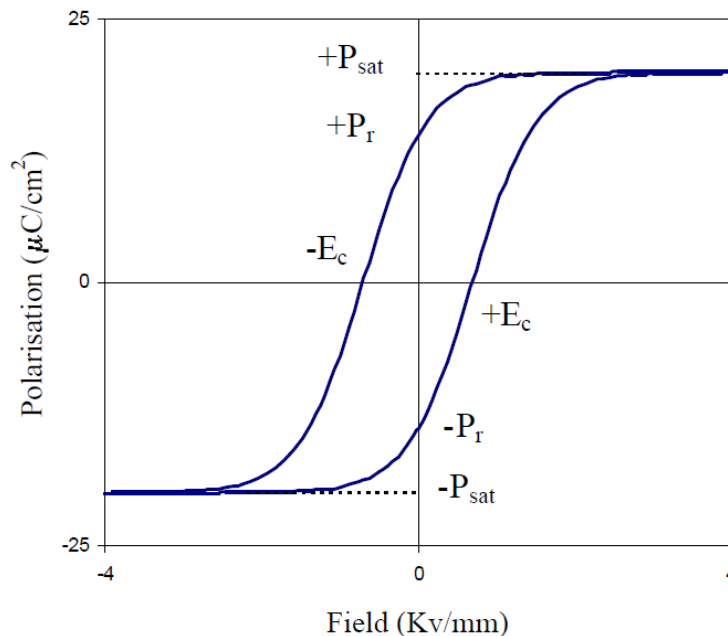


Figure 2. 13.: P-E hysteresis loop parameters for a ferroelectric material.

The strain field loops, S-E (typical plot for ferroelectrics is shown in Figure 1.12), are derived from sample displacement data, which are measured by a laser interferometer. The displacement is measured by splitting a monochromatic light source (helium neon laser) into two beams. One beam acts as a reference beam following a fixed path, and the second measuring beam goes to the sample and returns to join the reference beam. The interference fringes created are used to determine the displacement.

For the acquisition of a P-S-E loops, the initial triangle wave is formed by the generator, which is then amplified by the high voltage amplifier, and sends the amplified waveform to the sample. The current passing through the sample determines the charge accumulated on the surface of the capacitor. The P-E data are then sent to the PC for subsequent analysis.

These measures were performed using a ferroelectric tester (TF Analyzer 2000 E) (Figure 2. 14) and a high voltage amplifier. AixPlorer Software was used to acquire, interpret, and review measurement data.

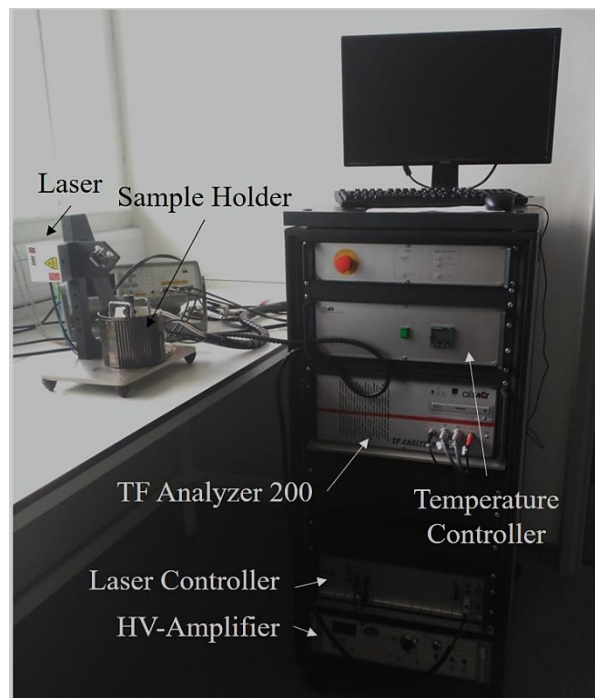


Figure 2. 14.: Image of the ferroelectric tester (TF Analyzer 2000 E)

2.6. Optical characterisation

2.6.1. Diffuse reflectance spectroscopy

When a beam of light impacts on a flat polished surface of a single crystal is partly reflected and partly refracted following Fresnel equations. In absorbing materials, the incident beam light is absorbed according the Lambert absorption law (Eq. 2.15):

$$I = I_0 e^{-Kx} \quad \text{Eq. 2.15}$$

Where I is the transmitted flux, I_0 is the initial flux, x is the thickness of a medium with an absorption coefficient, K . In polycrystalline materials, diffraction phenomena also occur. In powders of randomly oriented particles, part of the incident light goes back at all angles. If the particle size is similar or smaller than the wavelength (λ) of the beam, the light is scattered. The scattered light by a single particle has no isotropic distribution (Mie's theory). However, some investigations have shown, an isotropic distribution arises from the material with sufficiently large number of particles and layer thickness (x) and is defined as diffuse reflectance (Kortum 1969). The incident light is scattered according the Equation 2.16.

$$I = I_0 e^{-Sx} \quad \text{Eq. 2.16}$$

Where S is the scattering coefficient. Kubelka and Munk (K-M) proposed a system of differential equations based on the model of light propagation in plane-parallel homogeneous layer of thickness x . K-M model is based on assuming perfectly diffuse light incident and the only interactions of the light with the medium are scattering and absorption. The diffuse radiation flux in the negative and positive x directions are designed I and J , respectively (Figure 2. 15.).

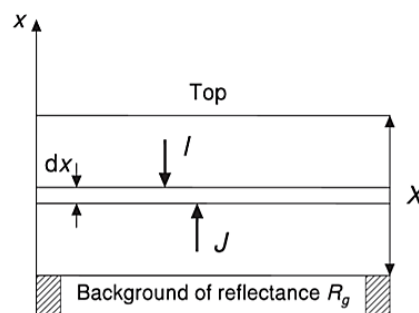


Figure 2. 15.: Cross sectional of a powder layer.

While the downward flux, I , passes through dx , it is decreased by amounts of Kdx and Sdx by the absorption and the scattering, and increased by an amount $SJdx$ by scattering, and a similar reasoning is made for the upward flux J , then the following differential equations (Eq. 2.17 and 2.18) can be derived:

$$-\frac{dI}{dx} = -(K + S)I + SJ \quad \text{Eq. 2.17}$$

$$\frac{dJ}{dx} = -(K + S)J + SI \quad \text{Eq. 2.18}$$

where K and S the absorption and scattering coefficient of the sample, respectively. Kubelka (1948) obtained explicit hyperbolic solutions to these equations that were later discussed in detail by Wyseck and Stiles (1982) and gave a solution in term of reflectance (R) (Eq. 2.19).

$$R = \frac{1 - R_g(a - b \coth bSX)}{a - R_g + b \coth bSX} \quad \text{Eq. 2.19}$$

where R_g is background reflectance, $\coth bSX$ the hyperbolic cotangent of bSX , $a=1+K/S$, and $b=(a^2-1)^{0.5}$. If layers are thick enough to ensure that a further increase in thickness does not change the reflectance, we can suppose that $x \rightarrow \infty$. Under these conditions, the reflectance is given by R_∞ and the Eq. 2.20 yields:

$$\frac{K}{S} = \frac{(1 - R_\infty)^2}{2R_\infty} = F(R_\infty) \quad \text{Eq. 2.20}$$

where $F(R_\infty)$ is K-M function.

In this work, band-gaps were determined from Tauc plots obtained from diffuse reflectance data. K-M function is proportional to the optical absorption. Hence the absorption coefficient, α , can be substituted by $F(R_\infty)$ in the Tauc equation (Eq. 2.21).

$$(h\nu\alpha)^{1/n} = [h\nu F(R_\infty)]^{1/n} \quad \text{Eq. 2.21}$$

where h is the Planck constant and ν frequency of vibration. The value of n denotes the nature of the sample transition. For the direct band-gap, the allowed transition is $n=1/2$, whilst for the indirect band-gap, the allowed transition is $n=2$. Subsequently, $[h\nu F(R_\infty)]^2$ and $[h\nu F(R_\infty)]^{1/2}$ curves were plotted against the photon energy, $h\nu$. The intersection point of the curve's tangent with horizontal axis determinates band-gap value of the sample. The Tauc method cannot determine conclusively if a band structure is direct or indirect.

Diffuse reflectance ultraviolet and visible (DRUV-VIS) spectra of ceramics were acquired at RT in the range 200-1600 nm using UV-VIS-NIR spectrometer (Shimadzu UV-3600) (Figure 2.16.) at Greatsolarcell, Manchester, United Kingdom.

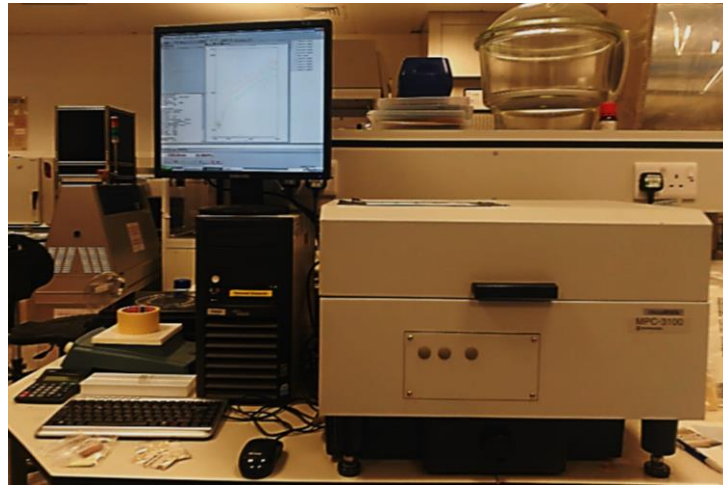


Figure 2. 16.: Image of UV-VIS-NIR spectrometer (Shimadzu UV-3600) at Greatsolarcell, Manchester, United Kingdom.

2.7. References

- Buchsbaum, C., & Schmidt, M. U. (2007). Rietveld refinement of a wrong crystal structure. *Acta Crystallographica Section B*, 63(6), 926–932. <https://doi.org/10.1107/S0108768107050823>
- Carter, C. B., & Norton, M. G. (2007). *Ceramic materials : science and engineering*. New York ; London: Springer.
- Chrisey, D. B., & Hubler, G. K. (1994). *Pulsed Laser Deposition of Thin Films* (Wiley-Inte). New York.
- Cullity, B. D. (2014). *Elements of x-ray diffraction* (Internatio). Pearson Education.
- Kittel, C., & Hellwarth, R. W. (1957). Introduction to Solid State Physics. *Physics Today*, 10(6), 43. <https://doi.org/10.1063/1.3060399>
- Martin, L. W., Chu, Y. H., & Ramesh, R. (2010). Advances in the growth and characterization of magnetic, ferroelectric, and multiferroic oxide thin films. *Mater. Sci. Eng. R-Reports*, 38, 133.
- Martín, M. J., Alfonso, J. E., Mendiola, J., Zaldo, C., Gill, D. S., Eason, R. W., &

- Chandler, P. J. (1997). Pulsed laser deposition of KNbO₃ thin films. *Journal of Materials Research*, 12(10), 2699–2706. <https://doi.org/DOI:10.1557/JMR.1997.0359>
- McCusker, L. B., Dreele, R. B. Von, Cox, D. E., Lou\er, D., & Scardi, P. (1999). Rietveld refinement guidelines. *Journal of Applied Crystallography*, 32(1), 36–50. <https://doi.org/10.1107/S0021889898009856>
- Perry, C. H., & Hall, D. B. (1965). Temperature dependence of the Raman spectrum of BaTiO₃. *Physical Review Letters*, 15(17), 700–702. <https://doi.org/10.1103/PhysRevLett.15.700>
- Van Benthem, K., Elsässer, C., & French, R. H. (2001). Bulk electronic structure of SrTiO₃: Experiment and theory. *Journal of Applied Physics*, 90(12), 6156–6164. <https://doi.org/10.1063/1.1415766>
- Waseda, Y., Matsubara, E., & Shinoda, K. (2011). *X-ray diffraction crystallography introduction, examples and solved problems*. Heidelberg ; New York: Springer.
- Young, R. A., & Wiles, D. B. (1982). Profile shape functions in Rietveld refinements. *Journal of Applied Crystallography*, 15(4), 430–438.

Chapter 3

Processing and Characterisation of KNbO_3 ceramics

3.1 Introduction

3.2 Method 1

3.2.1. Purity and crystal structure

3.3 Method 2

3.3.1 Purity and crystal structure

3.4 Comparison between method 1 and 2

3.4.1 X-Ray diffraction data

3.4.2 Stability in water

3.5 Structural and chemical characterisation

3.5.1 Raman Spectroscopy

3.5.2 SEM

3.5.3 EDX

3.6 Electric characterisation of stoichiometric KNbO_3 prepared via 2

3.6.1 Dielectric characterisation

3.6.2 Ferroelectric Characterisation

3.7 Optical characterisation

3.7.1 Diffuse reflectance spectroscopy

3.8. Discussion

3.9. Conclusions

3.10. References

3. Processing and Characterisation of KNbO_3 ceramics.

3.1. Introduction

The first part of this chapter is focused on the processability (powder synthesis and sintering) of KNbO_3 (KN) ceramics. Difficulties associated with the preparation of dense KN ceramics often limit the ability to fully characterise their electrical properties and rule out many technological applications of this material. Subsequently, the second part of this chapter is devoted to the dielectric, ferroelectric and optical characterisation of dense KN ceramics.

Potassium presents high volatility at 800 °C and its evaporation from the system is accelerated by moisture in the environment (Flueckiger & Arend, 1977). Potassium losses during ceramic processing make difficult the control of the stoichiometry in KN ceramics. As mentioned in Chapter 1, a secondary phase, $\text{K}_4\text{Nb}_6\text{O}_{17}$ (ICDD#: 00-031-1064), is easily formed due to potassium loss. This hygroscopic phase often leads to disintegration of non-fully dense ceramics due to absorption of atmospheric moisture. Another problem affecting the preparation of dense KN ceramics is the sintering temperature, which is very close to the melting point of this perovskite.

Various publications deal with the above shortcomings and proposed specific ceramic processing conditions. Table 3. 1 and Table 3. 2 list some of the investigations based on single and double calcination procedures, respectively. Moreover, it has been shown that the introduction of additives, such as LaFeO_3 (K. I. Kakimoto, Masuda, & Ohsato, 2003), CuO (Kim et al., 2014) and ZnO (Lv, Li, Wu, Xiao, & Zhu, 2016) among others, enhance density and electrical properties of KN ceramics. Kakimoto et al obtained high density

(98.8%) by substituting 0.2 % of LaFeO₃ into KN ceramics, which were sintered at 1020 °C in a potassium rich atmosphere provided by covering the green body with additional KN powder. In 2007, Matsumoto et al reported a density of KN as high as 96.3% when calcining two times and sintering at 1050 °C. In addition, the same authors also demonstrated that the addition of 1.2 wt% of MnCO₃ promotes the reduction of the electrical conductivity and enhances densification. This work shows a reputable 0.22% electric-field induced strain under unipolar field of 80 kV/cm (K Matsumoto, Hiruma, Nagata, & Takenaka, 2008). In 2016 Lv et al showed that the addition of ZnO to KN improves the electrical resistance and the stability in moisture.

Nevertheless, only few works reported on electrical properties of undoped KN ceramics, mainly due to the poor densification (H Birol, Damjanovic, & Setter, 2005; Dubernet & Ravez, 1998). In contrast, literature on the electric properties of KNN ceramics is vast, because those are more amenable preparation (Hansu Birol, Damjanovic, & Setter, 2006; Egerton & Dillon, 1959; Uniyal et al., 2003).

In this study, stoichiometric (KNbO₃), K-deficient (K_{0.95}NbO_{2.975}) and K-excess (KNb_{0.95}O_{2.875}) samples were prepared in order to evaluate the impact of an eventual potassium volatilisation during the processing. Moreover, two batches of KNbO₃, K_{0.95}NbO_{2.975} and KNb_{0.95}O_{2.875} ceramics were prepared by solid-state reaction following two different routes: standard (method 1) and optimised (method 2) ceramic processing. The two methods selected consist of two calcination steps, which allegedly are more effective in obtaining dense KN ceramics. Method 1 and method 2 are mainly inspired by the works of Matsumoto et al and Kakimoto et al, respectively.

The main findings in terms of purity, crystal structure and stability comparing both methods are presented in the first part of this chapter. Later, crystal structure, lattice dynamics, microstructure, stability of dense KN ceramics were investigated. The second part reports the dielectric, ferroelectric and optical properties for the stoichiometric composition. In addition, the optical properties of stoichiometric and non-stoichiometric were measured and compared.

Table 3. 1: KN ceramic processing methods in the literature using a single stage calcination step. Also, experimental relative permittivity (ϵ_r), Curie temperature (T_C), spontaneous polarisation (P_S) and maximum strain (S_{max}) values are included in this table.

Reference	Calcination conditions	Sintering conditions	Relative densities (%)	ϵ_r	T_C (°C)	P_S	S_{max}
(Tashiro, Nagamatsu, & Nagata, 2002)	900 °C (2h)	1090 °C-1170 °C	96.2	~4000	~400	20 μ C/cm ² at 30 kV/cm	-
(H Birol et al., 2005)	625°C (4h) 3°C/min	1035 °C	94	~3500	410	25 μ C/cm ² at 80 kV/cm	-
(Acker, Kungl, & Hoffmann, 2013)	775°C (5h)	1060°C	~85	-	-	-	-
(Lv et al., 2016)	800°C (4h)	1020°C (1-6 h)	-	~4000	430	23 μ C/cm ² at 30 kV/cm	-
(Park et al., 2017)	950°C (3h)	960°C (1-8 h)	98	~4000	406	26 μ C/cm ² at 80 kV/cm	0.17% at 80 kV/cm

Table 3. 2: KN ceramic processing in the literature using a double calcination step. Also, experimental relative permittivity (ϵ_r), Curie temperature (T_C), spontaneous polarisation (P_S) and maximum strain (S_{max}) values are included in this table.

Reference	Calcination conditions	Sintering conditions	Relative densities (%)	ϵ_r	$T_C(^{\circ}\text{C})$	P_S	S_{max}
(K. Kakimoto, Masuda, & Ohsato, 2005)	820°C (4h) + 850°C (4h)	1020°C-1280°C	90	~1200	420	7 $\mu\text{C}/\text{cm}^2$ at 40 kV/cm	0.02% at 40 kV/cm
(Kenji Matsumoto, Hiruma, Nagata, & Takenaka, 2007)	600°C (4h) + 1000°C (4h)	1055°C-1060°C (2h)	96.2	-	-	-	-
(Hajime Nagata, Matsumoto, Hirose, Hiruma, & Takenaka, 2007)	600°C (4h) + 1000°C (4h)	1055°C (2h)	>96	~3800	424°C	-	-
(Kim et al., 2014)	600°C (4h) + 1000°C (4h)	940°C-980°C (2h)	<70	-	-	-	-
Method 1 This study	625°C (4h) + 1000°C (4h)	1070 (4h)	-	-	-	-	-
Method 2 This study	850°C (4h) + 850°C (4h)	1085 (4h)	>94	~2600	398°C	17 $\mu\text{C}/\text{cm}^2$ at 80 kV/cm	0.092% at 80 kV/cm

3.2. Method 1

3.2.1. Purity and crystal structure

A series of KNbO_3 , $\text{K}_{0.95}\text{NbO}_{2.975}$ and $\text{KNb}_{0.95}\text{O}_{2.875}$ powders and ceramics were prepared by the conventional solid-state reaction method, following the two step calcination, proposed by Matsumoto et al, 2007.

Starting materials, were dried potassium carbonate (K_2CO_3) and niobium oxide (Nb_2O_5) weighed in required ratio, were mixed overnight in polyethylene bottles with zirconia milling media and using propan-2-ol as the milling medium. K_2CO_3 powder is hygroscopic and tends to absorb water when left open in air. Therefore, exposition of raw materials was kept to a possible minimum. The obtained slurries were dried, sieved and calcined, first at 625 °C and then at 1000°C, both for 4 hours with a heating rate of 3°C/min. Synthesis and sintering process was handled very carefully in order to avoid material losses, which would affect the sensitive stoichiometry of KNbO_3 . Subsequently, purity and crystal structure were examined by X-ray diffraction. Figure 3. 1 shows XRD patterns of KNbO_3 and non-stoichiometric KNbO_3 powders calcined at 625°C and 1000°C.

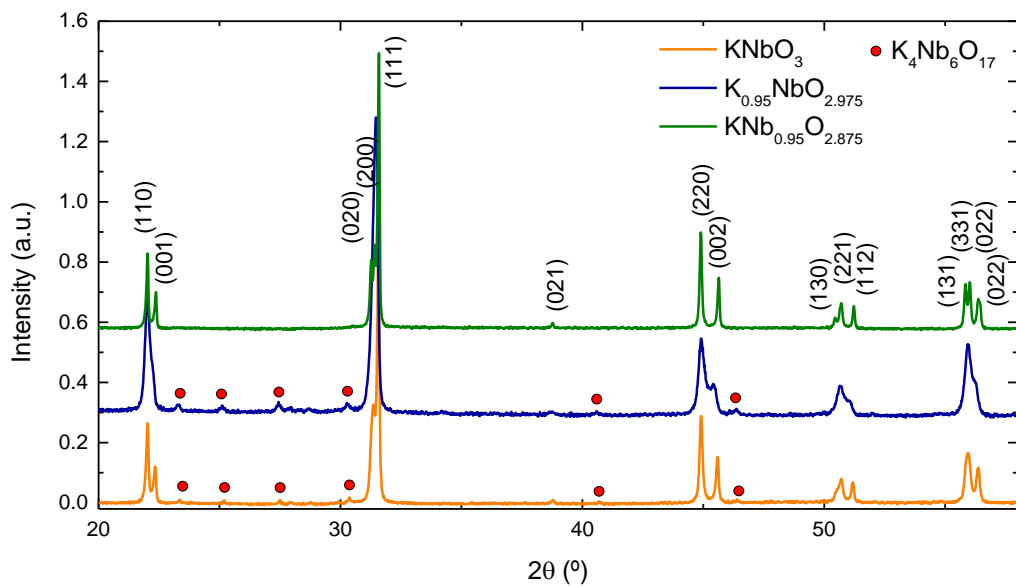


Figure 3. 1: XRD data of KNbO_3 , $\text{K}_{0.95}\text{NbO}_{2.975}$ and $\text{KNb}_{0.95}\text{O}_{2.875}$ powders after calcination at 625°C and 1000°C (Method 1). Red symbols indicate small amount of $\text{K}_4\text{Nb}_6\text{O}_{17}$.

XRD patterns of the three compounds look similar and can be ascribed to an orthorhombic perovskite. A small amount of secondary phase ($\text{K}_4\text{Nb}_6\text{O}_{17}$) appears in both stoichiometric and K-deficient powders, as indicated by the red circles. Differences on the degree of splitting of the quadruplet (131), (313), (022) and (202), suggest that a variation on the K/Nb ratios of the initial batches directly affect the purity but also the crystallisation of KNbO_3 . Higher degree of crystallinity is obtained for the K-excess composition (APPENDIX A).

Birol et al. reported that compact pellets should be fired at 1035°C in oxygen rich atmosphere. The furnace used in the present work is not equipped to control the firing environment. Samples fired at 1035°C were far from being densified. Hence, measurements of the shrinkage of pure KN after firing at different temperatures, was employed to experimentally determine the sintering temperature (Figure 3. 2).

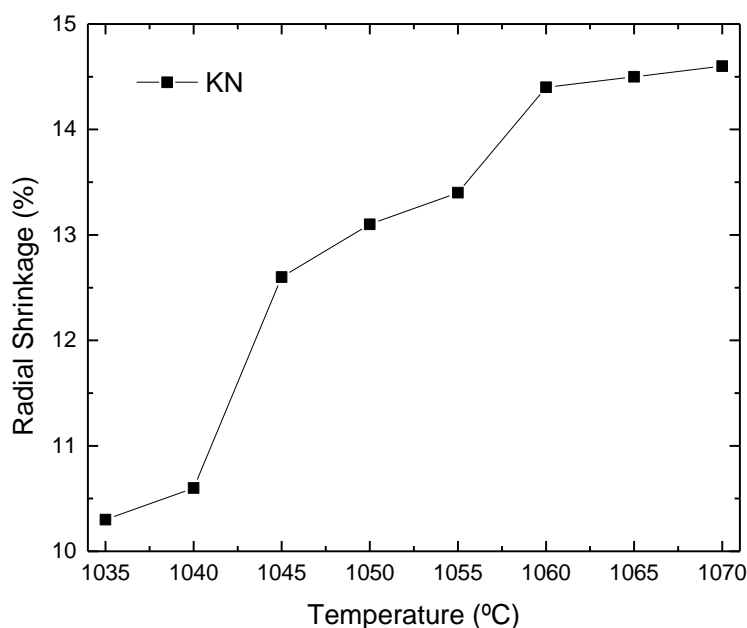


Figure 3. 2: Radial shrinkage as a function of the temperature for stoichiometric KN prepared by method 1.

The radial shrinkage of the pellet systematically increases with increasing firing temperature. From 1060°C to 1070°C its value is practically constant ($\sim 14.5\%$). At 1075°C the sample melts. Figure 3. 3 shows the room temperature X-Ray Diffraction data for KNbO_3 and non-stoichiometric KNbO_3 ceramics sintered at 1070°C .

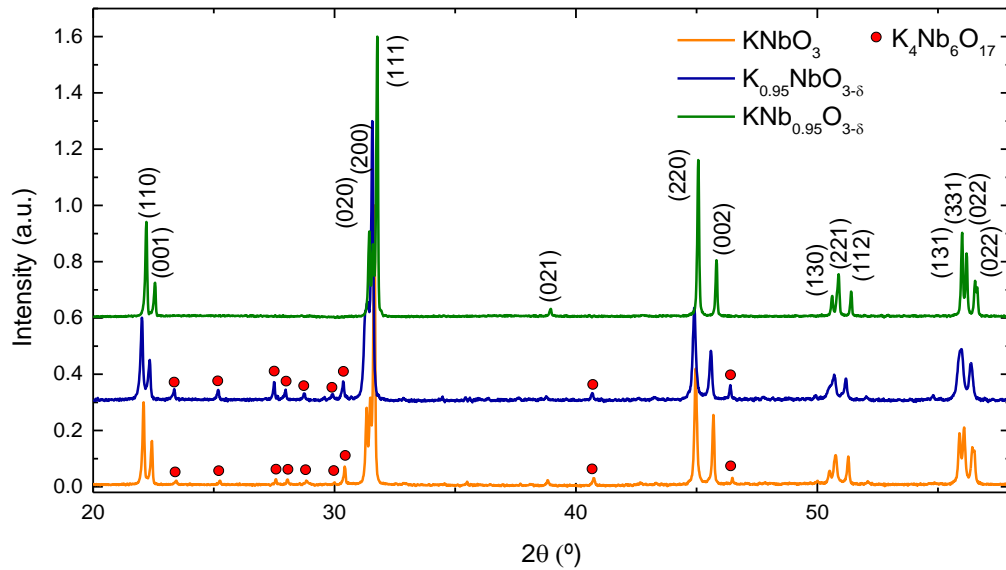


Figure 3. 3: XRD data of KNbO_3 , $\text{K}_{0.95}\text{NbO}_{2.975}$ and $\text{KNb}_{0.95}\text{O}_{2.875}$ pellets after sintering (method 1). Red symbols indicate the presence of $\text{K}_4\text{Nb}_6\text{O}_{17}$.

At first glance, it is apparent that the amount of secondary phase ($\text{K}_4\text{Nb}_6\text{O}_{17}$) in $\text{K}_{0.95}\text{NbO}_{2.975}$ and KNbO_3 increases considerably after sintering. As aforementioned this phase shows deliquescence when exposed to moisture. After sintering, K-deficient sample exhibits slightly higher concentration of this second phase. This fact leads to suggest that K losses are accelerated at high temperature in K-deficiency conditions. The 5 mol% of extra K in $\text{KNb}_{0.95}\text{O}_{2.875}$ samples seems to compensate for the losses during the processing, obtaining single-phase KN ceramics.

Peak splitting is better discernible in XRD patterns of KNbO_3 and $\text{KNb}_{0.95}\text{O}_{2.875}$ because of enhanced crystallisation. K-deficient samples may require higher firing temperature for better crystallisation, however they melt at 1075°C prior to full densification. The presence of $\text{K}_4\text{Nb}_6\text{O}_{17}$ phase, the accelerated K losses at high temperatures and the low melting temperature hinders the densification for K-deficient samples. Table 3. 3 shows the unit cell dimensions calculated by Rietveld refinements. However, experimental and relative densities were not measured because they were extremely low at first glance.

	KNbO_3		$\text{K}_{0.95}\text{NbO}_{2.975}$		$\text{KNb}_{0.95}\text{O}_{2.875}$
Space	89.4(5)%	10.6(3) %	84.9(5) %	15.1 (4) %	
Group	Amm2	Pna21	Amm2	Pna21	Amm2
Density (calculated) (g/cm^3)	4.6121(1)	3.9080(1)	4.5739(4)	3.9123(1)	4.5077(4)
a (Å)	3.9759(1)	33.0280(1)	3.9737(1)	33.019(2)	3.9734(1)
b (Å)	5.6961(1)	6.4861(1)	5.6924(1)	6.4828(6)	5.6951(1)
c (Å)	5.7225(1)	7.8204(1)	5.7187(2)	7.8178(8)	5.7216(1)
V/10^6 (pm^3)	64.799(2)	1675.3(1)	64.678(1)	1673.46(3)	64.7370(1)
R_{exp}	1.62276		1.53789		1.56951
R_{profile}	3.28346		3.28856		3.28807
R_{wp}	4.31841		4.24442		4.45203
GOF	7.08174		7.61707		8.04612

Table 3. 3: Theoretical density, lattice parameters and agreement indices for KNbO_3 , $\text{K}_{0.95}\text{NbO}_{2.975}$ and $\text{KNb}_{0.95}\text{O}_{2.875}$ calculate by Rietveld Refinement.

3.3. Method 2

3.3.1. Purity and crystal structure

A second series of KNbO_3 , $\text{K}_{0.95}\text{NbO}_{2.975}$ and $\text{KNb}_{0.95}\text{O}_{2.875}$ powders and ceramics was prepared by the solid state reaction method, but in this case following the route suggested in the literature by Kakimoto et al (method 2). Powders were compacted into big pellets of ~5 g each and calcined twice at 850°C (4h). After that, the pellets were crushed using a mortar and pestle until a very fine powder was obtained. XRD data of calcined powders for the three compositions prepared by Method 2 are shown in Figure 3. 4.

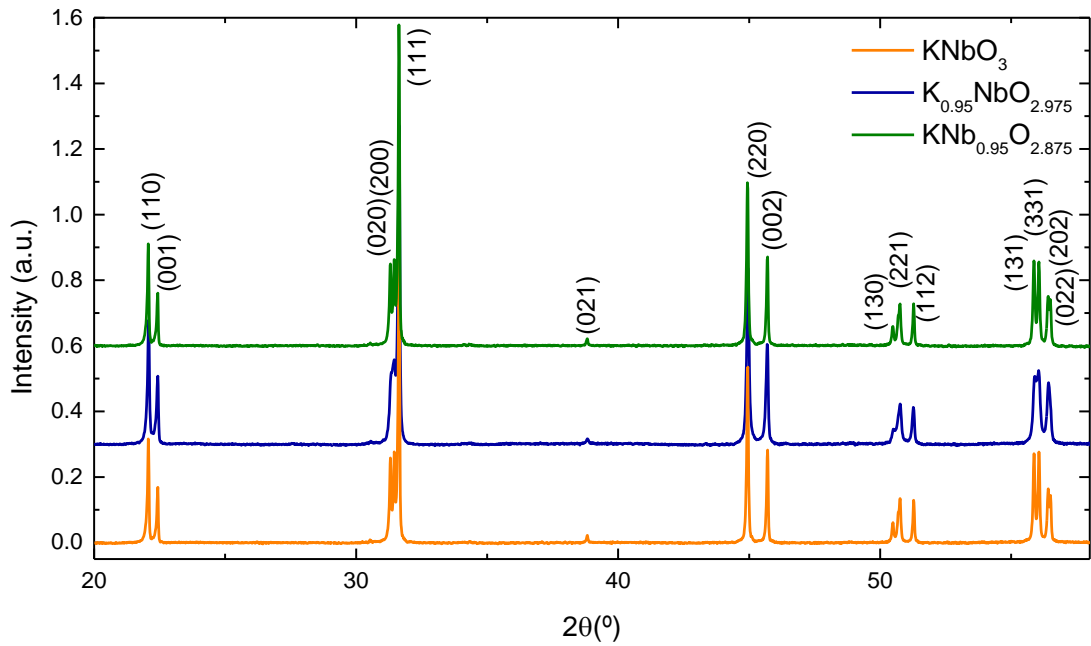


Figure 3. 4: XRD data of KNbO_3 , $\text{K}_{0.95}\text{NbO}_{2.975}$ and $\text{KNb}_{0.95}\text{O}_{2.875}$ powders after calcining two times at 850°C (Method 2).

After calcination, all XRD data for KNbO_3 , $\text{K}_{0.95}\text{NbO}_{2.975}$ and $\text{KNb}_{0.95}\text{O}_{2.875}$ exhibit well defined peaks and similar patterns. Reflections of the three compositions can be attributed to orthorhombic phase (Amm2 space group). Unexpectedly, $\text{K}_4\text{Nb}_6\text{O}_{17}$ secondary phase is not detected in the potassium deficiency composition. Peak splitting in KN is not as noticeable as in the other compositions.

For sintering, pellets were uniaxially pressed under 1 tonne and buried in powder of the same composition in a covered alumina crucible in order to inhibit volatilization of K. For this method, the pellets are not successfully densified at 1070°C . In the same way as in method 1, the monitoring of the radial shrinkage of the sample permits to determine the optimum sintering temperature of KN. Figure 3. 5 illustrates the evolution of the radial shrinkage of KN with the sintering temperature, from 1070°C to 1085°C (the sample melts at 1090°C).

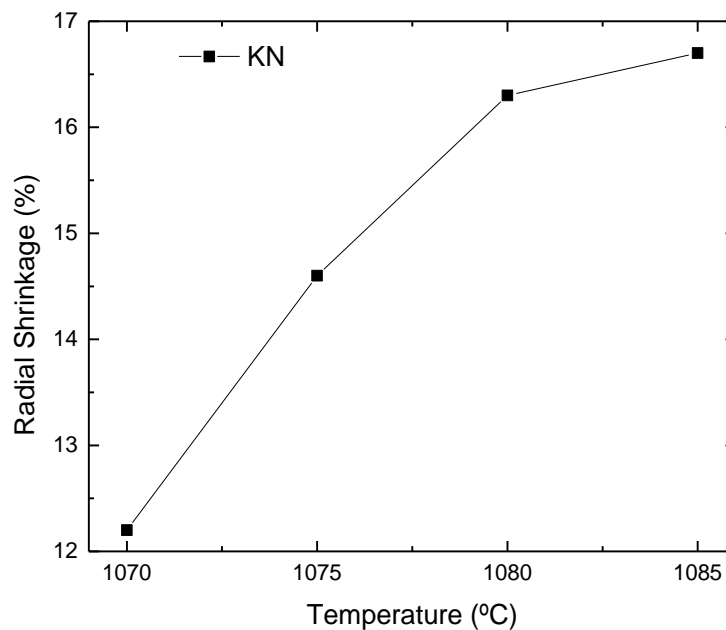


Figure 3. 5: Radial shrinkage versus sintering temperature for stoichiometric KN ceramics prepared by method 2.

Optimal sintering temperature for stoichiometric composition is 1085°C with a radial shrinkage of $\sim 16.5\%$. However, $\text{K}_{0.95}\text{NbO}_{2.975}$ and $\text{KNb}_{0.95}\text{O}_{2.875}$ melt at lower temperatures than pure KN. Table 3. 4 shows the sintering and melting temperatures for the three compounds.

Compound	Sintering Temperature (°C)	Melting Point (°C)
KNbO_3	1085	1090
$\text{K}_{0.95}\text{NbO}_{2.975}$	1080	1085
$\text{KNb}_{0.95}\text{O}_{2.875}$	1070	1075

Table 3. 4: Sintering and melting temperatures for KNbO_3 , $\text{K}_{0.95}\text{NbO}_{2.975}$ and $\text{KNb}_{0.95}\text{O}_{2.875}$ prepared following method 2.

Figure 3. 6 shows the room temperature XRD data for KNbO_3 and non-stoichiometric KNbO_3 ceramics sintered at 1070°C-1085°C for 4 hours.

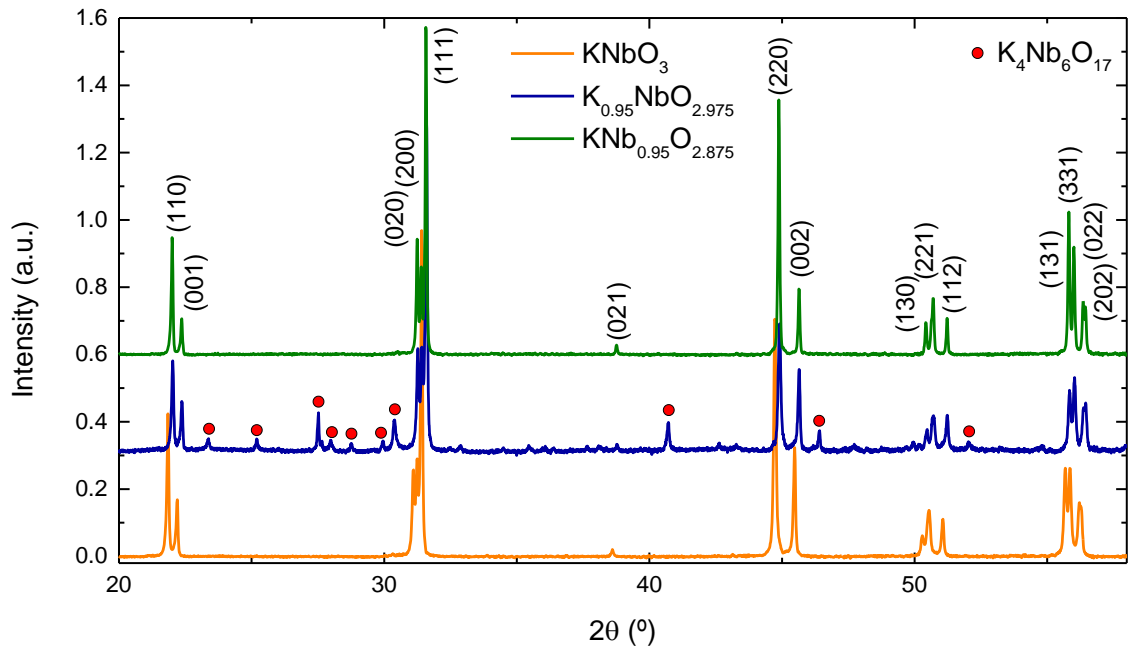


Figure 3. 6: XRD data of KNbO_3 , $\text{K}_{0.95}\text{NbO}_{2.975}$ and $\text{KNb}_{0.95}\text{O}_{2.875}$ pellets after sintering (method 2). Red symbols indicate reflections from $\text{K}_4\text{Nb}_6\text{O}_{17}$.

The stoichiometric and K-excess ceramics appear to be single-phase within the detection limits of the technique, whereas K-deficient $\text{K}_{0.95}\text{NbO}_{2.975}$ sample exhibits the presence of $\text{K}_4\text{Nb}_6\text{O}_{17}$ as a secondary phase after sintering. These results show how prone are KN ceramics to exhibit secondary phases when the K/Nb ratio is lower than 1.

Patterns for KNbO_3 and $\text{KNb}_{0.95}\text{O}_{2.875}$ were refined in the $\text{Amm}2$ space group and unit cell dimensions were calculated (Table 3. 5). A two-phase refinement was carried out for XRD data of $\text{K}_{0.95}\text{NbO}_{2.975}$ ceramics, using the $\text{Amm}2$ space group to model the orthorhombic KNbO_3 -based phase and the $\text{Pna}21$ space group to model the $\text{K}_4\text{Nb}_6\text{O}_{17}$ phase. The relative amounts of those two phases were calculated as $\sim 65\%$ and $\sim 35\%$, respectively.

	KNbO_3	$\text{K}_{0.95}\text{NbO}_{2.975}$		$\text{KNb}_{0.95}\text{O}_{2.875}$
Space Group	Amm2	64.8(5) % Amm2	35.1 (6) % Pna21	Amm2
Density (Experimental) (g/cm³)	4.35(3)	3.62(10)		3.87(5)
Density (calculated) (g/cm³)	4.6273(1)	4.3388(4) *		4.5077(4)
Relative Density (%)	94(1)	83(2) *		86(1)
a (Å)	3.9711(1)	3.9729(1)	32.995(3)	3.9705(2)
b (Å)	5.6909(1)	5.6905(2)	6.4773(7)	5.6905(3)
c (Å)	5.7158(1)	5.7175(2)	7.8207(4)	5.7173(2)
V/10⁶ (pm³)	64.576(2)	64.630(4)	1671.4(3)	64.589(5)
R_{exp}	1.26460	1.47829		0.90713
R_{profile}	2.97912	4.11528		5.02131
R_{wp}	4.65175	6.02513		9.53967
GOF	13.53086	16.61173		11.59170

Table 3. 5: Experimental and theoretical density, lattice parameters and agreement indices for KNbO_3 , $\text{K}_{0.95}\text{NbO}_{2.975}$ and $\text{KNb}_{0.95}\text{O}_{2.875}$ calculate by Rietveld Refinement. * Weighted averaged of the two phases.

Experimental density is estimated by the geometric method as explained in Chapter 3. Archimedes method is not suitable for this composition because of high sensitivity to water. Relative density is obtained comparing with the density calculated by Rietveld refinement. Stoichiometric samples present densities above 90%. In contrast, K-excess and K-deficient compositions presents low densities ($\sim 86\%$ and $\sim 79\%$, respectively). Lattice parameters of KNbO_3 , $\text{K}_{0.95}\text{NbO}_{2.975}$ and $\text{KNb}_{0.95}\text{O}_{2.875}$ are similar up to the third decimal and consequently they exhibit very similar volume values of the unit cells. Table 3. 5 also shows some indices that inform about the quality of the refinements. The reader is strongly encouraged to refer Appendix A where additional information is provided. Figure 3. 7 shows XRD pattern evolution of sintered KN pellet from RT up to 500°C. From 30°C to 150°C, the pattern is well ascribed as orthorhombic

phase (Amm2). From 200°C to 400°C, KN is tetragonal (P4mm) and over 400°C, cubic (Pm- $\bar{3}$ m).

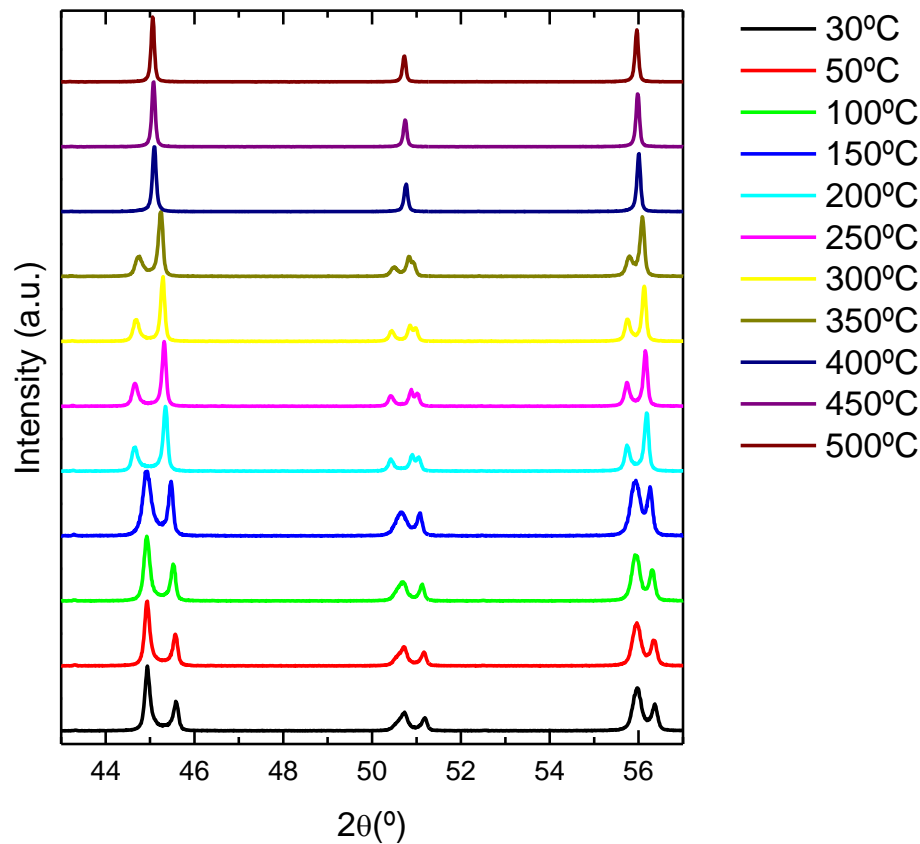


Figure 3. 7: Temperature dependence of XRD pattern of KN sintered ceramic from 30°C to 500°C.

3.4. Comparison between method 1 and 2

3.4.1. X-Ray diffraction data

The purpose of this section is to compare in terms of purity and stability KN and non-stoichiometric ceramics prepared by method 1 and method 2. Differences on purity and crystallinity will be highlighted and the potential origins for those will be discussed. Figure 3. 8 shows the XRD pattern of pure KN (a), K-deficient (b) and K-excess (c) prepared by method 1 and 2.

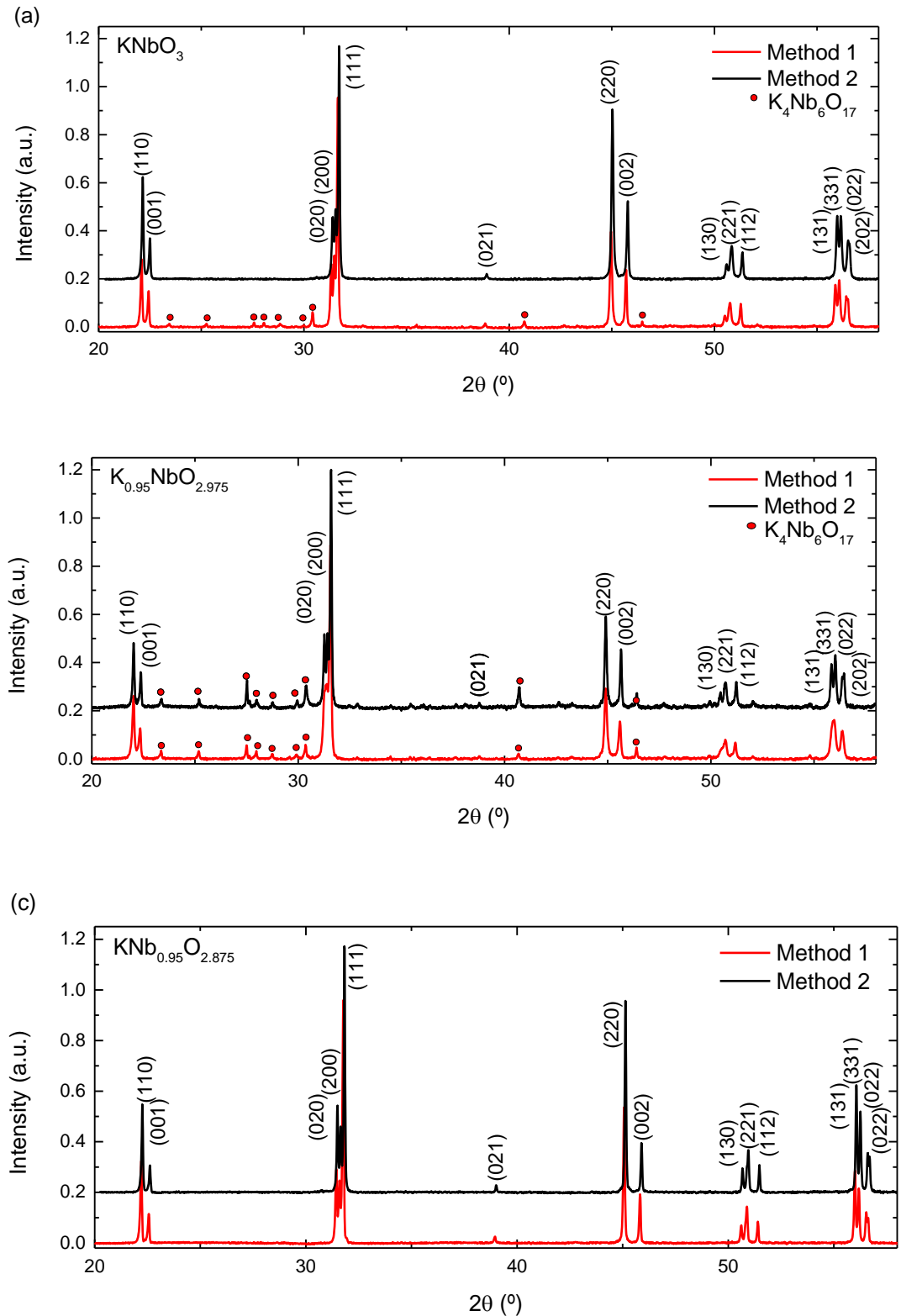


Figure 3. 8: Comparison of method 1 and 2 by inspection of XRD data of pure KN (a), K deficient (b) and K excess (c).

K losses in KN compounds are more remarkable when the materials are prepared by method 1. The only composition that is single phase is $\text{KNb}_{0.95}\text{O}_{2.875}$, because the K excess compensates for its losses during processing (Figure 3. 8 (c)). On the other hand,

both XRD data for pure KN and $K_{0.95}NbO_{2.975}$ reveal the presence of a secondary phase ($K_4Nb_6O_{17}$) which is strictly related with the loss of K, as explained above.

Method 2 appears to be an appropriate choice to prepare compounds based on KN. Its success may rely on: (1) the calcination of compacted powders and (2) imbedding pressed pellets into “atmospheric powder” during the sintering.

The use of atmospheric powders has been reported in the literature as a solution for inhibiting the volatility of some atomic species during ceramic processing, such as, Pb in PZT (Kington & Clark, 1983) and KNN, among others. The atmospheric powder, also known as sacrificial powder, must be the same composition as the sintered sample. Some authors reported this procedure to increase densities (Zhen & Li, 2006), others observed only enhancements in the grain size distribution (Pavlič, Malič, & Rojac, 2014).

3.4.2. Stability in water

In the previous sections it was shown that the high volatility of potassium prevents control of the stoichiometry in $KNbO_3$ ceramics during sintering process. This leads to poor densification and the formation of an unstable secondary phase, $K_4Nb_6O_{17}$, which causes disintegration of the ceramics when they are exposed to humidity.

Figure 3. 9 (a) and (b) show top external view of $KNbO_3$ ceramics pellets (KN_1 and KN_2) sintered by solid state reaction following method 1 and 2.

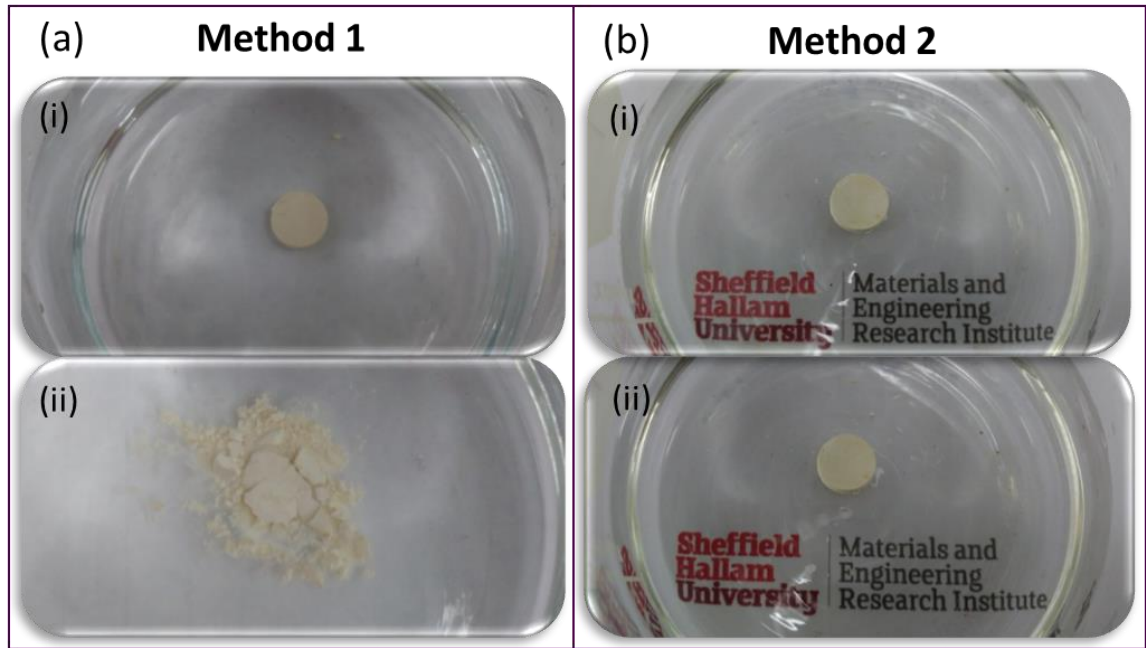


Figure 3. 9: KNbO_3 ceramic pellets immersed in water, prepared by method 1 (KN_1) and method 2 (KN_2). When sample KN_1 is immersed in water (Figure 3. 9 (a) (i)), the sintered body starts immediately to crack. After 5 minutes (Figure 3. 9 (a) (ii)), the sample is disintegrated. In contrast, the sample KN_2 shown in Figure 3. 9 (b) (i) and (ii) showed no reaction under water.

Figure 3. 10 (a) and (b) show the behaviour of $\text{K}_{0.95}\text{NbO}_{2.975}$ ceramics in water ($\text{K}_{0.95}\text{N}_1$ and $\text{K}_{0.95}\text{N}_2$) prepared by method 1 and 2, respectively. Both $\text{K}_{0.95}\text{N}_1$ and $\text{K}_{0.95}\text{N}_2$ samples are unstable in water. $\text{K}_{0.95}\text{N}_1$ showed in Figure 3. 10 (a) (i) and (ii) is decomposed in similar manner as KN_1 after 1 minute. The other specimen ($\text{K}_{0.95}\text{N}_2$) immediately exhibits high hygroscopic behaviour (Figure 3. 10 (b) (i) and (ii)). The pellet dissolves into water and the surroundings got muddy at the same time.

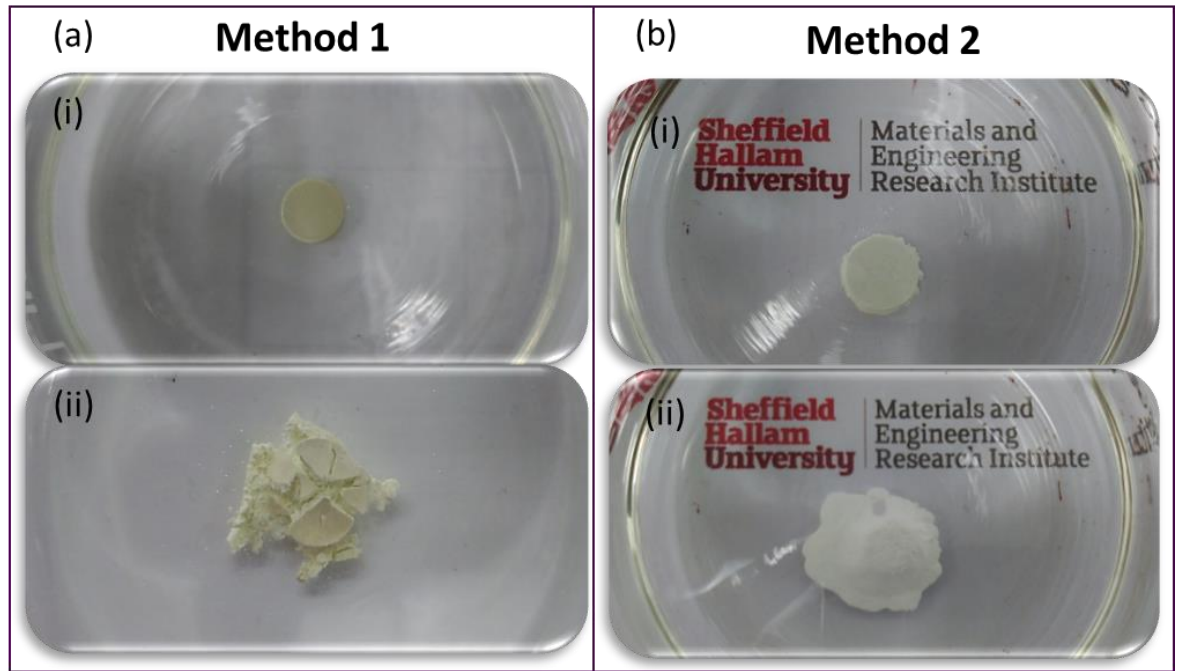


Figure 3. 10: $\text{K}_{0.95}\text{NbO}_{2.975}$ ceramic pellets immersed in water. Both $\text{K}_{0.95}\text{N}_1$ ((a) (i) and (ii)) and $\text{K}_{0.95}\text{N}_2$ ((b) (i) and (ii)) dissolve in water after few seconds.

Finally, the stability in water is checked for $\text{KNb}_{0.95}\text{O}_{2.875}$ samples ($\text{KN}_{0.95_1}$ and $\text{KN}_{0.95_2}$) (Figure 3. 11 (a) and (b)) prepared by method 1 and 2.

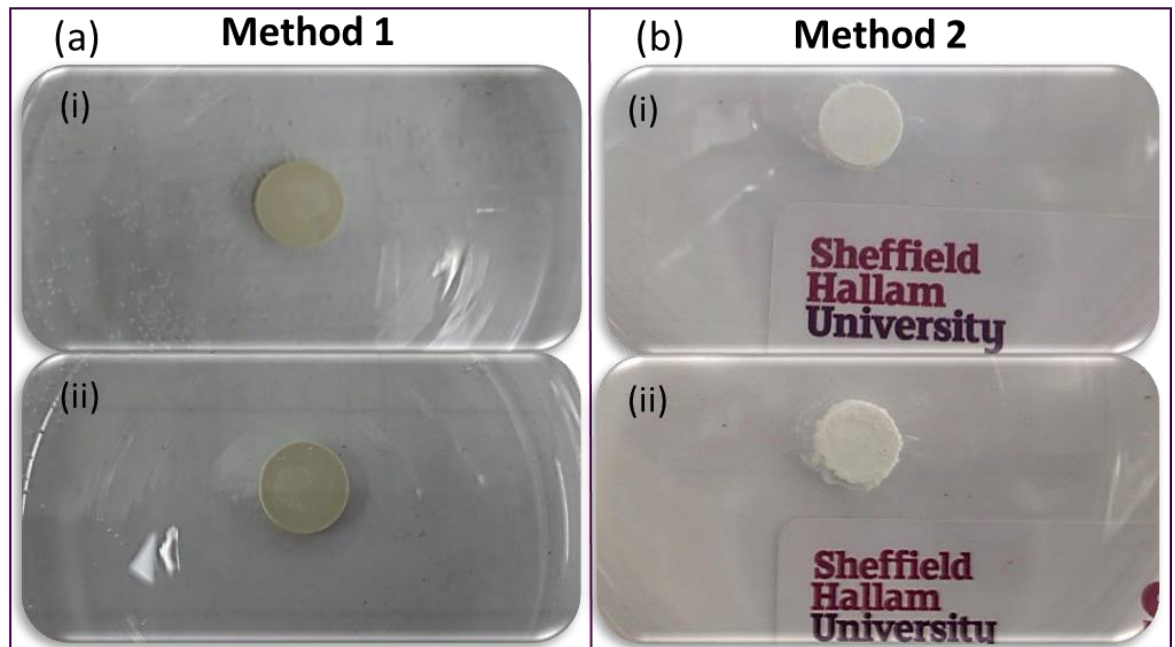


Figure 3. 11: $\text{KNb}_{0.95}\text{O}_{2.875}$ ceramic pellets immersed in water. Both $\text{KN}_{0.95_1}$ ((a) (i) and (ii)) and $\text{KN}_{0.95_2}$ ((b) (i) and (ii)) dissolve in water after few seconds.

$\text{KN}_{0.95_1}$ sample is stable in water after 3 hours. On the other hand $\text{KN}_{0.95_2}$ dissolved in water, probably due to its low density (85%).

Both method 1 and method 2 followed rigorous procedures for each processing step to reduce the reaction with environmental humidity and to avoid contamination. However, samples prepared by method 1 reveal larger potassium loss during the ceramic processing than samples prepared by method 2, leading to the appearance of $\text{K}_4\text{Nb}_6\text{O}_{17}$, a very hygroscopic phase.

The differences between the two methods concern heat treatment conditions. Firstly, second calcination in method 1 occurs at higher temperature than in method 2, which may lead to higher potassium volatility. Secondly, powders are compacted before calcination (method 2) instead of being directly heat treated (method 1). Thirdly, in method 2 the sintering is carried out under enriched potassium environment produced by a combination of using sacrificial powder and in addition covering the species with alumina crucibles. In contrast, sintering in method 1 is performed under room atmosphere.

These steps undertaken in method 2 effectively suppressed potassium losses during the ceramic processing. On the other hand, method 1 is suitable if extra quantity of K is added to the starting powder mixture to compensate the K evaporation. Due to high sensitivity of the stoichiometry in this system, it is considered more appropriate to follow the route suggested by method 2. All systems in the present study were prepared using at least two calcinations at temperatures no greater than 850°C .

3.5. Structural and chemical characterisation

3.5.1. Raman Spectroscopy

Room-temperature Raman spectra for KNbO_3 , $\text{K}_{0.95}\text{NbO}_{2.975}$ and $\text{KNb}_{0.95}\text{O}_{2.875}$ powder and sintered pellets prepared by method 2, are presented in Figure 3. 12 and Figure 3. 13, respectively. The three compositions exhibit analogous Raman spectra for powders and pellets. Consequently, the following analysis can be applied in both cases.

Orthorhombic KNbO_3 exhibits 12 Raman active optical modes of $4A_1 + 4B_1 + 3B_2 + A_2$ symmetries from group theory analysis. Modes in the following Raman spectra are labelled according to the single-crystal assignment by Quittet (1976): (i) a mixed sharp mode at 192 cm^{-1} ; (ii) a Fano-type interference dip at 197 cm^{-1} ; (iii) a broad B_1 (TO) mode

centered at 250 cm^{-1} ; (iv) a $B_1(\text{TO})$ at 272 cm^{-1} ; (v) a sharp mode at 278 cm^{-1} ; (vi) another mode at 294 cm^{-1} ; (vii) a $B_1(\text{TO})$ mode at $\sim 532\text{ cm}^{-1}$; (viii) a $A_1(\text{TO})$ mode at $\sim 600\text{ cm}^{-1}$ and (ix) a low intensity $A_1(\text{LO})$ mode at 831 cm^{-1} .

The sharp mode at 192 cm^{-1} is a mixed $B_1(\text{TO})$, $A_1(\text{TO})$, $A_1(\text{LO})$ and $B_2(\text{TO})$ mode. Similarly, the mode at 278 cm^{-1} is due to a broad $A_1(\text{TO})$ combined with a sharp A_2 , whilst the sharp mode at 294 cm^{-1} is due to $A_1(\text{LO})$ and $A_1(\text{TO})$, associated with a BO_6 bending vibration (Zhou, Deng, Yang, & Chu, 2014). However, because of the resolution limit of the instrument they all appear merged as a single peak

The occurrence of long-range polarisation in KNbO_3 is ultimately associated with the presence of the (i), (ii) and (vi) modes, which will therefore be used in this work to monitor the polar nature of KN-based solid solutions, (Luisman, Feteira, & Reichmann, 2011).

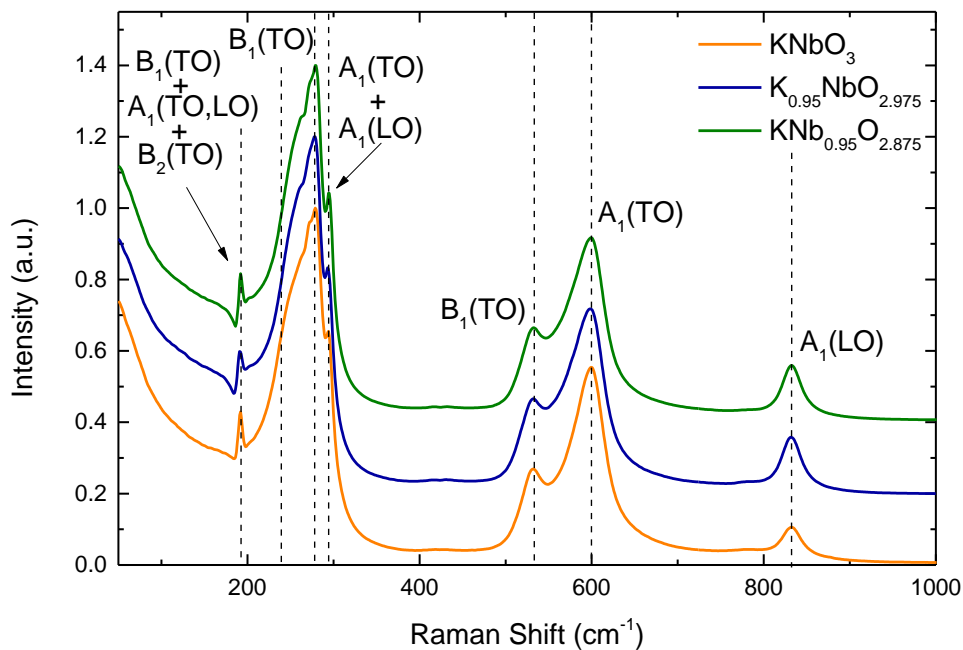


Figure 3. 12: Room temperature Raman Spectra of KNbO_3 and non-stoichiometric powders calcined twice at 850°C for 4 hours.

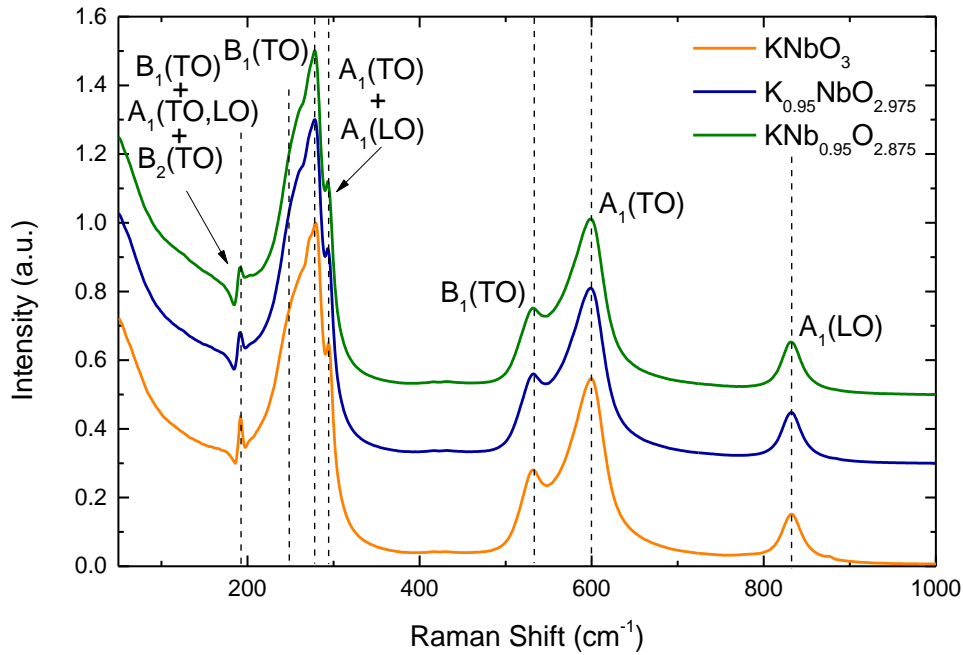


Figure 3. 13: Room-temperature Raman spectra of KNbO_3 and non-stoichiometric sintered pellets.

3.5.2. SEM

Scanning electron microscopy images of unpolished surfaces for stoichiometric, K-deficient and K-excess KNbO_3 sintered ceramics are shown in Figure 3. 14. Stoichiometric KN ceramic (a) exhibits the largest grain size (3-5 μm) among the rest of the microstructures. The grains are cubic shaped. In addition, the almost complete absence of porosity suggests high density, as was estimated in the previous section. On the other hand, microstructure of K-excess composition (b) exhibits a bimodal grain size distribution. Grains can be divided in two different categories: very small ones (~ 700 nm) and larger grains of maximum size of 1.5 μm . The grains maintain the cubic shape in K-excess composition. Finally, the microstructure of $\text{K}_{0.95}\text{NbO}_{2.975}$ (c) is significantly different of previous two. Grains do not present a homogeneous morphology, acquiring different polyhedral shapes. $\text{K}_{0.95}\text{NbO}_{2.975}$ ceramics seems to have finer grains sizes than KNbO_3 (a). In addition, (d) shows microstructure for K-deficient ceramics after one week left in air. The facility of absorbing moisture in this sample leads to the formation of a weak fused layer that covers the grains.

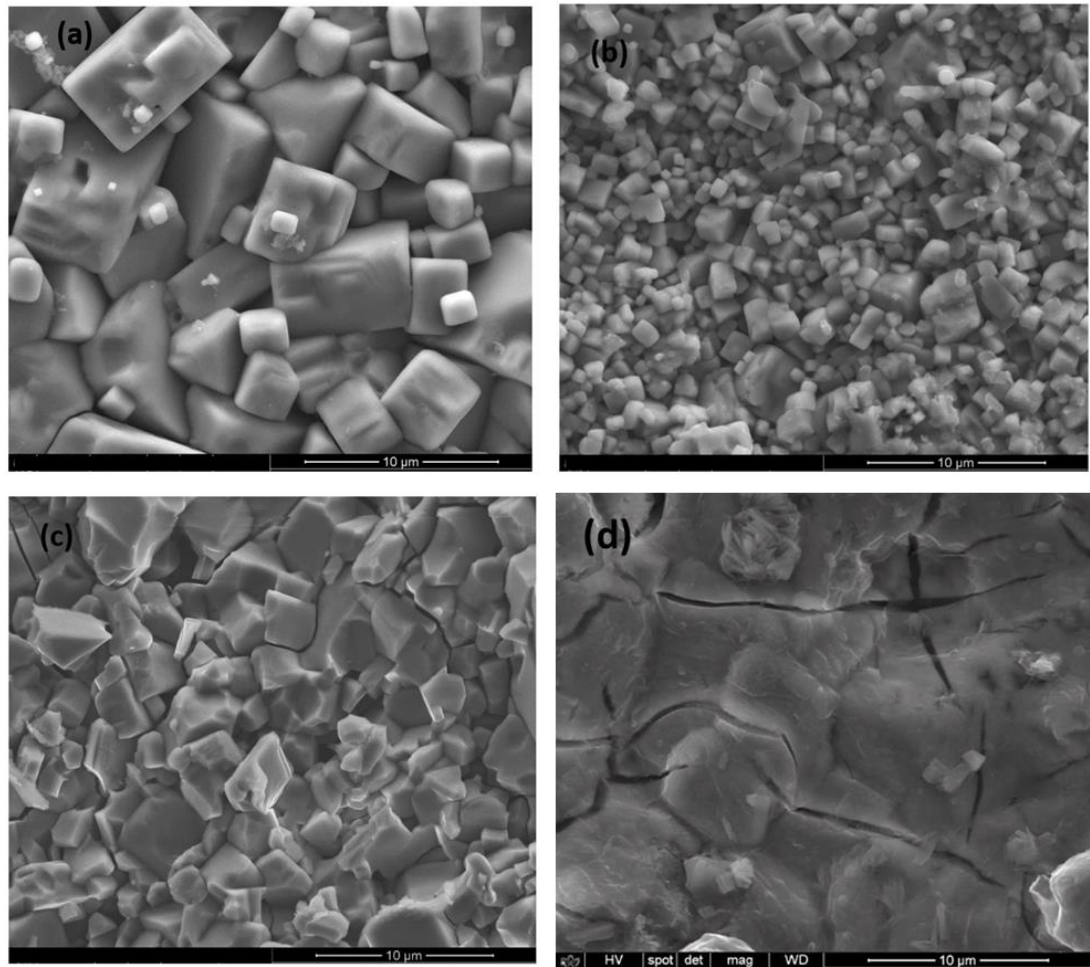


Figure 3. 14.: SEM images of unpolished surfaces for (a) KNbO_3 (b) $\text{K}_{0.95}\text{NbO}_{2.975}$, (c) $\text{KNb}_{0.95}\text{O}_{2.875}$ and (d) after one week $\text{KNb}_{0.95}\text{O}_{2.875}$ sintered pellets.

3.5.3. EDX

Table 3. 6 shows the experimental ratio between K and Nb for KNbO_3 , $\text{K}_{0.95}\text{NbO}_{2.975}$ and $\text{KNb}_{0.95}\text{O}_{2.875}$, calculated from energy-dispersive X-ray spectra (EDX data). This table includes the theoretical ratio for each composition.

Compound	$K/Nb_{\text{Experimental}}$	$K/Nb_{\text{Stoichiometric}}$	Relative Error (%)
KNbO_3	1.03(3)	1.00	~3%
$\text{K}_{0.95}\text{NbO}_{2.975}$	0.96(10)	0.95	~1%
$\text{KNb}_{0.95}\text{O}_{2.875}$	1.06(6)	1.05	~1%

Table 3. 6: Experimental and theoretical K/Nb ratios for pure, K-deficiency and K- excess KNbO_3 compounds.

EDX analysis reveals that KNbO₃ and KNb_{0.95}O_{2.875} samples are chemically homogeneous with K/Nb molar ratio being close to 1 and 1.05, respectively. K-excess and K-deficient samples exhibit slightly higher standard deviation than pure KN, which could be related with a lower homogeneity. This fact confirms again the sensibility of this system to the initial stoichiometry. Spectra and at% tables for each scan are available in Appendix A.

3.5 Electric characterisation of stoichiometric KNbO₃ prepared by method 2

In the previous section it was shown that dense single phase stoichiometric KNbO₃ ceramics can be successfully fabricated following method 2.

3.5.4. Dielectric characterisation

Electrical characterisation of non-stoichiometric K-deficient and K-excess ceramics was deemed unfeasible due to their poor densification (Table 3. 5), which renders them structurally weak. In addition, low density also prevents samples from withstanding high electric fields. Therefore, dielectric and ferroelectric measurements were carried out only for stoichiometric KNbO₃. The temperature dependence of the relative permittivity, ϵ_r , and dielectric loss, $\tan\delta$, for KNbO₃ ceramics measured at 1MHz, 250 kHz 100 kHz and 10 kHz is illustrated in Figure 3. 15 (a) and (b). The measurements were performed on heating and cooling in the temperature range 30-500 °C. KNbO₃ ceramics show two clear dielectric anomalies at ~206 °C and ~398 °C, which can be ascribed to the orthorhombic-to-tetragonal and to the tetragonal-to-cubic transitions, respectively (Figure 3. 15 (a)). On the single crystal, these transitions are reported to occur on heating at 220 °C and 420 °C (Shirane, Danner, Pavlovic, & Pepinsky, 1954). This difference may be caused by the impurities present in the starting raw materials, in particular, K₂CO₃, which has the lowest purity. The temperature of the highest anomaly determines the Curie temperature ($T_C \sim 400$ °C). A shift of ~0.5 °C to lower temperatures is observed for Curie temperature during cooling. The relative permittivity at T_C reaches a value of ~2600 on heating and ~2400 on cooling. On the other hand, relative permittivity at RT is ~300 and ϵ_r appears

frequency independent. Figure 3. 15 (b) shows dielectric losses become larger with increasing temperature and decreases with increasing frequencies.

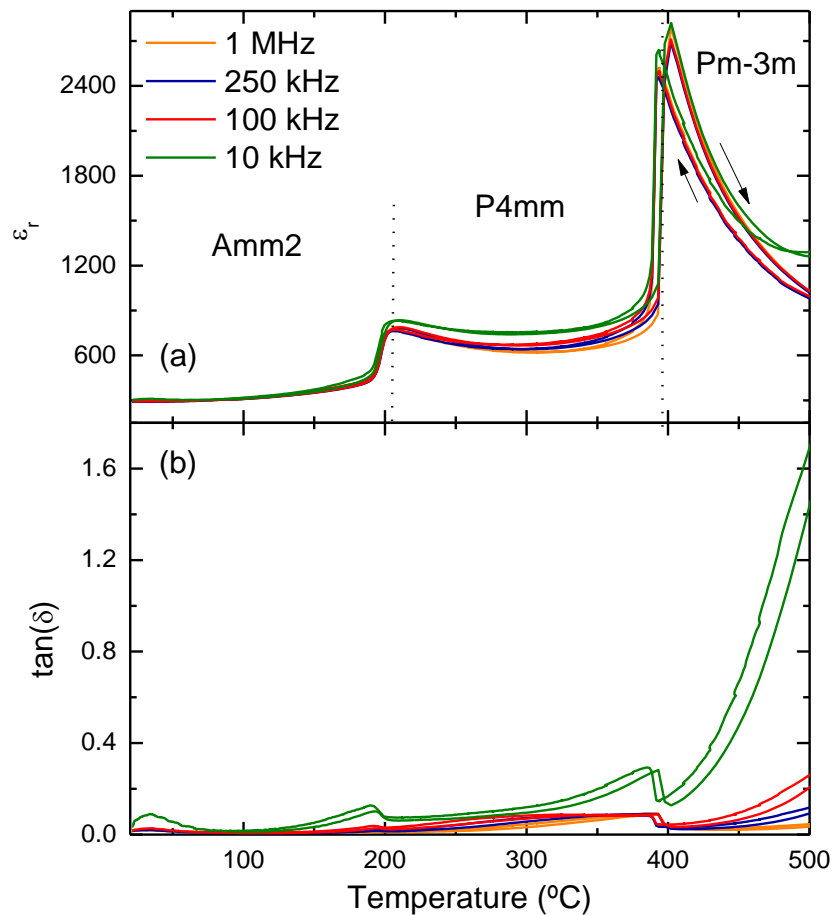


Figure 3. 15: Temperature dependence of the (a) relative permittivity and (b) $\tan(\delta)$ (1 MHz, 250 kHz, 100 kHz and 10 kHz) of KNbO_3 , during heating and cooling.

3.5.5. Ferroelectric Characterisation

Difficulties on measuring electrical properties of pure KN samples were encountered, but were circumvented. Samples left to ambient conditions present rounded ferroelectric loops (red loop in Figure 3. 16) which indicates some conductivity and consequently were unable to withstand higher electric fields. Hence, samples were dried at 200°C for 10 minutes. Figure 3. 16. (black loop) shows samples to become more resistive and exhibit a more typical ferroelectric loop. This fact suggests KN ceramics absorb very easily moisture from the environment. Drying ceramics up to 200°C before the electrical

measurements was systematically performed for all materials studied in this work. Figure 3. 17 shows the strain for KN left in open air and after drying.

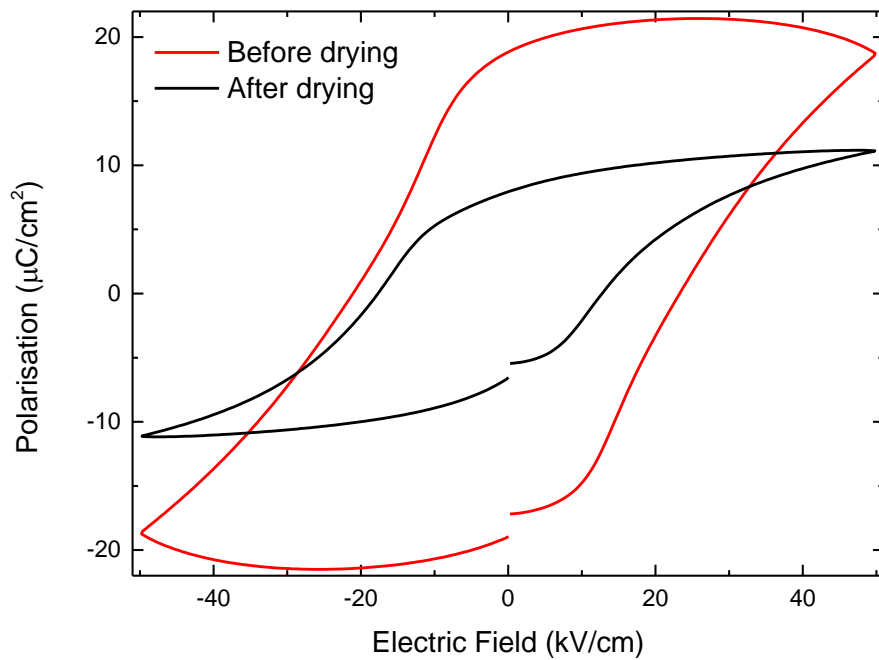


Figure 3. 16: Room temperature P-E loops of pure KNbO_3 ceramics under 50 kV/cm before (red curve) and after (black loop) drying at 200 °C.

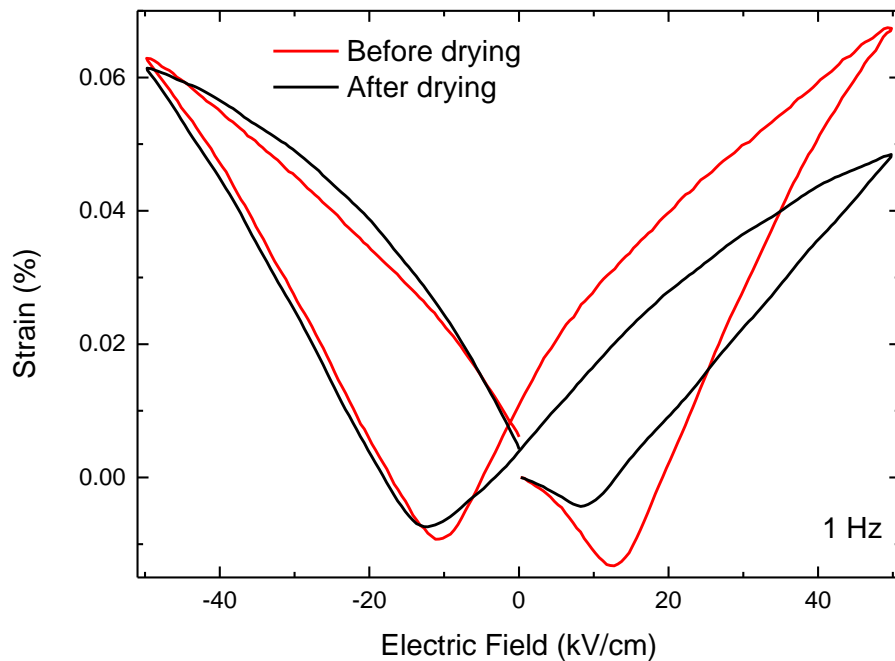


Figure 3. 17: Room temperature S-E loops of pure KNbO_3 ceramics under 50 kV/cm before (red curve) and after (black loop) drying at 200 °C.

The P-E loop measured before drying, resembles the hysteresis loop reported by Birol et al in 2005. Indeed, P_s , P_r and E_c values are very similar to the values measured in the present work, $\sim 20 \mu\text{C}/\text{cm}^2$, $\sim 18 \mu\text{C}/\text{cm}^2$ and $\sim 20 \text{kV}/\text{cm}$, respectively. In contrast, P-E loop measured after drying, resembles the hysteresis loop reported by Kakimoto et al in 2003. Again, P_s , P_r and E_c values are like the values obtained, $\sim 10 \mu\text{C}/\text{cm}^2$, $\sim 8 \mu\text{C}/\text{cm}^2$ and $\sim 20 \text{kV}/\text{cm}$, respectively. Significant differences are not observed for the S-E loops before and after drying. KN exhibits S_{max} value of approximately 0.06%, which is in agreement with values measured by Kakimoto et al. The absorbed water makes the ceramics more conductive and gives rise to current instead of inducing electric polarization with the applied electric field. Therefore, the high P_r values reported by Birol may be over-estimated.

Polarisation vs electric field (P-E) and strain vs electric field (S-E) loops measured at room temperature for KN ceramics under high electric fields up to 80 kV/cm, are shown in Figure 3. 18 and Figure 3. 19, respectively. Pure KN exhibits hysteresis loops typical for ferroelectric materials, which become larger with increasing electric field. Furthermore, KN sample is able to withstand an electric field of 80 kV/cm showing a maximum spontaneous polarisation (P_s) of $\sim 16.4 \mu\text{C}/\text{cm}^2$, a remnant polarization (P_r) of $\sim 13.8 \mu\text{C}/\text{cm}^2$ and a coercive field (E_c) of $\sim 27 \text{kV}/\text{cm}$. Table 3. 7 displays the P_s , P_r and E_c values under the different electric fields.

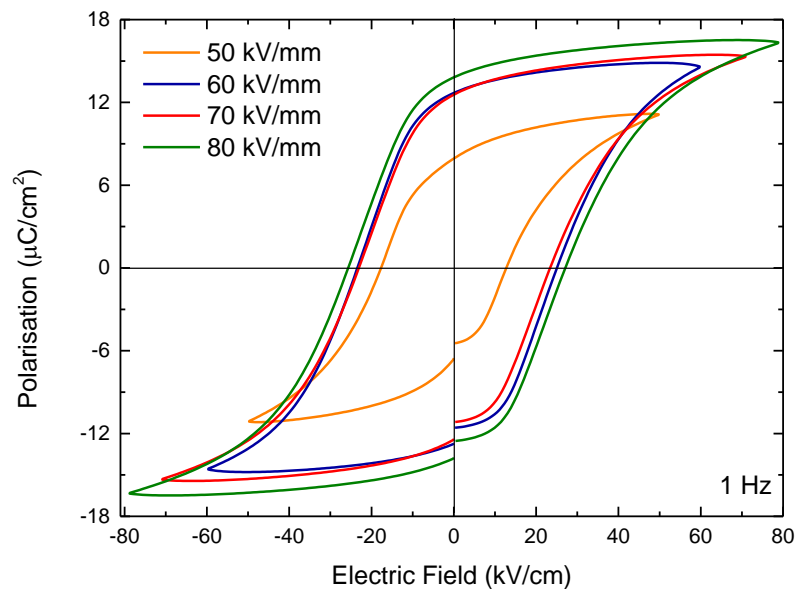


Figure 3. 18: Room temperature P-E loops of pure KNbO_3 ceramics under different electric fields (50 kV/cm, 60 kV/cm, 70 kV/cm and 80 kV/cm).

The shape of S-E curve is the standard butterfly curve that is usually observed in ferroelectrics (Figure 3. 19). The maximum strain (S_{max}) for KN is about 0.092% under 80 kV/cm. In addition, the S-E curve shows that the negative strain can reach $<0.02\%$, which is due to ferroelectric domain and domain wall switching. The S_{max} values under the different electric fields are also shown in Table 3. 7.

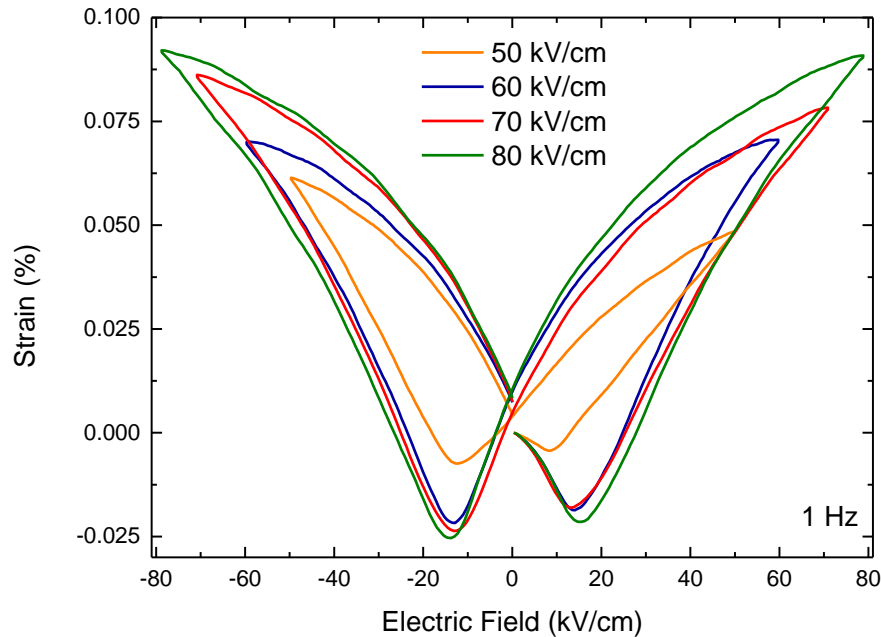


Figure 3. 19: Room temperature S-E loops of pure KNbO_3 ceramics under different electric fields (50 kV/cm, 60 kV/cm, 70 kV/cm and 80 kV/cm).

Electric Field (kV/cm)	P_s ($\mu\text{C}/\text{cm}^2$)	P_r ($\mu\text{C}/\text{cm}^2$)	E_c (kV/cm)	S_{max} (%)
50	11.20	7.94	13.00	0.062
60	14.83	12.67	23.5	0.070
70	15.51	12.67	24.81	0.086
80	16.56	13.85	27.43	0.092

Table 3. 7: P_s , P_r , E_c and S_{max} values of KN at RT under different electric fields (50 kV/cm, 60 kV/cm, 70 kV/cm and 80 kV/cm).

The characteristic ferroelectric parameters (P_s , P_r , E_c) and the maximum strain (S_{max}) of stoichiometric KN tend to increase with the increase of the electric field applied.

The temperature dependence of the ferroelectric loops (Figure 3. 20) and the strain curves (Figure 3. 21) are also investigated in this work. At first glance, when increasing the temperature, the hysteresis loops become narrower and taller. This can be translated into

an increase of P_s and P_r values and decrease of E_C with the temperature. Under 50 kV/cm, the maximum values are observed at 160°C: P_s of $\sim 23 \mu\text{C}/\text{cm}^2$, P_r of $20 \mu\text{C}/\text{cm}^2$ and E_C of $\sim 14 \text{ kV}/\text{cm}$. P_s , P_r , E_C and S_{\max} values at different temperatures, are shown in Table 3. 8.

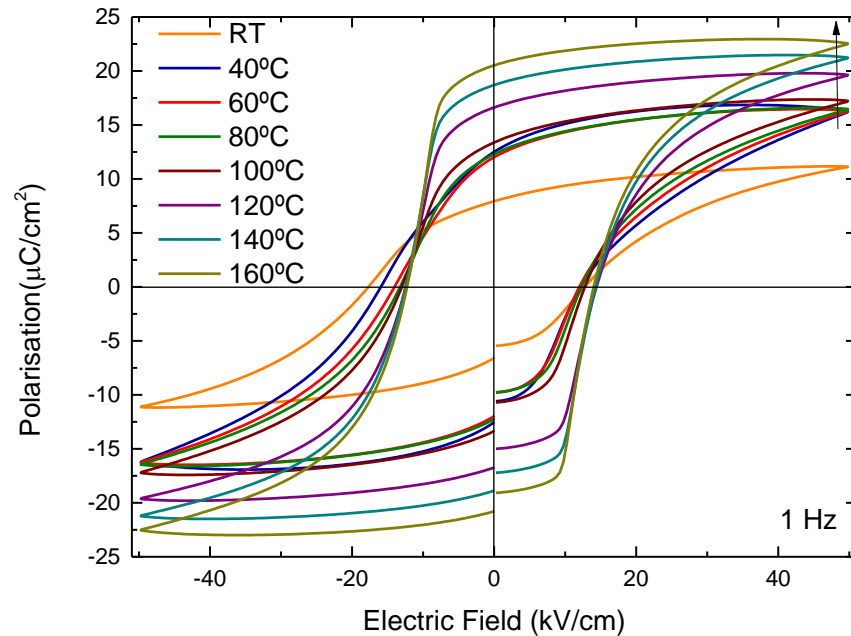


Figure 3. 20: P-E loops of pure KNbO_3 ceramics under 50kV/cm at different temperatures (RT, 40°C, 60°C, 80°C, 100°C, 120°C and 140°C).

The maximum strain (S_{\max}) for KN is about 0.097% under 50 kV/cm at 160°C. This value is slightly higher than the S_{\max} value at 80 kV/cm at RT. In addition, the S-E curve shows that the negative strain can reach $<0.025\%$, which is related with ferroelectric domain switching. S_{\max} values at different temperatures are shown in Table 3. 8.

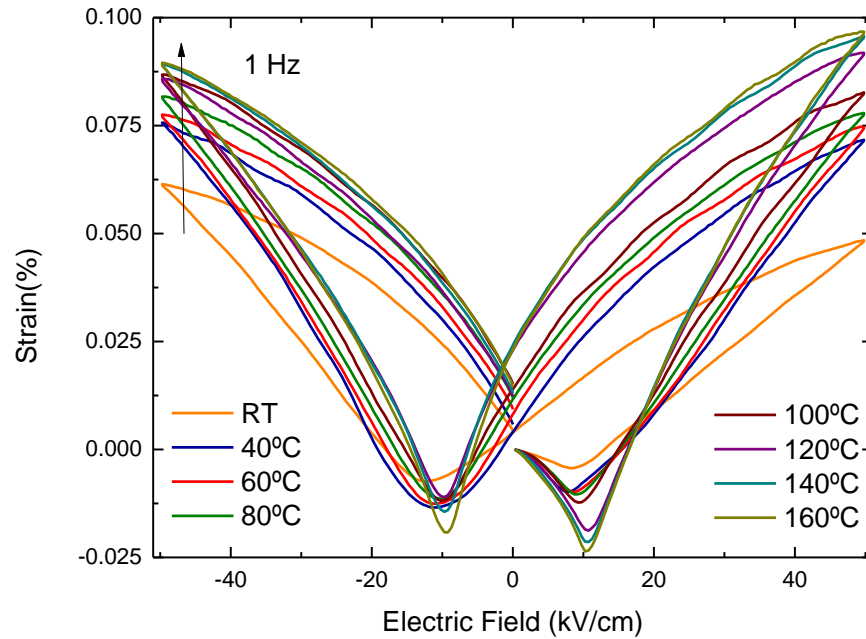


Figure 3. 21: P-E loops of pure KNbO_3 ceramics under 50 kV/cm at different temperatures (RT, 40°C, 60°C, 80°C, 100°C, 120°C and 140°C).

Temperature (°C)	P_s ($\mu\text{C}/\text{cm}^2$)	P_r ($\mu\text{C}/\text{cm}^2$)	E_c (kV/cm)	S_{\max} (%)
RT	11.19	7.92	12.52	0.061
40	16.18	12.34	12.52	0.071
60	16.18	11.86	12.29	0.075
80	16.42	12.19	12.61	0.078
100	17.16	13.25	13.02	0.083
120	19.62	16.51	14.58	0.091
140	21.21	18.58	14.44	0.096
160	22.50	20.45	14.17	0.097

Table 3. 8: P_s , P_r , E_c and S_{\max} values of KN under an electric field of 50kV/cm at different temperatures (RT, 40°C, 60°C, 80°C, 100°C, 120°C and 140°C).

Ferroelectric parameters of P_s , P_r and E_c of KN ceramic continuously increase with increasing temperature. This tendency goes against to results presented by Birol et al, where P_s decreases with increasing temperature. Again, this fact is an evidence of their measurements being strongly affected by conductivity on the samples. Basically, during their measurements, moisture is driven off on heating, and then polarisation apparently drops.

3.6. Optical characterisation

3.6.1. Diffuse Reflectance Spectroscopy

Figure 3. 22 shows diffuse reflectance data. Direct and indirect band-gaps were calculated from these measurements using the Kubelka-Munk function. As discussed in Chapter 1, there is controversy in the literature about the nature of band-gap for KNbO_3 . Therefore, direct and indirect band-gaps were determined (Figure 3. 23 and Figure 3. 24).

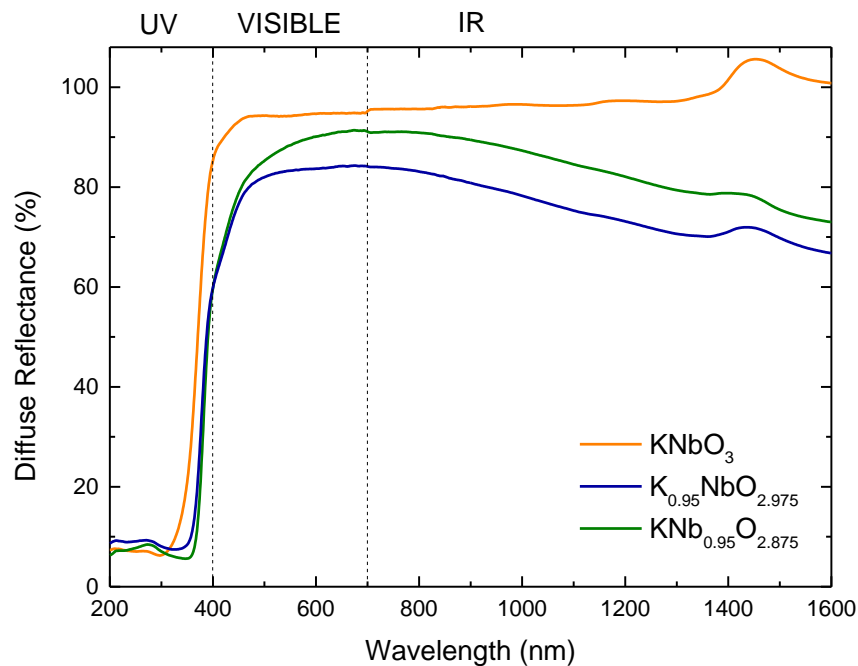


Figure 3. 22: Diffuse reflectance (%) data for KNbO_3 , $\text{K}_{0.95}\text{NbO}_{2.975}$ and $\text{KNb}_{0.95}\text{O}_{2.875}$ ceramics

Stoichiometric KN exhibits a direct band gap of 3.64 eV. Non-stoichiometric compositions present narrower band-gaps probably due to hybridised orbitals generated by oxygen vacancies. K-deficient and K- excess samples present 3.34 and 3.31 eV values respectively. Indirect band-gaps follow the same trend (Figure 3. 24). The narrowest band-gap is estimated for $\text{KNb}_{0.95}\text{O}_{2.875}$, which in principle has a larger concentration of oxygen vacancies. Indeed, in terms of defect chemistry it follows: $2V_{\text{Nb}}'''' + 5V_{\text{O}}^{\bullet\bullet}$ for $\text{KNb}_{0.95}\text{O}_{2.875}$ and $2V_{\text{K}}' + 5V_{\text{O}}^{\bullet\bullet}$ for $\text{K}_{0.95}\text{NbO}_{2.975}$.

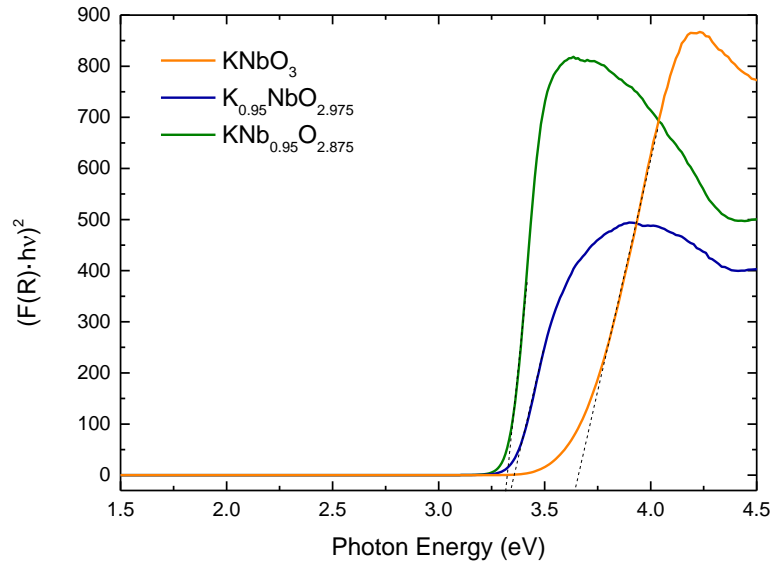


Figure 3. 23: Tauc plot for direct band-gaps of KNbO_3 , $\text{K}_{0.95}\text{NbO}_{2.975}$ and $\text{KNb}_{0.95}\text{O}_{2.875}$ ceramics.

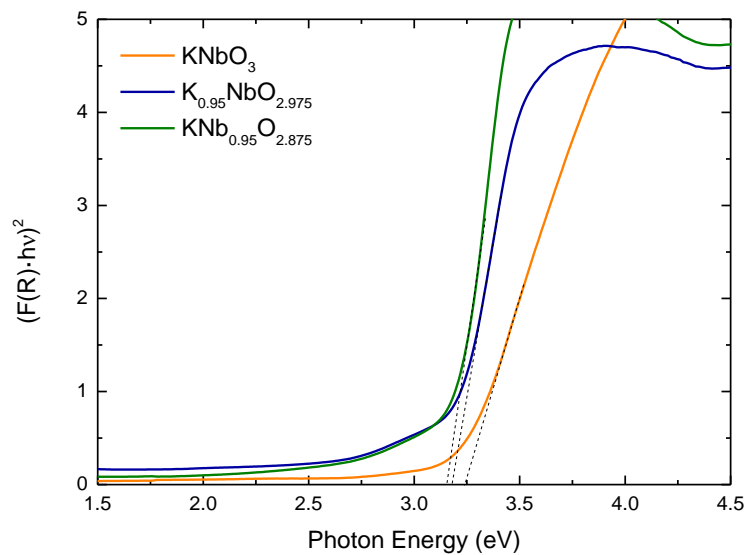


Figure 3. 24: Tauc plot for indirect band-gaps of KNbO_3 , $\text{K}_{0.95}\text{NbO}_{3.6}$ and $\text{KNb}_{0.95}\text{O}_{3.6}$ ceramics.

The indirect band-gap for stoichiometric composition is 3.23 eV. K-deficiency and K-excess samples show 3.18 and 3.15 eV values respectively. Calculated band-gaps are summarised in Table 3. 9 for pure KN and non-stoichiometric composition.

Band-gap	KNbO_3	$\text{K}_{0.95}\text{NbO}_{2.975}$	$\text{KNb}_{0.95}\text{O}_{2.875}$
Direct (eV)	3.64	3.34	3.31
Indirect (eV)	3.23	3.18	3.15

Table 3. 9: Direct and indirect values for pure KN and non-stoichiometric composition.

3.7. Discussion

Stoichiometric KNbO_3 ceramics and compositions altered with potassium and niobium deficiency were prepared by solid-state reaction to examine the impact of potassium losses during the ceramic processing. Indeed, potassium volatilisation hinders the control of the stoichiometry of KNbO_3 , which leads to the formation of secondary phase, $\text{K}_4\text{Nb}_6\text{O}_{17}$ (ICDD# 00-031-1064). This phase is highly hygroscopic. Two series of KNbO_3 , $\text{K}_{0.95}\text{NbO}_{2.975}$ and $\text{KNb}_{0.95}\text{O}_{2.875}$ were prepared following two different procedures, Method 1 and Method 2. All materials in this work are based on KNbO_3 , for this reason it was important to standardise a route which allows to prepare dense single-phase KNbO_3 ceramics.

Two main lines of KN ceramic preparation can be distinguished in the literature: (1) single calcination and (2) double calcination steps for the synthesis. Method 1 and Method 2 present two stages during calcination that should provide more effective route in obtaining dense KN ceramics. Method 1 is inspired on the most commonly used route in literature (Kim et al., 2014; K. Matsumoto et al., 2007; H. Nagata, Matsumoto, Hirose, Hiruma, & Takenaka, 2007). First calcination (625°C) occurs at lower temperature than the second calcination (1000°C), which is close to the sintering temperature. On the other hand, Method 2 is based on Kakimoto studies. Compact powders are doubly calcined at lower temperatures (850°C). By inspection of the crystal purity, the shrinkage behaviour and the stability in water of KNbO_3 , $\text{K}_{0.95}\text{NbO}_{2.975}$ and $\text{KNb}_{0.95}\text{O}_{2.875}$ ceramics, it is determined Method 2 is more appropriate for their preparation by conventional solid-state reaction.

Firstly, the volatility of K is exacerbated when the material is treated above 1000°C . Therefore, Method 1 promotes K losses and consequently the appearance of $\text{K}_4\text{Nb}_6\text{O}_{17}$. Secondly, K losses are also inhibited if the powders are compacted during the calcination. And thirdly, the control of firing environment with atmospheric powder and double crucible during the sintering, reduce the K losses and enhance the densification. High relative density ($>94\%$) is achieved for stoichiometric KN ceramics, as reported by Kakimoto et al.

Once the ceramic processing was optimised, KNbO₃, K_{0.95}NbO_{2.975} and KNb_{0.95}O_{2.875} ceramics were characterised in terms of the structure, morphology and electrical properties.

XRD and Raman results determined that KNbO₃, K_{0.95}NbO_{3-δ} and KNb_{0.95}O_{3-δ} ceramics can be described by an orthorhombic crystal structure (Amm2 space group). However, these three compositions exhibit significant differences. Stoichiometric KNbO₃ shows large cubic grains up to 3-5 μm. Being single-phase, these ceramics densify relatively well to 4.35(3) g/cm³ which corresponds to 94% relative density. KNbO₃ ceramics with potassium excess exhibit lower densification (~85%) and the grain growth is inhibited (600-800 nm). Finally, low density (<80%), deliquescence in water and the appearance of secondary phase (K₄Nb₆O₁₇) characterise the K-deficiency samples. Different temperatures are required to sinter KNbO₃, K_{0.95}NbO_{2.975} and KNb_{0.95}O_{2.875}. Worth to be underlined, the variation of only 5% of K content in KN ceramics induces changes in the purity, crystallisation, microstructure, stability and densification temperature of the samples. These results demonstrate the sensitivity of this compound to the stoichiometry and highlight the need of controlling the potassium losses during the processing.

Low densities in non-stoichiometry samples limit the study of electrical properties. Hence, only KN ceramics were electrically characterised. The mixed sharp peak centered at 192 cm⁻¹ in Raman spectra is the fingerprint of the long-range polar order in KN compounds. Indeed, KN is a typical ferroelectric material. Large anomalies in the relative permittivity (ϵ_r) as a function of temperature corroborate ferroelectric phase transitions, from cubic to tetragonal phases (P4mm) at 398 °C (Curie point) and from tetragonal to orthorhombic (Amm2) at 206°C. For single crystal phase transitions occur at 410°C and 200°C, exhibiting large temperature hysteresis between the heating and the cooling (Shirane et al., 1954). In contrast, ceramics do not show thermal hysteresis for orthorhombic-to-tetragonal transition but T_C during the heating is ~10°C higher than during cooling.

P-E loops reveal KN ceramics left in air absorb moisture from the environment, which makes the sample more conductive and leads to over-estimated P_s, P_r and E_c values, as in the case of FE loops reported by Birol et al. Prior drying at 200°C enables the application of 80 kV/cm at room temperature to KNbO₃ ceramics, which exhibit typical ferroelectric

polarisation-electric field loops, as previously reported by Kakimoto et al. Enhancement of spontaneous and remanent polarisation are observed when the temperature increases. Finally, direct (and indirect) band-gap of KNbO_3 was estimated at 3.64 eV (3.23 eV). However, non-stoichiometric compositions present narrower band-gaps. Indeed, K-excess compound has higher concentration of oxygen vacancies $2V_{\text{Nb}}'''' + 5V_{\text{O}}''$ than $2V_{\text{K}}' + V_{\text{O}}''$ on the K-deficiency compound, which may decrease the band-gap energy. This phenomenon was also observed on non-stoichiometric BaTiO_3 ceramics (Lee, Woodford, & Randall, 2008).

3.8. Conclusions

Densification issues on preparing pure KN ceramic are intimately related with the stoichiometry of the compound. The high volatility of K, the easy formation of a hygroscopic secondary phase ($\text{K}_4\text{Nb}_6\text{O}_{17}$) and moisture absorption during the process makes the manufacture of KNbO_3 ceramics difficult. In this chapter, these difficulties were circumvented through the introduction of appropriate measures to control K losses during the heat treatments. This investigation also demonstrates the susceptibility of KNbO_3 to small variations on potassium levels. Finally, dense single-phase KNbO_3 ceramics were prepared. Furthermore, in this chapter the dependence of dielectric, ferroelectric and piezoelectric properties for KNbO_3 with the temperature was shown. Spontaneous polarisation of $\sim 23 \mu\text{C}/\text{cm}^2$ and maximum strain of 0.1% is obtained under 50 kV/cm at 160°C. Finally, KNbO_3 , $\text{K}_{0.95}\text{NbO}_{2.975}$ and $\text{KNb}_{0.95}\text{O}_{2.875}$ exhibit direct (and indirect) band-gaps of 3.64 eV (3.23 eV), 3.34 eV (3.18 eV) and 3.31 eV (3.15 eV), respectively.

3.9. References

Acker, J., Kungl, H., & Hoffmann, M. J. (2013). Sintering and microstructure of potassium niobate ceramics with stoichiometric composition and with potassium- or niobium excess. *Journal of the European Ceramic Society*, 33(11). <https://doi.org/10.1016/j.jeurceramsoc.2013.03.011>

- Birol, H., Damjanovic, D., & Setter, N. (2005). Preparation and characterization of KNbO_3 ceramics. *Journal of the American Ceramic Society*, 88(7), 1754–1759. <https://doi.org/10.1111/j.1551.2916.2005.00347.x>
- Birol, H., Damjanovic, D., & Setter, N. (2006). Preparation and characterization of $(\text{K}_{0.5}\text{Na}_{0.5})\text{NbO}_3$ ceramics. *Journal of the European Ceramic Society*, 26(6), 861–866. <https://doi.org/10.1016/j.jeurceramsoc.2004.11.022>
- Dubernet, P., & Ravez, J. (1998). Dielectric study of KNbO_3 ceramics over a large range of frequency (102-109Hz) and temperature (300-800 K). *Ferroelectrics*, 211(1), 51–66. <https://doi.org/10.1080/00150199808232333>
- Egerton, L., & Dillon, M. D. (1959). Piezoelectric and Dielectric Properties of Ceramics in the System Potassium—Sodium Niobate. *Journal of the American Ceramic Society*, 42(9), 438–442. <https://doi.org/10.1111/j.1151-2916.1959.tb12971.x>
- Flueckiger, U., & Arend, H. (1977). Synthesis of KNbO_3 Powder. *Journal American Ceramic Society*, 56(575–7).
- Kakimoto, K.-I., Masuda, I., & Ohsato, H. (2005). Lead- free KNbO_3 piezoceramics synthesized by pressure- less sintering. *Journal of the European Ceramic Society*, 25(12), 2719–2722. <https://doi.org/10.1016/j.jeurceramsoc.2005.03.209>
- Kakimoto, K. I., Masuda, I., & Ohsato, H. (2003). Ferroelectric and piezoelectric properties of KNbO_3 ceramics containing small amounts of LaFeO_3 . *Japanese Journal of Applied Physics, Part 1: Regular Papers and Short Notes and Review Papers*, 42(9 B), 6102–6105. <https://doi.org/10.1143/JJAP.42.6102>
- Kim, D., Joung, M., Seo, I., Hur, J., Kim, J., Kim, B., ... Nahm, S. (2014). Influence of sintering conditions on piezoelectric properties of KNbO_3 ceramics. *Journal of the European Ceramic Society*, 34, 4193–4200.
- Kingon, A. I., & Clark, J. B. (1983). Sintering of PZT Ceramics: I, Atmosphere Control. *Journal of the American Ceramic Society*, 66(4), 253–256. <https://doi.org/10.1111/j.1151-2916.1983.tb15708.x>
- Lee, S., Woodford, W. H., & Randall, C. A. (2008). Crystal and defect chemistry influences on band gap trends in alkaline earth perovskites. *Applied Physics Letters*, 92(20). <https://doi.org/10.1063/1.2936091>

- Luisman, L., Feteira, A., & Reichmann, K. (2011). Weak-relaxor behaviour in Bi/Yb-doped KNbO_3 ceramics. *Applied Physics Letters*, 99(19). <https://doi.org/10.1063/1.3660255>
- Lv, X., Li, Z., Wu, J., Xiao, D., & Zhu, J. (2016). Lead-Free KNbO_3 :xZnO Composite Ceramics. *ACS Applied Materials & Interfaces*, 8(44), 30304–30311. <https://doi.org/10.1021/acsami.6b11677>
- Matsumoto, K., Hiruma, Y., Nagata, H., & Takenaka, T. (2007). Piezoelectric properties of KNbO_3 ceramics prepared by ordinary sintering. *Ferroelectrics*, 358(1 PART 4). <https://doi.org/10.1080/00150190701537166>
- Matsumoto, K., Hiruma, Y., Nagata, H., & Takenaka, T. (2008). Electric-field-induced strain in Mn-doped KNbO_3 ferroelectric ceramics. *Ceramics International*, 34(4), 787–791. <https://doi.org/http://dx.doi.org/10.1016/j.ceramint.2007.09.026>
- Nagata, H., Matsumoto, K., Hirose, T., Hiruma, Y., & Takenaka, T. (2007). Fabrication and electrical properties of potassium niobate ferroelectric ceramics. *Japanese Journal of Applied Physics, Part I: Regular Papers and Short Notes and Review Papers*, 46(10 B), 7084–7088. <https://doi.org/10.1143/JJAP.46.7084>
- Park, J., Kim, D.-H., Lee, T.-G., Cho, S.-H., Park, S.-J., Ryu, J., & Nahm, S. (2017). CuO-added KNbO_3 - BaZrO_3 lead-free piezoelectric ceramics with low loss and large electric field-induced strain. *Journal of the American Ceramic Society*, 100(7), 2948–2957. <https://doi.org/10.1111/jace.14826>
- Pavlič, J., Malič, B., & Rojac, T. (2014). Microstructural, structural, dielectric and piezoelectric properties of potassium sodium niobate thick films. *Journal of the European Ceramic Society*, 34(2), 285–295. <https://doi.org/10.1016/j.jeurceramsoc.2013.09.001>
- Quittet, A. M., Bell, M. I., Krauzman, M., & Raccach, P. M. (1976). Anomalous scattering and asymmetrical line shapes in Raman spectra of orthorhombic KNbO_3 . *Physical Review B*, 14(11), 5068–5072. <https://doi.org/10.1103/PhysRevB.14.5068>
- Shirane, G., Danner, H., Pavlovic, A., & Pepinsky, R. (1954). Phase Transitions in Ferroelectric KNbO_3 . *Physical Review*, 93(4), 672–673. <https://doi.org/10.1103/PhysRev.93.672>

- Tashiro, S., Nagamatsu, H., & Nagata, K. (2002). Sinterability and piezoelectric properties of KNbO_3 ceramics after substituting Pb and Na for K. *Japanese Journal of Applied Physics, Part 1: Regular Papers and Short Notes and Review Papers*, 41(11 B), 7113–7118. <https://doi.org/10.1143/JJAP.41.7113>
- Uniyal, M., Singh, K., Bhatt, S., Pant, R. P., Suri, D. K., & Semwal, B. S. (2003). Preparation, characterization and dielectric studies of $\text{K}_{1-x}\text{Na}_x\text{NbO}_3$. *Indian Journal of Pure and Applied Physics*, 4, 305–309.
- Zhen, Y., & Li, J.-F. (2006). Normal sintering of $(\text{K},\text{Na})\text{NbO}_3$ -based ceramics: Influence of sintering temperature on densification, microstructure, and electrical properties. *Journal of the American Ceramic Society*, 89(12). <https://doi.org/10.1111/j.1551-2916.2006.01313.x>
- Zhou, W., Deng, H., Yang, P., & Chu, J. (2014). Structural phase transition, narrow band gap, and room-temperature ferromagnetism in $[\text{KNbO}_3]_{1-x}[\text{BaNi}_{1/2}\text{Nb}_{1/2}\text{O}_{3-\delta}]_x$ ferroelectrics. *Applied Physics Letters*, 105(11), 111904. <https://doi.org/10.1063/1.4896317>

Chapter 4

System



4.1. Introduction

4.2. Structural and chemical characterisation

4.2.1. Purity and X-ray powder diffraction

4.2.2. Raman Spectroscopy

4.2.3. SEM

4.2.4. EDX

4.3. Electrical Characterisation

4.3.1. Dielectric Characterisation

4.3.2. Piezo- and Ferroelectric Characterisation

4.4. Optical Characterisation

4.4.1 Diffuse reflectance spectroscopy

4.5. Discussion

4.6. Conclusions

4.7. References

4. System $(1-x) \text{KNbO}_3-x(\text{Ba}_{0.5}\text{Bi}_{0.5})(\text{Zn}_{0.5}\text{Nb}_{0.5})\text{O}_3$

4.1. Introduction

This chapter is devoted to the synthesis and characterisation of powders and ceramics in the binary system $(1-x) \text{KNbO}_3-x \text{Ba}_{0.5}\text{Bi}_{0.5}\text{Nb}_{0.5}\text{Zn}_{0.5}\text{O}_3$ (KBBNZ) with $x=0, 0.05, 0.10, 0.15, 0.20$ and 0.25 . Details on ceramic processing, structural, dielectric, ferroelectric, piezoelectric and optical properties are presented.

The investigation of this system was motivated by a recent theoretical work on band-gap engineering of ferroelectric KN (F Wang, Grinberg, & Rappe, 2014). Their first principle calculations with HSE06 functional predict a band gap of 2.92 eV for $0.75 \text{KNbO}_3-0.25 (\text{Ba}_{0.5}\text{Bi}_{0.5})(\text{Zn}_{0.5}\text{Nb}_{0.5})\text{O}_3$ and a spontaneous polarisation of $\sim 38 \mu\text{C}/\text{cm}^2$, which is typical for a robust ferroelectric material. The origin of the band-gap narrowing allegedly relies on Zn^{2+} substitution for higher-valence Nb^{5+} in KNbO_3 , which gives rise to increased repulsion between the O 2p and Zn 3d states and thereby to a higher valence band maximum (VBM). The shift up of the VBM is driven by the repulsion between the non-bonding $3d^{10}$ orbitals of Zn^{2+} and the $2p^6$ orbitals of O^{2-} . In addition, the conduction band minimum (CBM) which mainly consists of Nb 4d states is essentially preserved from the parent KNbO_3 . Hence, the CBM is dependent on the off-centering direction of the B-site cation. Presumably, the combination of these two effects narrows the band-gap of the parent KN, moving it into the visible range.

In this work, KBBNZ system was prepared by solid state reaction and the experimental results validate previous first principles calculations of the band gap for $x = 0.25$, which also appears to be non-ferroelectric. In addition, a piezoelectric-to-electrostrictive crossover is also unveiled.

4.2. Structural and chemical characterisation

4.2.1. Purity and X-ray powder diffraction

KBBNZ powders were prepared by the solid-state reaction route. Starting oxides and carbonates (K_2CO_3 , Bi_2O_3 , BaCO_3 , Nb_2O_5 , and ZnO) were weighed in required molar ratios according to the $(1-x) \text{KNbO}_3 - x \text{Ba}_{0.5}\text{Bi}_{0.5}\text{Nb}_{0.5}\text{Zn}_{0.5}\text{O}_3$ formula and mixed for 24 h. Slurries were dried and subsequently passed through a 250 mesh sieve. Double calcination in air at 850°C was carried out following method 2 from Chapter 3. Room-temperature X-ray diffraction (XRD) data for KN-BBNZ powders are shown in Figure 4.

1.

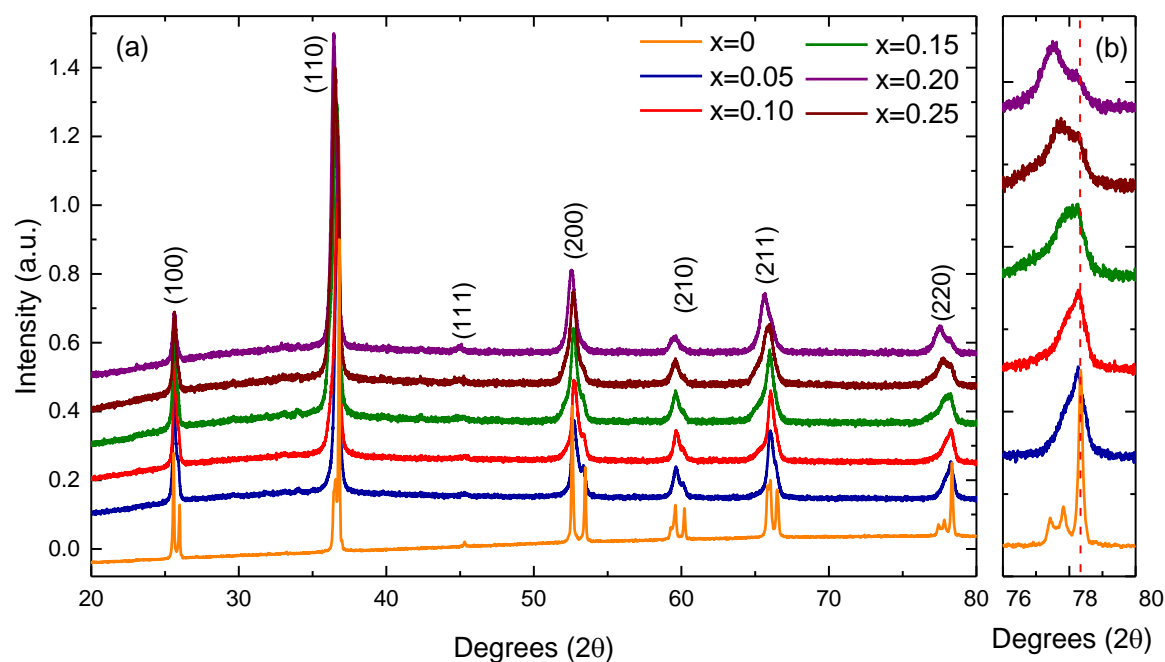


Figure 4. 1 Room temperature XRD data for KBBNZ $x=0, 0.05, 0.10, 0.15, 0.20$ and 0.25 powders after double calcination in air at 850°C .

After two calcinations at 850°C , all oxides and carbonates appear to have fully reacted, as supported by the absence of any reflection associated with those chemical precursors. Indeed, all reflections in the traces, shown in Figure 4. 1 can be assigned to phases with the perovskite structure. At first glance, all compositions appear to be single-phase, however a closer inspection reveals the appearance of nearly undoped phase. The latter

is indicated by the dashed line in part (b) of Figure 4. 1. From this figure it is also evident that the position of the reflection associated with the undoped phase remains virtually unchanged, however its intensity decreases with the increasing x . Basically this observation shows that at low dopant levels homogenisation is more difficult to achieve. Conversely, the shoulder that start appearing in KBBNZ $x=0.05$ shifts slightly towards lower angles with increasing x , making the peak splitting clear. This suggests there are some difficulties in the simultaneous incorporation of Ba^{+2} , Bi^{+3} , Zn^{+2} and Nb^{+5} into the KN lattice, using the processing conditions established in Chapter 3 for undoped KN.

The calcined powders were uniaxially pressed into pellets under 1 ton. Then, green bodies were fired in air for 12 hours at temperatures ranging from 1070 to 1100 °C, using a controlled heating rate of 3 °C/min. Room-temperature X-ray diffraction (XRD) data for KBBNZ ceramics are shown in Figure 4. 2.

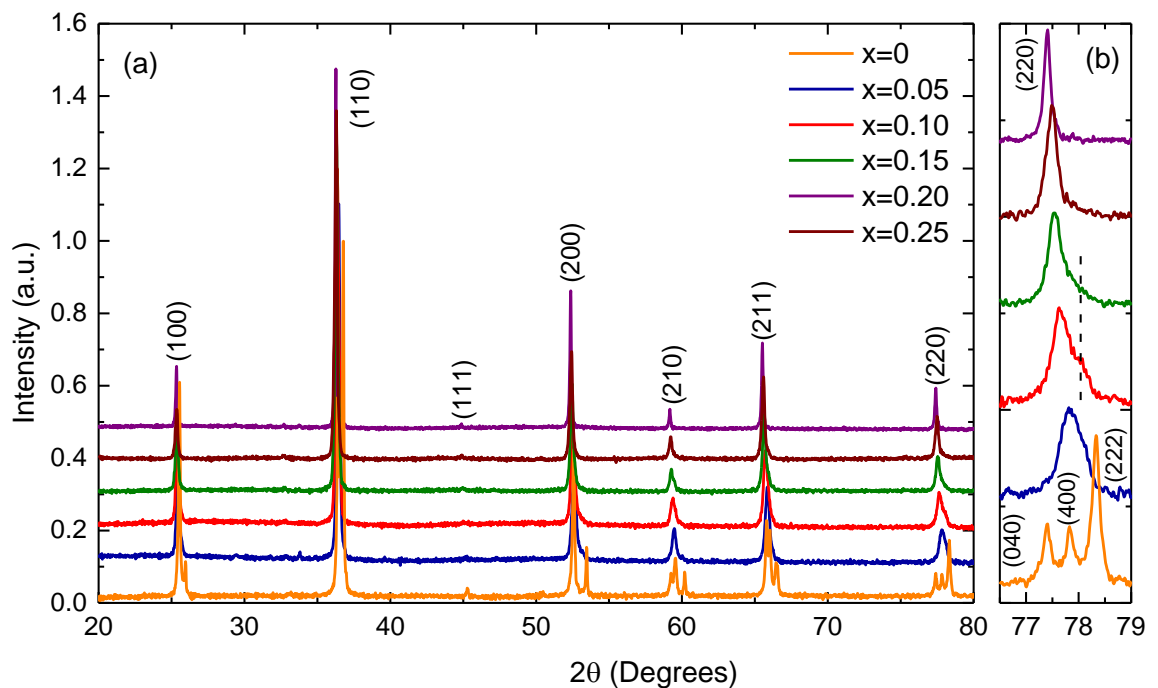


Figure 4. 2 Room temperature XRD data for KBBNZ $x=0, 0.05, 0.10, 0.15, 0.20$ and 0.25 ceramics sintered at 1100°C

The XRD pattern of KN ($x=0$) ceramics exhibits well-defined sharp peaks which can be indexed to an orthorhombic cell with $\text{Amm}2$ symmetry. All reflections for doped compositions shift systematically towards lower 2θ angles, indicating an increase of the unit cell size with increasing x . Figure 4. 2 (b) shows the evolution of the triplet indexed as (040), (400) and (222) for pure KN with increasing $\text{Ba}_{0.5}\text{Bi}_{0.5}\text{Nb}_{0.5}\text{Zn}_{0.5}\text{O}_3$ content. A

single peak is visible for the rest compositions. However, the wide peak for $x=0.05$ still exhibits an average orthorhombic symmetry. For $x=0.10$ and 0.15 , a shoulder is visible on the higher 2θ side indicating the coexistence of two phases. Finally, the sharp peaks for $x=0.20$ and 0.25 suggest an average cubic symmetry. Average lattice metrics calculated from the Rietveld refinement of XRD data for all KBBNZ ceramics are given in Table 4. 1 and Table 4. 2. Experimental and relative densities are also included in the tables.

Table 4. 1: Experimental and theoretical density, lattice parameters and agreement indices calculated by

	x=0	x=0.05	x=0.10	
Space Group	Amm2	Amm2	71.8(4) % Amm2	28(1) % Pm- $\bar{3}$ m
Density				
(Experimental)	4.35(3)	4.42(11)	4.86(6)	
(g/cm³)				
Density				
(calculated)	4.6273(1)	4.6523(4)	4.8888 (2)*	
(g/cm³)				
Relative				
Density (%)	94(1)	95(2)	98(1)*	
a (Å)	3.9711(1)	4.0057(1)	4.0266(1)	4.0204(1)
b (Å)	5.6909(1)	5.6763(3)	5.6927(1)	4.0204(1)
c (Å)	5.7158(1)	5.6935(3)	5.6822(1)	4.0204(1)
V/10⁶ (pm³)	64.576(2)	64.729(5)	65.128(3)	64.983(3)
R_{exp}	1.26460	1.45269	1.45707	
R_{profile}	2.97912	2.31942	2.03994	
R_{wp}	4.65175	3.29451	2.95423	
GOF	13.53086	5.14322	4.11080	

Rietveld Refinement for KBBNZ ($x=0, 0.05$ and 0.10). * Weighted averaged of the two phases.

	x=0.15		x=0.2	x=0.25
Space Group	28.5(3)% Amm2	71.5(6)% Pm- $\bar{3}$ m	Pm- $\bar{3}$ m	Pm- $\bar{3}$ m
Density				
(Experimental)		4.96(8)	4.42(11)	5.24(13)
(g/cm³)				
Density				
(calculated)		5.020(3)*	5.186(3)	5.3168(2)
(g/cm³)				
Relative				
Density (%)		98(1)*	96(2)	98 (2)
a (Å)	4.0399(6)	4.0268(1)	4.0276(1)	4.0331(1)
b (Å)	5.6730(20)	4.0268(1)	4.0276(1)	4.0331(1)
c (Å)	5.6810(20)	4.0268(1)	4.0276(1)	4.0331(1)
V/10⁶ (pm³)	65.100(3)	65.294(3)	65.334(4)	65.602(3)
R_{exp}		1.44527	1.44843	1.23751
R_{profile}		2.18202	2.40865	1.47899
R_{wp}		2.75964	3.17362	4.44817
GOF		3.64964	4.80078	9.04555

Table 4. 2: Experimental and theoretical density, lattice parameters and agreement indices calculated by Rietveld Refinement for KBBNZ (x=0.15, 0.20 and 0.25). * Weighted averaged of the two phases.

KBBNZ ceramics reached relative densities above 95% of theoretical density. As mentioned in Chapter 3, pure KN (x=0) is assigned to orthorhombic phase (symmetry group Amm2). XRD data of KBBNZ x=0.05 is also attributed to orthorhombic phase. Patterns for x=0.10 and x=0.15 are acceptably refined as a combination of orthorhombic phase (space group Amm2) and cubic phase (space group Pm- $\bar{3}$ m). The relative content of orthorhombic phase falls from ~70% (x=0.10) to ~30% (x=0.15). XRD results for x=0.20 and x=0.25 are well ascribed to cubic phase.

The unit cell volume for the orthorhombic phase (Amm2) increases linearly up to x=0.10. Orthorhombic and cubic symmetries coexist at x=0.10 and 0.15, but beyond these concentrations the unit cell volume for the cubic phase also increases linearly, as shown in Figure 4. 3. However, the volume of the orthorhombic phase for x=0.10 is larger than

the cubic phase, which is not consistent with XRD data in Figure 4. 2 (b). Probably, this inconsistency arises from the low resolution in XRD measurements, which generates difficulties with Rietveld refinement. The variation of the cell volume for the single-phase compositions follows Vegard's law.

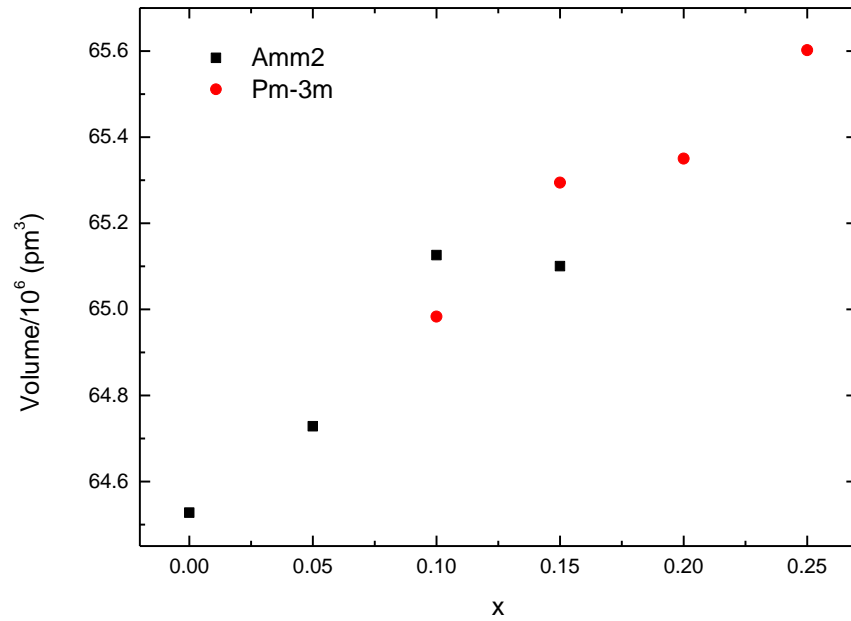


Figure 4. 3.: Compositional variation in the unit cell volume for $(1-x) \text{KNbO}_3-x (\text{Ba}_{0.5}\text{Bi}_{0.5}) (\text{Nb}_{0.5}\text{Zn}_{0.5}) \text{O}_3$ ($0 \leq x \leq 0.25$) ceramics.

4.2.2. Raman Spectroscopy

Room-temperature Raman spectra for KBBNZ powders calcined twice at 850°C are illustrated in Figure 4. 4. All doped compositions present the same general spectral features as undoped KN (orange spectrum). Raman modes for doped compositions become broader and slightly shift to lower wavenumbers. From these results the coexistence of orthorhombic and cubic phases is not immediately discernible, however the presence of orthorhombic phase in all compositions is corroborated by the presence of sharp mixed mode at 192 cm^{-1} and the $A_1(\text{TO})+A_1(\text{LO})$ peak. In contrast, significant changes appear in Raman spectra for KBBNZ ceramics (Figure 4. 5.).

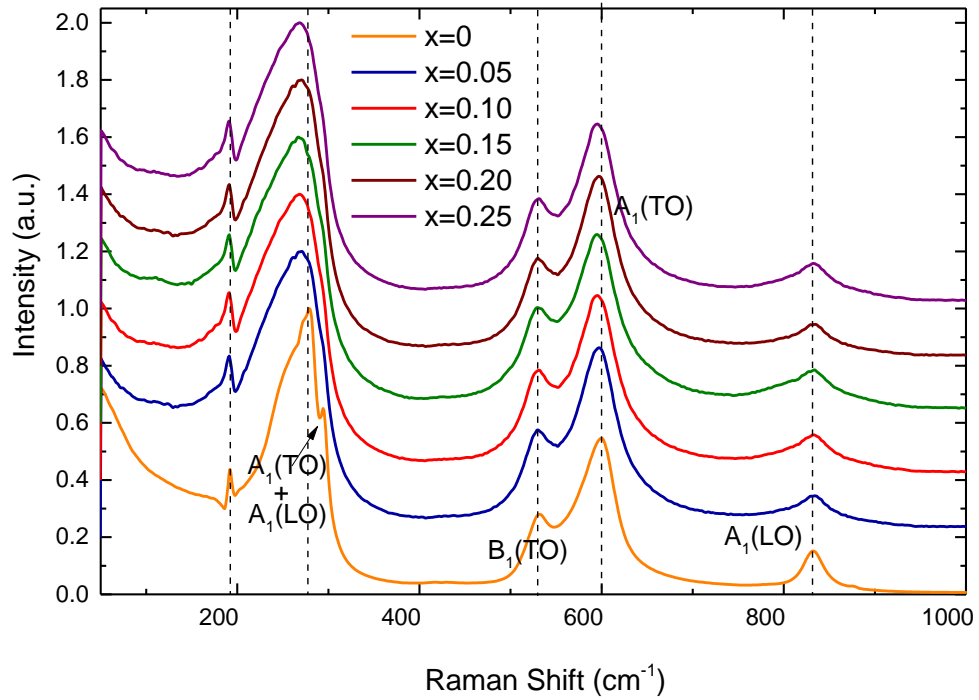


Figure 4. 4.: Room-temperature Raman spectra for KBBNZ ($0 \leq x \leq 0.25$) calcined powders at 850°C two times.

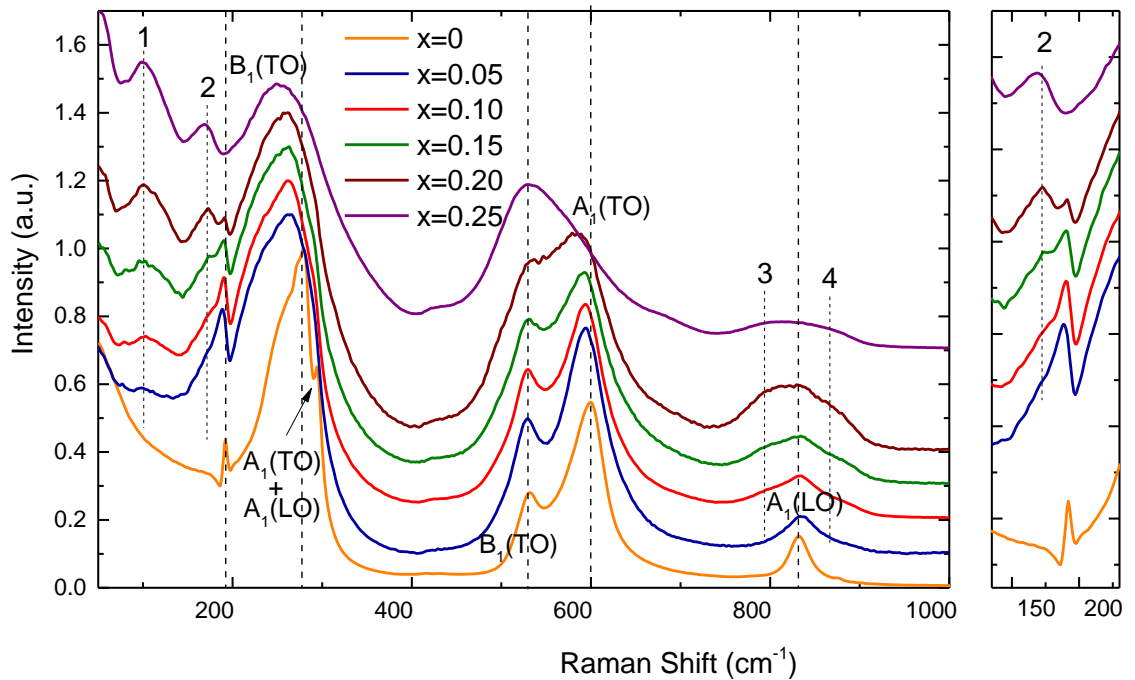


Figure 4. 5.: Room-temperature Raman spectra for KBBNZ ($0 \leq x \leq 0.25$) sintered ceramics at temperatures ranging from 1070 to 1100°C

The increasing broadening of modes in the Raman spectra with increasing x , is consistent with increasing lattice disorder. As described in Chapter 3, pure KN ($x=0$) exhibits 12 Raman active optical modes. KBBNZ ceramics exhibit similar features to KN. In addition, new modes emerged which are labelled as 1, 2, 3 and 4. At this point, their origin is purely speculative. Mode 1 emerges around $<100 \text{ cm}^{-1}$, whereas mode 2 appears at $<175 \text{ cm}^{-1}$, as a shoulder to the sharp mixed mode at 192 cm^{-1} . These modes are fairly static, as they only shift by $< 1 \text{ cm}^{-1}$ over the entire compositional range, but their relative intensity increases continuously. In the past, they have been associated to A-O vibrations within nm-sized clusters rich in either Bi^{+3} and/or K^+ cations. Modes 3 and 4 appear on both sides of the high frequency $A_1(\text{LO})$ mode. These have been previously associated with breathing of the BO_6 octahedra, when occupied by different B-cations. Doping also leads to softening of some modes. For example, the $A_1(\text{TO})$ mode at $< 600 \text{ cm}^{-1}$ for $x=0$ gradually softens to 585 cm^{-1} for $x=0.20$, due to the increase in the unit cell volume, as shown in Figure 4. 3. Indeed, softening of this O-Nb-O symmetric stretching mode is known to occur in undoped KN with increasing temperature, as expected from the lattice thermal expansion, which implies a lowering of the force constants. In contrast, the $B_1(\text{TO})$ mode at $< 532 \text{ cm}^{-1}$ shows no compositional shift. The relative intensity of the $A_1(\text{TO})$ in relation to the $B_1(\text{TO})$ decreases continuously with increasing x . For $x=0.25$, the $A_1(\text{TO})$ mode is considerably less intense than the $B_1(\text{TO})$. The occurrence of long-range polarisation in KN is ultimately associated with the presence of the mixed peak at 192 cm^{-1} , which therefore can be used to monitor the polar nature of KN-based solid solutions, as shown by Luisman et al, 2011. Figure 4. 6 illustrates the shifting of modes $B_1(\text{TO})$ and $A_1(\text{LO})$ for powders (dark squares) and ceramics (red circles). The shift of $B_1(\text{TO})$ mode is more accentuated in ceramics than powders. On the other hand, mode $A_1(\text{LO})$ is approximately constant in both, powders and ceramics.

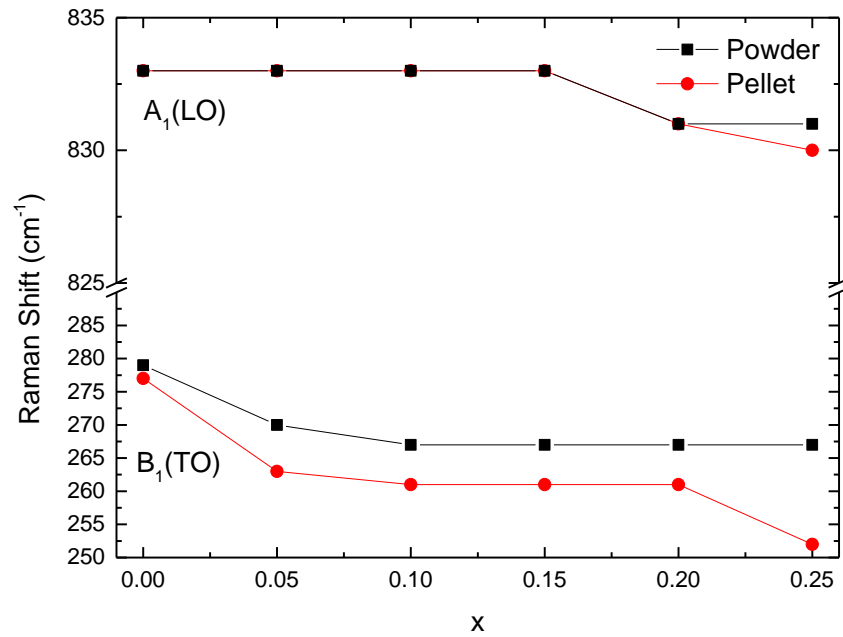


Figure 4. 6.: Shift of modes $B_1(\text{TO})$ and $A_1(\text{LO})$ for powders (dark squares) and ceramics (red circles) as a function of x .

In-situ Raman analysis between -180 and 280°C for KN (Figure 4. 7) clearly show the three different polymorphs (Rhombohedral, orthorhombic and tetragonal). In contrast, Figure 4. 8 suggests the crystal symmetry for $x=0.25$ is unchanged in this temperature range.

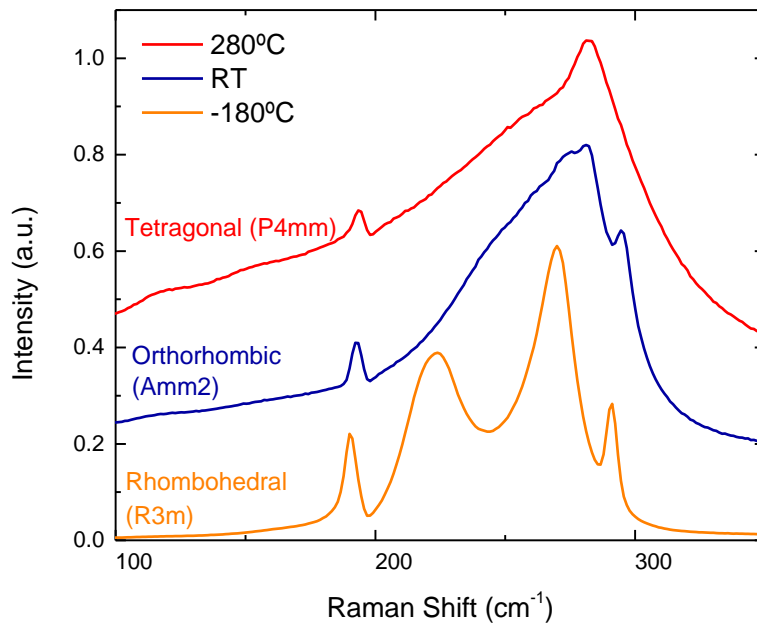


Figure 4. 7.: In-situ Raman for KNbO_3 showing the typical spectrum for each of the three ferroelectric polymorphs. The sharp modes are regarded as "fingerprints" for ferroelectricity. Data corrected with the Bose-Einstein factor.

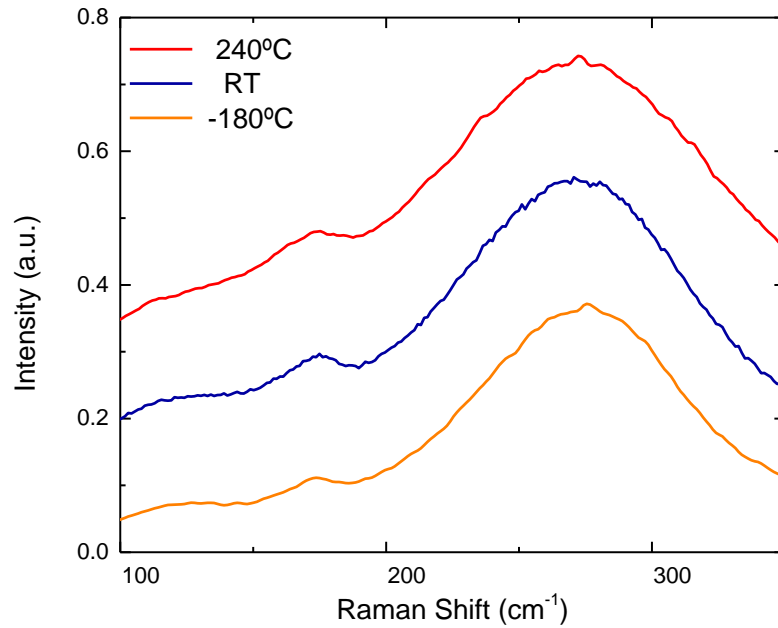


Figure 4. 8.: In-situ Raman for KN-BBNZ $x=0.25$, showing both the absence of structural phase transitions. Data corrected with the Bose-Einstein factor.

4.2.3. SEM

SEM images for KBBNZ ($x=0, 0.05, 0.10, 0.15, 0.20$ and 0.25) ceramics are shown in Figure 4. 9-13. Unpolished and polished surface were examined for KBBNZ ($x=0, 0.05, 0.10, 0.15$) composition because of difficulty to distinguish the grains, even after thermal etching.

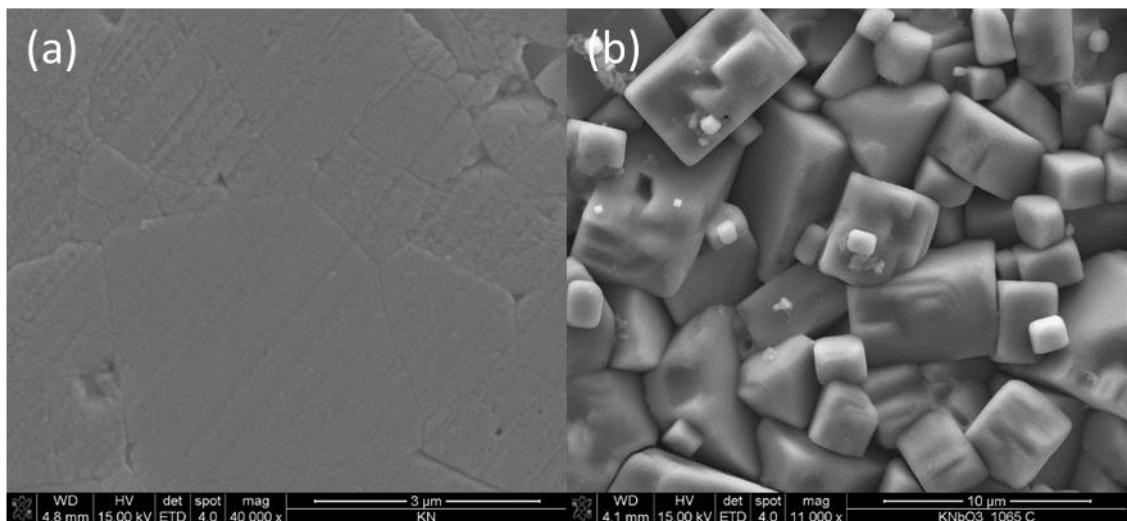


Figure 4. 9.: SEM image of polished (a) and unpolished (b) surface for KN ceramic.

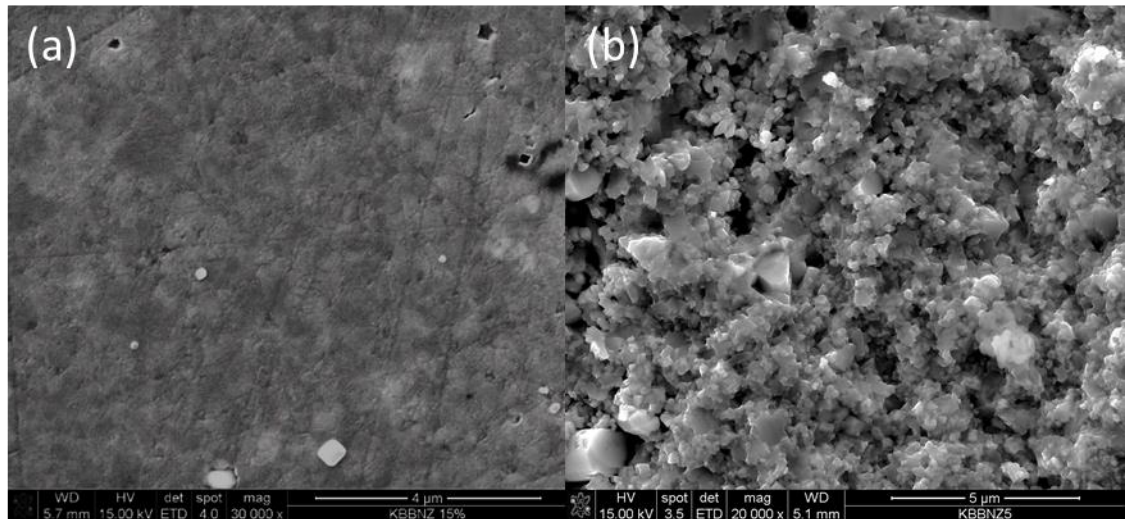


Figure 4.10.: SEM image of polished (a) and unpolished (b) surface for KBBNZ $x=0.05$ ceramic.

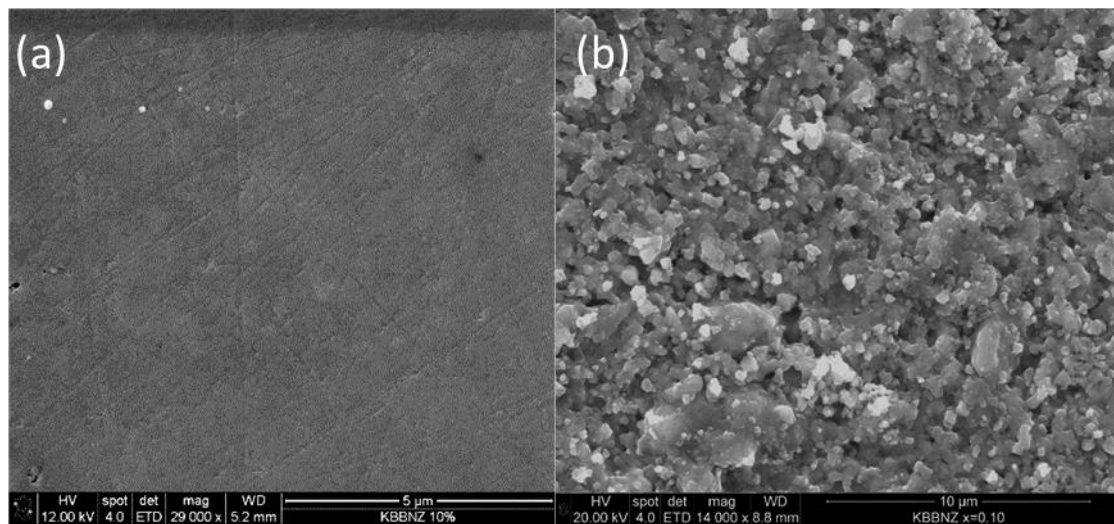


Figure 4. 11.: SEM image of polished (a) and unpolished (b) surface for KBBNZ $x=0.10$ ceramic.

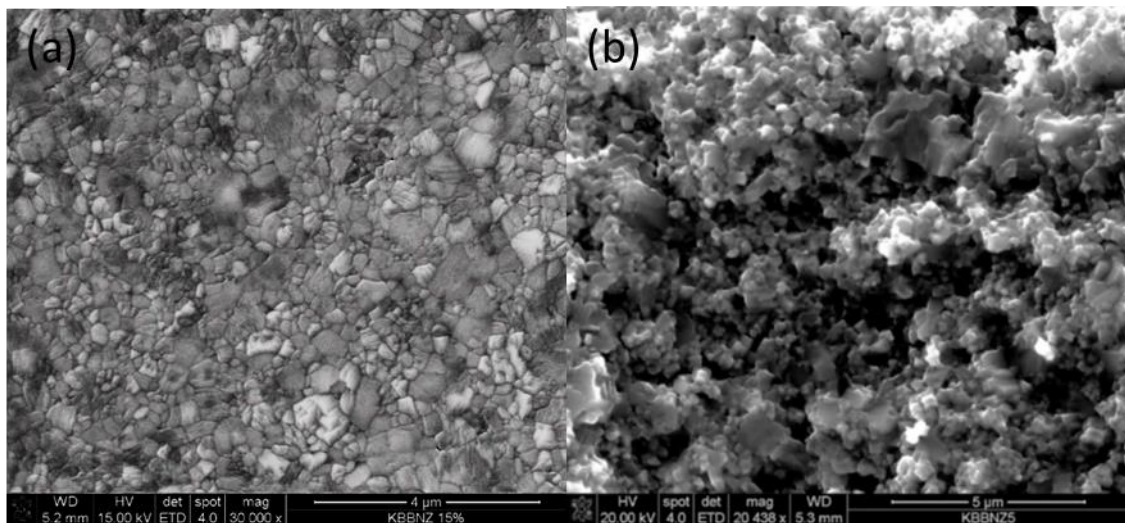


Figure 4. 12.: SEM image of polished (a) and unpolished (b) surface for KBBNZ $x=0.15$ ceramic.

Pure KN (Figure 4. 9.) ceramic exhibits cubic shaped grains, with smooth surface and their size varies from 3 μm to 5 μm . After doping, grain growth is inhibited, as shown in SEM image of KBBNZ $x=0.05$ (Figure 4.10), $x=0.10$ (Figure 4. 11.) and $x=0.15$ (Figure 4. 12.) microstructures. Grain size varies between 300 nm and 500 nm and has the tendency slightly increases with increasing x value. The absence of almost any porosity in polished surfaces confirm the high experimental density of the ceramics. SEM images of thermal etched KBBNZ $x=0.20$ and $x=0.25$ ceramics are given in Figure 4. 13 and Figure 4. 14.

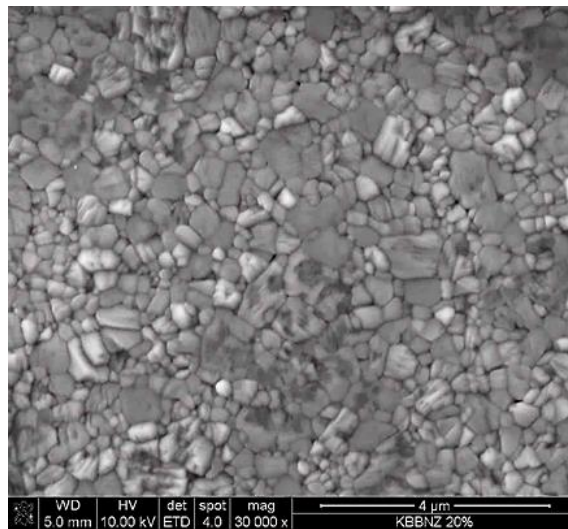


Figure 4. 13: SEM image of polished surface for KBBNZ $x=0.20$ ceramic

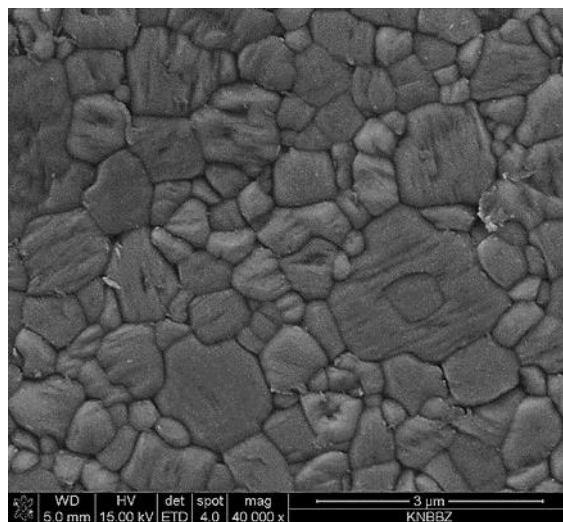


Figure 4. 14: SEM image of polished surface for KBBNZ $x=0.25$ ceramic.

Again, KBBNZ $x=0.20$ and $x=0.25$ ceramics reveal high density, in agreement with the experimental densities (both above 96%) reported in Table 4.2. Unlike the samples previously described, the growth in grain size is accentuated for these compositions, rising up to ~ 700 nm for $x=0.20$ and up to $\sim 1\mu\text{m}$ for $x=0.25$. In summary, the morphology of KBBNZ ceramics is strongly dependent on the $\text{Ba}_{0.5}\text{Bi}_{0.5}\text{Nb}_{0.5}\text{Zn}_{0.5}\text{O}_3$ content.

4.2.4. EDX

Chemical analyses and element distribution (K, Nb, Ba, Bi and Zn) for KBBNZ ($0.05 \leq x \leq 0.25$) ceramics are obtained by EDX analyses. Theoretical and experimental K/Ba, K/Bi, K/Nb and K/Zn ratios are reported and compared in Table 4. 3-7. Relative error is provided as a mathematical means for comparing experimental and theoretical values.

For $x=0.05$ (Table 4. 3), experimental K/Nb, K/Ba and K/Bi fractions match to theoretical ratios within margin of error. In contrast, K/Zn ratio is almost the double of theoretical ratio, which indicates concentration of Zn is much lower than it should be. This fact suggests ZnO presents difficulties on reacting with the rest of the oxides.

x=0.05			
	Theoretical	Experimental	Relative error (%)
K/Ba	38	34(3)	10
K/Bi	38	42(5)	10
K/Nb	0.974	1(2)	3
K/Zn	38	60(2)	58

Table 4. 3: Experimental (average) and theoretical K/Ba, K/Bi K/Nb and K/Zn ratios for $0.95 \text{KNbO}_3 - 0.05 \text{Ba}_{0.5}\text{Bi}_{0.5}\text{Zn}_{0.5}\text{Nb}_{0.5}\text{O}_3$ ceramic sintered at 1070°C .

Chemical inhomogeneities are found on the surface of KBBNZ $x=0.05$. For example, a big grain with fibre/cylindric shape is richer in Ba, Bi, and Zn and poorer in K, in comparison to the matrix. (Figure 4. 15). Difficulties on homogeneously incorporating small quantity of Ba^{+2} , Bi^{+3} and Zn^{+2} are found.

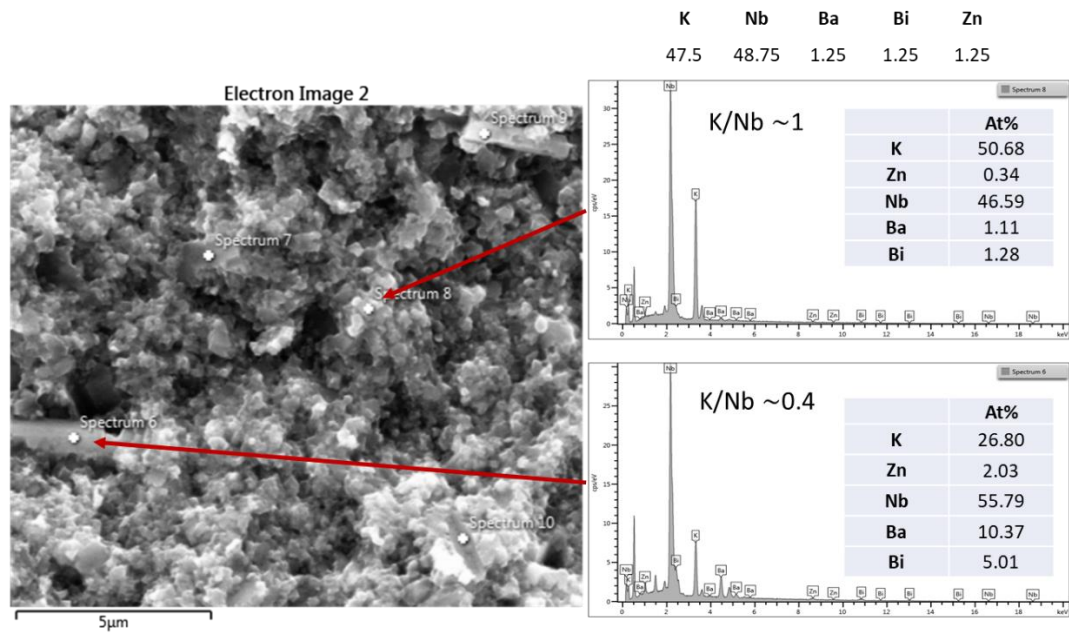


Figure 4. 15: Scanning electron image and EDX spectrograms of unpolished 0.95 $\text{KNbO}_3 - 0.05 \text{Ba}_{0.5}\text{Bi}_{0.5}\text{Nb}_{0.5}\text{Zn}_{0.5}\text{O}_3$ ceramic sintered at 1100°C .

Table 4. 4 shows the experimental and theoretical K/Nb, K/Ba, K/Bi and K/Zn ratios and relative error for $x=0.10$ composition.

x=0.10			
	Stoichiometric	Experimental	Relative error (%)
K/Ba	18	17(2)	5
K/Bi	18	24(6)	33
K/Nb	0.947	1(2)	6
K/Zn	18	28(6)	60

Table 4. 4: Experimental (average) and theoretical K/Ba, K/Bi K/Nb and K/Zn ratios for 0.90 $\text{KNbO}_3 - 0.10 \text{Ba}_{0.5}\text{Bi}_{0.5}\text{Zn}_{0.5}\text{Nb}_{0.5}\text{O}_3$ ceramic sintered at 1070°C .

Inside the margins of error, empirical K/Nb, K/Ba, K/Bi and K/Zn values fit with theoretical. Again, the high K/Zn value indicates low concentration of Zn. Big grains with fibre/cylindric shape are also detected on KBBNZ $x=0.10$ ceramic. These regions are characterised by low K concentration (calculated ratios in Figure 4. 16) but also Zn is not detected.

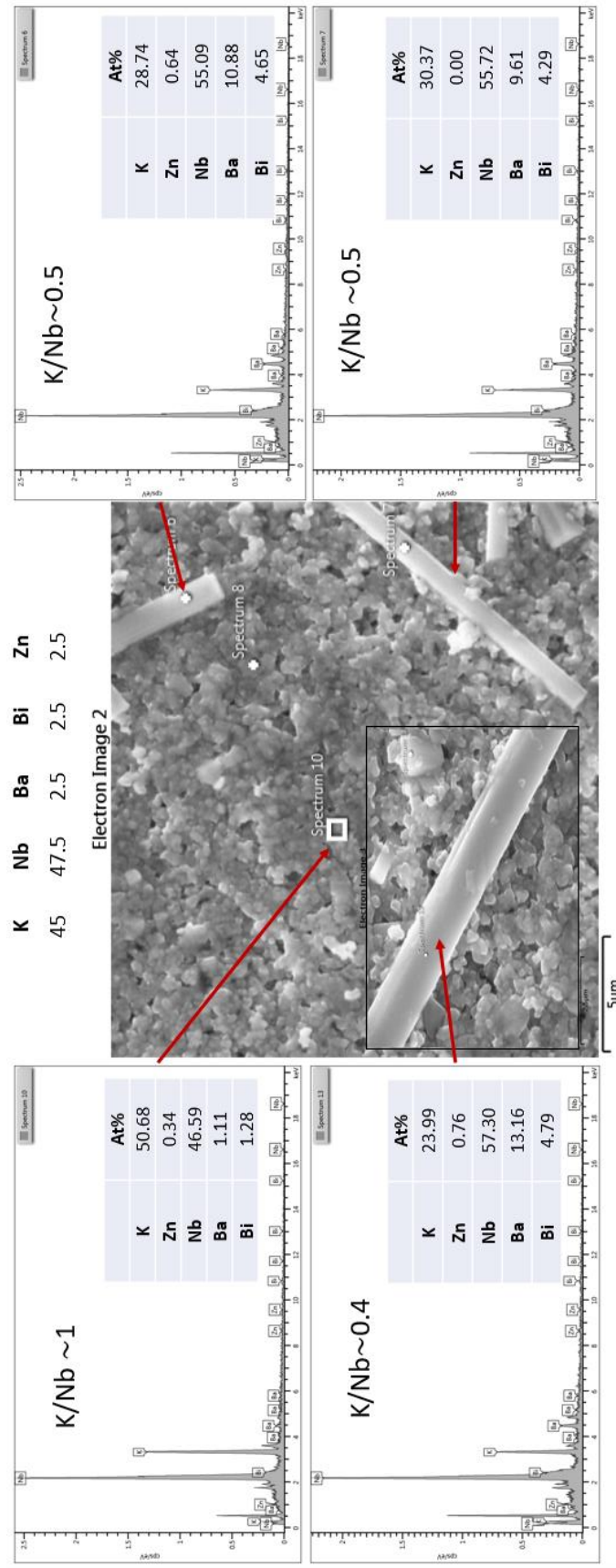


Figure 4. 16: Scanning electron image and EDX spectrograms of unpolished 0.90 $\text{KNbO}_3 - 0.10 \text{Ba}_{0.5}\text{Bi}_{0.5}\text{Nb}_{0.5}\text{Zn}_{0.5}\text{O}_3$ ceramic sintered at 1100°C .

Table 4. 5, Table 4. 6 and Table 4. 7 report the EDX results for KBBNZ $x=0.15$, $x=0.20$ and $x=0.25$ ceramics, respectively.

x=0.15			
	Stoichiometric	Experimental	Relative error (%)
K/Ba	11	10(2)	9
K/Bi	11	12(5)	8
K/Nb	0.919	1(2)	9
K/Zn	11	12(3)	9

Table 4. 5: Experimental (average) and theoretical K/Ba, K/Bi K/Nb and K/Zn ratios for $0.85 \text{KNbO}_3 - 0.15 \text{Ba}_{0.5}\text{Bi}_{0.5}\text{Zn}_{0.5}\text{Nb}_{0.5}\text{O}_3$ ceramic sintered at 1070°C .

x=0.20			
	Stoichiometric	Experimental	Relative error(%)
K/Ba	8	9(2)	12
K/Bi	8	8(4)	0
K/Nb	0.889	1(1)	12
K/Zn	8	10(3)	25

Table 4. 6: Experimental (average) and theoretical K/Ba, K/Bi K/Nb and K/Zn ratios for $0.80 \text{KNbO}_3 - 0.20 \text{Ba}_{0.5}\text{Bi}_{0.5}\text{Zn}_{0.5}\text{Nb}_{0.5}\text{O}_3$ ceramic sintered at 1070°C .

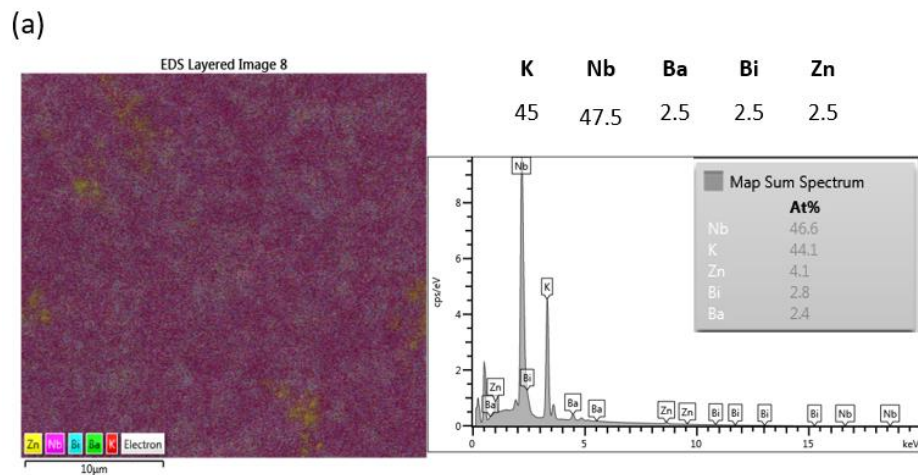
x=0.25			
	Stoichiometric	Experimental	Relative error (%)
K/Ba	6	5(1)	16
K/Bi	6	6(3)	0
K/Nb	0.857	1(3)	16
K/Zn	6	6(2)	0

Table 4. 7: Experimental (average) and theoretical K/Ba, K/Bi K/Nb and K/Zn ratios for $0.75 \text{KNbO}_3 - 0.25 \text{Ba}_{0.5}\text{Bi}_{0.5}\text{Zn}_{0.5}\text{Nb}_{0.5}\text{O}_3$ ceramic sintered at 1070°C .

The values reported in these tables are an average of a set of measurements, that can be referred in Appendix B.

From $x=0.15$ to $x=0.25$, experimental K/Ba, K/Bi, K/Nb and K/Zn ratios tend to continuously get closer to the theoretical stoichiometry. The high K/Zn ratio commented

for $x=0.05$ and $x=0.10$, is not observed in the rest of the compositions. This fact supports the hypothesis that difficulties on introducing Zn into KN matrix are more accentuated for low concentrations of Ba^{+2} , Bi^{+3} and Zn^{+2} . Indeed, relative errors are significantly lower. Standard errors also seem slightly lower for $x=0.15$, $x=0.20$ and $x=0.25$ than for $x=0.05$ and $x=0.10$. Therefore, compounds with low concentrations of x present more difficulties in obtaining a homogeneous element distribution. This statement is also supported by EDX mapping of K, Nb, Ba, Bi and Zn on KBBNZ $x=0.10$ sample (Figure 4. 17) and $x=0.25$ (Figure 4. 18). Overall, the elements are more homogeneously distributed on KBBNZ $x=0.25$ than $x=0.10$. Moreover, the presence of Zn-rich regions in KBBNZ $x=0.10$ confirm this oxide has more difficulties to diffuse into KN lattice than the other oxides, under the condition of low concentration of dopants.



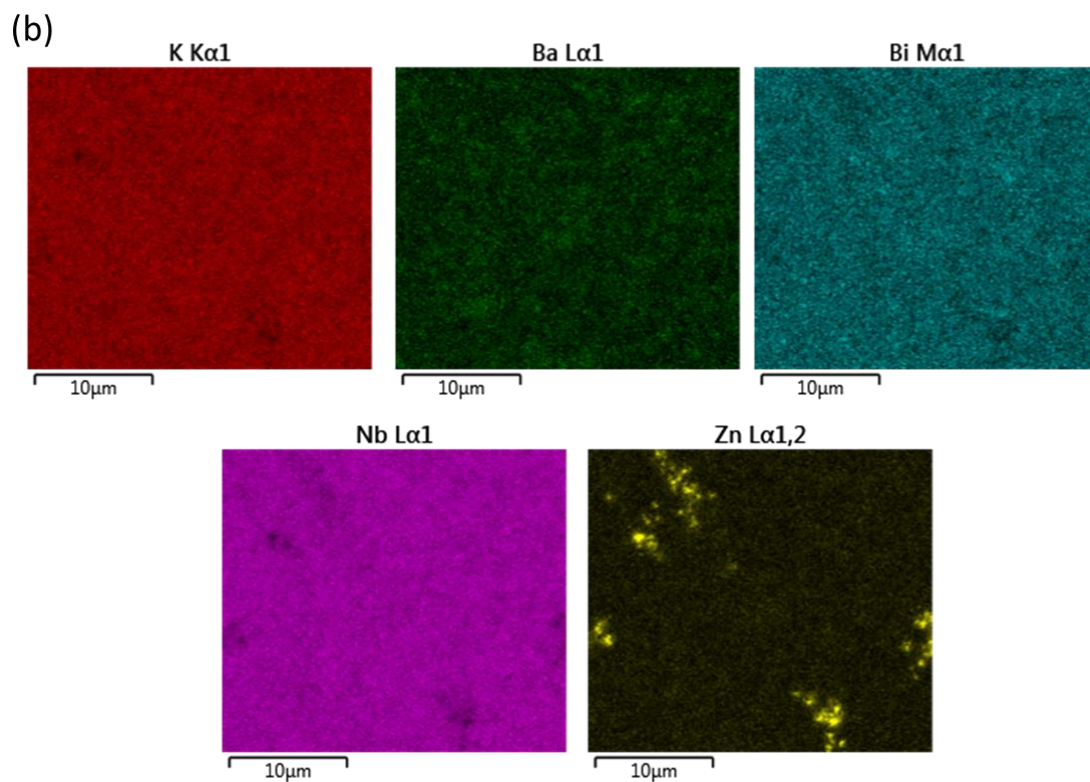
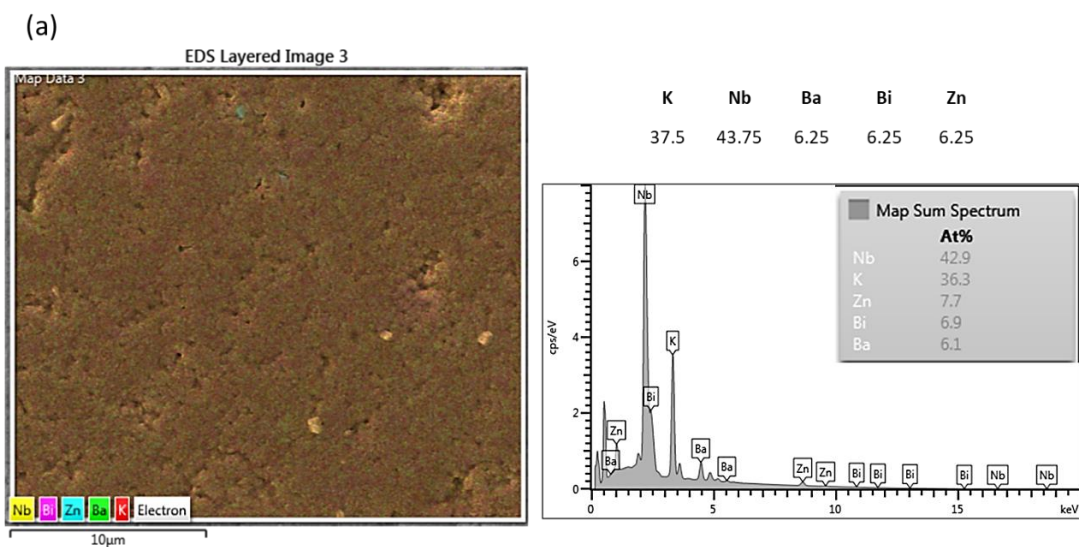


Figure 4. 17: (a) SEM image of the examined region with EDX spectra and experimental and theoretical atomic percent are provided. (b) EDX mapping of K, Ba, Bi, Nb and Zn for KBBNZ $x=0.10$.



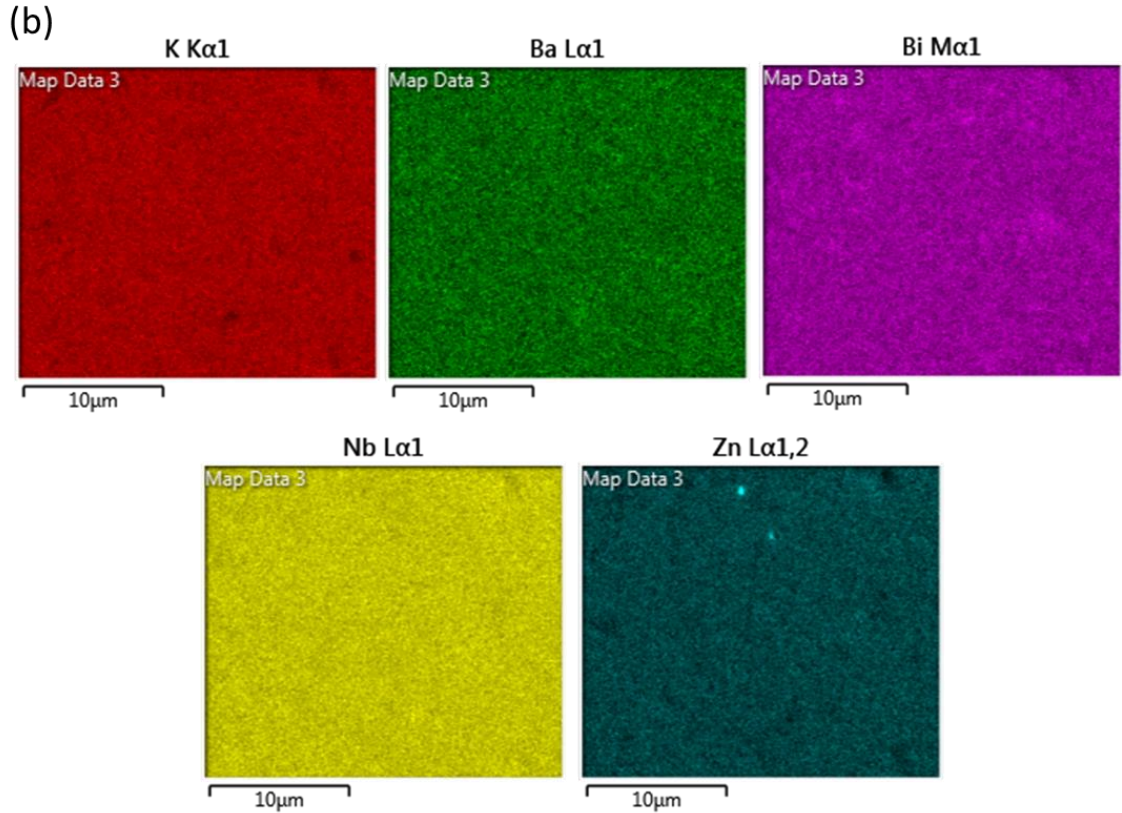


Figure 4. 18: (a) SEM image of the examined region with EDX spectra, experimental and theoretical atomic percent are provided. (b) EDX mapping of K, Ba, Bi, Nb and Zn for KBBNZ $x=0.25$.

4.3. Electrical Characterisation

4.3.1. Dielectric Characterisation

The temperature dependence of the permittivity, ϵ_r , for KBBNZ ceramics ($x = 0, 0.05, 0.10, 0.15, 0.20$ and 0.25) measured at 100 kHz is illustrated in Figure 4. 19 which gives information about the impact of doping on the phase transitions.

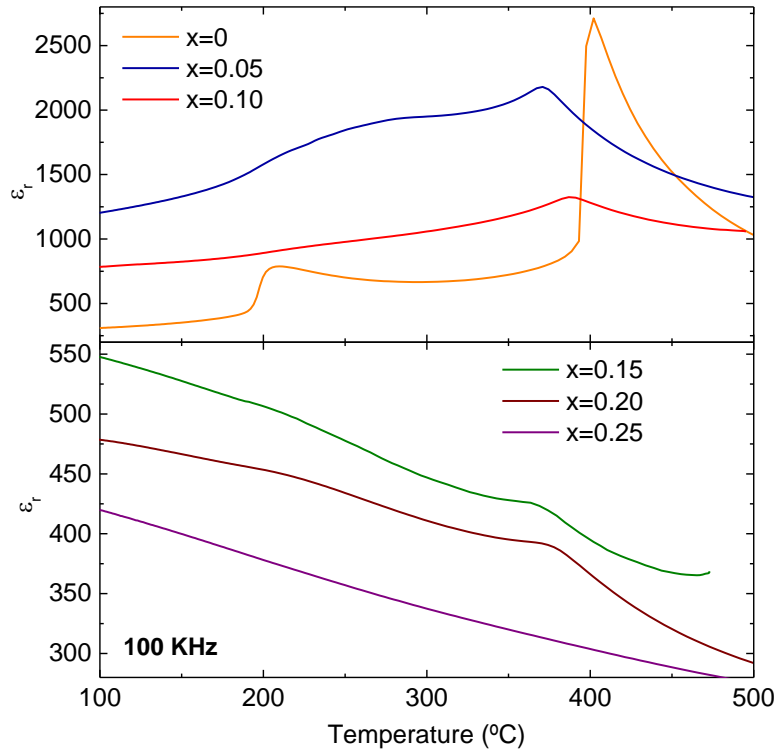


Figure 4. 19: Temperature dependence of ϵ_r for $(1-x)$ KNbO_3 - x $\text{Ba}_{0.5}\text{Bi}_{0.5}\text{Zn}_{0.5}\text{Nb}_{0.5}\text{O}_3$ solid solution at 100 kHz, during cooling.

As described in Chapter 3, KN ($x = 0$) shows two maxima at ~ 205 °C and ~ 400 °C (Curie temperature), respectively, corresponding to orthorhombic-to-tetragonal and the tetragonal-to-cubic phase transitions, respectively. In this system, dielectric anomalies are visible up $x=0.20$. With increasing x , T_C initially drops to ~ 370 °C for $x = 0.05$, then it increases to ~ 387 °C for $x = 0.10$ and subsequently goes down again to ~ 370 °C for $x = 0.15$. This non-monotonic T_C variation occurs within the multiphase composition range, which suggests a non-homogeneous distribution of dopants between the orthorhombic and cubic phases, as shown by the EDX results. For $x=0.20$, two dielectric anomalies, probably due to a residual orthorhombic phase are still present. Finally, for $x = 0.25$, ϵ_r decreases continuously upon increasing temperature. No dielectric anomalies are detected in this temperature range, which suggests that this composition has an average cubic crystal structure. It is noted, KBBNZ $x=0.15$, 0.20 and 0.25 ceramics exhibit larger ϵ_r values at lower temperatures.

Frequency-dependent measurements (100 kHz, 250 kHz and 1 MHz) of the relative permittivity and dielectric loss are provided for individual compositions, shown in Figure 4. 20-24. A strong frequency dependence is observed for $x=0.05$ and 0.10 , as illustrated in Figure 4. 20 and Figure 4. 21, respectively. The corresponding temperature for the

dielectric anomalies remains almost unaltered, but its magnitude decreases with increasing frequency. For $x=0.15$ and $x=0.20$, the frequency dependence is much less pronounced, as shown in Figure 4. 22 and Figure 4. 23. In these compositions, dielectric curves exhibit shoulders instead of maximum values at the phase transitions. Nevertheless, KBBNZ $x=0.25$ composition presents a flat dielectric response with temperature and it is not frequency dependent, as shown in Figure 4. 24.

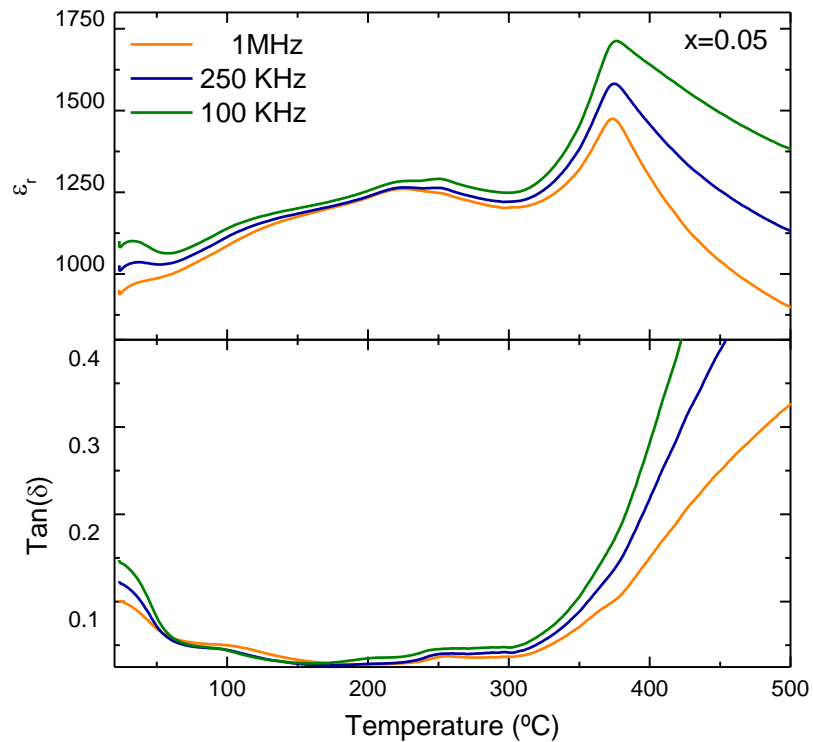


Figure 4. 20: Temperature dependence of ϵ_r and $\tan\delta$ for $0.95 \text{KNbO}_3-0.05 \text{Ba}_{0.5}\text{Bi}_{0.5}\text{Nb}_{0.5}\text{Zn}_{0.5}\text{O}_3$ solid solution at 100 kHz, 250 kHz and 1 MHz during cooling.

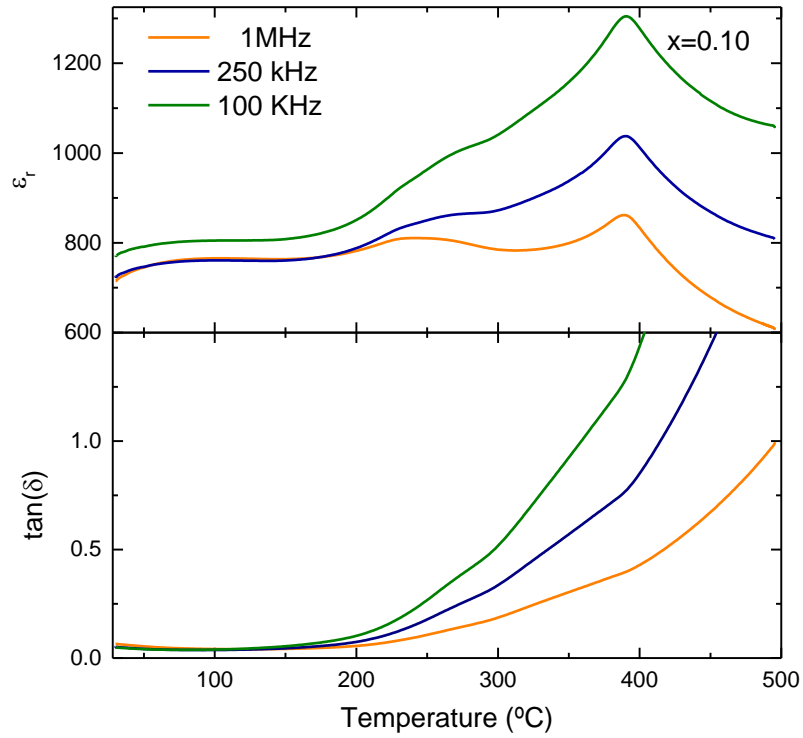


Figure 4. 21: Temperature dependence of ϵ_r and $\tan\delta$ for 0.90 KNbO_3 –0.10 $\text{Ba}_{0.5}\text{Bi}_{0.5}\text{Nb}_{0.5}\text{Zn}_{0.5}\text{O}_3$ solid solution at 100 kHz, 250 kHz and 1 MHz during cooling.

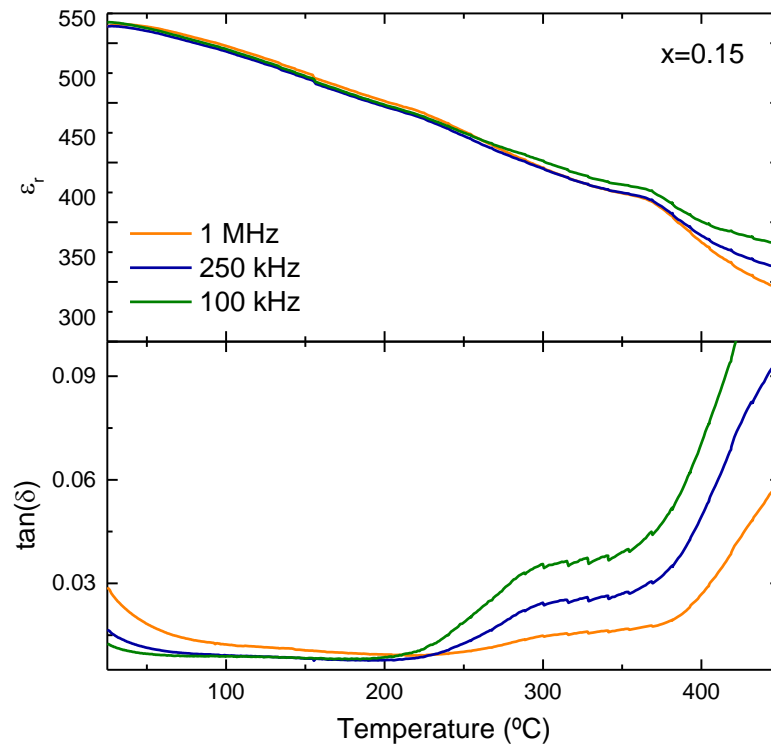


Figure 4. 22: Temperature dependence of ϵ_r and $\tan\delta$ for 0.85 KNbO_3 –0.15 $\text{Ba}_{0.5}\text{Bi}_{0.5}\text{Nb}_{0.5}\text{Zn}_{0.5}\text{O}_3$ solid solution at 100 kHz, 250 kHz and 1 MHz during cooling.

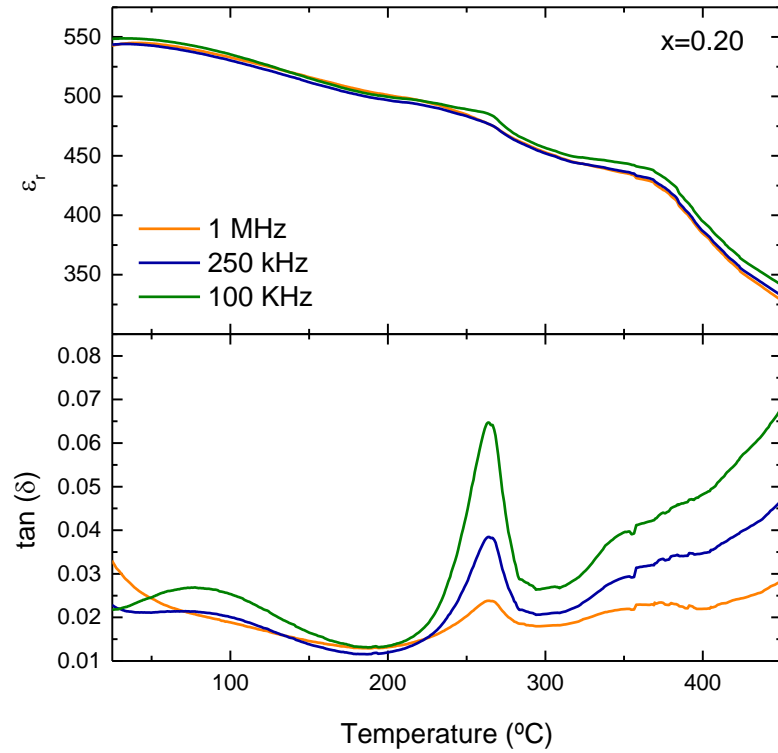


Figure 4. 23: Temperature dependence of ϵ_r and $\tan\delta$ for 0.80 KNbO_3 – $0.20 \text{ Ba}_{0.5}\text{Bi}_{0.5}\text{Nb}_{0.5}\text{Zn}_{0.5}\text{O}_3$ solid solution at 100 kHz, 250 kHz and 1 MHz during cooling.

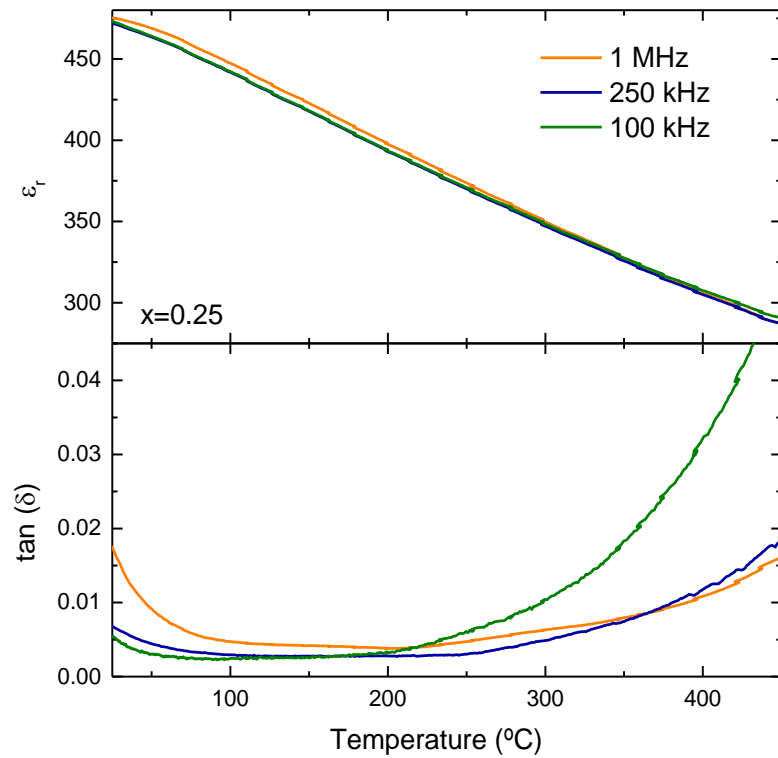


Figure 4. 24 Temperature dependence of ϵ_r and $\tan\delta$ for 0.75 KNbO_3 – $0.25 \text{ Ba}_{0.5}\text{Bi}_{0.5}\text{Nb}_{0.5}\text{Zn}_{0.5}\text{O}_3$ solid solution at 100 kHz, 250 kHz and 1 MHz during cooling.

4.3.2. Piezo- and Ferroelectric Characterisation

Polarisation vs. electric field (P–E) loops of KBBNZ ceramics measured at room temperature under an electric field of 80 kV/cm are shown in Figure 4. 25.

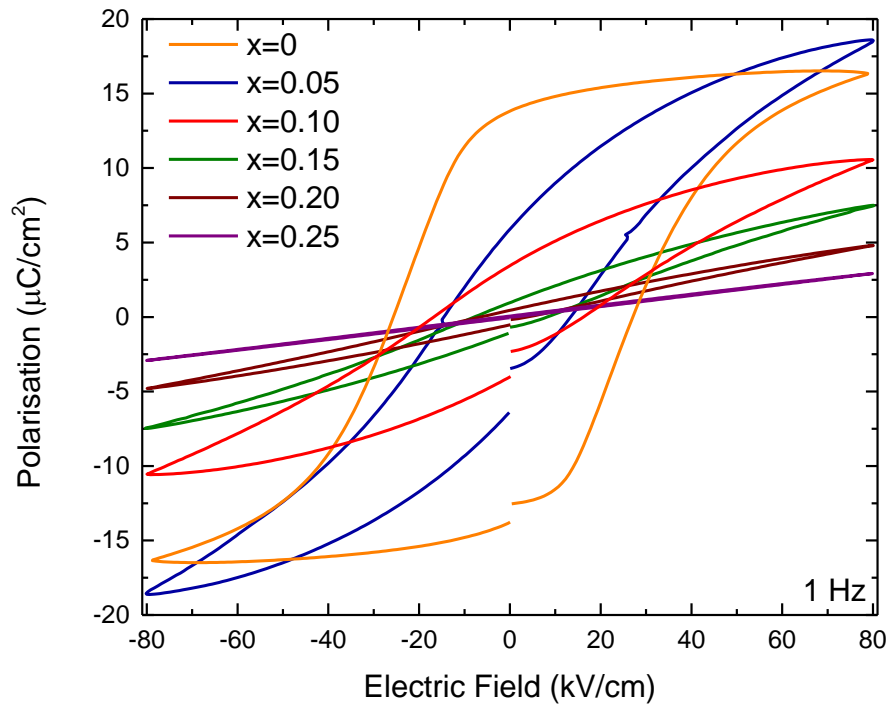


Figure 4. 25: P–E measurements for $(1-x) \text{KNbO}_3-x \text{Ba}_{0.5}\text{Bi}_{0.5}\text{Nb}_{0.5}\text{Zn}_{0.5}\text{O}_3$ ($x=0, 0.05, 0.10, 0.15, 0.20, 0.25$) ceramics.

Undoped KN ($x = 0$) exhibits a P–E loop typical of a ferroelectric response, (described in Chapter 4). When $\text{Ba}_{0.5}\text{Bi}_{0.5}\text{Nb}_{0.5}\text{Zn}_{0.5}\text{O}_3$ is substituted into the KN lattice, both P_r and E_c decrease dramatically and the P–E loops become increasingly slimmer as shown in Figure 4. 25. For single-phase $x = 0.25$ with an average cubic structure, the P–E curve is virtually linear (hysteresis free). Figure 4. 26 summarises the P_s , P_r and E_c values for all compositions at RT.

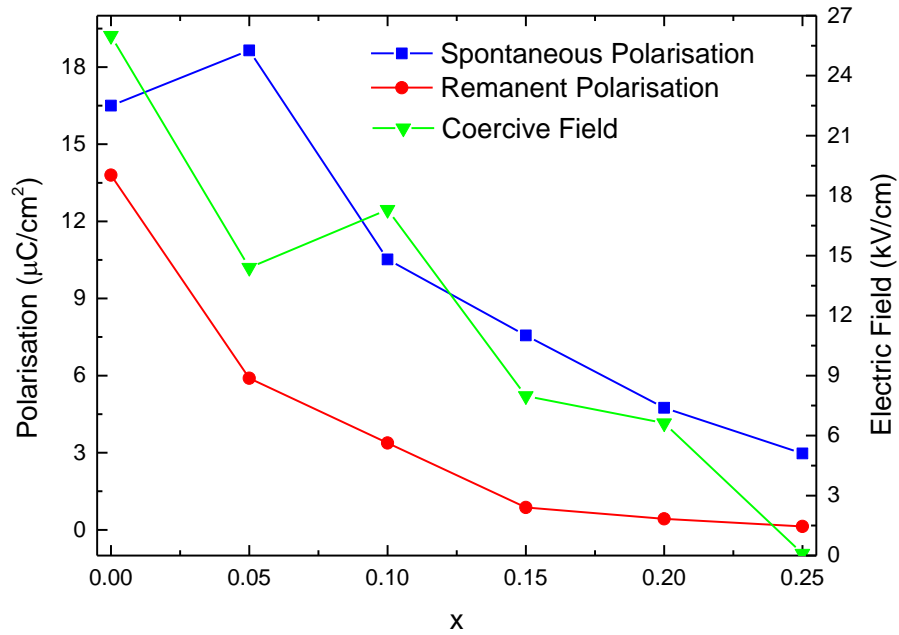


Figure 4. 26: Compositional evolution of the spontaneous polarisation, P_s , remanent polarisation, P_r and coercive field E_c under 80 kV/mm at RT.

KBBNZ $x=0.05$ ceramics show a spontaneous polarisation, P_s , of $\sim 18 \mu\text{C}/\text{cm}^2$, a remnant polarization, P_r , of $\sim 6 \mu\text{C}/\text{cm}^2$, which is roughly 3 times smaller in comparison with KN, and a coercive field, E_c , of $\sim 14 \text{ kV}/\text{cm}$. It is noted, that maximum polarisation for this composition is higher than pure KN. Many reasons such as grain size and orientation, domain size and density can be attributed to be at the origin of this counterintuitive result. For the multiphasic (orthorhombic + cubic) $x = 0.10, 0.15$ and 0.20 , P_s continuously drops from $\sim 10 \mu\text{C}/\text{cm}^2$ to $\sim 5 \mu\text{C}/\text{cm}^2$ as well as P_r , from $\sim 3 \mu\text{C}/\text{cm}^2$ to zero. Finally, KBBNZ $x = 0.25$ exhibits a linear response with a maximum polarisation of $\sim 2.3 \mu\text{C}/\text{cm}^2$.

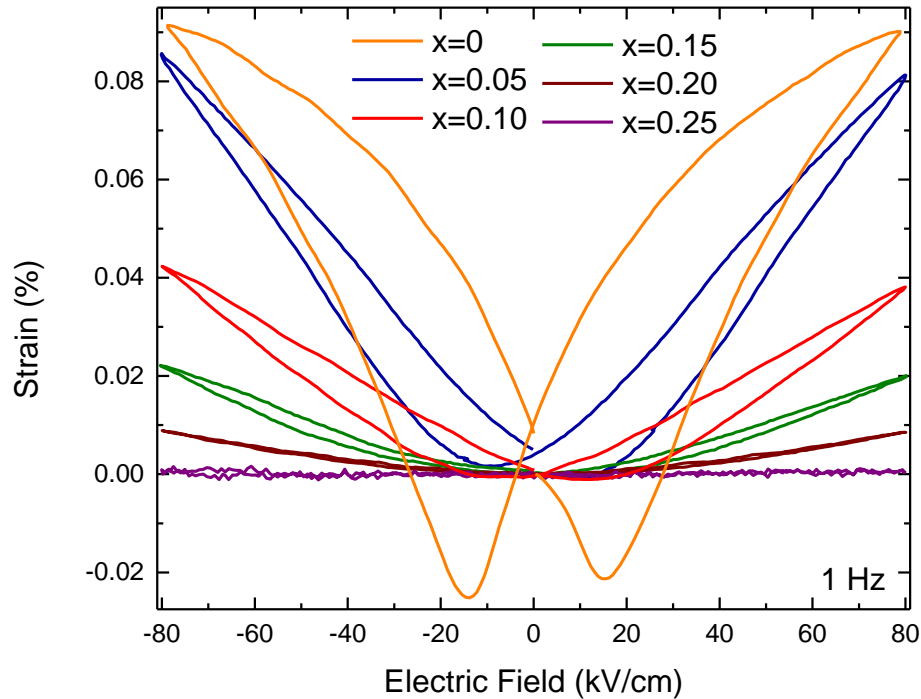


Figure 4. 27: S–E measurements for $(1 - x) \text{KNbO}_3-x \text{Ba}_{0.5}\text{Bi}_{0.5}\text{Nb}_{0.5}\text{Zn}_{0.5}\text{O}_3$ ($x=0, 0.05, 0.10, 0.15, 0.20, 0.25$) ceramics.

Again, a gradual decrease of the field induces strain with increasing x is observed. The induced strain drops from 0.091% for $x=0$ (butterfly shape) to zero ($x=0.25$). For $x = 0.10, 0.15$ and 0.20 , the S–E responses show almost parabolic shape (as expected for an electrostrictive material) and their maximum strains continuously decrease, from 0.041%, to 0.009%, respectively. KBBNZ $x=0.15$ and $x=0.20$ ceramics show more accentuated electrostrictive behaviour (Figure 4. 28 (a) and Figure 4. 29 (a)). Indeed, the electrostriction coefficient, Q , can be determined from the $S=QP^2$ relationship, where S and P represent the strain and polarisation, respectively. Thus, this coefficient is easily calculated from $S-P^2$ curves of $x=0.15$ and $x=0.20$ (Figure 4. 28 (b) and Figure 4. 29 (b)). The electrostrictive coefficient, Q , for $x=0.15$ is $0.037 \text{ m}^4\text{C}^{-2}$ and for $x=0.20$ Q is $0.035 \text{ m}^4\text{C}^{-2}$.

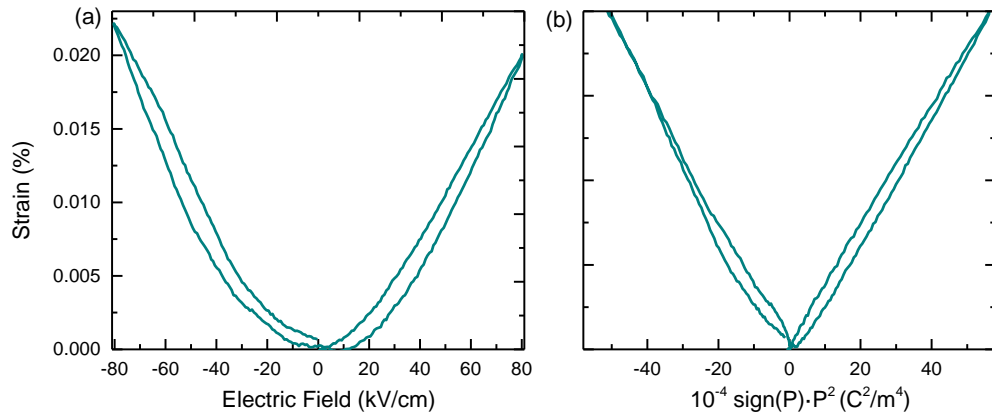


Figure 4. 28: (a) Parabolic S-E response and (b) S-P² curve for KBBNZ $x=0.15$ ceramics.

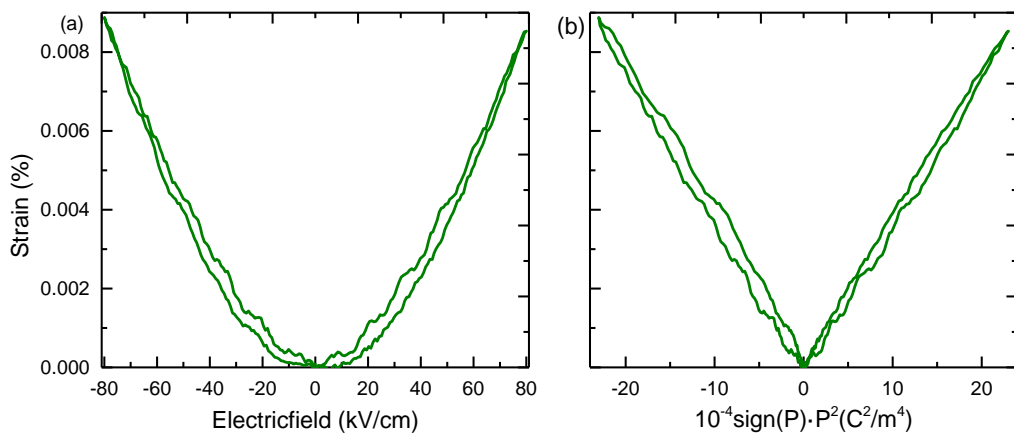


Figure 4. 29: (a) Parabolic S-E response and (b) S-P² curve for KBBNZ $x=0.20$ ceramics.

Evolution of P-E and S-E loops under different electric fields from 20 kV/cm to 80 kV/cm at RT and their dependence with temperature from RT to 180 °C, are provided for individual compositions in APPENDIX B (section B.3). Temperature measurements are performed under electric field of 50 kV/cm at 1 Hz, to avoid dielectric breakdown (APPENDIX B, section B.3).

Figure 4. 30, Figure 4. 31 and Figure 4. 32 summarise the results of spontaneous polarisation (P_s), coercive field (E_C) and maximum strain (S_{\max}) as a function of the temperature and the composition (x).

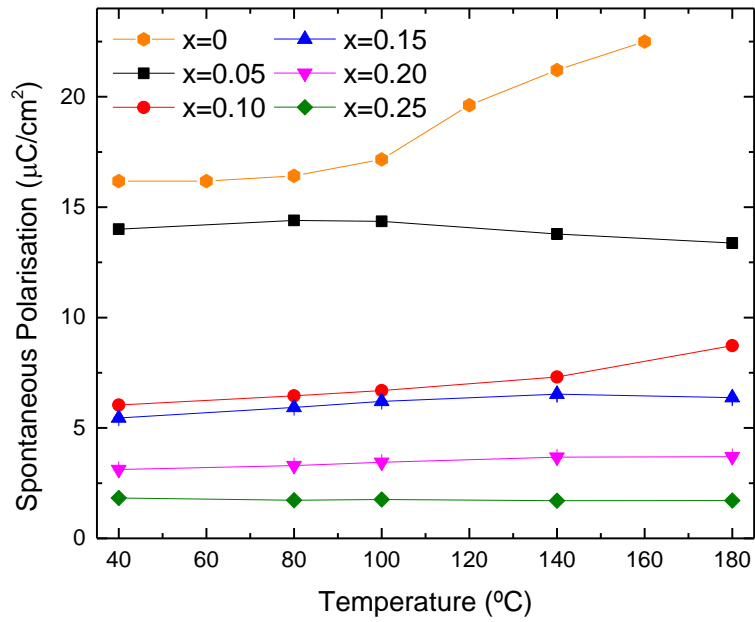


Figure 4. 30: Temperature dependence of P_s for KBBNZ ($x=0, 0.5, 0.10, 0.15, 0.20$ and 0.25) ceramics measured under electric field of 50kV/cm (1 Hz).

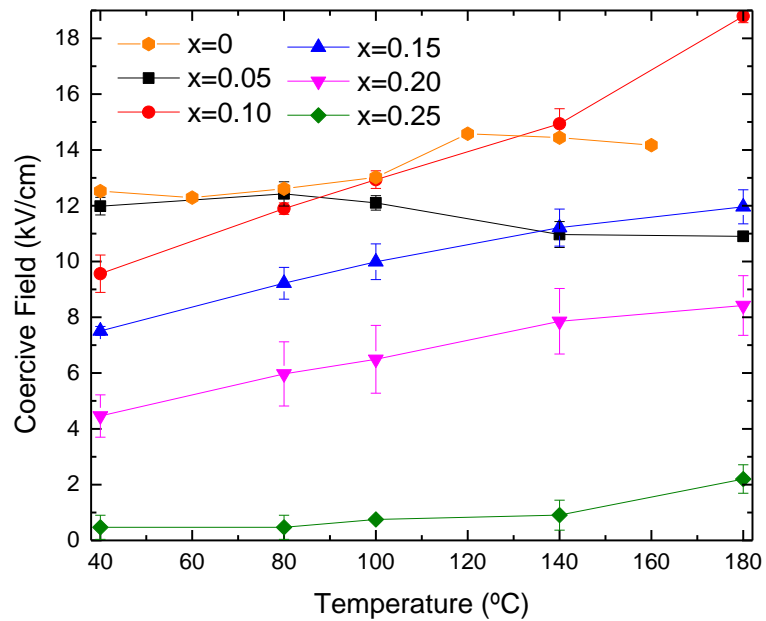


Figure 4. 31: Temperature dependence of E_c for KBBNZ ($x= 0, 0.5, 0.10, 0.15, 0.20$ and 0.25) ceramics measured under electric field of 50kV/cm (1 Hz).

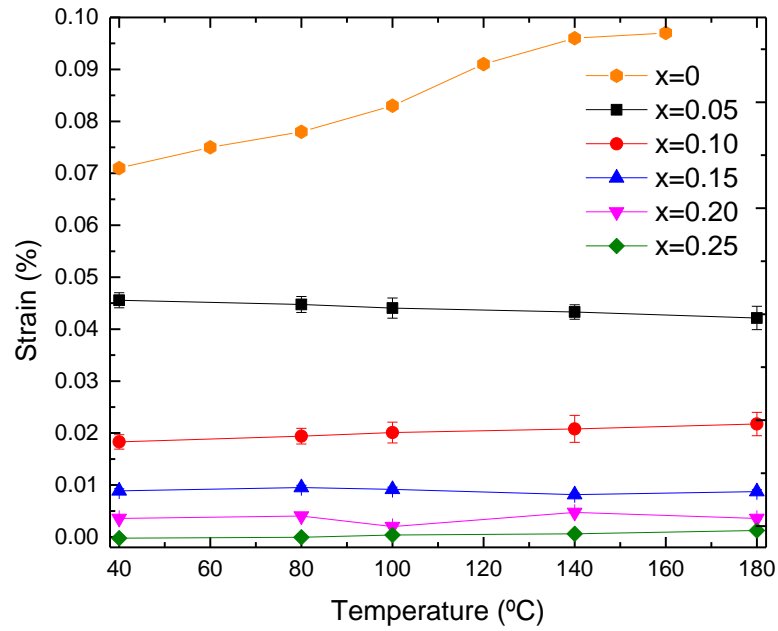


Figure 4. 32: Temperature dependence of S_{\max} for KBBNZ ($x=0.5, 0.10, 0.15, 0.20$ and 0.25) ceramics measured under electric field of 50kV/cm (1 Hz).

P_s , E_c and S_{\max} parameters for KBBNZ $x=0.05$ ceramic slightly decreases with increasing temperature. This behaviour is due to the proximity of the composition to the phase transition from orthorhombic-to-tetragonal at $\sim 200^\circ\text{C}$. Indeed, the polarisation decrease in this region is reported by theoretical calculations for KNbO_3 (Fontana, Metrat, Servoin, & Gervais, 1984). In contrast, P_s , E_c and S_{\max} values for KBBNZ $x=0.10$ ceramic increases with the temperature. Probably, this different tendency relies on the ferroelectric unsaturation of KBBNZ $x=0.10$ at 50 kV/cm . If the spontaneous polarisation values for KBBNZ $x=0.05$ and $x=0.10$ at RT under an electric field 80 kV/cm are compared with the ones at 40°C under 50kV/cm , a larger difference is noticed for $x=0.10$ ($\sim 12\ \mu\text{C/cm}^2$) than for $x=0.05$ ($\sim 4\ \mu\text{C/cm}^2$), indicating this last composition is closer to be saturated (Figure 4. 33). P_s , E_c and S_{\max} parameters for KBBNZ $x=0.15, 0.20$ and 0.25 ceramics are virtually maintained constant from RT to 180°C .

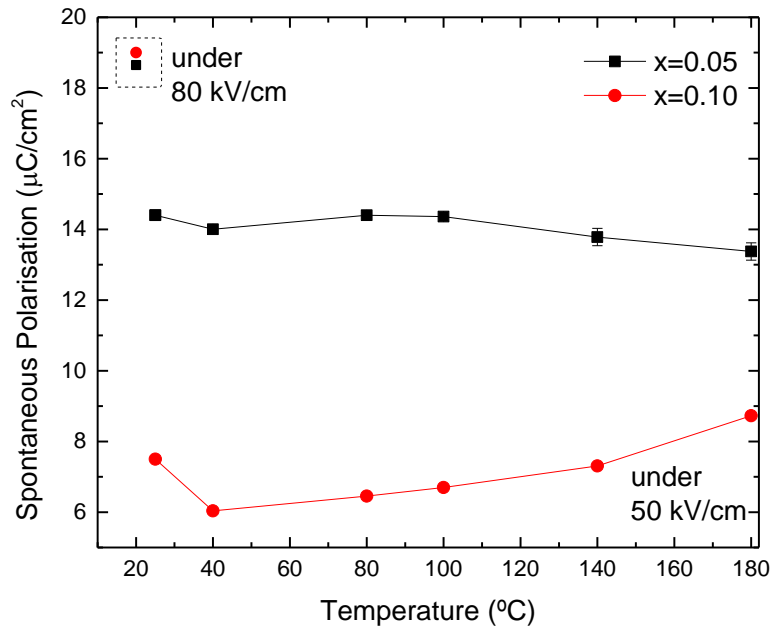


Figure 4. 33: Comparison of Ps values at RT under an electric field of 80 kV/cm with the Ps evolution increasing the temperature under an electric field of 50 kV/cm.

4.4. Optical Characterisation

4.4.1 Diffuse reflectance spectroscopy

The excitation across the band gap in KBBNZ ceramics is essentially a charge transfer from the O 2p states at the valence band maximum (VBM) to the Nb 4d states at the conduction band minimum (CBM). Some insight into the band structure and other charge transitions can be gathered from the response to photons of different energies.

Experimental optical band gaps are obtained from the extrapolation of the linear part of the curve $(F(R) \cdot hv)^n$ in the Tauc plots, where $F(R)$ is Kubelka-Munk formula, R is experimental diffuse reflectance data and n determines the nature of the band-gap, direct ($n=2$) or indirect ($n=1/2$). Diffuse reflectance (raw data) against wavenumbers is shown in Figure 4. 34. Moreover, Tauc plots for KNBN $0 \leq x \leq 0.25$ ceramics are constructed for direct (Figure 4. 35) and indirect (Figure 4. 36) band-gaps.

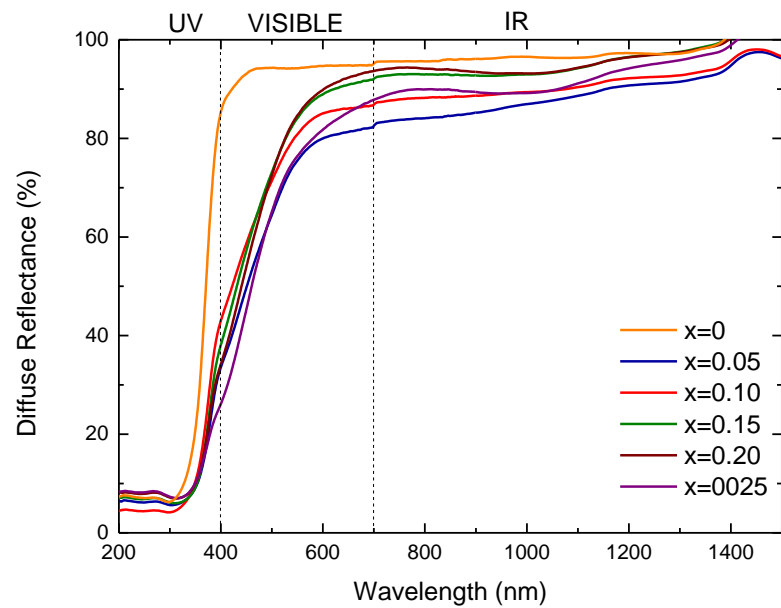


Figure 4. 34: Diffuse reflectance as a function of wavelength for KBBNZ system (raw data).

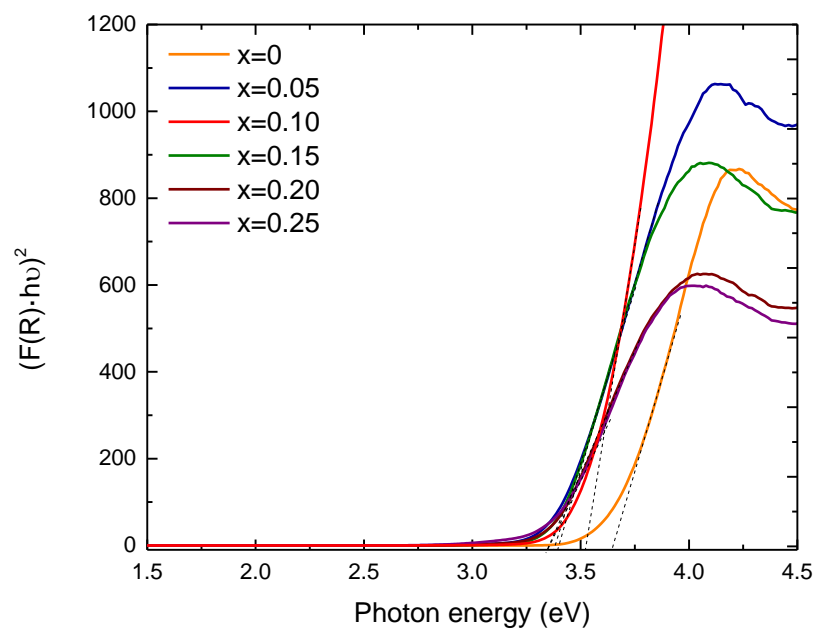


Figure 4. 35: Tauc's plot for direct band gaps for KBBNZ ceramics

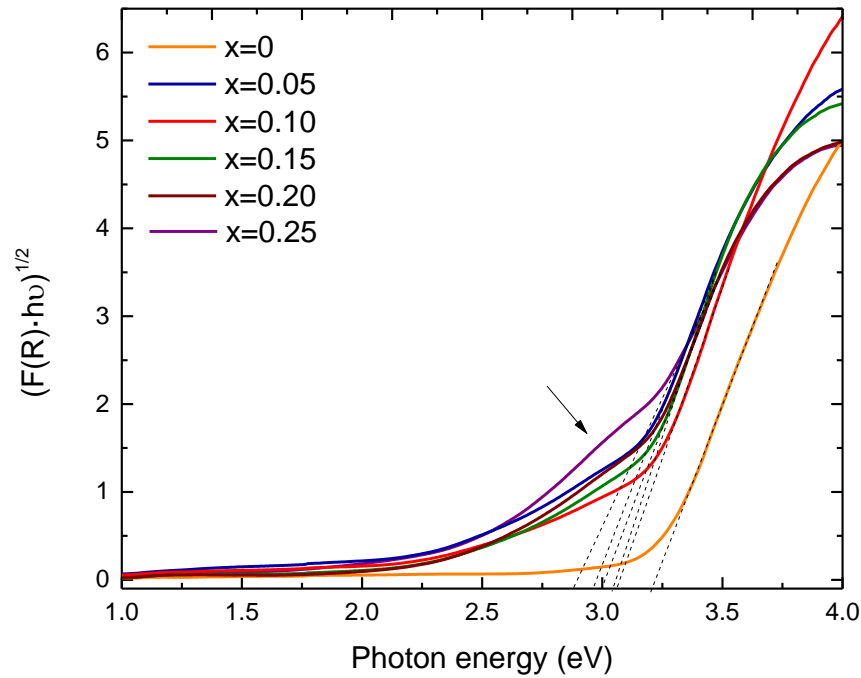


Figure 4. 36: Tauc's plot for indirect band gaps for KBBNZ ceramics.

First, reflectivity spectra for KBBNZ ceramics are very similar, all compositions mainly reflect in the region from 300 nm to 500 nm wavelength, and they do not follow any trend in respect to their compositions. Direct band-gaps narrow from 3.42 eV ($x=0$) to 3.13 eV ($x=0.25$). On the other hand, indirect band-gaps vary from 3.22 eV for $x = 0$ to 2.89 eV for $x = 0.25$, in broad agreement with the first-principles calculations (F Wang et al., 2014) and also with experimental results for KNbO_3 (Shi, Zhang, Zhou, & Chen, 2015). The emergence of Urbach tails reveals lattice disorder in the KBBNZ compositions, indicated by an arrow in Figure 4. 36. From the analysis of the Urbach tails, it is possible to obtain the information pertaining to the dynamics of the electronic transitions, and in principle to evaluate the impact of defects on those transitions. For example, the Urbach energy, E_U , for KBBNZ when $x = 0.25$ was calculated as 0.22 eV. Moreover, these band gaps are consistent with the ability of KBBNZ ceramics to withstand electric fields as high as 80 kV cm^{-1} , as previously shown in Figure 4. 25. Finally, Table 4. 8 summarises the direct and indirect band-gap values from Tauc's plots.

	$x=0$	$x=0.05$	$x=0.10$	$x=0.15$	$x=0.20$	$x=0.25$
Direct band-gaps (eV)	3.64	3.40	3.52	3.38	3.34	3.34
Indirect band-gaps (eV)	3.22	2.96	3.06	3.03	2.99	2.89

Table 4. 8: Direct and Indirect band-gaps derived from Tauc's plot.

4.5. Discussion

Spontaneous polarisation of $\sim 38 \mu\text{C}/\text{cm}^2$ and a band gap of $\sim 2.9 \text{ eV}$ were predicted by first principle calculations for $0.75\text{KNbO}_3-0.25(\text{Ba}_{0.5}\text{Bi}_{0.5})(\text{Zn}_{0.5}\text{Nb}_{0.5})\text{O}_3$ composition (F Wang et al., 2014). Motivated by this study, the $(1-x) \text{KNbO}_3-x (\text{Ba}_{0.5}\text{Bi}_{0.5})(\text{Zn}_{0.5}\text{Nb}_{0.5})\text{O}_3$ ($x=0, 0.05, 0.10, 0.15, 0.20$ and 0.25) system was prepared by solid-state reaction.

XRD patterns of sintered ceramics reveal that the simultaneous incorporation of Ba^{+2} , Bi^{+3} and Zn^{+2} into the KNbO_3 parent phase is accompanied with an increase of the unit cell volume and a change in the crystal symmetry from orthorhombic ($x=0$) to cubic ($x=0.25$)

Even if the XRD pattern for $x=0.05$ does not show the typical splitting of the peaks, still it is ascribed to orthorhombic symmetry. For $x=0.10$ and $x=0.15$, XRD patterns are interpreted as a combination of KN-based phase (space group $\text{Amm}2$) and a cubic phase (space group $\text{Pm}\bar{3}\text{m}$). In addition, a fibre-shaped K-deficient phase is detected by SEM. XRD pattern of KBBNZ $x=0.20$ is consistent with cubic symmetry. However, the presence of spontaneous polarisation ($\sim 5 \mu\text{C}/\text{cm}^2$) even in this composition suggests the presence of some residual orthorhombic ($\text{Amm}2$) phases, but at a level below the detection limit of the in-house XRD. This is consistent with the decrease of the relative intensity of the Raman mode at 192 cm^{-1} (fingerprint of the long-range polar order) in comparison with the mode 2, as illustrated in the expanded region of Figure 4. 5. The presence of this residual orthorhombic phase is also responsible for dielectric anomalies in $x=0.20$ ceramics, as shown Figure 4. 24

Finally, XRD pattern for $x=0.25$ is also attributed to cubic symmetry. Nevertheless, the presence of intense broad modes in the Raman spectrum of these samples provides ample evidence that their local crystal symmetry cannot be described by the cubic $\text{Pm}\bar{3}\text{m}$ space group. The presence of K^+ , Ba^{2+} and Bi^{3+} in the A-sites and Nb^{5+} and Zn^{2+} in the B-sites not only induces local strains due to the difference in ionic radii, but also due to the hybridization between the $6s^2$ lone-pair of electrons of Bi^{3+} with both empty $6p^0$ orbitals of Bi^{3+} and $2p^6$ electrons of O^{2-} which foreshortens the Bi-O covalent bonds. Bi^{3+} cations in perovskite compounds tend to off-center, often inducing rhombohedral distortions, thereby relieving the tensile bond strain of shorter Bi-O bonds. All the aforementioned local deformations allow for strong Raman scattering on materials, whose average crystal

structure may be described by the cubic $\text{Pm}\bar{3}\text{m}$ space group, since the ions are locally displaced away from the centre of inversion. Octahedral tilting due to smaller Bi^{3+} , which is a common distortion mechanism for reducing the A-O bond strain in perovskites, can be partially counteracted by the equivalent concentration of larger Ba^{2+} in KBBNZ ceramics. In summary, the Raman spectrum for $x=0.25$ provides a strong spectroscopic indication for the occurrence of short-range lattice deformations, which could not be resolved from the XRD data, but also rules out spontaneous polarisation in those ceramics.

The change of the crystal structure with the increase of the $(\text{Ba}_{0.5}\text{Bi}_{0.5})(\text{Zn}_{0.5}\text{Nb}_{0.5})\text{O}_3$ content into KNbO_3 generates changes on the electrical and optical properties of the materials. Gradual loss of the FE properties occurs with increasing x . This fact is suggested by monitoring the Raman peak at 192 cm^{-1} and confirmed by P-E measurements (Figure 4. 25) in combination with S-E curves (Figure 4. 27) and dielectric data (Figure 4. 19).

The strain curves evolve from a butterfly shape ($x=0$) to non-response ($x=0.25$). For intermediary compositions (0.15 and 0.20), S-E responses show almost parabolic shapes, as shown in Figure 4. 28 and Figure 4. 29. Their maximum strain values drop to 0.021% and 0.009% and the electrostriction coefficients for $x=0.20$ and $x=0.25$ are estimated, $0.037\text{ m}^4\text{C}^{-2}$ and $0.035\text{ m}^4\text{C}^{-2}$, respectively. These values are even larger than the well-known electrostrictive material $\text{Pb}(\text{Mg}_{1/3}\text{Nb}_{2/3})\text{O}_3$ (PMN) having Q of $0.024\text{ m}^4\text{C}^{-2}$ (Kuwata, Uchino, & Nomura, 1980) with a maximum strain of 0.12% at 40 kV cm^{-1} . However, the value of strain of $x = 0.05$ is comparatively low. Electrostriction in Pb-free materials has been investigated in recent years (Bai, Li, Wang, Shen, & Zhai, 2015; Feifei Wang, Jin, Yao, & Shi, 2013; Zhang, Yan, Yang, & Cao, 2010; Zuo et al., 2016). Q values ranging from 0.021 to $0.027\text{ m}^4\text{C}^{-2}$ were reported in $\text{Bi}_{0.5}\text{Na}_{0.5}\text{TiO}_3$ - BaTiO_3 - $\text{K}_{0.5}\text{N}_{0.5}\text{NbO}_3$ ceramics (Zhang et al., 2009). More recently, Pb-free ferroelectric ceramics have been reported to exhibit giant electrostrictive coefficients as large as $0.05\text{ m}^4\text{C}^{-2}$ (Jin et al., 2016). A piezoelectric-to-electrostrictive crossover is also unveiled. The normal-to-relaxor ferroelectric crossover in Pb-free ceramics is now well documented, and it has been recently reviewed by Shvartsman & Lupascu in 2012. Interestingly, heterovalent substitution in $\text{K}_{0.5}\text{Na}_{0.5}\text{NbO}_3$ (KNN), which is isostructural with KN, induces quenched random fields due to the local charge imbalance and the local elastic fields. These fields hinder long-range ordering thus leading to polar nanometric-size regions, often referred

to as PNRs. The degree of transformation into relaxor behaviour varies between different systems, as observed for KNN-SrTiO₃ (Guo, Kakimoto, & Ohsato, 2004) and KNN-BiScO₃ (Du et al., 2008).

Indirect band-gaps for the KBBNZ system narrow from 3.22 eV for $x = 0$ to 2.89 eV for $x = 0.25$, in broad agreement with the first-principles calculations.

Crystal chemistry arguments can be recalled to explain the moderate band gap narrowing as follows: (i) the replacement of Nb⁵⁺ by Zn²⁺ creates underbonded O²⁻ ions adjacent to the Zn²⁺, which form ZnO₆ octahedra, (ii) Bi³⁺ ions which tend to be off-center, create short, strong Bi–O (covalent) bonds that partially compensate for the aforementioned loss of B–O bonding and (iii) Ba²⁺ ions are not off-center and are less prone to compensate the decrease of B–O bonding. As a result, the repulsion between the non-bonding O charge densities and Zn 3d states is relatively weak, leading to a moderate upshift of valence band maxima (VBM), which is composed of O 2p and Zn 3d states. It is worth noting that the observed Raman shift of the broad A₁(TO₁), Figure 4. 6. may be a manifestation of the strong Bi–O bonds, whereas the general broadening of Raman modes results from an increased lattice disorder, which manifests itself by the emergence of Urbach tails, as shown in Figure 4. 36.

In summary, a combination of competition between covalent and ionic bonds and a distribution of effective cation radii in the KNbO₃-Ba_{0.5}Bi_{0.5}Nb_{0.5}Zn_{0.5}O₃ system leads simultaneously to a piezoelectric-to-electrostrictive crossover and a modest narrowing of the optical band gaps.

4.6. Conclusions

Dense KBBNZ ($0 \leq x \leq 0.25$) ceramics were prepared by the solid-state reaction method. XRD data show the average crystal structure to evolve from orthorhombic at $x=0$ to pseudocubic at $x=0.25$. Raman spectroscopy suggests the absence of polar order for $x \geq 0.25$ ceramics. SEM and EDX analyses revealed second phases fiber shaped with K-deficiency. Moreover, low solutes concentrations have more difficulties in achieving the chemical homogenisation, especially Zn⁺². From a point of view of electric characterisation, continuous decrease of spontaneous polarisation and strain with

increasing x is observed. Electromechanical characterisation reveals a piezoelectric-to-electrostrictive crossover. An electrostriction coefficient of $0.037 \text{ m}^4\text{C}^{-2}$ and $0.035 \text{ m}^4\text{C}^{-2}$ were measured for KBBNZ $x=0.15$ and $x=0.20$, respectively.

4.7. References

- Bai, W., Li, L., Wang, W., Shen, B., & Zhai, J. (2015). Phase diagram and electrostrictive effect in BNT-based ceramics. *Solid State Communications*, 206, 22–25. <https://doi.org/http://dx.doi.org/10.1016/j.ssc.2015.01.004>
- Du, H., Zhou, W., Luo, F., Zhu, D., Qu, S., Li, Y., & Pei, Z. (2008). Design and electrical properties' investigation of $(\text{K}_{0.5}\text{Na}_{0.5})\text{NbO}_3\text{--BiMeO}_3$ lead-free piezoelectric ceramics. *Journal of Applied Physics*, 104(3), 34104. <https://doi.org/10.1063/1.2964100>
- Fontana, M., Metrat, G., Servoin, J., & Gervais, F. (1984). Infrared spectroscopy in KNbO_3 through the successive ferroelectric phase transitions. *Journal of Physics C: Solid State Physics*, 16, 483–514. <https://doi.org/10.1088/0022-3719/17/3/020>
- Guo, Y., Kakimoto, K., & Ohsato, H. (2004). Dielectric and piezoelectric properties of lead-free $(\text{Na}_{0.5}\text{K}_{0.5})\text{NbO}_3\text{--SrTiO}_3$ ceramics. *Solid State Communications*, 129(5), 279–284. <https://doi.org/http://dx.doi.org/10.1016/j.ssc.2003.10.026>
- Jin, L., Huo, R., Guo, R., Li, F., Wang, D., Tian, Y., ... Liu, G. (2016). Diffuse Phase Transitions and Giant Electrostrictive Coefficients in Lead-Free Fe^{3+} -Doped $0.5\text{Ba}(\text{Zr}_{0.2}\text{Ti}_{0.8})\text{O}_3\text{--}0.5(\text{Ba}_{0.7}\text{Ca}_{0.3})\text{TiO}_3$ Ferroelectric Ceramics. *ACS Applied Materials & Interfaces*, 8(45), 31109–31119. <https://doi.org/10.1021/acsami.6b08879>
- Kuwata, J., Uchino, K., & Nomura, S. (1980). Electrostrictive coefficients of $\text{Pb}(\text{Mg}_{1/3}\text{Nb}_{2/3})\text{O}_3$ ceramics. *Japanese Journal of Applied Physics* 19(11), 2099–2103. Retrieved from <http://jjap.jsap.jp/link?JJAP/19/2099/>
- Luisman, L., Feteira, A., & Reichmann, K. (2011). Weak-relaxor behaviour in Bi/Yb-doped KNbO_3 ceramics. *Applied Physics Letters*, 99(19). <https://doi.org/10.1063/1.3660255>

- Shi, H. F., Zhang, C. L., Zhou, C. P., & Chen, G. Q. (2015). Conversion of CO_2 into renewable fuel over Pt-g- $\text{C}_3\text{N}_4/\text{KNbO}_3$ composite photocatalyst. *Rsc Advances*, 5(113), 93615–93622. <https://doi.org/10.1039/c5ra16870h>
- Shvartsman, V. V., & Lupascu, D. C. (2012). Lead-Free Relaxor Ferroelectrics. *Journal of the American Ceramic Society*, 95(1), 1–26. <https://doi.org/10.1111/j.1551-2916.2011.04952.x>
- Wang, F., Grinberg, I., & Rappe, A. M. (2014). Semiconducting ferroelectric photovoltaics through Zn^{2+} doping into KNbO_3 and polarization rotation. *Physical Review B - Condensed Matter and Materials Physics*, 89(23).
- Wang, F., Jin, C., Yao, Q., & Shi, W. (2013). Large electrostrictive effect in ternary $\text{Bi}_{0.5}\text{Na}_{0.5}\text{TiO}_3$ -based solid solutions. *Journal of Applied Physics*, 114(2), 27004. <https://doi.org/10.1063/1.4811812>
- Zhang, S.-T., Kouna, A. B., Jo, W., Jamin, C., Seifert, K., Granzow, T., Damjanovic, D. (2009). High-Strain Lead-free Antiferroelectric Electrostrictors. *Advanced Materials*, 21(46), 4716–4720. <https://doi.org/10.1002/adma.200901516>
- Zhang, S.-T., Yan, F., Yang, B., & Cao, W. (2010). Phase diagram and electrostrictive properties of $\text{Bi}_{0.5}\text{Na}_{0.5}\text{TiO}_3\text{-BaTiO}_3\text{-K}_{0.5}\text{Na}_{0.5}\text{NbO}_3$ ceramics. *Applied Physics Letters*, 97(12), 122901. <https://doi.org/10.1063/1.3491839>
- Zuo, R., Qi, H., Fu, J., Li, J., Shi, M., & Xu, Y. (2016). Giant electrostrictive effects of $\text{NaNbO}_3\text{-BaTiO}_3$ lead-free relaxor ferroelectrics. *Applied Physics Letters*, 108(23), 232904. <https://doi.org/10.1063/1.4953457>

Chapter 5

System (1-x) KNbO₃- x BiFeO₃

5.1. Introduction

5.2. Structural and chemical characterisation

5.2.1. Purity and X-ray powder diffraction

5.2.2. Raman spectroscopy

5.2.3. SEM

5.2.4. EDX

5.3. Electrical Characterisation

5.3.1. Dielectric Characterisation

5.4. Optical Characterisation

5.4.1 Diffuse reflectance spectroscopy

5.5. Preparation of thin film

5.5.1. Pulsed laser deposition

5.5.2. Photovoltaic cell

5.5. Discussion

5.6. Conclusions

5.7. References

5. System (1-x) $\text{KNbO}_3\text{-x BiFeO}_3$

5.1. Introduction

In the first part of this chapter, the crystal structure, dielectric characteristics and band-gap of compositions in (1-x) $\text{KNbO}_3\text{-x BiFeO}_3$ (KNBF) ($0 \leq x \leq 0.25$) system are investigated using XRD combined with Raman spectroscopy, capacitance measurements and diffuse reflectance ultraviolet and visible (DRUV-vis) spectroscopy. This system has been previously studied with the aim of finding new Pb-free FE and multiferroic materials. Structural phase transitions and electrical characterisation are mostly reported for high concentration of x in KNBF system (J. H. Choi, Kim, Hong, Chae, & Cheon, 2012; Dash, Choudhary, Das, & Kumar, 2014; Lennox et al., 2015; Nakashima, Shimura, Sakamoto, & Yogo, 2007; Teslenko et al., 2017). Fe^{3+} substitution for higher-valence Nb^{5+} may give rise to increased repulsion between the O 2p and Fe 3d states and thereby to a higher VBM, whereas Bi^{3+} substituting for K^+ inhibits the formation of oxygen vacancies. KNBF $x=0.25$ retains ferroelectricity and decreases its band-gap around 1 eV in comparison with KN.

The second part of the chapter explores the best conditions to deposit this composition by PLD. Moreover, the photo-response of KNBF $x=0.25$ was measured.

BiFeO_3 is probably the most widely studied multiferroic material, due to the observation of ferroelectric ($T_c \sim 800^\circ\text{C}$) and antiferromagnetic ($T_N \sim 635\text{ K}$) ordering at room temperature (Catalan & Scott, 2009). As mentioned in Chapter 1, BiFeO_3 exhibits an optical band-gap of $\sim 2.2\text{ eV}$ (Gao et al., 2006).

To our knowledge, there is no literature about the band-gap measurements of this system. However, band-gap tunability has been studied on other solid-solutions based on BiFeO_3 , such as $(1-x)\text{BiFeO}_3\text{-}x\text{SrTiO}_3$, where FE properties are improved compared with BiFeO_3 (Wu, Yao, Yang, & Zhang, 2017), and $(1-x)\text{Bi}_{0.5}\text{K}_{0.5}\text{TiO}_3\text{-}x\text{BiFeO}_3$ (Tuan et al., 2017) with a considerable band-gap narrowing, from 3.22 eV down to 1.39 eV.

5.2. Structural and chemical characterisation

5.2.1. Purity and X-ray powder diffraction

KNBF ceramics were fabricated as described in Chapter 2 using the following precursor powders, K_2CO_3 , Nb_2O_5 , Bi_2O_3 and Fe_2O_3 . After mixing 24 hours and sieve, powders were calcined twice in air at 850 °C for 4 hours with heating rate of 3 °C/min. XRD data of KNBF ($0 \leq x \leq 0.25$) calcined powders are shown in Figure 5. 1.

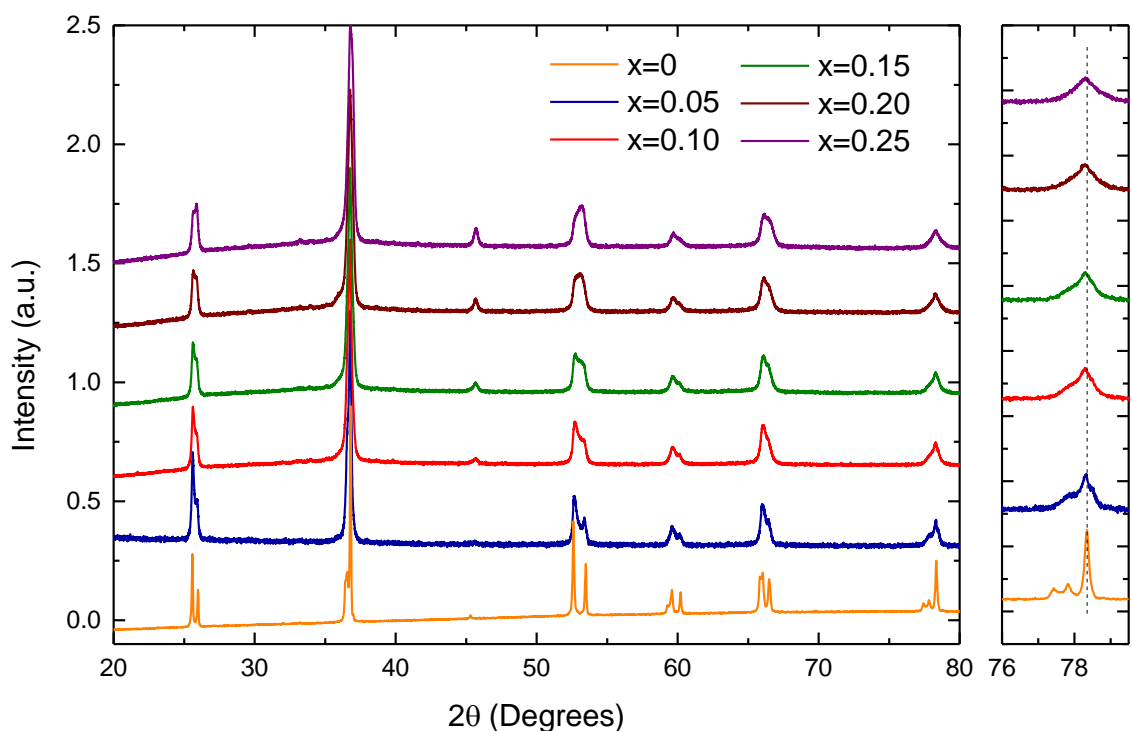


Figure 5. 1: Room-temperature XRD data of KNBF powders after double calcination at 850°C.

As described in Chapter 3, XRD patterns for KN calcined powder exhibit well defined sharp peaks, which can be attributed to an orthorhombic structure. In contrast, the rest of

the compositions present broader peaks than pure KN, which hinders the assignment of the corresponding crystal symmetry. Some reflections in the patterns of doped compositions are coincident with those of undoped KN, suggesting the coexistence of virtually undoped KN with doped-KN. No other secondary phases are detected. This chemical inhomogeneity appears to vanish upon sintering, as shown below.

Compacted powders into pellets were fired at 1085°C for 4 hours with a heating rate of 3°C/min. Figure 5. 2. shows XRD data for KNBF ceramics at room temperature.

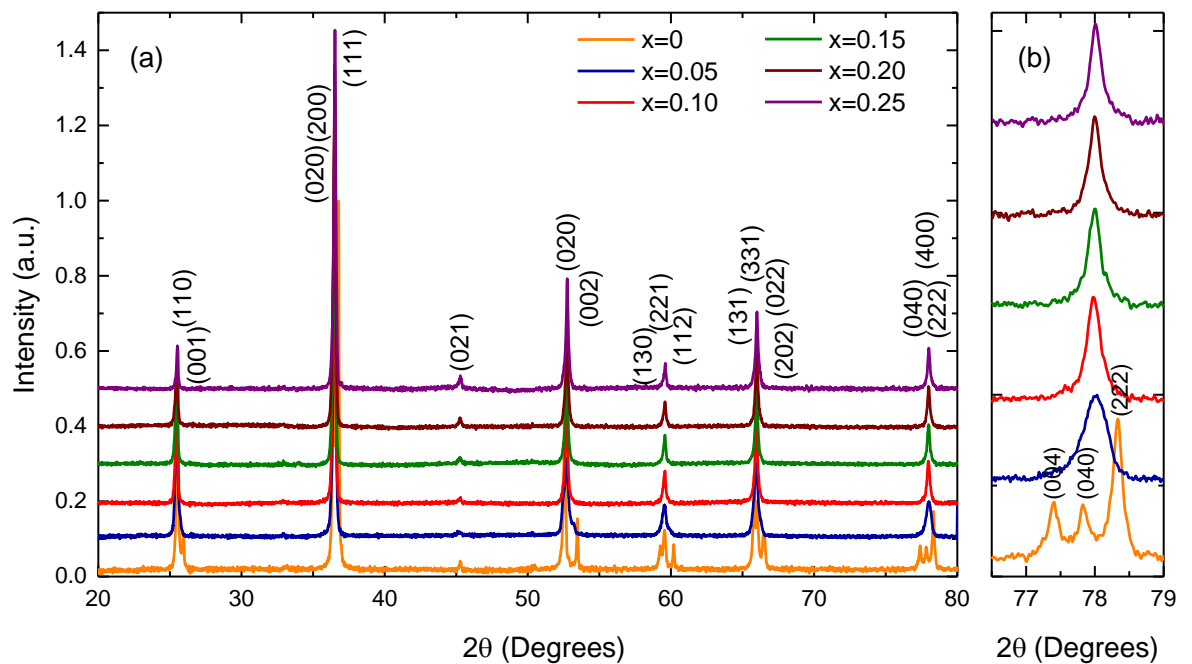


Figure 5. 2.: Room-temperature XRD data of KNBF ceramics after sintering at 1085°C.

Within the detection limits of the technique, all ceramics are single-phase. KN exhibits typical peak splitting expected for a perovskite with orthorhombic crystal symmetry (space group $\text{Amm}2$), but within the resolution of our measurements only single peaks are visible for doped ceramics. Indeed, the triplet for KN became a single peak for the other compositions, as shown in Figure 5. 2. Reflections shift slightly but almost systematically towards higher 2θ angles with increasing x , indicating that the co-solubility of $\text{Bi}^{+3}/\text{Fe}^{+3}$ and KNbO_3 is accompanied by a decrease of the unit cell volume. XRD patterns were refined by the Rietveld method. Lattice parameters, theoretical and experimental densities are reposted in Table 5. 1 and Table 5. 2.

	x=0	x=0.05	x=0.10
Space Group	Amm2	Amm2	Amm2
Density (Experimental) (g/cm³)	4.35(3)	4.43(4)	4.6(1)
Density (calculated) (g/cm³)	4.6273(1)	4.8093(4)	4.9871(4)
Relative Density (%)	94(1)	92(1)	92(2)
a (Å)	3.9711(1)	3.9987(2)	4.0013(2)
b (Å)	5.6909(1)	5.6668(3)	5.6640(3)
c (Å)	5.7158(1)	5.6871(3)	5.6786(3)
V/10⁶ (pm³)	64.576(2)	64.434(6)	64.348(6)
R_{exp}	1.26460	1.43385	1.41668
R_p	2.97912	2.19462	2.21614
R_{wp}	4.65175	3.64457	3.42608
GOF	13.53086	6.46074	5.84859

Table 5. 1: Experimental and theoretical density, lattice parameters and agreement indices calculated by Rietveld Refinement for KNBF (x=0, 0.05 and 0.10).

	x=0.15	x=0.2	x=0.25
Space Group	Amm2	Amm2	Amm2
Density (Experimental) (g/cm³)	4.6 (2)	4.7(4)	4.9(3)
Density (calculated) (g/cm³)	5.1597 (5)	5.3288(5)	5.4971(7)
Relative Density (%)	90(4)	89(4)	90(6)
a (Å)	4.0014(2)	4.0030(2)	4.0031(1)
b (Å)	5.6612(4)	5.6618(4)	5.6618(1)
c (Å)	5.6799(3)	5.6795(4)	5.6825(5)
V/10⁶ (pm³)	64.333(7)	64.361(5)	64.397(8)
R_{exp}	1.39445	1.39349	1.45637
R_p	2.40295	2.31442	2.60597
R_{wp}	3.77848	3.43919	3.98020
GOF	7.34224	6.09119	7.46907

Table 5. 2: Experimental and theoretical density, lattice parameters and agreement indices calculated by Rietveld Refinement for KNBF (x=0.15, 0.20 and 0.25).

For x=0.05, 0.10 and 0.15, relative densities exceed 90% comparing with theoretical density, and for x=0.20 and 0.25, they are somewhat below 90%. All compositions are acceptably refined into orthorhombic phase (symmetry group Amm2). Figure 5. 3 shows the compositional evolution of the unit cell volume and lattice parameters for KNBF ceramics calculated by Rietveld refinement.

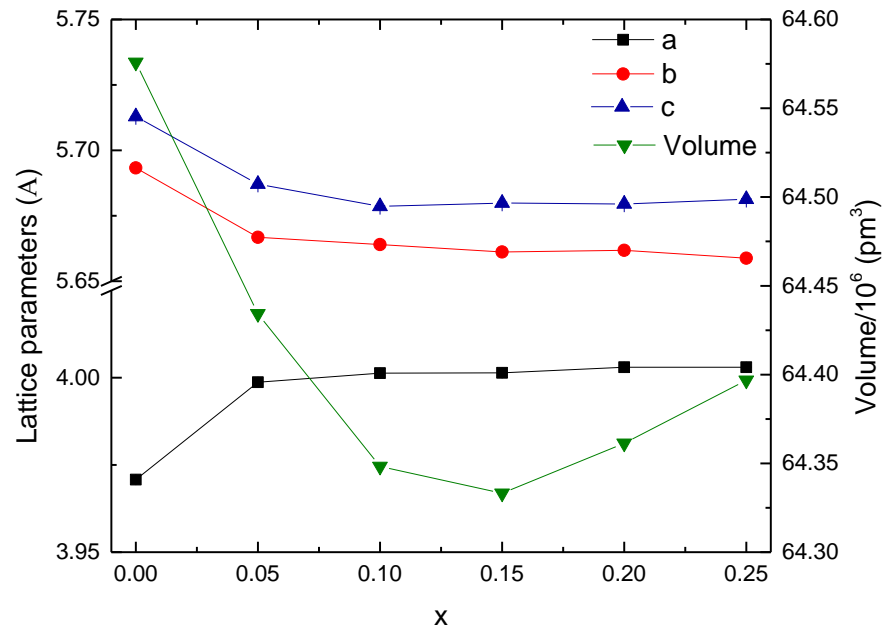


Figure 5. 3: Evolution of the unit cell volume and lattice parameters with x for $(1-x)\text{KNbO}_3\text{-}x\text{BiFeO}_3$ ($0 \leq x \leq 0.25$) ceramics.

From $x=0$ to $x=0.15$, b and c lattice parameters decrease while a parameter increases, resulting in a smaller unit cell volume than KN. Then, from $x=0.15$ to 0.25 , the unit cell volume increases slightly. However, a , b and c lattice parameters practically remain constant between $x=0.05$ and $x=0.25$, indicating variations of the unit cell volume values are very small.

5.2.2. Raman spectroscopy

Room-temperature Raman spectra for KNBF ($0 \leq x \leq 0.25$) powders calcined at 850°C twice for 4 hours using heating rate of $3^\circ\text{C}/\text{min}$ are shown in Figure 5. 4. The typical spectral features exhibited by the ferroelectric KN orthorhombic polymorph (described in Chapter 3) are also visible in the Raman spectra of all doped powders. Raman modes became broader and slightly shift towards lower wavenumbers ($\sim 20\text{ cm}^{-1}$) with increasing Bi^{+3} and Fe^{+3} contents. Room-temperature Raman spectra for KNBF ($0 \leq x \leq 0.25$) sintered ceramics at 1085°C for 4 hours using heating rate of $3^\circ\text{C}/\text{min}$ are shown in Figure 5. 5.

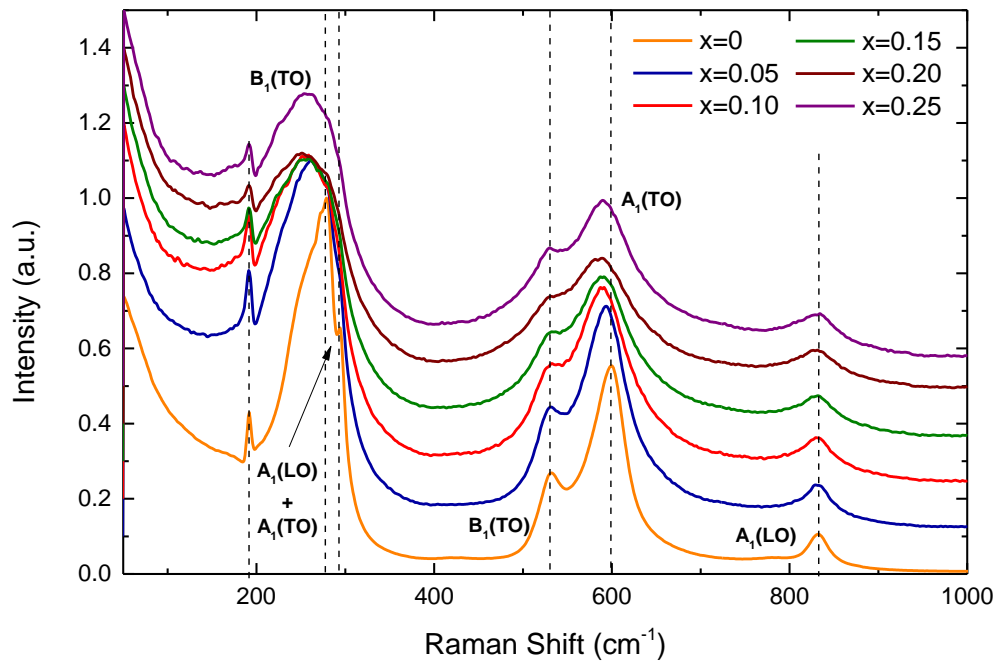


Figure 5. 4: Room-temperature Raman spectra for KNBF ($0 \leq x \leq 0.25$) calcined powders at 850°C two times.

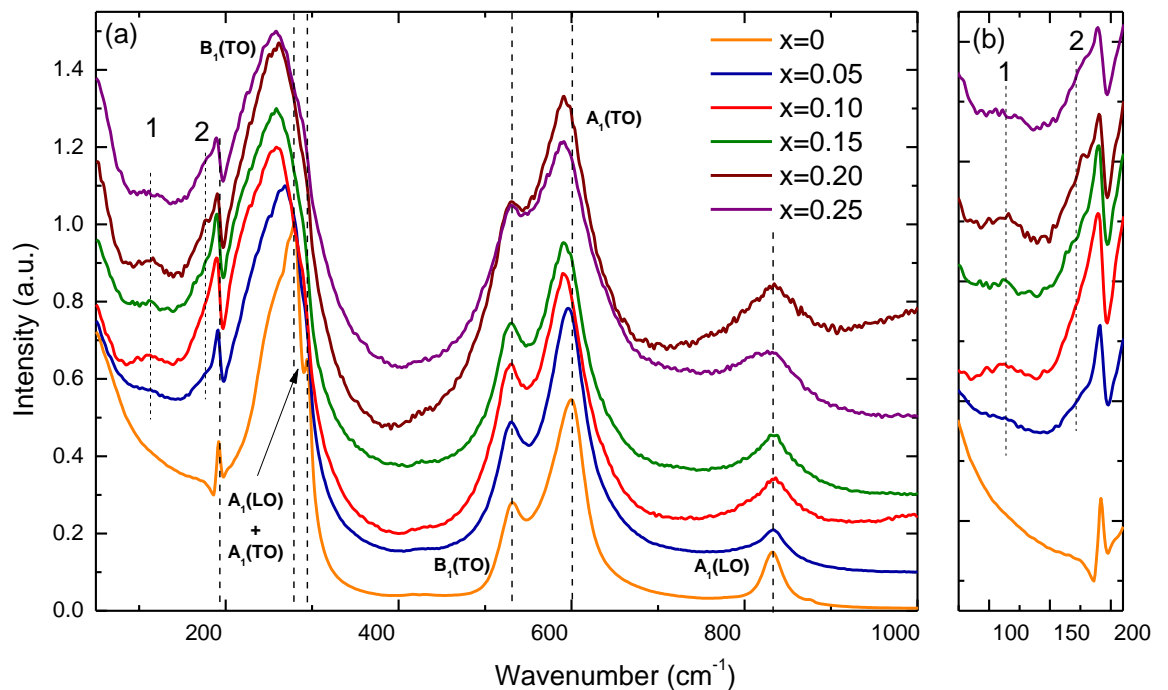


Figure 5. 5: Room-temperature Raman spectra for KNBF ($0 \leq x \leq 0.25$) ceramics sintered at 1085°C . New modes (1 and 2) emerge in KNBF ($x \geq 0.05$) pellets spectra. Attached graph: monitoring of mixed sharp mode at 192 cm^{-1} .

The average orthorhombic crystal symmetry for the doped compositions is also corroborated by the Raman spectroscopy data. The typical spectral features for undoped KN are still visible in the Raman spectra of all doped ceramics. This spectral similarity is

sufficient to simultaneously ascertain the orthorhombic crystal symmetry and the occurrence of long-range polar order in the doped materials.

Upon doping new modes emerge in the low frequency regime. They are labelled as 1 and 2 and their origin is unclear. The new mode 1 is relatively broad and appears $\sim 110\text{ cm}^{-1}$, whereas mode 2 appears as a shoulder to the sharp mixed mode at 192 cm^{-1} . Relative intensity of mode 2 appears to increase with increasing x . In Chapter 4, these modes have been associated to A-O vibrations, in particular to nm-sized clusters rich in either Bi^{3+} or K^+ cations. Finally, the $\text{A}_1(\text{LO})$ mode at 831 cm^{-1} appears to become broader with increasing BiFeO_3 content. This broadening may be associated with the emergence of new modes too, also perceived in KBBNZ system, due to breathing of the octahedra, when occupied by different B cations. The general broadening of the Raman modes from the doped ceramics (that results from increased lattice disorder) and the shift towards lower wavenumbers are shown for the most intense peaks in Figure 5. 6.

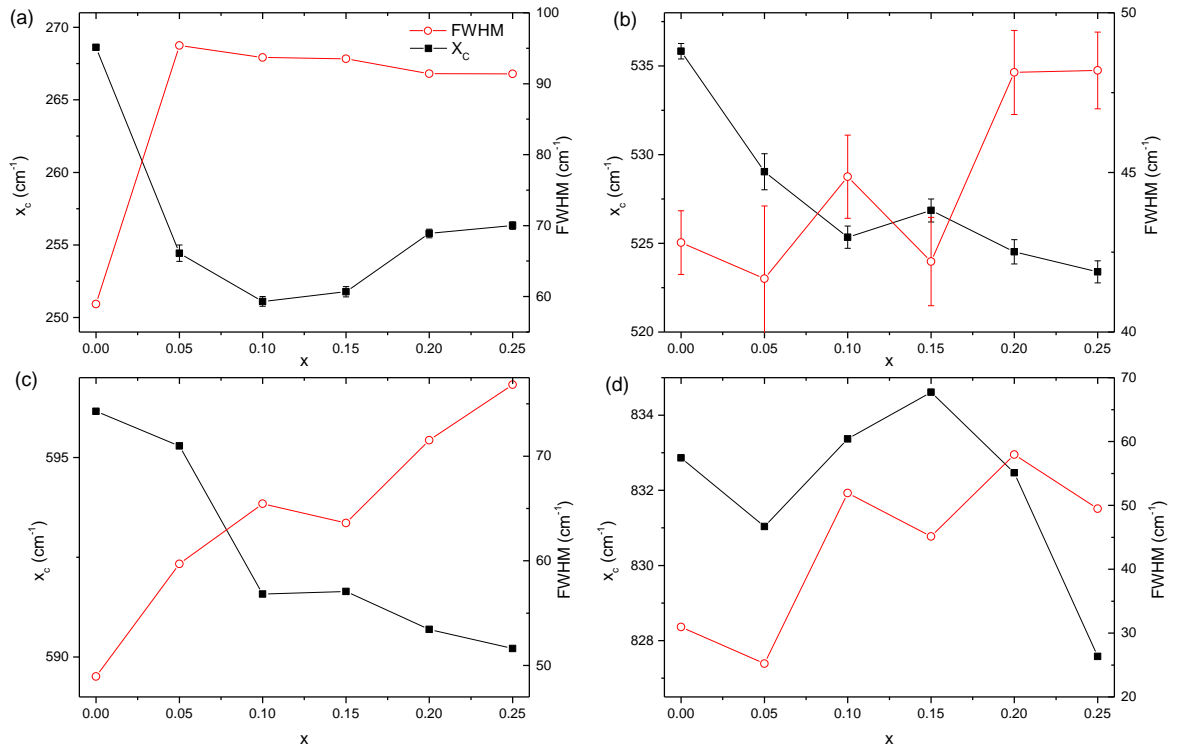


Figure 5. 6: Compositional evolution of the position, X_c , and the width, FWHM, of main Raman modes for doped compositions, (a) $\text{B}_1(\text{TO})$ at $\sim 270\text{ cm}^{-1}$, (b) $\text{B}_1(\text{TO})$ at $\sim 530\text{ cm}^{-1}$, (c) $\text{A}_1(\text{TO})$ at $\sim 600\text{ cm}^{-1}$ and (d) $\text{A}_1(\text{LO})$ at $\sim 830\text{ cm}^{-1}$.

The presence of a sharp mode at 192 cm^{-1} suggests the occurrence of long-range polar order in all compositions studied. *In-situ* Raman spectroscopy analyses were carried out

in the $-80\text{ }^\circ\text{C}$ to $200\text{ }^\circ\text{C}$ temperature range. Dependence of Raman spectra with temperature for KNBF $x=0.05$ and $x=0.20$ are illustrated in Figure 5. 7 and Figure 5. 8.

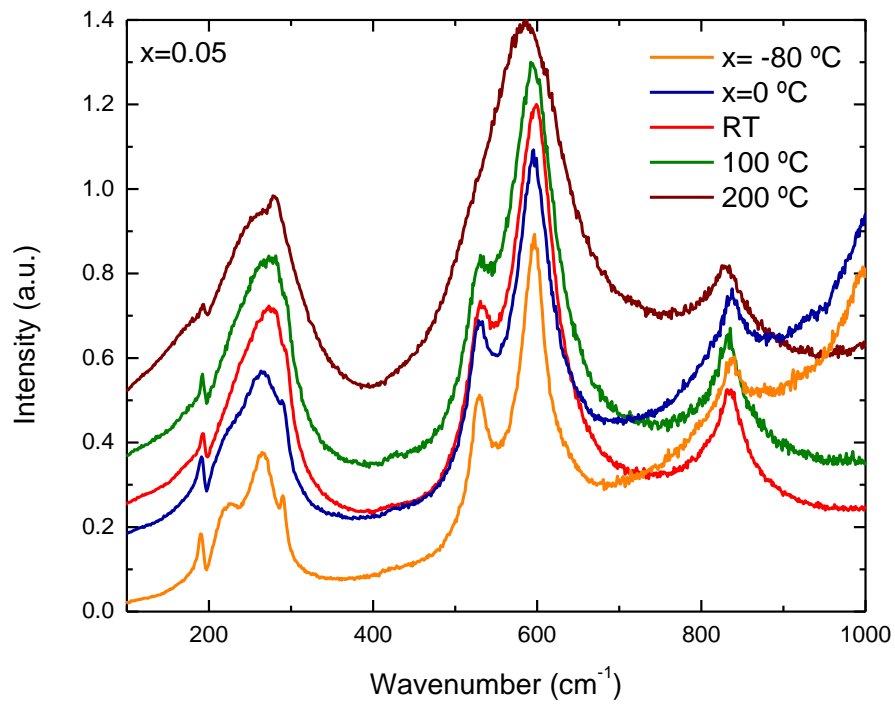


Figure 5. 7: Raman spectra evolution from $-80\text{ }^\circ\text{C}$ to $200\text{ }^\circ\text{C}$ for KNBF $x=0.05$ ceramic.

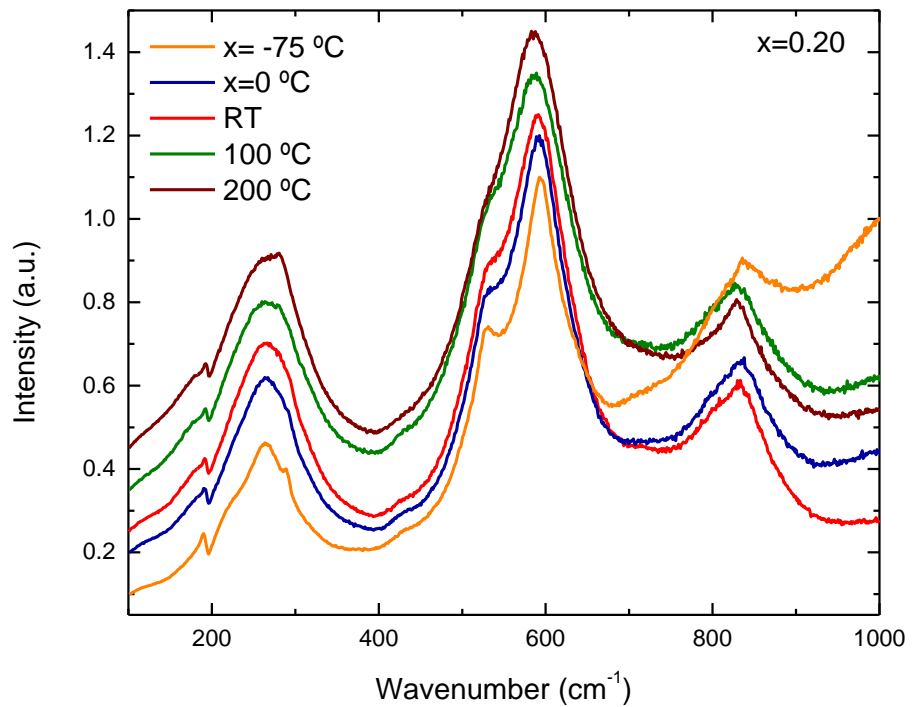


Figure 5. 8: Raman spectra evolution from $-75\text{ }^\circ\text{C}$ to $200\text{ }^\circ\text{C}$ for KNBF $x=0.20$ ceramic.

Both compositions show rhombohedral-to-orthorhombic and orthorhombic-to-tetragonal transitions in the temperature range between -100°C and 200°C . The phase identification was carried out comparing the temperature evolution for KN Raman spectrum, described in Chapter 3; therefore, a detailed discussion of the modes assignment is not given here.

In order to assert the presence of long-range polar order over a wide temperature range, Raman spectra for KN, $x=0.05$ and 0.20 are compared at three different temperatures (-100°C , 25°C and 200°C) in Figure 5. 9. The spectra collected at -100°C show in the $150\text{-}300\text{ cm}^{-1}$ region the spectral signature typical for the ferroelectric rhombohedral polymorph (Figure 5. 9 (c)). On heating, to 25°C , the low frequency region becomes consistent with the ferroelectric orthorhombic polymorph, as shown in Figure 5. 9. (b). Finally, at 200°C , the phase transition to tetragonal phase (as will be determined by dielectric properties, section 5.3.1), that can be monitored by the appearance of a Raman mode at 270 cm^{-1} , indicated with an arrow in Figure 5. 9. (a). Splitting between $B_1(\text{TO})$ and $A_1(\text{TO})$ modes in the medium frequency range becomes less evident as x increases, all compositions however, still show the features of long-range polar order. Therefore, all ceramics are polar in a wide temperature range.

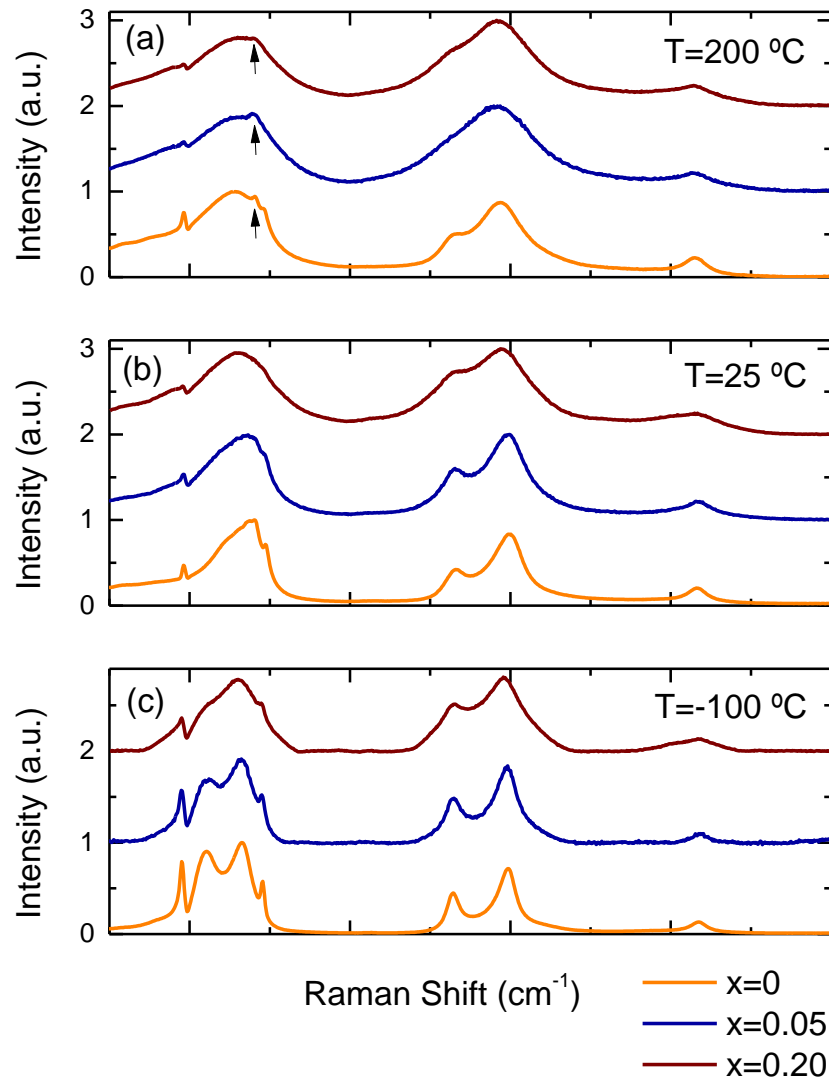


Figure 5. 9.: *In-situ* Raman KNbF, $x=0$, $x=0.05$ and $x=0.20$ ceramics. Bose-Einstein factor applied to data.

5.2.3. SEM

SEM images of polished surfaces of KNbF ($x=0$, 0.05, 0.10, 0.15, 0.20 and 0.25) ceramics are shown in Figure 5. 10. (a-f). Large grains having average grain diameter of $\sim 3\mu\text{m}$ are observed for pure KN (Figure 5. 10. (a)). Upon doping, grain growth is inhibited, showing grain size falls below $1\mu\text{m}$. The non-appearance of porosity confirms highly dense ceramics (Table 5. 1).

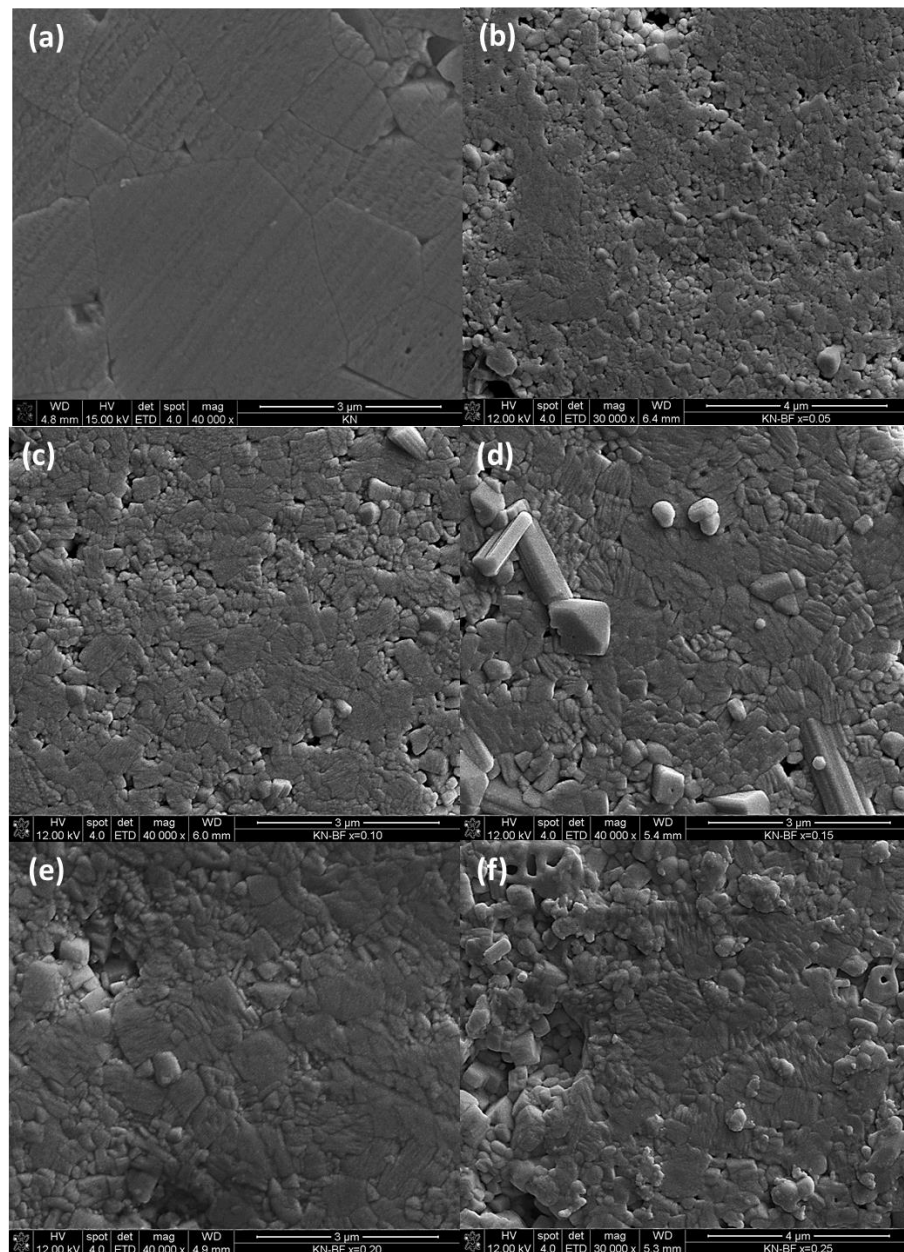


Figure 5. 10.: Microstructure evolution for $(1-x)\text{KNbO}_3\text{-}x\text{BiFeO}_3$ (KNBF) ceramics for $x=0$ (a), $x=0.05$ (b), $x=0.10$ (c), $x=0.15$ (d), $x=0.20$ (e) to $x=0.25$ (f).

5.2.4. EDX

Compositional analyses of KNBF ($x=0, 0.05, 0.10, 0.15, 0.20$ and 0.25) ceramics were performed by EDX spectroscopy, which enables us to study how efficient is the incorporation of $\text{Bi}^{+3}/\text{Fe}^{+3}$ into the KN lattice. Table 5. 3, Table 5. 4 and Table 5. 5 report the experimental and theoretical relations of K/Nb, K/Bi and K/Fe and relative errors, for $x=0.05, x=0.10$ and $x=0.15$.

x=0.05			
	Theoretical	Experimental	Relative error (%)
K/Nb	1	1.1(1)	10
K/Bi	19	17(4)	11
K/Fe	19	29(10)	53

Table 5. 3.: Experimental (average) and theoretical K/Nb, K/Bi and K/Fe ratios for 0.95 KNbO_3 – 0.05 BiFeO_3 ceramic sintered at 1085°C

x=0.10			
	Theoretical	Experimental	Relative error (%)
K/Nb	1	1.0(1)	0
K/Bi	9	11(3)	22
K/Fe	9	17(4)	90

Table 5. 4: Experimental (average) and theoretical K/Nb, K/Bi and K/Fe ratios for 0.90 KNbO_3 – 0.10 BiFeO_3 ceramic sintered at 1085°C

x=0.15			
	Theoretical	Experimental	Relative error (%)
K/Nb	1	1.0(1)	0
K/Bi	~5.67	6(2)	6
K/Fe	~5.67	8(3)	41

Table 5. 5.: Experimental (average) and theoretical K/Nb, K/Bi and K/Fe ratios for 0.85 KNbO_3 – 0.15 BiFeO_3 ceramic sintered at 1085°C.

$x=0.05$, $x=0.10$ and $x=0.15$ compositions exhibit K/Nb ratios close to unity. Molar K/Bi ratio is similar to the intended stoichiometry. In contrast, K/Fe differ from the theoretical value, indicating low concentration of the solutes Fe^{3+} . Evidence of the appearance of a common secondary phase exists, ~0.70 KNbO_3 -0.30 BiFeO_3 , are shown in Figure 5. 11. (a) for $\text{KNBF } x=0.05$, Figure 5. 11. (b) for $x=0.10$ and Figure 5. 11. (c) for $x=0.15$.

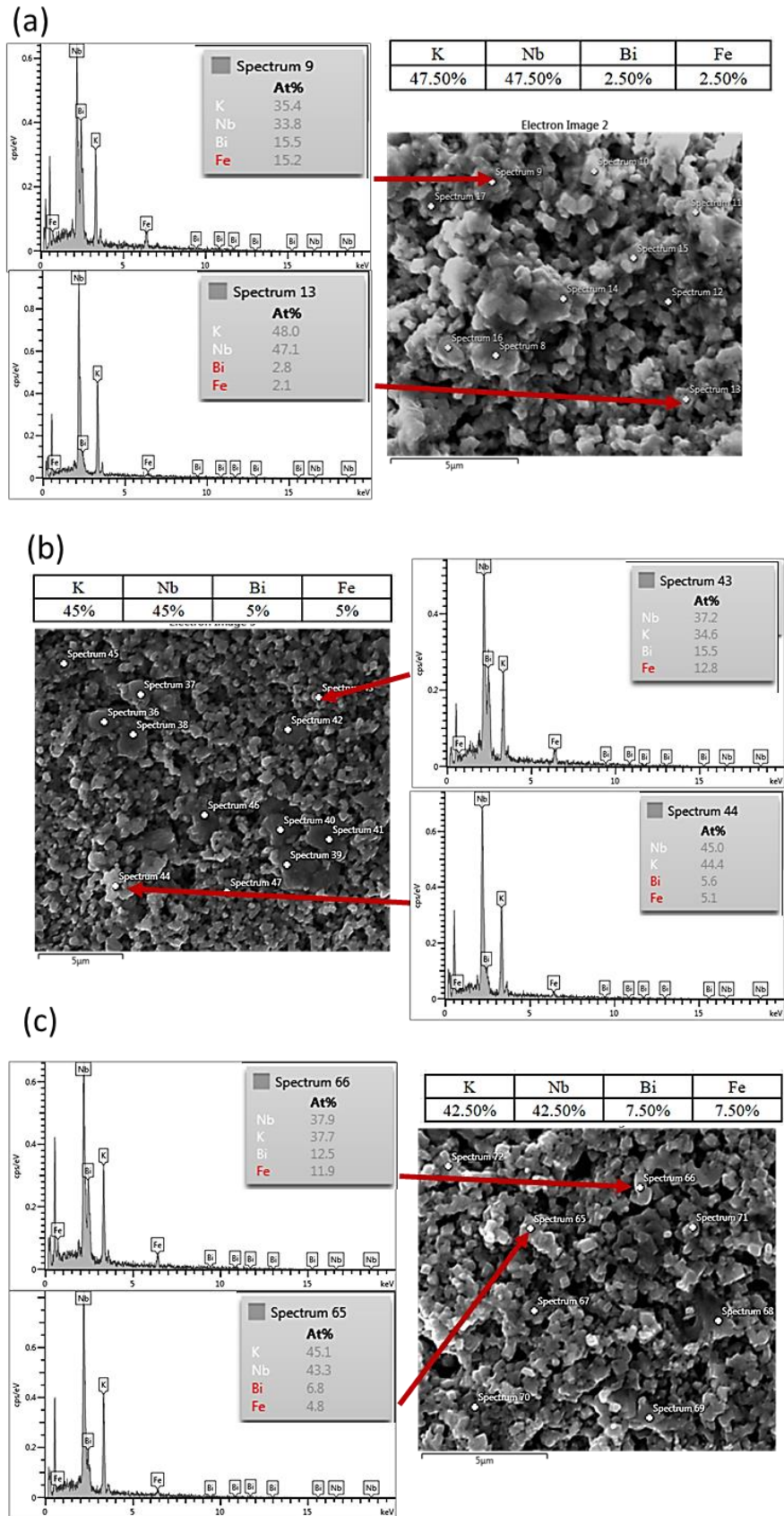


Figure 5. 11.: SEM image and EDX spectra of unpolished ceramics for (a) $x=0.05$, (b) $x=0.10$ and (c) $x=0.15$.

On the other hand, Table 5. 6 and Table 5.7 inform about experimental and theoretical K/Nb, K/Bi and K/Fe ratios and relative errors, for $x=0.20$ and $x=0.25$.

x=0.20			
	Theoretical	Experimental	Relative error (%)
K/Nb	1	1.1(2)	10
K/Bi	4	5(2)	25
K/Fe	4	6(3)	50

Table 5. 6.: Experimental (average) and theoretical K/Nb, K/Bi and K/Fe ratios for $0.80 \text{KNbO}_3 - 0.20 \text{BiFeO}_3$ ceramic sintered at 1085°C .

x=0.25			
	Theoretical	Experimental	Relative error (%)
K/Nb	1	1.0(1)	0
K/Bi	3	2.5(9)	15
K/Fe	3	3(1)	0

Table 5. 7.: Experimental (average) and theoretical K/Nb, K/Bi and K/Fe ratios for $0.75 \text{KNbO}_3 - 0.25 \text{BiFeO}_3$ ceramic sintered at 1085°C .

The indicated experimental molar ratios for K/Nb, K/Bi and K/Fe closely approximate to theoretical values. For $x=0.20$ and $x=0.25$, the intended solid-solutions seems to be easily formed than for $x=0.05$, $x=0.10$ and $x=0.15$. Nevertheless, a minor quantity of $0.5 \text{KNbO}_3\text{-}0.5 \text{BiFeO}_3$ secondary phase is detected on both compositions, as shown in Figure 5. 12. (a) and (b).

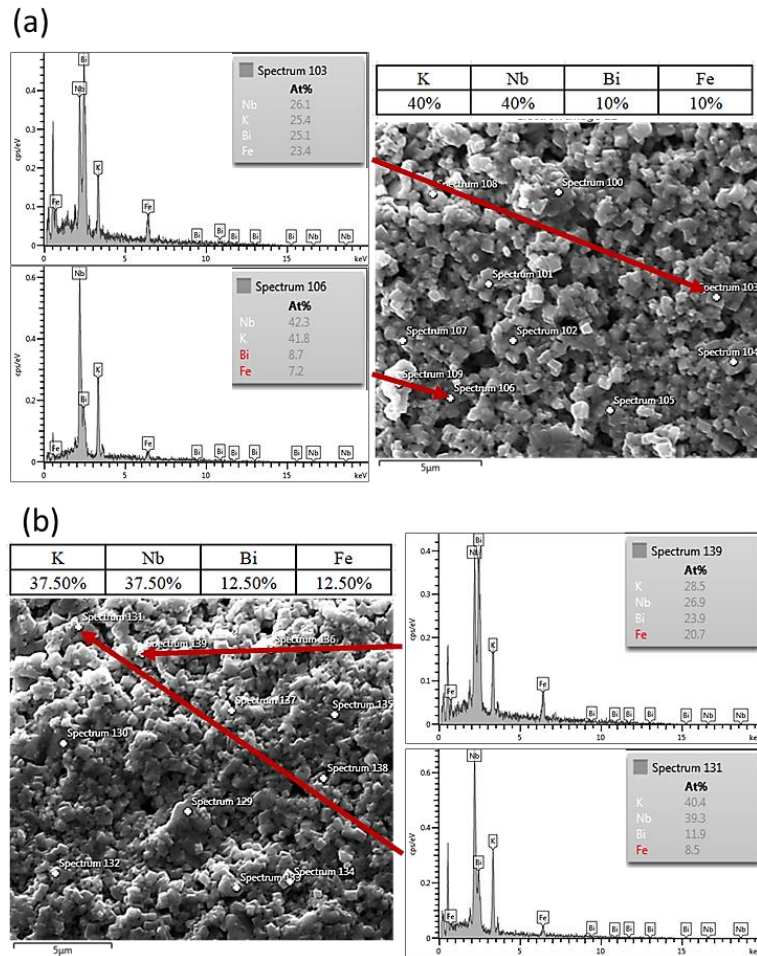


Figure 5. 12.: SEM image and EDX spectra of unpolished ceramics for (a) $x=0.20$ and (b) $x=0.25$.

EDX mapping detected the Bi/Fe-rich regions that were mentioned before for KNbF $x=0.05$ (Figure 5. 13). Despite these inhomogeneities, chemical distribution seems to be more homogeneous than for other systems studied in this thesis, for low concentration of x . EDX mapping on KNbF $x=0.25$ ceramic (Figure 5. 14) reveal more homogeneous distribution of the species, K, Nb, Bi and Fe, than $x=0.05$. Also, rich-K/Nb and rich-Bi/Fe regions are detected but only in traces, which is in agreement with what was described previously.

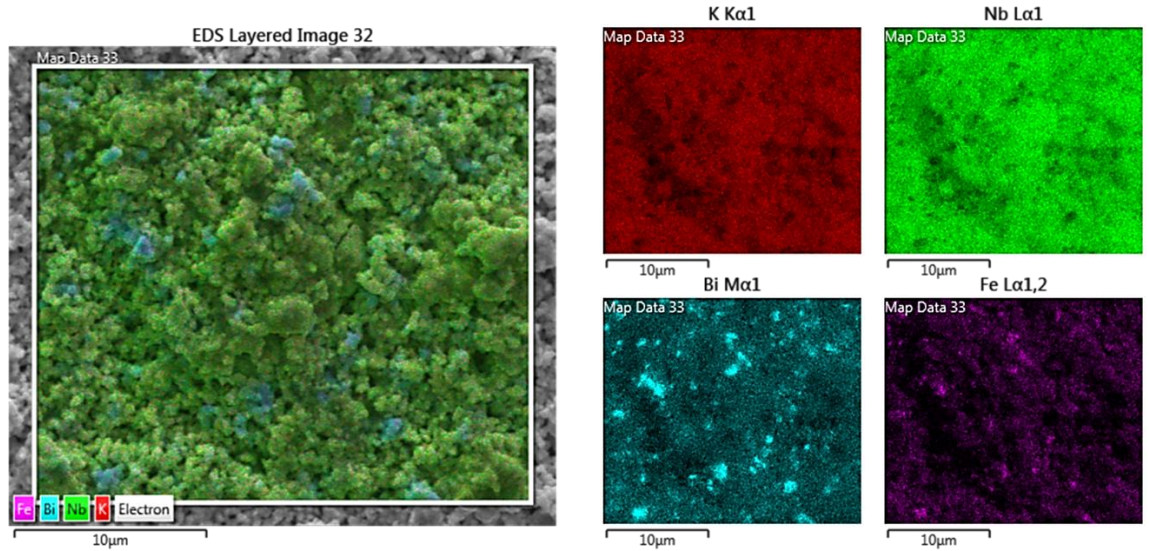


Figure 5. 13: SEM image of the examined region and EDX mapping of K, Nb, Bi and Fe for KNBF $x=0.05$.

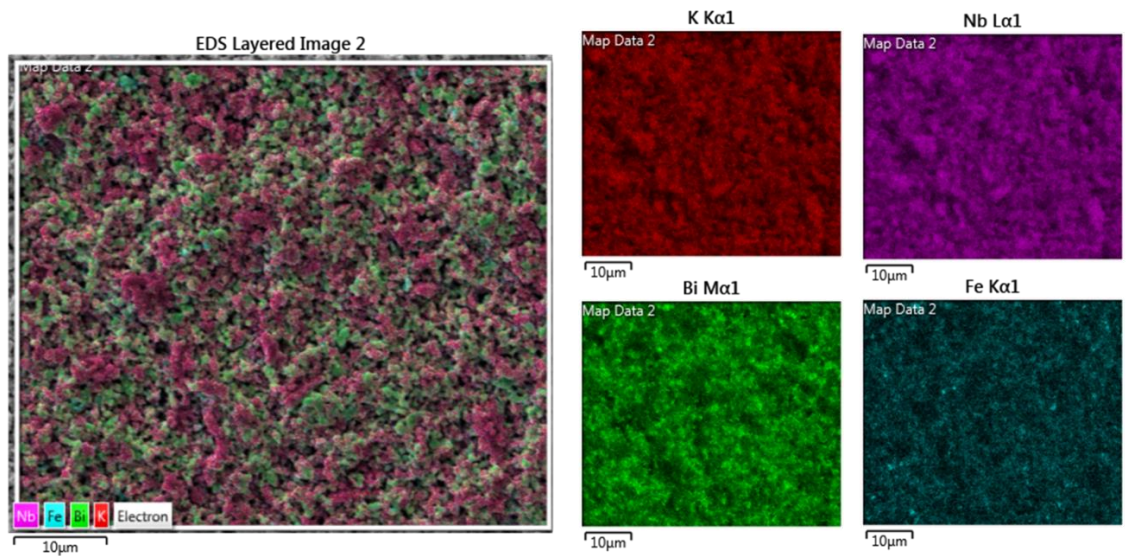


Figure 5. 14: SEM image of the examined region and EDX mapping of K, Nb, Bi and Fe for KNBF $x=0.25$.

5.3. Electrical Characterisation

5.3.1. Dielectric Characterisation

Frequency dependence of relative permittivity, ϵ_r (10kHz, 100 kHz, 250 kHz and 1 MHz) and dielectric loss are provided for individual compositions, shown in Figure 5. 15-19.

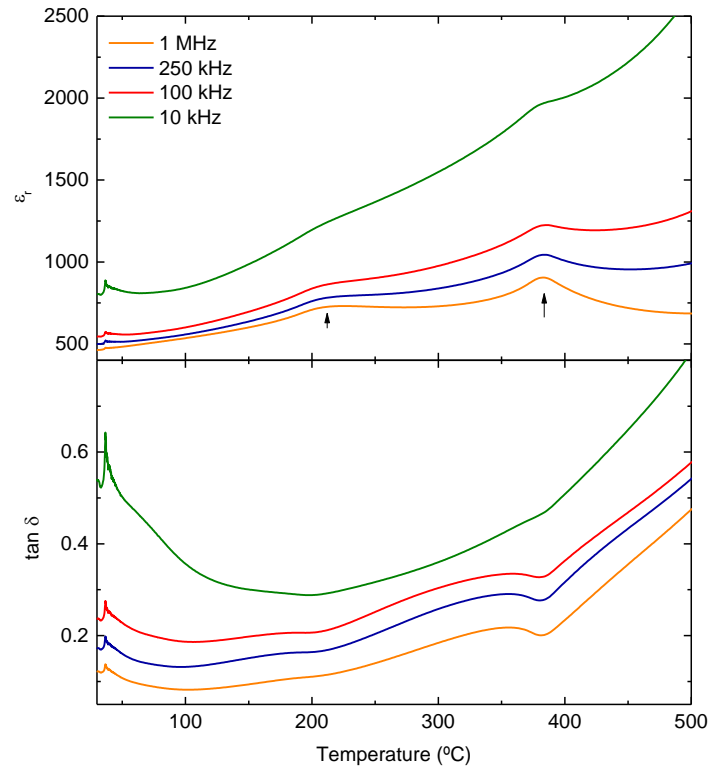


Figure 5. 15.: Temperature dependence of ϵ_r and $\tan\delta$ for $0.95 \text{ KNbO}_3\text{-}0.05 \text{ BiFeO}_3$ solid ceramics at 10 kHz, 100 kHz, 250 and 1 MHz during cooling.

For $x=0.05$ (Figure 5. 15) two dielectric anomalies are observed at $\sim 220^\circ\text{C}$ and $\sim 390^\circ\text{C}$. The temperatures for the ϵ_r anomalies are constant, but its magnitude decreases with increasing frequency. It is worth to mention, dielectric measurements for $x=0.10$ (Figure 5. 16.), $x=0.15$ (Figure 5. 17.) and $x=0.20$ (Figure 5. 18.) are strongly affected by the conductivity of the samples, making it difficult to describe the dielectric anomalies, especially for low frequency values. Dielectric losses, $\tan\delta$, for these compositions are two orders of magnitude higher than in undoped KN, KNBF $x=0.05$ and KNBF $x=0.25$ ceramics.

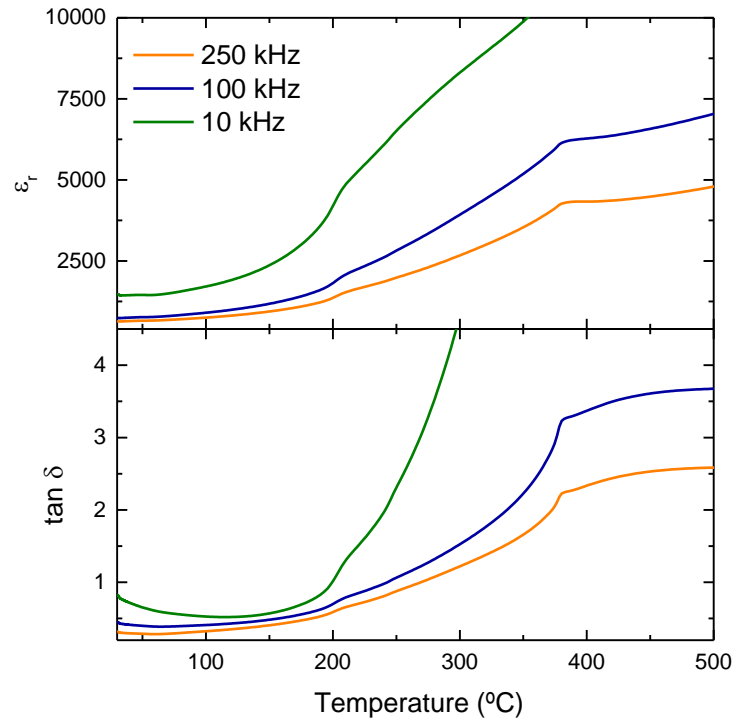


Figure 5. 16.: Temperature dependence of ϵ_r and $\tan\delta$ for 0.90 $\text{KNbO}_3\text{-0.10 BiFeO}_3$ solid solution at 10 kHz, 100 kHz and 250 kHz during cooling.

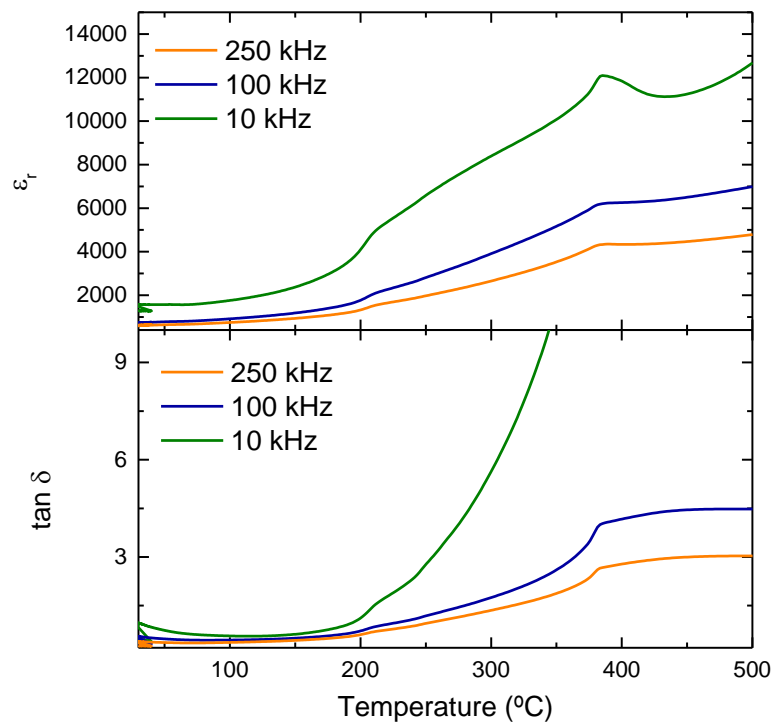


Figure 5. 17.: Temperature dependence of ϵ_r and $\tan\delta$ for 0.85 $\text{KNbO}_3\text{-0.15 BiFeO}_3$ solid solution at 10 kHz, 100 kHz and 250 kHz during cooling.

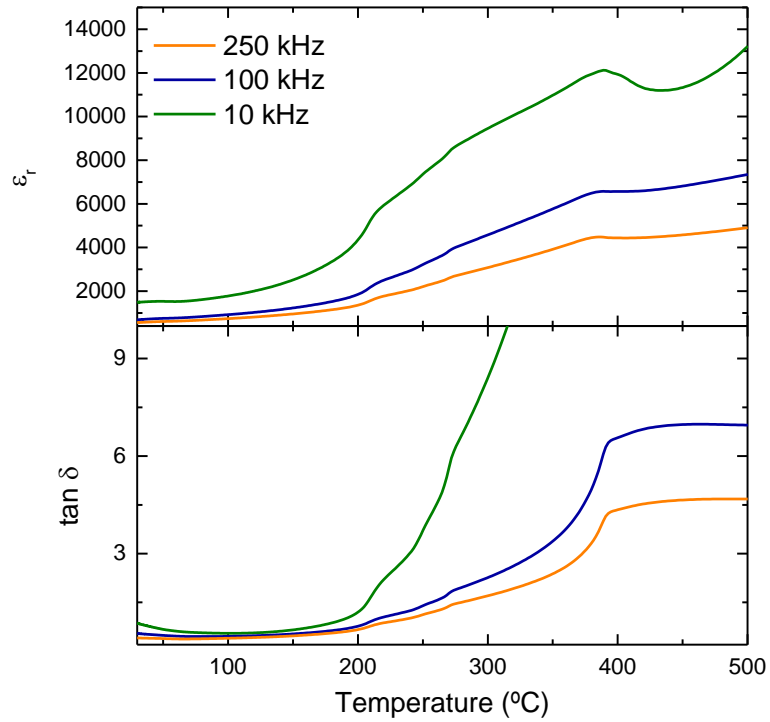


Figure 5. 18.: Temperature dependence of ϵ_r and $\tan\delta$ for 0.80 $\text{KNbO}_3\text{-0.20 BiFeO}_3$ solid solution at 10 kHz, 100 kHz and 250 kHz during cooling.

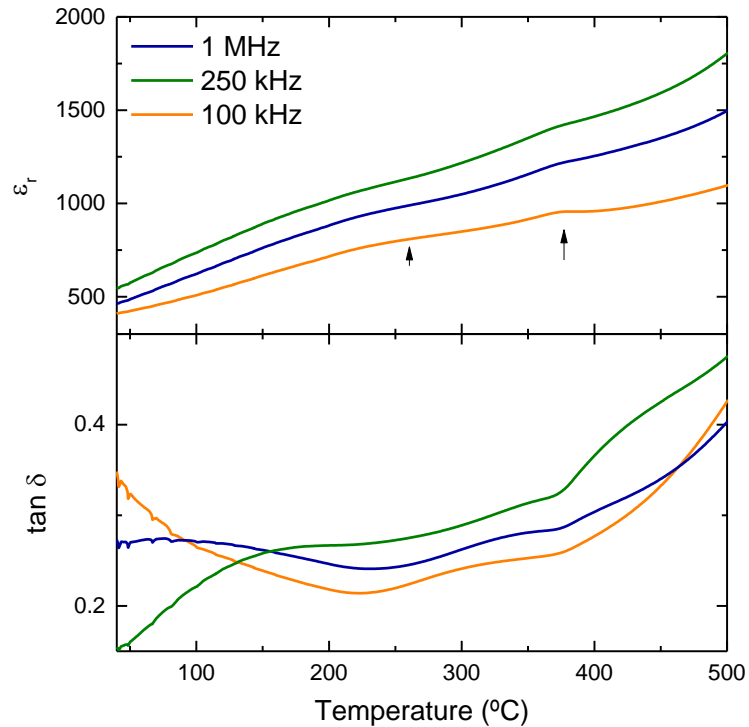


Figure 5. 19.: Temperature dependence of ϵ_r and $\tan\delta$ for 0.75 $\text{KNbO}_3\text{-0.25 BiFeO}_3$ solid solution at 10, 100 kHz, 250 kHz and 1 MHz during cooling.

Dielectric anomalies are still visible for $x=0.25$, at $\sim 220^\circ\text{C}$ and $\sim 390^\circ\text{C}$ and the dielectric losses are in the same order as in KNBF $x=0.05$ ceramic.

The temperature dependence of the relative permittivity for KNBF ($x=0, 0.05$ and 0.25) ceramics measured at 100 kHz is compared in Figure 5. 20.

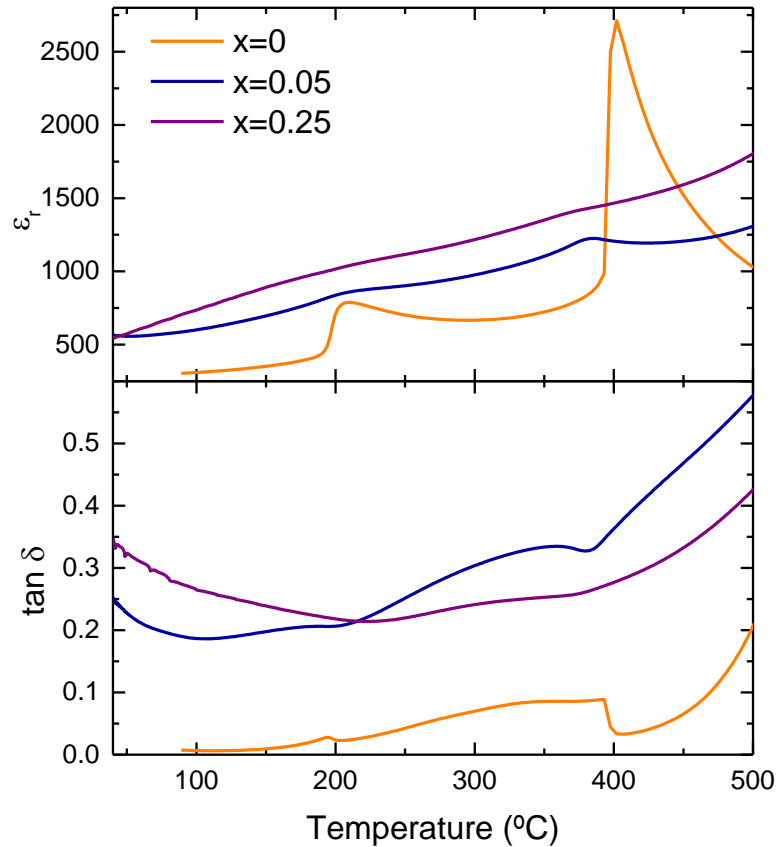


Figure 5. 20.: Temperature dependence of ϵ_r for KNBF, $x=0$, $x=0.05$ and $x=0.25$ ceramics at 100 kHz.

As described in Chapter 3, KN shows two clear dielectric anomalies at ϵ_r at $\sim 205^\circ\text{C}$ and $\sim 400^\circ\text{C}$, can be ascribed to the orthorhombic-to-tetragonal and to tetragonal-to-cubic and structural phase transitions. $x=0.25$ ceramics show the highest apparent relative permittivity over the entire temperature range considered, but this may be a consequence of the fact that it has the lowest band gap, as will be discussed later. KN exhibits lower dielectric losses than $x=0.05$ and $x=0.25$ which have similar leaky behaviour.

5.3.2. Ferroelectric Characterisation

Polarization, P , vs electric field, E , measurements are considered an inconclusive proof for determining ferroelectricity, because of the conductive nature of the samples. Figure 5. 21. shows the P - E ferroelectric hysteresis loops at RT for KN and KNBF $x=0.05$. The shape of the hysteresis loop for the pure KN ceramic indicates a normal ferroelectric behaviour (Figure 5. 21. (a)). In contrast, a lossy capacitor hysteresis loop is clearly observed for KNBF $x=0.05$ (Figure 5. 21. (b)).

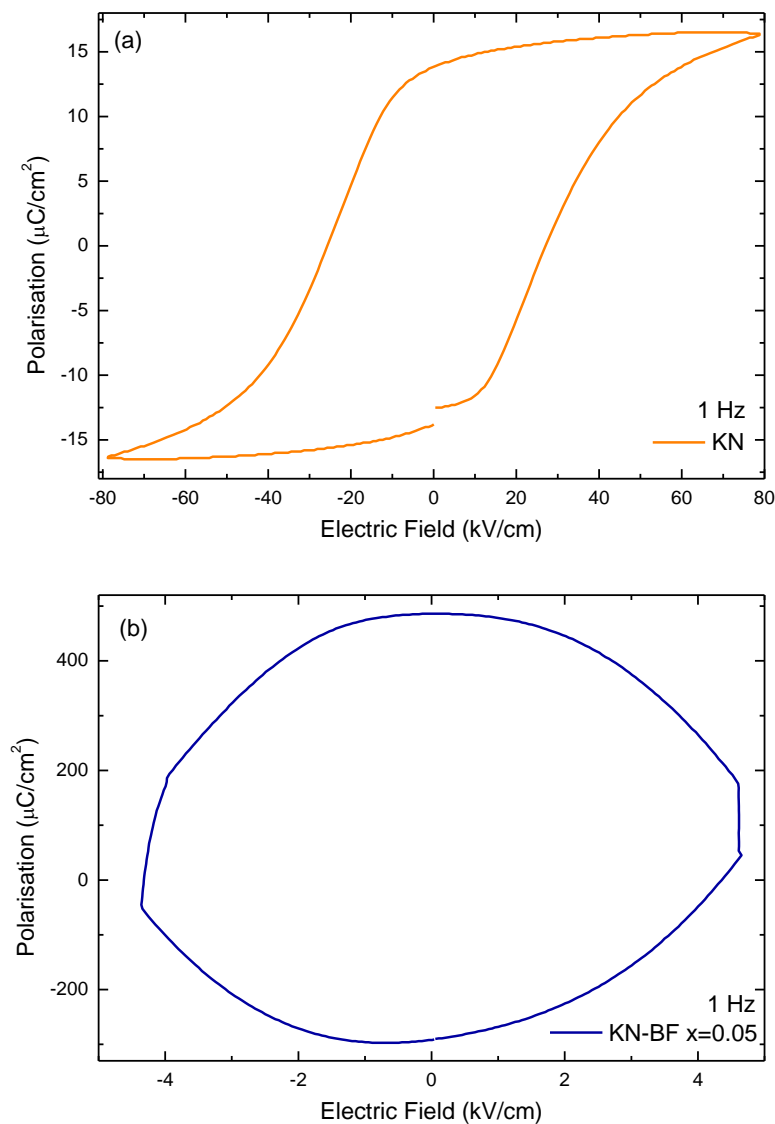


Figure 5. 21.: P - E measurements for (a) KN and (b) KNBF $x=0.05$ at room temperature.

P-E measurements for $\text{KNbO}_3\text{-BiFeO}_3$ $x=0.05$ were performed at very low field from 0.2 kV/cm to 3 kV/cm, revealing ‘lemon’ shaped loops, which confirms the leaky nature of the sample (Figure 5. 22.).

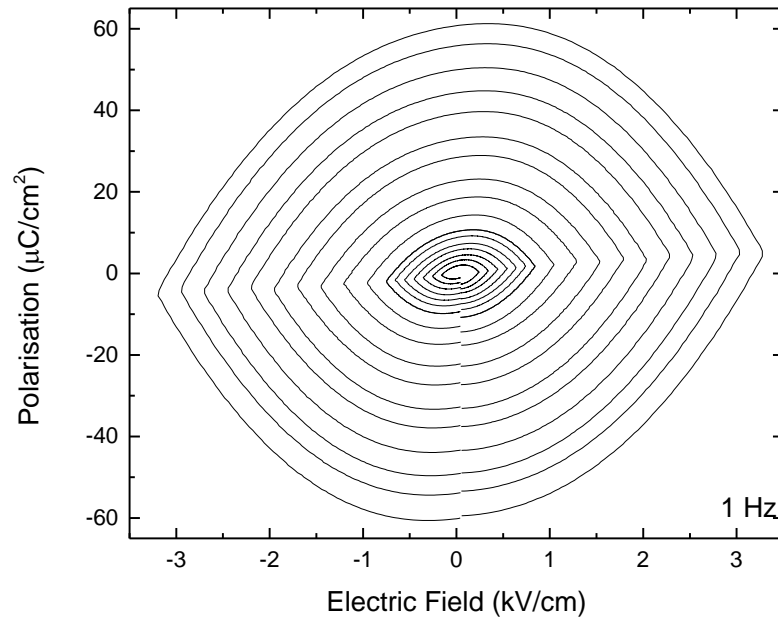


Figure 5. 22.: Low field P-E loops measured for $\text{KNbO}_3\text{-BiFeO}_3$ $x=0.05$ at room temperature.

However, $x=0.05$ sample was able to withstand an electric field up to 30 kV/cm at sub-ambient temperature (Figure 5. 23.). The sample was cooled down by immersion in liquid nitrogen before applying the electric field. Unsaturated loops were recorded.

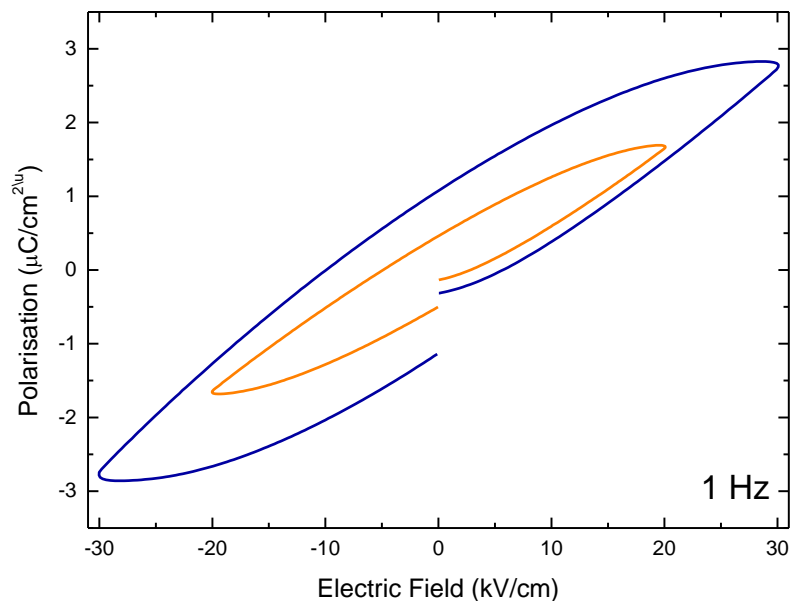


Figure 5. 23.: P-E measurements for $\text{KNbO}_3\text{-BiFeO}_3$ $x=0.05$ at sub-ambient temperature

5.4. Optical Characterisation

5.4.1 Diffuse reflectance spectroscopy

Diffuse reflectance spectroscopy was carried out using photons with wavelengths ranging from 200 to 1600 nm (Figure 5. 24).

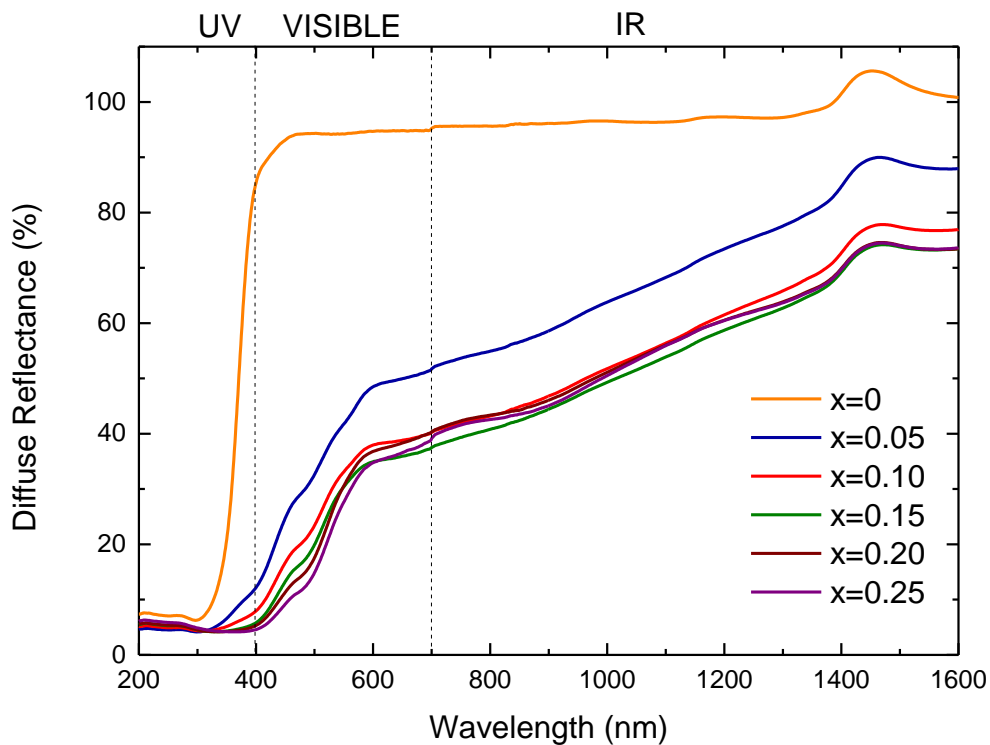


Figure 5. 24: Diffuse reflectance data as a function of wavelength for KNBF system.

The band gaps for KNBF ceramics were determined using the Tauc plots in Figure 5. 25 and Figure 5. 26. The band gap energies are obtained from the intercept of the tangent line in the plot of $(F(R) \cdot hv)^n$ vs energy. *A priori* there is no reason why the band gaps of KNBF ceramics should be direct or indirect. Hence, Tauc plots are constructed for $n=2$ (direct band-gaps, Figure 5. 25.) and for $n=1/2$ (indirect band-gaps, Figure 5. 26).

The value extracted for direct band-gap of KN is 3.66 eV, a high value but within the range reported in the literature (Chapter 1, Table 1.4), and consistent with the fact that these ceramics were able to withstand an applied electric field of 80 kV/cm.

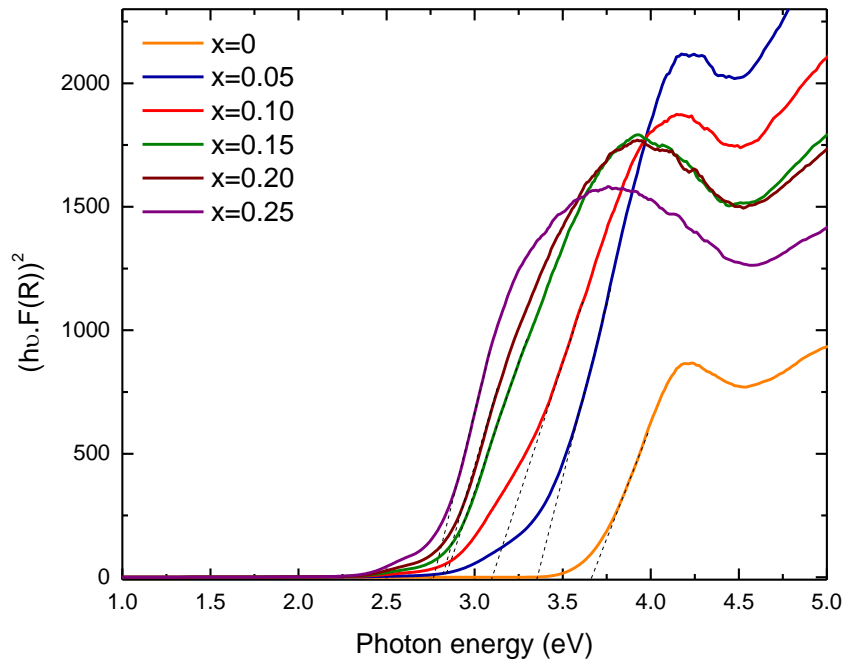


Figure 5. 25.: Tauc plot for direct band gaps for KNBF ceramics.

In Figure 5. 26, the Tauc plot is constructed using $n=1/2$ (indirect band gap). The extracted band gaps for KNBF $x=0$ and $x=0.05$ are 3.22 eV and ~ 2.5 eV, respectively, consistent with their electrical resistances. With increasing x , the band gap narrows continuously, reaching ~ 2.25 eV for $x=0.25$. We note that the apparent increase of the relative permittivity, Figure 5. 20., appears to follow the narrowing of the band gaps.

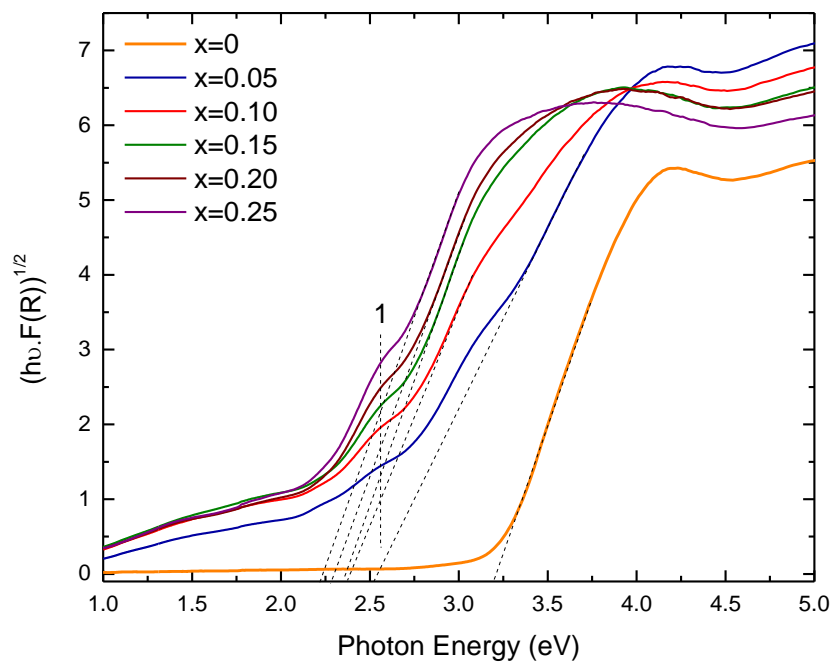


Figure 5. 26: Tauc plot for indirect band gaps for KNBF ceramics

Around 2.5 eV there is a clear shoulder, present in all doped materials (labelled as 1 in Figure 5. 26), and whose magnitude increases with increasing x. The optical absorption spectra of Fe^{3+} containing substances are known to exhibit three types of electronic transitions. Namely, Fe^{3+} cations ligand field transitions or the d-d transitions, ligand to metal charge transfer transitions, and pair excitations resulting from the simultaneous excitation of two neighbouring Fe^{3+} that are magnetically coupled.

In 2016, Burkert et al carried out an optical spectroscopy study in BiFeO_3 and observed three well-defined absorption features at 1.22 eV, 1.66 eV, and 2.14 eV, which were assigned to charge-transfer excitons and in-gap defect states probably related to oxygen vacancies. All KNBF show Urbach tails, however their appearance in optical absorption near band edges is expected in any material with disorder. The general broadening of the Raman modes from the doped ceramics, Figure 5. 3, results from increased lattice disorder, which manifests itself by the emergence of Urbach tails in the Tauc plots. An alternative interpretation of these absorption regions is intraband transitions originated by $\text{Bi}^{+3}/\text{Fe}^{+3}$ -rich impurities.

5.5. Preparation of thin films

5.5.1. Pulsed laser deposition

The starting conditions for depositing KNBF $x=0.25$ were taken from the literature (Martín et al., 1997; Nakagawara et al., 2000; Zaldo, Gill, Eason, Mendiola, & Chandler, 1994). The main limitation to deposit this material is the potassium loss, which has a detrimental influence on the purity of the sample.

Deposition conditions were optimised from a systematic study in order to achieve thin film with good quality. KNBF $x=0.25$ was deposited at 600°C and 650°C under an oxygen pressure of 0.1 mBar and 0.75 mBar using KrF laser with a focused energy of $\sim 1 \text{ J/cm}^2$ operating at 5 Hz (background pressure was $\sim 10^{-4}$ mBar). In addition, both STO (001) and MgO (001) were used as substrates, which makes in total 8 films. Purity and structural properties of the films are examined by XRD at RT, as shown in Figure 5. 27 and Figure 5. 28.

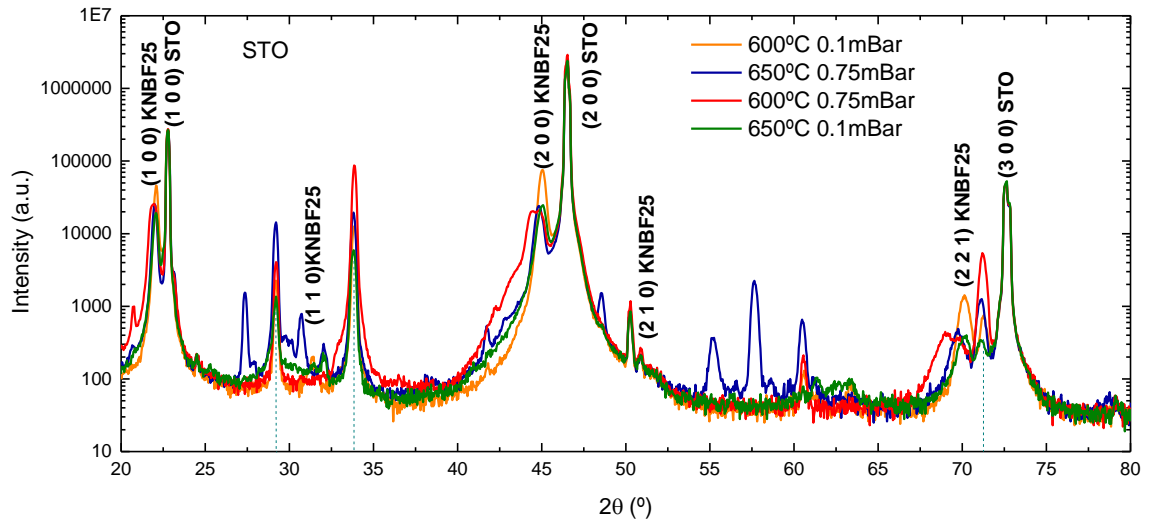


Figure 5. 27: XRD data for $\text{KNBF } x=0.25$ thin films deposited at 600°C and 650°C under oxygen pressure of 0.75 mBar and 1 mBar on STO.

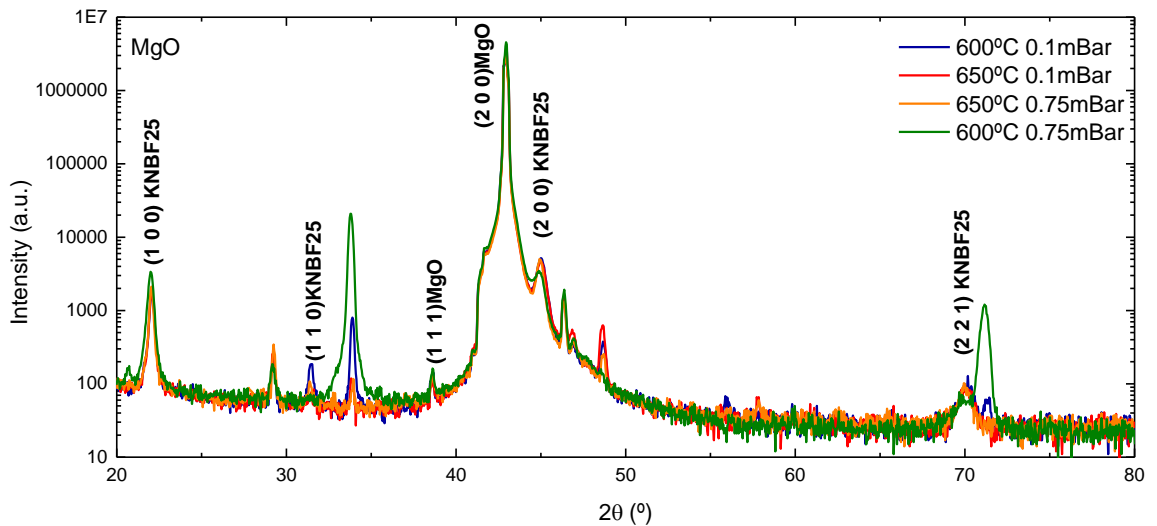


Figure 5. 28: XRD data for $\text{KNBF } x=0.25$ thin films deposited at 600°C and 650°C under oxygen pressure of 0.75 mBar and 1 mBar on MgO.

For both substrates, the best conditions to deposit $\text{KNBF } x=0.25$ are at 600°C under an oxygen pressure of 0.15 mBar, that correspond to the patterns with less unindexed peaks. Low deposition temperature prevents the K volatilisation and low pressure decreases the resistance of the atoms from the target to the substrate.

Figure 5. 29 shows XRD pattern of $\text{KNBF } x=0.25$ deposited at these conditions on STO and MgO. $\text{KNBF } x=0.25$ films are less crystallised on MgO than on STO.

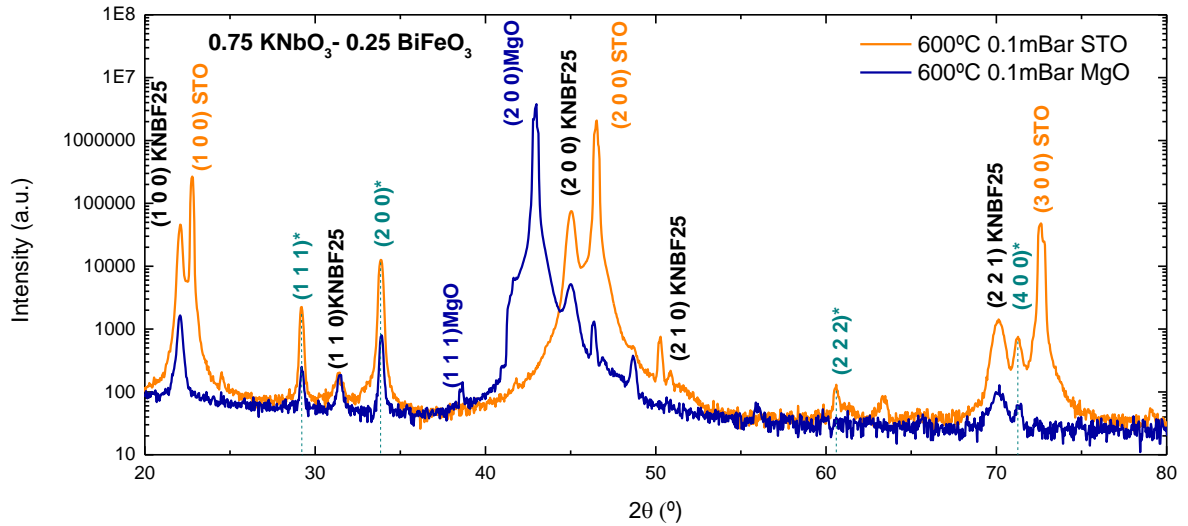


Figure 5. 29: Room-temperature XRD pattern of KNBF $x=0.25$ thin film deposited at 600°C under oxygen pressure 0.1 mBar on STO and MgO. Unknown secondary phase is indicated with blue asterisks.

Almost all the peaks can be indexed to a pseudo-cubic structure of KNBF $x=0.25$ and to the substrates. Peaks indicated by blue asterisks in Figure 5. 29, belong to an unknown phase. Table 5. 8 shows that there is a relationship among these peaks.

2θ (°)	d-spacing (Å)	Miller indices
29.17	3.06	(1 1 1)
33.87	2.64	(2 0 0)
60.62	1.53	(2 2 2)
71.265	1.32	(4 0 0)

Table 5. 8.: Unknown secondary phase indexing

The unknown phase presents cubic symmetry with a cell size of ~ 5.28 Å. This second phase is observed in all films. However, its origin is completely unknown, after verifying that there is no coincidence with the data base.

In-situ XRD for KNBF $x=0.25$ target is compared with the films deposited in Figure 5. 30 and Figure 5. 31.

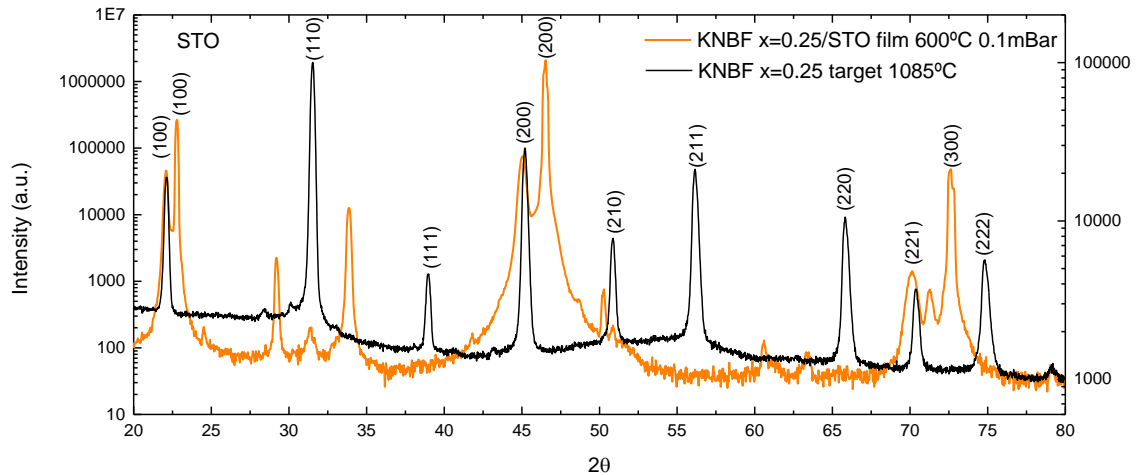


Figure 5. 30: Room-temperature XRD pattern of KNBF $x=0.25$ film (deposited at 600°C under oxygen pressure 0.1 mBar on STO) compared with *in-situ* XRD of the target.

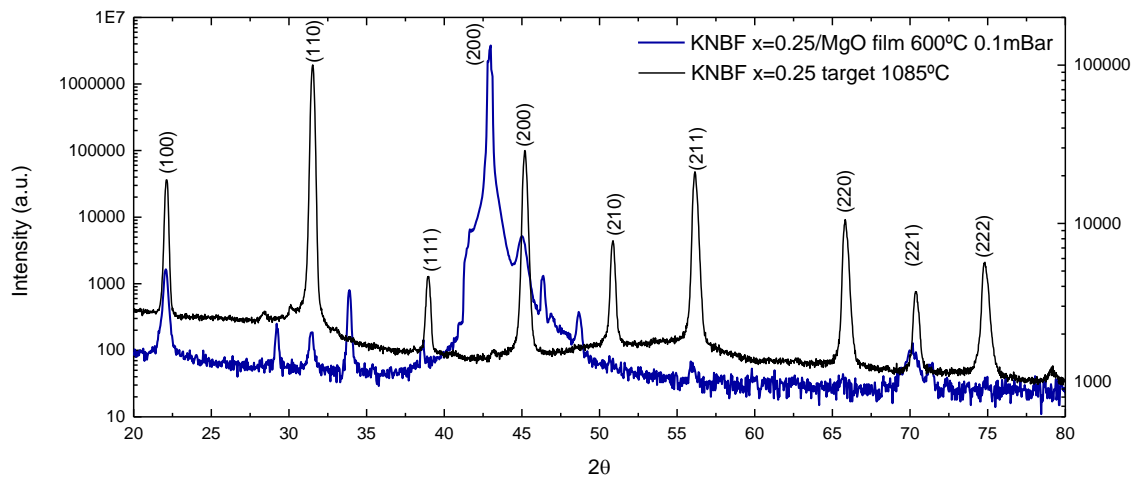


Figure 5. 31: Room-temperature XRD pattern of KNBF $x=0.25$ film (deposited at 600°C under oxygen pressure 0.1 mBar on MgO) compared with *in-situ* XRD of the target.

However, KNBF $x=0.25$ still requires further optimisation before functional characterisation.

5.5.2. Photovoltaic cell

Photoresponse was measured in ferroelectric photovoltaic (FEPV) cell for KNBF $x=0.25$. The fabrication of the cell was performed at the Universidade Federal de Pelotas (Brasil). The photoelectrical measurements were made under white light (210-1500 nm) and in the dark. For direct current measurements, the positive pole was connected to FTO/KNBF025

side, while the negative pole to FTO/carbon side. Also, reverse measurements were performed (positive connected to FTO/carbon and negative to FTO/KNBF025). The fabrication FEPV cell is explained in Chapter 2: Methodology (section 2.3.2.).

Figure 5. 32 displays I-V plots during the illumination and at dark for unpoled KNBF $x=0.25$ at RT. From this graph the open circuit photovoltage V_{oc} (the intersection points with the V-axis for the I-V curves) and the short circuit photocurrent, I_{sc} , (the intersection points with the I-axis for the I-V curves) can be determined. The current density is given by Equation 5.1:

$$J_{sc} = \frac{I_{sc}}{A} \quad \text{Eq. 5.1.}$$

where A is the area of the cell (in this study $A=1 \text{ cm}^2$).

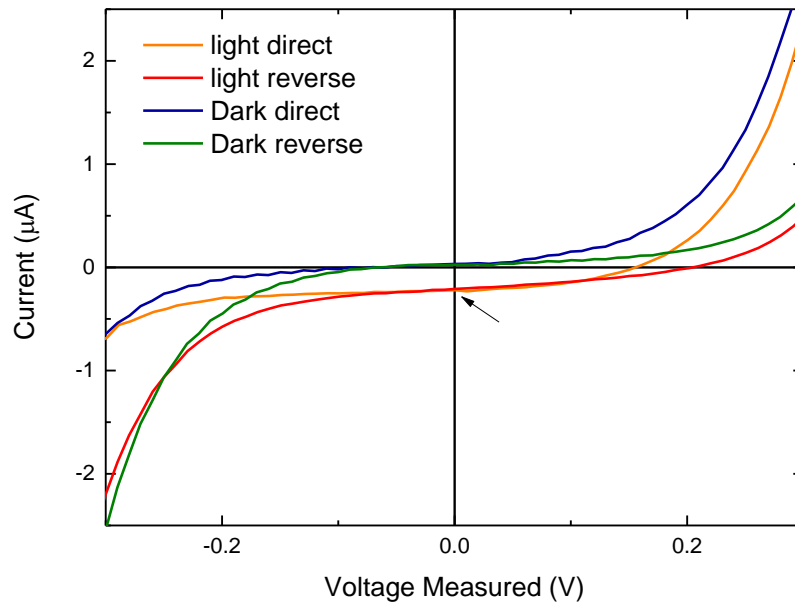


Figure 5. 32: Dependence of the photovoltaic current on voltage for KNBF $x=0.25$ film under direct and reverse illumination.

For direct illumination, J_{sc} and V_{oc} are about 0.16 V and $0.24 \mu\text{A}/\text{cm}^2$, respectively. On the other hand, for reverse illumination, 0.21 V and $0.23 \mu\text{A}/\text{cm}^2$. It is worth noting that our J_{sc} is higher than $0.1 \mu\text{A}/\text{cm}^2$ reported for KN-BNN thick film by Grinberg et al in 2013. Moreover, our J_{sc} is also greater than $40 \text{ nA}/\text{cm}^2$ obtained at 77 K for the same composition.

The Fill Factor, FF, for KNBF $x=0.25$ cell is given by the ratio between the maximum operational power of the cell, P_{max} , (grey rectangle in Figure 5. 33) and the product of V_{oc} and I_{sc} (black rectangle in Figure 5. 33). For direct light, KNBF $x=0.25$ film exhibits an

operational P_{\max} of 15.7 nW, a theoretical P_{\max} of 38.4 nW and a FF of $\sim 41\%$. From the I-V curves obtained for reverse light, a FF of 33%, was estimated. For further information about the Fill Factor, please refer to Chapter 1, Introduction (section 1.4.2.: Photovoltaic effect).

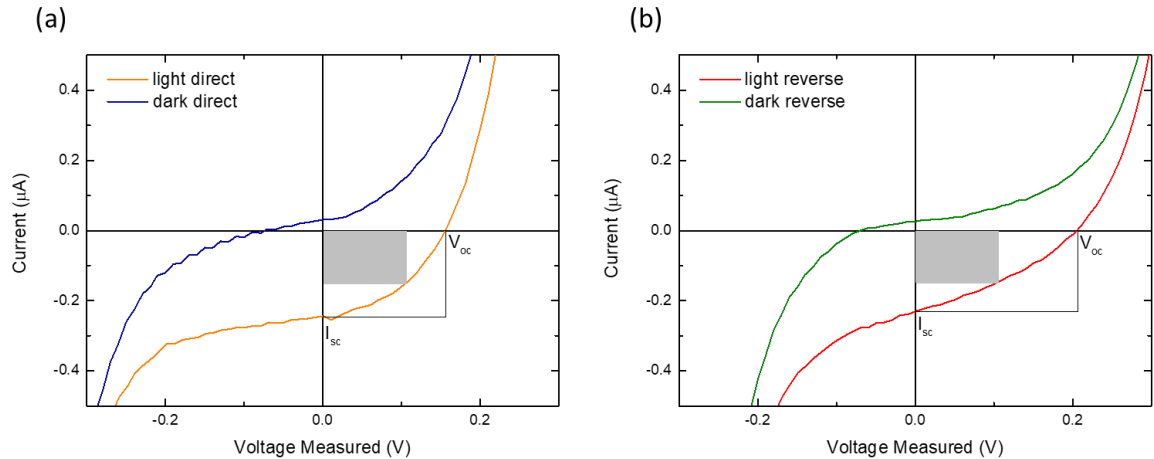


Figure 5.33: I-V plot and schemes to calculate the FF for (a) direct light and (b) indirect light.

Unfortunately, it is not possible to calculate the efficiency conversion (Chapter 1. Equation 1.14) of the cell because the incident light power during the operation of the lamp is not known.

5.5. Discussion

Room temperature XRD data for KNBF $x=0, 0.05, 0.10, 0.15, 0.20$ and 0.25 , combined with Raman spectroscopy analysis show the polar orthorhombic crystal structure (Amm2 space group) to persist up to $x=0.25$. In addition, *in-situ* Raman spectroscopy corroborates the polar nature of all compositions in the temperature range -100 to 200 $^{\circ}\text{C}$ (Figure 5. 9). Reflections of KNBF patterns shift slightly to higher angles indicating a decrease of the unit cell volume up to $x=0.15$ (Figure 5. 2).

Based on both permittivity measurements (Figure 5. 20) and Raman spectroscopy analysis all ceramics studied exhibit dielectric anomalies associated with structural phase transitions and their ferroelectric nature is corroborated by the presence of a Fano-type resonant dip in their Raman spectra (Figure 5. 5)

SEM imaging confirms dense sample by the almost absence of porosity (Figure 5. 10). However, chemical inhomogeneities are detected by EDX spectroscopy, which are not perceived by XRD, such as Bi/Fe-rich regions (Figure 5. 11). Also, minor quantity of secondary phase, $0.5 \text{ KNbO}_3\text{-}0.5 \text{ BiFeO}_3$, is detected in KNBF $x=0.20$ and 0.25 .

The unclear nature of the band-gap for KNBF system requires the study of both, direct and indirect, transitions. Direct band-gap continuously decreases from 3.66 eV ($x=0$) to 2.70 eV ($x=0.25$). On the other hand, indirect bandgap narrows monotonically from 3.2 eV ($x=0$) down to 2.22 eV ($x=0.25$), consistent with the inability of KNBF $x=0.05$ to withstand an electrical field as low as 0.2 kV/cm (Figure 5. 22). Indeed, all KNBF ceramics are electrically conductive, suggesting band gaps lower than 3 eV.

It is demonstrated the polar order is retained up to $x=0.25$, which also exhibits the lowest band-gap of the KNBF system (2.22 eV), making this composition interesting for photoinduced phenomena. In order to measure the photoresponse of this composition, thin film of KNBF $x=0.25$ were tentatively deposited by PLD. The most appropriate temperature, oxygen pressure and substrate to deposit KNBF $x=0.25$ were 600°C, 0.15 mBar and STO, respectively. Low temperature avoids K losses, low pressure facilitates the motion of the atoms from the target to the STO. Polycrystalline KNBF $x=0.25$ film was obtained by PLD, therefore is still required further optimisation before measuring photoresponse on these films.

Nonetheless, photoresponse was measured on other KNBF $x=0.25$ cell, fabricated by coating a FTO glass. The measured V_{oc} and I_{sc} were about 0.16 V and $0.24 \mu\text{A}/\text{cm}^2$, respectively. Table 5. 9 informs about V_{oc} and J_{sc} values found in the literature for ferroelectric films and assuming the area of the cells is $\sim 1 \text{ cm}^2$, P_{max} is estimated.

Material	V_{oc}	J_{sc}	P_{max}	Reference
KN-BNN at RT	0.7 mV	$0.1 \mu\text{A}/\text{cm}^2$	0.07 nW	(Grinberg et al., 2013)
KN-BNN at 77K	3.5 V	$40 \text{ nA}/\text{cm}^2$	140 nW	(Grinberg et al., 2013)
PLZT at RT	0.84V	$25 \text{ nA}/\text{cm}^2$	21 nW	(Poosanaas, Dogan, Thakoor, & Uchino, 1998)
KNMN at RT	5 V	$3.2 \text{ nA}/\text{cm}^2$	16 nW	(Park, Won, Ahn, & Kim, 2013)
BTO	8 V	0.2 nA	1.6 nW	(Spanier et al., 2016)
BFO	535 mV	$54 \mu\text{A}/\text{cm}^2$	28 μW	(T. Choi, Lee, Choi, Kiryukhin, & Cheong, 2009)
KNBF $x=0.25$ at RT	0.16 V	$0.24 \mu\text{A}/\text{cm}^2$	38.4 nW	This study

Table 5. 9. V_{oc} and J_{sc} values reported in the literature for photoresponses of ferroelectric materials. Theoretical P_{max} values were calculated by the the product of V_{oc} and I_{sc} and assuming PV cells of 1 cm^2 .

As previously discussed, our J_{sc} is higher than $0.1 \mu\text{A}/\text{cm}^2$ and $40 \text{ nA}/\text{cm}^2$ reported at RT and 77 K for KN-BNN thick film by Grinberg et al. In addition, J_{sc} for KNBF $x=0.25$ is also superior than $8 \text{ nA}/\text{cm}^2$ for a PLZT sample or $25 \text{ nA}/\text{cm}^2$ for KNMN or 0.2 nA for BTO samples measured under ultraviolet illumination. However, our result is still lower than the photoresponse for BiFeO_3 reported for a 70-mm sample under green-light illumination.

The ability to control the band gap while maintaining the spontaneous polarisation makes the KNBF system specially interesting for photoinduced processes in a wide temperature range.

5.6. Conclusions

Dense KNBF ceramics were prepared by solid-state reaction. Orthorhombic symmetry is maintained up to $x=0.25$ as corroborated by XRD, Raman spectroscopy and dielectric measurements. SEM images confirms the absence of porosity and EDX revealed some regions rich in solutes. Finally, it was demonstrated that the band gap of undoped KN can be systematically narrowed by 1 eV (i.e. a ~30% reduction) via co-substitution of K and Nb by Bi and Fe, respectively. Polar KNBF $x=0.25$ with a band gap of 2.2 eV is a promising candidate as a photoferroelectric. Indeed, a photocurrent of $0.24 \mu\text{A}/\text{cm}^2$ was measured on FEPV cell, which is much higher than other values reported in the literature for ferroelectrics (Table 5. 9).

5.7. References

- Burkert, F., Kreisel, J., & Kuntscher, C. A. (2016). Optical spectroscopy study on the photo-response in multiferroic BiFeO_3 . *Applied Physics Letters*, *109*(18). <https://doi.org/10.1063/1.4966548>
- Catalan, G., & Scott, J. F. (2009). Physics and applications of bismuth ferrite. *Advanced Materials*, *21*(24). <https://doi.org/10.1002/adma.200802849>
- Choi, J. H., Kim, J. S., Hong, S. B., Chae, K. W., & Cheon, C. Il. (2012). Crystal structure and piezoelectric properties of $\text{KNbO}_3\text{-BiFeO}_3$ ceramics. *Journal of the Korean Physical Society*, *61*(6), 956–960. <https://doi.org/10.3938/jkps.61.956>
- Choi, T., Lee, S., Choi, Y. J., Kiryukhin, V., & Cheong, S.-W. (2009). Switchable ferroelectric diode and photovoltaic effect in BiFeO_3 . *Science*, *324*(5923). <https://doi.org/10.1126/science.1168636>
- Dash, S., Choudhary, R. N. P., Das, P. R., & Kumar, A. (2014). Effect of KNbO_3 modification on structural, electrical and magnetic properties of BiFeO_3 . *Applied Physics A: Materials Science and Processing*, *118*(3), 1023–1031. <https://doi.org/10.1007/s00339-014-8862-9>
- Gao, F., Yuan, Y., Wang, K. F., Chen, X. Y., Chen, F., Liu, J. M., & Ren, Z. F. (2006).

- Preparation and photoabsorption characterization BiFeO_3 nanowires. *Applied Physics Letters*, 89(10), 2004–2007. <https://doi.org/10.1063/1.2345825>
- Grinberg, I., West, D. V., Torres, M., Gou, G., Stein, D. M., Wu, L., ... Rappe, A. M. (2013). Perovskite oxides for visible-light-absorbing ferroelectric and photovoltaic materials. *Nature*, 503(7477). <https://doi.org/10.1038/nature12622>
- Lennox, R. C., Taylor, D. D., Vera Stimpson, L. J., Stenning, G. B. G., Jura, M., Price, M. C., ... Arnold, D. C. (2015). PZT-like structural phase transitions in the BiFeO_3 – KNbO_3 solid solution. *Dalton Trans.*, 44(23), 10608–10613. <https://doi.org/10.1039/C5DT00140D>
- Martín, M. J., Alfonso, J. E., Mendiola, J., Zaldo, C., Gill, D. S., Eason, R. W., & Chandler, P. J. (1997). Pulsed laser deposition of KNbO_3 thin films. *Journal of Materials Research*, 12(10), 2699–2706. <https://doi.org/DOI:10.1557/JMR.1997.0359>
- Nakagawara, O., Shimuta, T., Makino, T., Arai, S., Tabata, H., & Kawai, T. (2000). Epitaxial growth and dielectric properties of (111) oriented $\text{BaTiO}_3/\text{SrTiO}_3$ superlattices by pulsed-laser deposition. *Applied Physics Letters*, 77(20), 3257–3259. <https://doi.org/10.1063/1.1324985>
- Nakashima, Y., Shimura, T., Sakamoto, W., & Yogo, T. (2007). Fabrication and Properties of BiFeO_3 – KNbO_3 Ceramics. *Ferroelectrics*, 356(1), 180–184. <https://doi.org/10.1080/00150190701512151>
- Park, J., Won, S. S., Ahn, C. W., & Kim, I. W. (2013). Ferroelectric photocurrent effect in polycrystalline lead-free $(\text{K}_{0.5}\text{Na}_{0.5})(\text{Mn}_{0.005}\text{Nb}_{0.995})\text{O}_3$ thin film. *Journal of the American Ceramic Society*, 96(1). <https://doi.org/10.1111/j.1551-2916.2012.05430.x>
- Poosanaas, P., Dogan, A., Thakoor, S., & Uchino, K. (1998). Influence of sample thickness on the performance of photostrictive ceramics. *Journal of Applied Physics*, 84(3).
- Spanier, J. E., Fridkin, V. M., Rappe, A. M., Akbashev, A. R., Polemi, A., Qi, Y., ... Johnson, C. L. (2016). Power conversion efficiency exceeding the Shockley–Queisser limit in a ferroelectric insulator. *Nature Photonics*, 10(9), 611–616. <https://doi.org/10.1038/nphoton.2016.143>

- Teslenko, P., Pavlenko, A. V., Reznichenko, L. A., Rudskaya, A. G., Kofanova, N., Kabirov, Y., Kupriyanov, M. F. (2017). *Advanced Materials* (Vol. 193, pp. 133–144). https://doi.org/10.1007/978-3-319-56062-5_12
- Tuan, N. H., Bac, L. H., Cuong, L. V., Van Thiet, D., Van Tam, T., & Dung, D. D. (2017). Structural, Optical, and Magnetic Properties of Lead-Free Ferroelectric $\text{Bi}_{0.5}\text{K}_{0.5}\text{TiO}_3$ Solid Solution with BiFeO_3 Materials. *Journal of Electronic Materials*, 46(6), 3472–3478. <https://doi.org/10.1007/s11664-017-5328-9>
- Wu, X., Yao, L., Yang, S., & Zhang, Y. (2017). Enhanced ferroelectricity and band gap engineering of $(1-x)\text{BiFeO}_3\text{-}x\text{SrTiO}_3$ thin films. *Journal of Sol-Gel Science and Technology*, 83(3), 653–659. <https://doi.org/10.1007/s10971-017-4441-9>
- Zaldo, C., Gill, D. S., Eason, R. W., Mendiola, J., & Chandler, P. J. (1994). Growth of KNbO_3 thin films on MgO by pulsed laser deposition. *Applied Physics Letters*, 65(4), 502–504. <https://doi.org/10.1063/1.112280>

Chapter 6

System (1-x) KNbO₃-x BiMnO₃

6.1. Introduction

6.2. Structural and chemical characterisation

6.2.1. Purity and X-ray diffraction

6.3.2. Raman spectroscopy

6.3.3. SEM

6.3.4. EDX

6.4. Electrical Characterisation

6.4.1. Dielectric Characterisation

6.5. Optical Characterisation

6.5.1 Diffuse reflectance spectroscopy

6.6. Discussion

6.7. Conclusions

6.8. References

6. System (1-x) $\text{KNbO}_3\text{-x BiMnO}_3$

6.1. Introduction

This chapter is devoted to the synthesis and characterisation of powders and ceramics from the binary system (1-x) $\text{KNbO}_3\text{-x BiMnO}_3$ (KNBM) with $x=0, 0.05, 0.10, 0.15, 0.20$ and 0.25 . Ceramic processing, structural, dielectric and optical characterisation are detailed below. For this system, ferroelectric and piezoelectric measurements are not carried out due to all KNBM ceramics being electrically very leaky. Indeed, band-gap narrowing is observed with increasing $\text{Bi}^{+3}/\text{Mn}^{+3}$ contents.

BiMnO_3 has been known since 1960, but recently the search for multiferroic materials has renewed the interest in this compound. Concerning the physical properties of BiMnO_3 , ferromagnetic order has been confirmed by several researchers. The Curie temperature was reported at around 100 K. In contrast, the ferroelectric nature of BiMnO_3 has been a controversial issue.

Indeed, the exact crystal symmetry of BiMnO_3 has also been a matter of debate as shown by the large number of studies (Alexei A. Belik, 2012). The first crystal symmetry proposed for BiMnO_3 was based on the non-centrosymmetric $C2$ space group (Atou, Chiba, Ohoyama, Yamaguchi, & Syono, 1999; Moreira dos Santos et al., 2002). However, posterior studies suggested BiMnO_3 to be better described as $C2/n$ space group (nonpolar phase) (A.A. Belik et al., 2007; Montanari et al., 2005; Toulemonde et al., 2009; Yang et al., 2008). Theoretical studies determined $C2/n$ symmetry to be more stable than the $C2$ model at RT (Baettig, Seshadri, & Spaldin, 2007). In addition, ferroelectricity for BiMnO_3 compound is still controversial. P-E loops in bulk BiMnO_3 are reported with the P_r values of 0.043 mC/cm^2 at 200 K (Moreira dos Santos et al., 2002) and 0.06 mC/cm^2

at RT (Chi et al., 2007). Conversely, some reports affirmed ferroelectricity is not detected in bulk BiMnO_3 (Alexei A. Belik, 2012). Optical band-gap of 0.9 eV based on X-ray emission and absorption spectra has been reported (McLeod et al., 2010).

6.2. Structural and chemical characterisation

6.2.1. Purity and X-ray diffraction

KNBM ($x=0, 0.05, 0.10, 0.15, 0.20$ and 0.25) ceramics were prepared by the solid-state reaction method. K_2CO_3 , Nb_2O_5 , Bi_2O_3 and Mn_2O_3 powders weighed in the required stoichiometric ratios were mixed overnight in polyethylene bottles with zirconia milling media and isopropanol as solvent. After drying, the mixed powders were sieved and calcined twice in air first at 800°C and then at 900°C . Subsequently, pellets were fired in air for 4 hours at 1070°C using a controlled heating rate of $3^\circ\text{C}/\text{min}$. In the literature, BiMnO_3 is reported to be synthesised under high pressure conditions (Sugawara, Iiida, Syono, & Akimoto, 1968). The room-temperature XRD data for KNBM ($0 \leq x \leq 0.25$) powders are shown in Figure 6. 1.

A significant amount of manganese oxide (Mn_2O_3) is present in KNBM $x \geq 0.10$ (indicated with grey squares on Figure 6. 1.). XRD data for undoped KN (Orange pattern) is assigned to an orthorhombic perovskite described by the $\text{Amm}2$ space group. For KNBM $x=0.05$, data are also consistent with the formation of a single-phase perovskite. Moreover, the absence of any secondary phase or residual precursor phase supports the incorporation of Bi^{+3} and Mn^{+3} into KN lattice. This is also accompanied by a gradual disappearance of the peak splitting typical for the orthorhombic structure. With increasing x , Mn_2O_3 appears as a second phase, showing that under the chosen processing conditions the homogenisation process is incomplete. This is further corroborated by the presence of some residual KN (indicated with black circles on Figure 6. 1.(a) and dashed line in Figure 6. 1.(b)), which remained virtually undoped, as clearly shown by the XRD data for $x=0.10$ and $x=0.15$. Figure 6. 2. shows the room-temperature XRD data for KNBM ceramics. After sintering at 1070°C for 4 hours, the secondary phase (Mn_2O_3) disappears, supporting the complete incorporation of Mn into the KN lattice. Nevertheless, a closer

inspection of the XRD data, shows the coexistence of two KN-based polymorphs, as discussed below.

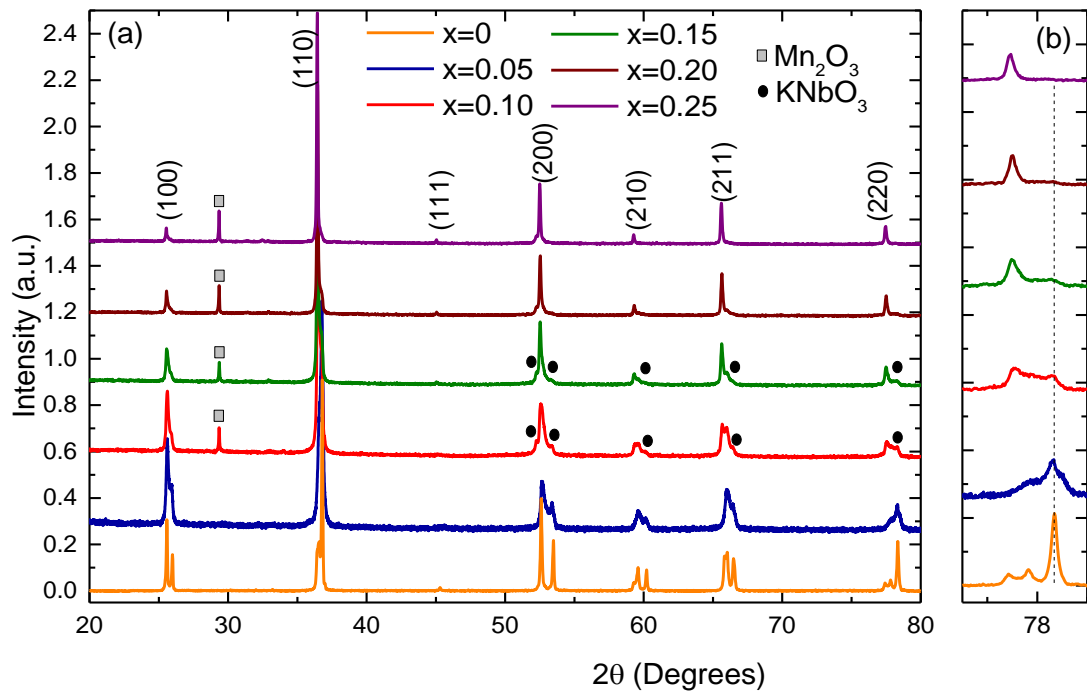


Figure 6. 1.: Room-temperature XRD data of KNBM ($x=0, 0.05, 0.10, 0.15, 0.20$ and 0.25) powders. Second phase at $\sim 30^\circ$ is associated with Mn_2O_3 (grey square). In addition, some pure KN remains in $x=0.10$ and $x=0.15$ (black circles).

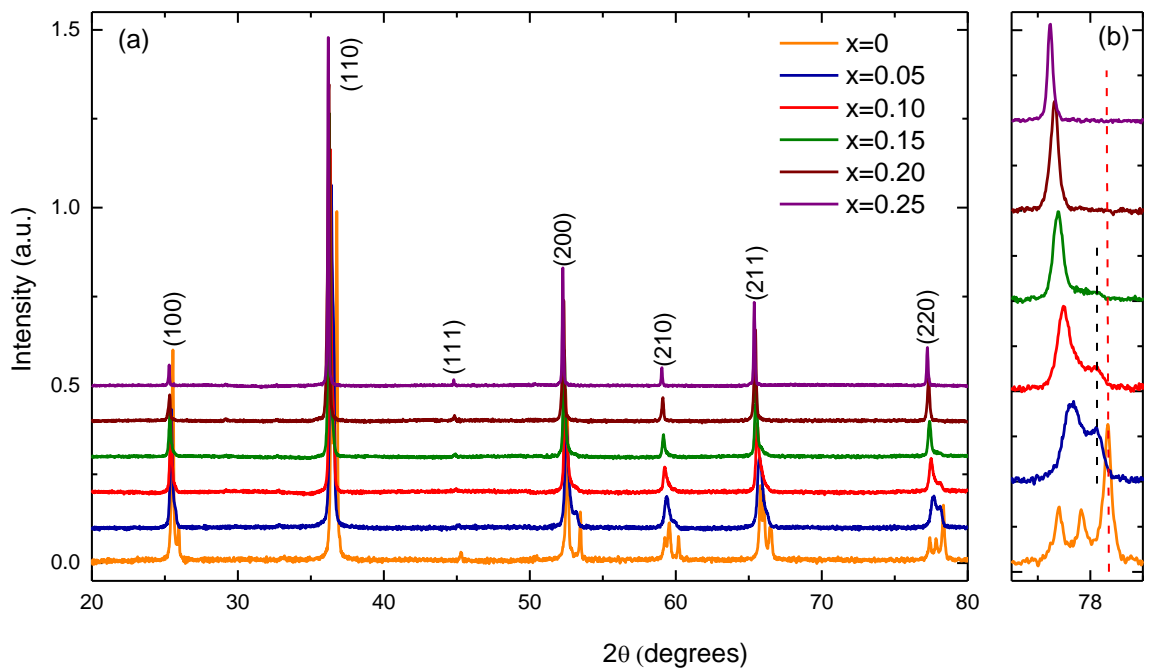


Figure 6. 2: (a) Room-temperature XRD data of KNBM ($x=0, 0.05, 0.10, 0.15, 0.20$ and 0.25) ceramics. (b) Coexistence of two phases: orthorhombic KN-based phase (black dashed line) and cubic phase.

Firstly, reflections of doped compositions shift towards lower 2θ angles, which means there is an increase of the unit cell volume with increasing $\text{Bi}^{+3}/\text{Mn}^{+3}$ contents. This is consistent with the replacement of Nb^{+5} ($r_{\text{VI}} = 0.64 \text{ \AA}$) by larger Mn^{+3} ($r_{\text{VI}} = 0.645 \text{ \AA}$). Assuming high spin state, which may give rise to a Jahn-Teller distortion. The presence of larger Mn^{+2} , should not be discarded.

Secondly, the triplet between 77° and 80° ($x=0$) evolve to a single peak accompanied by a lower intensity reflection at higher 2θ angles (Figure 6. 2 (b)). With increasing x , this reflection looks less intense and disappears for KNBM $x=0.20$ and $x=0.25$. Speculatively, this reflection (black dash line, Figure 6. 2 (b)) could be associated with an orthorhombic KN-based phase (red dash line, Figure 6. 2 (b)), which is slightly shifted towards lower 2θ angles in comparison with undoped KN due to the simultaneous incorporation of Bi^{+3} and Mn^{+3} . The fact that this reflection does not shift for $x > 0.05$, suggests that the solubility limit in orthorhombic KN is limited to $x \sim 0.05$. This is supported by the Rietveld refinements in Table 6. 1 and Table 6. 2, which also show XRD data of these compositions are successfully refined as a combination of an orthorhombic phase (space group $\text{Amm}2$) and cubic phase (space group $\text{Pm}\bar{3}\text{m}$). Finally, the typical peak splitting expected for $\text{Amm}2$ crystal is not visible

Table 6. 1 and Table 6. 2 show the results of Rietveld refinements for all compositions. In addition, experimental and relative density values are included.

	x=0	x=0.05		x=0.10	
Space Group	Amm2	Amm2 22.8(7) 8%	Pm- $\bar{3}m$ 77.2(1) %	Amm2 14.1(5) %	Pm- $\bar{3}m$ 85.9(1) %
Density (Experimental) (g/cm³)	4.35(3)	4.34(22)		4.21(10)	
Density (calculated) (g/cm³)	4.6273(1)	4.7829(7)	4.7568(4)	4.9560(8)	4.8890(2)
Relative Density (%)	94(1)	91(4)*		86(2)*	
a (Å)	3.9711(1)	3.9883(3)	4.0234(2)	4.0003(3)	4.0325(1)
b (Å)	5.6909(1)	5.6979 (6)	4.0234(2)	5.6855(5)	4.0325(1)
c (Å)	5.7158(1)	5.7007(5)	4.0234(2)	5.6914(6)	4.0325(1)
V/10⁶ (pm³)	64.576(2)	64.77(1)	65.130(7)	64.72(1)	65.572(3)
R_{exp}	1.26460	0.69640		0.84829	
R_{profile}	2.97912	1.34817		2.17999	
R_{wp}	4.65175	1.91855		3.16955	
GOF	13.53086	7.58975		13.96061	

Table 6. 1.: Rietveld refinement results for KNBM x=0, x=0.05 and x=0.10 ceramics. (*) Relative densities compared with the weighted average of the theoretical densities from the two coexisting phases.

	x=0.15		x=0.20	x=0.25
Space Group	Amm2 5.4(3) %	Pm- $\bar{3}$ m 94.6(8) %	Pm- $\bar{3}$ m	Pm- $\bar{3}$ m
Density (Experimental) (g/cm³)		4.29(19)	4.32(16)	4.20(10)
Density (calculated) (g/cm³)	5.1267(7)	5.0480(2)	5.2137(4)	5.3657(9)
Relative Density (%)		85(5)*	83(3)	78(1)
a (Å)	3.9874(3)	4.0353(1)	4.0356(8)	4.0406(1)
b (Å)	5.6800(7)	4.0353(1)	4.0356(8)	4.0406(1)
c (Å)	5.7176(8)	4.0353(1)	4.0356(8)	4.0406(1)
V/10⁶ (pm³)	64.748(10)	65.711(3)	65.723(3)	65.97(1)
R_{exp}		0.83353	0.6694	0.68507
R_{profile}		2.27072	1.54564	1.33107
R_{wp}		3.85881	2.48361	2.22667
GOF		21.43187	13.76548	10.56425

Table 6. 2.: Rietveld refinement for KNBM x=0.15, x=0.20 and 0.25. (*) Relative densities compared with the weighted average of the theoretical densities from the two coexisting phases.

All compositions have a relative density above 80% except KNBM x=0.25. The relative content of orthorhombic phase falls from ~23% for x=0.05 to ~ 5% for x=0.15. KNBM x=0.20 and x=0.25 are acceptably refined as cubic phase (Pm- $\bar{3}$ m). Figure 6. 3. shows the unit cell volumes as a function of x.

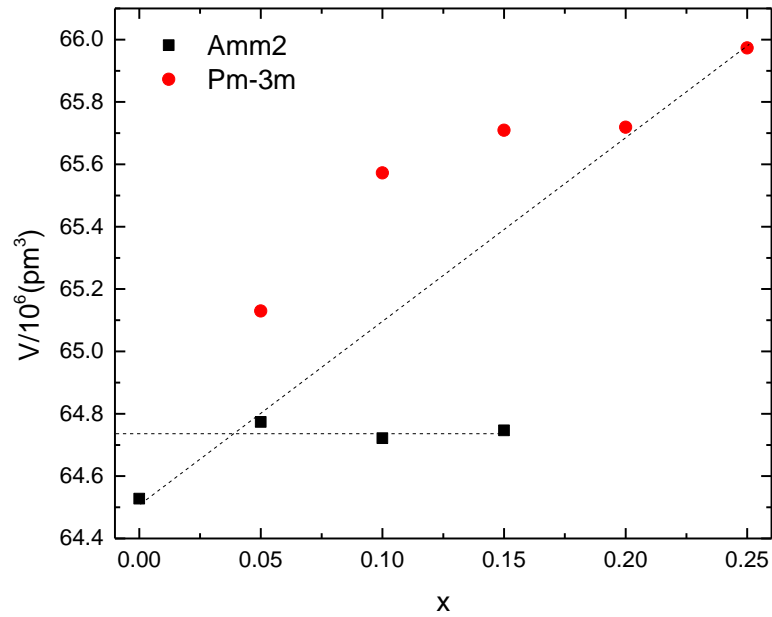


Figure 6. 3.: Graphical representation of unit cell volumes with x . Black square represents orthorhombic phase (Amm2) and red circles the cubic phase (Pm- $\bar{3}m$)

The orthorhombic phase for KNBM $0 \leq x \leq 0.15$ presents an average volume of $\sim 64.7 \cdot 10^6 \text{ pm}^3$ and this value remains almost constant. On the other hand, the volume of the cubic phase Pm- $\bar{3}m$ increases systematically with x . This fact suggests limited incorporation of $\text{Bi}^{+3}/\text{Mn}^{+3}$ into the orthorhombic phase. Therefore, difficulties on homogenising the dopants into the KN lattice are observed at low concentration of x .

6.3.2. Raman spectroscopy

Room-temperature Raman spectra for KNBM $0 \leq x \leq 0.25$ powders are shown in Figure 6. 4.. Spectra for all compositions present the same general features as reported for KN. Detailed description of Raman modes for pure KN can be found in Chapter 3.

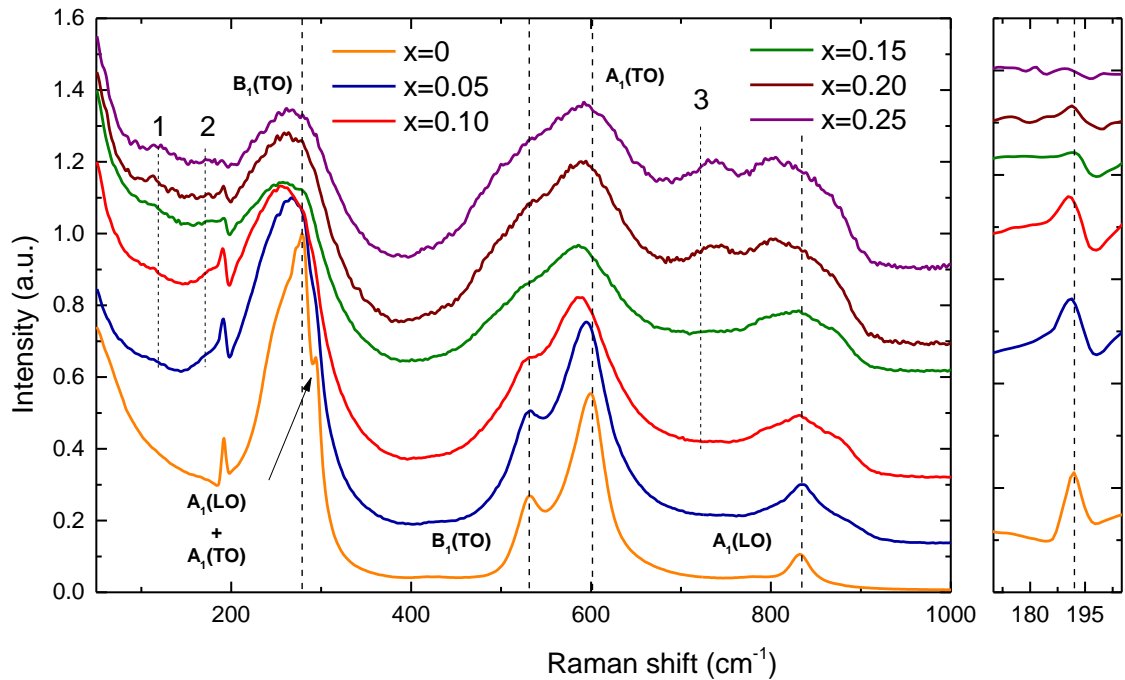


Figure 6. 4.: Room-temperature Raman spectra for KNBM ($0 \leq x \leq 0.25$) powders. New modes (1,2 and 3) emerge in KNBM ($x \geq 0.15$) powders spectra. Inset graph: monitoring of mixed sharp mode at 192 cm^{-1} .

The modes for doped compositions for this system become broader (which is directly related with the disorder of the material) and slightly shift to lower wavenumbers. As explained in previous chapters, the occurrence of long-range polarisation in KN is associated with the presence of a mixed sharp mode at 192 cm^{-1} . Therefore, it can be used to monitor the polar phases. The presence of this sharp mode up to $x=0.25$ (attached graph on the right in Figure 6. 4) can be interpreted in two different ways. Firstly, KNBM system exhibits polar nature and secondly and more likely, the incomplete homogenisation, as shown by the XRD data, leads to powders containing residual orthorhombic KN. In addition, new modes start emerging for compositions with $x \geq 0.10$, which are indicated as 1, 2, and 3. These extra modes are better observed in Raman spectra recorded for KNBM ($0 \leq x \leq 0.25$) ceramics in Figure 6. 5.

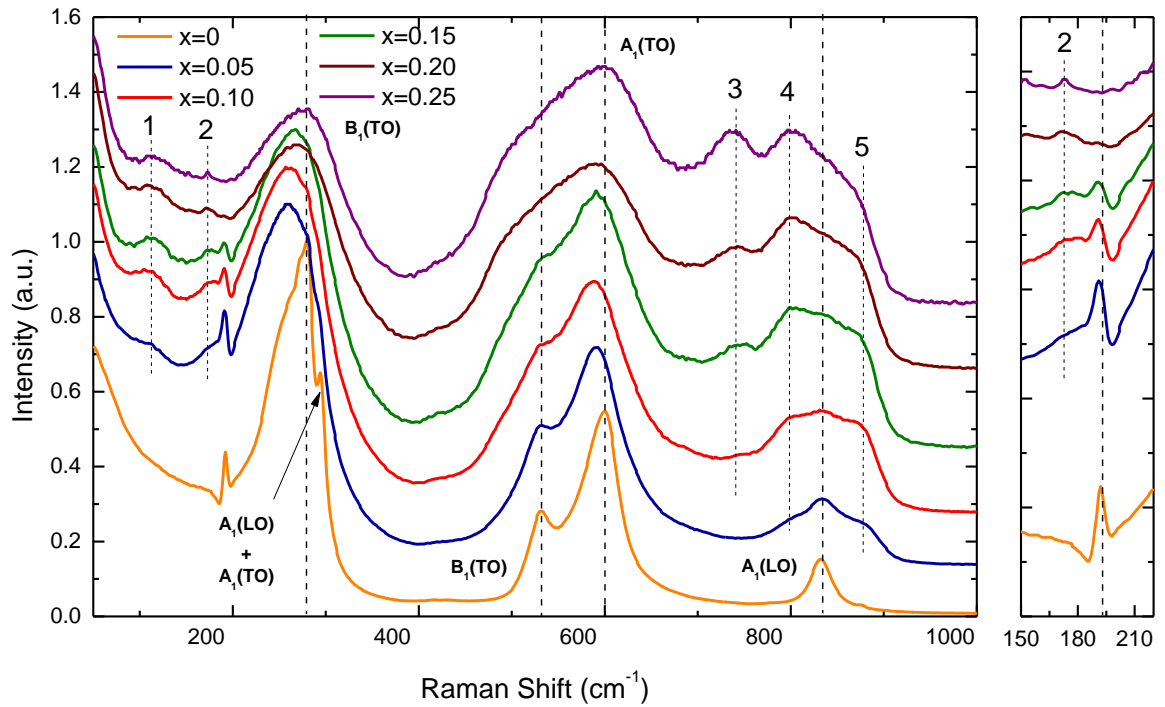


Figure 6. 5.: Room-temperature Raman spectra for KNBM ($0 \leq x \leq 0.25$) ceramics. New modes (1,2,3,4 and 5) emerge in KNBM ($x \geq 0.15$) ceramics spectra. Inset graph: monitoring of mixed sharp mode at 192 cm^{-1}

New modes are labelled as 1,2,3,4 and 5. Mode 1 appears around $\sim 100 \text{ cm}^{-1}$ and mode 2 emerges at $\sim 175 \text{ cm}^{-1}$ as a shoulder of the sharp peak at 192 cm^{-1} . Both modes do not shift and the intensity increases systematically. Indeed, these modes have been observed and explained in Chapter 5 and they were speculatively associated with to A-O vibrations within nm-sized clusters rich in either Bi^{3+} and/or K^+ cations. For sintered ceramics, the sharp mode at 192 cm^{-1} is present up to $x=0.15$, which supports the presence of an orthorhombic KN-based phase (ferroelectric phase). Moreover, the sharp mode become less intense with x , in agreement with the drop in the percentage of orthorhombic phase in KNBM ($0.05 \leq x \leq 0.15$) ceramics calculated by the Rietveld refinements. Modes 3 and 4 appear at 740 cm^{-1} and 800 cm^{-1} respectively and their relative intensity increase with x . Finally, mode 5, the least intense, continuously shifts by $\sim 10 \text{ cm}^{-1}$ to lower wavenumbers. The absence of the sharp mode at 192 cm^{-1} for $x \geq 0.20$, is consistent with the disappearance of orthorhombic KN-based phases, but the presence of Raman modes for $x \geq 0.20$, shows that the local structures is not purely cubic, as Raman activity is absent from crystals described by the centrosymmetric $\text{Pm}\bar{3}\text{m}$ space group. Figure 6. 6 and Figure 6. 7 show the temperature dependence of Raman spectra for KNBM $x=0.15$ and $x=0.25$, respectively. The presence of a polar phase for $x=0.15$ is confirmed in a

temperature range between -180°C and 20°C . In contrast KNBM $x=0.25$ maintains the non-polar nature from 340 to -180°C .

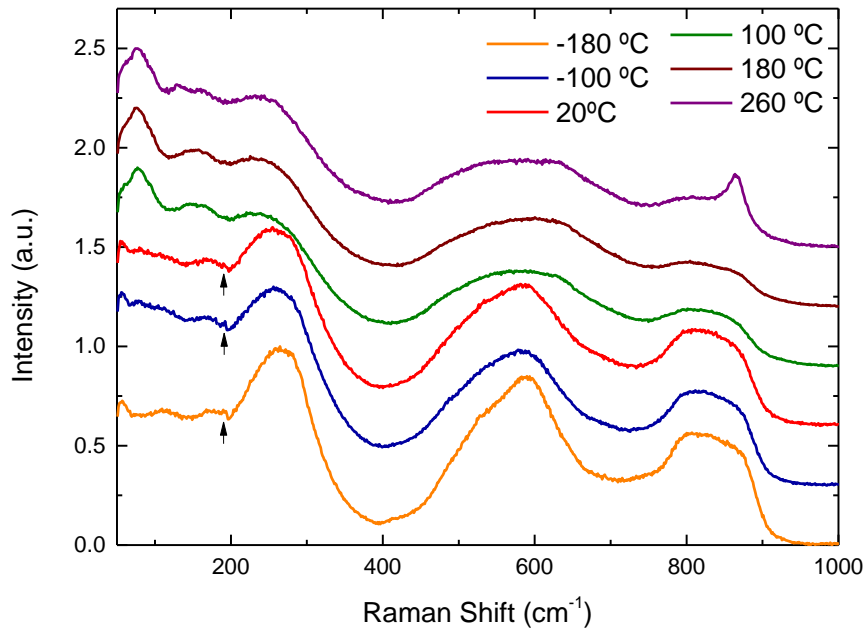


Figure 6. 6: Raman spectra evolution from -100°C to 200°C for KNBM $x=0.15$ ceramic.

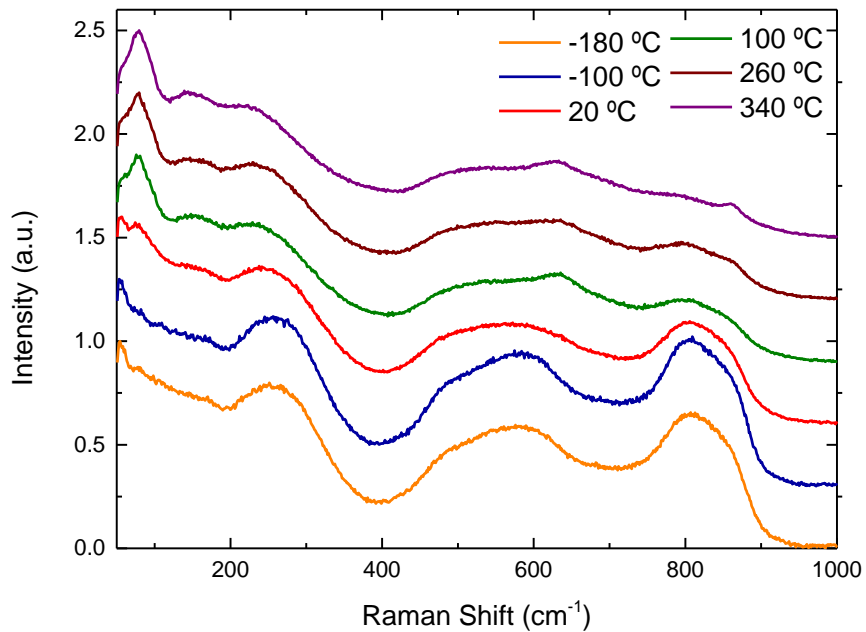


Figure 6. 7: Raman spectra evolution from -100°C to 200°C for KNBM $x=0.25$ ceramic

6.3.3. SEM

Scanning electron microscopy (SEM) images of unpolished surfaces KNBM $0 \leq x \leq 0.25$ ceramics are shown in Figure 6. 8(a-f).

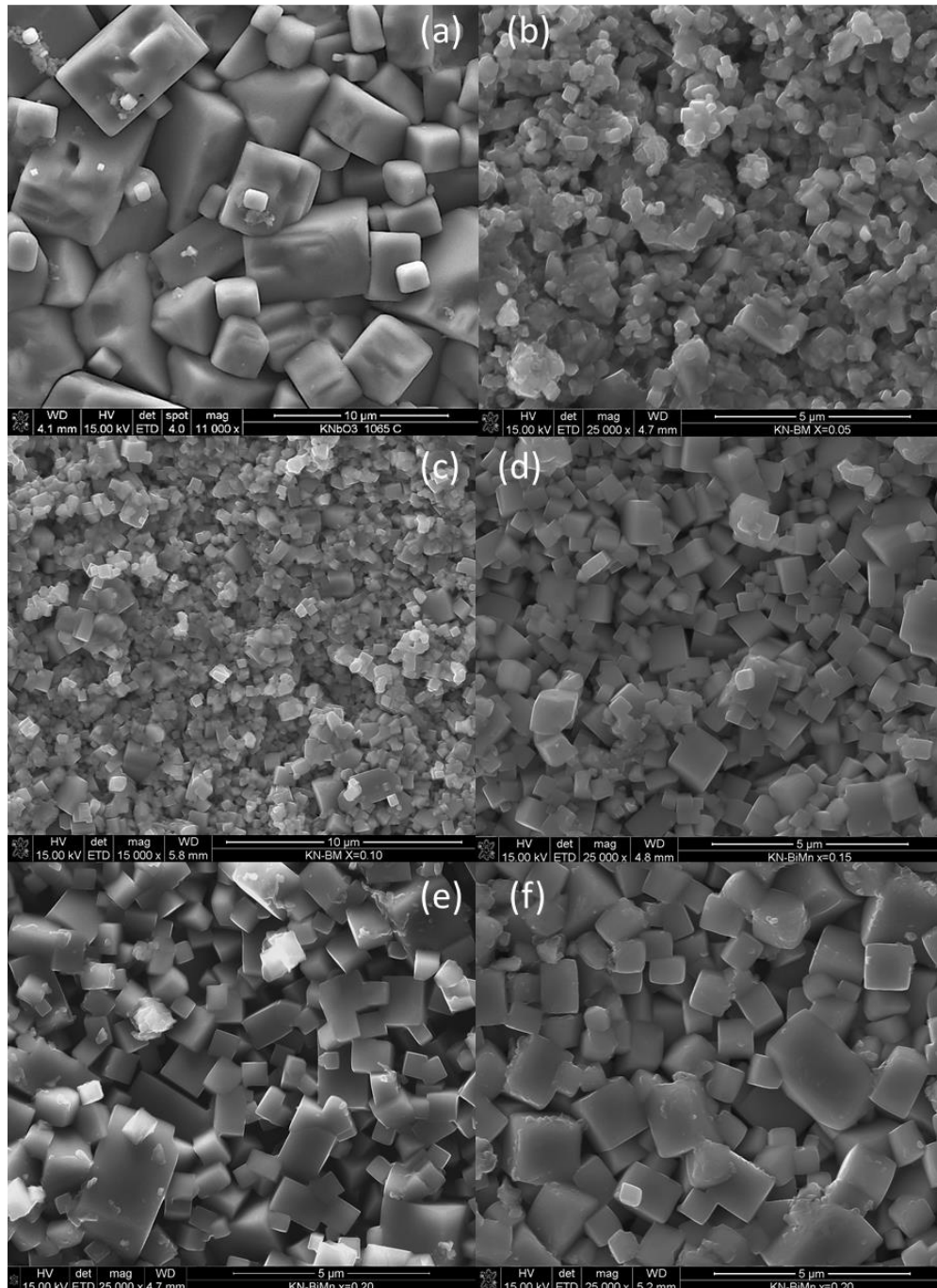


Figure 6. 8.: SEM images of KNBM ceramics with (a) $x=0$, (b) $x=0.05$, (c) $x=0.10$, (d) $x=0.15$, (e) $x=0.20$ and (f) $x=0.25$.

Pure KN ceramics (Figure 6. 8 (a)) exhibit cubic shaped grains. The grain size varies from $3\mu\text{m}$ to $5\mu\text{m}$. A distinctive grain size decrease is observed for $x=0.05$ and $x=0.10$ (Figure

6. 8 a-c). The grain sizes for KNBM $x=0.05$ and $x=0.10$ are in a range between 300 and 500 nm. Grain growth is inhibited upon 5% substitution of Bi^{+3} for K^{+1} in A-site and Mn^{+3} for Nb^{+5} in the B-site. This behaviour has been reported previously in the literature. The microstructures of KNBM $x=0.10$ and $x=0.15$ (Figure 6. 8 c-d) show different grain morphology such as cubic or irregular shape. The grain size for $x=0.15$, $x=0.20$ and $x=0.25$ (Figure 6. 8 d-f) rises continuously reaching 1 μm . This increase is accompanied by the appearance of cubic shaped grains. This phase could be related with the cubic phase ($\text{Pm}\bar{3}\text{m}$) previously described. Important to note, some big grains are detected on KNBM $x=0.10$ and $x=0.15$ surface with different appearance, which will be examined by EDX.

6.3.4. EDX

The chemical composition for KNBM $x=0, 0.05, 0.10, 0.15, 0.20$ and 0.25 ceramics were studied by EDX analysis. Moreover, this study evaluates how homogeneous the distribution of the elements (K, Nb, Bi and Mn) across the samples is. Table 6. 3 and Table 6. 4. shows the experimental and theoretical molar ratios for undoped KN and KNBF $x=0.05$, respectively.

x=0			
	Theoretical	Experimental	Relative Error (%)
K/Nb	1	1.03(3)	3

Table 6. 3.: Experimental (average) and theoretical molar K/Nb, ratio for KNbO_3 ceramic sintered at 1085°C.

x=0.05			
	Theoretical	Experimental	Relative Error (%)
K/Nb	1	1.0 (1)	0
K/Bi	19	7(3)*	63
K/Mn	19	20(9)*	5

Table 6. 4.: Experimental (average) and theoretical molar K/Nb, K/Bi and K/Mn ratios for 0.95 $\text{KNbO}_3 - 0.05 \text{BiMnO}_3$ ceramic sintered at 1070°C.

Experimental K/Bi and K/Mn ratios (indicated with an * in Table 6. 4.) do not reflect the average chemical profile of KNBM. The species are not well homogenised in this

material, as observed in EDX measurements provided in APPENDIX C. Indeed, high value of standard deviation for K/Mn ratio is evidence of the non-homogeneous distribution of Mn in the sample. Table 6. 5 shows EDX results for KNBM $x=0.10$.

$x=0.10$			
	Theoretical	Experimental	Relative Error (%)
K/Nb	1	1.2 (3)	20
K/Bi	9	6(2)	33
K/Mn	9	9(4)	0

Table 6. 5.: Experimental (average) and theoretical molar K/Nb, K/Bi and K/Mn ratios for 0.90 KNbO_3 – 0.10 BiMnO_3 ceramic sintered at 1070°C.

Experimental K/Bi value markedly diverges from the theoretical molar ratio, contrary to K/Nb and K/Mn ratios which are within the error margins. However, high standard deviation for K/Mn suggest difficulties of incorporating Mn. Some big grains with smooth surface can be detected between irregular grain aggregates on KNBM $x=0.10$ surface (Figure 6. 9).

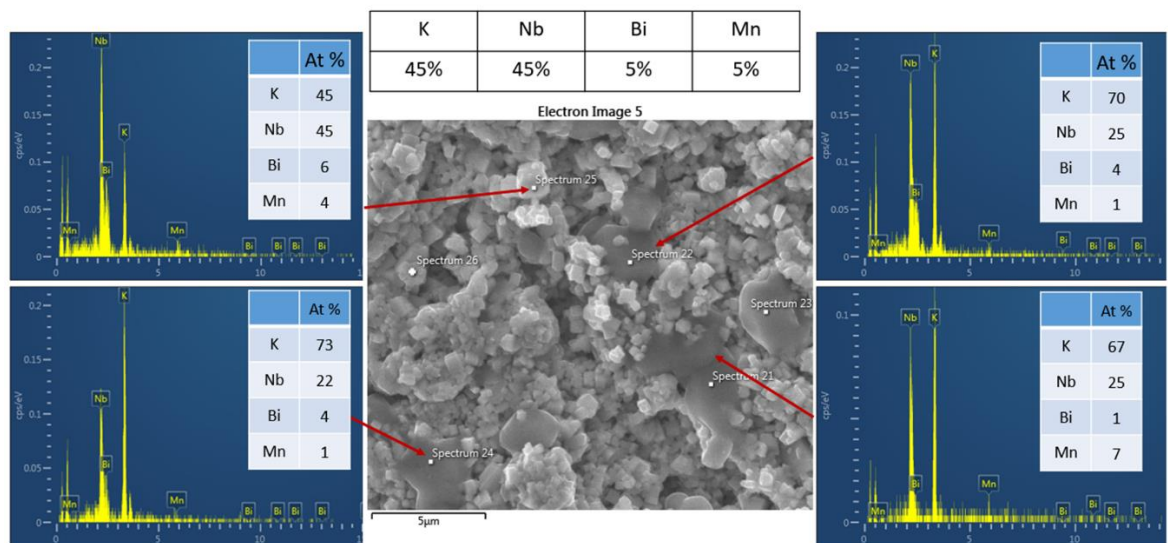


Figure 6. 9.: SEM image and EDX spectra of unpolished 0.90 KNbO_3 – 0.10 BiMnO_3 ceramic sintered at 1070°C reveal also the appearance of grains with high concentration of K and Nb

EDX analysis reveals that these regions are K-rich and Nb, Bi and Mn are detected only in minor quantity. This fact confirms the coexistence of different phases. These large grains can be attributed to a second perovskite with stoichiometry $\sim A_3\text{BO}_9$. Moreover, it is demonstrated that different morphologies are associated with different chemical compositions. Table 6. 6 shows EDX results for KNBM $x=0.15$.

$x=0.15$			
	Theoretical	Experimental	Relative Error (%)
K/Nb	1	1.3 (6)	30
K/Bi	~ 5.67	7(4)	23
K/Mn	~ 5.67	7(3)	23

Table 6. 6.: Experimental (average) and theoretical molar K/Nb, K/Bi and K/Mn ratios for 0.85 $\text{KNbO}_3 - 0.15 \text{BiMnO}_3$ ceramic sintered at 1070°C.

Experimental K/Nb, K/Bi and K/Mn ratios differ from the stoichiometric ratios, particularly K/Bi and K/Mn with a relative error of 23%. The high standard deviation for K/Bi and K/Mn reveals high spreading of the values above and below the mean. In other words, there is not a homogeneous distribution of the elements. Furthermore, the coexistence of two phases is shown in Figure 6. 10.

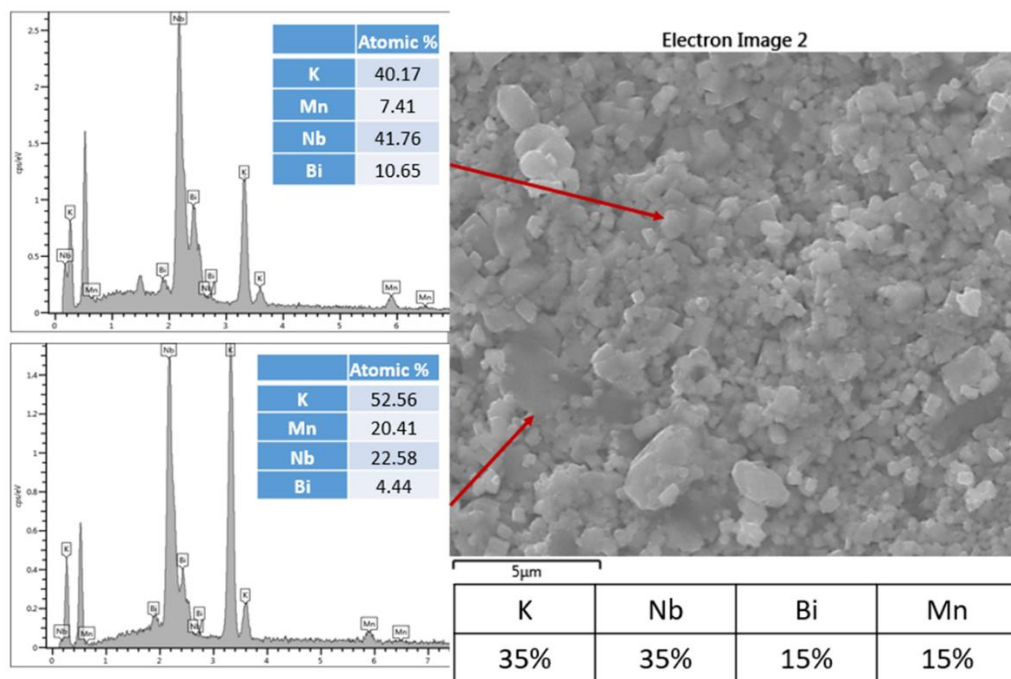


Figure 6. 10.: SEM image and EDX spectra of unpolished 0.85 $\text{KNbO}_3 - 0.15 \text{BiMnO}_3$ ceramic sintered at 1070°C reveal also the appearance of grains with high concentration of K and Nb.

Again, EDX spectroscopy reveals a region that is K-rich and speculatively can be ascribed to a second perovskite with stoichiometry $\sim \text{A}_2\text{B}_3\text{O}_9$. Therefore, the coexistence of two phases is confirmed for KNBM $x=0.15$ as well. Table 6. 7 and Table 6. 8. present EDX results for KNBM $x=0.20$ and $x=0.25$, respectively.

x=0.20			
	Theoretical	Experimental	Relative Error (%)
K/Nb	1	1.0(4)	0
K/Bi	4	4.0(3)	0
K/Mn	4	5.2(5)	30

Table 6. 7: Experimental (average) and theoretical K/Nb, K/Bi and K/Mn ratios for 0.80 $\text{KNbO}_3 - 0.20$ BiMnO_3 ceramic sintered at 1070°C.

x=0.25			
	Theoretical	Experimental	Relative Error (%)
K/Nb	1	0.95(2)	5
K/Bi	3	2.2(1)	27
K/Mn	3	2.8(3)	7

Table 6. 8.: Experimental (average) and theoretical K/Nb, K/Bi and K/Mn ratios for 0.75 $\text{KNbO}_3 - 0.25$ BiMnO_3 ceramic sintered at 1070°C.

For $x=0.20$ and $x=0.25$, experimental K/Nb, K/Bi and K/Mn ratios are closer to the theoretical than the previous compositions described. However, EDX spectroscopy has detected regions composed mainly of undoped KN, Bi-deficient and K-rich areas. Therefore, conventional ceramic processing strongly limits chemical homogenisation of the samples, especially for low concentrations of x .

EDX mapping of K, Nb, Bi and Mn on KNBM $x=0.05$ and $x=0.25$ ceramics are shown in Figure 6. 11 and Figure 6. 12, respectively. Overall, the solutes are more homogeneously diffused in the lattice, for KNBM $x=0.25$ than $x=0.05$. The existence of Mn-rich regions in KNBM $x=0.05$ demonstrates that Mn^{+3} has more difficulties to disperse than Bi^{+3} .

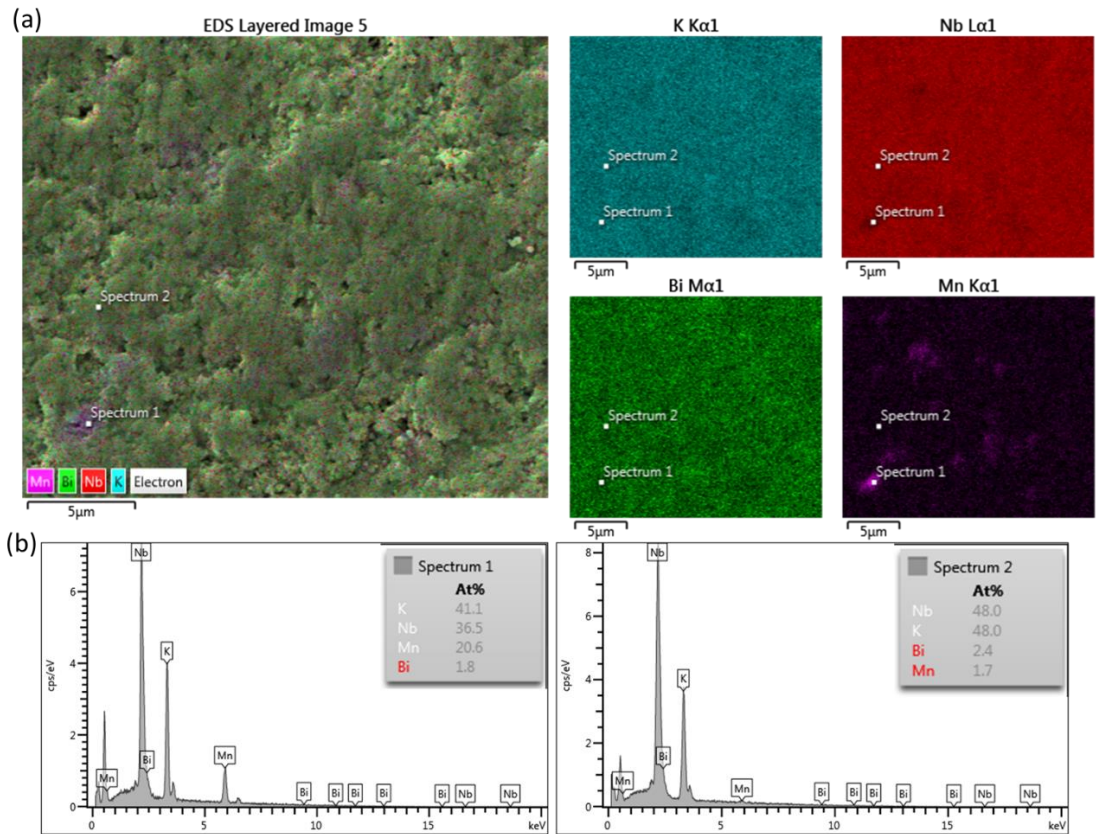


Figure 6. 11: (a) SEM image of the examined region and EDX mapping of K, Nb, Bi and Mn for KNBM $x=0.05$ (b) EDX spectra of Mn-rich region (Spectrum 1) is compared homogeneous region.

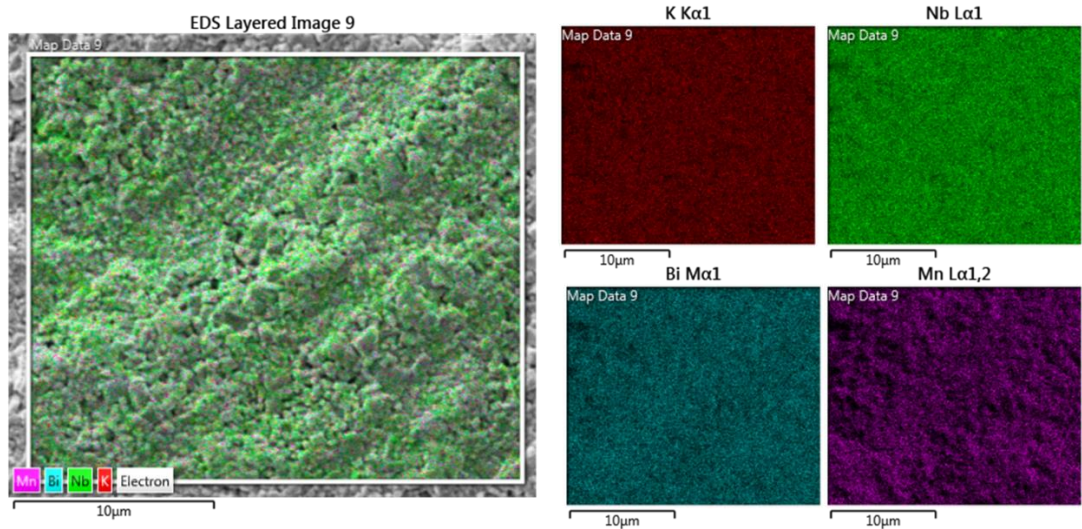


Figure 6. 12: SEM image of the examined region and EDX mapping of K, Nb, Bi and Mn for KNBM $x=0.25$

6.4. Electrical Characterisation

6.4.1. Dielectric Characterisation

Temperature dependence of the permittivity (ϵ_r) and dielectric losses ($\tan\delta$) for KN-BM ceramics ($x= 0.05, 0.10, 0.15, 0.20$ and 0.25) are measured at 10 kHz, 100 kHz and 250 kHz (Figure 6. 13-17). For $x=0.05$ (Figure 6. 13) and for $x=0.10$ (Figure 6. 14.), two broad dielectric anomalies are visible at $\sim 220^\circ\text{C}$ and $\sim 400^\circ\text{C}$, corresponding to orthorhombic-to-tetragonal and tetragonal-to-cubic transitions, respectively. Therefore, this corroborates the presence of an orthorhombic ferroelectric phase. A third anomaly around 100°C emerges in all compositions (indicated with an arrow). At this stage, the origin of this anomaly is unknown, however it can arise from a secondary phase. Interestingly, it is present in $x=0.25$, which according to data in the previous sections appears to be single-phase material.

The temperature for the ϵ_r anomalies remains almost constant, but their magnitude decreases with frequency. Also, frequency dependence is less marked between 100 kHz and 250 kHz. KNBM $x=0.15$ shows a dielectric relaxation which is indicated with an arrow at $\sim 400^\circ\text{C}$ (Figure 6. 15). This is consistent with the 5% of orthorhombic phase calculated for KNBM $x=0.15$ by Rietveld refinement. Compositions for $x\geq 0.20$ only show a dielectric protuberance around 100°C (Figure 6. 16 and Figure 6. 17).

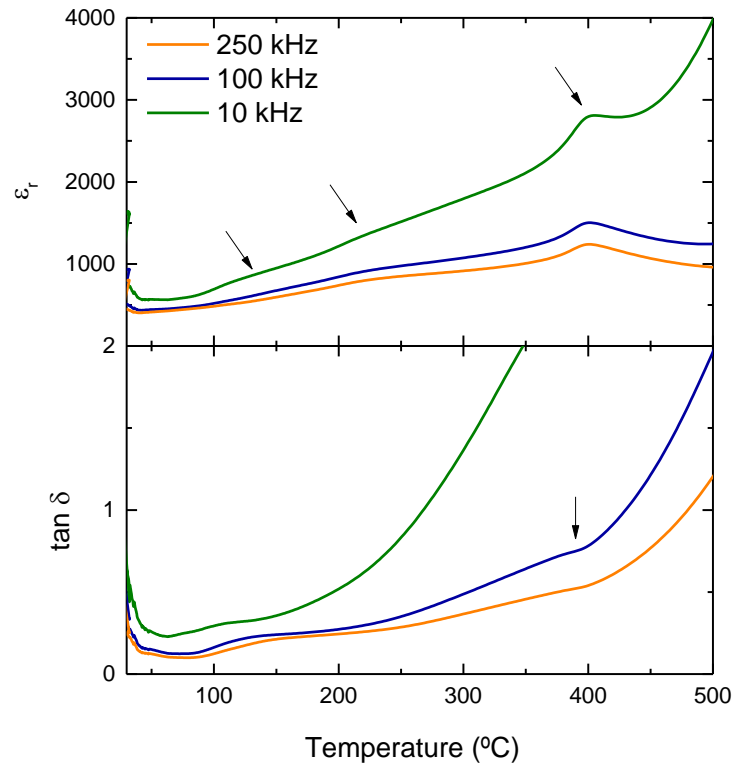


Figure 6. 13.: Temperature dependence of ϵ_r and $\tan \delta$ for 0.95 $\text{KNbO}_3\text{-0.05 BiMnO}_3$ ceramics at 10 kHz, 100 kHz and 250 kHz during cooling.

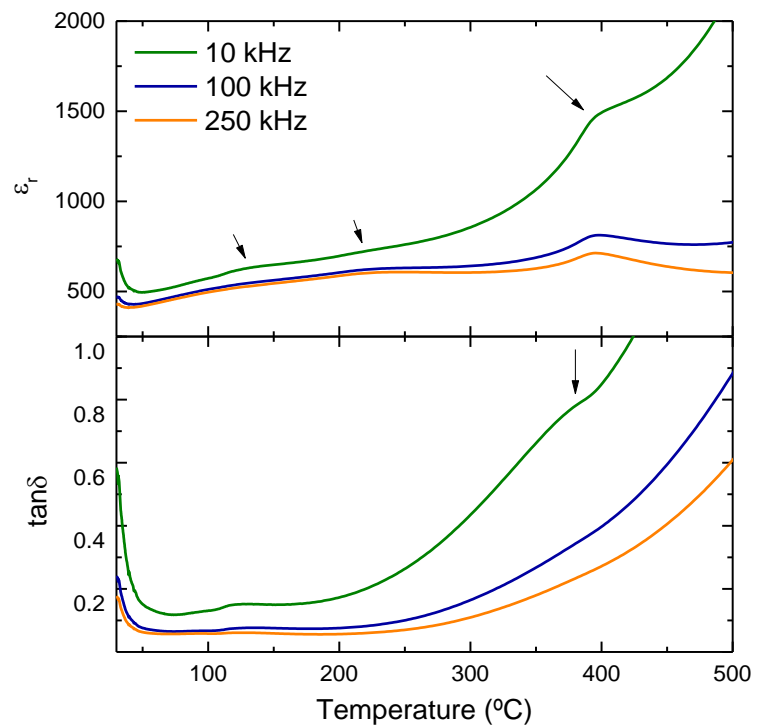


Figure 6. 14.: Temperature dependence of ϵ_r and $\tan \delta$ for 0.90 $\text{KNbO}_3\text{-0.10 BiMnO}_3$ ceramics at 10 kHz, 100 kHz and 250 kHz during cooling.

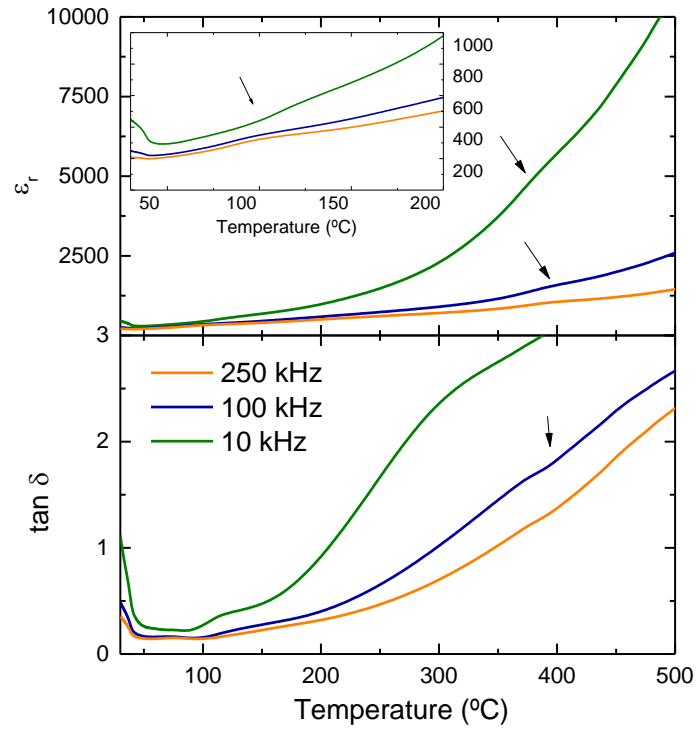


Figure 6. 15.: Temperature dependence of ϵ_r and $\tan \delta$ for 0.85 $\text{KNbO}_3\text{-0.15 BiMnO}_3$ ceramics at 10 kHz, 100 kHz and 250 kHz during cooling.

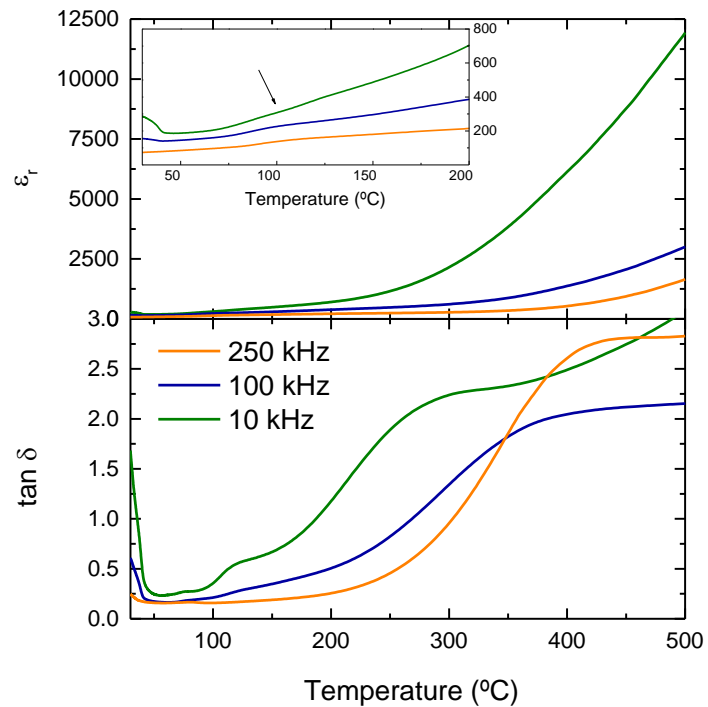


Figure 6. 16.: Temperature dependence of ϵ_r and $\tan \delta$ for 0.80 $\text{KNbO}_3\text{-0.20 BiMnO}_3$ ceramics at 10 kHz, 100 kHz and 250 kHz during cooling.

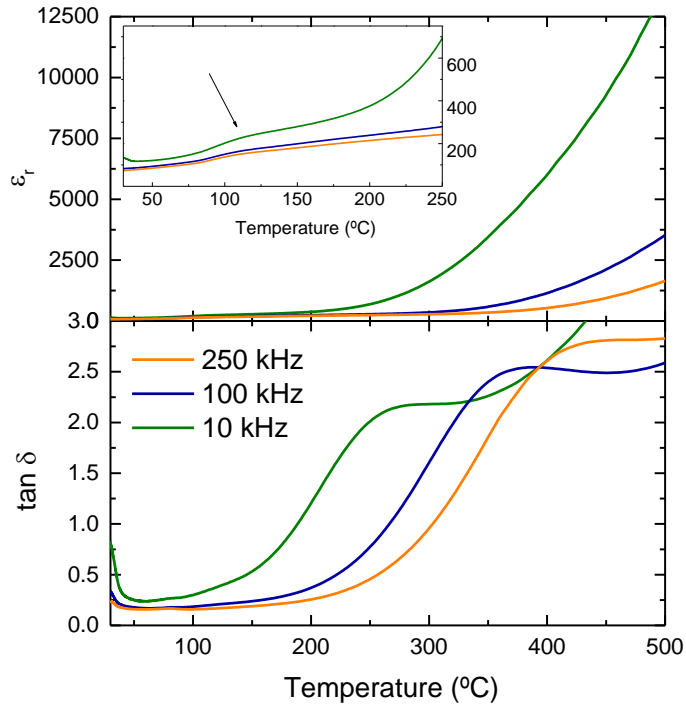


Figure 6. 17.: Temperature dependence of ϵ_r and $\tan\delta$ for $0.75 \text{ KNbO}_3\text{-}0.25 \text{ BiMnO}_3$ ceramics at 10 kHz, 100 kHz and 250 kHz during cooling.

Relative permittivity versus temperature curves at 100 kHz for KNBM $0 \leq x \leq 0.25$ ceramics are compared in Figure 6. 18. Orange curve (pure KN) shows two clear dielectric anomalies at 206°C and 394°C , these anomalies are still visible for $x=0.05$ and $x=0.10$, but less intense and at lower temperature. For $x=0.15$, a bump (indicated with an arrow in Figure 6. 15) is noticed at $\sim 400^\circ\text{C}$ in the dielectric curve. This demonstrates the presence of an orthorhombic phase in KNBM $x=0.05$, $x=0.10$ and $x=0.15$ observed and also described in XRD, SEM and Raman results. KNBM $x=0.20$ and $x=0.25$ show only one anomaly at 100°C .

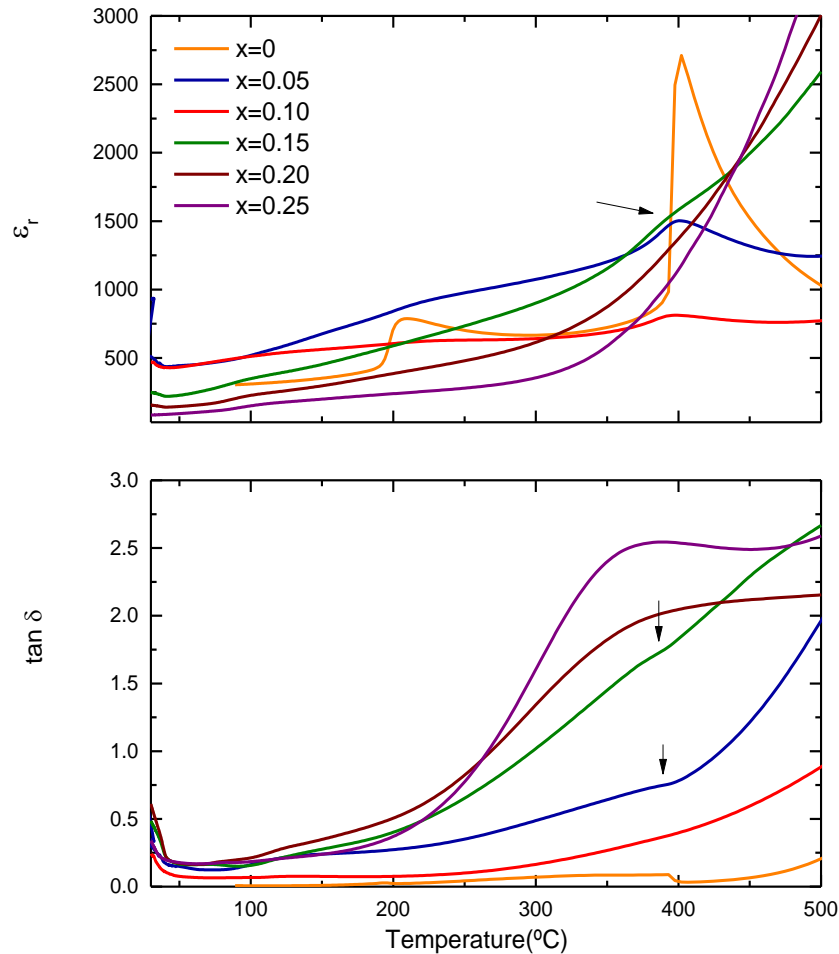


Figure 6. 18.: Temperature dependence of ϵ_r and $\tan\delta$ for KNBM $0 \leq x \leq 0.25$ ceramics at 100kHz

The dielectric losses of doped compositions are higher than for undoped KN. KNBM ceramics become more conductive with the increase of x (apart from the case of KNBM $x=0.10$, explained before). This behaviour could be directly related with the band-gap narrowing, as discussed later.

6.5. Optical Characterisation

6.5.1 Diffuse reflectance spectroscopy

Diffuse reflectance spectroscopy was carried out in the range of 200 - 1400 nm. Band-gaps are obtained from the intersection of the tangent line in the plot of $[h\nu F(R)]^n$ with

the x-axis, $F(R)$, being the Kubelka-Munk function and R , the diffuse reflectance data (Figure 6. 19.). The n value determines the kind of transition, $n=2$ is used to plot direct band gaps and $n=1/2$ for indirect band gaps. In this study, both direct and indirect band-gaps are considered because it is difficult to determine the nature of KNBM band-gap from the Tauc plot.

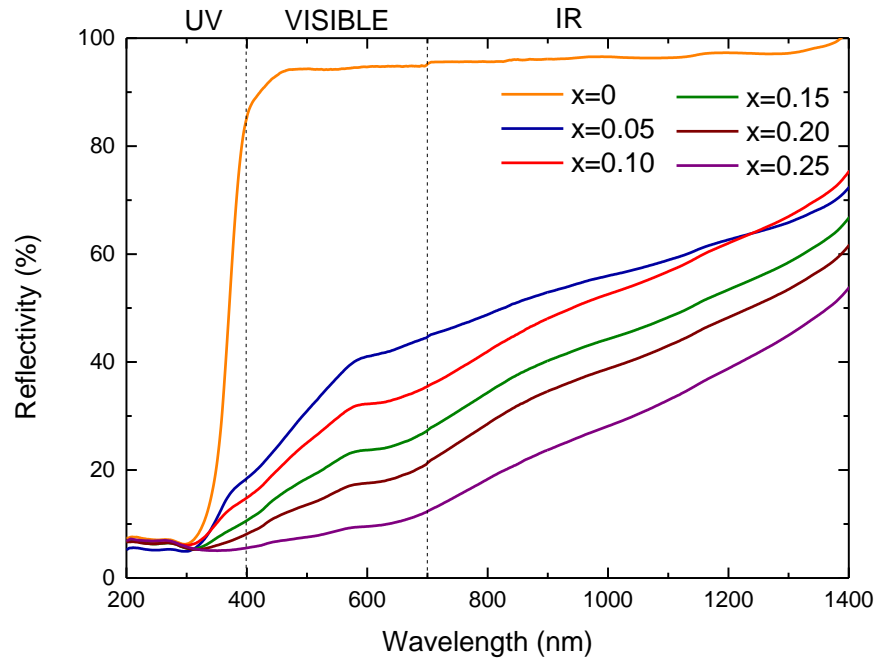


Figure 6. 19.: Diffuse reflectance as a function of wavelength for KNBM system (raw data).

The Tauc plot of KNBM $0 \leq x \leq 0.25$ ceramics is constructed for $n=2$ (direct band-gap) in Figure 6. 20. Band-gaps narrow systematically from 3.66 eV ($x=0$) to 2.44 eV ($x=0.25$). A shoulder (indicated with 1 in Figure 6. 20.) is observed for KNBM with $x \geq 0.15$ around 2.8 eV and its magnitude increases with increasing x . Purple curve (KNBM $x=0.25$) shows two extra features at ~ 2 eV and ~ 2.25 eV (indicated with arrows).

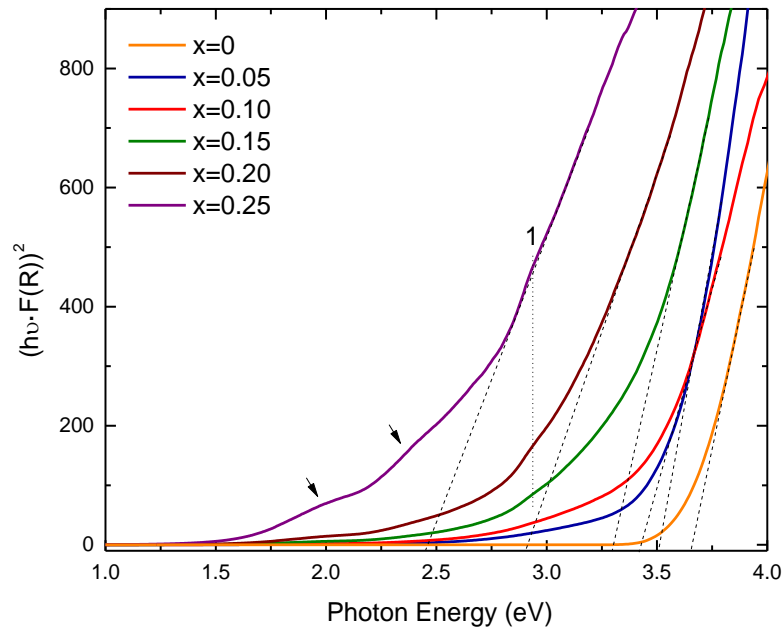


Figure 6. 20.: Tauc plot for direct band gaps for KNBM $0 \leq x \leq 0.25$ ceramics.

The Tauc plot of KNBM ceramics constructed for $n=1/2$ (indirect band-gap) is shown in Figure 6. 21. In this case, it is difficult to determine the band-gap. With the increase of x , band- gaps narrow from 3.22 eV ($x=0$) to 1.29 eV ($x=0.25$). Three broad shoulders (indicated with 1, 2 and 3 in Figure 6. 21.) are present in all doped compositions at ~ 1.8 eV, ~ 2.4 eV and ~ 2.8 eV. These modes are clearer for higher concentrations of x .

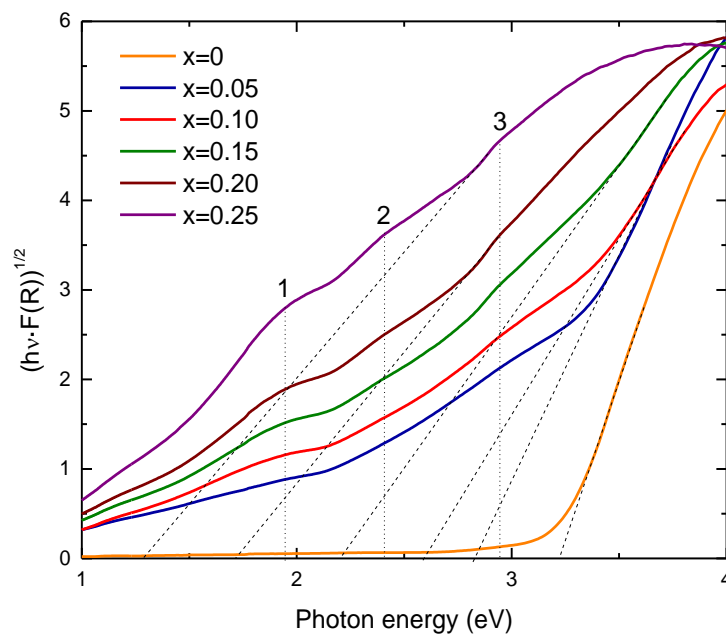


Figure 6. 21.: Tauc plot for indirect band gaps for KNBM $0 \leq x \leq 0.25$ ceramics.

Figure 6. 22 shows direct and indirect band-gap values as a function of x . Both follow the same trend, band-gaps narrow systemically with the increase of x .

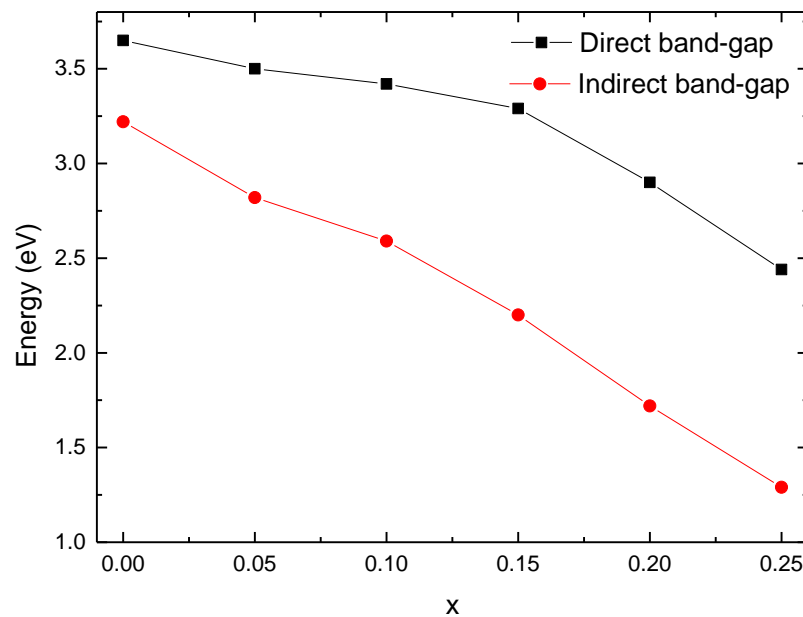


Figure 6. 22.: Dependence of direct and indirect band gap with x for KNBM $0 \leq x \leq 0.25$ ceramics

6.6. Discussion

Room temperature XRD data of KNBM ($0 \leq x \leq 0.25$) ceramics (Figure 6. 2) show a phase transition from orthorhombic ($x=0$) to pseudocubic ($x=0.25$). All reflections of doped compositions shift continuously towards lower angles, indicating an increase of the unit cell volume with increasing x . The presence of a reflection at $\sim 78^\circ 2\theta$ (Figure 6. 2(b)) suggests the coexistence of two phases in KNBM $0.05 \leq x \leq 0.15$ ceramics, an orthorhombic KN-based phase (space group $\text{Amm}2$) and a cubic phase (space group $\text{Pm-}3\text{m}$). This reflection remains at $\sim 78^\circ 2\theta$ and its intensity decreases with x , therefore the relative volume of this phase falls systematically until it disappears at $x=0.20$. Rietveld refinement calculated a concentration of 23% of the orthorhombic phase in KNBM $x=0.05$ which drops to 5% in KNBM $x=0.15$. Raman spectroscopy, SEM images and dielectric characterisation support the hypothesis of coexistence of these two phases.

First, the existence of a polar orthorhombic KN-based phase in KNBM $0 \leq x \leq 0.15$ ceramics is supported by the presence of the sharp Raman mode centred at 192 cm^{-1} in Raman spectra (Figure 6. 5). This peak becomes less intense with the increase of x and

disappears in KNBM $x=0.20$ spectra, following the same trend described for XRD patterns. Indeed, this is also consistent with the Rietveld refinements results, which calculate a drop of the orthorhombic phase, from 23% ($x=0$) to 5% ($x=0.15$).

Second, SEM images of KNBM $x=0.10$ clearly show two different morphologies: some big grains with smooth surface stand out in a small cubic grains agglomerate (Figure 6. 8). EDX analyses reveals a K-rich concentration in these regions. Overall, significant decrease of the grain size is observed on SEM images, from $3\mu\text{m}$ ($x=0$) to 300 nm ($x=0.10$). Then, the grain size increases until it reaches $1\mu\text{m}$ ($x=0.25$). KNBM ceramics look well densified and the grains are cubic shaped.

Finally, the coexistence of these two phases is also corroborated by the appearance of three broad dielectric anomalies as a function of temperature in KNBM $0\leq x\leq 0.15$ ceramics (Figure 6. 13-15). Two anomalies are attributed to the orthorhombic-to-tetragonal at $\sim 220\text{ }^\circ\text{C}$ and the tetragonal-to-cubic at $\sim 400\text{ }^\circ\text{C}$ phase transition of the orthorhombic KN-based phase, where the solutes Bi^{+3} and Mn^{+3} are not incorporated. Indeed, the ferroelectric-to-paraelectric transition ($\sim 400\text{ }^\circ\text{C}$) confirms the polar nature of the KN-based phase in KNBM $0\leq x\leq 0.15$. The third anomaly around $100\text{ }^\circ\text{C}$ maybe associated to the pseudocubic phase. In 2011, Luisman et al observed a frequency dependent broad anomaly in $\text{KNbO}_3\text{-BiYbO}_3$ ceramics with an average pseudocubic structure.

From reflectivity data, direct band-gap values of KNBM system continuously narrow from 3.66 eV ($x=0$) to 2.44 eV ($x=0.25$). On the other hand, indirect band-gaps decrease from 3.22 eV ($x=0$) to 1.29 eV ($x=0.25$). However, there are not enough signs to identify the nature of KNBM band-gaps.

6.7. Conclusions

The co-solubility of Bi and Mn into the orthorhombic phase of KN is limited to less than 5% mol. Ceramics in the $0\leq x\leq 0.15$ region were refined as a combination of orthorhombic and pseudocubic phases. For $x\geq 0.20$, XRD suggests a cubic structure for KNBM ceramics, but Raman shows that their local structure is non-cubic. Direct band-gaps

varying from 3.66 eV down to 2.44 eV and indirect band-gaps from 3.22 eV to 1.29 eV, are estimated from reflectivity data.

6.8. References

- Atou, T., Chiba, H., Ohoyama, K., Yamaguchi, Y., & Syono, Y. (1999). Structure determination of ferromagnetic perovskite BiMnO_3 . *Journal of Solid State Chemistry*, 145(2).
- Baettig, P., Seshadri, R., & Spaldin, N. A. (2007). Anti-polarity in ideal BiMnO_3 . *Journal of the American Chemical Society*, 129(32). <https://doi.org/10.1021/ja073415u>
- Belik, A. A. (2012). Polar and nonpolar phases of BiMO_3 : A review. *Journal of Solid State Chemistry*, 195, 32–40. <https://doi.org/10.1016/j.jssc.2012.01.025>
- Belik, A. A., Iikubo, S., Yokosawa, T., Kodama, K., Igawa, N., Shamoto, S., ... Takayama-Muromachi, E. (2007). Origin of the monoclinic-to-monoclinic phase transition and evidence for the centrosymmetric crystal structure of BiMnO_3 . *Journal of the American Chemical Society*, 129(4). <https://doi.org/10.1021/ja0664032>
- Chi, Z. H., Yang, H., Feng, S. M., Li, F. Y., Yu, R. C., & Jin, C. Q. (2007). Room-temperature ferroelectric polarization in multiferroic BiMnO_3 . *Journal of Magnetism and Magnetic Materials*, 310. <https://doi.org/10.1016/j.jmmm.2006.10.335>
- Luisman, L., Feteira, A., & Reichmann, K. (2011). Weak-relaxor behaviour in Bi/Yb-doped KNbO_3 ceramics. *Applied Physics Letters*, 99(19). <https://doi.org/10.1063/1.3660255>
- McLeod, J. A., Pchelkina, Z. V., Finkelstein, L. D., Kurmaev, E. Z., Wilks, R. G., Moewes, A., ... Takayama-Muromachi, E. (2010). Electronic structure of BiMnO_3 multiferroics and related oxides. *Physical Review B - Condensed Matter and Materials Physics*, 81(14), 1–10. <https://doi.org/10.1103/PhysRevB.81.144103>
- Montanari, E., Righi, L., Calestani, G., Migliori, A., Gilioli, E., & Bolzoni, F. (2005). Room temperature polymorphism in metastable BiMnO_3 prepared by high-pressure synthesis. *Chemistry of Materials*, 17(7). <https://doi.org/10.1021/cm048250s>

- Moreira dos Santos, A., Cheetham, A. K., Atou, T., Syono, Y., Yamaguchi, Y., Ohoyama, K., ... Rao, C. N. R. (2002). Orbital ordering as the determinant for ferromagnetism in biferroic BiMnO_3 . *Physical Review B - Condensed Matter and Materials Physics*, 66(6). <https://doi.org/10.1103/PhysRevB.66.064425>
- Sugawara, F., Iiida, S., Syono, Y., & Akimoto, S.-I. (1968). Magnetic properties and crystal distortions of BiMnO_3 and BiCrO_3 . *Journal of the Physical Society of Japan*, 25(6). <https://doi.org/10.1143/JPSJ.25.1553>
- Toulemonde, P., Darie, C., Goujon, C., Legendre, M., Mendonca, T., Alvarez-Murga, M., ... Mezouar, M. (2009). Single crystal growth of BiMnO_3 under high pressure-high temperature. *High Pressure Research*, 29(4). <https://doi.org/10.1080/08957950903467050>
- Yang, H., Chi, Z. H., Jiang, J. L., Feng, W. J., Cao, Z. E., Xian, T., ... Yu, R. C. (2008). Centrosymmetric crystal structure of BiMnO_3 studied by transmission electron microscopy and theoretical simulations. *Journal of Alloys and Compounds*, 461(1–2). <https://doi.org/10.1016/j.jallcom.2007.06.085>

Chapter 7

System (1-x) KNbO₃- x BiCoO₃

7.1. Introduction

7.2. Structural and chemical characterisation

7.2.1. Purity and X-ray powder diffraction

7.2.2. Raman spectroscopy

7.2.3. SEM

7.2.4. EDX

7.3. Electrical Characterisation

7.3.1. Dielectric Characterisation

7.4. Optical Characterisation

7.4.1 Diffuse reflectance

7.5. Discussion

7.6. Conclusions

7.7. References

7. System (1-x) $\text{KNbO}_3\text{-x BiCoO}_3$

7.1. Introduction

This chapter addresses the synthesis and characterisation of powders and ceramics from the binary system (1-x) $\text{KNbO}_3\text{-x BiCoO}_3$ (KNBC) with $x=0, 0.05, 0.10, 0.15, 0.20$ and 0.25 . First, KNBC ceramics were prepared by conventional route and were characterised in terms of crystal structure (XRD and Raman spectroscopy) and chemical homogeneity (EDX). Then, the impact of different quantities of Bi^{+3} and Co^{+3} into KN lattice was examined by the evolution of dielectric and optical properties. Ferro- and piezoelectric characterisation was not performed because of the high conductivity and low density of the samples. Indeed, difficulties in dielectric measurements were encountered and detailed below.

BiCoO_3 is a polar compound (P4mm space group) similar to well-known FE materials, such as BaTiO_3 and PbTiO_3 (Izyumskaya, Alivov, & Morkoç, 2009). Theoretically, BiCoO_3 exhibits antiferromagnetic ordering as well as giant ferroelectric polarization. First principles calculations for BiCoO_3 gave a P_s value as high as $170\text{--}179 \mu\text{C}/\text{cm}^2$ (Oguchi, 2005; Ravindran, Vidya, Eriksson, & Fjellvåg, 2008). However, polarisation switching of BiCoO_3 has not yet been demonstrated experimentally. The number of experimental investigations on BiCoO_3 (Oka et al., 2010; Sudayama et al., 2011) is still rather small compared with the number of theoretical works, probably because of preparation difficulties that require high pressure conditions, 6 GPa (Belik et al., 2006). Finally, a band-gap of 1.7 eV was measured for BiCoO_3 by X-Ray absorption spectra XAS (McLeod et al., 2010).

7.2. Structural and chemical characterisation

7.2.1. Purity and X-ray powder diffraction

KNBC ($x=0, 0.05, 0.10, 0.15, 0.20$ and 0.25) powders were prepared by the solid-state reaction route. Required amounts of K_2CO_3 , Nb_2O_5 , Bi_2O_3 and Co_3O_4 were mixed for 24 hours, then dried and the resulting powder was sieved. This powder was calcined twice in air at 850°C for 4 hours using a heating rate of $3^\circ\text{C}/\text{min}$. XRD patterns of KNBC ($0 \leq x \leq 0.25$) calcined powders are shown in Figure 7. 1.

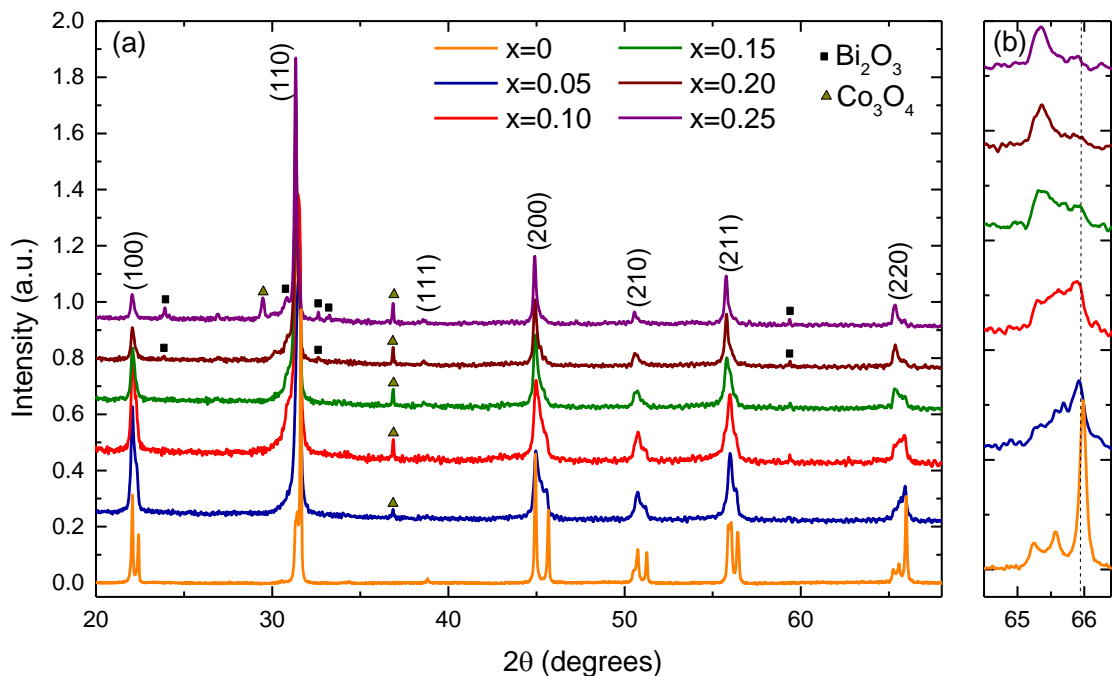


Figure 7. 1: Room-temperature X-Ray diffraction data of KNBC ($0 \leq x \leq 0.25$) powders. Secondary phases are identified as Bi_2O_3 (black square) and Co_3O_4 (yellow triangle). Probably, some pure KN remains in all compositions (black dash line).

Main reflections can be assigned to the perovskite structure, indicating that the most of starting oxides reacted to form KNBC ($x=0, 0.05, 0.10, 0.15, 0.20$ and 0.25). Nevertheless, some unreacted Bi_2O_3 (black square) and Co_3O_4 (yellow triangle) are detected. The appearance of these phases is more accentuated for compositions with higher x values. Doped compounds exhibit broader peaks in comparison with pure KN ($x=0$), which makes the assignment of the corresponding crystal structure difficult. A

closer inspection shows nearly undoped KN to be formed in all compositions, as indicated the dashed black line (Figure 7. 1).

Pellets were fired in air for 4 hours at 1090 °C using a controlled heating rate of 3 °C/min. Figure 7. 2 shows XRD data of KNBC ($0 \leq x \leq 0.25$) sintered ceramics.

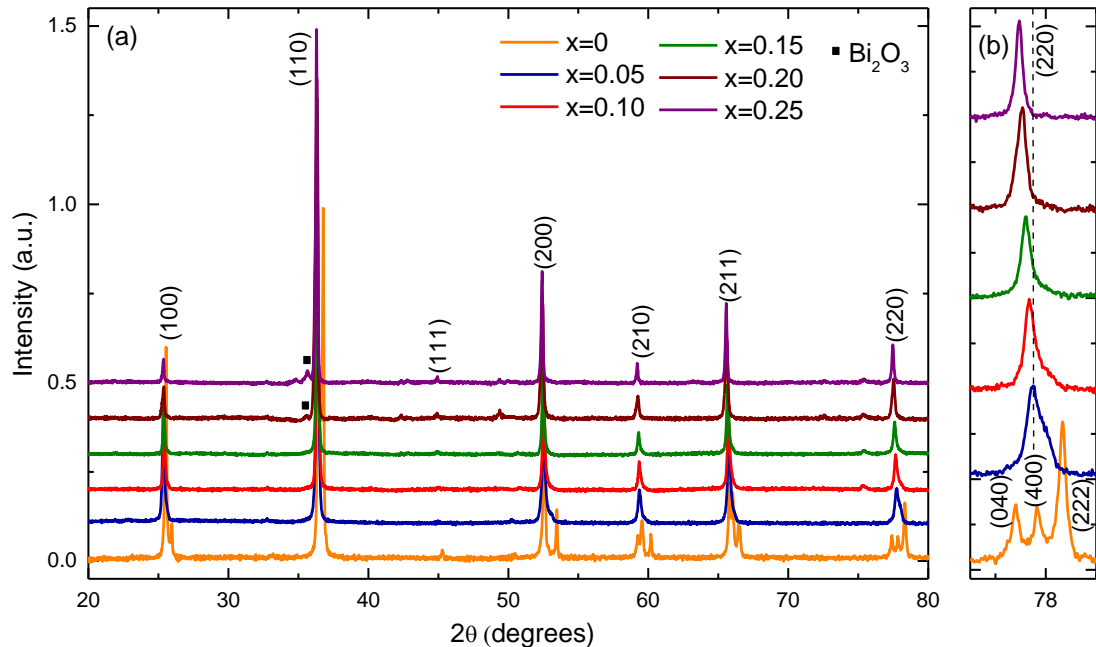


Figure 7. 2: Room temperature XRD patterns for KNBC ($x=0, 0.05, 0.10, 0.15, 0.20$ and 0.25) ceramics sintered at 1080-1090°C. Black squares indicate secondary phase of Bi_2O_3 . The attached graph on the right illustrates how the triplet for $x=0$ evolves to a single peak for $x=0.25$.

Sharp peaks and reduction of secondary phases confirm both a higher degree of crystallisation and enhanced purity for KNBC ceramics in comparison with powders. However, a small amount of Bi_2O_3 is still present in KNBC $x=0.20$ and $x=0.25$ ceramics. A continuous shift of the XRD peaks towards lower 2θ angles indicates an increase of the unit cell size with the increase of BiCoO_3 content.

Figure 7. 2 (b) shows in detail the XRD patterns from 75° to 80° 2θ with increasing x . For $x=0$, a triplet is observed corresponding to (040), (400) and (222) Miller indices for the orthorhombic symmetry. For the rest of compositions, a single peak is perceptible within the resolution of the measurement. This single peak is accompanied by a remarkable shoulder in $x=0.05$ which also appears in $x=0.10$ pattern but is less intense. For $0.15 \leq x \leq 0.25$ compositions, a sharp peak is observed which could be attributed to (220) Miller index for the cubic symmetry. However, the assignment of the phases for this system was ambiguous, due to the resolution of the measurements. Complete

characterisation of these compounds will help to determine the crystal structure evolution with increasing $\text{Bi}^{+3}/\text{Co}^{+3}$. The refinement of the XRD patterns by Rietveld method provides information about the space group, lattice parameters and theoretical density of KNBC ceramics (Table 7. 1 and Table 7. 2). Experimental and relative density are added in the tables.

	x=0	x=0.05		x=0.10
Space Group	Amm2	8.1 (6) % Amm2	91.9(2)% Pm- $\bar{3}$ m	Pm- $\bar{3}$ m
Density (Experimental) (g/cm³)	4.35(3)	4.19(17)		4.21(22)
Density (calculated) (g/cm³)	4.6273(1)	4.7960(2)*		4.9436(4)
Relative Density (%)	94(1)	87(1)*		85(2)
a (Å)	3.9711(1)	3.9868(4)	4.0150(1)	4.0211(2)
b (Å)	5.6909(1)	5.6829(7)	4.0150(1)	4.0211(2)
c (Å)	5.7158(1)	5.7080(1)	4.0150(1)	4.0211(2)
V/10⁶ (pm³)	64.576(2)	64.723(3)	64.66(2)	65.02(1)
R_{exp}	1.26460	1.21332		1.3220
R_p	2.97912	2.56084		4.1034
R_{wp}	4.65175	3.17835		5.83102
GOF	13.53086	6.8620		19.4552

Table 7. 1: Experimental and theoretical density, lattice parameters and agreement indices calculated by Rietveld Refinement for KNBC (x=0, 0.05 and 0.10). *Weighed average for the phases.

	x=0.15	x=0.2	x=0.25
Space Group	Pm- $\bar{3}$ m	Pm- $\bar{3}$ m	Pm- $\bar{3}$ m
Density (Experimental) (g/cm³)	4.26(7)	4.25(20)	4.18(10)
Density (calculated) (g/cm³)	5.4590(2)	5.2651(4)	5.4269(2)
Relative Density (%)	78(2)	81(4)	77(2)
a (Å)	4.0245(1)	4.0276(2)	4.0304(1)
b (Å)	4.0245(1)	4.0276(2)	4.0304(1)
c (Å)	4.0245(1)	4.0276(2)	4.0304(1)
V/10⁶ (pm³)	65.183 (2)	65.333(5)	65.465 (3)
R_{exp}	1.30162	1.26475	1.26090
R_p	3.32856	4.35045	3.01453
R_{wp}	4.94895	6.57066	4.73736
GOF	14.45641	26.9903	14.1159

Table 7. 2: Experimental and theoretical density, lattice parameters and agreement indices calculated by Rietveld Refinement for KNBC (x=0.15, 0.20 and 0.25).

Low relative density values (below 90%) for all KNBC ceramics were obtained. This fact could be related to the unsuccessful densification of BiCoO_3 ceramics at ambient conditions (Belik et al., 2006). KNBC x=0.05 is reasonably refined as a combination of orthorhombic phase (space group $\text{Amm}2$) and cubic phase (space group $\text{Pm-}\bar{3}\text{m}$) as shown in Figure E.2 (Appendix E). XRD patterns for x=0.10, x=0.15, x=0.20 and x=0.25 can be ascribed as cubic phase ($\text{Pm-}\bar{3}\text{m}$). However, there is evidence which suggests these compositions are neither single phase nor truly cubic, as will be explained below. However, a linear relation between unit cell volume and x is obtained (Figure 7. 3).

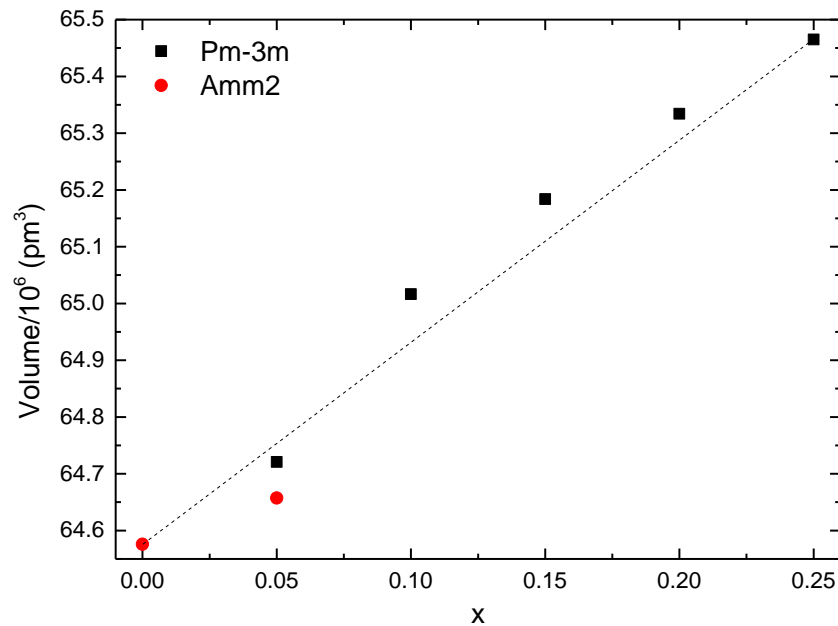


Figure 7. 3: Evolution of the unit cell volume with x for KNBC ($0 \leq x \leq 0.25$) ceramics.

Overall, the unit cell volume increases linearly with x. This fact indicates there is a systematic incorporation of Bi^{+3} and Co^{+3} into KNbO_3 structure. Probably, there is coexistence of phases in the intermediary concentrations, but X'Pert software was not able to fit two phases.

7.2.2. Raman spectroscopy

Room-temperature Raman spectra for KNBC ($0 \leq x \leq 0.25$) powders are illustrated in Figure 7. 4. All KNBC powders present similar Raman spectra. Main features reported for KN (orange pattern) are found in the other spectra (bold dashed line). However, these modes seem to be wider and slightly displaced to lower wavenumbers (by $\sim 11 \text{ cm}^{-1}$). New modes arise for high concentrations of $\text{Bi}^{+3}/\text{Co}^{+3}$ and labelled as 1, 2 and 3. In addition, small bumps pointed with '*' could be interpreted as impurities. The sharp mode at 192 cm^{-1} discloses the polar ordering in KN compounds. This mode is detected in all KNBC powders spectra, which supports the hypothesis proposed in the XRD section about the presence of nearly pure orthorhombic KN, which reveals chemical inhomogeneities in KNBC powders. Room-temperature Raman spectra for KNBC ($0 \leq x \leq 0.25$) ceramics sintered 1090°C are examined in Figure 7. 4 and Figure 7. 5.

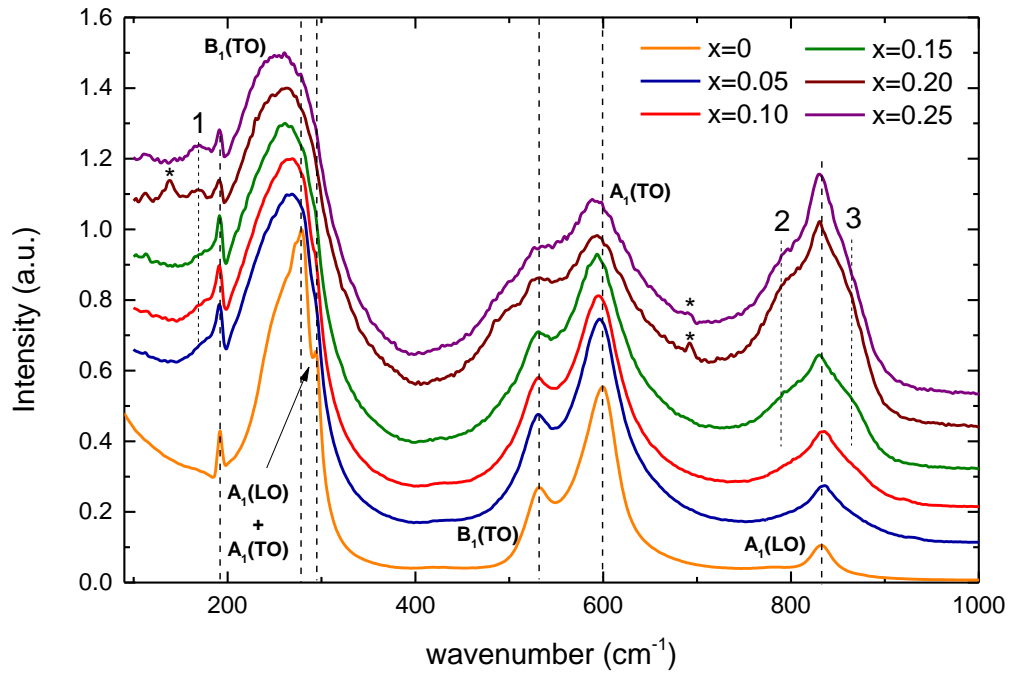


Figure 7. 4: Room-temperature Raman spectra for KNBC ($0 \leq x \leq 0.25$) powders calcined at 850°C two times. New modes (1, 2 and 3) emerge in KNBM ($x \geq 0.05$) powders. Small modes indicated with '*' can be associated with local impurities.

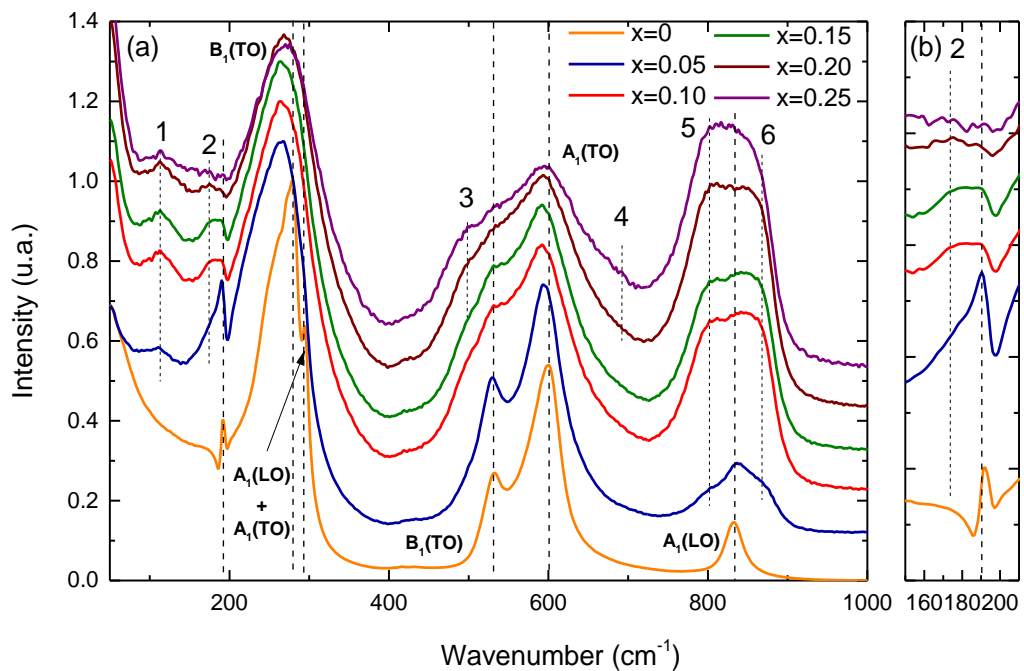


Figure 7. 5: (a) Room-temperature Raman spectra for KNBC ($0 \leq x \leq 0.25$) ceramics sintered at $1080\text{-}1090^\circ\text{C}$. New modes (1, 2, 3, 4, 5 and 6) emerge in KNBC ($x \geq 0.05$) pellets spectra. (b) Attached graph shows the monitoring of mixed sharp mode at 192 cm^{-1} .

Raman spectra for KNBC ($0 \leq x \leq 0.25$) ceramics show some differences in comparison with powder spectra. New arising modes are labelled as 1, 2, 3, 4, 5, and 6. Mode 1 and

2, also visible in the powders, appear at 114 cm^{-1} and 174 cm^{-1} (as a shoulder of the mixed peak centred at 192 cm^{-1}). Both modes keep their position constant. The intensities of mode 1 is practically equal for all compositions, in contrast, the intensity of mode 2 seems to reach a maximum for $x=0.10$ and 0.15 and then gradually decreases. These modes appear in all the systems investigated in this work, and are attributed to A-O vibrations within nm-sized clusters rich in either Bi^{3+} and/or K^+ cations. The absence of the sharp mixed peak at 192 cm^{-1} and the interference dip at 197 cm^{-1} support the cubic symmetry assigned for $x=0.20$ and $x=0.25$ in the XRD analysis section. Evidence of the coexistence of orthorhombic phase (polar phase) and cubic phase (nonpolar phase) for intermediary concentrations is shown in Figure 7. 5 (b). The sharp mode can be intuited up to $x=0.20$ and its intensity decreases with x . The polar phase may be only in traces for $x=0.10$ and $x=0.15$, because it was not detected by XRD. Modes 3 and 4 appear at $\sim 500\text{ cm}^{-1}$ and $\sim 700\text{ cm}^{-1}$ only for $x=0.20$ and $x=0.25$. Finally, the intensity of mode 5 ($\sim 800\text{ cm}^{-1}$) and mode 6 ($\sim 870\text{ cm}^{-1}$) considerably increases with increasing x .

7.2.3. SEM

SEM images of unpolished KNBC ($0 \leq x \leq 0.25$) ceramics are shown in Figure 7. 6 (a-f).

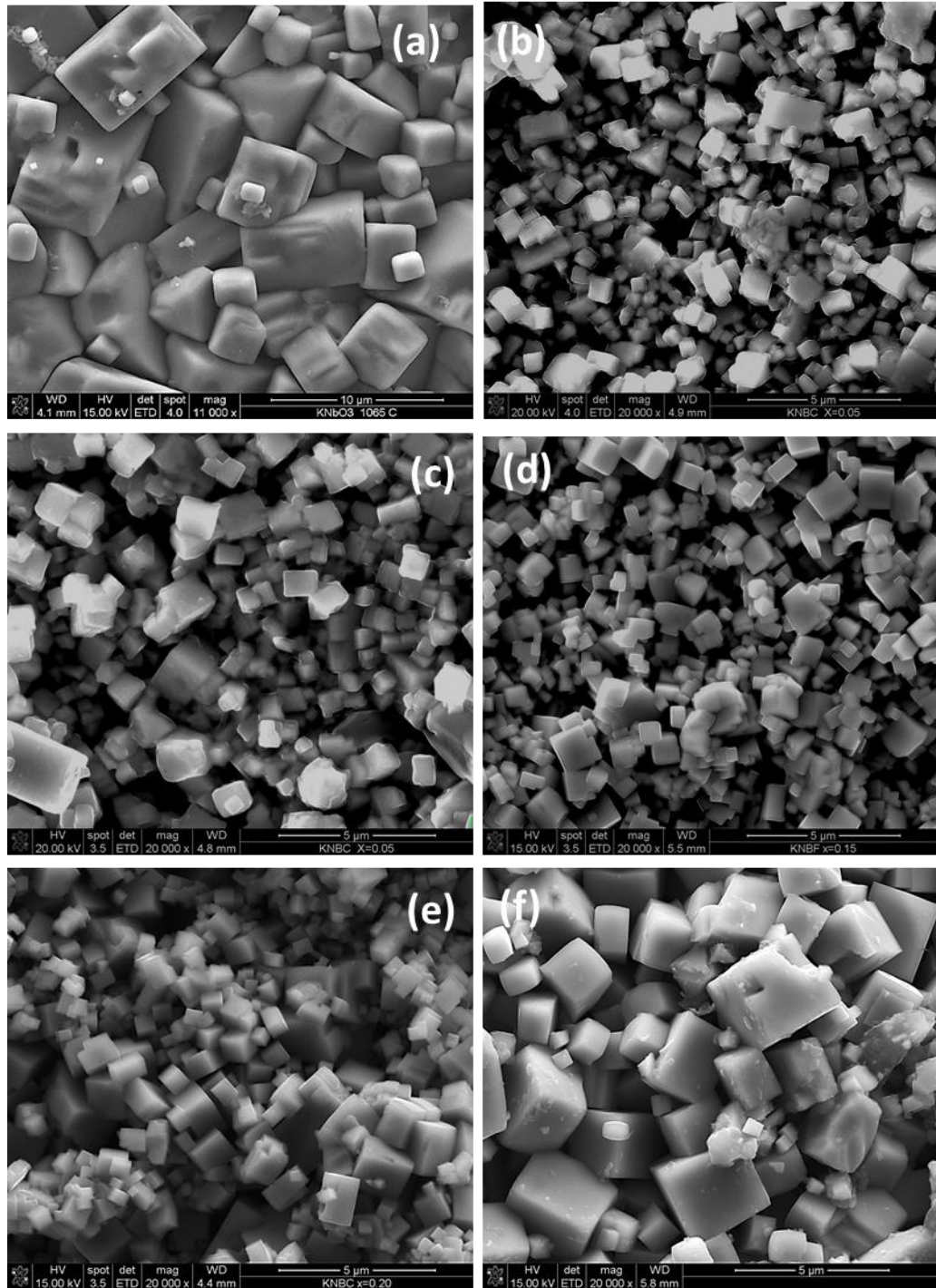


Figure 7. 6: Microstructure evolution for KNBC ceramics for (a) $x=0$, (b) $x=0.05$, (c) $x=0.10$, (d) $x=0.15$, (e) $x=0.20$ and (f) $x=0.25$.

Grain growth is inhibited with the incorporation of Bi^{3+} and Co^{3+} into the KNbO_3 lattice. However, grains preserve the cubic shape in all compositions. Microstructures for $x=0.05$,

$x=0.10$ and $x=0.15$ present very similar morphology (Figure 7. 6. (b-d)). Grain size varies between 600 nm and 800 nm for these compositions. For $x=0.20$, large cubic grains ($\sim 1\mu\text{m}$) but still a wide grain size spectrum is distinguished in its microstructure start appearing. KNBC $x=0.20$ and $x=0.25$ exhibit smooth surfaces. Grain size grows up to 2 μm but still different grain sizes in the surface of $x=0.25$ can be found.

7.2.4. EDX

Element distribution (K, Nb, Bi and Co) and chemical analyses were performed in all KNBC ($0.05 \leq x \leq 0.25$) ceramics by EDX. Experimental and theoretical K/Nb, K/Bi and K/Co ratios and relative errors for KNBC $x=0.05$ are given in Table 7. 3.

x=0.05			
	Theoretical	Experimental	Relative error (%)
K/Nb	1	0.99(3)	1
K/Bi	19	18(4)	5
K/Co	19	34(12)	79

Table 7. 3: Experimental and theoretical molar K/Nb, K/Bi and K/Co ratios for $0.95 \text{KNbO}_3 - 0.05 \text{BiCoO}_3$ ceramic sintered at 1090°C .

The experimental K/Nb and K/Bi ratios match with the theoretical values within deviation margins. On the other hand, K/Co considerably differs from theoretical value (79%). The high standard deviation value indicates non-homogeneous distribution of Bi and Co across the sample. An example of different degree of Bi^{+3} and Co^{+3} solubility is shown in Figure 7. 7.

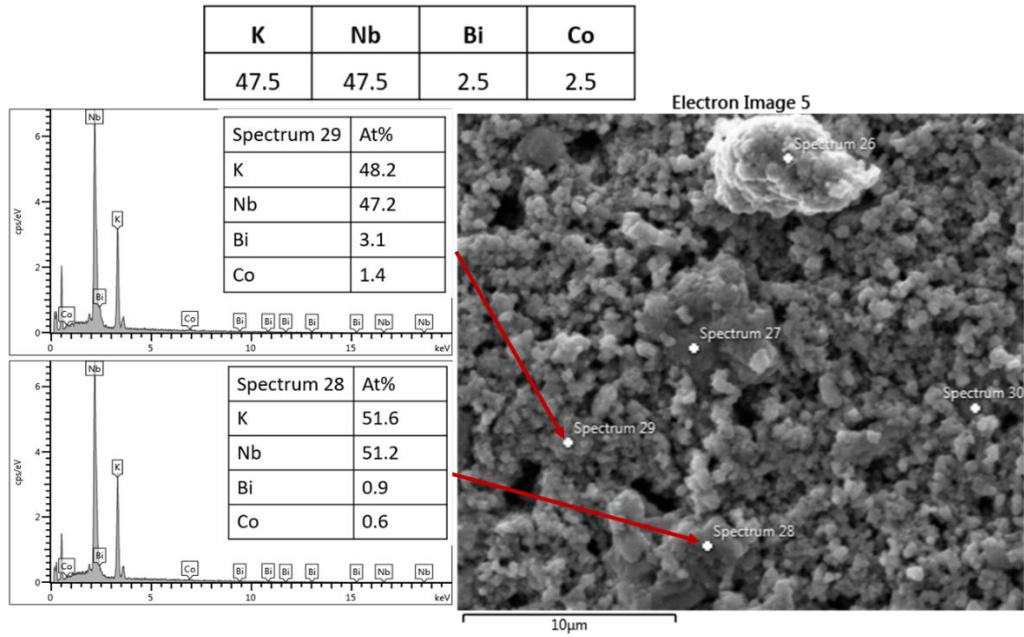


Figure 7. 7: SEM image and EDX spectra of unpolished $0.95 \text{KNbO}_3 - 0.05 \text{BiCoO}_3$ ceramic sintered at 1090°C .

The existence of such disparities amongst experimental K/Bi ratios reveals the difficulties of uniformly incorporating a small amount of $\text{Bi}^{+3}/\text{Co}^{+3}$ into KNbO_3 .

Table 7. 4 shows the experimental and theoretical K/Nb, K/Bi and K/Co relations and relative errors for KNBC $x=0.10$ composition.

x=0.10			
	Theoretical	Experimental	Relative error (%)
K/Nb	1	1.2(4)	20
K/Bi	9	5(2)	44
K/Co	9	7(3)	22

Table 7. 4 Experimental and theoretical K/Nb, K/Bi and K/Co ratios for $0.90 \text{KNbO}_3 - 0.10 \text{BiCoO}_3$ ceramic sintered at 1090°C .

Despite margin of error, empirical K/Bi and K/Co ratios still diverge from theoretical ratios. Their lower values reveal high concentration of K and Nb, suggesting difficulties in incorporating Bi^{+3} and Co^{+3} into the KNbO_3 lattice. Figure 7. 8 shows a SEM image and the EDX spectra as evidence of inhomogeneous distribution of the species.

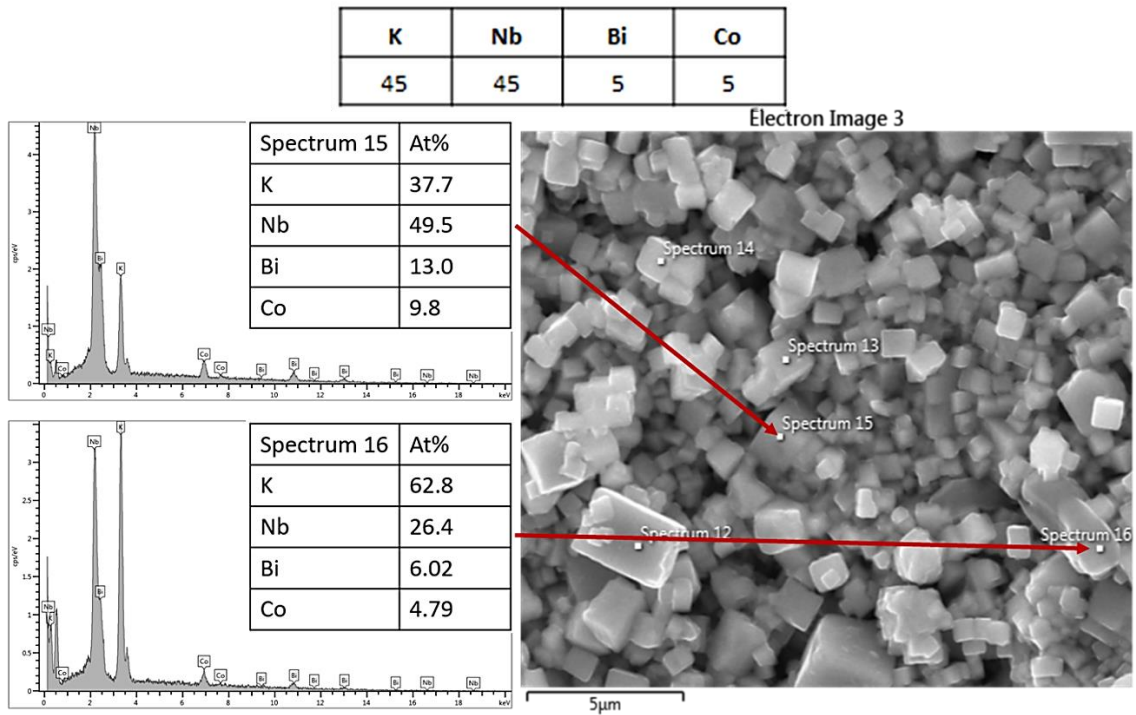


Figure 7. 8: SEM image and EDX spectra of unpolished $0.90 \text{KNbO}_3 - 0.10 \text{BiCoO}_3$ ceramic sintered at 1090°C .

High concentration of K is detected in some regions, suggesting the appearance of other phase ($\sim \text{A}_2\text{BO}_6$). Table 7. 5 show the experimental and theoretical K/Nb, K/Bi and K/Co relations and relative errors for KNBC $x=0.15$ composition.

x=0.15			
	Theoretical	Experimental	Relative error (%)
K/Nb	1	1.0(1)	0
K/Bi	5.67	5(1)	12
K/Co	5.67	7(2)	23

Table 7. 5: Experimental and theoretical K/Nb, K/Bi and K/Co ratios for $0.85 \text{KNbO}_3 - 0.15 \text{BiCoO}_3$ ceramic sintered at 1090°C .

In this case, experimental K/Nb, K/Bi and K/Co ratios are in agreement with the theoretical stoichiometry of KNBC $x=0.15$ within the margin error. Table 7. 6 reports the EDX results for KNBC $x=0.20$.

x=0.20			
	Theoretical	Experimental	Relative error
K/Nb	1	1.0(1)	0
K/Bi	4	3.5(5)	12
K/Co	4	5(1)	25

Table 7. 6: Experimental and theoretical K/Nb, K/Bi and K/Ni ratios for 0.80 KNbO_3 – 0.20 BiCoO_3 ceramic sintered at 1090°C.

Experimental values acceptably coincide with theoretical values, beside presenting lower standard deviation. This fact implies a substantial enhancement of Bi^{+3} and Co^{+3} solubility into KNbO_3 . However, Co-rich particles are detected on the surface of the sample (Figure 7. 9). Finally, K/Nb, K/Bi and K/Co ratios for KNbO_3 x=0.25 have the closest values to the intended stoichiometry (Table 7. 7). As commented above, low standard deviation values indicate more homogeneous chemical distribution. These results confirm the solubility of $\text{Bi}^{+3}/\text{Co}^{+3}$ into KNbO_3 is more effective under conditions of high concentration of BiCoO_3 .

x=0.25			
	Theoretical	Experimental	Relative error
K/Nb	1	1(1)	0
K/Bi	3	3(1)	0
K/Co	3	4(1)	33

Table 7. 7.: Experimental and theoretical K/Nb, K/Bi and K/Co ratios for 0.75 KNbO_3 – 0.25 BiCoO_3 ceramic sintered at 1090°C.

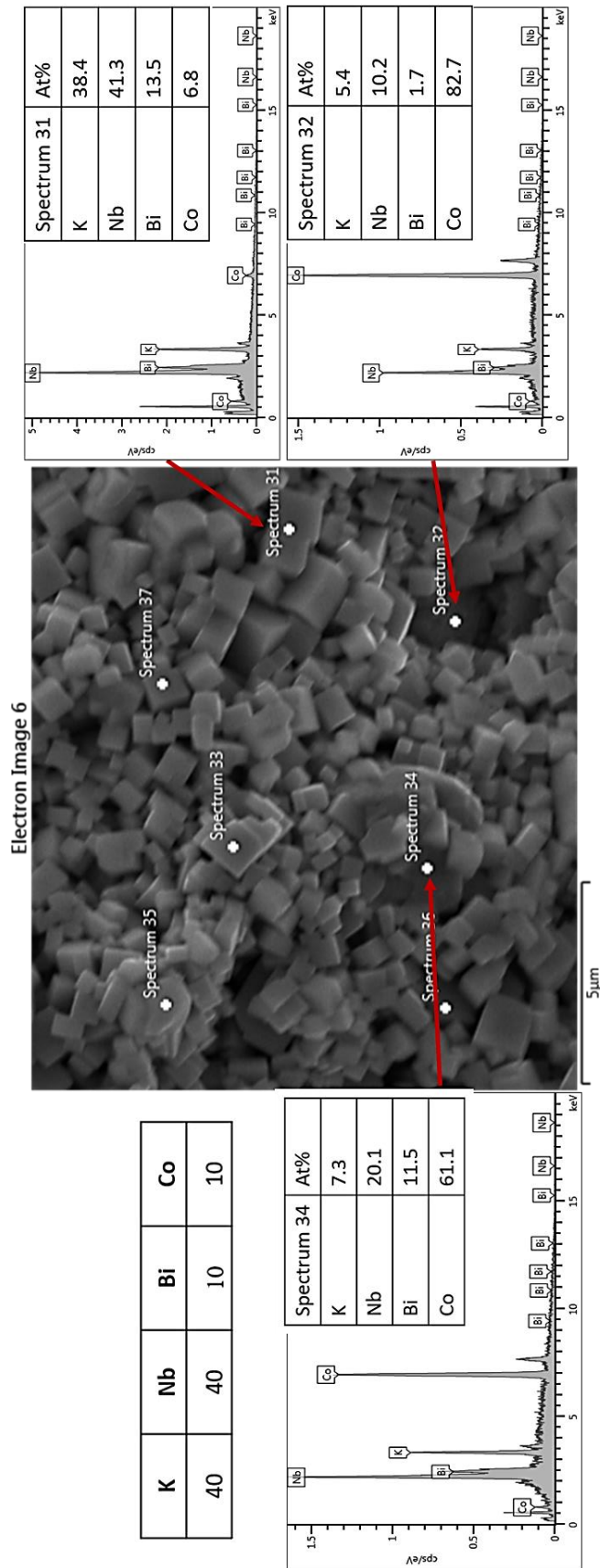


Figure 7. 9: SEM image and EDX spectra of unpolished 0.80 KNbO_3 – 0.20 BiCoO_3 ceramic sintered at 1090°C.

In the same way as noted in the other systems, KNBC presents difficulties in forming the solid solution, especially for low concentration of x . In contrast, KNBC $x=0.20$ and $x=0.25$ exhibit more accurate K/Nb, K/Bi and K/Co values than the rest. This is also supported by EDX mapping of K, Nb, Bi and Co on KNBC $x=0.05$ sample (Figure 7. 10) and $x=0.25$ (Figure 7. 11). Globally, the elements are more homogeneously dispersed on KNBC $x=0.25$ than $x=0.05$. The existence of Co-rich regions in KNBC $x=0.05$ demonstrates that Co^{+3} has difficulties to diffuse into KN lattice. Despite the large concentration of porosity that is visible for $x=0.25$, a better diffusion of Co^{+3} is achieved. Some K-rich region are detected.

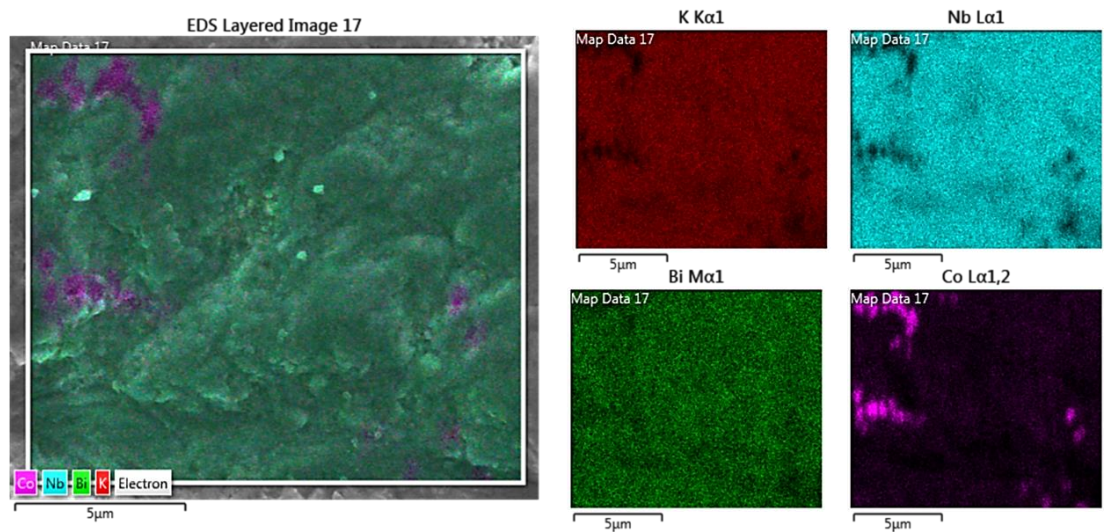


Figure 7. 10: SEM image of the examined region and EDX mapping of K, Nb, Bi and Co for KNBC $x=0.05$.

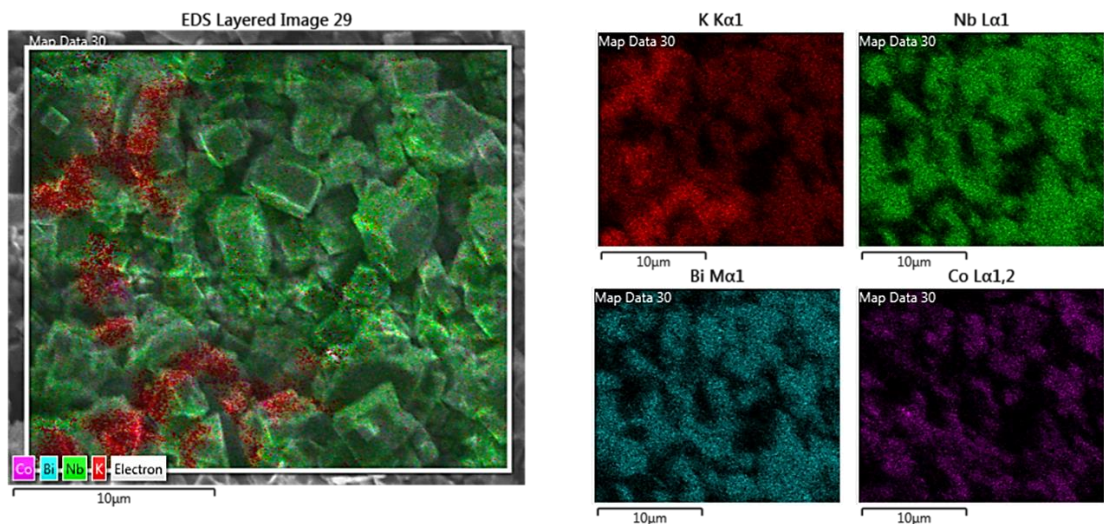


Figure 7. 11: SEM image of the examined region EDX mapping of K, Nb, Bi and Co for KNBC $x=0.25$.

7.3. Electrical Characterisation

7.3.1. Dielectric Characterisation

The temperature dependence of the permittivity, ϵ_r , and dielectric losses, $\tan\delta$, for KNBC ceramics ($x= 0.05, 0.10, 0.15, 0.20$ and 0.25) measured at 1 kHz, 10 kHz, 100 kHz and 250 kHz are shown in Figure 7. 12-16. It must not be forgotten that KNBC ceramics reveal relative densities below 90%, which promotes the sensitivity to crack and directly affects the physical properties such as electrical conduction.

The only sample that presents two dielectric anomalies (dashed line in Figure 7. 12) is KNBC $x=0.05$: one at 215°C and the other at 381°C. These anomalies can be attributed to the orthorhombic solid solution as well as to some pure KN-based phase left, detected in EDX. Dielectric response and losses show dependency with frequency. For $x=0.10$, only a broad relaxation is visible at 390°C (dashed line in Figure 7. 13). Again, ϵ_r and $\tan\delta$ are heavily influenced by frequency. By inspection of Figure 7. 14-16, dielectric anomalies are not perceived, and the frequency dependence is less marked for KNBC $x=0.15, 0.20$ and 0.25 . Moreover, a protuberance is perceived around 100°C in KNBC $x=0.10$ and $x=0.15$, which could be supposedly originated by the pseudocubic phase.

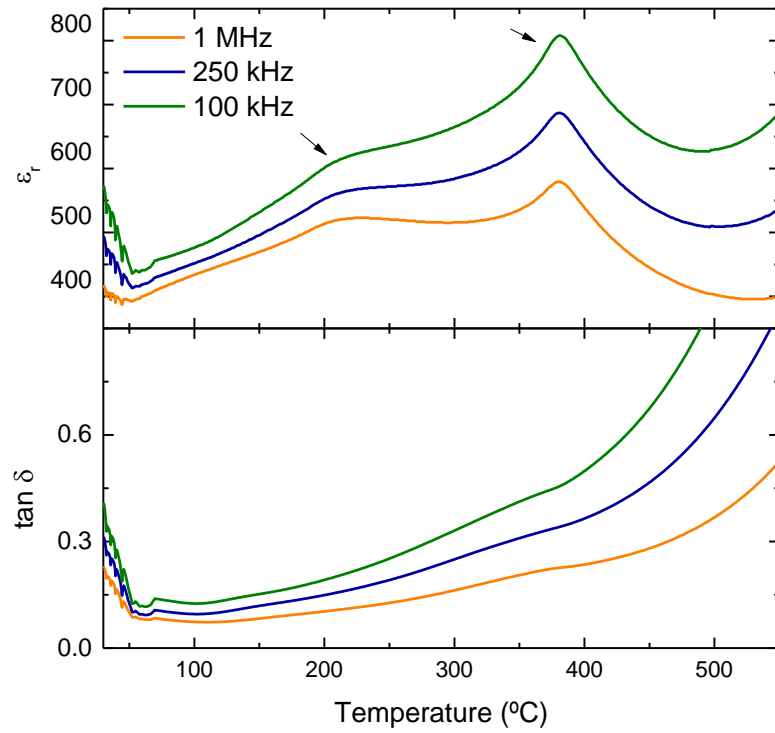


Figure 7. 12: Temperature dependence of ϵ_r and $\tan \delta$ for 0.95 $\text{KNbO}_3\text{-0.05 BiCoO}_3$ ceramic at 1 kHz, 10 kHz and 100 kHz during cooling.

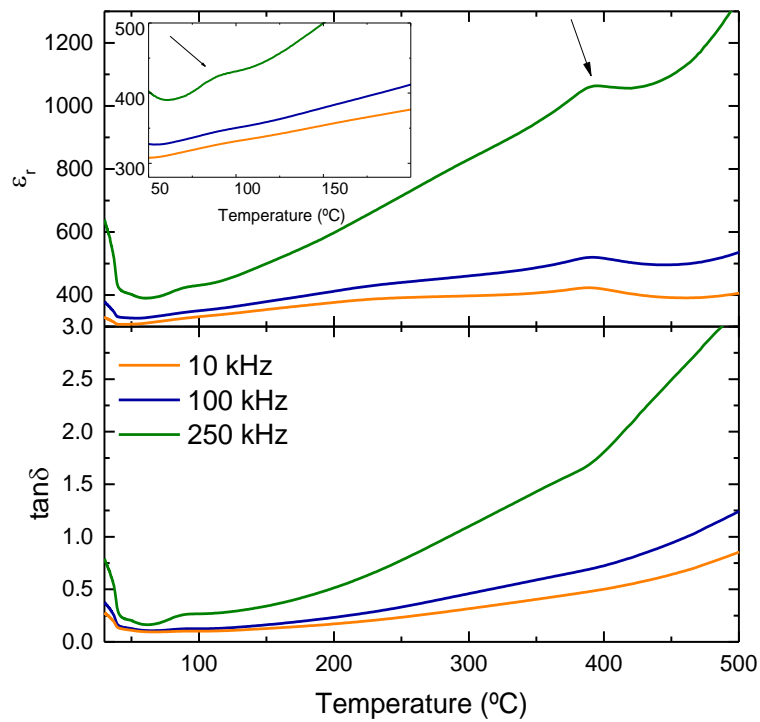


Figure 7. 13: Temperature dependence of ϵ_r and $\tan \delta$ for 0.90 $\text{KNbO}_3\text{-0.10 BiCoO}_3$ solid solution at 1 kHz, 10 kHz and 100 kHz during cooling.

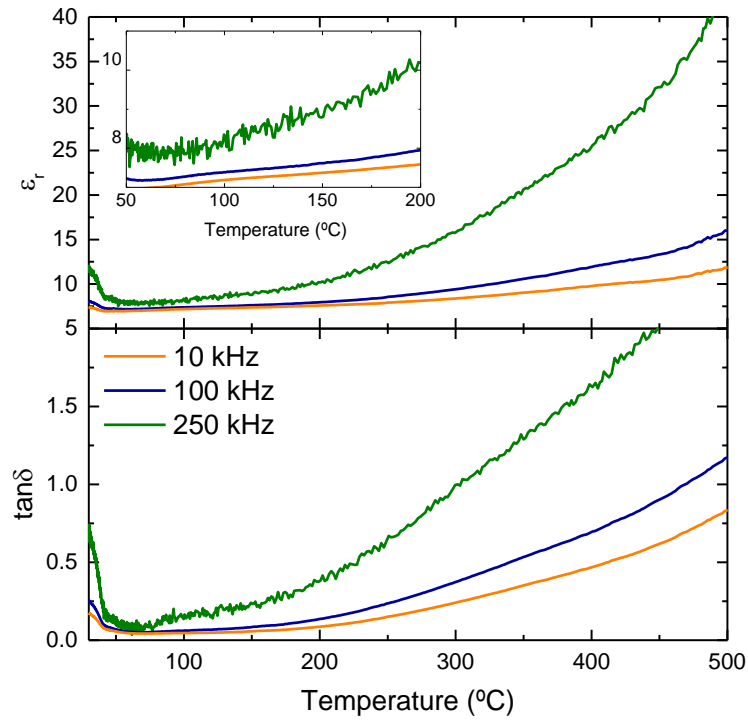


Figure 7. 14: Temperature dependence of ϵ_r and $\tan\delta$ for 0.85 $\text{KNbO}_3\text{-}0.15 \text{BiCoO}_3$ solid solution at 1 kHz, 10 kHz and 100 kHz during cooling.

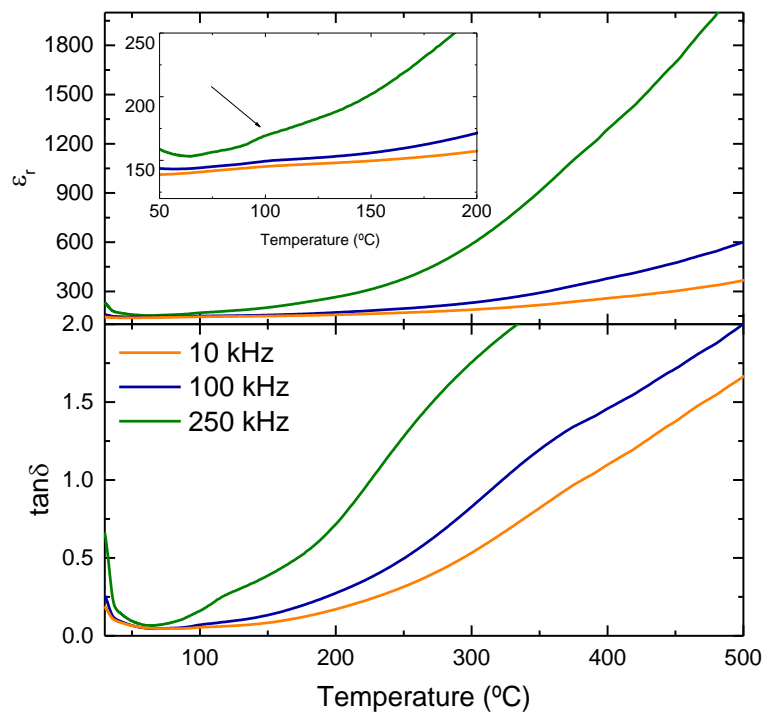


Figure 7. 15: Temperature dependence of ϵ_r and $\tan\delta$ for 0.80 $\text{KNbO}_3\text{-}0.20 \text{BiCoO}_3$ solid solution at 1 kHz, 10 kHz and 100 kHz during cooling.

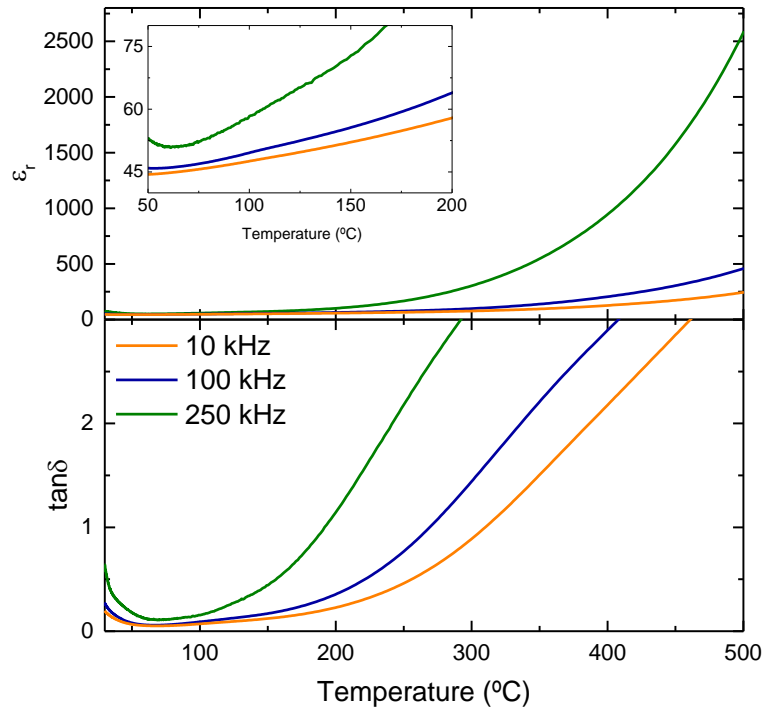


Figure 7. 16: Temperature dependence of ϵ_r and $\tan\delta$ for 0.75 $\text{KNbO}_3\text{-}0.25 \text{ BiCoO}_3$ solid solution at 1 kHz, 10 kHz and 100 kHz during cooling.

The temperature dependence of the permittivity, ϵ_r , for KNBC ceramics ($x = 0, 0.05, 0.10, 0.15, 0.20$ and 0.25) measured at 100 kHz is illustrated in Figure 7. 17. Upon doping, the $\epsilon_r(T)$ curves become flatter than KN curve, which shows two maxima at 205 °C and 400 °C. Those two dielectric anomalies are associated with phase transitions. As mentioned before, KNBC $x=0.05$ is the only one that exhibits two anomalies but much less intense than undoped KN.

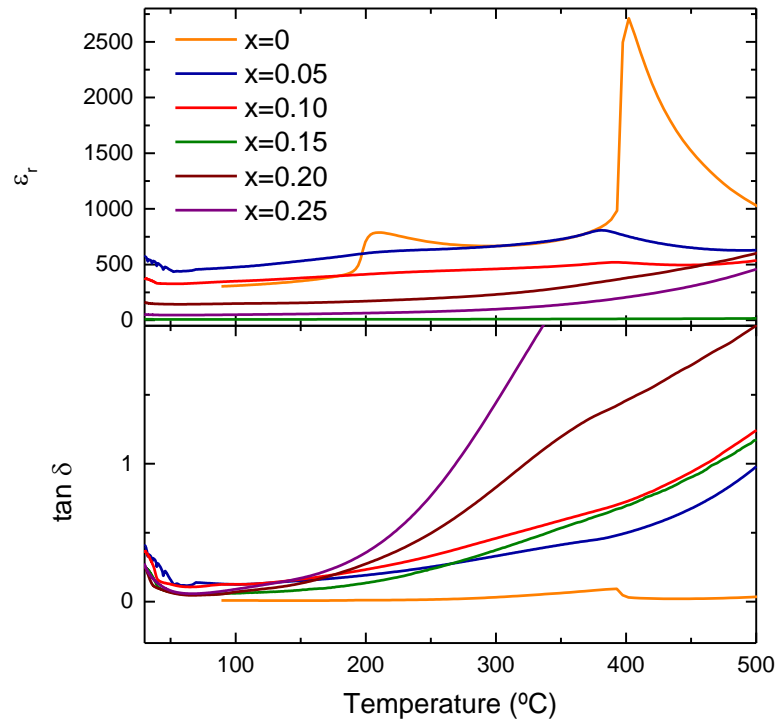


Figure 7. 17: Temperature dependence of relative permittivity and dielectric losses for $(1-x)\text{KNbO}_3-x\text{BiCoO}_3$ ($0 \leq x \leq 0.25$) ceramics at 100 kHz.

7.4. Optical Characterisation

7.4.1 Diffuse reflectance spectroscopy

Direct and indirect band-gaps for KNBC ceramics ($x = 0, 0.05, 0.10, 0.15, 0.20$ and 0.25) were determined using the Tauc plots from the reflectivity data (Figure 7. 18) Direct band-gaps continuously narrow from 3.62 eV ($x=0$) to 2.60 eV ($x=0.25$) with increasing of Bi^{+3} and Co^{+3} contents into the KN lattice (Figure 7. 19).

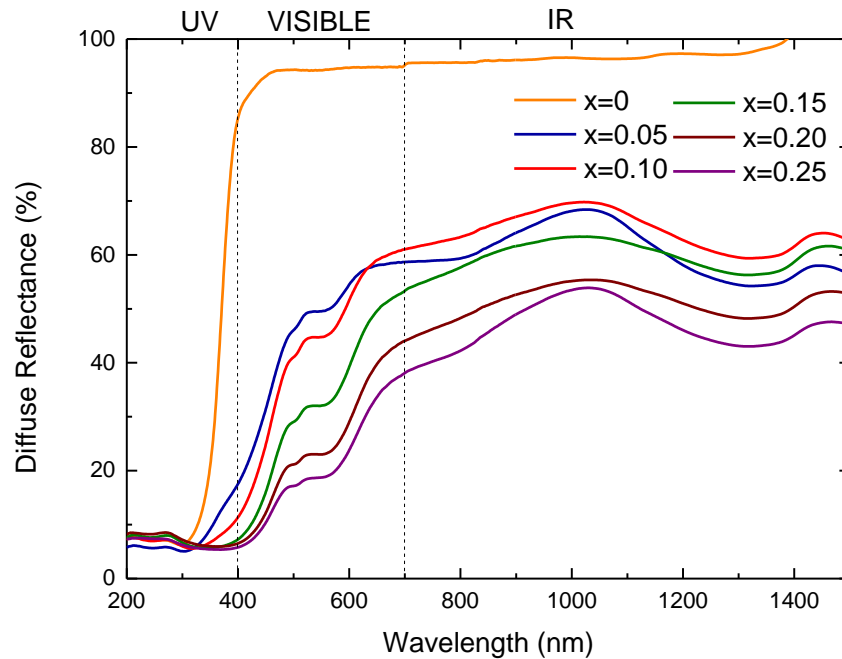


Figure 7.18: Diffuse reflectance as a function of wavelength for KNBC system (raw data).

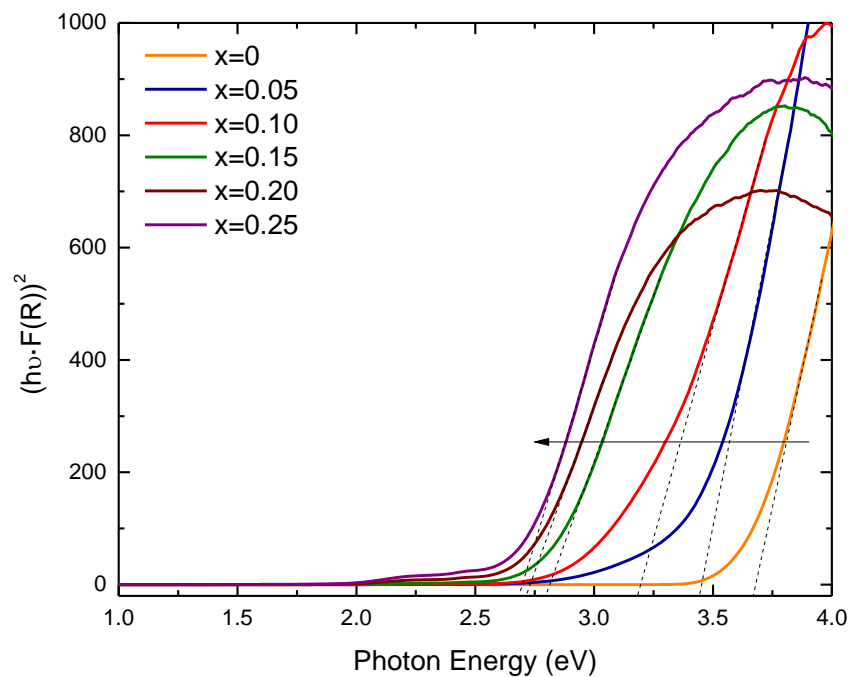


Figure 7.19: Tauc plot for direct band gaps for KNBC $0 \leq x \leq 0.25$ ceramics

If the electron excitation occurs through an indirect path, the bandgap narrows with increasing x , reaching 2.15 eV for $x=0.25$ (Figure 7.20). Two bumps (labelled as 1 and 2) arise at 2.21 eV and 2.45 eV in all the spectra, which become more intense with x . These absorption regions could be related with d-d transitions, hybridized orbitals or energetic levels within the band gap.

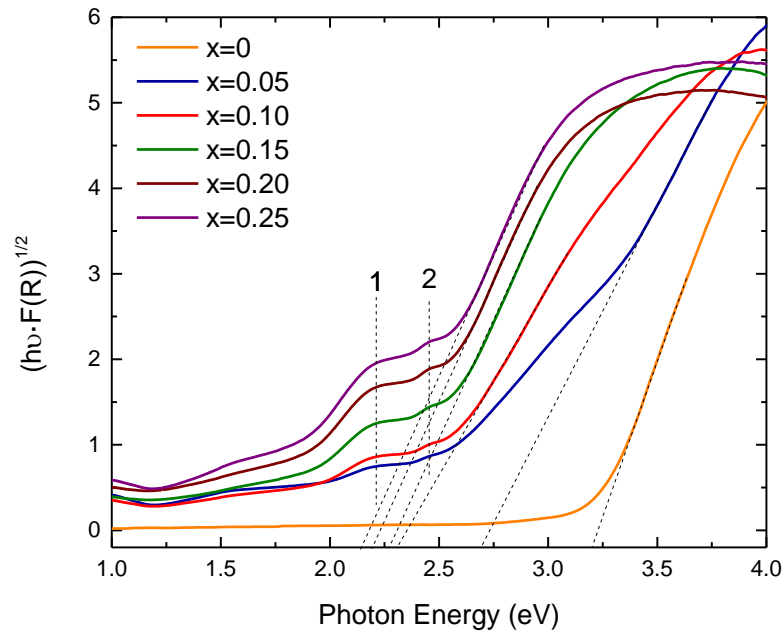


Figure 7. 20: Tauc plot for indirect band gaps for KNBC $0 \leq x \leq 0.25$ ceramics.

Figure 7. 21 plots the band-gap narrowing as a function of x for direct and indirect transitions.

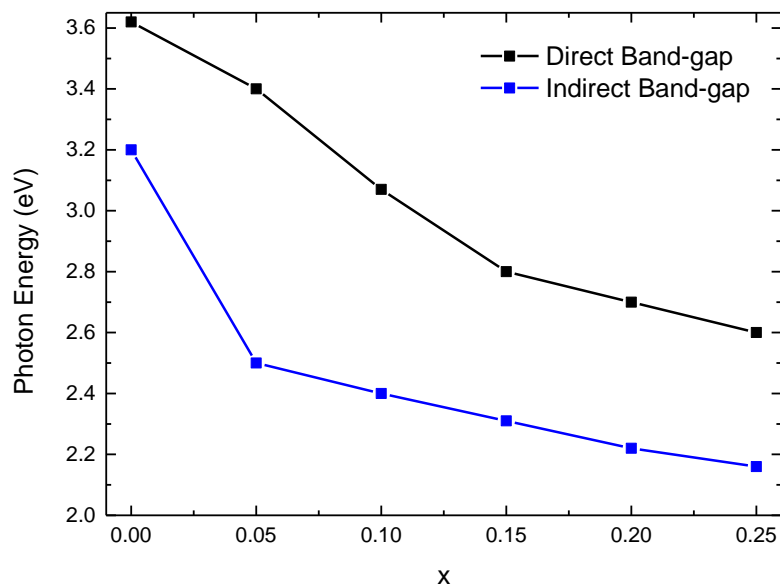


Figure 7. 21: Compositional evolution of direct and indirect band-gap for KNBC $0 \leq x \leq 0.25$ ceramics.

Predictably, direct band-gaps present higher values than indirect band-gaps. In addition, both show the same trend of narrowing with increasing x . For indirect band-gaps, the most pronounced decrease occurs in between $x=0$ and $x=0.05$. On the other hand, direct band-gaps constantly narrow with increasing $\text{Bi}^{+3}/\text{Co}^{+3}$ contents.

7.5. Discussion

Unreacted bismuth and cobalt oxides were detected in KNBC calcined powders by XRD. After sintering, small amount of Bi_2O_3 was perceived in KNBC $x=0.20$ and $x=0.25$ ceramics. The main problem found during the ceramic processing of this system was the impossibility of obtaining high density ceramics. Densities below 85% lead to very weak samples, generating stability problems in air and preventing a reliable electric characterisation. There are only few papers that have reported BiCoO_3 solid-solutions prepared by conventional route at ambient pressure (Wu et al., 2011; Zhou, Liu, Li, Yuan, & Chen, 2009), probably due to difficulties in the ceramic processing.

XRD patterns of KNBC ceramics show all reflections constantly move towards lower 2θ angles with increasing x . KNBC $x = 0.05$ is acceptably refine as a combination of cubic and orthorhombic phases. With further increase of the Bi^{+3} and Co^{+3} , the system evolves to a pseudocubic phase, which is accompanied by a linear increase of the unit cell volume. In contrast, a polymorphic phase transition between the orthorhombic and the rhombohedral phase for a similar system, $(1-x) \text{K}_{0.5}\text{Na}_{0.5}\text{NbO}_3\text{-}x \text{BiCoO}_3$, was described approximately at $0.01 \leq x \leq 0.02$ (Wu et al., 2011).

The presence of the Raman mode at 192 cm^{-1} and the dip at 197 cm^{-1} indicates the presence of a polar phase up to $x=0.15$, that was not detected by XRD. The absence of the mixed Raman mode at 192 cm^{-1} corroborates the centrosymmetric phase for KNBC $x=0.20$ and $x=0.25$. However, Raman activity confirms local distortions up to $x=0.25$.

SEM imaging and EDX analyses show different solubility degrees of Bi^{+3} and Co^{+3} for low concentration of x , revealing solid-state reaction is not adequate processing method, as already commented in other similar solid-solutions. For $x=0.20$ and $x=0.25$, better homogenisation of the chemicals leads to the appearance of larger cubic grains.

Dielectric anomaly associated with ferroelectric-to-paraelectric transition is visible for KNBC $x=0.05$ and $x=0.10$. Based on EDX results it seems the ferroelectric behaviour in this system is due to orthorhombic KNbO_3 -based. In contrast, dielectric maxima are not detected for $x=0.15$, $x=0.20$ and $x=0.25$, however electrical measurements are not reliable due to the low density, which affects the integrity of the samples.

By inspection of constructed Tauc plots, direct (and indirect) band-gaps continuously narrow from 3.62 eV (3.22 eV) to 2.60 eV (2.15 eV), with increasing Bi^{+3} and Co^{+3} content into the KN lattice.

7.6. Conclusions

Low density KNBC ceramics were prepared by solid state reaction. Coexistence of polar and non-polar phases for $x=0.05$ and $x=0.10$ is suggested by XRD, Raman and dielectric measurements. The polar phase is attributed to the presence of KN-rich regions where Bi^{+3} and Co^{+3} are not well diffused, as revealed by SEM and EDX analyses. In contrast, KNBC $x=0.20$ and $x=0.25$ are assigned to pseudocubic symmetry as supported by XRD and Raman spectroscopy analyses. EDX confirms a better homogenisation of the chemicals, which is accompanied by grain growth. Finally, systematic band-gap narrowing for KNBC system is observed with increasing x .

7.7. References

- Belik, A. A., Iikubo, S., Kodama, K., Igawa, N., Shamoto, S. I., Niitaka, S., ... Takayama-Muromachi, E. (2006). Neutron powder diffraction study on the crystal and magnetic structures of BiCoO_3 . *Chemistry of Materials*, 18(3), 798–803. <https://doi.org/10.1021/cm052334z>
- Izyumskaya, N., Alivov, Y., & Morkoç, H. (2009). Oxides, oxides, and more oxides: High-oxides, ferroelectrics, ferromagnetics, and multiferroics. *Critical Reviews in Solid State and Materials Sciences*, 34(3–4). <https://doi.org/10.1080/10408430903368401>
- McLeod, J. A., Pchelkina, Z. V., Finkelstein, L. D., Kurmaev, E. Z., Wilks, R. G., Moewes, A., ... Takayama-Muromachi, E. (2010). Electronic structure of BiMO_3 multiferroics and related oxides. *Physical Review B - Condensed Matter and Materials Physics*, 81(14), 1–10. <https://doi.org/10.1103/PhysRevB.81.144103>
- Oguchi, Y. U. and T. S. and F. I. and T. (2005). First-Principles Predictions of Giant Electric Polarization. *Japanese Journal of Applied Physics*, 44(9S), 7130.

<http://stacks.iop.org/1347-4065/44/i=9S/a=7130>

Oka, K., Azuma, M., Chen, W., Yusa, H., Belik, A. A., Takayama-Muromachi, E., ... Shimakawa, Y. (2010). Pressure-Induced Spin-State Transition in BiCoO_3 . *Journal of the American Chemical Society*, 132(27), 9438–9443.

<https://doi.org/10.1021/ja102987d>

Ravindran, P., Vidya, R., Eriksson, O., & Fjellvåg, H. (2008). Magnetic-instability-induced giant magnetoelectric coupling. *Advanced Materials*, 20(7), 1353–1356.

<https://doi.org/10.1002/adma.200701889>

Sudayama, T., Wakisaka, Y., Mizokawa, T., Wadati, H., Sawatzky, G. A., Hawthorn, D. G., ... Shimakawa, Y. (2011). Co-O-O-Co superexchange pathways enhanced by small charge-transfer energy in multiferroic BiCoO_3 . *Phys. Rev. B*, 83(23), 235105.

<https://doi.org/10.1103/PhysRevB.83.235105>

Wu, W., Xiao, D., Wu, J., Liang, W., Li, J., & Zhu, J. (2011). Polymorphic phase transition-induced electrical behavior of BiCoO_3 -modified $(\text{K}_{0.48}\text{Na}_{0.52})\text{NbO}_3$ lead-free piezoelectric ceramics. *Journal of Alloys and Compounds*, 509(29), L284–L288.

<https://doi.org/10.1016/j.jallcom.2011.05.004>

Zhou, C., Liu, X., Li, W., Yuan, C., & Chen, G. (2009). Structure and electrical properties of $\text{Bi}_{0.5}\text{Na}_{0.5}\text{TiO}_3\text{-Bi}_{0.5}\text{K}_{0.5}\text{TiO}_3\text{-BiCoO}_3$ lead-free piezoelectric ceramics. *Journal of Materials Science*, 44(14), 3833.

<https://doi.org/10.1007/s10853-009-3519-3>

Chapter 8

System (1-x) KNbO₃- x BiNiO₃

8.1. Introduction

8.2. Structural and chemical characterisation

8.2.1. Purity and X-ray diffraction

8.2.2. Raman spectroscopy

8.2.3. SEM

8.2.4. EDX

8.3. Electrical Characterisation

8.3.1. Dielectric Characterisation

8.4. Optical Characterisation

8.4.1 Diffuse reflectance spectroscopy

8.5. Discussion

8.6. Conclusions

8.7. References

8. System (1-x) $\text{KNbO}_3\text{-x BiNiO}_3$

8.1. Introduction

This chapter is devoted to the processing and characterisation of ceramics from the binary system (1-x) $\text{KNbO}_3\text{-x BiNiO}_3$ (KNBN) with x=0, 0.05, 0.10, 0.15, 0.20 and 0.25. First, the optimal powder processing heat-treatment was established. This was followed by an evaluation of the crystal structure using combined XRD and Raman Spectroscopy analyses. Then the impact of Bi^{+3} and Ni^{+3} into KNbO_3 was investigated by the evolution of ferroelectric and dielectric properties. Finally, a band-gap narrowing is observed in this system with the increase of Bi^{+3} and Ni^{+3} content.

The triclinic BiNiO_3 (symmetry group $\text{P}\bar{1}$) is centrosymmetric, and therefore not polar (Belik, 2012). In this chapter, the effect of non-polar BiNiO_3 doping on the long-range polar order of KNbO_3 is investigated. BiNiO_3 compound is mainly reported in the literature due to its unusual charge distribution (McLeod et al., 2010). At ambient pressure, BiNiO_3 exhibits $\text{Bi}_{0.5}^{3+}\text{Bi}_{0.5}^{5+}\text{Ni}^{2+}\text{O}_3$ charge distribution with ordering of Bi^{3+} and Bi^{5+} charges in the A site in a highly distorted perovskite structure (Carlsson et al., 2008; Ishiwata et al., 2002; Mizumaki et al., 2009; Wadati et al., 2005). This fact may lead to interesting conductivity phenomena in the boundary between insulator and metal. A band-gap of 1.1(5) eV based on X-ray emission and absorption spectra (Azuma et al., 2007) has been reported. Furthermore, with increasing pressure BiNiO_3 acquires Pnma symmetry (Azuma et al., 2007) which is accompanied by a different charge distribution ($\text{Bi}^{3+}\text{Ni}^{3+}\text{O}_3$) which leads to insulator-to-metal electronic changes, and a 2.6% volume reduction (Azuma et al., 2011). BiNiO_3 also presents weak ferromagnetism ($T_N \sim 300$ K) (Carlsson et al., 2008; Ishiwata et al., 2002). However, there is no experimental evidence for BiNiO_3 being a multiferroic (Catalan, 2008). To the best of our knowledge, there are

only few reports about BiNiO_3 -based solid solution, such as $\text{Na}_{0.5}\text{K}_{0.5}\text{NbO}_3\text{-BiNiO}_3\text{-LiSbO}_3$ (Liu, Liu, Jiang, & Ma, 2010).

8.2. Structural and chemical characterisation

8.2.1. Purity and X-ray diffraction

$(1-x)\text{KNbO}_3\text{-}x\text{BiNiO}_3$ (KNBN) with $x=0, 0.05, 0.10, 0.15, 0.20$ and 0.25 ceramics were prepared by the solid-state reaction method. K_2CO_3 , Nb_2O_5 , Bi_2O_3 and NiO powders were weighed in the required stoichiometric ratios and mixed overnight (24 hours) by ball milling in isopropanol. The dried mixed powders were then calcined twice in air at 850°C for 4 hours using a heating rate of $3^\circ\text{C}/\text{min}$. Figure 8. 1 shows XRD data of KNBN ($0 \leq x \leq 0.25$) calcined powders.

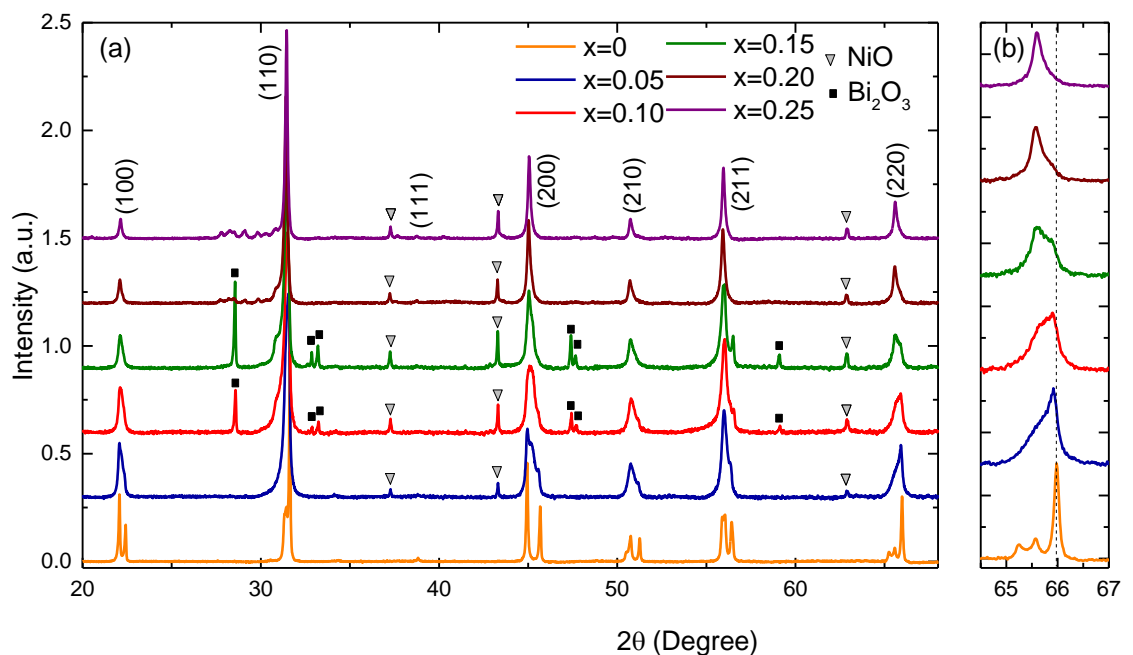


Figure 8. 1: XRD data of $(1-x)\text{KNbO}_3\text{-}x\text{BiNiO}_3$ (KNBN) with $x=0, 0.05, 0.10, 0.15, 0.20$ and 0.25 powders after calcining twice at 850°C . Grey triangles and black squares indicate secondary phases, NiO and Bi_2O_3 respectively.

The main peaks can be ascribed to a perovskite structure which means KNBN ($x=0, 0.05, 0.10, 0.15, 0.20$ and 0.25) forms a solid solution. Although KN calcined powder exhibits well defined peaks (orange pattern) and an orthorhombic crystal structure, broader peaks for KNBN $x>0.05$ compositions are observed, which makes difficult to assign the

corresponding crystal structure. Moreover, considerable amount of two second phases are identified in this system, nickel oxide (NiO) in all compositions (grey triangle) and bismuth oxide (Bi_2O_3) in KNBN $0.10 \leq x \leq 0.15$ compounds (black square), indicating low reactivity. There is also some small amount of impurity in KNBN $0.20 \leq x \leq 0.25$ compositions labelled with ‘?’, because those impurities could not be identified. KNBN $0.05 \leq x \leq 0.25$ powders were again calcined at 850°C for 4 hours with heating rate of $3^\circ\text{C}/\text{min}$ in order to further react NiO and Bi_2O_3 . Figure 8. 2 shows the XRD patterns of KNBN ($0 \leq x \leq 0.25$) powders after the third calcination.

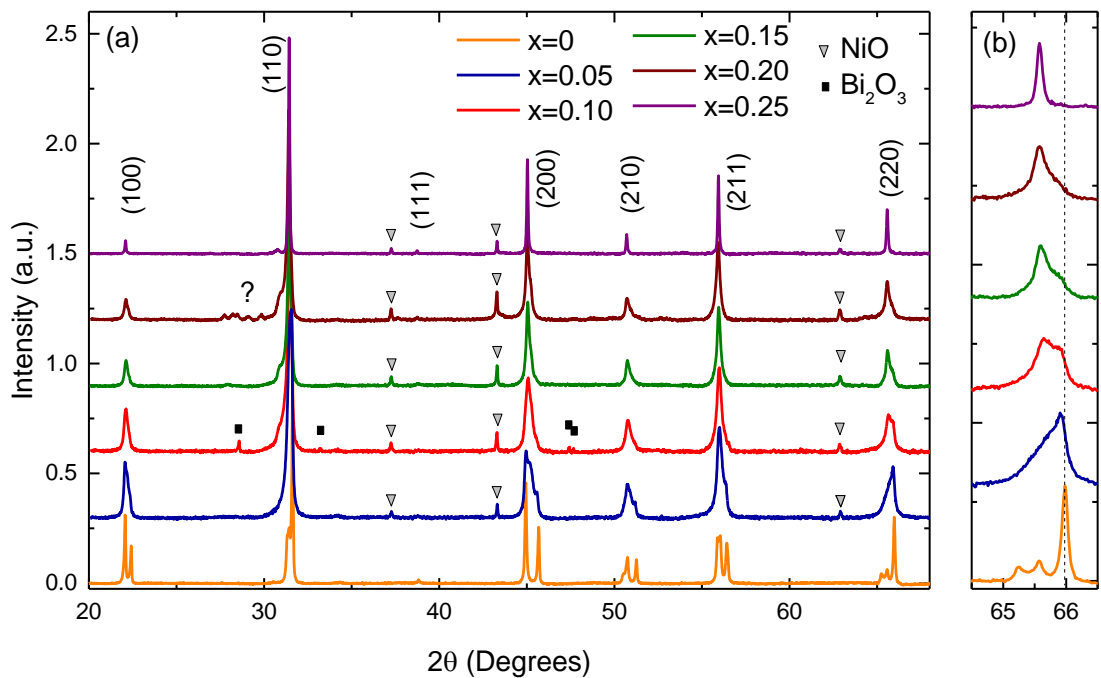


Figure 8. 2: XRD data of $(1-x)\text{KNbO}_3\text{-}x\text{BiNiO}_3$ (KNBN) with $x=0, 0.05, 0.10, 0.15, 0.20$ and 0.25 calcined powders three times at 850°C . Grey triangles and black squares indicate secondary phases, NiO and Bi_2O_3 respectively.

After the third calcination, some residual Bi_2O_3 is still present in KNBN $x=0.10$ but it is absent in KNBN $x=0.15$. The amount of NiO decreases compared with the previous calcination but there is still a considerable quantity of second phase in all compositions. The unknown impurity (‘?’) is only present in KNBN $x=0.20$. The triplet from KN powder pattern ($64^\circ\text{-}67^\circ$) evolves to a single peak (KNBN $x=0.25$) (Figure 8. 2 (b)). The intermediary compositions exhibit one broad peak with a shoulder. For $x=0.05$, the peak at higher 2θ is linked to some orthorhombic KN-based phase where Bi^{+3} and Ni^{+3} are not diffused. Between KNBN $x=0.05$ and $x=0.10$, the peak and the shoulder swap positions,

indicating the better diffusion of the solutes with increasing x . In contrast, this swapping occurred between KNBN $x=0.10$ and $x=0.15$ in the first calcinations (Figure 8. 1).

Figure 8. 3 shows XRD data of KNBN ($0 \leq x \leq 0.25$) pellets sintered at 1070°C for 4 hours using a heating rate of $3^\circ\text{C}/\text{min}$.

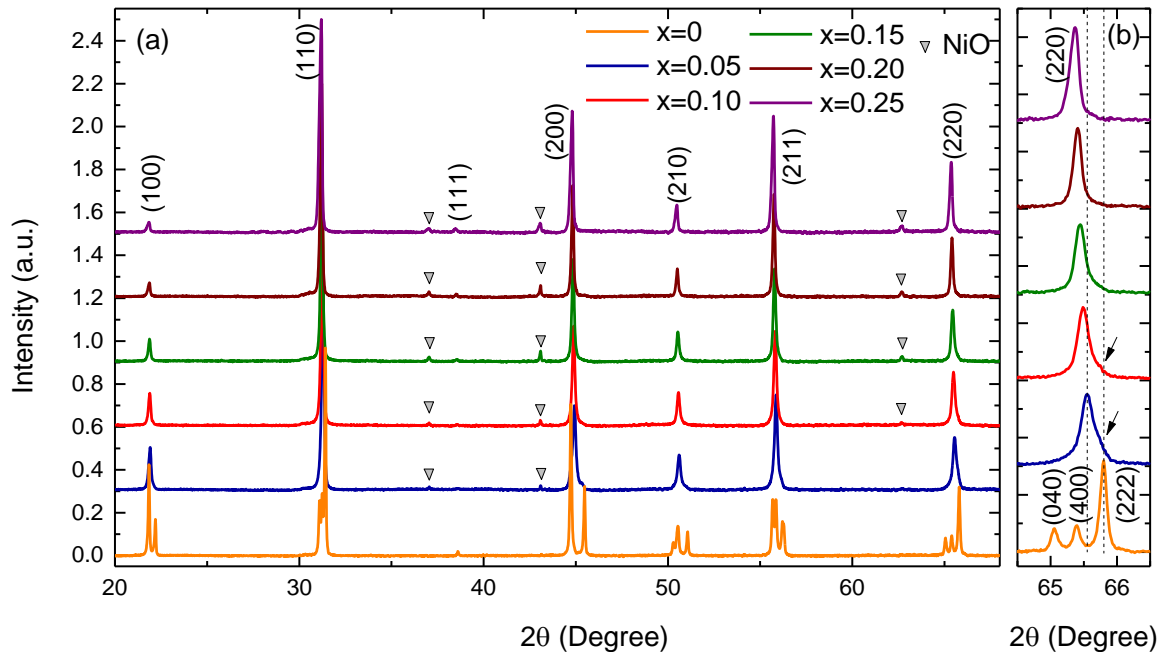


Figure 8. 3.: XRD data of $(1-x)\text{KNbO}_3\text{-}x\text{BiNiO}_3$ (KNBN) with $x=0, 0.05, 0.10, 0.15, 0.20$ and 0.25 ceramics sintered at 1070°C for 4h. Grey triangles indicate secondary phase of NiO. The attached graph on the right illustrates the evolution from the triplet in KN to a sharp single peak.

All reflections for KNBN ($0 \leq x \leq 0.25$) pellets shift systematically towards lower 2θ angles, indicating an increase of the unit cell size with increasing Bi^{3+} and Ni^{3+} contents. The presence of some residual NiO suggests incomplete reaction.

Figure 8. 3. (b) shows the evolution of the triplet from $x=0$ to $x=0.25$. A single peak is visible for the rest of the compositions within the resolution of our measurements. For $x=0.05$ and $x=0.10$, an asymmetry of the peak shape is observed on the higher 2θ side (pointed with arrows in Figure 8. 3) indicating a distortion away from cubic symmetry. Indeed, complications in refining these patterns were found. For $0.15 \leq x \leq 0.25$, single and sharp peak is observed which could be associated with cubic structure but a simple visual inspection of XRD patterns is impossible to determine the crystal structure. Only a full characterisation of this system will provide enough information to elucidate crystal structure evolution with x . Crystal metrics for each composition were calculated by Rietveld refinement, and are listed in Table 8. 1 and Table 8. 2 alongside theoretical and

relative density values for the ceramics. The relative densities decrease from 94% for undoped ceramics to 76%.

	x=0	x=0.05		x=0.10
Space Group	Amm2	27.9 (7) % Amm2	72.1(9) % Pm- $\bar{3}$ m	Pm- $\bar{3}$ m
Density (Experimental) (g/cm³)	4.35(3)		4.19(17)	4.21(22)
Density (calculated) (g/cm³)	4.6273(1)		4.801(1)*	4.9671(4)
Relative Density (%)	94(1)		87(1)*	85(2)
a (Å)	3.9711(1)	3.9868(4)	4.0118(1)	4.0146(1)
b (Å)	5.6909(1)	5.6829(7)	4.0118(1)	4.0146(1)
c (Å)	5.7158(1)	5.7080(1)	4.0118(1)	4.0146(1)
V/10⁶ (pm³)	64.576(2)	64.68(2)	64.570(3)	64.703(3)
R_{exp}	1.26460		1.26990	1.31667
R_p	2.97912		2.77807	3.66920
R_{wp}	4.65175		4.07684	4.60483
GOF	13.53086		10.30640	12.23126

Table 8. 1: Experimental and theoretical density, lattice parameters and agreement indices calculated by Rietveld Refinement for KNBC (x=0., 0.05 and 0.10). *Weighed average for the phases.

	x=0.15	x=0.2	x=0.25
Space Group	Pm- $\bar{3}$ m	Pm- $\bar{3}$ m	Pm- $\bar{3}$ m
Density (Experimental) (g/cm³)	4.26(7)	4.25(20)	4.18(10)
Density (calculated) (g/cm³)	5.1331(2)	5.3013(2)	5.4705(2)
Relative Density (%)	83(2)	80(4)	76(2)
a (Å)	4.0167(1)	4.0181(1)	4.0192(1)
b (Å)	4.0167(1)	4.0181(1)	4.0192(1)
c (Å)	4.0167(1)	4.0181(1)	4.0192(1)
V/10⁶ (pm³)	64.805 (3)	64.873(3)	64.926 (3)
R_{exp}	1.34213	1.36698	1.47013
R_p	3.25375	4.21412	4.28872
R_{wp}	4.70176	5.75481	6.14752
GOF	12.27251	17.72312	17.48605

Table 8. 2: Experimental and theoretical density, lattice parameters and agreement indices calculated by Rietveld Refinement for KNBC (x=0.15, 0.20 and 0.25).

As largely discussed in this work, pure KN (x=0) is described as an orthorhombic phase. XRD data of KNBN x=0.05 is refined as a combination of orthorhombic phase (symmetry group Amm2) and cubic phase (symmetry group Pm- $\bar{3}$ m). As commented before, x=0.10 shows a small shoulder (Figure 8. 3 (b)) which made the phase assignment difficult. Different symmetries were attempted, such as orthorhombic, cubic or a combination of both, which based on previous systems seemed to be the most likely option. However, the software was not able to refine the coexistence of both phases. Alternative refinement into orthorhombic phase for x=0.10 is shown in Appendix F. x=0.15, x=0.20 and x=0.25 patterns are ascribed to cubic symmetry (Pm- $\bar{3}$ m). Even if the XRD patterns seems to describe cubic symmetry, some evidence suggests the presence of a polar phase up to x=0.25, as will be explained below. Figure 8. 4 shows compositional evolution of the unit cell volume for KNBN (0≤x≤0.25) ceramics calculated by Rietveld refinement.

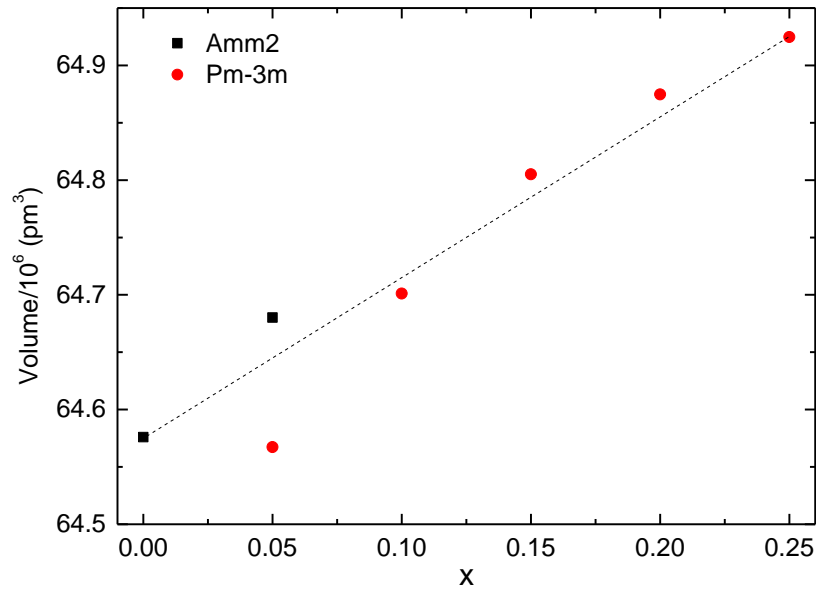


Figure 8. 4: Evolution of the unit cell volume with x for $(1-x)\text{KNbO}_3\text{-}x\text{BiNiO}_3$ ($0 \leq x \leq 0.25$) ceramics. The unit cell volume increases linearly with increasing x , which means the compositional evolution for KNBN system follows Vegard's law. However, the unit cell volume of the orthorhombic phase for $x=0.05$ is larger than the cubic phase, which is not consistent with XRD data in Figure 8. 1(b). Figure F.3 (Appendix F) shows the inability of Rietveld method to refine the orthorhombic phase.

8.2.2. Raman spectroscopy

Room-temperature Raman spectra for KNBN ($0 \leq x \leq 0.25$) powders calcined at 850°C three times are shown in Figure 8. 5. All compositions present the same general modes as reported for KN (bold dashed lines), but these are broader due to disorder of the material and slight shift to lower wavenumbers. Moreover, new modes emerge with the increase of Bi^{+3} and Ni^{+3} contents into KNbO_3 , labelled as 1, 2, 3, 4, 5 and 6. As demonstrated in previous chapters, the presence of the sharp mode at 192 cm^{-1} indicates the long-range polar order for all KN-BN ($0.05 \leq x \leq 0.25$) powders. Modes 5 and 6 indicate undoped KN in agreement with XRD data in Figure 8. 1. Room-temperature Raman spectra for KN-BN ($0 \leq x \leq 0.25$) ceramics sintered at 1070°C are also examined in Figure 8. 6.

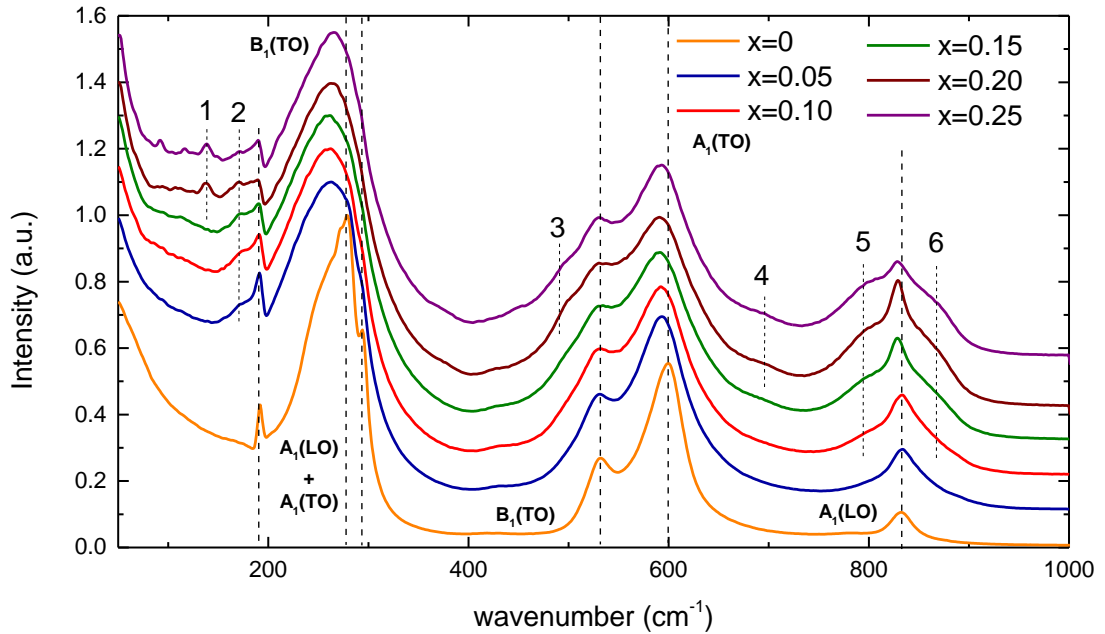


Figure 8. 5: Room-temperature Raman spectra for KNBN ($0 \leq x \leq 0.25$) powders calcined three times at 850°C . New modes (1,2,3,4 and 5) emerge in KNBN ($x \geq 0.05$).

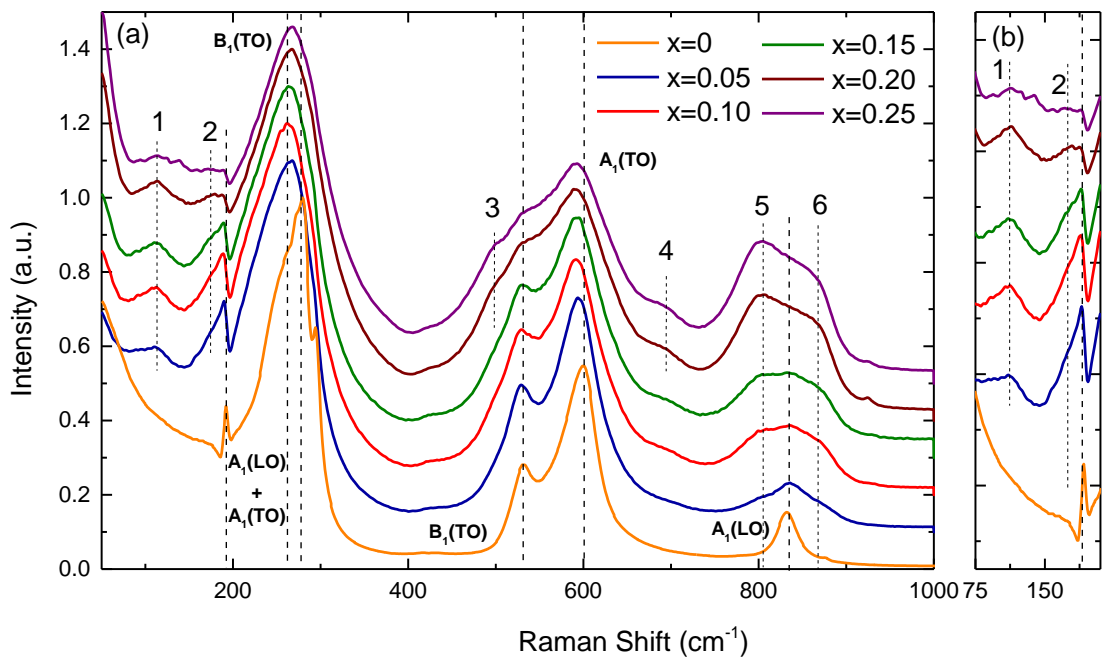


Figure 8. 6: (a) Room-temperature Raman spectra for KNBN ($0 \leq x \leq 0.25$) ceramics sintered at 1070°C . New modes (1, 2, 3, 4, 5 and 6) emerge in KNBN ($x \geq 0.05$) pellets spectra. (b) Monitoring of mixed sharp mode at 192 cm^{-1} .

Raman spectra for KNBN ($0 \leq x \leq 0.25$) ceramics exhibit same general features with the powders (labelled with dashed lines). Emerging modes are indicated by 1, 2, 3, 4, 5, and 6. Mode 1 arises at 114 cm^{-1} and mode 2 appears at $\sim 175\text{ cm}^{-1}$ as a shoulder of the sharp

peak at 192 cm^{-1} . Both modes do not shift and the intensity is maintained constant with the increase of x . Modes 1 and 2 are observed in almost all the systems studied in this work and hypothetically attributed to A-O vibrations within nm-sized clusters rich in either Bi^{3+} and/or K^+ cations. Mode 1 is present in all doped ceramics but not in all powders. The sharp mode at 192 cm^{-1} and the interference dip at 197 cm^{-1} are visible in all compositions, which supports the existence of orthorhombic phase (polar phase) up to $x=0.25$ (attached graph in Figure 8. 6). The intensity of the sharp mode decreases with increasing x , which it may confirm the systematic reduction of the orthorhombic phase. Modes 3 and 4 emerge at $\sim 500\text{ cm}^{-1}$ and $\sim 700\text{ cm}^{-1}$ only for KNBN $x=0.20$ and $x=0.25$. Finally, the intensity of mode 5 ($\sim 800\text{ cm}^{-1}$) and mode 6 ($\sim 875\text{ cm}^{-1}$) systematically rises with increasing x .

The temperature dependence of Raman spectra for KNBN $x=0.05$ and KNBN $x=0.25$ is shown in Figure 8. 7 and Figure 8. 8, respectively. In this range of temperatures (from -180°C to 340°C), the transitions from rhombohedral to orthorhombic to tetragonal are visible for KNBN $x=0.05$. The sharp mode (indicated with arrows) is apparent up to 340°C for KNBN $x=0.05$, suggesting polar phase is still present. Indeed, this temperature is below its Curie temperature ($\sim 390^\circ\text{C}$, Figure 8. 18). For $x=0.25$, this sharp mode disappears at 180°C suggesting a phase transition from polar to non-polar state at this temperature. Interestingly, this transition occurs at lower temperature than observed for orthorhombic KN-based solid solutions ($\sim 400^\circ\text{C}$). This phenomenon may be linked with the appearance of a broad dielectric anomaly at $\sim 130^\circ\text{C}$ (Figure 8. 22).

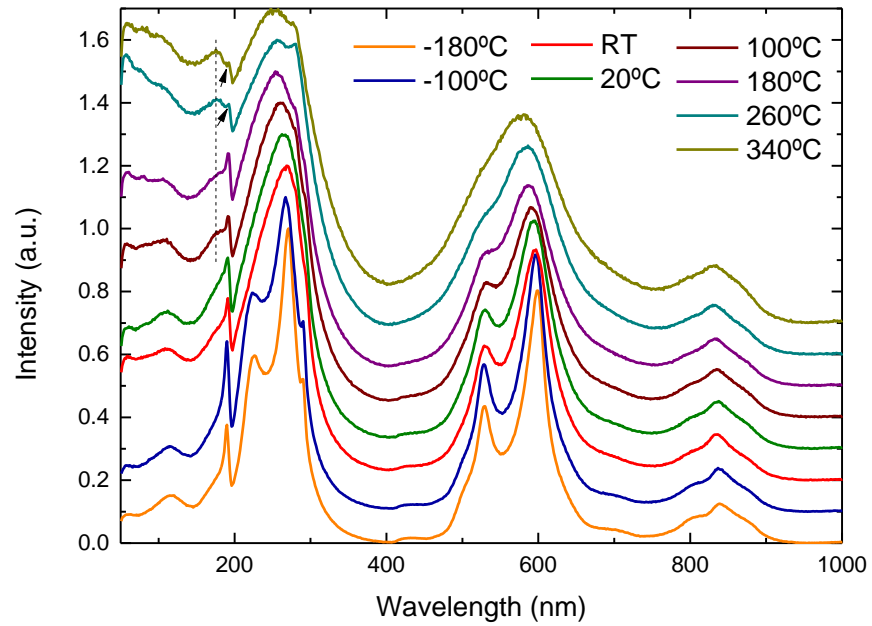


Figure 8. 7: Raman spectra evolution from -180°C to 340°C for KNBN $x=0.05$ ceramics.

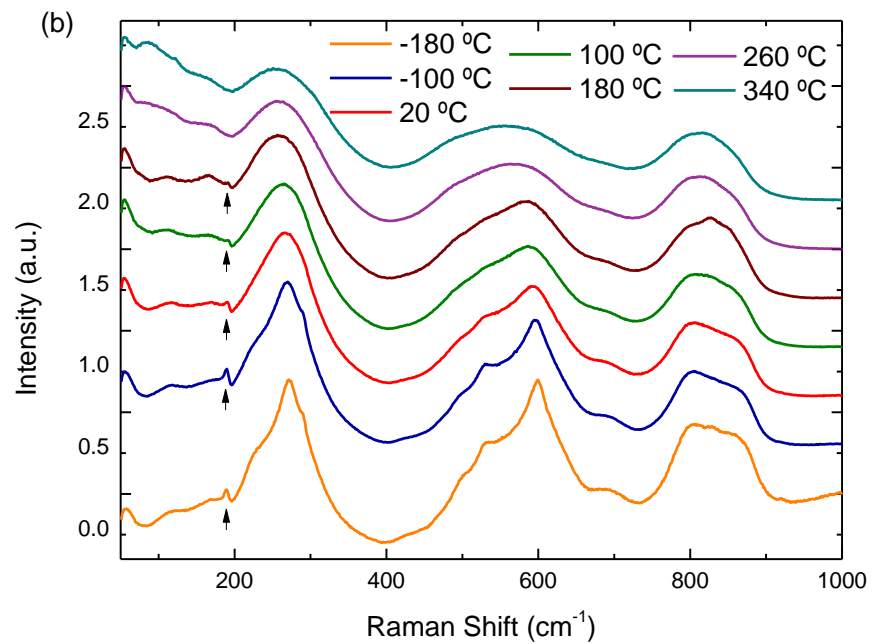


Figure 8. 8: Raman spectra evolution from -180°C to 340°C for KNBN $x=0.25$ ceramics.

8.2.3. SEM

SEM surface images of unpolished KNBN ($0 \leq x \leq 0.25$) ceramics are shown in Figure 8.9 (a-f). Upon $\text{Bi}^{+3}/\text{Ni}^{+3}$ doping into the KN lattice, cubic large grains of $\sim 3\mu\text{m}$ for $x=0$

(Figure 8. 9 a) become round small grains of $\sim 500\text{nm}$ ($x=0.05$, Figure 8. 9 b). The inhibition of the grain growth is also observed in all systems studied in this investigation. A heterogenous grain size distribution is perceived in KNBN ($0.05 \leq x \leq 0.25$) ceramics, which is accompanied by different grain morphologies such as agglomerates of small grains, irregular shaped grains as well as cubic grains. However, cubic grains seem to continuously emerge with increasing x (Figure 8. 9. c-e). For $x=0.25$, mostly all grains are cubic shaped with the grain size in between $\sim 500\text{ nm}$ and $\sim 1\text{ }\mu\text{m}$. The complex microstructures for KNBN ceramics can be associated firstly, with the coexistence of multiple phases, as supported by XRD and Raman results. And secondly, to difficulties on forming solid solutions and consequently inhomogeneous incorporation of the dopants in the grains. To validate this statement, energy dispersive x-ray spectra and mapping are collected for all compositions in the KNBN system.

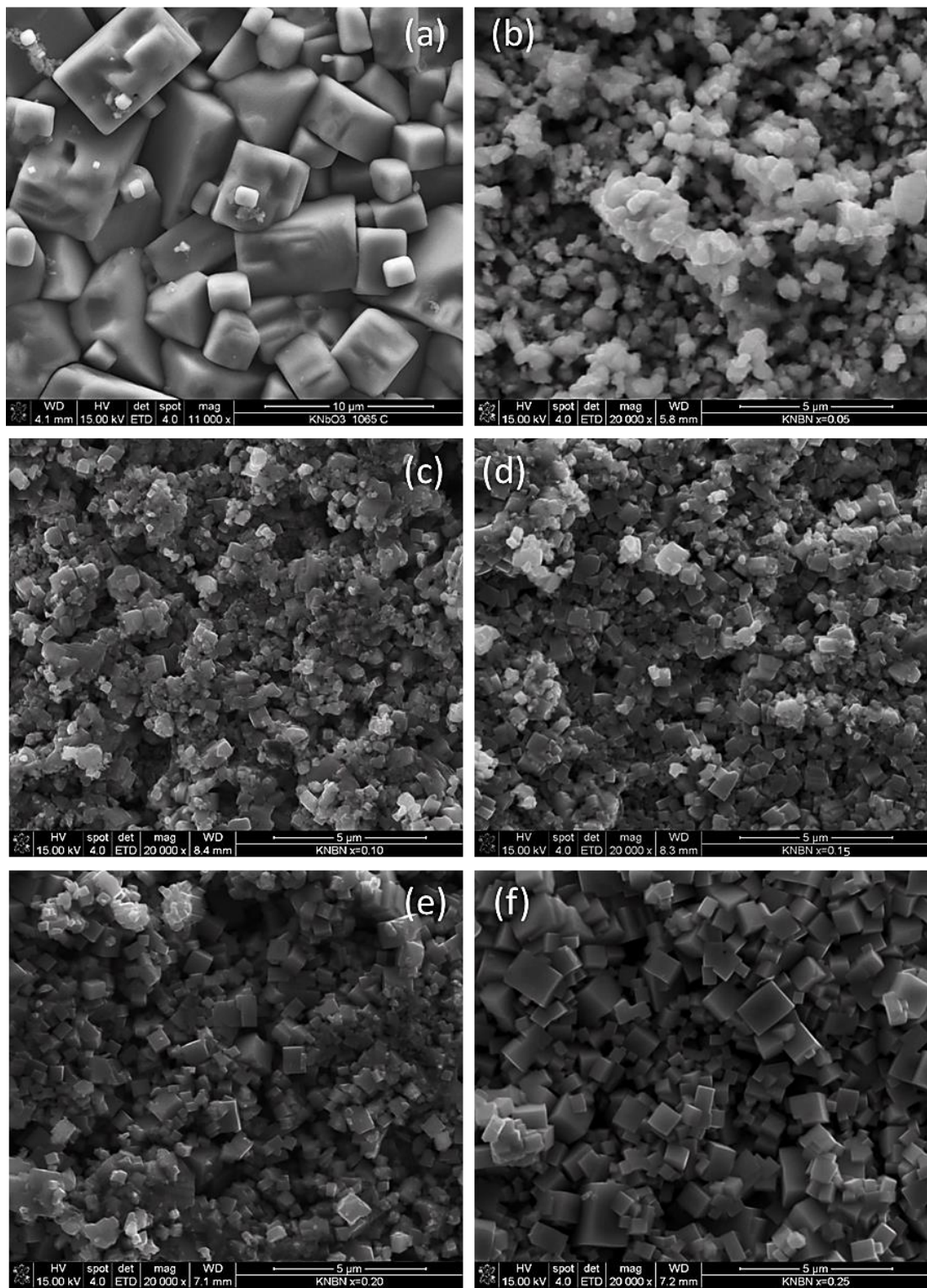


Figure 8.9 (a-f): Microstructure evolution for $(1-x)\text{KNbO}_3\text{-}x\text{BiNiO}_3$ ceramics from (a) $x=0$, (b) $x=0.05$, (c) $x=0.10$, (d) $x=0.15$, (e) $x=0.15$ and (f) $x=0.25$.

8.2.4. EDX

The chemical composition for $\text{KNbO}_3\text{-BiNiO}_3$ $x=0, 0.05, 0.10, 0.15, 0.20$ and 0.25 ceramics is studied by EDX analysis, showing the non-homogeneous distribution of the elements (K, Nb, Bi and Ni) across the samples. Table 8. 3 reports the experimental and theoretical ratios and relative error of the different elements for $x=0.05$.

$x=0.05$			
	Theoretical	Experimental	Relative error (%)
K/Nb	1	0.97(5)	3
K/Bi	19	21(7)	10
K/Ni	19	31(9)	64

Table 8. 3: Experimental (average) and theoretical molar K/Nb, K/Bi and K/Ni ratios for $0.95 \text{KNbO}_3 - 0.05 \text{BiNiO}_3$ ceramic sintered at 1070°C .

K/Ni ratio is much larger than the theoretical, an indication of Ni-rich regions. This fact supports the difficulties of NiO reacting with the rest of the oxides. Evidence of unreacted NiO is shown in Figure 8. 10.

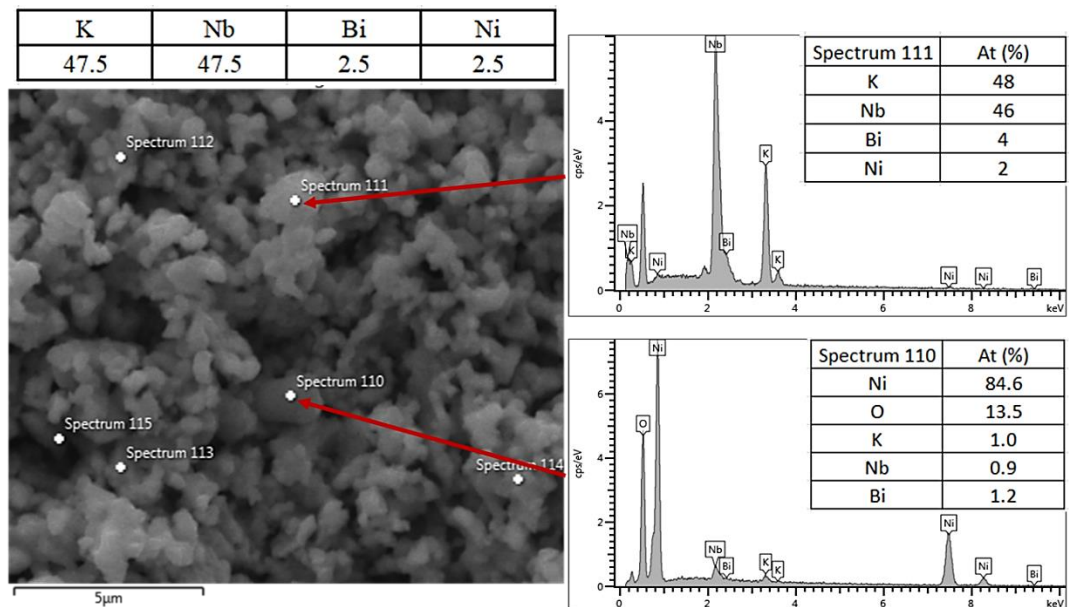


Figure 8. 10: SEM image and EDX spectra of unpolished $0.95 \text{KNbO}_3 - 0.05 \text{BiNiO}_3$ ceramic sintered at 1070°C .

EDX analysis detected NiO particles, in agreement with XRD data Table 8. 4 informs the experimental and theoretical molar K/Nb, K/Bi and K/Ni ratios and relative errors for $x=0.10$ composition.

x=0.10

	Stoichiometric	Experimental	Relative error (%)
K/Nb	1	1.07(5)	7
K/Bi	10	10(4)	0
K/Ni	10	16(7)	60

Table 8. 4.: Experimental (average) and theoretical molar K/Nb, K/Bi and K/Ni ratios for 0.90 KNbO_3 – 0.10 BiNiO_3 ceramic sintered at 1070°C.

Within the margin of errors, empirical K/Nb and K/Bi ratios are in agreement with the desired stoichiometry. The high K/Ni fraction again reveals concentration of Ni is lower in KNbO_3 x=0.10. Figure 8. 11. demonstrates non-uniform distribution of the species across the sample.

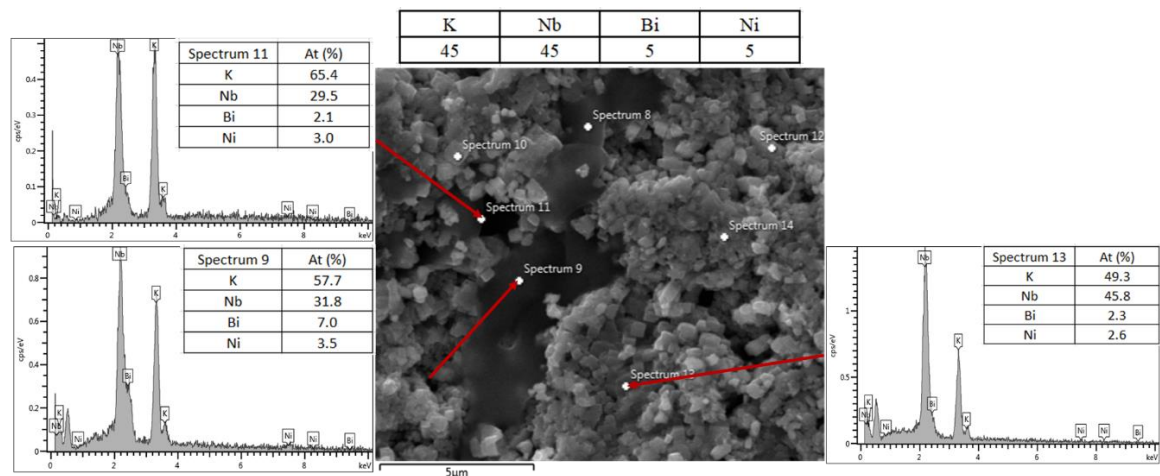


Figure 8. 11: SEM image and EDX spectra of unpolished 0.90 KNbO_3 – 0.10 BiNiO_3 ceramic sintered at 1070°C.

Large grains with smooth surface stand out above the agglomerates of irregular small grains. EDX spectra reveal high concentration of K, approximately the double of Nb. Indeed, this could be related with the formation of a second perovskite with stoichiometry $\sim \text{A}_2\text{BO}_6$. Table 8. 5 presents EDX results for KNbO_3 x=0.15.

$x=0.15$

	Theoretical	Experimental	Relative error (%)
K/Nb	1	0.99(4)	1
K/Bi	5.67	6(1)	6
K/Ni	5.67	10(2)	75

Table 8. 5: Experimental (average) and theoretical K/Nb, K/Bi and K/Ni ratios for 0.85 KNbO_3 – 0.15 BiNiO_3 ceramic sintered at 1070°C.

Once more, K/Ni ratio is high for this composition. In contrast, molar K/Nb and K/Bi relations match with the intended stoichiometry of KNbN $x=0.15$ within the margin of error. Grains of NiO are found on the ceramic surface (Figure 8. 12) which confirms the same tendency of non-homogeneous chemical distribution as observed in previous samples.

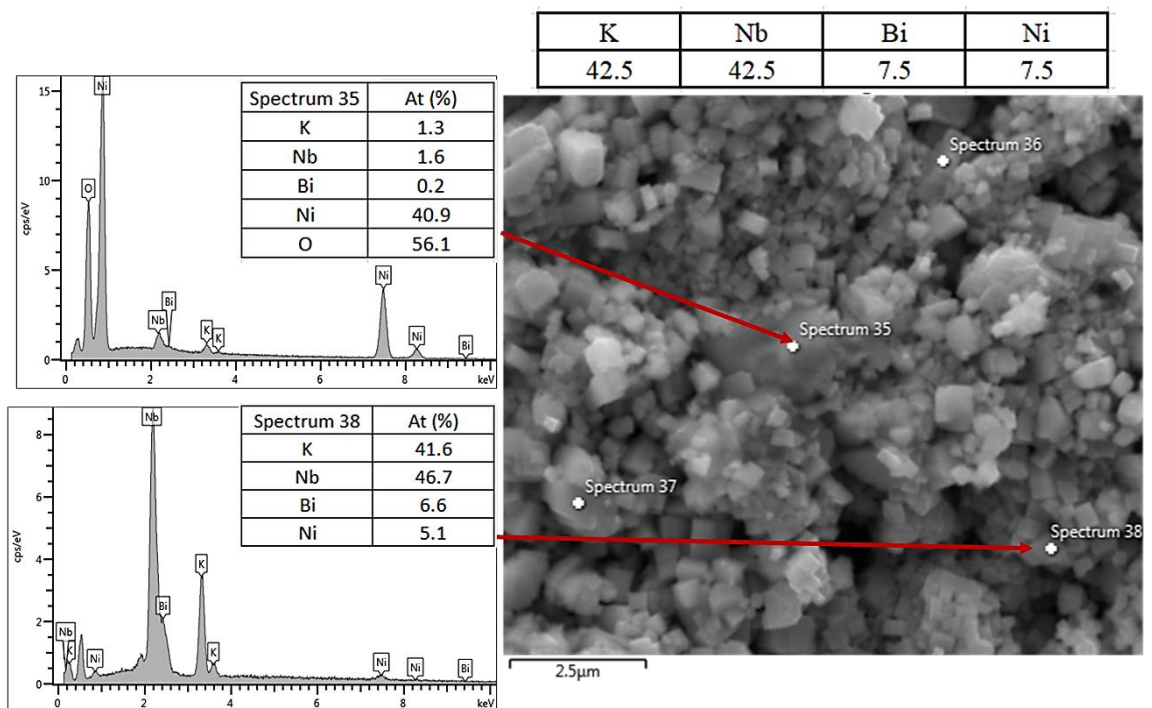


Figure 8. 12: SEM image and EDX spectra of unpolished 0.85 KNbO_3 – 0.15 BiNiO_3 ceramic sintered at 1070°C.

EDX analysis reveals more homogeneous chemical distribution for $x \geq 0.20$ (Table 8. 6.) However, secondary phases are again detected, such as NiO particles (Figure 8. 13) and K -rich regions ($\sim \text{A}_2\text{BO}_6$) (Figure 8. 14) also observed for $x=0.15$.

$x=0.20$

	Theoretical	Experimental	Relative error (%)
K/Nb	1	0.95(4)	5
K/Bi	4	4(1)	0
K/Ni	4	7(1)	75

Table 8. 6: Experimental (average) and theoretical K/Nb, K/Bi and K/Ni ratios for 0.80 KNbO_3 – 0.20 BiNiO_3 ceramic sintered at 1070°C.

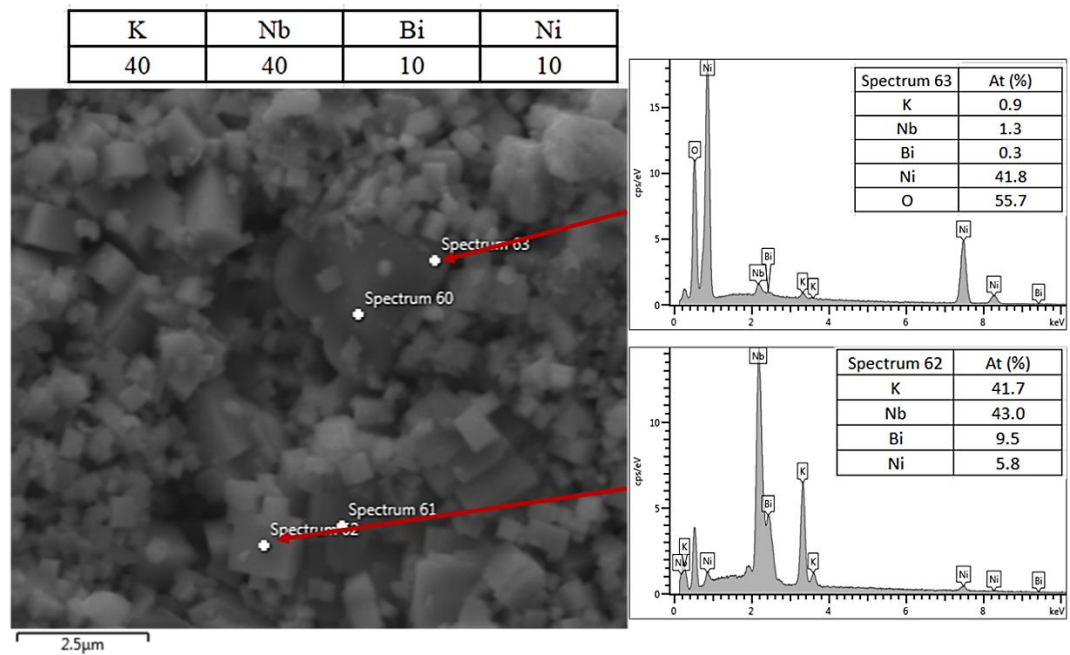


Figure 8. 13: SEM image and EDX spectra of unpolished 0.80 KNbO_3 – 0.20 BiNiO_3 ceramic sintered at 1070°C. NiO is detected.

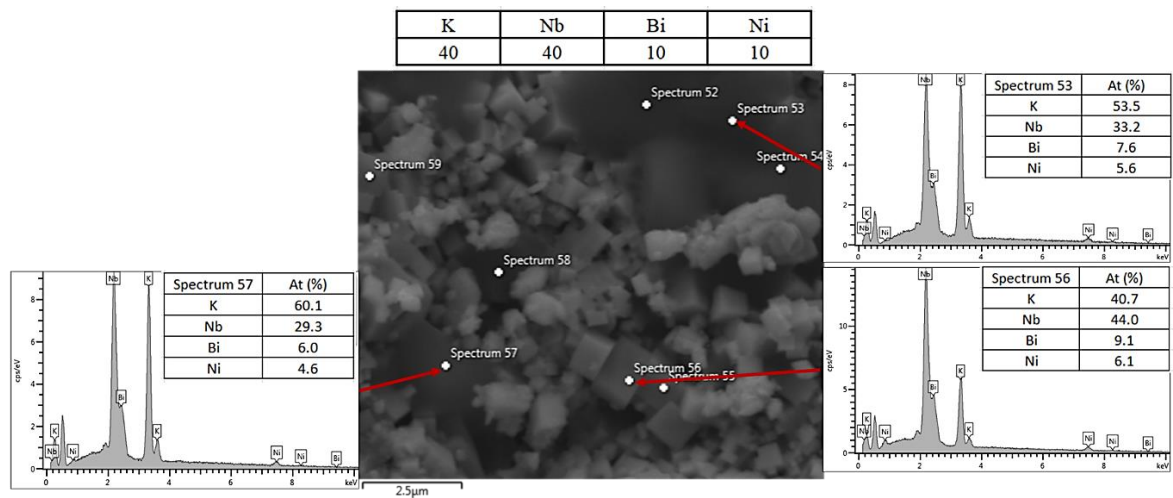


Figure 8. 14: SEM image and EDX spectra of unpolished 0.80 KNbO_3 – 0.20 BiNiO_3 ceramic sintered at 1070°C reveal also the appearance of grains with high concentration of K and Nb.

Finally, KNBN $x=0.25$ shows the closest experimental molar relations to the intended stoichiometry. Higher concentration of Bi^{+3} and Ni^{+3} enhance the solubility of these species (Table 8. 7). Nevertheless, K-rich regions are also detected in this composition (Figure 8. 15).

$x=0.25$			
	Stoichiometric	Experimental	Relative error (%)
K/Nb	1	0.94(7)	6
K/Bi	3	3.4(5)	13
K/Ni	3	4 (1)	33

Table 8. 7: Experimental (average) and theoretical K/Nb, K/Bi and K/Ni ratios for 0.75 $\text{KNbO}_3 - 0.25 \text{BiNiO}_3$ ceramic sintered at 1070°C.

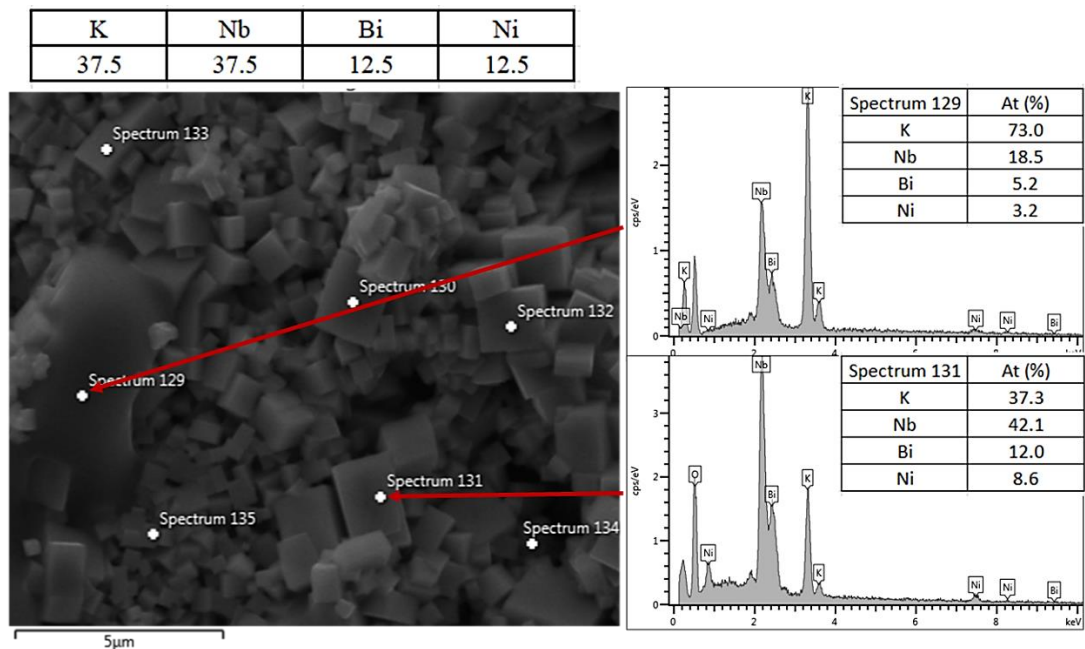


Figure 8. 15: SEM image and EDX spectra of unpolished 0.75 $\text{KNbO}_3 - 0.25 \text{BiNiO}_3$ ceramic sintered at 1070°C.

Summarising, KNBN system shows difficulties to achieve the intended stoichiometry, especially for Ni. Unreacted NiO (Figure 8. 16) leads to low concentration of Ni in the solid-solution. Indeed, high molar K/Ni values are obtained in all KNBN composition. Elements are more homogeneously dispersed in KNBN $x=0.20$ and $x=0.25$, as confirmed by EDX mapping. NiO particles and K-rich regions are detected for $x=0.05$ and $x=0.20$ by EDX mapping.

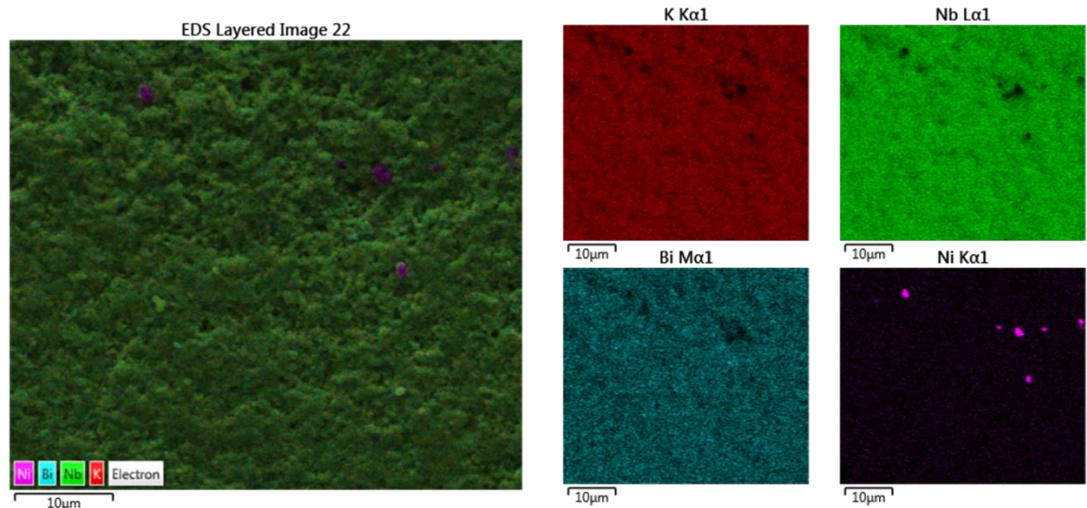


Figure 8. 16: SEM image of the examined region EDX mapping of K, Nb, Bi and Ni for KNBN $x=0.05$

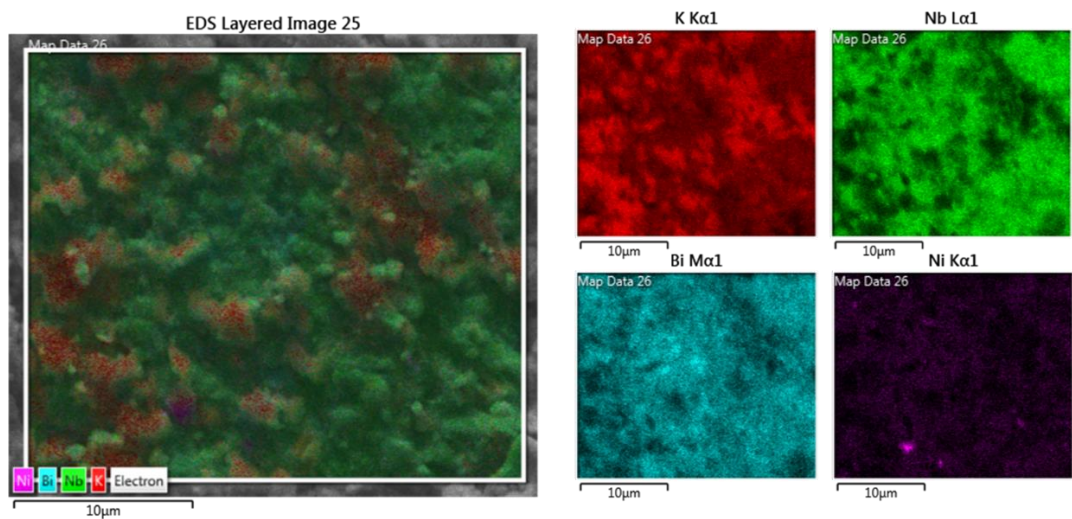


Figure 8. 17: SEM image of the examined region EDX mapping of K, Nb, Bi and Ni for KNBN $x=0.20$

8.3. Electrical Characterisation

8.3.1. Dielectric Characterisation

The temperature dependence of the permittivity, ϵ_r , and dielectric losses, $\tan\delta$, for KNBN ceramics ($x= 0.05, 0.10, 0.15, 0.20$ and 0.25) measured at 1 kHz, 10 kHz, 100 kHz and 250 kHz is shown in the following figures (Figure 8. 18-22)). The impact of doping on phase transitions is examined and compared with dielectric anomalies of undoped KN.

For $x=0.05$ (Figure 8. 18), $x= 0.10$ (Figure 8. 19) and $x=0.15$ (Figure 8. 20), three broad dielectric anomalies are observed at ~ 100 °C, at ~ 220 °C and ~ 390 °C. The first anomaly can be hypothetically attributed to a pseudocubic secondary phase. As described in Chapter 3 the two maxima values of ϵ_r at ~ 200 °C and ~ 400 °C, are related to the orthorhombic-to-tetragonal and the tetragonal-to-cubic structural phase transitions, respectively. The temperature for these anomalies remains almost constant, but their magnitude decreases with x . Moreover, a strong frequency dependence of both ϵ_r and $\tan\delta$ is measured for all the compositions. Nevertheless, KNBN $x\geq 0.20$ compositions only show the broad dielectric anomaly at ~ 100 °C and the frequency dependence is less marked, as shown in Figure 8. 21 and Figure 8. 22.

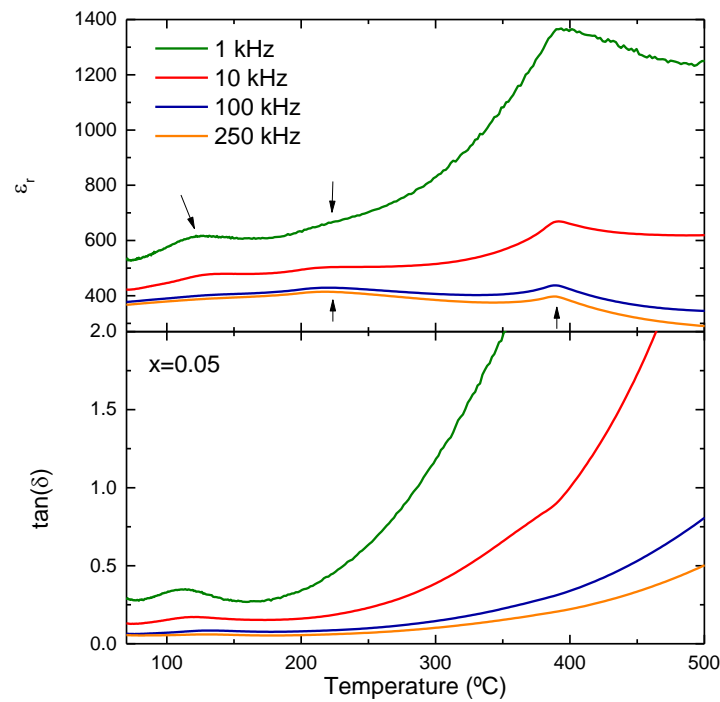


Figure 8. 18: Temperature dependence of ϵ_r and $\tan\delta$ for 0.95 $\text{KNbO}_3\text{-}0.05$ BiNiO_3 solid solution at 1 kHz, 10 kHz and 100 kHz during cooling.

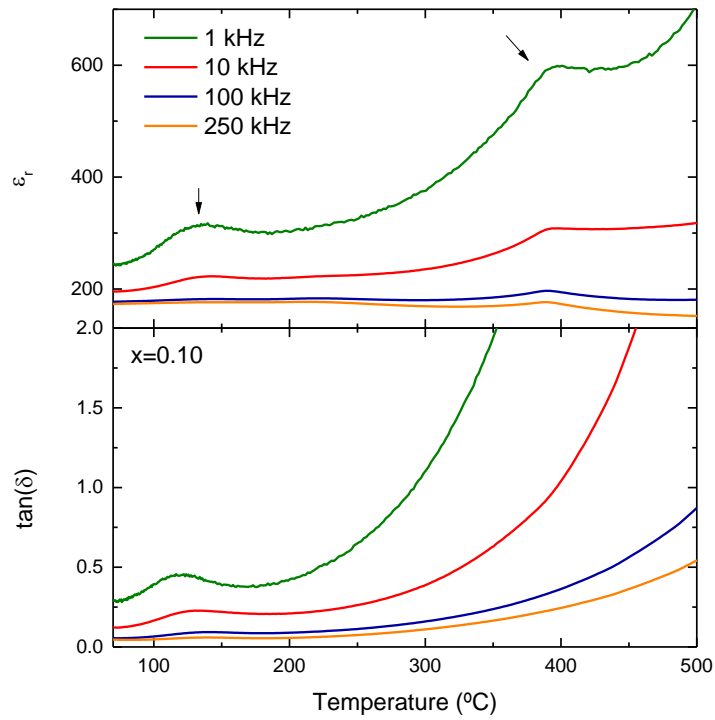


Figure 8. 19 Temperature dependence of ϵ_r and $\tan\delta$ for 0.90 $\text{KNbO}_3\text{-}0.10$ BiNiO_3 solid solution at 1 kHz, 10 kHz and 100 kHz during cooling.

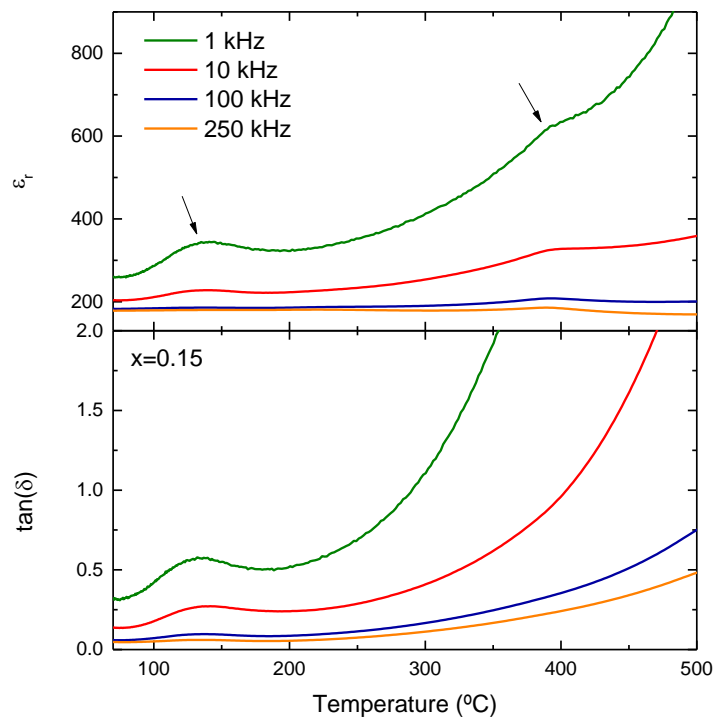


Figure 8. 20: Temperature dependence of ϵ_r and $\tan\delta$ for 0.85 $\text{KNbO}_3\text{-}0.15$ BiNiO_3 solid solution at 1 kHz, 10 kHz and 100 kHz during cooling.

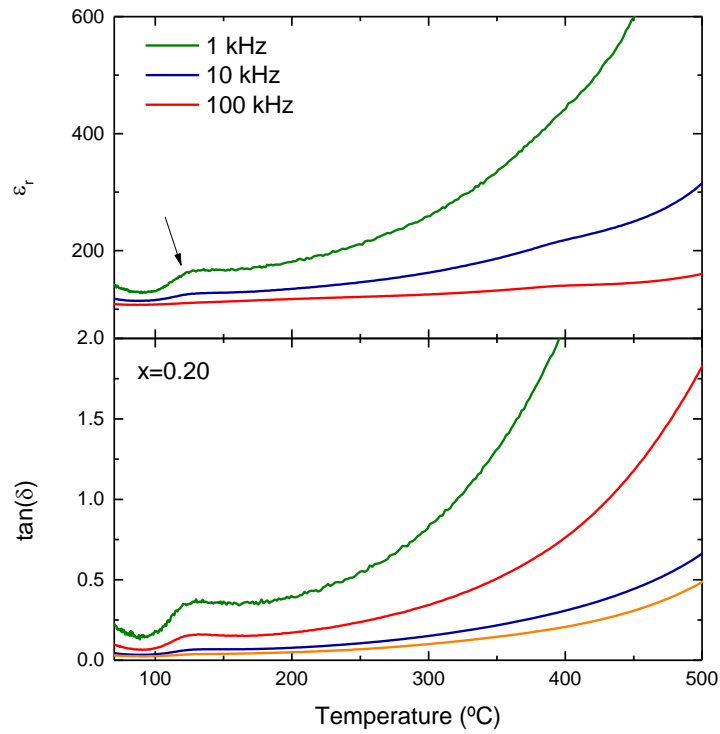


Figure 8. 21: Temperature dependence of ϵ_r and $\tan\delta$ for $0.80\text{KNbO}_3\text{-}0.20\text{ BiNiO}_3$ solid solution at 1 kHz, 10 kHz and 100 kHz during cooling.

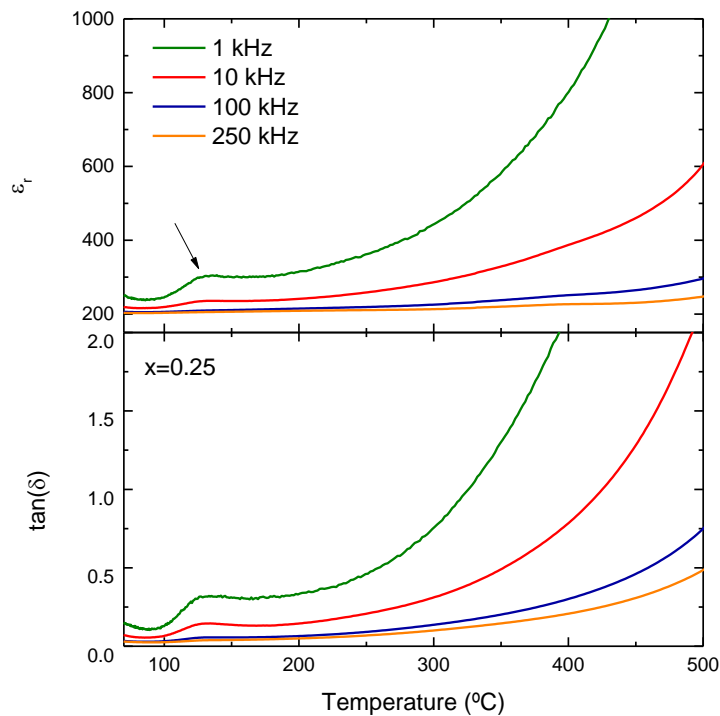


Figure 8. 22: Temperature dependence of ϵ_r and $\tan\delta$ for $0.75\text{ KNbO}_3\text{-}0.25\text{ BiNiO}_3$ solid solution at 1 kHz, 10 kHz and 100 kHz during cooling.

$\text{KNbO}_3-x\text{BiNiO}_3$ $x=0.25$ only shows the broad anomaly at $\sim 100^\circ\text{C}$, which might be linked to the phase described for this sample from Raman spectrum evolution with temperature in section 8.7. Indeed, the polar-to-non-polar phase transition is observed in the same temperature range as the dielectric anomaly.

The temperature dependence of relative permittivity and dielectric losses for $\text{KNbO}_3-x\text{BiNiO}_3$ ceramics at 100 kHz is shown in Figure 8. 23.

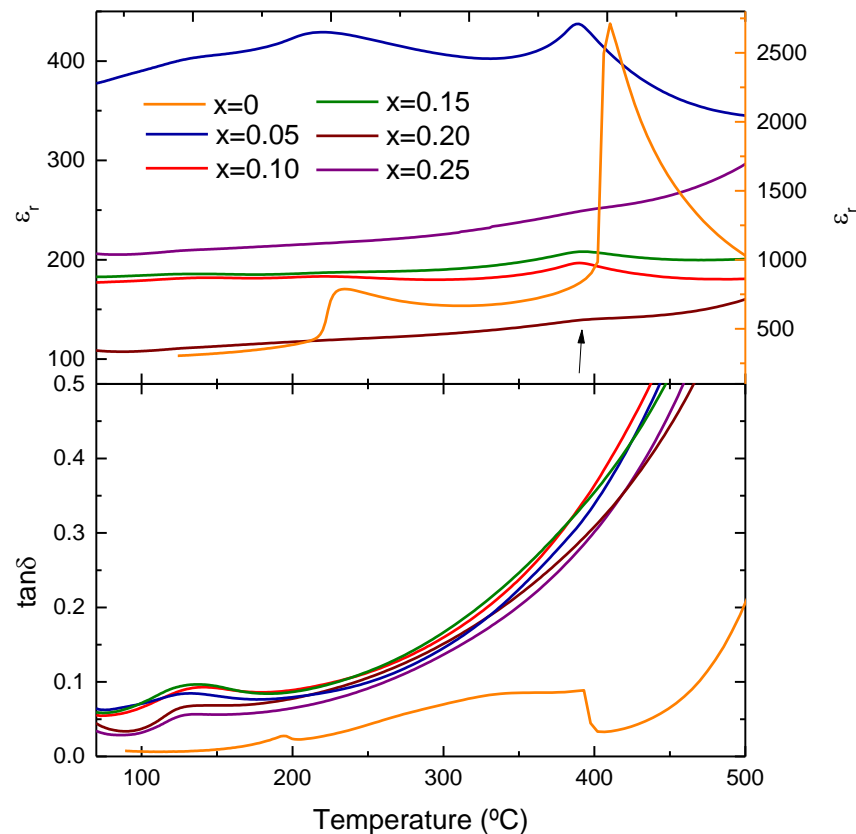


Figure 8. 23: Temperature dependence of relative permittivity and dielectric losses for $(1-x)\text{KNbO}_3-x\text{BiNiO}_3$ ($0 \leq x \leq 0.25$) ceramics at 100 kHz. Note dielectric response for KN (orange curve) has different scale (right axes).

As explained in Chapter 4, KN ($x = 0$) shows two maxima values of ϵ_r at $\sim 205^\circ\text{C}$ and $\sim 400^\circ\text{C}$, which are related with the orthorhombic-to-tetragonal and the tetragonal-to-cubic structural phase transitions, respectively. These anomalies are visible up to $x=0.15$, suggesting the presence of a polar phase, even if it was not detected by XRD. No anomalies are measured for $x=0.20$ and $x=0.25$. The protuberance at 100°C is unnoticeable for 100 kHz. Undoped KN exhibit lower dielectric losses than the rest of the compositions.

8.4. Optical Characterisation

8.4.1 Diffuse reflectance spectroscopy

Tauc plots for KNBN $0 \leq x \leq 0.25$ ceramics are constructed from diffuse reflectance data (Figure 8. 24) and shown in Figure 8. 25 (direct optical band-gaps) and Figure 8. 26. (indirect optical band-gap). The maximum of the valence band of KNBN compositions can be attributed to O 2p orbital and the conduction band minimum to Nb 4d states. Direct band-gaps narrow from 3.62 eV ($x=0$) to 3.32 eV ($x=0.25$) with increasing $\text{Bi}^{+3}/\text{Ni}^{+3}$ contents into the KN lattice.

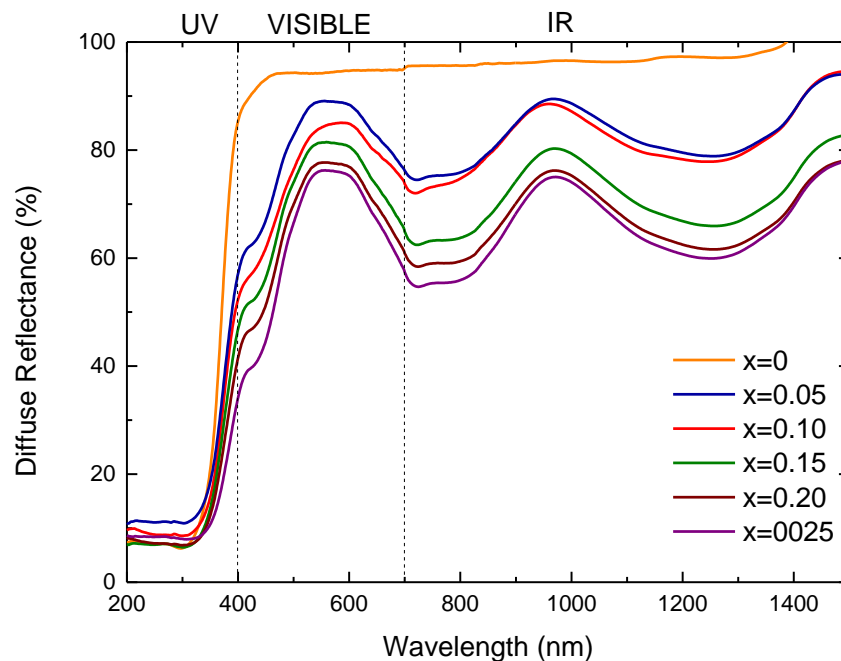


Figure 8. 24: Diffuse reflectance as a function of wavelength for KNBN system (raw data).

In the case of KNBN compounds they present indirect optical band gaps, the narrowing is produced from 3.20 eV ($x=0$) to 2.87 eV ($x=0.25$). Four lumps (labelled as 1, 2, 3 and 4 in Figure 8. 26) emerge at 1 eV, 1.53 eV, 1.73 eV and 2.82 eV in all the spectra. Similar pattern is reported in literature for KN-BNN compositions (Wu et al., 2016). These absorption bands are related with d-d transitions by Ni^{+2} ions within the bulk or from hybridized Ni 3d and O 2p to Nb 4d states transitions. Indeed as mentioned in Chapter 1, low band gap in KN solid solutions doped with Ni may arise from inadequate interpretation of these absorbance regions.

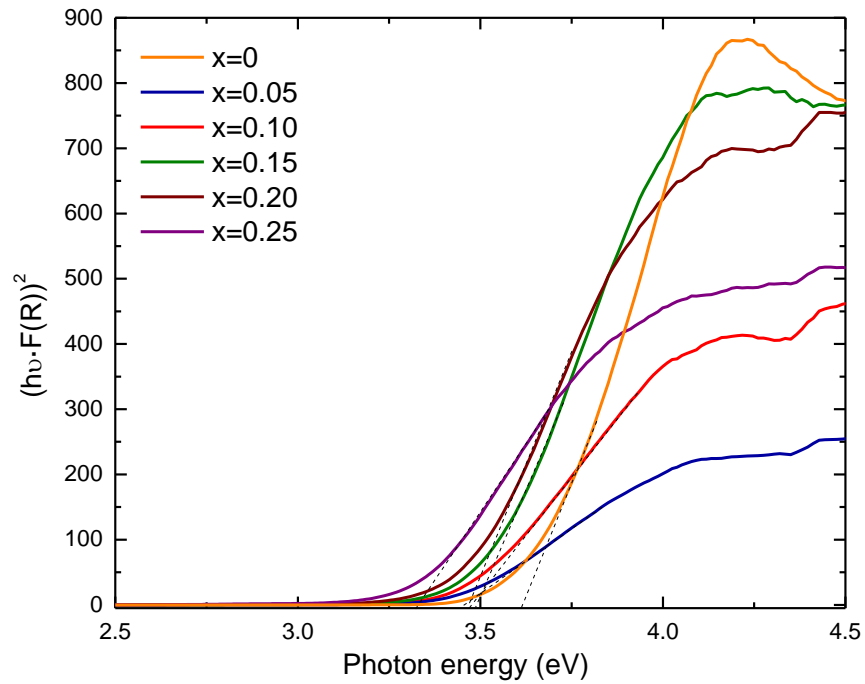


Figure 8. 25: Tauc plot for direct band gaps for KNBN $0 \leq x \leq 0.25$ ceramics.

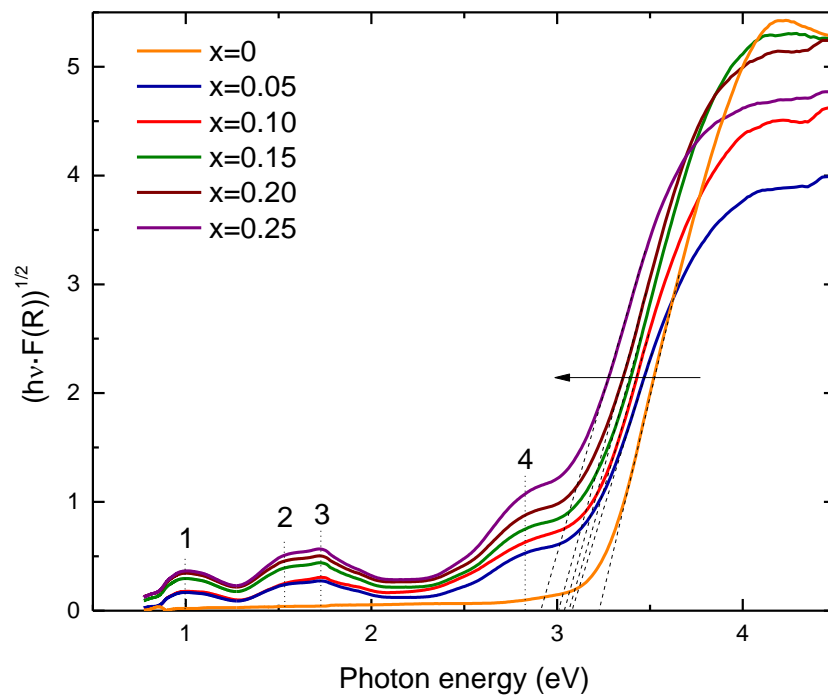


Figure 8. 26.: Tauc plot for indirect band gaps for KNBN $0 \leq x \leq 0.25$ ceramics.

Evolution of direct and indirect band-gap values as a function of x is illustrated in Figure 8. 27.

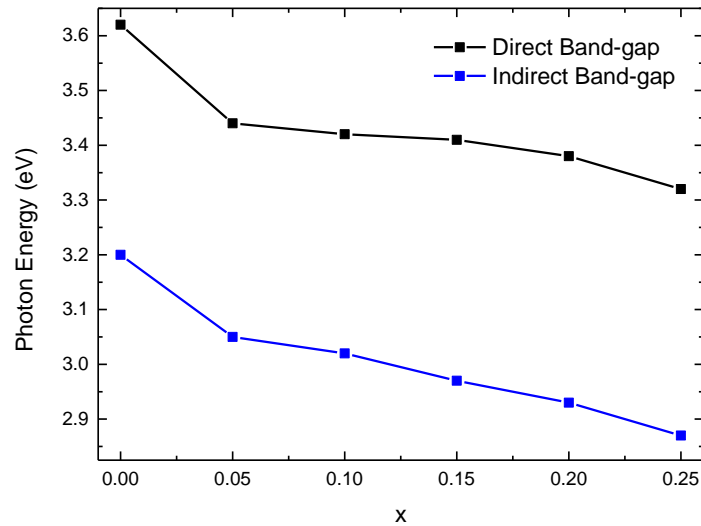


Figure 8. 27: compositional evolution of direct and indirect band-gap for KNBN $0 \leq x \leq 0.25$ ceramics.

As expected, direct band gaps present larger values than indirect band gaps. Both decrease following the same trend. The largest reduction happens in between $x=0$ and $x=0.05$. Apart from that, the values decrease systematically with x .

8.5. Discussion

Unreacted oxides, Bi_3O_2 and NiO , were detected in ceramic powders after two calcinations by XRD analyses. An extra heat treatment at 850°C for 4 hours helped the reaction, indeed Bi_3O_2 phase disappeared and the amount of NiO phase was considerably reduced as shown in XRD results. NiO particles were detected in SEM images due to their morphology and in EDX analyses due to their chemical composition. Unreacted NiO particles cause low concentration of Ni in KNBN system (Table 8. 8), especially for $x=0.05$, $x=0.10$ and $x=0.15$. This phenomenon evidences the enhancement of NiO solubility for larger concentration of $\text{Bi}^{+3}/\text{Ni}^{+3}$. Moreover, high deviation errors mean heterogeneous chemical distributions, as it is shown in Appendix E.

	$x=0.05$	$x=0.10$	$x=0.15$	$x=0.20$	$x=0.25$
$(K/Ni)_{\text{Experimental}}$	31 (9)	16(7)	10(2)	7(1)	4(1)
$(K/Ni)_{\text{Theoretical}}$	19	10	5.67	4	3

Table 8. 8.: Experimental and theoretical K/Ni ratios for $(1-x)\text{KNbO}_3\text{-}x\text{BiNiO}_3$ ($0.5 \leq x \leq 0.25$) ceramics sintered at 1070°C .

Difficulties on crystal structure assignment were also encountered for this system. Firstly, XRD results do not provide enough resolution to accurately determine the crystal symmetries. XRD data were refined by Rietveld method and cubic symmetry ($\text{Pm}\bar{3}\text{m}$) was attributed up to $x=0.25$. The coexistence of orthorhombic ($\text{Amm}2$) and cubic ($\text{Pm}\bar{3}\text{m}$) phase is only ascribed for $x=0.05$. However, the appearance of the sharp mode at 192 cm^{-1} and the interference dip at 197 cm^{-1} in Raman spectra and dielectric anomalies with temperature at $\sim 220^\circ\text{C}$ and $\sim 390^\circ\text{C}$ for KNBN $x=0.05$, $x=0.10$ and $x=0.15$ demonstrate the occurrence of a polar phase up to $x=0.15$. For the rest of the compositions, neither dielectric anomalies nor sharp peaks in Raman spectra are visible, which agrees with the cubic symmetry assignment. Raman activity reveal non- truly cubic symmetry.

Despite these difficulties, the incorporation of $\text{Bi}^{+3}/\text{Ni}^{+3}$ into KNbO_3 lattice is supported by: first, reflections in XRD patterns shift towards lower 2θ angles with x , which means the unit cell increases with increasing x . Second, EDX analyses show that ceramics have the tendency to get closer to the intended stoichiometry within the standard deviation margins. Third, systematic band-gap narrowing is observed with increasing x .

Locally, different facts also show non-homogeneous incorporation of the dopants into KNbO_3 . First, multiphase formation as explained above. Second, broader Raman modes with increasing BiNiO_3 content, which indicates more disorder in the lattice. Furthermore, extra modes emerge in Raman spectra, which can be related with local impurities. Third, SEM images show a wide spectrum of grain morphologies that is accompanied with changes in the chemical composition (detected by EDX analyses). Fourth, broad dielectric anomalies exist as a function of the temperature.

8.6. Conclusions

KNBN system required three calcinations to react the starting oxides and carbonates. XRD revealed unreacted NiO phase in the sintered ceramics, promoting low concentrations in all compositions. Upon doping, the pseudocubic unit cell volume continuously increases with increasing x . However, Raman results combined with dielectric measurements proved the occurrence of a polar phase up to $x=0.15$. For

compositions with low concentrations of $\text{Bi}^{+3}/\text{Ni}^{+3}$ ($0.05 \leq x \leq 0.15$) non-homogeneous microstructure and regions with different chemical compositions were detected by XRD, Raman spectroscopy, SEM and EDX. However, EDX mapping confirmed a better homogenisation of the chemicals for $x=0.20$ and $x=0.25$, which is accompanied by grain growth. Despite all these problems, a systematic band-gap narrowing was observed with increasing x .

8.7. References

- Azuma, M., Carlsson, S., Rodgers, J., Tucker, M. G., Tsujimoto, M., Ishiwata, S., Attfield, J. P. (2007). Pressure-induced intermetallic valence transition in BiNiO_3 . *Journal of the American Chemical Society*, 129(8), 14433–6. <https://doi.org/10.1021/ja074880u>
- Azuma, M., Chen, W., Seki, H., Czapski, M., Olga, S., Oka, K., Attfield, J. P. (2011). Colossal negative thermal expansion in BiNiO_3 induced by intermetallic charge transfer. *Nature Communications*, 2, 347. <https://doi.org/10.1038/ncomms1361>
- Belik, A. A. (2012). Polar and nonpolar phases of BiMO_3 : A review. *Journal of Solid State Chemistry*, 195, 32–40. <https://doi.org/10.1016/j.jssc.2012.01.025>
- Carlsson, S. J. E., Azuma, M., Shimakawa, Y., Takano, M., Hewat, A., & Attfield, J. P. (2008). Neutron powder diffraction study of the crystal and magnetic structures of BiNiO_3 at low temperature. *Journal of Solid State Chemistry*, 181(3), 611–615. <https://doi.org/10.1016/j.jssc.2007.12.037>
- Catalan, G. (2008). Progress in perovskite nickelate research. *Phase Transitions*, 81(7–8), 729–749. <https://doi.org/10.1080/01411590801992463>
- Ishiwata, S., Azuma, M., Takano, M., Nishibori, E., Takata, M., Sakata, M., & Kato, K. (2002). High pressure synthesis, crystal structure and physical properties of a new Ni(ii) perovskite BiNiO_3 . *Journal of Materials Chemistry*, 12(12), 3733–3737. <https://doi.org/10.1039/b206022a>
- Liu, C., Liu, X., Jiang, M., & Ma, J. (2010). Microstructure and piezoelectric properties of $\text{Na}_{0.5}\text{K}_{0.5}\text{NbO}_3\text{-BiNiO}_3\text{-LiSbO}_3$ lead-free ceramics. *Journal of Alloys and*

Compounds, 503(1), 209–212.
<https://doi.org/http://dx.doi.org/10.1016/j.jallcom.2010.04.234>

McLeod, J. A., Pchelkina, Z. V., Finkelstein, L. D., Kurmaev, E. Z., Wilks, R. G., Moewes, A., Takayama-Muromachi, E. (2010). Electronic structure of BiMO_3 multiferroics and related oxides. *Physical Review B - Condensed Matter and Materials Physics*, 81(14), 1–10. <https://doi.org/10.1103/PhysRevB.81.144103>

Mizumaki, M., Ishimatsu, N., Kawamura, N., Azuma, M., Shimakawa, Y., Takano, M., & Uozumi, T. (2009). Direct observation of the pressure-induced charge redistribution in BiNiO_3 by X-ray absorption spectroscopy. *Physical Review B - Condensed Matter and Materials Physics*, 80(23), 2–5. <https://doi.org/10.1103/PhysRevB.80.233104>

Wadati, H., Takizawa, M., Tran, T. T., Tanaka, K., Mizokawa, T., Fujimori, A., ... Takano, M. (2005). Valence changes associated with the metal-insulator transition in $\text{Bi}_{1-x}\text{La}_x\text{NiO}_3$. *Physical Review B*, 72(15), 155103. <https://doi.org/10.1103/PhysRevB.72.155103>

Wu, P., Wang, G., Chen, R., Guo, Y., Ma, X., & Jiang, D. (2016). Advances Enhanced visible light absorption and photocatalytic activity of gel based Pechini method. *RSC Advances*, 6, 82409–82416. <https://doi.org/10.1039/C6RA15288K>

Chapter 9

Ferroelectric and optical properties for

KNbO_3 vs $\text{K}_{0.90}\text{Ba}_{0.1}\text{Nb}_{0.95}\text{Ni}_{0.05}\text{O}_3$

$\text{K}_{0.5}\text{Na}_{0.5}\text{NbO}_3$ vs

$\text{K}_{0.49}\text{Na}_{0.49}\text{Ba}_{0.02}\text{Nb}_{0.99}\text{Ni}_{0.01}\text{O}_3$

9.1. Introduction

9.2. Structural and chemical characterisation

9.2.1. Purity and X-ray powder diffraction

9.2.1.1. Results for KN and KN-BNN powders and ceramics

9.2.1.2. Results for KNN and KNN-BNN powders and ceramics

9.2.2. Raman spectroscopy

9.2.3. SEM

9.2.4. EDX

9.3. Electrical Characterisation

9.3.1. Piezo- and Ferroelectric Characterisation

9.4. Optical Characterisation

9.4.1 Diffuse reflectance spectroscopy

9.5. Discussion

9.6. Conclusions

9.7. References

9. Ferroelectric and optical properties for:



9.1. Introduction

Following the 2013's Nature letter claiming 0.90 KNbO_3 - $0.10 \text{ BaNi}_{0.5}\text{Nb}_{0.5}\text{O}_3$ (KN-BNN) to be a polar perovskite at room temperature, with a direct band-gap of 1.39 eV and exhibiting a photocurrent density of ~ 50 times larger than $(\text{Pb}_{0.5}\text{La}_{0.5})(\text{Zr}_{0.5}\text{Ti}_{0.5})\text{O}_3$, some other researchers investigated the $(1-x) \text{ KNbO}_3$ - $x \text{ BaNi}_{0.5}\text{Nb}_{0.5}\text{O}_3$ system (Ilya Grinberg et al., 2013). The aforementioned results were also rationalised by different theoretical works (F. Wang, Grinberg, & Rappe, 2014; Fenggong Wang & Rappe, 2015). Details on the origin of the band-gap narrowing in the KN-BNN solid solutions were reviewed in section 1.5. of this thesis. A few researchers reported band-gaps as wide as 3.20 eV, as listed in Table 9. 1, which also includes spontaneous polarisation values. A more detailed review of these works is provided in Chapter 1. In the initial report (Ilya Grinberg et al., 2013) KN-BNN was deemed too conductive at room-temperature to attempt the evaluation of its polarisation response to a large electric field for this reason that measurement was carried out between 77 K and 170 K, and a spontaneous polarisation of $20 \mu\text{C}/\text{cm}^2$, measured under 250 kV/m was reported. Spontaneous polarisation for KN-BNN ceramics seems to reach $\sim 10 \mu\text{C}/\text{cm}^2$ at RT under 80 kV/cm (Bai, Siponkoski, Peräntie, Jantunen, & Juuti, 2017). One of the motivations of this Chapter is the attempt to resolve the controversial issues surrounding this compound.

KN- BNN		
Reference	Band-gap (eV)	Ps
(I. Grinberg et al., 2013)	1.39	20 $\mu\text{C}/\text{m}^2$ at 170 K under 250 kV/m
(Song et al., 2017)	1.8	-
(Zhou, Deng, Yang, & Chu, 2014)	1.8	-
(Bai, Siponkoski, et al., 2017)	1.48	$\sim 10 \mu\text{C}/\text{cm}^2$ at RT under 80 kV/cm
(Zhou, Deng, Yang, & Chu, 2016)	2.51	-
(Wu et al., 2016)	3.20	-

Table 9. 1: Experimental band gap and spontaneous polarisation values for KN-BNN (0.9 KNbO₃- 0.10 BaNi_{0.5}Nb_{0.5}O₃) ceramic found in the literature.

In 2017, Bai et al investigated a similar compound based on 0.98 K_{0.5}Na_{0.5}NbO₃- 0.02 BaNi_{0.5}Nb_{0.5}O₃ (KNN-BNN), which is able to withstand at room-temperature an electric field of 90 kV/cm leading to Ps=26 $\mu\text{C}/\text{cm}^2$ and shows a band-gap as narrow as 1.6 eV (Table 9. 3). Interestingly, FE properties of KNN-BNN are apparently comparable to those of undoped K_{0.5}Na_{0.5}NbO₃ (KNN) but with ~ 1 eV band-gap narrower (Table 9. 2).

KNN			
Reference	Band-gap (eV)	Reference	Ps
(Sun et al., 2017)	2.70	(Birol, Damjanovic, & Setter, 2006)	$\sim 25 \mu\text{C}/\text{cm}^2$ at RT under 80 kV/cm

Table 9. 2: Experimental band gap and spontaneous polarisation value for KNN (K_{0.5}Na_{0.5}NbO₃) ceramic found in the literature.

KNN-BNN		
Reference	Band-gap (eV)	Ps
(Bai, Tofel, et al., 2017)	1.60	26 $\mu\text{C}/\text{cm}^2$ at RT under 90 kV/cm

Table 9. 3.: Experimental band gap and spontaneous polarisation value for KNN-BNN (0.98 $\text{K}_{0.5}\text{Na}_{0.5}\text{NbO}_3$ -0.02 $\text{BaNi}_{0.5}\text{Nb}_{0.5}\text{O}_3$) ceramic found in the literature.

In summary, this chapter addresses the incongruence in the literature previously described. $\text{K}_{0.90}\text{Ba}_{0.1}\text{Nb}_{0.95}\text{Ni}_{0.05}\text{O}_3$ (KN-BNN) ceramic is prepared by solid-state reaction. In addition, $\text{K}_{0.49}\text{Na}_{0.49}\text{Ba}_{0.02}\text{Nb}_{0.99}\text{Ni}_{0.01}\text{O}_3$ (KNN-BNN) ceramic is prepared in order to reproduce the recent promising photoferroelectric properties reported. Their crystal structure, chemical composition, FE and optical properties will be characterised and compared to KNbO_3 and $\text{K}_{0.5}\text{Na}_{0.5}\text{NbO}_3$ results.

9.2. Structural and chemical characterisation

9.2.1. Purity and X-ray powder diffraction

KN, KN-BNN, KNN and KNN-BNN ceramics were prepared by solid-state reaction method. Stoichiometric ratios of K_2CO_3 , Nb_2O_5 , Na_2CO_3 , BaCO_3 and NiO powders were milled overnight and sieved for obtaining fine powder. The mixed powders were calcined in air at 850 °C two times for 4 hours with heating rate of 3°C/min. Powders were compacted into pellets and fired in air for 4 hours at 1070-1180°C using a controlled heating rate of 3 °C /min.

9.2.1.1. Results for KN and KN-BNN powders and ceramics

Figure 9. 1 and Figure 9. 2 illustrate RT XRD data for KN and KN-BNN calcined powders and sintered pellets, respectively.

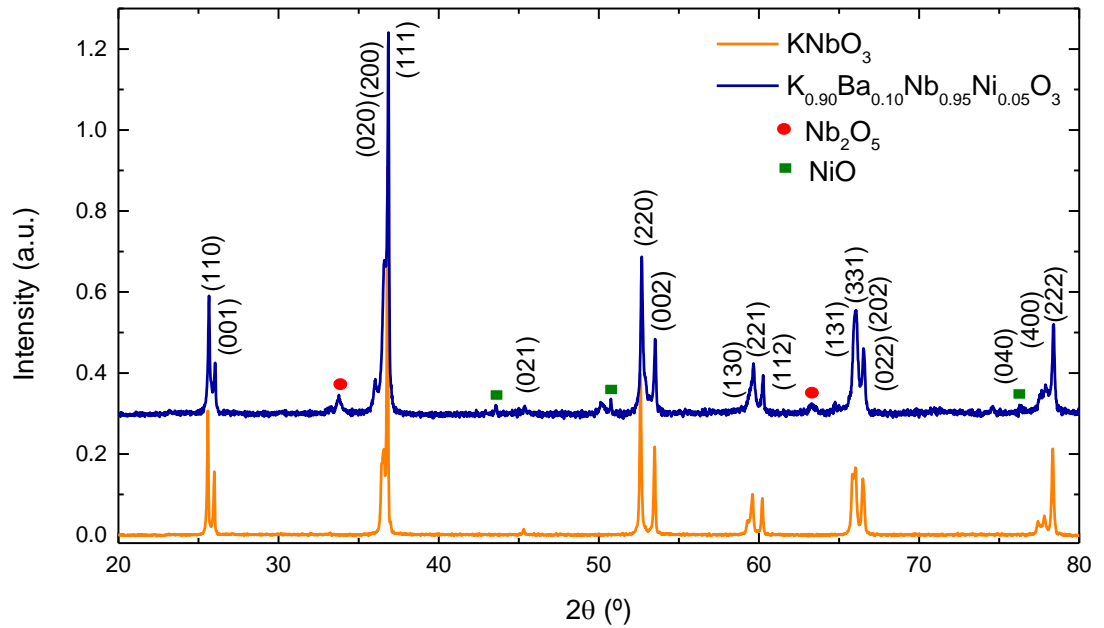


Figure 9. 1: Room-temperature XRD patterns of KN and KN-BNN calcined powders. Secondary phases, Nb_2O_5 and NiO , are indicated with red and green symbols, respectively.

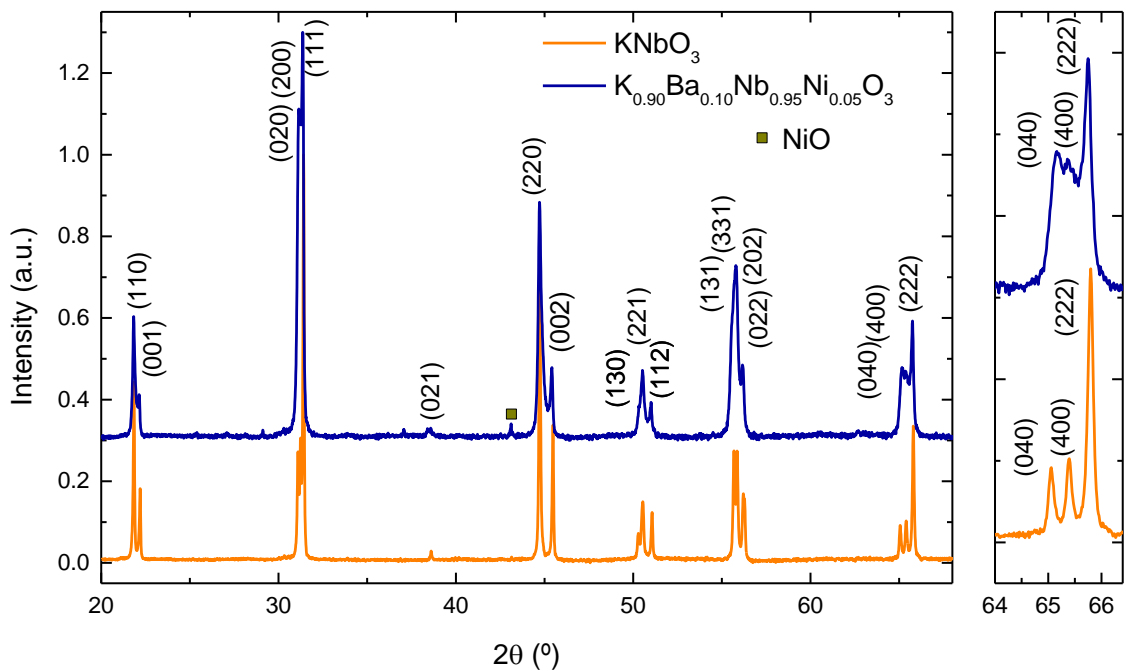


Figure 9. 2: Room-temperature XRD patterns of KN and KN-BNN sintered pellets.

XRD pattern of KN-BNN ceramic can be ascribed to orthorhombic crystal structure (Amm2 symmetry) as well as KN pattern. However, KN-BNN pattern exhibits broader peaks and peak splitting is not as clear as for KN, which could be related to the crystals size. After calcination, minor amounts of starting reactants (Nb_2O_5 and NiO) are detected, and after sintering, a small quantity of NiO is still present. This result is in agreement

with the literature (Bai, Siponkoski, et al., 2017; Ilya Grinberg et al., 2013). As demonstrated in Chapter 8, NiO exhibits major difficulties in reacting with the rest of oxides. Lattice parameters are calculated by Rietveld method as $a=3.9820(2)$ Å, $b=5.6927(3)$ Å and $c=5.7041(3)$ Å. The unit cell volume is only 0.12% larger than for KN. The sintering and the melting temperature of KN-BNN ceramic are very close, generating difficulties in the densification. Indeed, this compound only reached a relative density of 87% after firing at 1075°C for 4 h, while it melted at 1080°. Rietveld refinements results are summarised in Table 9. 4.

9.2.1.2. Results for KNN and KNN-BNN powders and ceramics

Room-temperature XRD analysis for KNN and KNN-BNN calcined powders and sintered ceramics are shown in Figure 9. 3 and Figure 9. 4, respectively.

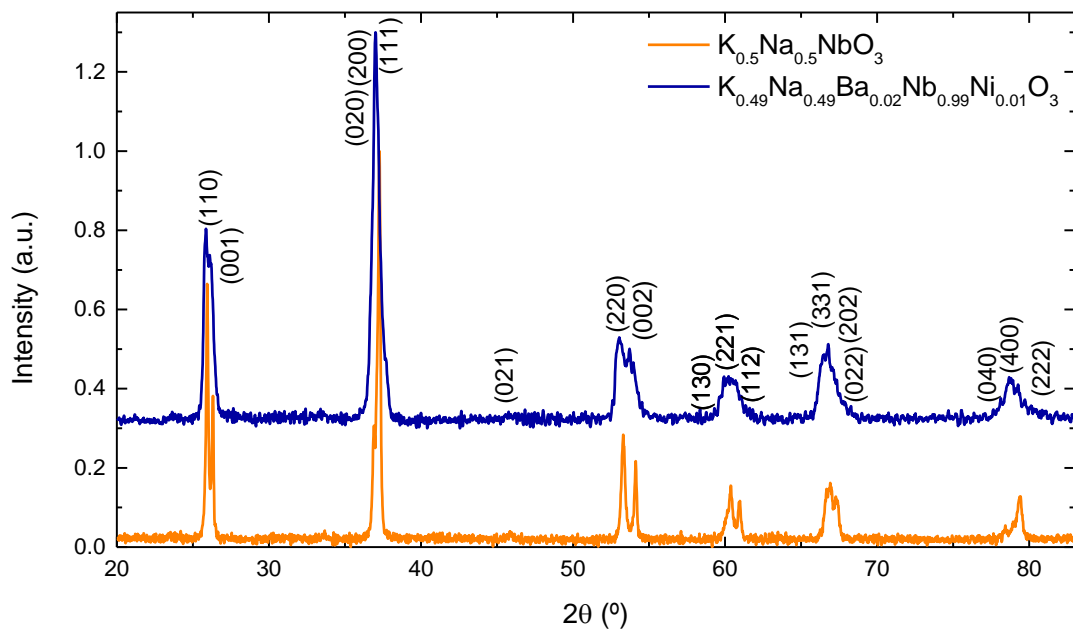


Figure 9. 3: Room-temperature XRD patterns of KNN and KNN-BNN calcined powders.

XRD pattern for KNN-BNN powder exhibits much broader peaks than KNN, preventing to distinguish the peak splitting. Broader peaks are often associated with non-homogeneity in powders produced by solid-state reaction method.

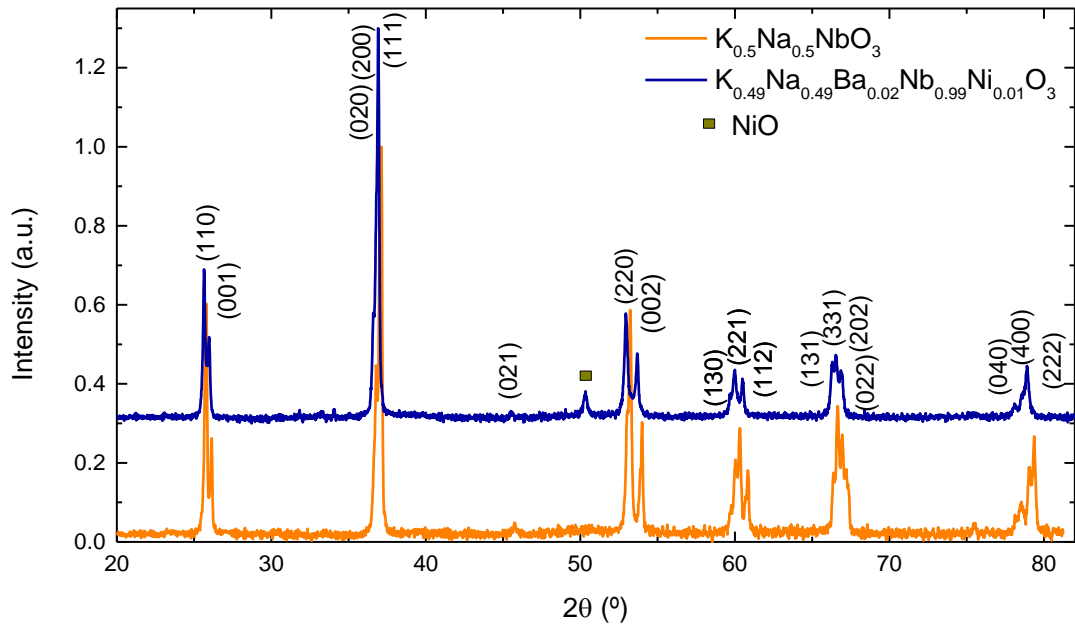


Figure 9. 4: Room-temperature XRD patterns of KNN and KNN-BNN sintered ceramics.

Again, KNN-BNN ceramics exhibit well-defined sharp peaks, which can be indexed to an orthorhombic cell with $Amm2$ symmetry. Both KNN and KNN-BNN show very similar XRD patterns. The same secondary phase (NiO) is found on KNN-BNN, which again evidences chemical inhomogeneity in the sample. This second phase was also reported by Bai in 2017. Rietveld refinement estimates lattice parameters for KNN-BNN: $a=3.9488 \text{ \AA}$, $b=5.6394(4) \text{ \AA}$ and $c=5.6648(3) \text{ \AA}$ and its unit cell volume is 1.25% larger than KNN. In addition, KN-BNN ceramic was sintered at 1175°C in contrast to KNN that was sintered at 1100°C and reached a relative density of 95%. Rietveld refinements results are shown in Table 9. 4.

	KN	KN-BNN	KNN	KNN-BNN
Space Group	Amm2	Amm2	Amm2	Amm2
Density (Experimental) (g/cm³)	4.35(3)	4.22(16)	4.29(10)	4.35(12)
Density (calculated) (g/cm³)	4.6273(1)	4.8310(4)	4.5831(5)	4.5731(4)
Relative Density (%)	94(1)	87(3)	90(2)	95(2)
a (Å)	3.9711(1)	3.9820(2)	3.9299(2)	3.9488(2)
b (Å)	5.6909(1)	5.6927(3)	5.6148(4)	5.6394(3)
c (Å)	5.7158(1)	5.7041(3)	5.6460(3)	5.6648(3)
V/10⁶ (pm³)	64.576(2)	64.651(6)	62.291(6)	63.074(5)
R_{exp}	1.26460	1.32958	2.15325	2.27382
R_{profile}	2.97912	2.33741	2.84928	2.99204
R_{wp}	4.65175	3.55947	3.89764	3.87318
GOF	13.53086	7.16704	3.27654	2.90151

Table 9. 4: Experimental and theoretical density, lattice parameters and agreement indices for KN (KNbO₃), KN-BNN, KNN and KNN-BNN calculate by Rietveld Refinement.

9.2.2. Raman spectroscopy

9.2.2.1. Results for KN and KN-BNN

The Raman spectrum for KN-BNN calcined powders is very similar to that of undoped KN (Figure 9. 5). All Raman modes for KN (described in Chapter 4) can be assigned to KN-BNN spectra, confirming the orthorhombic symmetry. Nevertheless, some differences are perceived in the Raman spectrum for KN-BNN sintered pellets in comparison to KN spectrum (Figure 9. 6) such as broader peaks and shifted to lower wavenumber. The shift at low and high frequencies is $\sim 12 \text{ cm}^{-1}$ and $\sim 6 \text{ cm}^{-1}$, respectively. In addition, the emergence of (1) and (2) modes, one at 104 cm^{-1} and other at 164 cm^{-1} as

a shoulder of the sharp peak at 192 cm^{-1} (indicated with arrows) was also observed and described in other systems (Chapters 4,5,6,7 and 8)). It is noted, mode (1) was already in the KN-BNN powder and the bump labelled as '?' in Figure 9. 5 disappears in ceramics.

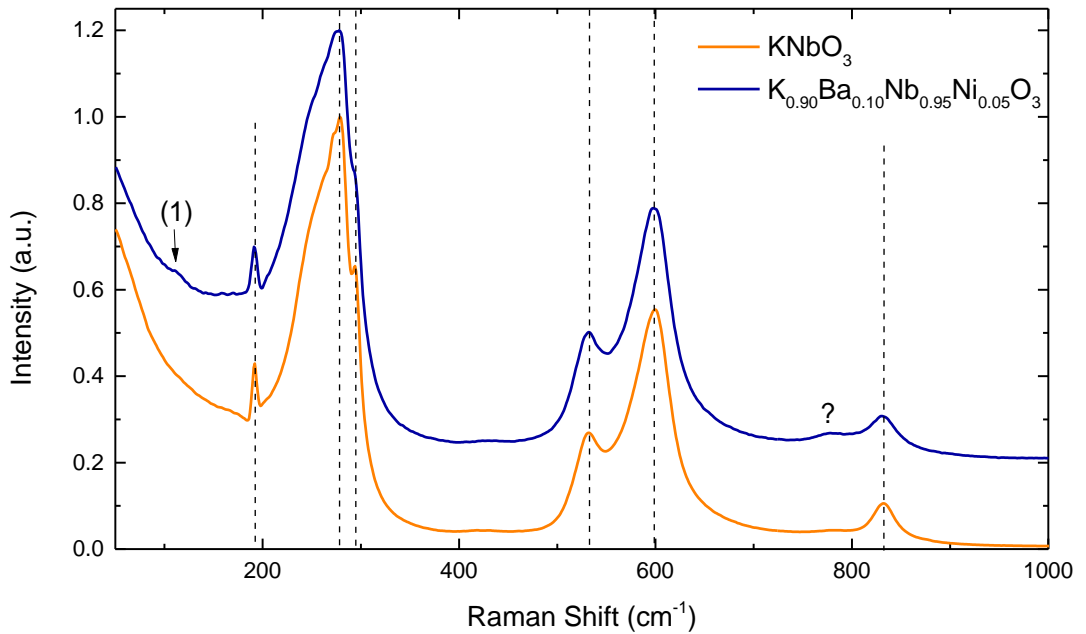


Figure 9. 5: Room-temperature Raman spectra for KN and KN-BNN calcined powders.

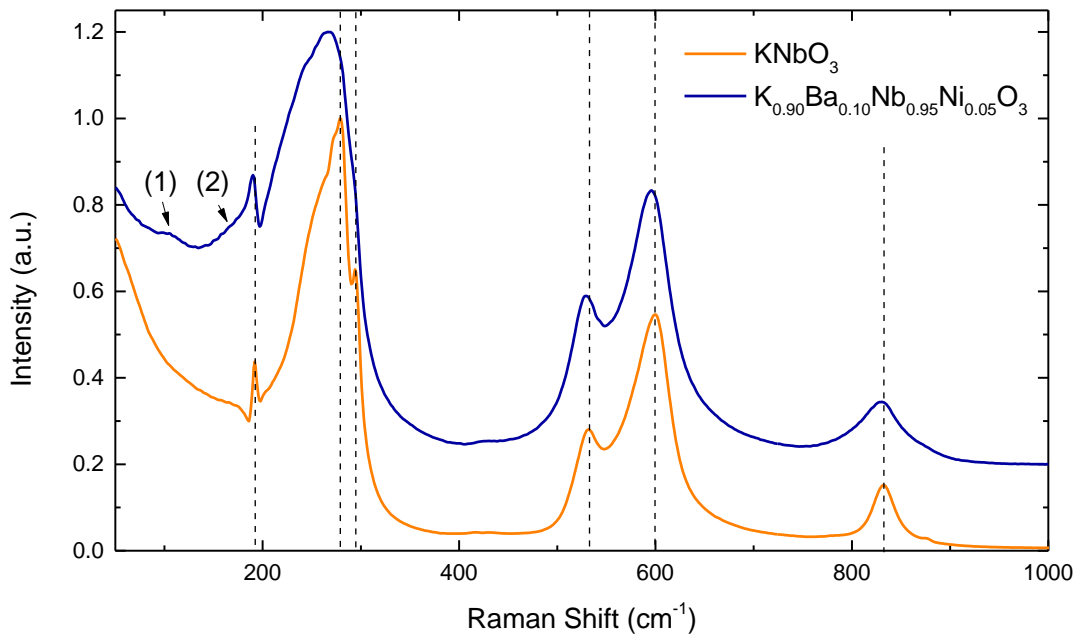


Figure 9. 6: Room-temperature Raman spectra for KN and KN-BNN sintered pellets.

9.2.2.2. Results for KNN and KNN-BNN

Room-temperature Raman spectra for KNN and KNN-BNN calcined powders and sintered ceramics are shown in Figure 9. 7 and Figure 9. 8, respectively. All spectra present the typical features for KNN, which has 12 Raman-active optical modes of $4A_1+4B_1+3B_2+A_2$, which are labelled according to the assignment by Kakimoto et al in 2005.

Vibrational modes can be separated into translational modes of an isolated cation and internal modes of coordination polyhedra. In that case, the vibrations of the NbO_6 octahedra consist of $1A_{1g}(v_1)+1E_g(v_2)+2F_{1u}(v_3, v_4)+F_{2g}(v_5)+F_{2u}(v_6)$. Of these vibrations, $1A_{1g}(v_1)+1E_g(v_2)+2F_{1u}(v_3, v_4)$ are stretching and the rest are bending modes. The other internal vibrational modes of NbO_6 octahedra appear in a wide range from 200 to 900 cm^{-1} . In particular, v_1 (615 cm^{-1}) and v_5 (256 cm^{-1}) are detected as relatively strong scatterings. The v_6 mode of NbO_6 also appears at 141 cm^{-1} , although its peak intensity is still much lower than the other internal vibrational modes, its intensity increases for ceramics. The weak peaks (humps) observed at around 60 and 196 cm^{-1} , which appear to the left of v_5 as a shoulder, are assigned to the translational modes of Na^+/K^+ and K^+ cations versus NbO_6 octahedra, respectively.

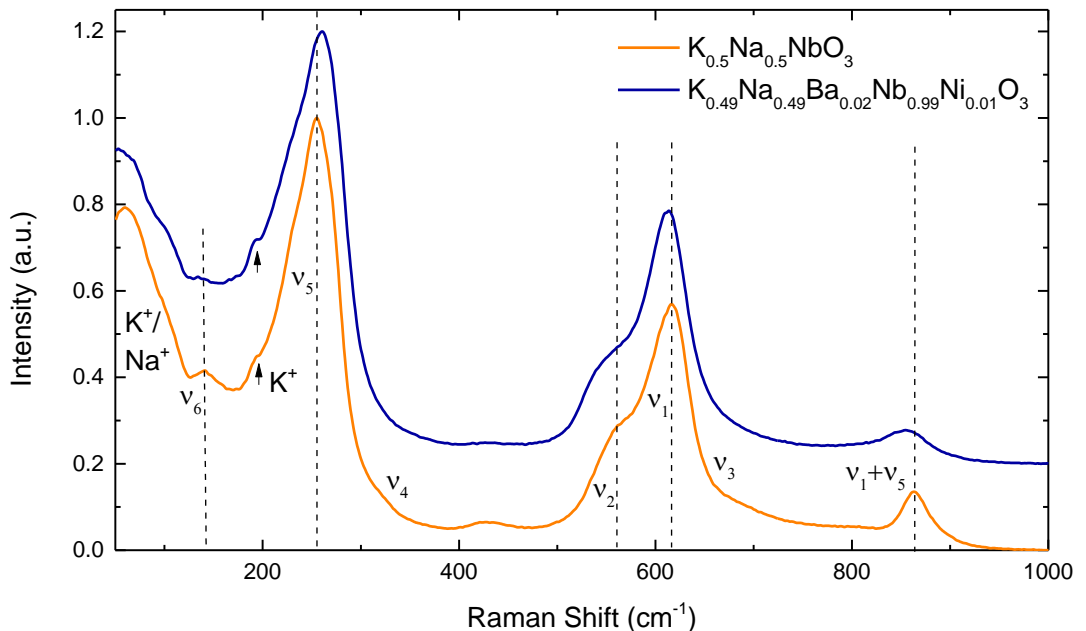


Figure 9. 7: Room-temperature Raman spectra for KNN and KNN-BNN calcined powders.

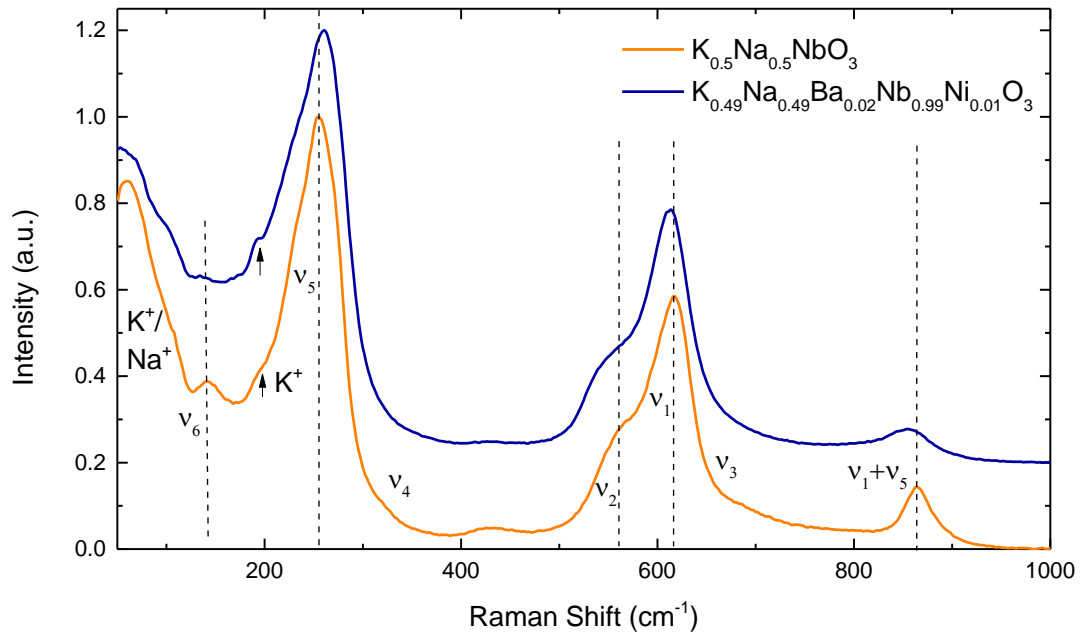


Figure 9. 8: Room-temperature Raman spectra for KNN and KNN-BNN sintered pellets.

9.2.3. SEM

SEM images of unpolished surfaces of KN vs KN-BNN and KNN vs KNN-BNN ceramics are illustrated in Figure 9. 9. (a and b) and Figure 9. 10 (a and b).

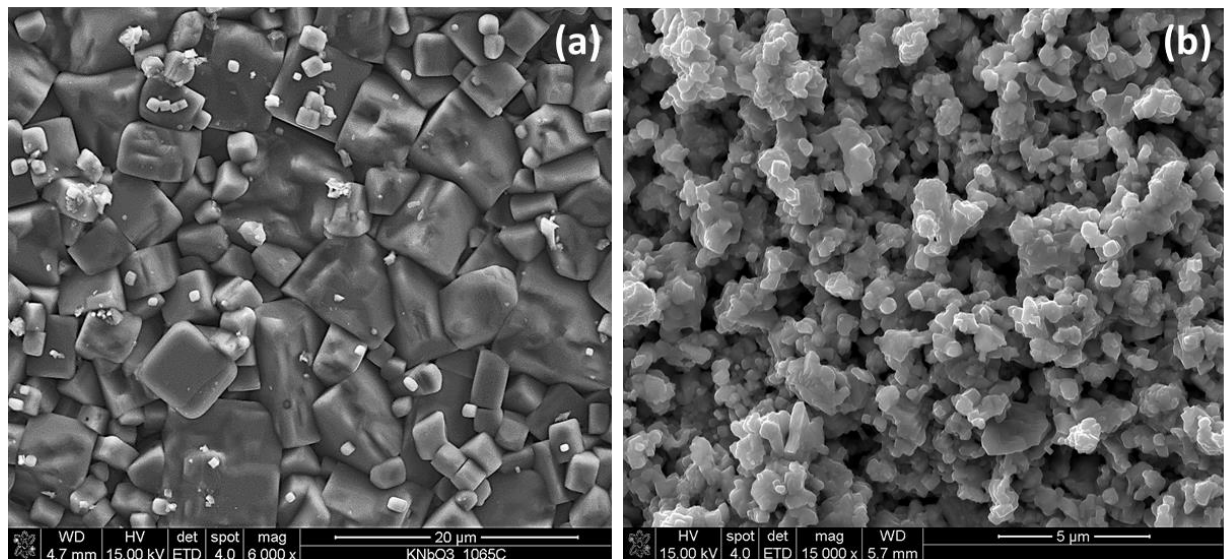


Figure 9. 9: Secondary electron images of (a) KN and (b) KN-BNN.

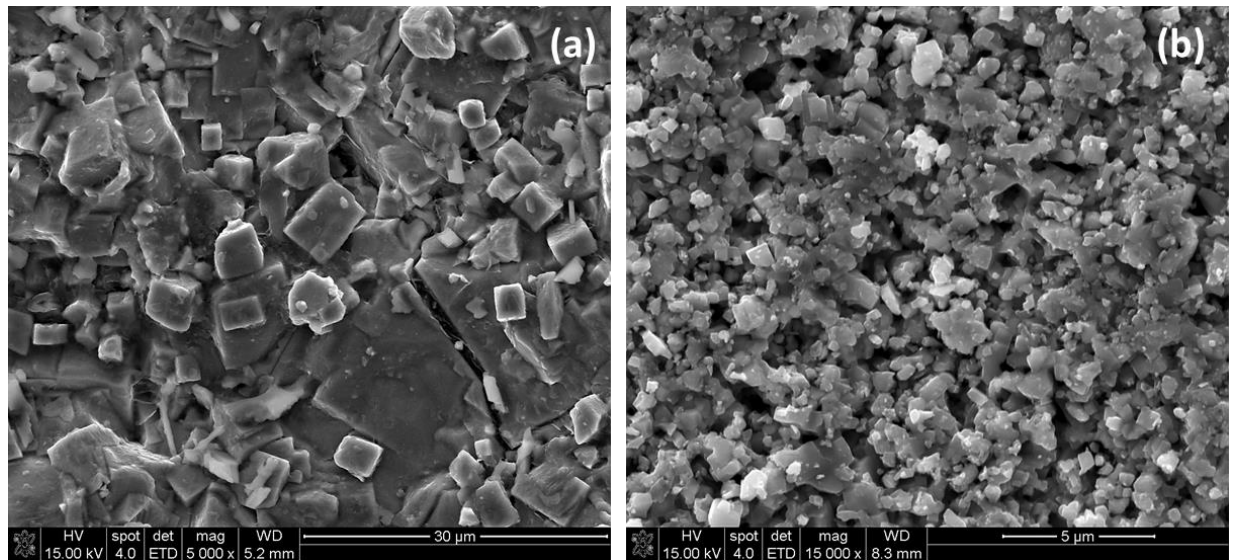


Figure 9. 10: Secondary electron images of (a) KNN and (b) KNN-BNN.

Both KN and KNN ceramics (Figure 9. 9 and Figure 9. 10(a)) morphologies, displaying well-defined cubic grains. Also, the absence of almost any porosity confirms the high density obtained in the previous section. Even if different grain sizes can be detected in both ceramics, the average grain size of KNN seems to be slightly larger ($\sim 10 \mu\text{m}$) than KN ($\sim 5 \mu\text{m}$). The incorporation of Ba and Ni in KN leads to a dramatic reduction of the grain size of the final microstructure. This marked alteration on the microstructure of KN-BNN and KNN-BNN, is also noticed in all systems for low concentration of dopants (x) investigated in the present work.

9.2.4. EDX

The chemical composition of KN, KN-BNN, KNN and KNN-BNN ceramics was determined by EDX analyses. Moreover, chemical inhomogeneities can be detected combining this analyses with SEM imaging. Table 9. 5 and Table 9. 6 shows experimental and theoretical molar K/Nb, K/Ba and K/Ni relations for KN and KN-BNN.

KN			
	Theoretical	Experimental	Relative error (%)
K/Nb	1	1.03(3)	3

Table 9. 5: Theoretical and experimental molar K/Nb ratio for KN. Relative error between the two values is included.

KN-BNN			
	Theoretical	Experimental	Relative error (%)
K/Nb	~0.95	1.1 (1)	15
K/Ba	9	15(9)	67
K/Ni	18	38(18)	>100

Table 9. 6: Theoretical and experimental molar K/Nb, K/Ba, K/Ni ratio for KN. Relative error between the two values is included.

While experimental stoichiometry for KN is acceptably adjusted to theoretical, stoichiometry for KN-BNN considerably differs from theoretical. Also, high standard deviation errors indicate a non-homogeneous chemical distribution on the surface, especially for Ni. Indeed, in some regions Ni is not detected at all as shown in Figure 9. 11.

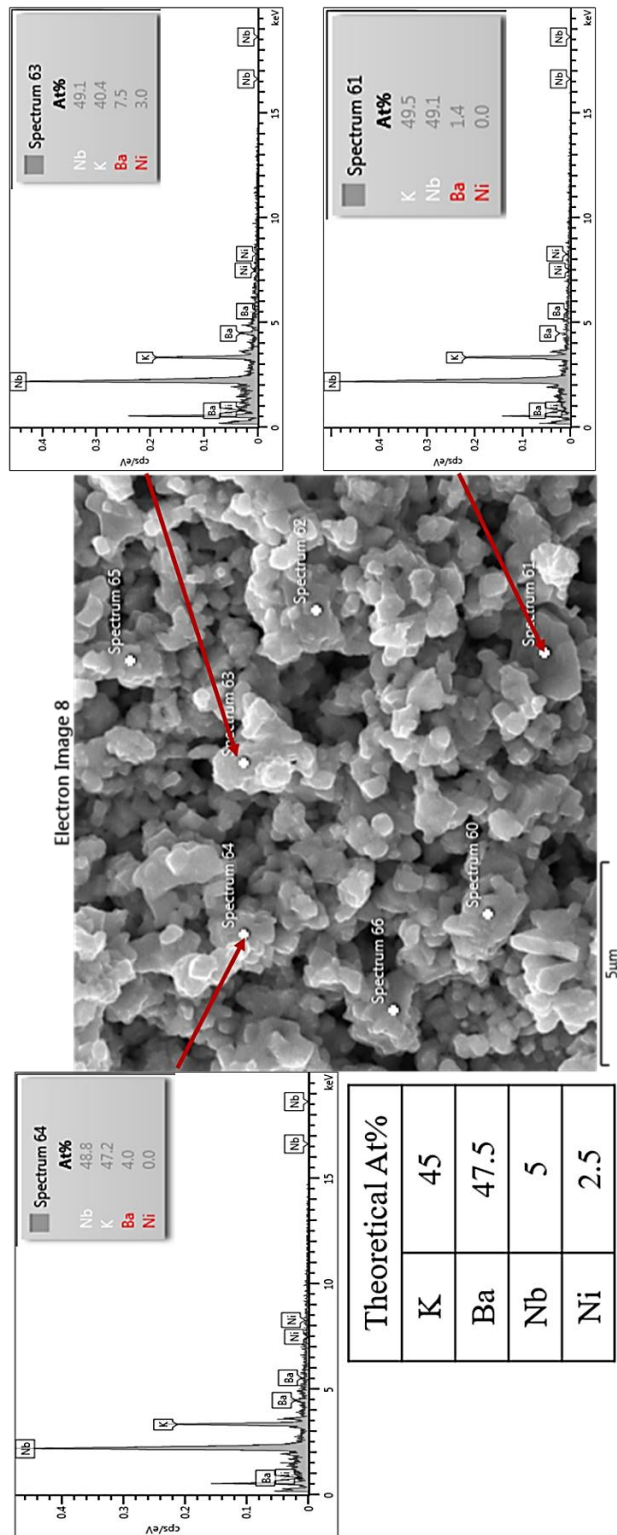


Figure 9. 11: SEM image and EDX spectra of unpolished KN-BNN ceramic sintered at 1085°C.

Spectrum 63 gives the ideal atomic percent for intended KN-BNN solid solution. However, other regions reveal low concentration of Ba and Ni (if it is detected at all). In addition, some large grains ($>10 \mu\text{m}$) with different morphology are observed (Figure 9. 12 and Figure 9. 13). Both EDX spectra reveals low concentration of K and the absence

of Ni. Indeed, this could be related with the formation of a second perovskite with the following stoichiometry: $K_{1/3}Ba_{1/3}NbO_3$.

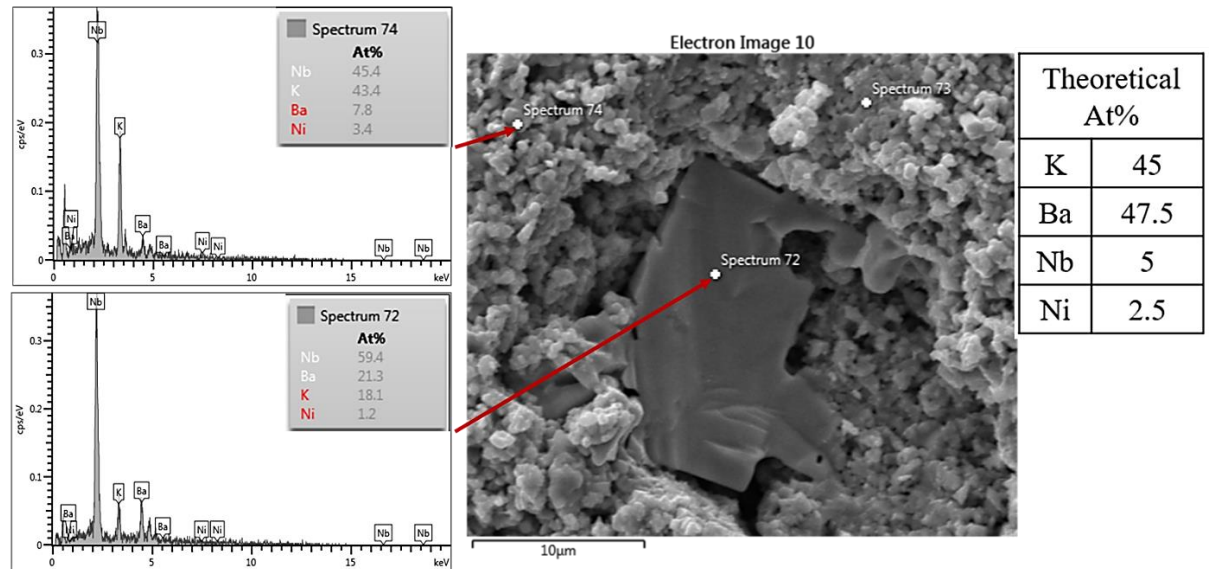


Figure 9. 12: SEM image and EDX spectra of second phase detected on unpolished surface of KN-BNN ceramic.

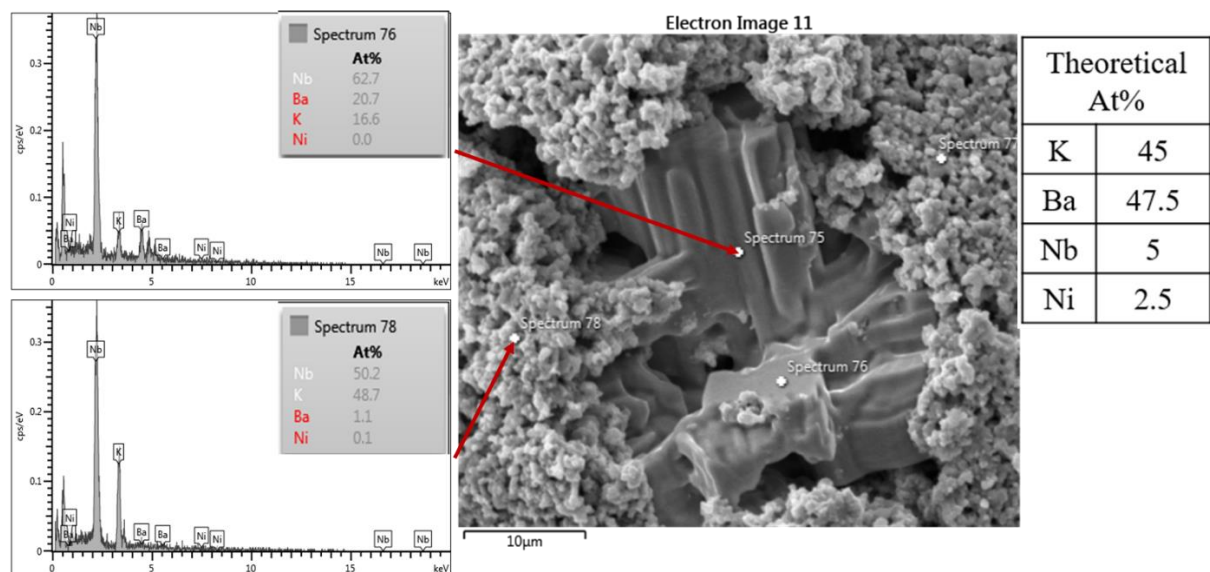


Figure 9. 13: SEM image and EDX spectra of second phase detected on unpolished surface of KN-BNN ceramic.

Experimental and theoretical molar K/Nb, K/Ba, K/Nb and K/Ni ratios for KNN and KNN-BNN are shown in Table 9. 7 and Table 9. 8, respectively.

KNN			
	Theoretical	Experimental	Relative error (%)
K/Na	1	0.9(4)	10
K/Nb	0.5	0.4(1)	20

Table 9. 7.: Theoretical and experimental molar K/Na and K/Nb ratio for KNN. Relative error between the two values is included.

Experimental stoichiometry for KNN coincides with theoretical, within error margins and consequently low relative errors. Nevertheless, some chemical inhomogeneities are perceived, as exposed in Figure 9. 14.

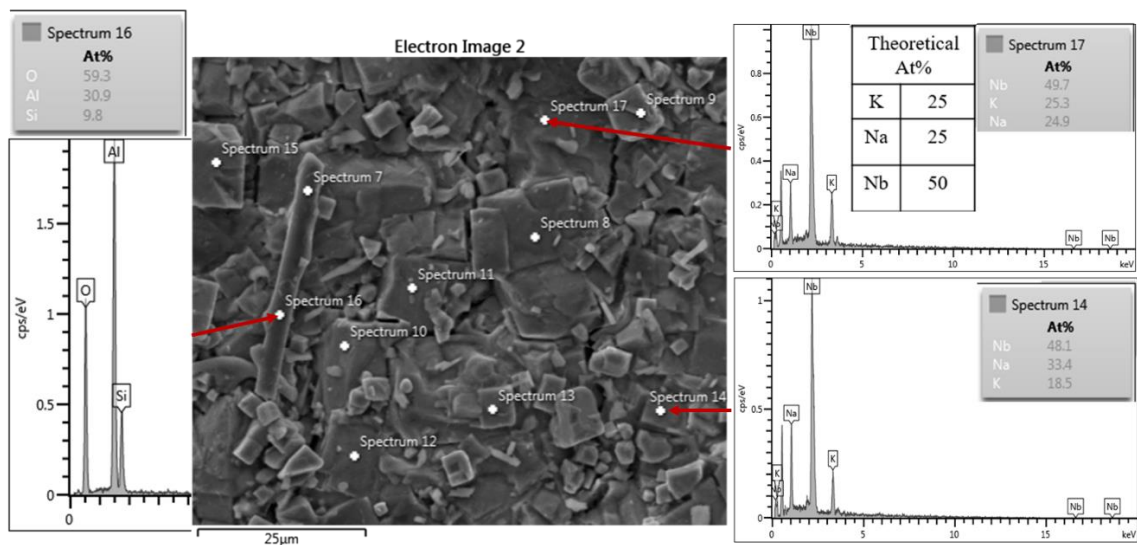


Figure 9. 14: SEM image and EDX spectra of second phase detected on unpolished surface of KNN ceramic.

While small grains on the ceramic surface reveal slightly lower K concentration than theoretical, large grains present the desired stoichiometry. In addition, a fibre shaped grain rich in Si and Al is detected which can be attributed to a possible contamination from the firing environment or from the equipment.

Table 9. 8. provides EDX results for KNN-BNN ceramic and it is perceived this compound presents the same difficulties in homogenising the species as described for KN-BNN ceramic. First, Ni is absent in some areas of the ceramics, as shown in Figure 9. 15. Second, regions mostly made of KNN are identified, where Ba and Ni are found in trace quantities (Figure 9. 15). And third, big grains with smooth surface that stand out from the small grains (Figure 9. 16.), are K and Ni deficient, similarly to the second phase found on KN-BNN.

KNN-BNN			
	Theoretical	Experimental	Relative error (%)
K/Na	1	1.0(4)	0
K/Ba	24.5	21(14)	14
K/Nb	0.5	0.4 (1)	20
K/Ni	49	56(54)	14*

Table 9. 8: Theoretical and experimental molar K/Na, K/Na, K/Nb and K/Ni ratios for KNN-BNN. Relative error between the two values is included.

Summarising, the experimental results confirm KN and KNN ceramics have the desired stoichiometry and do not show second phases. In contrast, both KN-BNN and KNN-BNN ceramics are heterogeneous. EDX analyses revealed regions depleted of Ni or where Ba and Ni are in trace quantities or K-deficient areas. Therefore, the chemical homogeneity is not achieved in these compositions by conventional ceramic processing. The main reason of this failure is attempting to homogenise a small quantity of $BaNb_{0.5}Ni_{0.5}O_3$ into KN and KNN lattice, which at the same time are very sensitive materials to moisture absorption and to K losses.

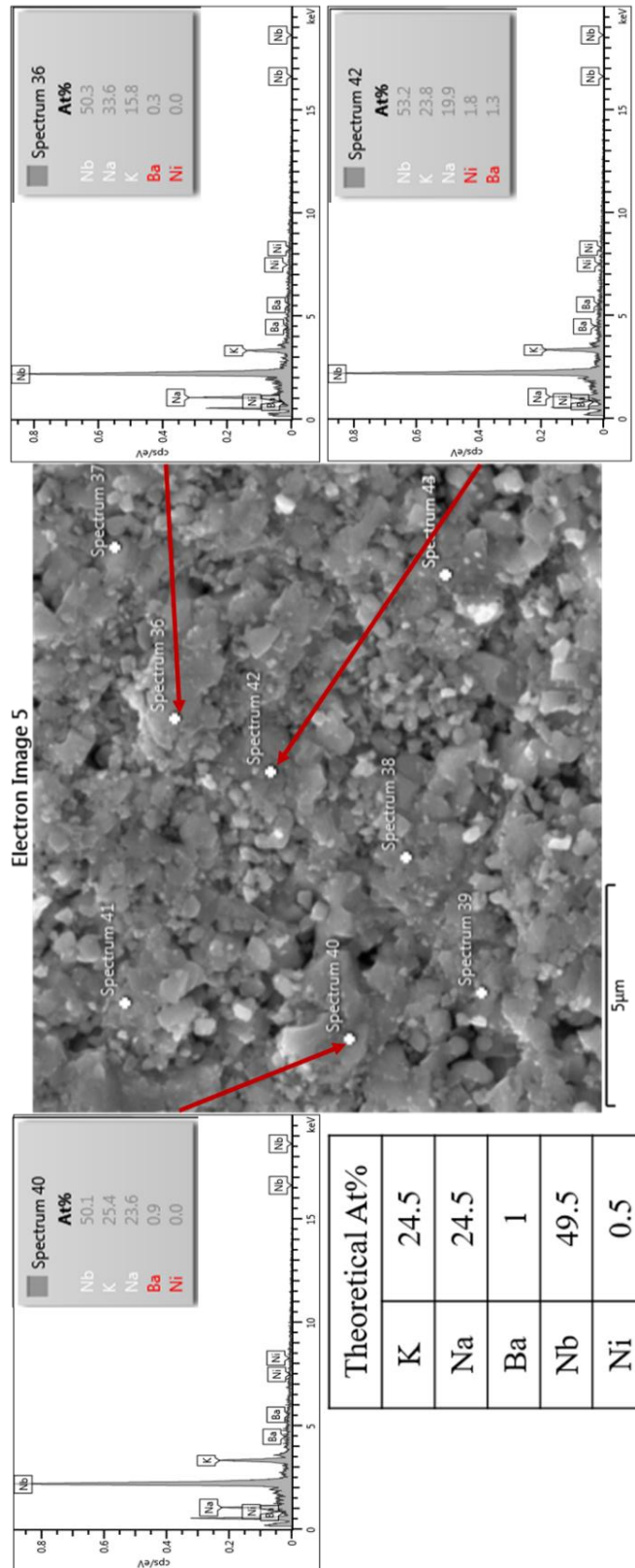


Figure 9. 15: SEM image and EDX spectra of second phase detected on unpolished surface of KNN-BNN ceramics.

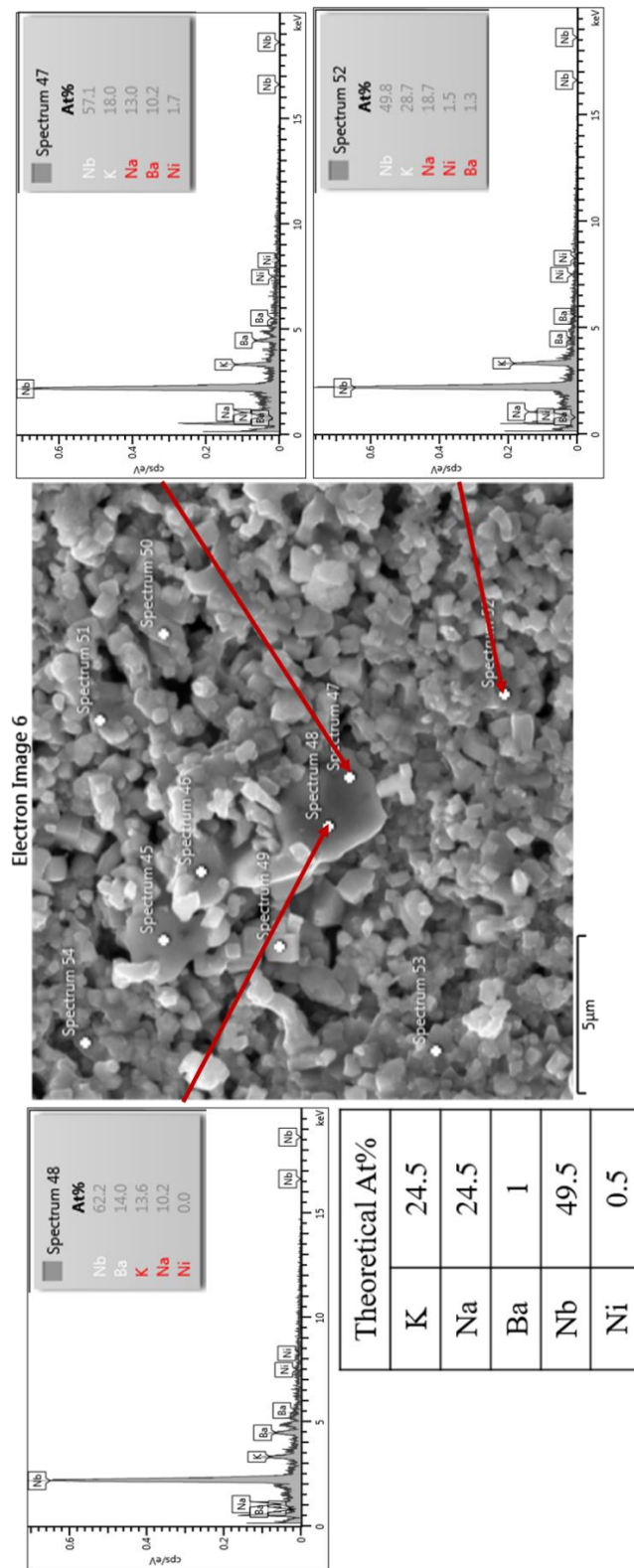


Figure 9. 16: SEM image and EDX spectra of second phase detected on unpolished surface of KNN-BNN ceramic.

9.3. Electrical Characterisation

9.3.1. Dielectric measurements

Dielectric, piezo- and ferroelectric characterisation for undoped KN is shown in Chapter 3. KN-BNN sample is conductive, as observed by Grinberg et al, only dielectric response was measured. At ambient conditions, KNN ceramics get pulverised, making it impossible to measure any electrical property.

Temperature dependence of the permittivity (ϵ_r) and dielectric losses ($\tan\delta$) for KN-BNN and KNN-BNN ceramics, measured at 1 kHz, 10 kHz, 100 kHz and 250 kHz, are shown in Figure 9. 17 and Figure 9. 18, respectively. KN-BNN exhibits two dielectric anomalies at ~ 210 °C and ~ 405 °C, corresponding to orthorhombic-to-tetragonal and tetragonal-to-cubic transitions, respectively. The values of the relative permittivity are extremely low in comparison with KN. On the other hand, dielectric anomalies for KNN-BNN are visible at ~ 167 °C and ~ 375 °C. These results are consistent with the assignment to orthorhombic phase for the two compositions by Rietveld refinement. The temperature for the ϵ_r anomalies does not change, but the magnitude decreases with frequency for KN-BNN. Also, frequency dependence is more marked for KN-BNN than KNN-BNN. The dielectric losses are on the same order for both compositions.

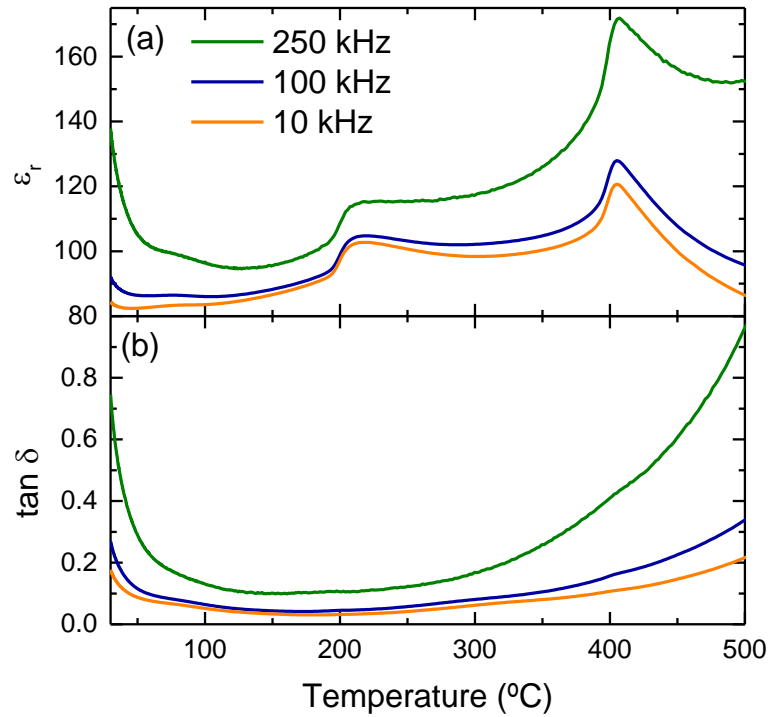


Figure 9. 17.: Temperature dependence of the (a) relative permittivity and (b) $\tan(\delta)$ (250 kHz, 100 kHz and 10 kHz) of KN-BNN, during cooling.

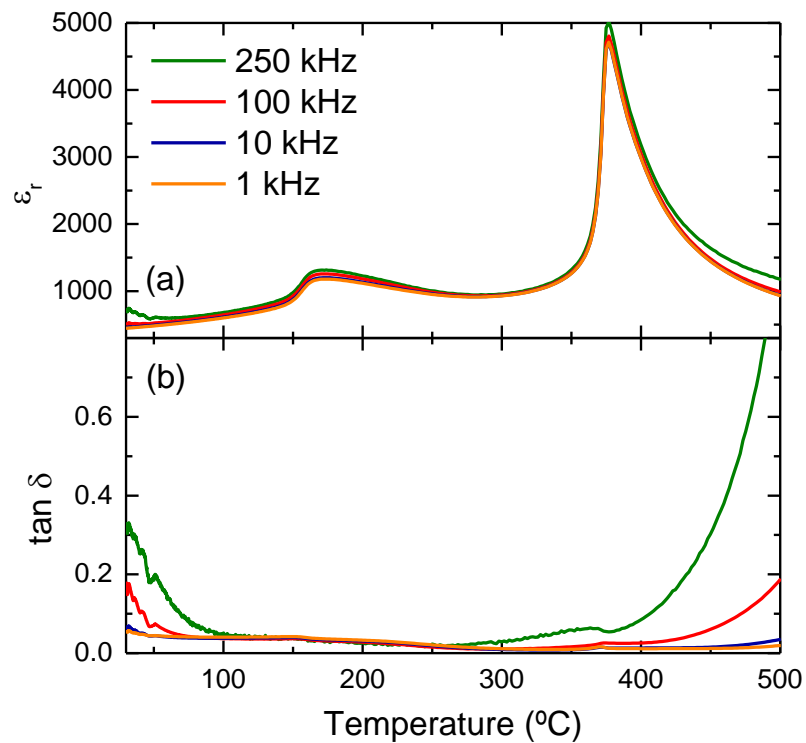


Figure 9. 18.: Temperature dependence of the (a) relative permittivity and (b) $\tan(\delta)$ (250 kHz, 100 kHz, 10 kHz and 1kHz) of KNN-BNN, during cooling.

9.3.2. Piezo- and Ferroelectric Characterisation

Evolution of P-E and S-E loops for KNN-BNN ceramic under different electric fields from 20 kV/cm to 60 kV/cm at RT is shown in Figure 9. 19 and Figure 9. 20. KNN-BNN sample is able to withstand 60 kV/cm. This ceramic shows a spontaneous polarisation, P_s , of $\sim 20 \mu\text{C}/\text{cm}^2$, a remnant polarization, P_r , of $\sim 17 \mu\text{C}/\text{cm}^2$ and a coercive field, E_c , of $\sim 14 \text{ kV}/\text{cm}$. The bipolar electric-field induced strain for KNN-BNN reaches about 0.10% under a field of 60 kV cm^{-1} , as shown in Figure 9. 20. The strain curve shows that the negative strain can reach $\sim 0.04\%$, which is due to the ferroelectric domain and domain wall switching.

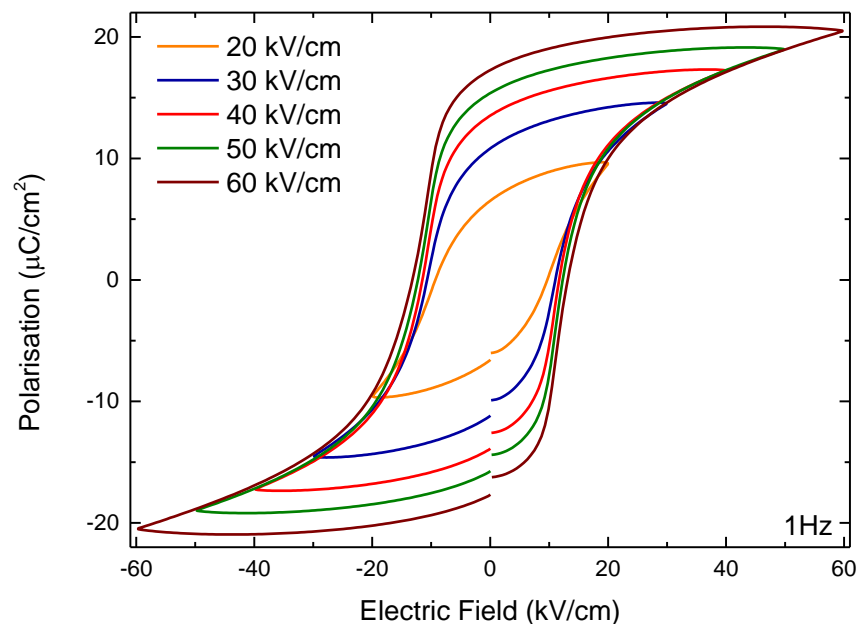


Figure 9. 19: P-E loops for KNN-BNN ceramics under electric field from 20 kV/cm up to 60 kV/cm at RT.

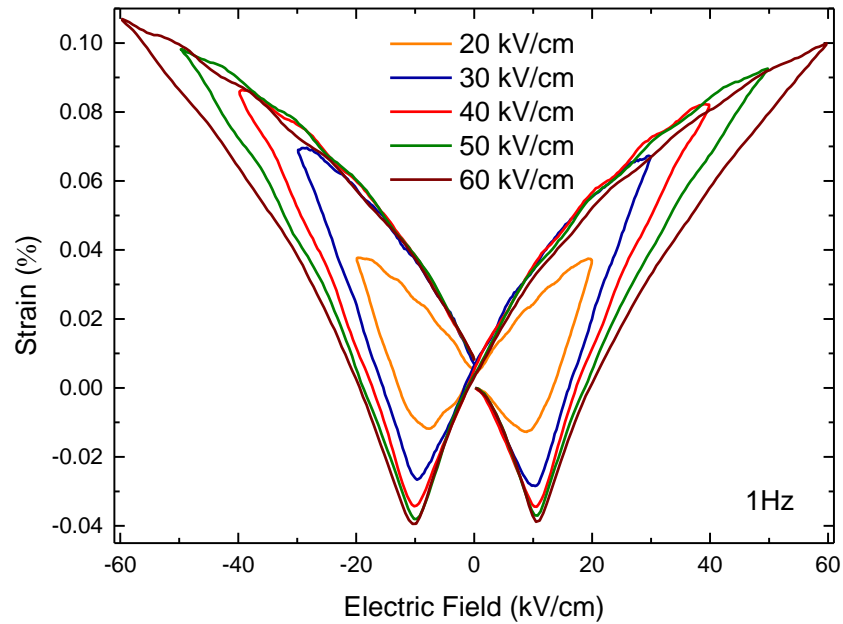


Figure 9. 20: S-E loops for KNN-BNN ceramics under electric field from 20 kV/cm up to 60 kV/cm at RT. Temperature dependence of P-E and S-E loops from RT to 140°C under an electric field of 50 kV/cm is shown in Figure 9. 21 and Figure 9. 22, respectively. Spontaneous polarisation, P_s rises to $\sim 21 \mu\text{C}/\text{cm}^2$ at 60°C but then P_s drops to $\sim 18 \mu\text{C}/\text{cm}^2$ at 180°C. This tendency of slightly decreasing P_s values with increasing the temperature was observed in KN (Chapter 3) and KBBNZ $x=0.05$ ceramics (Chapter 4). This behaviour was attributed to the proximity of the composition to the phase transition from orthorhombic-to-tetragonal ($\sim 180^\circ\text{C}$). In contrast, maximum strain value continuously increases up to $\sim 0.12\%$ with increasing temperature.

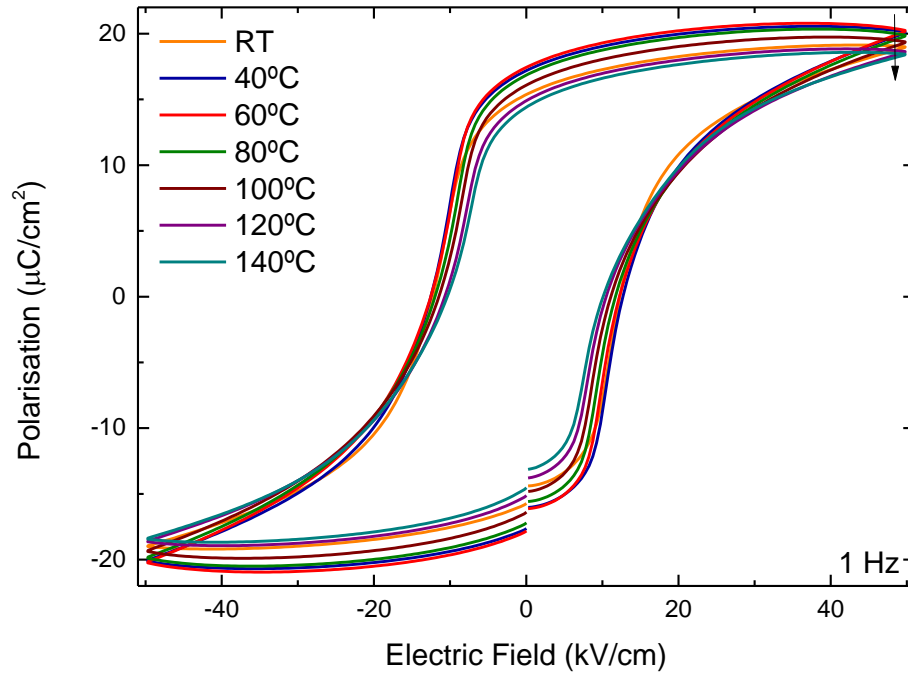


Figure 9. 21: P-E loops from RT up to 140° under electric field of 50 kV/cm for KNN-BNN

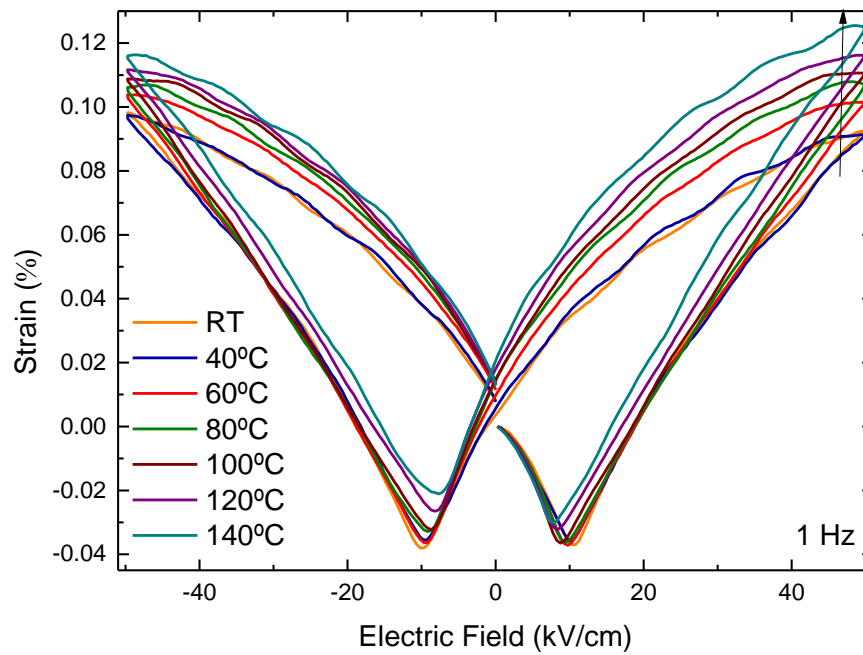


Figure 9. 22.: P-E loops from RT up to 140° under electric field of 50 kV/cm for KNN-BNN.

9.4. Optical Characterisation

9.4.1 Diffuse reflectance spectroscopy

Direct and indirect band-gaps are estimated from reflectivity data plotted in relation to wavelength (Figure 9. 23).

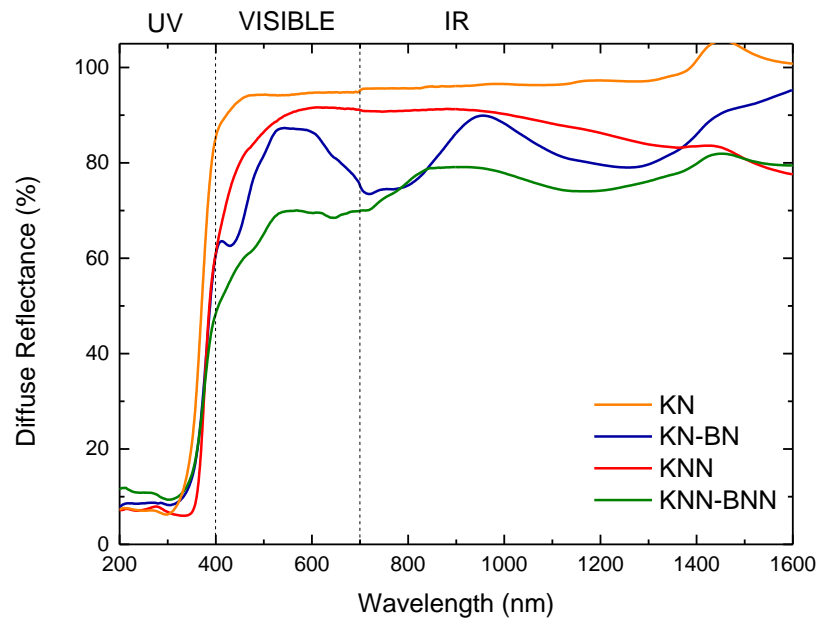


Figure 9. 23.: Diffuse reflectance as a function of wavelength for KN, KN-BNN, KNN and KNN-BNN (raw data)

Direct and indirect band-gap values are determined from $(F(R)hv)^2$ and $(F(R)hv)^{1/2}$ curves vs photon energy, shown in Figure 9. 24 and Figure 9. 25.

The nature (direct or indirect) and the value of KN band-gap were largely discussed in Chapter 1 and experimentally validated in Chapter 3. It is strongly recommended that the reader refers to these chapters. Supposedly, KN exhibits an indirect band-gap of 3.2 eV.

Direct and indirect band-gaps for KN-BNN ceramic are calculated as 3.37 eV and 3 eV, contrary to works (Bai, Siponkoski, et al., 2017; I. Grinberg et al., 2013) that reported direct band-gaps as low as 1.4 eV.

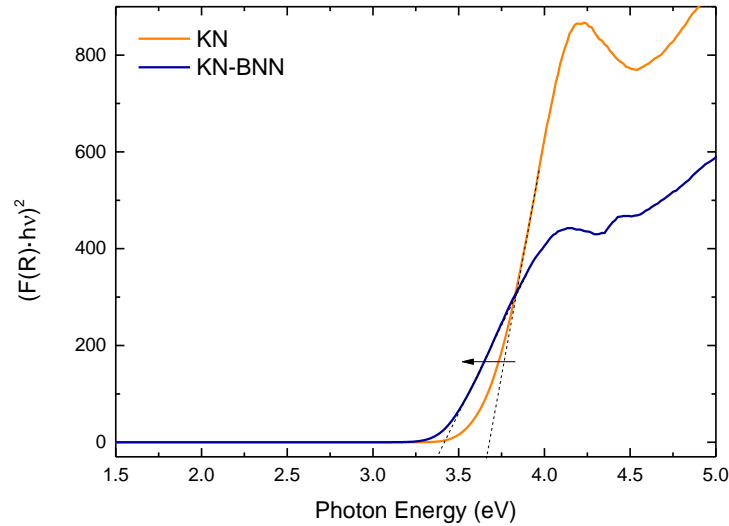


Figure 9. 24: Tauc plot for direct band gaps of KN and KN-BNN ceramics.

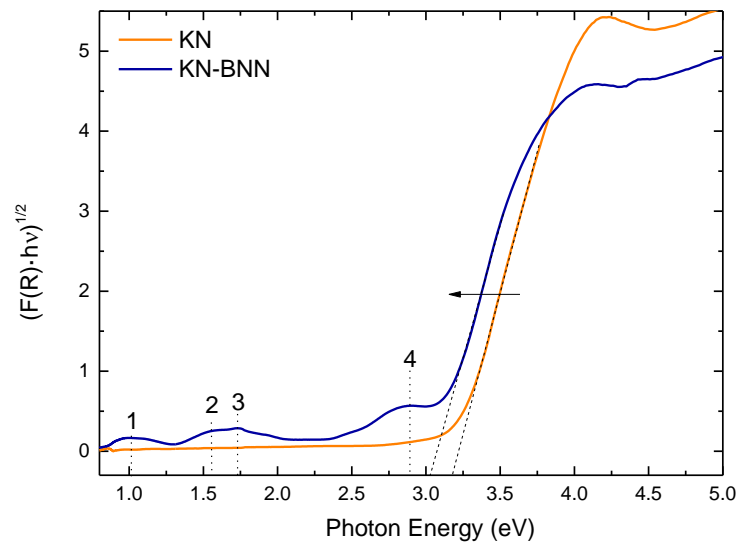


Figure 9. 25: Tauc plot for indirect band gaps of KN and KN-BNN ceramics.

Also, four absorption bands (labelled as 1, 2, 3 and 4 in Figure 9. 25) emerge at 1 eV, 1.56 eV, 1.73 eV and 2.90 eV in KN-BNN spectra, which were also observed in KNBN system (Chapter 8). These protuberance bands are attributed to d-d transitions by Ni^{+2} ions within the bulk or from hybridized Ni 3d and O 2p to Nb 4d states transitions (Wu et al., 2016). Again, direct and indirect band-gaps are considered for KNN and KNN-BNN, because there are not enough indications to determinate the nature of their band-gaps. Tauc plots constructed for $n=2$ and $n=1/2$ are illustrated in Figure 9. 26. and Figure 9. 27., respectively.

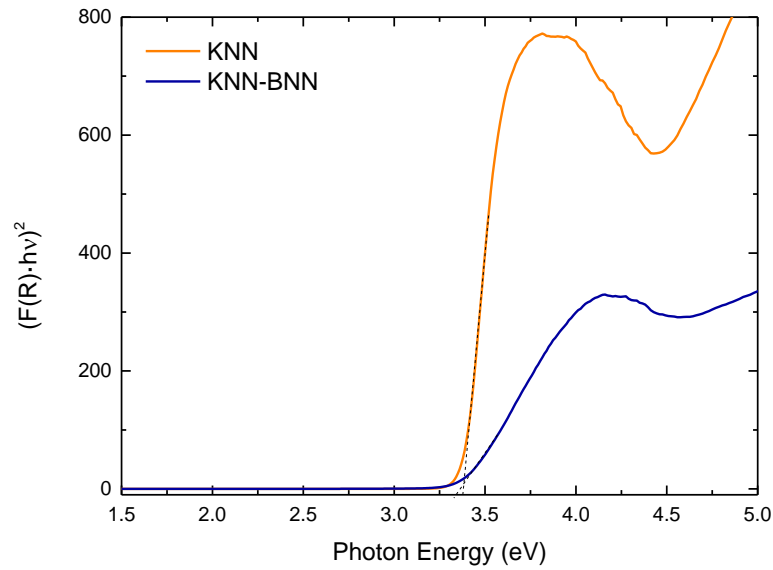


Figure 9. 26 Tauc plot for direct band gaps of KNN and KNN-BNN ceramics

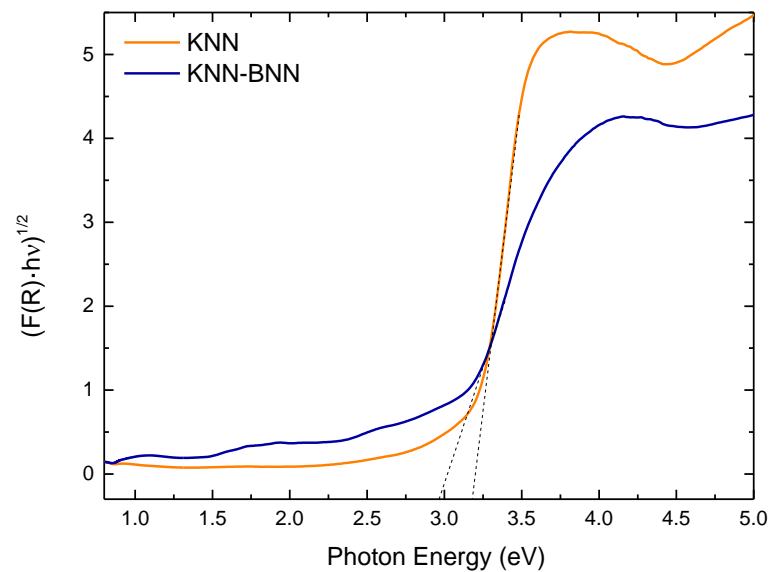


Figure 9. 27.: Tauc plot for indirect band gaps of KNN and KNN-BNN ceramics.

A direct band-gap of 3.38 eV for KNN and slightly lower value for KNN-BNN, 3.34 eV is determined from the Tauc plots. In the same way, indirect band-gaps are calculated as 3.18 eV and 2.95 eV for KNN and KNN-BNN, respectively. Table 9. 9. Summarises all band- gap obtained for the four compositions under study.

	Direct band-gap (eV)	Indirect band-gap (eV)
KN	3.65	3.20
KN-BNN	3.37	3.00
KNN	3.38	3.18
KNN-BNN	3.34	2.95

Table 9. 9: Direct and indirect band-gap extrapolated from Tauc plots for KN, KN-BNN, KNN and KNN-BNN ceramics.

9.5. Discussion

KN-BNN composition was proposed as promising photoferroelectric material in an influential journal such as Nature (I. Grinberg et al., 2013). It did not take long for investigations on this compound to appear (Table 9. 1). As explained in Chapter 1 and in the introduction of this chapter, the large discrepancy in band-gap value of KN-BNN in the literature, motivated us to investigate this controversy. Very recently, a similar compound, KNN-BNN, has been reported to have even better FE properties than KN-BNN, and a low band-gap of 1.60 eV (Bai, Tofel, et al., 2017)

KN-BNN and KNN-BNN ceramics were prepared by solid state reaction following the methodology detailed in Chapter 3 and their characterisation is compared with the parent KN and KNN compounds.

In terms of crystal structure symmetry, KN-BNN and KNN-BNN are isostructural and can be described by the orthorhombic Amm2 space group, like their parent KN and KNN compounds. XRD in combination with Raman spectra support this statement. In agreement with literature, XRD data of both KN-BNN and KNN-BNN reveal the presence of small amounts of NiO, suggesting difficulties in homogenisation of Ni. Raman spectra of KN-BNN shows the same general features as KN and the same happens for KNN-BNN and KNN.

To the best of our knowledge, there are no studies about morphology and chemistry of KN-BNN and KNN-BNN ceramics by SEM and EDX. The first thing to notice, is a drastic change in the microstructure of KN and KNN when $\text{BaNb}_{0.5}\text{Ni}_{0.5}\text{O}_3$ is incorporated, generating inhibition of the grain growth. This phenomenon occurs in all the systems studied in this work and also is reported in the literature (Saito & Takao,

2006; Zuo, Rödel, Chen, & Li, 2006). The appearance of small crystals ($<1\mu\text{m}$) can be related with the broadening of the XRD peaks for KN-BNN and KNN-BNN.

KN and KNN ceramics are free of secondary phase and show the expected stoichiometry. In contrast, considerable compositional deviations are found in KN-BNN and KNN-BNN ceramics. EDX analysis identified regions in both compounds where: Ni is not detected at all, KN or KNN compositions are predominant (minor quantities of Ba and Ni) or K is deficient, leading to the formation of secondary phases. These compositional inhomogeneities are not perceived by XRD.

These results evidence the difficulties of obtaining homogenised samples by solid state reaction, especially when a small quantity of dopants has to be uniformly incorporated. Indeed, $\text{BaNb}_{0.5}\text{Ni}_{0.5}\text{O}_3$ represents only 10% and 2% of the entire composition for KN-BNN and KNN-BNN, respectively. Similar issues regarding solid state reaction procedure are reported in the literature for Nb-doped BT ceramics (Masó et al., 2006). Therefore, even if macroscopically KN-BNN and KN-BNN are single phase (except for NiO), the presence of chemical inhomogeneities could be a source of error when interpreting the experimental results.

FE measurements at RT of KN-BNN ceramic were not possible to perform. Just one study was able to apply an electric field of 80 kV/cm to KN-BNN ceramic at RT, showing unsaturated FE loops (Bai, Siponkoski, et al., 2017). The same authors also reported FE loops and a spontaneous polarisation above $25\mu\text{C}/\text{cm}^2$ for KNN-BNN composition. Experimental evidence corroborates the ferroelectric nature at RT of this composition, reaching a spontaneous polarisation, of $\sim 20\mu\text{C}/\text{cm}^2$, a remnant polarization of $\sim 17\mu\text{C}/\text{cm}^2$ and a coercive field of $\sim 14\text{ kV}/\text{cm}$ under an electric field of 60 kV/cm. Also, electromechanical properties were studied and a strain deformation of 0.10% was obtained.

Finally, to resolve the discrepancy of the band-gap values, the diffuse reflectance of KN, KN-BNN, KNN and KNN-BNN ceramics was measured and compare with the largely reported band-gap of MAPbI_3 (1.58 eV). In addition, direct and indirect band-gaps were considered, because there is not enough experimental evidence to be sure of the origin of the transition. Reflectivity data and Tauc plots constructed for direct and indirect band gaps of KN, KN-BNN, KNN, KNN-BNN and MAPbI_3 are shown in Figure 9. 28, Figure 9. 29 and Figure 9. 30.

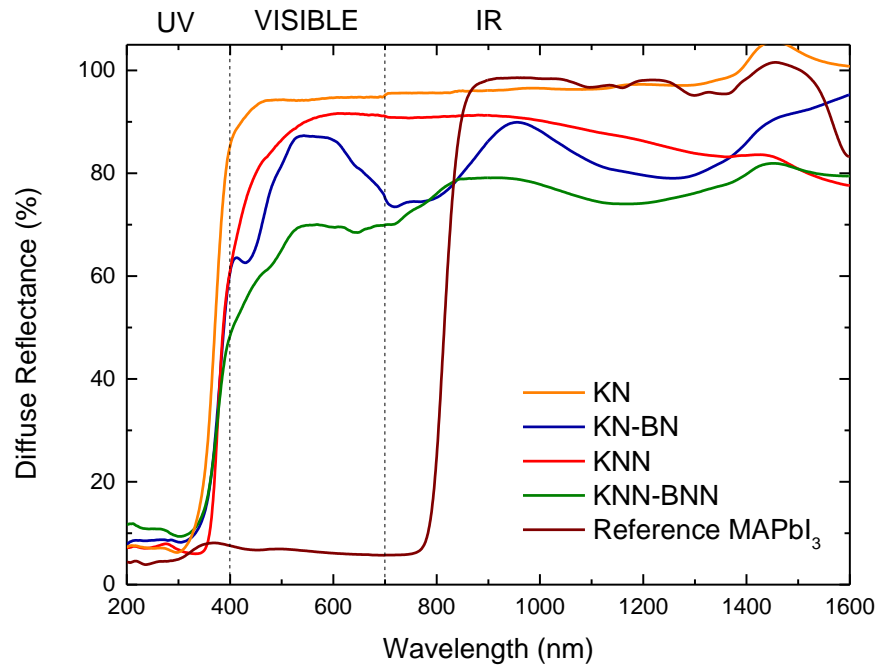


Figure 9.28: Reflectance (%) data for KN, KN-BNN, KNN, KNN-BNN and MAPbI₃ compounds.

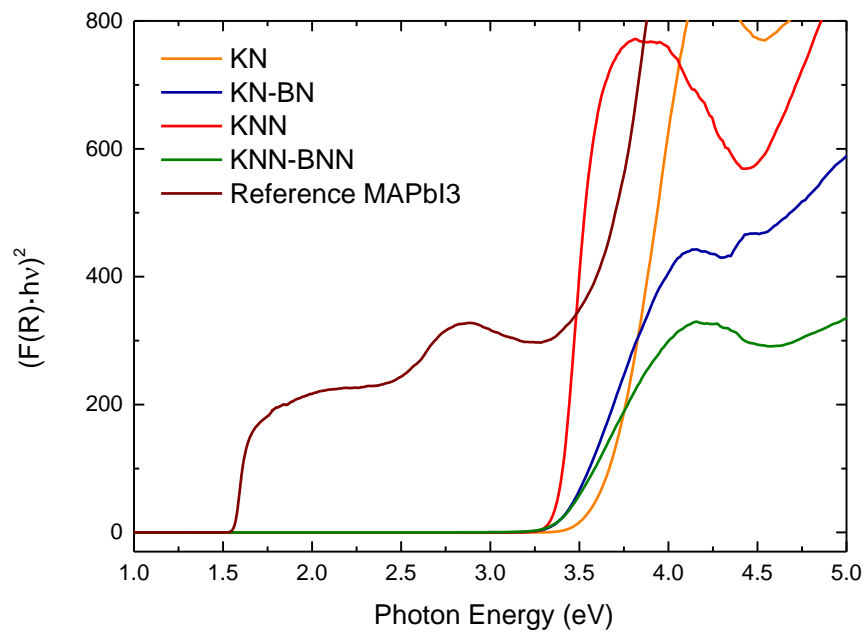


Figure 9.29 Tauc plot for direct band gaps of KN, KN-BNN, KNN, KNN-BNN and MAPbI₃ compounds.

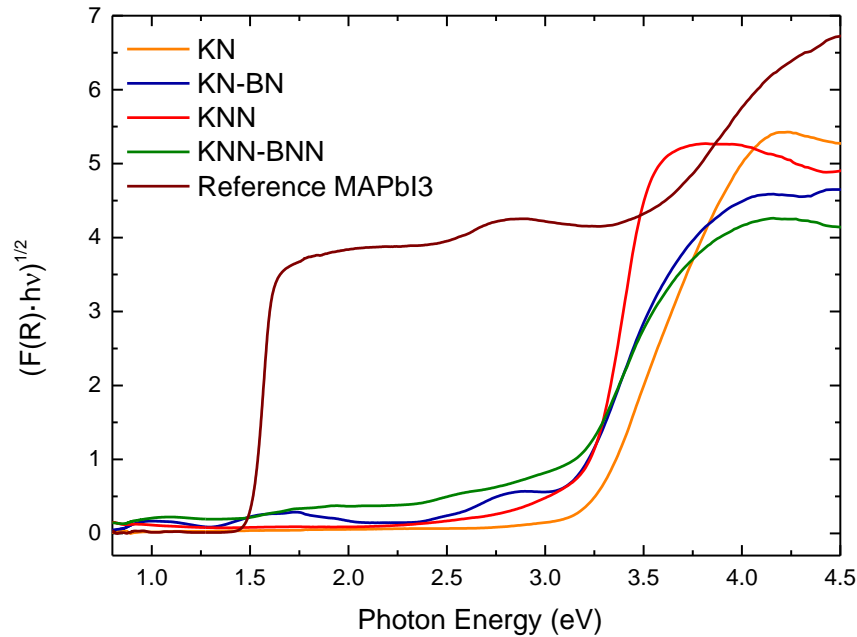


Figure 9. 30: Tauc plot for indirect band gaps of KN, KN-BNN, KNN, KNN-BNN and MAPbI₃ compounds. The major absorption region in terms of light energy for KN, KN-BNN, KNN and KNN-BNN correspond to ranges from 3.25 eV to 3.6 eV for direct transitions and from 3 eV to 3.25 eV for indirect transitions. Ba and Ni modifications slightly narrow the KN band-gap (only 0.12 eV) which is similar with results reported by Wu et al in 2016. On the other hand, KNN seems to have even lower band-gap than KNN-BNN in contradiction to reported results (Bai, et al 2017).

The Tauc plot constructed for $n=1/2$ (Figure 9. 25 and Figure 9. 27) shows four broad bumps below the band-gap for KN-BNN and KNN-BNN that were attributed to d-d transitions generated by Ni cations. Wu et al. proposed the misinterpretation of these absorption regions might be the origin of the discrepancy of the band-gap values for KN-BNN. However, Grinberg and Bai reported direct nature for the band-gaps of KN-BNN and KNN-BNN in their respective studies.

Finally, we realised that depending on the scale at which the $(F(R) \cdot h\nu)^2$ curve is plotted, the band-gap values from the intercept of the x-axis and the tangent line of the curve may be different. Indeed, it is demonstrated here that by zooming at the bottom part of the Tauc plot, we obtained band-gap values for KN-BNN and KNN-BNN as low as 1.42 eV and 1.46 eV, respectively (Figure 9. 31). Coincidentally, these values are in broad agreement with those reported by Grinberg and Bai.

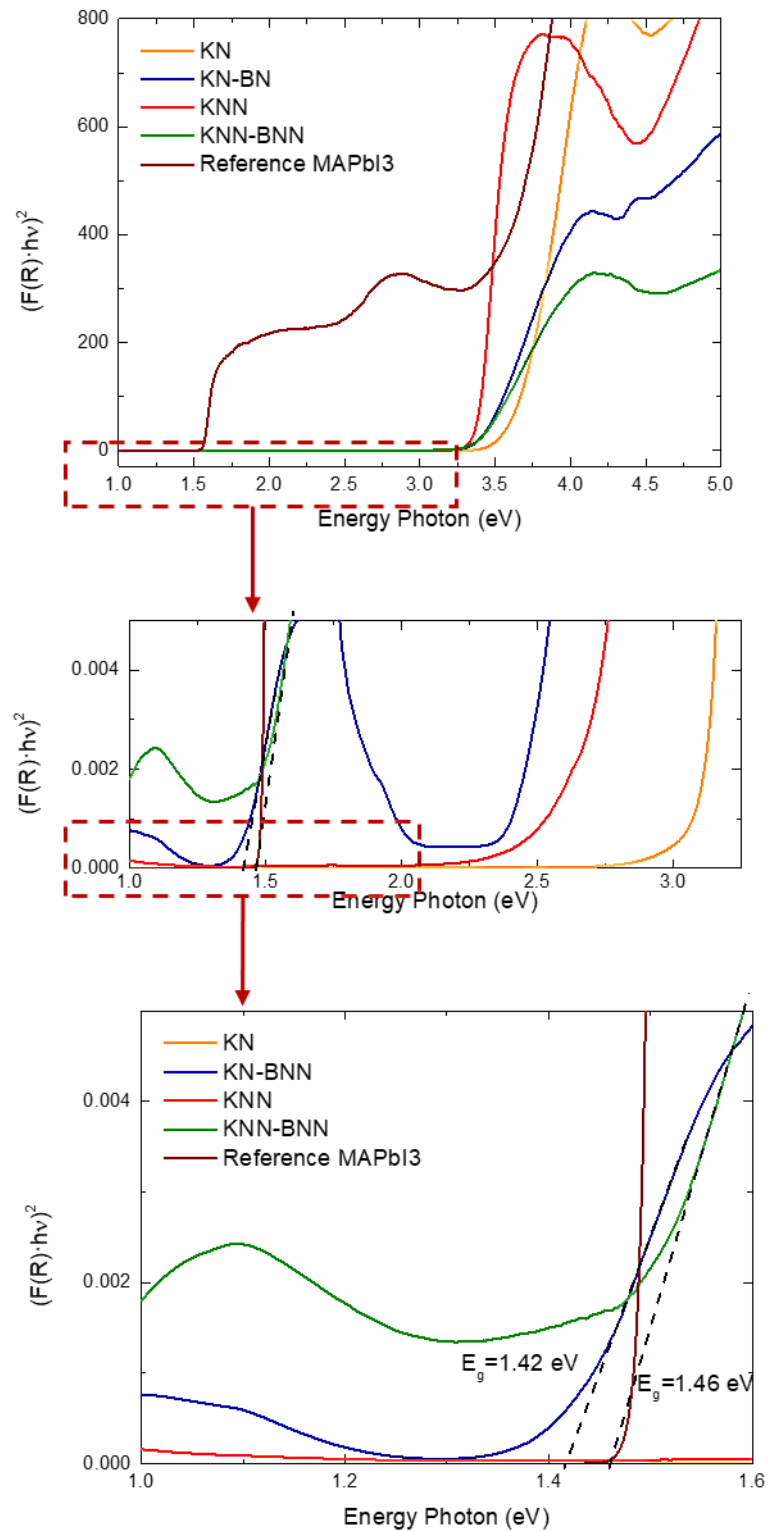


Figure 9. 31 Zoom of Tauc plot for direct band gaps of KN, KN-BNN, KNN, KNN-BNN and MAPbI₃ compounds

9.6. Conclusions

SEM and EDX analyses evidence the difficulties of obtaining chemically homogenised samples of KN-BNN and KNN-BNN by conventional ceramic processing. Band-gaps of 3.37 eV and 3.34 eV are obtained for these compositions from reflectivity data. These results are consistent with the ability of KNN-BNN to withstand an electric field as high as 60 kV/cm up to 140°C. Discrepancies of band-gap values in the literature are attributed to: firstly, non-adequate processing route that may lead to the appearance of chemical inhomogeneities which modify the physical properties, secondly a misinterpretation of some absorption regions below the band-gap due to d-d transitions in the Tauc plot and thirdly the use of non-standardised scale for the Tauc plots.

9.7. References

- Bai, Y., Siponkoski, T., Peräntie, J., Jantunen, H., & Juuti, J. (2017). Ferroelectric, pyroelectric, and piezoelectric properties of a photovoltaic perovskite oxide. *Applied Physics Letters*, *110*(6). <https://doi.org/10.1063/1.4974735>
- Bai, Y., Tofel, P., Palosaari, J., Jantunen, H., & Juuti, J. (2017). A Game Changer : A Multifunctional Perovskite Exhibiting Giant Ferroelectricity and Narrow Bandgap with Potential Application in a Truly Monolithic Multienergy Harvester or Sensor, *Advance Materials*, *29*, 1700767, 1–7. <https://doi.org/10.1002/adma.201700767>
- Birol, H., Damjanovic, D., & Setter, N. (2006). Preparation and characterization of (K_{0.5}Na_{0.5})NbO₃ ceramics. *Journal of the European Ceramic Society*, *26* (6), 861–866. <https://doi.org/10.1016/j.jeurceramsoc.2004.11.022>
- Grinberg, I., West, D. V., Torres, M., Gou, G., Stein, D. M., Wu, L, Rappe, A. M. (2013). Perovskite oxides for visible-light-absorbing ferroelectric and photovoltaic materials. *Nature*, *503* (7477), 509. <https://doi.org/10.1038/nature12622>
- Kakimoto, K., Akao, K., Guo, Y., & Ohsato, H. (2005). Raman Scattering Study of Piezoelectric (Na_{0.5}K_{0.5})NbO₃ -LiNbO₃ Ceramics. *Japanese Journal of Applied Physics*, *44* (9B), 7064–7067. <https://doi.org/10.1143/JJAP.44.7064>

- Masó, N., Beltrán, H., Cordoncillo, E., Flores, A. A., Escribano, P., Sinclair, D. C., & West, A. R. (2006). Synthesis and electrical properties of Nb-doped BaTiO₃. *Journal of Materials Chemistry*, *16*(30), 3114–3119. <https://doi.org/10.1039/B601251E>
- Saito, Y., & Takao, H. (2006). High performance lead-free piezoelectric ceramics in the (K,Na)NbO₃-LiTaO₃ solid solution system. *Ferroelectrics* (Vol. 338). <https://doi.org/10.1080/00150190600732512>
- Song, B., Wang, X., Xin, C., Zhang, L., Song, B., Zhang, Y., Wang, Y., Wang, J., Zhiguo, L., Yu, S., Tang, J. (2017). Multiferroic properties of Ba/Ni co-doped KNbO₃ with narrow band-gap. *Journal of Alloys and Compounds* *703*, 67-72. <https://doi.org/10.1016/j.jallcom.2017.01.180>.
- Sun, H., Liu, J., Wang, X., Zhang, Q., Hao, X., & An, S. (2017). (K,Na)NbO₃ ferroelectrics: a new class of solid-state photochromic materials with reversible luminescence switching behavior. *Journal of Materials Chemistry C* *5*, 9080-9087 <https://doi.org/10.1039/c7tc03076b>
- Wang, F., Grinberg, I., Rappe, A. M. (2014). Band gap engineering strategy via polarization rotation in perovskite ferroelectrics. *Applied Physics Letters*, *104* (15). <https://doi.org/10.1063/1.4871707>
- Wang, F., Rappe, A. M. (2015). First-principles calculation of the bulk photovoltaic effect in KNbO₃ and (K,Ba)(Ni,Nb)O_{3-δ}. *Physical Review B*, *91* (16), 165124. <https://doi.org/10.1103/PhysRevB.91.165124>
- Wu, P., Wang, G., Chen, R., Guo, Y., Ma, X., & Jiang, D. (2016). Advances Enhanced visible light absorption and photocatalytic activity of gel based Pechini method. *Royal Society of Chemistry Advances*, *6*, 82409–82416. <https://doi.org/10.1039/C6RA15288K>
- Zhou, W., Deng, H., Yang, P., & Chu, J. (2014). Structural phase transition, narrow band gap, and room-temperature ferromagnetism in [KNbO₃]_{1-x}[BaNi_{1/2}Nb_{1/2}O_{3-δ}]_x ferroelectrics. *Applied Physics Letters*, *105*(11), 111904. <https://doi.org/10.1063/1.4896317>
- Zhou, W., Deng, H., Yang, P., & Chu, J. (2016). Investigation of microstructural and optical properties of (K,Ba)(Ni,Nb)O_{3-δ} thin films fabricated by pulsed laser deposition. *Materials Letters*, *181*, 178–181.

<https://doi.org/http://dx.doi.org/10.1016/j.matlet.2016.06.032>

Zuo, R., Rödel, J., Chen, R., & Li, L. (2006). Sintering and Electrical Properties of Lead-Free $\text{Na}_{0.5}\text{K}_{0.5}\text{NbO}_3$ Piezoelectric Ceramics. *Journal of the American Ceramic Society*, 89(6), 2010–2015. <https://doi.org/10.1111/j.1551-2916.2006.00991.x>

Chapter 10

Discussion

10.1. Ceramic processing

10.2. $(1-x)$ KNbO_3 - x BiMeO_3 ($\text{Me}=\text{Fe}, \text{Mn}, \text{Co}, \text{Ni}$) ($0 \leq x \leq 0.25$) systems

10.3. Photovoltaic effect in orthorhombic 0.75 KNbO_3 -0.25 BiFeO_3 solid-solution

10.4. Experimental validation and non-reproducibility of band-gap narrowing in solid solutions based on KNbO_3 from literature

10.4. Band-gap narrowing

10.5. References

10. Discussion

10.1. Ceramic processing

The solid-state reaction method, also known as conventional processing, was selected for preparing all the compositions presented in this work. The main processing issue with KNbO_3 concerns K loss during heat treatments, which promotes the appearance of the hygroscopic phase, $\text{K}_4\text{Nb}_6\text{O}_{17}$. This secondary phase affects the structural integrity of KN ceramics. In order to mitigate this issue, several strategies have been explored. For example, preparation methods that require lower sintering temperature than conventional, such as sol-gel processing (Nazeri-Eshghi, Kuang, & Mackenzie, 1990) and co-precipitation methods (K. K. and T. I. and H. Ohsato, 2008), or the introduction of additives, such as CuO and ZnO, that were described in detail in Chapter 3.

In this work, it was shown that is possible to prepare high density undoped KN ceramics (~94%) by solid state reaction. Ceramic processing involved the synthesis of deliberately non-stoichiometric KN ceramics, in order to gather some in-sight of the effect of potential K-loss on properties. Comparison of two routes based on general recommendations reported in the literature was carried out (Chapter 3, Table 3.1. and Table 3.2.).

The selection of calcination temperatures was crucial to obtain single-phase samples. These temperatures must not exceed 1000°C, to control K losses. KN samples were successfully synthesised after double calcination at 850°C during 4 hours with a heating rate of 3°C/min. Also, the control of the firing environment during the sintering using atmospheric powder and double crucible was decisive to inhibit the K losses during sintering (Figure 10. 1). The sintering temperature was at 1075°C for 4 hours with a heating rate of 3°C/min.

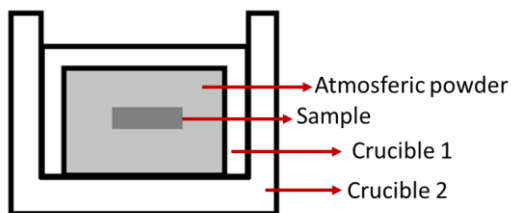


Figure 10. 1: Schematic representation of the sintering environment. The green body is imbedded into atmospheric powder and covered with two crucibles.

Most powders for the KN-based systems, presented in this thesis, were double calcined at 850°C. KNBM and KNBN systems were exceptions. KNBM powders were calcined at 800°C and 900°C, because literature shows BiMnO_3 to require higher reacting temperature than BiFeO_3 (Woo, Tyson, Croft, Cheong, & Woicik, 2001) and the KNBN system needed three calcinations to react the starting oxides, as shown in this thesis.

Nevertheless, some issues regarding the solid-state route were noticed during the powders preparation. After the synthesis, most of the compositions presented some orthorhombic KNbO_3 -based phase, where the solutes were not well incorporated, due to an incomplete reaction among the reactants. The presence of nearly undoped-KN was detected by XRD combined with Raman analysis.

Diffusion of low concentration of dopants ($x \leq 0.15$) into the KNbO_3 lattice was incomplete even after sintering, generating compositionally inhomogeneous regions. Cations of the transition metals (Mn^{+3} , Fe^{+3} , Co^{+3} , $\text{Ni}^{+3/+2}$ and Zn^{+2}) appeared to be more difficult of being incorporated into KNbO_3 than Bi^{+3} and Ba^{+2} , specially, $\text{Ni}^{+3/+2}$ and Zn^{+2} (Table 10. 1). Unreacted NiO was detected by XRD and EDX analyses in all system that contained Ni^{+3} (KNBN from $x=0.05$ to $x=0.25$, KN-BNN and KNN-BNN compounds). This phenomenon has been reported in the literature (Bai, Siponkoski, Peräntie, Jantunen, & Juuti, 2017; Grinberg et al., 2013; Hawley et al., 2017).

Chemical homogeneity was achieved in most systems for $x=0.20$ and $x=0.25$, as confirmed by EDX mapping analysis. To avoid chemical inhomogeneities for low concentration of solutes, higher and longer heat treatments would be required, but in turn, would promote K and O losses. Alternatively, the number of calcinations can be increased or the use of master-batch method which enables a precise control of the composition. This method relies on a sequential mixing process. Firstly, same quantity of solutes and solvent is mixed up. Subsequently, the solvent is progressively added until the desired stoichiometry is obtained.

The solid-state reaction shows some limitations to prepare these solid solutions, and therefore, it would be interesting to investigate new synthesis and sintering routes, such as sol-gel (Masó et al., 2006), combustion (Pecchi, Cabrera, Delgado, García, & Jimenez, 2013), HP-HT (high pressure and high temperature) (Chi et al., 2007) and SPS (spark-plasma-sintering) (Jiang, Nan, Wang, Liu, & Shen, 2008).

Polarisation measurement of single-phase KN are strongly affected by the moisture absorption from the environment. A simple experiment enables us to demonstrate this phenomenon and it is easily reproducible. A P-E loop for undoped KN sample left in air is round and resembles the loop and the values reported by Birol et al, 2005 (P-E loop 1, Figure 10. 2). Then, if the sample is dried at over 200°C for 10 minutes, it becomes more resistive, showing a typical ferroelectric loop as reported by Kakimoto et al in 2004 (P-E loop 2, Figure 10. 2). Moreover, the sample was again left at room conditions for 10 minutes, which caused an increase of the polarisation (P-E loop 3, Figure 10. 2). The conductivity of the KN sample increases by the absorption of water, giving rise to the current instead of the electric polarization under electric field and over-estimating the P_r values of undoped KN.

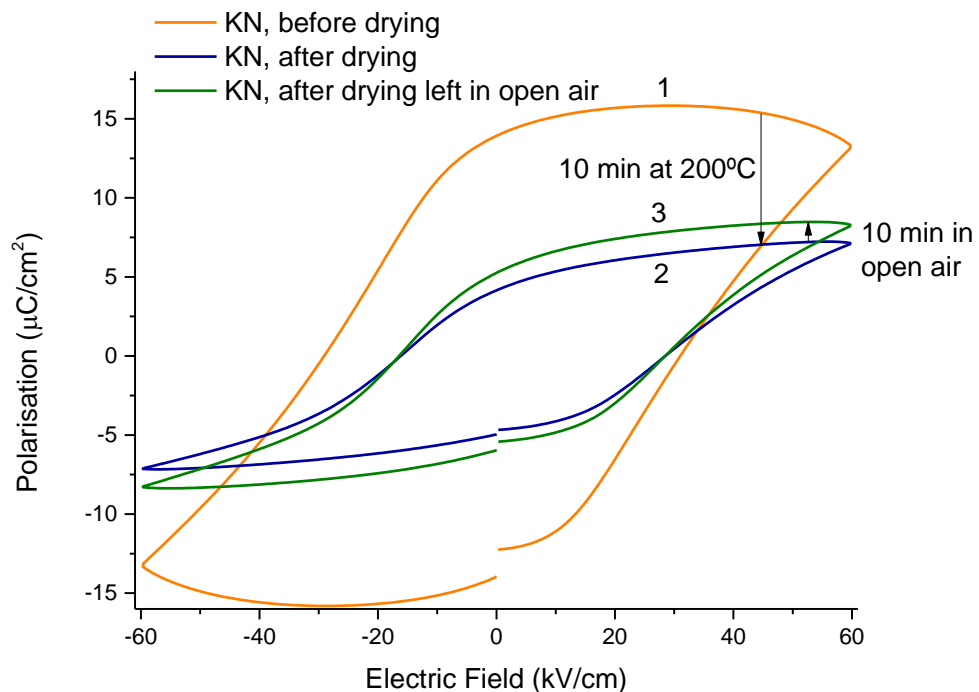


Figure 10. 2.: Reproducibility of the experiment described in Chapter 3, section 3.6.2 (Figure 3. 16). RT P-E loops for undoped KN ceramics under 60 kV/cm before (P-E loop 1) and after (P-E loop 2) drying at 200 °C. An increase of the spontaneous polarisation is noticed if the same sample is left for 10 min in open air (P-E loop 3).

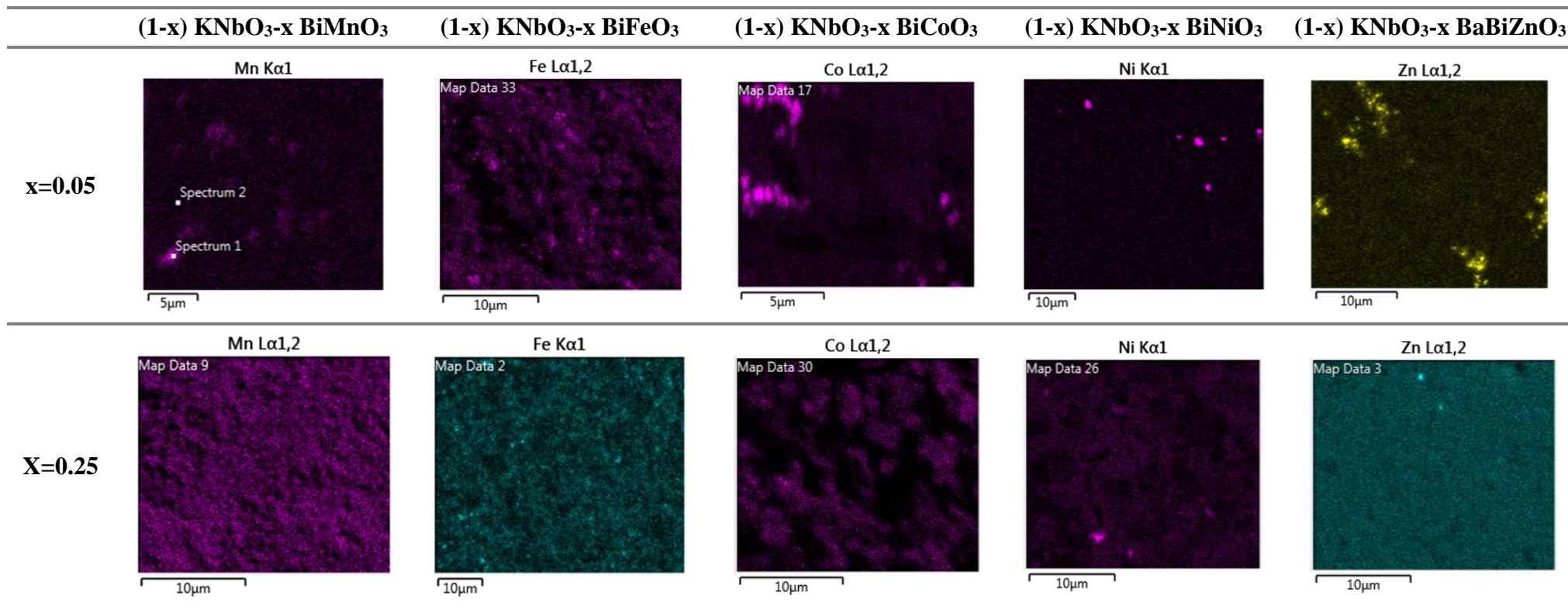


Table 10. 1: EDX mapping for $x=0.05$ and $x=0.25$ of the transition metals for the systems object of this thesis, KNBM, KNBF, KNBC, KNBN and KBBNZ. Low concentrations ($x=0.05$) of metal transition cations, Mn^{+3} , Fe^{+3} , Co^{+3} , Ni^{+3} and Zn^{+2} , show difficulties of being diffuse into the $KNbO_3$, leading the appearance of compositionally inhomogeneous regions, specially, Ni^{+3} and Zn^{+2} : On the other hand, for high concentration of solutes ($x>0.25$) a more homogeneous distribution is observed. Porosity can induce misinterpretation of the EDX mapping, as for example KNBC $x=0.25$. KNBF exhibits better diffusion of Fe^{+3} in comparison with the other systems.

10.2. (1-x) KNbO₃-x BiMeO₃ (Me=Fe, Mn, Co, Ni) (0≤x≤0.25) systems

(1-x) KNbO₃-x BiMeO₃ (Me=Fe, Mn, Co, Ni) (0≤x≤0.25) systems were prepared with the objective of retaining the spontaneous polarisation of the parent compound (KNbO₃) while narrowing the band-gap, through the modification of the electronic configuration of B-site but without generating oxygen vacancies, which would lead to recombination of photocarriers. K⁺¹ is substituted by a higher valence cation, Bi⁺³, whereas Nb⁺⁵ is replaced by a transition metal, Me⁺³, in order to maintain charge neutrality. The structural and chemical characterization of KNBM, KNBC and KNBN systems revealed coexistence of different polymorphs (Amm2 and Pm- $\bar{3}$ m) for some ranges of x. For some compositions, it was difficult to identify secondary phases by XRD. Reflections corresponding to secondary phases were very weak in intensity and sometime overlapped, making very ambiguous the identification of the phases present. Hence the characterisation of each system was accomplished through the combination of analyses of data obtained from different techniques, as shown below.

Firstly, the coexistence of a pseudocubic phase with a residual orthorhombic KN-based phase was inferred from XRD data. In some cases, like the KNBM system, it was easier to identify the residual orthorhombic phase. Secondly, imaging (SEM) and elemental mapping by EDX showed K-rich regions with different morphology than the rest of grains, that were attributed to this orthorhombic phase. Thirdly, the monitoring of Raman modes at 192 cm⁻¹ and 830 cm⁻¹ (more evident in powders) which indicate the polar order in undoped KN. Indeed, the sharp mode at 192 cm⁻¹ suggests the occurrence of spontaneous polarisation, which is fundamental to develop the anomalous photovoltaic effect. Finally, two dielectric anomalies linked to the orthorhombic-to-tetragonal and tetragonal-to-cubic phase transition of ferroelectric KN. The combination of these results demonstrated the presence of the ferroelectric-orthorhombic phase in some compositions. On the other hand, and simultaneously, the pseudocubic phase was monitored by XRD and Raman spectroscopy. The third broad dielectric anomaly around 100°C, visible in KNBM, KNBC and KNBN systems, was speculatively attributed to a weak-relaxor behaviour of a pseudocubic phase that was reported by Luisman et al for similar solid-solution, KNbO₃-BiYbO₃, in 2011. This phase could be hypothetically connected with the phase revealed by Raman spectroscopy with temperature in KNBN x=0.25

ceramic, which presented a polar-to-non-polar phase transition in the same temperature range with the appearance of the dielectric anomaly.

Another similarity among KNBM, KNBC and KNBN systems was the tendency to macroscopically evolve to a pseudocubic symmetry with increasing x (Figure 10. 3), resulting in the absence of long-range polar ordering. On the other hand, microscopically all compositions show distortions from the cubic phase. This phenomenon was previously described in $(1-x)$ PbTiO_3 - $x\text{BiMnO}_3$ solid solutions (Reaney, 2004), while authors were attempting to validate the hypothesis that coupling of the Jahn–Teller effect of BiMnO_3 could enhance the spontaneous strain in the tetragonal structure close to the MPB in the BiMnO_3 – PbTiO_3 solid solution.

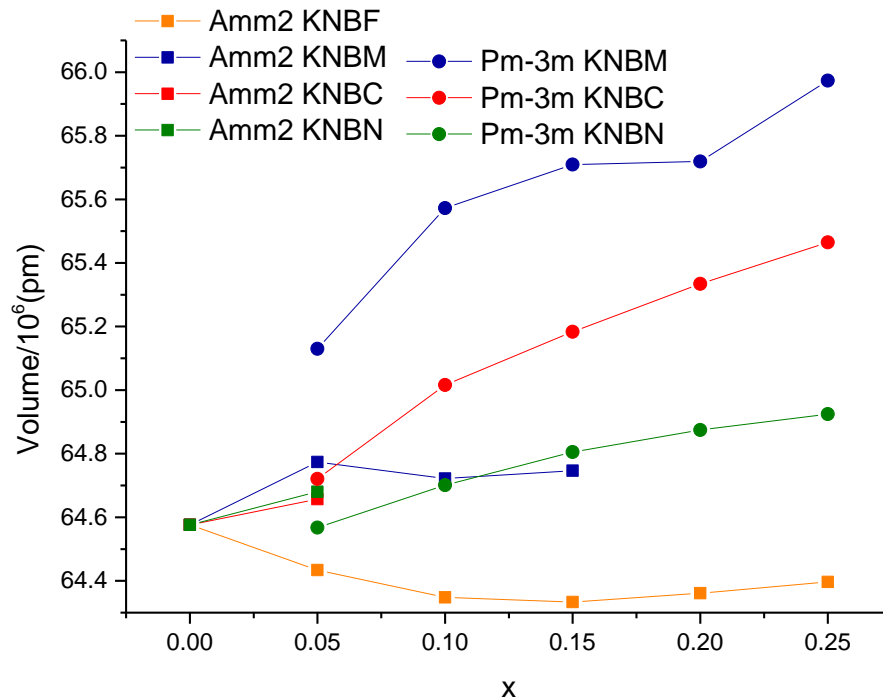


Figure 10. 3: Compositional unit cell volume evolution for KNBM, KNBF, KNBC and KNBN. Squares and circles indicate orthorhombic and cubic phases, respectively.

For KNBC and KNBN systems, the two polymorphs coexist up to $x=0.05$. In KNBM system while the content of orthorhombic phase drops continuously until it disappears, the cubic and orthorhombic phases coexist up to $x=0.15$. In summary, upon doping systems have the tendency of being ascribed to “cubic” lattice, which results from a set of microdomains of small orthorhombic distortion. Furthermore, the unit cell volume increases with increasing x .

In contrast, KNBF system seems to be single phase and maintains the polar phase up to $x=0.25$. Also, the unit cell volume decreases with x . Immediately, a question arises, what makes KNBF different from the other systems?

To address this question, it is required to go back to some basic concepts.

Formation of substitutional solid solutions between two compounds is governed by the following rules, also known as Hume-Rothery rules (Kittel & Hellwarth, 1957): (a) Size difference between the atoms of solute and the parent compound should be less than 15%. (b) The electronegativity difference between the metals should be small. (c) For complete solubility over the entire range of compositions the crystal structures of the solute and the solvent must be the same. (d) Similar valence between the metals.

Table 10. 2 informs about the coordination numbers, ionic radii and electronegativity for K^{+1} , Bi^{+3} , Nb^{+5} , Mn^{+3} , Fe^{+3} , Co^{+3} and Ni^{+3} cations.

A-site			
	Coordination	Ionic radius (Å)	Electronegativity
K⁺¹	XII	1.64	0.82
Bi⁺³	XII	1.33	2.02
B-site			
Nb⁺⁵	VI	0.64	1.60
Mn⁺³	VI	0.645	1.55
Fe⁺³	VI	0.645	1.83
Co⁺³	VI	0.61	1.88
Ni⁺³	VI	0.60	1.91

Table 10. 2: Coordination numbers, ionic radii and electronegativity for the cations involved in KNBM, KNBF, KNBC and KNBN (Shannon, 1976).

B-site cations have very similar ionic radii to Nb^{+5} . In contrast, there is a considerable difference of size in A-site cations and more than double of electronegativity. This aspect could hinder the formation of the solid-solutions. As described in Figure 10. 3, the unit cell volume of the solid solutions increases monotonically with increasing amount of substitution. However, this tendency cannot be explained by the difference in the ionic radii of substitution ions (Table 10. 2). Bi^{+3} (1.33 Å, XII) exhibits a smaller cation size than K^{+} (1.64 Å, XII), while Mn^{+3} , Fe^{+3} , Co^{+3} and Ni^{+3} have ionic radii equivalent to that of Nb^{5+} (0.64 Å, VI). Therefore, the incorporation of a smaller cation (Bi^{+3}) into the K^{+}

site should decrease the dimensions of the unit cell. In contrast, the opposite behaviour is observed. This may be due to the incorporation of Bi^{+5} (0.76 Å, VI) into the B-site position, replacing Nb^{+5} and promoting an increase of the unit cell volume. Other possibility could be the occurrence of the Jahn-Teller effect that produces octahedral distortions which in turn might lead to the increase of the unit cell volume.

Table 10. 3. shows the crystal symmetry and the lattice parameters for KNbO_3 , BiMnO_3 , BiFeO_3 and BiNiO_3 .

		Crystal symmetry	Lattice parameters		Volume ($\text{pm}^3/10^6$)	Ref.
KNbO₃	Amm2	Polar	a= 3.971 Å	$\alpha = \beta = \gamma$ =90°	64.74	[1]
	Orthorhombic		b=5.697 Å c=5.723 Å			
BiMnO₃	C2/c	Non-polar	a=9.464 Å	$\beta = 110.70^\circ$ $\alpha = \gamma = 90^\circ$	61.78	[2]
	Monoclinic		b=5.479 Å c=9.585 Å			
BiFeO₃	R3c	Polar	$a_{rh} = b_{rh} = c_{rh}$ =5.581 Å	$\alpha_{rh} = \beta_{rh}$ = $\gamma_{rh} = 59.3^\circ$	62.30	[3]
	Rhombohedral		$a_h = b_h = 5.58 \text{Å}$ $c_h = 4.720 \text{Å}$			
BiCoO₃	P4mm	Polar	a=3.719 Å	$\alpha = \beta = \gamma$ =90°	65.70	[4]
	Tetragonal		b=3.719 Å c=4.720 Å			
BiNiO₃	P $\bar{1}$	Non-polar	a=5.385 Å	$\alpha = 91.95^\circ$ $\beta = 89.81^\circ$ $\gamma = 91.54^\circ$	58.57	[5]
	Triclinic		b=5.650 Å c=7.708 Å			

Table 10. 3: Crystal symmetry and lattice parameters for KNbO_3 , BiMnO_3 , BiFeO_3 and BiNiO_3 (A.A. Belik, 2012). Refereces: [1] (Shuvaeva, V.A., & Antipin, 1995), [2] (A.A. Belik et al., 2007), [3](Sosnowska, Schäfer, Kockelmann, Andersen, & Troyanchuk, 2002)[4] (Alexei A. Belik et al., 2006) and [5] (Ishiwata et al., 2002).

None of the solute perovskites crystallises with the same symmetry as KNbO_3 . Indeed, BiMO_3 compounds (being M transition materials from the 4th period) that have incomplete d^n orbitals, are predisposed to acquire centrosymmetric crystal structure (A.A.

Belik, 2012). However, BiFeO₃ and BiCoO₃ can be considered as exceptions from this general tendency (Catalan & Scott, 2009; Oka et al., 2010).

Another point to be considered is the transition metals (Me) have multiple potential oxidation states, because unpaired electrons in 3d orbitals are unstable and tend to bond with other chemical species. During traditional sintering, there is no-control of oxidation states, which may result in cations getting reduced (gain electrons) or oxidised (lose electrons) to achieve the stability and react with other species, and not being in the desired state. Sintering at high pressure prevents the appearance of unusual oxidation states. A study on ferroelectric and piezoelectric properties of KNbO₃ doped with small amount of Fe⁺³, La⁺³ and Mn⁺³ (K. K. and I. M. and H. Ohsato, 2003) revealed the non-control of the oxidation states for manganese cations (Mn⁺⁴/Mn⁺³/Mn⁺²), while Fe⁺³ (being a multivalent ion as well), maintained its valence state.

Finally, stoichiometric BiMnO₃, BiNiO₃ and BiCoO₃ can be only synthesized at high pressure. From our point of view, this aspect would be an important contribution to the sintering issue presented in this work.

BiMnO₃ is not stable at atmospheric pressure, and it requires pressures of approximately 6 GPa and temperatures of approximately 1100 K to be fabricated in bulk from a mixture of Bi₂O₃ and Mn₂O₃ (A.A. Belik et al., 2007). Under ambient pressure the reaction of the metal oxides is Bi₂O₃+Mn₂O₃→0.5 Bi₂Mn₄O₉+0.5 Bi₂O₃ (Levin, Robbins, & McMurdie, 1964) and it is therefore an inaccessible material to synthesise at ambient pressure. In the same way, BiCoO₃ and BiNiO₃ ceramics are only stable at high-pressures and thus to be regarded as metastable under ambient conditions (Gilioli & Ehm, 2014; Oka et al., 2010; Yasui et al., 2008). However, BiFeO₃ is again unusual compound among the Bi-based perovskites because it can be prepared under ambient conditions.

As was described, there are several factors that could affect the formation of single-phase solid solutions. However, BiFeO₃ is an exception among the Bi-based compounds because it crystallises in a polar phase and can be prepared by conventional methods at ambient pressure, and this is reflected on KNBF system that displays completely different development from KNBM, KNBC and KNBN systems. Indeed, there are a wide spectrum of applications and studies for solid solution based on BiFeO₃, specially to examine piezoelectric properties in the MPB such as KNa_{0.5}Nb_{0.5}O₃-BiFeO₃ (Sun et al., 2008) or PbTiO₃-BiFeO₃ (Woodward, Reaney, Eitel, & Randall, 2003). In addition, Kowal et al

reported in 2017 that BiFeO₃-BaTiO₃ solid solutions possess both ferroelectric and weak ferromagnetic properties.

In all these systems, KNBM, KNBF, KNBC and KNBN, a continuous band-gap narrowing was achieved as well as the formation of the solid -solutions, that was proved through the validation of Vegard's law. Theoretically, the mechanism which leads to the band-gap narrowing is the local imbalance created by Me⁺³ substitution in B-site of KNbO₃, giving rise to the repulsion between non-bonding 3d orbitals of the Me⁺³ and 2p orbitals of O⁻² and consequently upshifting the VBM. The transition metals were chose following the periodic table order in the fourth period, Fe, Mn, Co and Ni. Ferroelectric characterisation was unfeasible due to the high conductivity of these samples.

10.3. Photovoltaic effect in orthorhombic 0.75 KNbO₃-0.25 BiFeO₃ solid-solution

KNBF x=0.25 ceramic retains the polar order in a wide range of temperatures and its band-gap is narrowed by 1eV in comparison with undoped KN, making this composition interesting for photoinduced phenomena. To measure the photoresponse of this composition, thin films of KNBF x=0.25 were deposited by PLD. The most appropriate temperature, oxygen pressure and substrate to deposit KNBF x=0.25 were 600°C, 0.15 mBar and STO, respectively. Undesirable polycrystalline thin films were obtained, therefore further optimisation is still required before measuring photoresponse. However, we were able to measure photoresponse in a cell filled by KNBF x=0.25 paste. The measured V_{oc} and J_{sc} are about 0.16 V and 0.24 μA/cm², respectively and a P_{max} of 0.016 μW and FF of ~41%. Table 5.9. (Chapter 5) informs about V_{oc} and J_{sc} values found in the literature for ferroelectric films. It is important to note, our J_{sc} is higher than 0.1 μA/cm² reported for KN-BNN thick film at RT by Grinberg et al in 2013. Moreover, our J_{sc} is also greater than 40 nA/cm² obtained at 77 K for the same composition.

10.4. Experimental validation and non-reproducibility of band-gap narrowing in solid solutions based on KNbO₃ from literature

The first part of this section addresses the experimental validation of ferroelectricity in KNbO₃-based material proposed by a theoretical study that predicted low band-gaps upon doping. This part exposes both the helpfulness and the limitation of this kind of studies.

In 2014, Wang et al proposed six KNbO₃- based solid solutions doped with Zn²⁺, together with charge compensation by different combinations of higher-valence A-site cations (free vacancies). Their first principles calculations predicted a band gap of 2.92 eV for 0.75 KNbO₃-0.25 (Ba_{0.5}Bi_{0.5}) (Zn_{0.5}Nb_{0.5}) O₃ and a spontaneous polarisation of ~38 μC/cm². Our experimental results validate the optical band-gap value, but not the ferroelectric behaviour. Structural, dielectric, ferroelectric, piezoelectric and optical characterisation and discussion of (x-1) KNbO₃-x (Ba_{0.5}Bi_{0.5}) (Zn_{0.5}Nb_{0.5}) O₃ (KBBNZ) system are provided in detail in Chapter 4.

Upon doping, the crystal structure of KBBNZ system evolves from orthorhombic (x=0) to pseudocubic (x=0.25) symmetry, continuing the same trend seen in KNBM, KNBC, and KNBN systems. Moreover, the coexistence of these two polymorphs is verified for x=0.10 and x=0.15. SEM and EDX analysis revealed chemical inhomogeneities mainly associated with Zn. The overall chemical homogeneity is enhanced for higher values of solutes. Compositional evolution is accompanied by a gradual loss of the FE properties. The typical butterfly loop characteristic of FE became a parabola and then no field induced strain is observed.

In summary, it is not possible to experimentally validate the results predicted by first-principles, though this paper was fundamental in our research. The rest of the systems which are the object of this thesis were inspired on the band-gap narrowing strategy, described in this study (F Wang et al., 2014).

Chapter 11 is focused on the controversy found in the literature about the compound K_{0.9}Ba_{0.1}Nb_{0.95}Ni_{0.05}O₃ (KN-BNN) (motivated and explained in detail Chapter 1 and Chapter 10). We were not able to reproduce the results reported by the Nature paper (Grinberg et al., 2013).

Nevertheless, we demonstrated that KNbO_3 presents difficulties in incorporating multiple solutes by conventional sintering, especially if it is a small amount. XRD is not sufficient evidence for the formation of homogeneous single-phase solid solutions. Indeed, SEM imaging combined with EDX analysis for KN-BNN revealed: undoped KN regions, NiO particles and different concentration of solutes.

Ferroelectric characterisation was not performed because of the leaky comportment of the KN-BNN sample, in contrast to P-E loops reported at RT in the literature by Grinberg and Bai. Similar band-gap values to the parent KNbO_3 were obtained. However, some absorption bands are visible at 1 eV, 1.56 eV, 1.73 eV and 2.90 eV in KN-BNN spectra, which were also observed in $(1-x) \text{KNbO}_3-x \text{BiNiO}_3$ system (Chapter 8). These protuberance bands could be related to d-d transitions by Ni^{+2} ions within the bulk or from hybridized Ni 3d and O 2p to Nb 4d states transitions from the NiO particles. The misinterpretation of these absorption regions could be the origin of the discrepancy of the band-gap values for KN-BNN in the literature. Furthermore, we realised that depending on the scale with which the $(F(R) \cdot hv)^2$ curve is plotted, the band-gap values from the intercept of the x-axis and the tangent line of the curve may be different. Indeed, it is demonstrated that when zooming in the bottom part of the Tauc plot, we obtained low band-gaps for KN-BNN. These suppositions can be extrapolated to $\text{K}_{0.49}\text{Na}_{0.49}\text{Ba}_{0.02}\text{Nb}_{0.99}\text{Ni}_{0.01}\text{O}_3$ (KNN-BNN) as well.

The band-gap narrowing in ferroelectric KN-BNN is supported by theoretical calculations (Fengsong Wang & Rappe, 2015). However, as also discussed for KBBNZ, sometimes theoretical studies cannot be experimentally proven. We are not saying that the theory is wrong but conventional synthesis and sintering processing is not able to prepare this compound and hence impossible to experimentally reproduce.

10.4. Band-gap narrowing

Tauc plots for direct and indirect band-gaps of KN and $0.75 \text{KNbO}_3-0.25 \text{BiMeO}_3$ (Me= Mn, Fe; Co and Ni) systems are shown in Figure 10. 4-5. The most homogeneous samples were obtained for $x=0.25$, as was explained in the first section of this chapter. Also, the solar spectrum is illustrated, and the IR, VIS and UV regions are schematically indicated.

Even if the sun emits in all the energetic range, the maximum energy is allocated in the visible range.

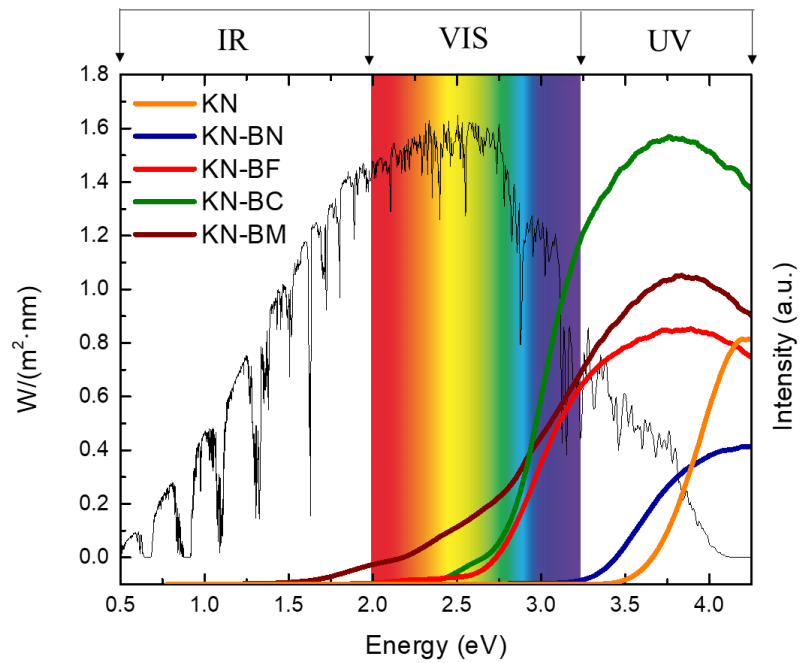


Figure 10. 4: $[F(R) \cdot hv]^2$ against photon energy for KN and $0.75 \text{ KNbO}_3\text{-}0.25 \text{ BiMeO}_3$ (Me= Mn, Fe; Co and Ni) systems.

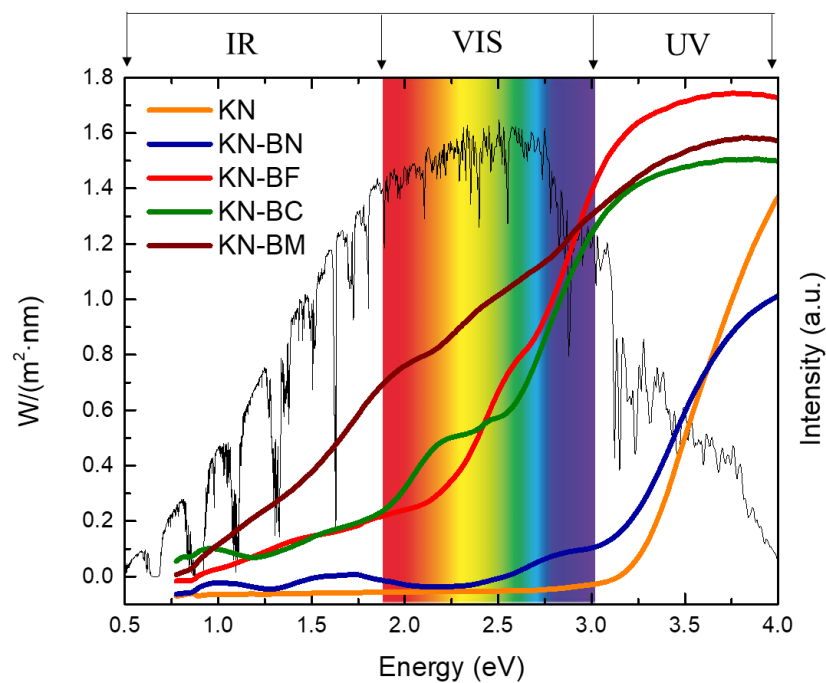


Figure 10. 5: $[F(R) \cdot hv]^{1/2}$ against photon energy for KN and $0.75 \text{ KNbO}_3\text{-}0.25 \text{ BiMeO}_3$ (Me= Mn, Fe; Co and Ni) systems.

As mentioned in Chapter 2, Tauc plots cannot determine conclusively if a band structure is direct or indirect, therefore, both band-gap values are extracted. Direct and indirect band-gaps follow the same trend, KNBM (2.4 eV) < KNBC (2.6 eV) < KNBF (2.8 eV) < KNBN (3.3 eV) < KN (3.6 eV) and KNBM (1.3 eV) < KNBC (2.1 eV) < KNBF (2.2 eV) < KNBN (2.87 eV) < KN (3.2 eV), respectively.

As shown in Figure 10. 6. a linear relationship is found between the optical band gaps (direct and indirect) and the pseudocubic unit cell volume, leaving aside the KNBF compound that presents orthorhombic symmetry.

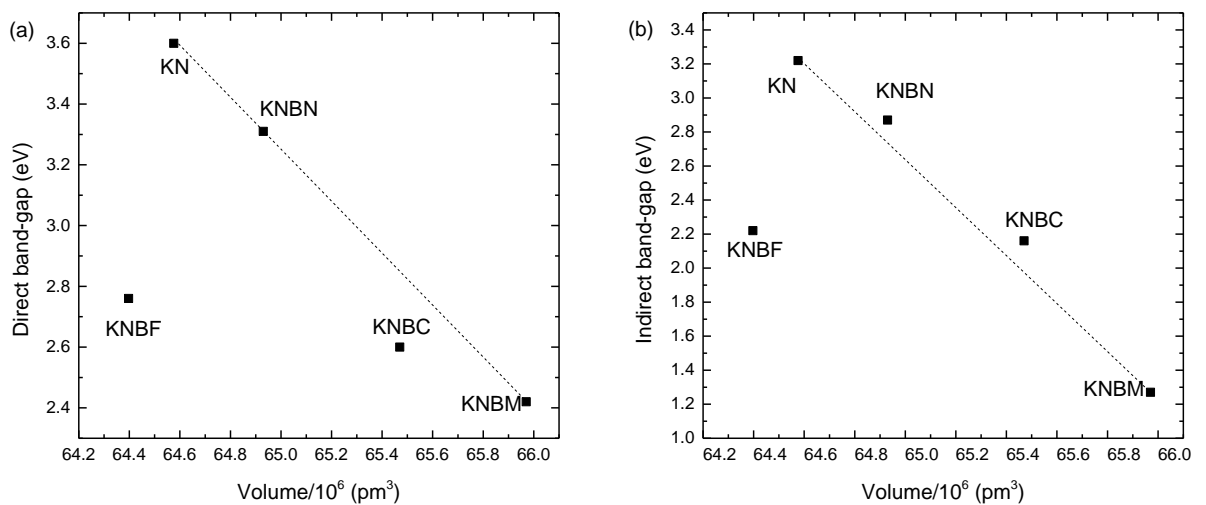


Figure 10. 6: Direct (a) and indirect (b) band gap energies as a function of pseudocubic unit cell volume shows a linear dependency.

The band gap decreases with increasing lattice volume. On the other hand, the lattice volume increase with B-site ionic radius, in the order Mn^{+3} , Co^{+3} and Ni^{+3} . Moreover, electronegativity also decreases with ionic radii and therefore increases with increasing band-gap energy. This trend with lattice volume for each solid is comparable to that reported by Lee et al, which described a set of perovskites with A-site alkaline earth whose optical band-gap varied linearly with lattice volume and the Goldschmidt tolerance factor. Also, it is in agreement with the classical work for covalent semiconductors, where a linear increase in band gap is noticed for smaller bond lengths (Phillips, 1973).

The relationship between optical band-gap and Goldschmidt tolerance factor is also examined in Figure 10. 7. The Goldsmith tolerance factor for a solid solution was calculated using Equation 10.1.

$$t_{SS} = \frac{(0.75 \cdot r_K) + (0.25 \cdot r_{Bi}) + r_O}{\sqrt{2}((0.75 \cdot r_{Nb}) + (0.25 \cdot r_{Me}) + r_O)} \quad \text{Eq.10.1}$$

where r_K , r_{Bi} , r_{Nb} , r_{Me} and r_O denote the ionic radii for K^{+1} , Bi^{+3} , Nb^{+5} , Me^{+3} and O^{2-} , respectively (Table 10. 2).

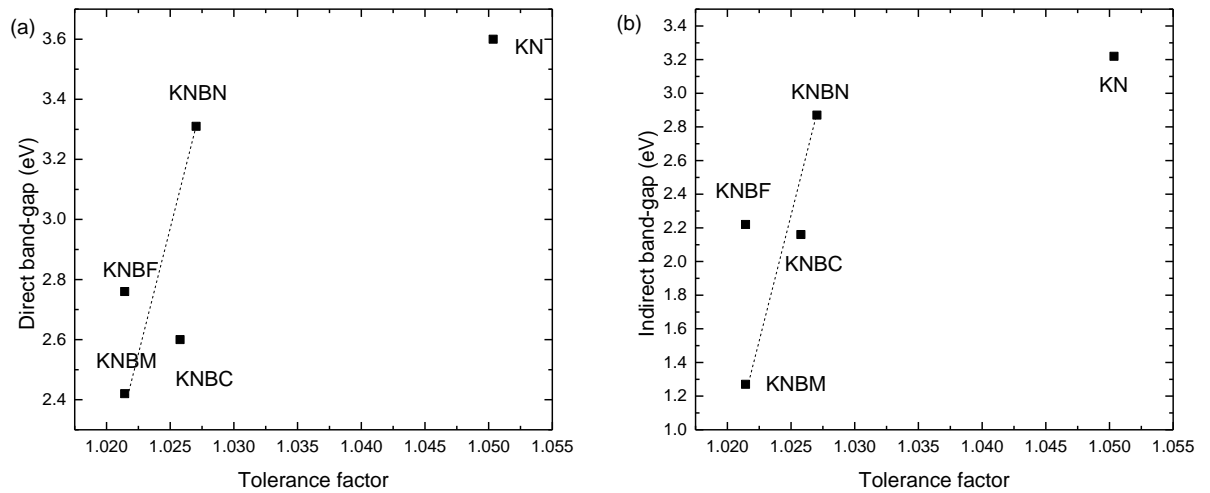


Figure 10. 7: Direct (a) and indirect (b) band gap energies as a function of tolerance factor.

All the systems, KNBM, KNBF, KNBC and KNBN have similar tolerance factor which considerably differs from KN. In general, solid solutions with high tolerance factor show broad band-gaps. If we draw a line from KNBN to KNBM, we can observe the other two values for KNBF and KNBC, are close to this line. However, it is not possible to determine a linear dependence between the tolerance factor and the band-gaps values.

10.5. References

- Bai, Y., Siponkoski, T., Peräntie, J., Jantunen, H., & Juuti, J. (2017). Ferroelectric, pyroelectric, and piezoelectric properties of a photovoltaic perovskite oxide. *Applied Physics Letters*, *110*(6). <https://doi.org/10.1063/1.4974735>
- Belik, A. A. (2012). Polar and nonpolar phases of BiMO₃: A review. *Journal of Solid State Chemistry*, *195*. <https://doi.org/10.1016/j.jssc.2012.01.025>
- Belik, A. A., Iikubo, S., Kodama, K., Igawa, N., Shamoto, S. I., Niitaka, S., ... Takayama-Muromachi, E. (2006). Neutron powder diffraction study on the crystal and magnetic

- structures of BiCoO₃. *Chemistry of Materials*, 18(3), 798–803. <https://doi.org/10.1021/cm052334z>
- Belik, A. A., Iikubo, S., Yokosawa, T., Kodama, K., Igawa, N., Shamoto, S., Takayama-Muromachi, E. (2007). Origin of the monoclinic-to-monoclinic phase transition and evidence for the centrosymmetric crystal structure of BiMnO₃. *Journal of the American Chemical Society*, 129(4). <https://doi.org/10.1021/ja0664032>
- Birol, H., Damjanovic, D., & Setter, N. (2005). Preparation and characterization of KNbO₃ ceramics. *Journal of the American Ceramic Society*, 88(7). <https://doi.org/10.1111/j.1551-2916.2005.00347.x>
- Catalan, G., & Scott, J. F. (2009). Physics and applications of bismuth ferrite. *Advanced Materials*, 21(24). <https://doi.org/10.1002/adma.200802849>
- Chi, Z. H., Yang, H., Feng, S. M., Li, F. Y., Yu, R. C., & Jin, C. Q. (2007). Room-temperature ferroelectric polarization in multiferroic BiMnO₃. *Journal of Magnetism and Magnetic Materials*, 310(2 SUPPL. P). <https://doi.org/10.1016/j.jmmm.2006.10.335>
- Gilioli, E., & Ehm, L. (2014). High pressure and multiferroics materials: a happy marriage. *IUCrJ*, 1(Pt 6), 590–603. <https://doi.org/10.1107/S2052252514020569>
- Grinberg, I., West, D. V., Torres, M., Gou, G., Stein, D. M., Wu, L., ... Rappe, A. M. (2013). Perovskite oxides for visible-light-absorbing ferroelectric and photovoltaic materials. *Nature*, 503(7477), 509. <https://doi.org/10.1038/nature12622>
- Hawley, C. J., Wu, L., Xiao, G., Grinberg, I., Rappe, A. M., Davies, P. K., & Spanier, J. E. (2017). Structural and ferroelectric phase evolution in [KNbO₃]_{1-x}[BaNi_{1/2}Nb_{1/2}O_{3-δ}]_x (x=0,0.1). *Physical Review B*, 96(5), 1–8. <https://doi.org/10.1103/PhysRevB.96.054117>
- Ishiwata, S., Azuma, M., Takano, M., Nishibori, E., Takata, M., Sakata, M., & Kato, K. (2002). High pressure synthesis, crystal structure and physical properties of a new Ni (ii) perovskite BiNiO₃. *Journal of Materials Chemistry*, 12(12), 3733–3737. <https://doi.org/10.1039/b206022a>
- Jiang, Q., Nan, C., Wang, Y., Liu, Y., & Shen, Z. (2008). Synthesis and properties of multiferroic BiFeO₃ ceramics. *Journal of Electroceramics*, 21(1), 690–693.

<https://doi.org/10.1007/s10832-007-9265-5>

- Kakimoto, K., Masuda, I., & Ohsato, H. (2004). Solid-Solution Structure and Piezoelectric Property of KNbO_3 Ceramics Doped with Small Amounts of Elements. *Japanese Journal of Applied Physics*, 43(9S), 6706. <http://stacks.iop.org/1347-4065/43/i=9S/a=6706>
- Kittel, C., & Hellwarth, R. W. (1957). Introduction to Solid State Physics. *Physics Today*, 10(6), 43. <https://doi.org/10.1063/1.3060399>
- Kowal, K., Guzdek, P., Kowalczyk, M., & Jartych, E. (2017). Compositional dependence of hyperfine interactions and magnetoelectric coupling in $(\text{BiFeO}_3)_x\text{-(BaTiO}_3)_{1-x}$ solid solutions. *Nukleonika*, 62(2), 117–122. <https://doi.org/10.1515/nuka-2017-0016>
- Lee, S., Woodford, W. H., & Randall, C. A. (2008). Crystal and defect chemistry influences on band gap trends in alkaline earth perovskites. *Applied Physics Letters*, 92(20). <https://doi.org/10.1063/1.2936091>
- Levin, E. M., Robbins, C. R., & McMurdie, H. F. (1964). *Phase Diagrams for Ceramists* (American C, Vol. Vol. 1). Columbus.
- Luisman, L., Feteira, A., & Reichmann, K. (2011). Weak- relaxor behaviour in Bi/ Yb-doped KNbO_3 ceramics. *Applied Physics Letters*, 99(19). <https://doi.org/10.1063/1.3660255>
- Masó, N., Beltrán, H., Cordoncillo, E., Flores, A. A., Escribano, P., Sinclair, D. C., & West, A. R. (2006). Synthesis and electrical properties of Nb-doped BaTiO_3 . *Journal Materials Chemistry*, 16(30), 3114–3119. <https://doi.org/10.1039/B601251E>
- Nazeri-Eshghi, A., Kuang, A. X., & Mackenzie, J. D. (1990). Preparation and properties of KNbO_3 via the sol-gel method. *Journal of Materials Science*, 25(7), 3333–3337. <https://doi.org/10.1007/BF00587695>
- Ohsato, K. K. and I. M. and H. (2003). Ferroelectric and Piezoelectric Properties of KNbO_3 Ceramics Containing Small Amounts of LaFeO_3 . *Japanese Journal of Applied Physics*, 42(9S), 6102. Retrieved from <http://stacks.iop.org/1347-4065/42/i=9S/a=6102>
- Ohsato, K. K. and T. I. and H. (2008). Synthesis of KNbO_3 Piezoelectric Ceramics Using

- Citrate Precursors. *Japanese Journal of Applied Physics*, 47(9S), 7669. Retrieved from <http://stacks.iop.org/1347-4065/47/i=9S/a=7669>
- Oka, K., Azuma, M., Chen, W., Yusa, H., Belik, A. A., Takayama-Muromachi, E., ... Shimakawa, Y. (2010). Pressure-Induced Spin-State Transition in BiCoO₃. *Journal of the American Chemical Society*, 132(27), 9438–9443. <https://doi.org/10.1021/ja102987d>
- Pecchi, G., Cabrera, B., Delgado, E. J., García, X., & Jimenez, R. (2013). Activity of KNbO₃ as catalyst for soot combustion: Effect of the preparation method. *Applied Catalysis A: General*, 453(Supplement C), 341–348. <https://doi.org/https://doi.org/10.1016/j.apcata.2012.12.030>
- Phillips, J. C. (1973). *Bonds and Bands in Semiconductors* (Academic). New York.
- Reaney, D. I. W. and I. M. (2004). A structural study of ceramics in the (BiMnO₃)_x – (PbTiO₃)_{1-x} solid solution series. *Journal of Physics: Condensed Matter*, 16(49), 8823. Retrieved from <http://stacks.iop.org/0953-8984/16/i=49/a=002>
- Shannon, R. D. (1976). Revised Effective Ionic Radii and Systematic Studies of Interatomic Distances in Halides and Chalcogenides Central Research and Development Department, Experimental Station, E. L. Du Pont de Nemours The effective ionic radii of Shannon & Prewitt [*Acta Crystallogr. Sec., A*, 32, 751.
- Shuvaeva, V.A., & Antipin, M. Y. (1995). Structural disorder in KNbO₃ crystal from X-ray diffraction and EXAFS spectroscopy. *Crystallography Reports*, 40(3), 466–471.
- Sosnowska, I., Schäfer, W., Kockelmann, W., Andersen, K. H., & Troyanchuk, I. O. (2002). Crystal structure and spiral magnetic ordering of BiFeO₃ doped with manganese. *Applied Physics A*, 74(1), s1040–s1042. <https://doi.org/10.1007/s003390201604>
- Sun, X., Chen, J., Yu, R., Xing, X., Qiao, L., & Liu, G. (2008). BiFeO₃-doped (Na_{0.5}K_{0.5})NbO₃ lead-free piezoelectric ceramics. *Science and Technology of Advanced Materials*, 9(2), 25004. <https://doi.org/10.1088/1468-6996/9/2/025004>
- Wang, F., Grinberg, I., & Rappe, A. M. (2014). Semiconducting ferroelectric photovoltaics through Zn²⁺ doping into KNbO₃ and polarization rotation. *Physical Review B - Condensed Matter and Materials Physics*, 89(23).

- Wang, F., & Rappe, A. M. (2015). First-principles calculation of the bulk photovoltaic effect in KNbO_3 and $(\text{K,Ba})(\text{Ni,Nb})\text{O}_{3-d}$. *Physical Review B*, *91*(16), 165124. <https://doi.org/10.1103/PhysRevB.91.165124>
- Woo, H., Tyson, T. A., Croft, M., Cheong, S.-W., & Woicik, J. C. (2001). Correlations between the magnetic and structural properties of Ca-doped BiMnO_3 . *Phys. Rev. B*, *63*(13), 134412. <https://doi.org/10.1103/PhysRevB.63.134412>
- Woodward, D. I., Reaney, I. M., Eitel, R. E., & Randall, C. A. (2003). Crystal and domain structure of the BiFeO_3 – PbTiO_3 solid solution. *Journal of Applied Physics*, *94*(5), 3313–3318. <https://doi.org/10.1063/1.1595726>
- Yasui, S., Naganuma, H., Okamura, S., Nishida, K., Yamamoto, T., Iijima, T., ... Funakubo, H. (2008). Crystal Structure and Electrical Properties of {100}-Oriented Epitaxial BiCoO_3 – BiFeO_3 Films Grown by Metalorganic Chemical Vapor Deposition. *Japanese Journal of Applied Physics*, *47*(9S), 7582. Retrieved from <http://stacks.iop.org/1347-4065/47/i=9S/a=7582>

Chapter 11

Conclusions, contributions to the field and future work

12.1. Conclusions

12.2. Future work

12.3. Contributions to the field

12.4. References

11. Conclusions, contributions to the field and future work

11.1. Conclusions

Ferroelectric KNbO_3 (KN) ceramic is the central compound of this thesis. An intensive study on processing, electrical and optical characterization of KN ceramic was conducted. Following results were obtained:

- High density and pure KN ceramics were prepared by solid state reaction. It was demonstrated purity and stability are intimately related with the stoichiometry of KN. Double calcination of powders compacted at 850°C for 4 hours and the control of the sintering environment through atmospheric powder and double crucible, enabled to inhibit the K losses during the ceramic processing, keeping KN stoichiometric.
- Stoichiometric KN, K-deficient and K-excess compounds were also prepared in order to evaluate eventual K losses. XRD and Raman results determined the orthorhombic phase (Amm2 space group). Slight deviations from the nominal stoichiometry induces changes in the purity, crystallisation, microstructure, stability, density and sintering temperature of the samples.
- Electrical characterisation of non-stoichiometric compounds was unfeasible due to their poor densification. In addition, samples should be dried at 200°C for 10 min, because KN ceramics left in air absorb moisture from the environment, making the samples more conductive.
- KN ceramics showed two clear dielectric anomalies at $\sim 206^\circ\text{C}$ and $\sim 398^\circ\text{C}$, which can be attributed to the orthorhombic-to-tetragonal and to the tetragonal-

to-cubic transitions, respectively. Spontaneous polarisation of $\sim 23 \mu\text{C}/\text{cm}^2$ and maximum strain of 0.1% is obtained under 50 kV/cm at 160°C.

- The narrowest band-gap (3.15 eV) corresponds to K-excess compound, which supposedly has the largest concentration of oxygen vacancies. Direct and indirect band-gaps for stoichiometric KN are estimated 3.64 eV and 3.23 eV, respectively.

The following binary systems based on KN, $(1-x) \text{KNbO}_3-x \text{Ba}_{0.5}\text{Bi}_{0.5}\text{Nb}_{0.5}\text{Zn}_{0.5}\text{O}_3$ (KBBNZ), $(1-x) \text{KNbO}_3-x \text{BiFeO}_3$ (KNBF), $(1-x) \text{KNbO}_3-x \text{BiMnO}_3$ (KNBF), $(1-x) \text{KNbO}_3-x \text{BiCoO}_3$ (KNBC), $(1-x) \text{KNbO}_3-x \text{BiNiO}_3$ (KNBN), $0.90 \text{KNbO}_3-0.10 \text{BaNb}_{0.5}\text{Ni}_{0.5}\text{O}_3$ (KN-BNN), $\text{KNa}_{0.5}\text{Nb}_{0.5}\text{O}_3$ (KNN) and $0.98 \text{KNa}_{0.5}\text{Nb}_{0.5}\text{O}_3-0.10 \text{BaNb}_{0.5}\text{Ni}_{0.5}\text{O}_3$ (KNN-BNN), being $x=0, 0.05, 0.10, 0.15, 0.20$ and 0.25 , were prepared by solid state reaction, following the same route as KN. However, some problems appeared during the ceramic processing:

- After the synthesis, most of the compositions present some orthorhombic KNbO_3 -based phase due to incomplete diffusion of the species.
- The solubility of low concentration of solutes ($x \leq 0.15$) into the KNbO_3 lattice was insufficient during sintering, generating compositionally inhomogeneous regions.
- Solid-state reaction may not be the most adequate method to prepare these solid solutions.

This thesis underpins the structural, vibrational, microstructural, elemental, electrical (if feasible) and optical characterisation of the systems listed above. The main conclusions are summarised below:

- Upon doping, KBBNZ system evolves from orthorhombic to cubic symmetry, which is accompanied by a piezoelectric-to-electrostrictive crossover in the compositional range, $0 \leq x \leq 0.25$. A progressive decrease of FE and piezoelectric properties is observed. Indeed, KBBNZ $x=0.25$ is non-ferroelectric in contradiction with a theoretical study (Wang, Grinberg, & Rappe, 2014). Electrostrictive coefficient for $x=0.15$ is $0.037 \text{ m}^4\text{C}^{-2}$ and for $x=0.20$ Q is $0.035 \text{ m}^4\text{C}^{-2}$.
- The band gap of KBBNZ ceramics narrows slightly from 3.22 eV for $x=0$ to 2.89 eV for $x=0.25$, in agreement with first-principles calculations (Wang et al., 2014).

Common results were obtained for KNBM, KNBC and KNBN systems:

- XRD data suggests these systems evolve from an orthorhombic phase ($x=0$) to cubic symmetry with an increase of x . There is a solubility limit for orthorhombic KN phase. The cubic solid-solution is confirmed by the validation of Vegard's law.
- Cubic and orthorhombic phases coexist at intermediary values of x , more specifically, up to $x=0.15$ for the KNBM system and up to $x=0.10$ for the KNBC and KNBN systems.
- The polar phase (Amm2) was monitored by: (i) the occurrence of the Raman modes at 192 cm^{-1} and 830 cm^{-1} . (ii) SEM imaging combined with elemental EDX analyses, which reveals the presence of KN-rich regions. (iii) The appearance of the two dielectric anomalies associated with KN.
- Globally, $x=0.20$ and $x=0.25$ compositions can be ascribed as cubic phase ($Pm\bar{3}m$), but the existence of Raman modes demonstrates that locally they are not purely cubic.
- Systematic band-gap narrowing was observed with increasing x . A linear dependence is found between the optical band gaps (direct and indirect) and the pseudocubic unit cell volumes.

However, the KNBF system was an exception in all aspects:

- KNBF system retained polar order up to $x=0.25$ in a wide range of temperatures and continuously narrowed its band-gap with x .
- Polar ordering and a lower band-gap. $\sim 1\text{eV}$ in comparison with undoped KN, makes KNBF $x=0.25$ interesting for photoinduced phenomena. The measured V_{oc} and J_{sc} are about 0.16 V and $0.24\text{ }\mu\text{A}/\text{cm}^2$, respectively and a P_{max} of $0.016\text{ }\mu\text{W}$ and FF of $\sim 41\%$.

Finally, KN-BNN and KNN-BNN showed:

- Impossibility of obtaining chemically homogenised samples by conventional ceramic processing, as revealed by XRD, SEM and EDX.
- Band-gaps of 3.37 eV and 3.34 eV were estimated, respectively.
- Controversy of band-gap values in the literature are attributed to: (i) conventional processing route may lead to the appearance of chemical inhomogeneities which modify the physical properties. (ii) ambiguity on interpretation of Tauc plots.

11.2. Contributions to the field

- (1) First comprehensive study on processing-structure-property relationships in $\text{KNbO}_3\text{-BiMeO}_3$, where Me is Fe, Mn, Co and Ni. Demonstration for first time of a photovoltaic effect in the KN-BF system.
- (2) Demonstration for first time of a piezoelectric-to-electrostrictive crossover on KBBNZ system and corroboration of first principle calculations of the band-gap (Wang et al., 2014).
- (3) Contribute with a hypothesis why there are controversies in the band-gaps reported for KN-BNN (Grinberg et al., 2013) and possibly in KNN-BNN (Bai, Tofel, Palosaari, Jantunen, & Juuti, 2017).

11.3. Future work

The research presented in this thesis seems to have opened new horizons to explore. There are several lines of research arising from this work which should be pursued.

- (1) Sample synthesis using alternative routes to improve homogeneity.
- (2) X-ray synchrotron study to obtain better resolution and address the problems related with Rietveld refinement.
- (3) Raman spectroscopy with temperature for KNBC $x=0.15$.
- (4) Low- temperature P-E loops to avoid the conductivity issues.
- (5) Fabrication and characterisation of solar cells, using the most promising materials.
- (6) Temperature dependence of the band-gap to investigate the nature of the band-gaps. Furthermore, development of some simulations by first principles calculations for better understanding.
- (7) All systems should be investigated in all compositional range from KN to BiMeO_3 .
- (8) Control of the oxidation states.

11.4. References

Bai, Y., Tofel, P., Palosaari, J., Jantunen, H., & Juuti, J. (2017). A Game Changer : A Multifunctional Perovskite Exhibiting Giant Ferroelectricity and Narrow Bandgap with Potential Application in a Truly Monolithic Multienergy Harvester or Sensor, *1700767*, 1–7. <https://doi.org/10.1002/adma.201700767>

Grinberg, I., West, D. V., Torres, M., Gou, G., Stein, D. M., Wu, L., ... Rappe, A. M. (2013). Perovskite oxides for visible-light-absorbing ferroelectric and photovoltaic materials. *Nature*, *503*(7477). <https://doi.org/10.1038/nature12622>

Wang, F., Grinberg, I., & Rappe, A. M. (2014). Semiconducting ferroelectric photovoltaics through Zn^{2+} doping into $KNbO_3$ and polarization rotation. *Physical Review B - Condensed Matter and Materials Physics*, *89*(23).

[word count: 53415 (excluding appendices and references)]